Project No. 12-3730

Probabilistic Multi-Hazard Assessment of Dry Cask Structures

Fuel Cycle Research and Development

Bora Bencturk
University of Houston

In collaboration with:
Rice University
University of Illinois at Urbana-Champaign

JC de la Garza, Federal POC
Ken Sorenson, Technical POC

NEUP Nuclear Energy University Programs
U.S. Department of Energy

PROBABILISTIC MULTI-HAZARD ASSESSMENT OF DRY CASK STRUCTURES

STANDARD RESEARCH
CONTRACT NO. 00128931

Project Period: Oct. 1, 2012 – Sept. 30, 2016

Bora Gencturk and Kaspar Willam
University of Houston

Jamie Padgett
Rice University

Rizwan Uddin
University of Illinois at Urbana-Champaign

FINAL REPORT

LIST OF ACRONYMS

ASR .....Alkali silica reaction / reactivity
ASTM .....American Society for Testing and Materials
CG .....Center of gravity
CSCM .....Continuous surface cap model
C-S-H.....Calcium silicate hydrates
CV .....Cross validation
EDP .....Engineering demand parameters
EDS .....Energy-dispersive X-ray spectroscopy
FE.....Finite element
FFT .....Fast Fourier transform
IM .....Intensity measure
ISFSI .....Independent spent fuel storage installations
MAT.....Management aptitude test
MSB .....Multi-assembly sealed basket
NCHRP .....National cooperative highway research program
NIST .....National Institute of Standards and Technology
NPP.....Nuclear power plants
NRC.....U.S. Nuclear Regulatory Commission
NT .....Nordtest
OD .....Oven dry
PGA.....Peak ground accelerations
PSD .....Particle size distribution
PSDM.....Probabilistic seismic demand models
RCPT .....Rapid chloride penetration test
RH.....Relative humidity
SCC .....Self-consolidating concrete
SEM .....Scanning electron microscopy
SSD .....Saturated surface dry
T.....Temperature
THCM.....Thermo-hygro-chemo-mechanical
TRIGA.....Training, research, isotopes, and general atomics
TSC.....Transportable storage canister
UH .....University of Houston
UHRS .....Uniform hazard response spectra
UIUC .....University of Illinois at Urbana Champaign
UPV.....Ultrasonic pulse velocity
USGS.....U.S. Geological Survey
VCC .....Ventilated concrete cask

TABLE OF CONTENTS

SUMMARY 7
PROJECT OBJECTIVES 7
KEY RESEARCH FINDINGS 7
PROJECT PRODUCTS 8
Thesis 8
Journal Papers and Reports 9
Presentations or Conference Papers 9
CHAPTER 1 12
1.1. PROBLEM STATEMENT 12
1.2. SCOPE 12
1.3. REPORT ORGANIZATION 13
CHAPTER 2 14
2.1. INTRODUCTION 14
2.2. REVIEW OF DRY-STORAGE SYSTEMS 15
2.2.1. Dry Cask Types 15
2.2.2. Examples of Dry Cask Storage 16
2.3. SELECTION OF A CASK DESIGN FOR DETAILED INVESTIGATION 21
2.3.1. Cask Geometry and Similitude 21
2.3.2. Fabrication of the Scaled Cask Models 23
2.4. CONCLUSIONS 25
2.5. REFERENCES 26
CHAPTER 3 27
3.1. INTRODUCTION 27
3.1.1. Alkali-Silica Reactivity in Concrete 27
3.1.2. Corrosion in Reinforced Concrete 28
3.1.3. Accelerated Aging 30
3.2. EXPERIMENTAL PROGRAM 32
3.2.1. Design of Concrete Mixtures 32
3.2.2. Design of Concrete Mixtures 38
3.2.3. Testing Plan for First Phase of Specimens 40
3.2.4. Testing Plan for Second Phase of Specimens 42

3.2.5. Testing Plan for Already Aged Specimens Obtained from a Research Nuclear Reactor 43
3.3. RESULTS 45
3.3.1. Fresh Properties of Concrete 45
3.3.2. Physical Properties of Hardened Concrete 47
3.3.3. Mechanical Properties of Concrete 55
3.3.4. Non-Destructive Testing 63
3.3.5. Other Measurements 80
3.4. CONCLUSIONS 80
3.5. REFERENCES 81
CHAPTER 4 90
4.1. INTRODUCTION 90
4.2. THERMAL LOADING OF DRY CASKS 90
4.3. ESTIMATION OF TEMPERATURE DISTRIBUTION IN DRY CASKS 91
4.3.1. Evaluation of Temperature Distribution in Concrete 91
4.3.2. Consideration of Volumetric Heat Source in the Concrete Layer. 94
4.4. COMPUTATIONAL FLUID DYNAMICS OF DRY CASKS 98
4.4.1. Mesh Generation 98
4.4.2. Boundary Conditions 99
4.4.3. Grid Independence Studies 99
4.4.4. CFD Results for Dry Cask under Normal, Summer and Winter Conditions 110
4.5. CONCLUSIONS 129
4.6. REFERENCES 130
CHAPTER 5 131
5.1. INTRODUCTION 131
5.2. MONITORING OF AGING 131
5.2.1. Schmidt Hammer Test Results 131
5.2.2. Visual Inspection 132
5.2.3. Ultrasonic Pulse Velocity Test Results 136
5.2.4. Half-Cell Potential Test Results 137
5.3. EXPERIMENTAL PROGRAM FOR IMPACT TESTING 138
5.3.1. Test Setup 138
5.3.2. Sensors and Instrumentation 139
5.4. IMPACT TEST RESULTS 143

5.4.1. End-Drop Tests 143
5.4.2. Side-Drop Tests 149
5.4.3. Analytical Results and Comparisons with Experimental Data 159
5.5. SERVICE-LIFE PREDICTION 161
5.6. CONCLUSIONS 170
5.7. REFERENCES 171
CHAPTER 6 174
6.1. INTRODUCTION 174
6.2. CREEP AND SHRINKAGE MODELING OF CASKS 174
6.2.1. Introduction 174
6.2.2. Evaluating the Creep and Shrinkage Based on B4 Model 175
6.2.3. Creep and Shrinkage Modeling of Dry Cask Structure 180
6.2.4. Conclusions 190
6.3. THERMO-HYGRO MODEL 191
6.3.1. Modeling of Heat transfer in Porous Media 191
6.3.2. Modeling of Moisture Transfer in Porous Media 192
6.3.3. A Validation for Coupled Moisture/Thermal Model 197
6.3.4. Thermo-Hygro Modeling of Dry Cask Structure 202
6.4. ALKALI-SILICA REACTION (ASR) SWELLING MODEL 206
6.4.1. A Comparison between the Hydration Process 206
6.4.2. 1st-Order ASR Reaction Kinetics 214
6.4.3. Benchmark Problems of the ASR Model 219
6.4.4. ASR model of Dry Cask Structure 225
6.5. CRASH ANALYSIS OF DRY CASK STRUCTURE IN LS-DYNA 227
6.5.1. Constitutive Behavior of Concrete Material Model in LS-DYNA 227
6.5.2. Drop Test of a Thick-Walled Concrete Cylinder subjected to Shrinkage and Expansion 238
6.5.3. Tip-Over Simulation of Model Dry Cask Structure Using the Reference Concrete 245
6.5.4. Tip-Over Simulation of Prototype Dry Cask Made of Reference Concrete 258
6.5.5. Tip-Over Simulation of Model Dry Cask Using the ASR Affected Concrete 263
6.6. CONCLUSIONS 266
6.7. REFERENCES 266
CHAPTER 7 271

7.1. INTRODUCTION 271
7.2. PROBABILISTIC SEISMIC ANALYSIS OF THE VERTICAL DRY CASK 271
7.2.1. Model Development 271
7.2.2. Virtual Experimental Design 275
7.2.3. Earthquake Selection 275
7.2.4. Probabilistic Seismic Demand Modeling 276
7.2.5. Seismic Fragility Analysis 281
7.2.6. Parameter Study 282
7.2.7. Seismic Risk Estimation for Sliding and Tip-Over 283
7.3. ANALYSIS OF IMPACT FROM TIP-OVER 284
7.3.1. Model Development 284
7.3.2. Virtual Experimental Design 287
7.3.3. Impact Demand Model Development 287
7.3.4. Impact Fragility Analysis 289
7.4. CONCLUSIONS 291
7.5. REFERENCES 291
CHAPTER 8 293
8.1. CONCLUSIONS 293
8.2. RECOMMENDATIONS FOR FUTURE RESEARCH 294
APPENDIX A 295
APPENDIX B 325

SUMMARY

PROJECT OBJECTIVES

Reinforced concrete performs multiple roles in dry-storage systems. For canister-based storage systems the concrete shall not only provide shielding but insures stability of the upright canister, facilitates anchoring, allows ventilation, and provides physical protection against theft, severe weather and natural (seismic) as well as man-made events (blast incidences). Given the need to remain functional for 40 years or even longer in case of interim storage, the concrete outerpack and the internal canister components need to be evaluated with regard to their long-term ability to perform their intended design functions. Just as evidenced by deteriorating concrete bridges, there are reported visible degradation mechanisms of dry storage systems especially when high corrosive environments are considered in maritime locations. The degradation of reinforced concrete is caused by multiple physical and chemical mechanisms, which may be summarized under the heading of environmental aging. The underlying hygro-thermal transport processes are accelerated by irradiation effects, hence creep and shrinkage need to include the effect of chloride penetration, alkali aggregate reaction as well as corrosion of the reinforcing steel.

In light of the above, the two main objectives of this project are to (1) develop a probabilistic multi-hazard assessment framework, and (2) through experimental and numerical research perform a comprehensive assessment under combined earthquake loads and aging induced deterioration, which will also provide data for the development and validation of the probabilistic framework.

KEY RESEARCH FINDINGS

The key research findings of this project are summarized below. Detailed findings are provided at the end of each chapter.

- Three scaled (approximately 1/3 scale) physical models of concrete dry casks with an exposed concrete surface have been manufactured. Two of the casks were subjected to accelerated aging due to corrosion and alkali-silica reactivity (ASR). After 2 years of degradation, the casks were tested under tip-over impact to compare their performance under aged conditions to the condition of the control (unaged) cask.
- Material studies on plain and reinforced concrete indicated that addition of $CaCl_2$ and NaOH work effectively for accelerators of rebar corrosion and ASR of concrete, respectively. Based on the outcomes of the material level studies, these techniques were successfully applied to accelerate the degradation in concrete outerpacks of scaled physical models of dry casks.
- 4% and 0.8% by weight of cement addition of $CaCl_2$ and NaOH to fresh concrete and has resulted in observable degradation (cracking) due to reinforcing bar corrosion and ASR in scaled models.
- Three tip-over impact tests were performed on each scaled cask model. It was observed that the degraded casks underwent substantially more distress in the form of cracking

and spalling compared to the control (unaged) cask. Particularly, the corrosion damaged cask showed substantial spalling of the cover concrete. Some yielding of the steel liner was also observed. However, the overall performance of all three casks were found to be satisfactory with no major disintegration of the cask. Furthermore, the deformations of the steel liner were limited and canister integrity in this regard is not compromised although the damage due to severe decelerations reaching to over 100 g should be investigated separately.

- Detailed probabilistic simulations and analysis were performed and it was found out that the annual probability of exceeding the predefined sliding limit state (of a quarter of the cask diameter) and tip-over are on the order of 10^{-5} to 10^{-6} for locations in Western, Central, and Eastern U.S. These probabilities are considerably lower than those of the major failures modes of other key infrastructure such as bridges.
- The results of the fragility (probabilistic) analysis showed the high sensitivity of the response and fragility to thickness of the pad and the soil shear wave velocity. Based on this observation, in order to minimize the impact loads applied to dry casks in case of tip-over, the pad thickness should be as small as possible, acknowledging that there are practical limits to ensure adequate foundation.
- It was found through detailed computational fluid dynamics analysis that the temperature difference between the inside and outside surfaces of the dry cask concrete over pack might as high as 39 °C in winter conditions. The same number is 32 °C and 22 °C for summer and normal conditions, respectively. This temperature gradient might result in the deterioration of the concrete in the long term and needs to be investigated in more detail in future studies. The highest temperature on the interior surface of concrete was found to be 104 °C in summer conditions. This high temperature might also accelerate degradation processes such as corrosion of steel reinforcement and alkali-silica reactivity of aggregates in concrete.
- It was also found through thermal analysis that conventional scaling laws do not work to obtain the temperature distributions and a fully detailed analysis is required to obtain the temperature distributions in scaled models.
- Numerical simulations using state-of-the-art creep and shrinkage formulations indicate that the stresses induced in the concrete due these phenomena is negligible due to the nature of the applied loads (gravity only). However, the ASR degradation simulations followed by tip-over numerical experiments confirmed the findings of tests performed on the scaled casks that this issue needs to be investigated for even longer durations of ASR aging.

PROJECT PRODUCTS

Thesis

1. Sichani, M. “Seismic Risk Assessment of Vertical Concrete Dry Casks,” PhD Dissertation (in progress), Department of Civil Engineering, Rice University, Houston, Texas.

2. Attar. A. (2016) "Accelerated Alkali-Silica Reaction and Corrosion of Reinforcing Steel in Concrete: Application of Dry Casks," PhD Dissertation, Department of Civil Engineering, University of Houston, Houston, Texas.
3. Hanifehzadeh, M., "Experimental and Numerical Investigation of Multi-Hazard Performance of Dry Cask Structures", PhD Dissertation (in progress), Department of Civil Engineering, University of Houston, Houston, TX.
4. Champiri, M. D., "Crash Analysis of Degraded Concrete Dry Cask Structures Including Alkali-Silica-Reaction", PhD Dissertation (in progress), Department of Civil Engineering, University of Houston, Houston, TX.

Journal Papers and Reports

1. Sichani, M. and Padgett, J. "Probabilistic Seismic Analysis of Concrete Dry Cask Structures", Earthquake Engineering & Structural Dynamics (under review).
2. Attar, A., Gencturk, B., Willam, K., Wei, J., (2016). "Accelerated Alkali-Silica Reaction and Corrosion of Reinforcing Steel in Reinforced Concrete for Large-Scale Studies," Construction & Building Materials (under review).
3. Attar, A., Gencturk, B., Hanifehzadeh M. and Willam, K. (2016). "Accelerated Aging of Concrete Dry Cask Storage Systems for Nuclear Waste," Journal of Advanced Concrete Technology, 14 (6).
4. Zhou, Y., Gencturk, B., Willam, K. and Attar A. (2015). "Carbonation-Induced and Chloride-Induced Corrosion in Reinforced Concrete Structures," Journal of Materials in Civil Engineering, 27(9).
5. Xotta, G., Beizaee, S. and Willam, K. "Bifurcation Investigations of Coupled Damage-Plasticity Models for Concrete Materials," International Journal of Computer Methods in Applied Mechanics and Engineering (under review).
6. Xotta, G., Mazzucco, G., Salomoni, V. A., Majorana, C. E., and Willam, K. J. "Composite Behavior of Concrete Materials under High Temperatures," International Journal of Solids and Structures (in press).
7. Willam, K., Xi, Y., Naus, D., and Graves, H. L. (2013) "A Review of the Effects of Radiation on Microstructure and Properties of Concrete Used in Nuclear Power Plants," NUREG/CR Report under preparation, U.S. Nuclear Regulatory Commission, Washington, DC.

Presentations or Conference Papers

The following presentations were made or will be made by the PIs on the project or on related topics.

1. Sichani, M. and Padgett, J. (2017). "Sensitivity Analysis of Seismic Performance of Dry Cask Structures", *16th World Conference on Earthquake Engineering*, January 9-13, Chile.
2. Sichani, M. and Padgett, J. (2016). "Probabilistic Seismic Demand Models for Sliding Response of Dry Cask Structures", *1st Symposium on Probabilistic Modeling in Engineering and Science*, October 31, Bethlehem, Pennsylvania.
3. Mousavi, M.M.R., Champiri, M. and Willam, K. (2016). "Efficiency of damage-plasticity models in capturing compaction-expansion transition of concrete under different

compression loading conditions", *European Congress on Computational Methods in Applied Sciences and Engineering*, June 5–10, Crete Island, Greece.

4. Champiri, M., Mousavi, M.M.R., Hanifehzadeh, M., Attar, A., Willam, K. and Gencturk, B. (2016). "Drop test of a thick-walled concrete cylinder subjected to shrinkage and expansion", *9th International Conference on Fracture Mechanics of Concrete and Concrete Structures*, Berkeley, May 29-June 1, California.
5. Sichani, M. and Padgett, J. (2016). "Probabilistic Seismic Performance of Dry Cask Structures under Strong Ground Motions", *Probabilistic Mechanics & Reliability Conference*, May 22-25, Nashville, Tennessee.
6. Champiri, M., Attar, A., Hanifehzadeh, M., Willam, K. and Gencturk, B. (2015). "Tip-Over Simulation of Degraded Dry Storage Structures", *International Mechanical Engineering Congress and Exposition*, November 13-17, Houston, Texas.
7. Gencturk B. and Hanifehzadeh, M. (2015). "Performance of Deteriorated Dry Cask Storage Systems Subjected to Impact Loading", *American Concrete Institute (ACI) Fall 2015 Convention*, November, 7-11, Denver, Colorado.
8. Champiri, M., Attar, A., Hanifehzadeh, M., Willam, K. and Gencturk, B. (2015). "Long-Term Performance of Dry Storage Structures", *Mechanics and Physics of Creep, Shrinkage, and Durability of Concrete and Concrete Structures, CONCREEP-10*, September 21-23, Vienna, Austria.
9. Gencturk, B. and Attar, A. (2015). "Material Durability Performance of Reinforced Concrete Dry Cask Storage Systems for Nuclear Waste", *ASCE Structures Congress*, April, 23-25, Portland, Oregon.
10. Sichani, M. and Padgett, J. (2015). "Probabilistic Seismic Demand models for Rocking Response of Dry Cask Structures", *Earthquake Engineering Research Institute Annual Meeting*, March 31 – April 3, Boston, Massachusetts.
11. Xotta, G., Willam, K. Champiri, M. and Beizaee, S. (2014). "Multiscale evaluation of concrete degradation due to Alkali-Silica Reaction", *11th World Congress on Computational Mechanics*, July 20-25, Barcelona, Spain.
12. Beizaee, S., Xotta, G. and Willam, K. (2013). "Modeling of Post-Peak Response Behavior by Coupling Softening Elastoplasticity with Discontinuous XFEM Techniques", *International Mechanical Engineering Congress and Exposition,* November 17-21, San Diego, California.
13. Zhou, Y., Willam, K., Ayoub, A., Gencturk, B., Padgett, J. and Uddin, R. (2013). "Multi-Hazard Assessment of Dry Casks for Interim Storage of Spent Nuclear Fuel", *22nd International Conference on Structural Mechanics in Reactor Technology*, August 18-23, San Francisco, California.
14. Xotta, G., Willam, K., Gencturk B. and Xi, Y. (2013). "Damage Assessment of Interim Dry Storage Casks for Spent Nuclear Fuel", *22nd International Conference on Structural Mechanics in Reactor Technology*, August 18-23, San Francisco, California.
15. Willam, K., Xotta, G., Beizaee, S. and Mousavi, M.M.R. (2013). "Damage-Plasticity Models for Concrete Materials", *Engineering Mechanics Institute Conference*, August 4–7, Northwestern University, Evanston, Illinoi.

16. Bisadi, V. and Padgett, J. (2013). "Probabilistic demand models and fragility estimates for dry storage casks", *Engineering Mechanics Institute Conference,* August 4–7, Northwestern University, Evanston, Illinoi.
17. Beizaee, S. and Willam, K. (2013). "Modeling Plastic Fracture Mechanics by Inelastic Extended Finite Element Method (IXFEM)", *12th U.S. National Congress on Computational Mechanics*, July 22-25, Rayleigh, North Carolina.
18. Xotta, G., Beizaee, S. and Willam, K. (2013). "The Coupling of Damage and Plasticity for Concrete Materials", *12th U.S. National Congress on Computational Mechanics*, July 22-25, Rayleigh, North Carolina.
19. Mousavi, M.M.R., Acun, B. and Willam, K. (2013). "Mechanical Interaction of Brick and Mortar Interface in Unreinforced Masonry Triplets subjected to Shear and Compression", *12th U.S. National Congress on Computational Mechanics*, July 22-25, Rayleigh, North Carolina.
20. Xotta, G., Willam, K., Majorana, C. and Salomoni, V. (2013). "A Thermo-Hygro-Mechanical Model of Concrete Deterioration due to Alkali-Silica Reaction", 3rd *International Conference on Computational Modeling of Fracture and Failure of Materials and Structures*, June 5-7, Prague, Czech Republic.
21. Beizaee, S., Willam K. and Xotta, G. (2013). "On the Effect of Perforation on the Brittle Ductile Fracture in Ferrous Flat Bars", *8th International Conference on Fracture Mechanics of Concrete and Concrete Structures*, March 10-14, Toledo, Spain.
22. Mohammadipour, A., Willam, K. and Ayoub, A. (2013). "Experimental Studies of Brick and Mortar Composites Using Digital Image Analysis", *8th International Conference on Fracture Mechanics of Concrete and Concrete Structures*, March 10-14, Toledo, Spain *(Keynote Presentation)*.
23. Willam, K., Beizaee S. and Xotta, G. (2012). "Fixed vs. Rotating Cracking: That is the Question?", *International Mechanical Engineering Congress & Exposition*, November 9-15, Houston, Texas *(Keynote Presentation).*
24. Xotta G. and Willam, K. (2012). "Effect of Aggregate Inclusions on Concrete under Thermal Exposure: a Meso-Mechanical Response Study", *International Mechanical Engineering Congress & Exposition*, November 9-15, Houston, Texas.

CHAPTER 1
INTRODUCTION

1.1. PROBLEM STATEMENT

In the absence of permanent/long-term options for the storage of spent nuclear fuel in the United States, the nuclear waste has to be stored in short-term and mid-term storage facilities such as spent fuel pools and dry cask structures. The dry casks are located at independent spent fuel storage installations (ISFSI) with the intended lifetime of 20 years with possible extension to 40 years. However, they have to be used for longer periods of time due to the lack of a long-term storage solution in the United States. The long-term performance of the dry casks should be studied under different conditions to avoid catastrophic consequences of any damage to these nuclear waste containers.

1.2. SCOPE

This study is focused on vertical concrete dry casks and their structural performance in seismic and tip-over events, aiming for risk estimation of large seismically induced motions (large sliding and tip-over) and structural damage due to the tip-over loads. Both numerical and experimental work was conducted to investigate the long-term performance of the concrete outerpacks with an exposed surface. Material level studies provided additional data to the existing literature on how to accelerate the corrosion and alkali-silica reactivity (ASR) in concrete without altering the key properties of the material to observe significant levels of deterioration in a short period of time. The developed methods are specifically geared towards large-scale applications of structural systems. Detailed thermal analysis was performed to determine the temperature distributions in both prototype and scaled casks. Tip-over experiments were performed on both intact and aged physical models of concrete casks to compare the structural performance in terms under combined aging and mechanical loading. The influence of shrinkage, creep and gravity loading in the long-term and combined ASR and tip-over impact were investigated using detailed numerical simulations. In the probabilistic assessments, the effect of different sources of aleatory and epistemic uncertainties on the structural performance of the dry casks are studied, and probabilistic models are developed for some of the key structural responses. Fragility curves are developed for seismic sliding motion and tip-over, as well as large acceleration in case of tip-over, and effect of different parameters' variations on the response is studied herein. Probabilistic seismic analysis on a portfolio of vertical concrete dry casks is performed in this study considering common cask configurations in the United States. Probabilistic seismic demand models for the maximum sliding distance and maximum angle of rotation of the casks are developed, and seismic fragility analysis and parameter study are performed. Seismic risk of large sliding motions and tip-over is estimated. In addition, finite element models are developed to analyze the structural response of a dry cask to impact tip-over loads considering the influence of material and structural parameter variations. Impact fragility curves are developed for the mean maximum acceleration of the cask in tip-over events, and effect of geometric and material properties on the response is investigated.

1.3. REPORT ORGANIZATION

In Chapter 2, a brief review of dry cask storage systems currently in use in the United States is provided. Then the selection and scaling of cask dimensions for model structures and the fabrication of the three cask models is described. Chapter 3 is dedicated to the material level analysis to determine the appropriate accelerated aging techniques for concrete dry casks to study their long-term performance under combined aging and mechanical loading. In Chapter 4, thermal analysis of dry cask under normal, summer, and winter conditions is conducted. Chapter 5 describes the monitoring of the casks over a 2 year period to observe the degradation. Additionally, the results from impact tests are provided. The degradation of concrete cask is investigated using numerical techniques in Chapter 6. Seismic analysis and impact analysis of the dry casks are performed in Chapter 7. Moreover, probabilistic models for some of the key structural responses in seismic and tip-over events are developed in this chapter, and risk of seismically induced large motions (large sliding and tip-over) and structural damage due to tip-over is estimated. Chapter 8 summarizes the findings of this research and lists recommendations for furture studies.

CHAPTER 2

CASE STUDY CASK CONFIGURATION

2.1. INTRODUCTION

Dry cask storage systems are intended to provide temporary onsite storage of spent nuclear fuel (SNF). The SNF assemblies, composed of several fuel rods, are placed in SNF pools for several years after being removed from the nuclear reactor for cooling and radiation shielding purposes. Dry cask systems emerged as a convenient temporary storage option. After a minimum of one year storage in the SNF pool, the fuel temperature and radioactivity decreases sufficiently for the SNF to be removed from the pool and placed in the cask. The first cask installation was licensed by the United States Nuclear Regulatory Commission (NRC) in 1986 at the Surry Nuclear Power Plant in Virginia, since then cask sites have constantly increased exceeding 60 sites around the United States at the time of writing of this report. In the canister-based cask designs, the SNF is sealed in a cylinder filled with inert gas, called the canister, and then the canister is placed in the cask which has thick outerpack made of steel, concrete, or both, to provide further radiation shielding. Both horizontal and vertical cask configurations are used in the United States. In this report, a vertical configuration is investigated for its vulnerability to tip-over impact event. A typical configuration of a vertical concrete storage system is shown in Figure 2-1.

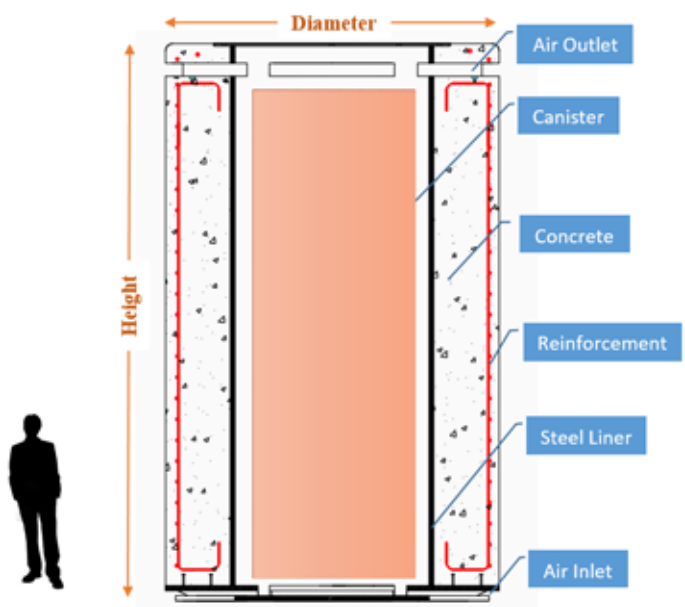

Figure 2-1 Typical configuration of vertical dry storage system.

A tip-over event is a hypothetical accident which may happen during the regular handling or in the case of an extreme event such as a strong earthquakes or a tornado or explosions. Based on the standard review plans developed by the United States Nuclear Regulatory Commission (NRC), the structures should be evaluated under normal and off-normal environmental conditions as well as under hypothetical accidents (NUREG, 2000). For most vertical cask, the casks are

freestanding on a concrete pad. This leads to stability concerns in terms of sliding and tipping over in seismic areas which threatens the safety of the canister and the fuel rods. The most important parameter for SNF integrity under impact loading is the induced g-load, which could be used as a measure for performance evaluation.

Several impact tests have been performed mostly on the transfer casks (used to transfer the canister from a storage to a transportation cask) over the past two decades. In the United States, the first series of testing including impact and fire tests were performed in 1970s at Sandia National Laboratories (Shappert 1970). The Oak Ridge National Laboratory built an impact pad at the tower shielding facility, which has a large lift capacity, sufficient to elevate a 75-ton weight to a height of about 60 m. In 1974, the first cask specimens weighting from 2,700 kg to 5400 kg were dropped from a height of 9 m onto a steel impacting surface (Shappert and Ludwig 2004). Vecchio and Sato (Vecchio and Sato 1988) performed a study on 9 m free drop and 1 m drop onto a steel pin using a half-scale concrete cask weighting 6.6 tons. Furthermore, a series of drop tests were performed on 1/3 scale models of steel dual purpose casks produced by Hitachi in 2000s (Shimizu and Hoshikawa 2004). To the knowledge of the authors, the only published tip-over test on a concrete cask (in this case, a 1/3 scale model) is presented in Kim et al. (2006). Further, the tip-over impact performance of vertical concrete casks subjected to environmental degradation has not been investigated before.

2.2. REVIEW OF DRY-STORAGE SYSTEMS

A comprehensive review of different types of dry casks that are being used today was performed and the design details was identified. Although some of the design specifications are not publically available, it was possible to obtain sufficient information from the reports submitted to NRC to develop a generic cask design.

2.2.1. Dry Cask Types

There are various dry cask storage system designs. In certain designs, the steel cylinders containing the fuel are placed vertically in a concrete vault; other designs orient the cylinders horizontally. The concrete vaults provide the radiation shielding. The number of different types of casks in the United States as well as their classification based on configuration and fabrication materials are presented in Figure 2-2 and Figure 2-3. Other cask designs orient the steel cylinder vertically on a concrete pad at a dry cask storage site and use both metal and concrete outer cylinders for radiation shielding. The cost is a chief consideration; therefore, recently there is a tendency towards higher use of concrete design rather than all-metal cask designs. There are two basic types of storage systems, which are widely in use in the United States. Canister-based systems consisting of a metal canister inside a cask or storage module made of steel or composite steel and concrete, and non-canistered designs where bare-fuel is stored in a thick-walled or metal shielded cask. As presented in Figure 2-2, most of the dry storage employed in the United States are canister-based with concrete outerpacks (HI-STORM, NAC-MAGNASTOR, NAC-UMS, VSC 24). That is also the reason for focusing on vertical concrete cask performance in this study.

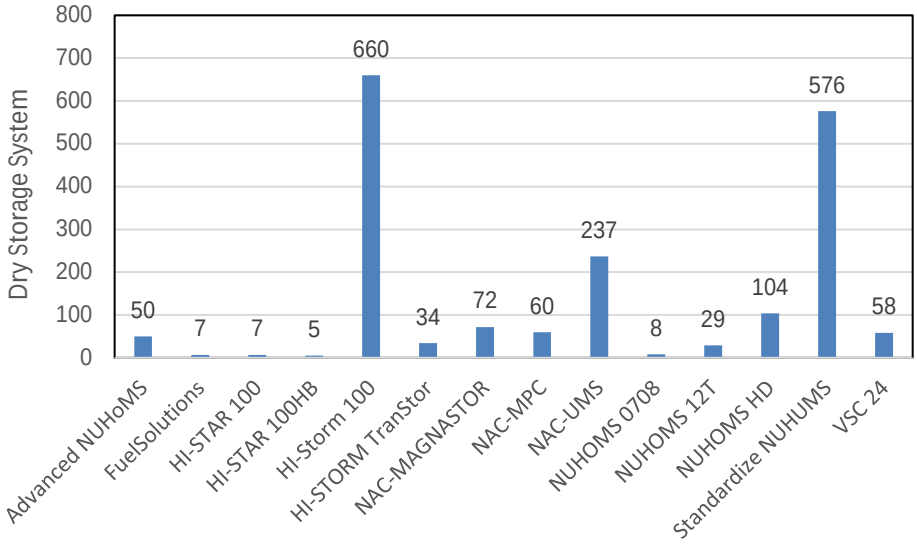

Figure 2-2 Horizontal versus vertical storage (Greene et al., 2013).

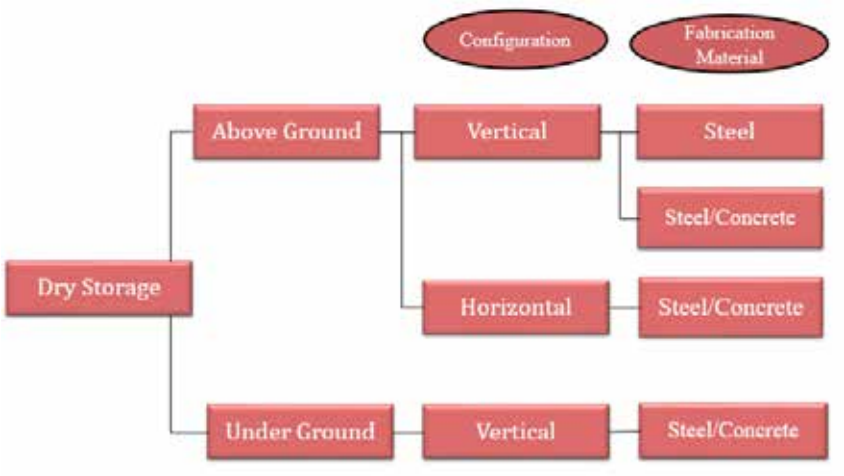

Figure 2-3 Classification of dry storage based on configuration and fabrication material.

2.2.2. Examples of Dry Cask Storage

There are five major companies in the U.S., which provide approved dry cask storage and transportation systems: NAC International, Holtec International, Areva Group, BNG Fuel Solutions Corporation and Transnuclear. The list of approved spent fuel storage casks with the related manufacturer is available at http://www.nrc.gov/waste/spent-fuel-storage/designs.html. There are also other brands which are obsolete at the present time. In the following, a short description is provided for some of the most commonly used concrete cask designs. More information about various storage and transportation casks is available in Greene et al. (2013).

2.2.2.a. HI-STORM 100 (Holtec International)

HI-STORM 100 system has both concrete and structural steel components, see Figure 2-4. The concrete is poured between inner and outer steel shells that are connected to each other by four vertical oriented radial plates, and top and bottom closure plates. The main structural function is provided by the carbon steel parts. The plain concrete has shielding functionality. The concrete is made of Type II Portland cement and has a compressive strength of 27.5 MPa and a minimum density of 2340 kg/m^3. Vertical channels attached to the inner surface of the liner provide guidance for canister insertion and removal and also energy absorption during the tip-over event, while still allowing the cooling airflow to circulate around the canister (Holtec, 2012).

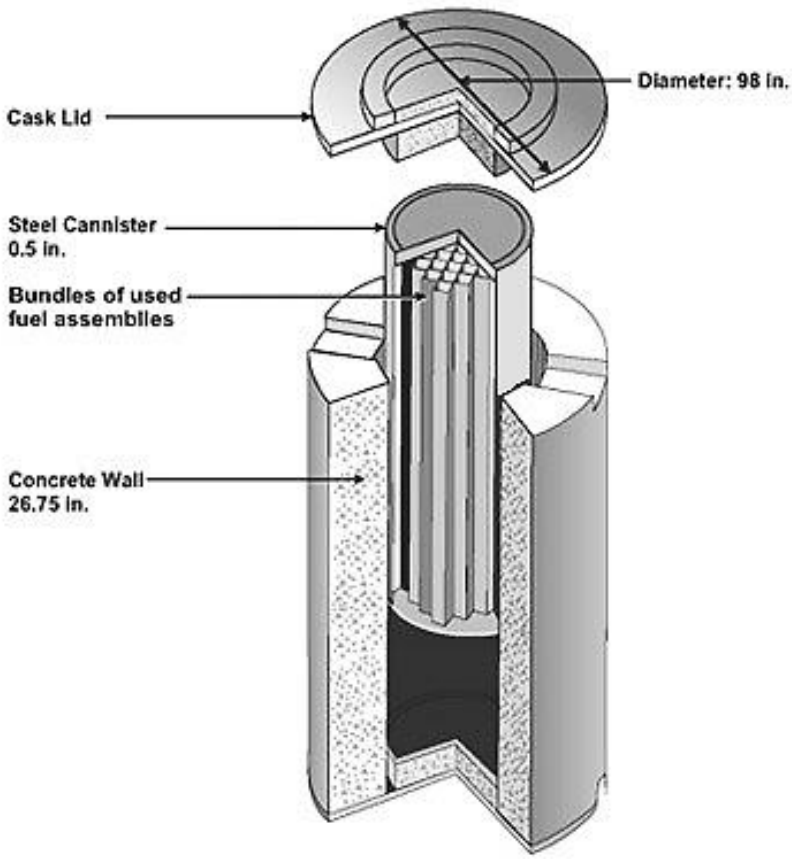

Figure 2-4 HI-STORM 100 (Holtec, 2012).

There are three HI-STORM designs: HI-STORM 100, HI-STORM 100S, HI-STORM 100S Version B. The differences among the three are:

- Over-pack height
- Canister pedestal height
- Location of the air outlet ducts
- Vertical alignment of the inlet and outlet air ducts

There are two variants of the HI-STORM 100S over-pack design, differing only in height and weight.

2.2.2.b. VSC-24 (BNG Fuel Solution Corporation)

This system consists of three major structural components: the Ventilated Concrete Cask (VCC), the Multi-Assembly Sealed Basket (MSB), and the MSB Transfer Cask. The main structural member of the VCC is the concrete layer with reinforcing bars. The concrete cask is a reinforced concrete cylinder with an outside diameter of 3.35 m and an overall height that varies from 5 m to 5.72 m. The internal cavity of the concrete cask has an inside diameter of 1.79 m and is formed by a 44.5 mm thick cylindrical steel liner. The liner is a stay-in-place form and its thickness is determined by shielding requirements. The reinforcing steel in the VCC body is located to provide adequate strength for the design loading conditions. The concrete is Type II Portland cement with 2306 kg/m^3 density and 27.5 MPa compressive strength. Type II Portland cement is typically used because of its higher sulfate resistance and lower heat of hydration in comparison to general purpose Type I cement.

The VSC system is designed to be stored outdoors without additional weather protection. Therefore, the cask is designed to withstand the design basis daily and seasonal temperature fluctuations, and tornado, wind, flood, seismic, snow, and ice loads. In design, the 24°C normal temperature was used to evaluate the long-term concrete properties and to serve as the base temperature for thermal cycle evaluations (BNG, 2005). The general configuration of the system is presented in Figure 2-5.

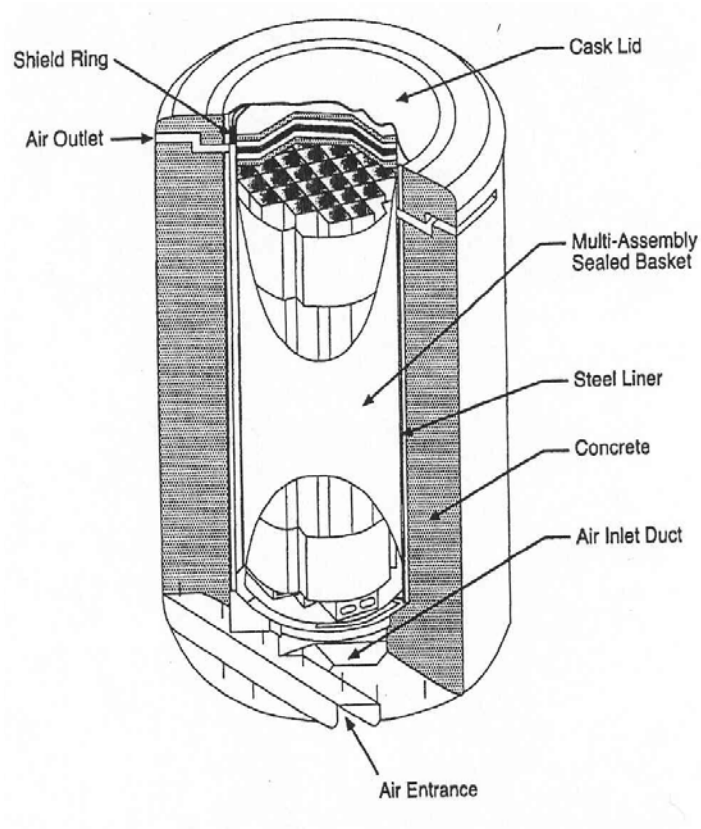

Figure 2-5 VSC-24 (BNG, 2005).

2.2.2.c. UMS (NAC International, Inc.)

The NAC-UMS system is a portable dry storage system that accommodates stainless steel transportable storage canister (TSC). The cask provides radiation shielding and allows heat removal of spent fuel contents by natural air circulation around the canister wall through the air ventilation path. The NAC-UMS is designed to store up to 24 Pressurized Water Reactor (PWR) or up to 56 Boiling Water Reactor (BWR) spent fuel assemblies. There are five TSCs of different lengths, each to accommodate a different class of PWR or BWR fuel assembly. Each TSC has an outside diameter of about 1701 mm and the lengths vary from about 4445 mm to 4953 mm long. The maximum weight of a loaded PWR TSC is slightly less than 36.5 tons. Five concrete casks of different heights, ranging from about 5309 mm 5740 mm, are each designed to accommodate a different TSC. Each VCC design has an outside diameter of about 3454 mm. The five VCC's vary in weight between 111 tons and 119 tons empty. The VCC side walls consist of about 711 mm of reinforced concrete (Type II Portland cement), with a 64 mm thick carbon steel liner. The VCC provides structural support, shielding, protection from environmental conditions, and natural convection cooling of the TSC during long-term storage. General configuration of the system is presented in Figure 2-5.

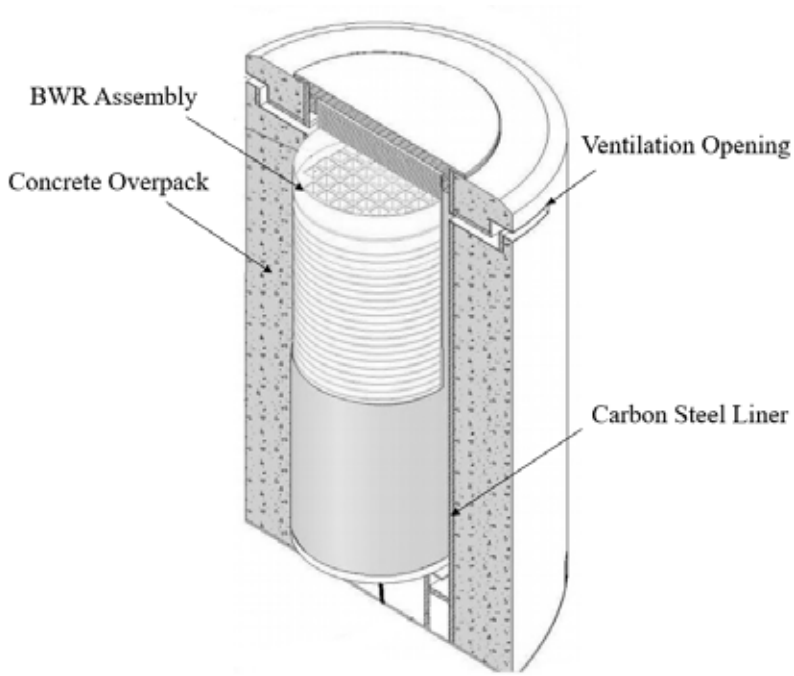

Figure 2-6 NAC UMS (Pennington, 2013).

2.2.2.d. MAGNASTOR (NAC International, Inc.)

The MAGNASTOR system is designed to safely store up to 37 undamaged PWR fuel assemblies in the 37 PWR basket assembly or up to 87 BWR fuel assemblies. MAGNASTOR has been designed and analyzed for a 50-year service life. The concrete cask provides structural support, shielding, protection from environmental conditions, and natural convection cooling of the transportable storage canister (TSC) during long-term storage (NAC, 2011).

The concrete cask is a reinforced concrete structure with a structural steel inner liner and base (see Figure 2-7). The reinforced concrete wall and steel liner provide the neutron and gamma radiation shielding for the stored spent fuel. The reinforced concrete wall provides the structural strength to protect TSC and its contents in natural phenomena events such as tornado wind loading and wind-driven missiles, and during non-mechanistic tip-over events. The concrete cask provides an annular air passage to allow the natural circulation of air around the TSC to remove the decay heat from the contents. Fabrication of the concrete cask requires no unique or unusual forming, concrete placement, or reinforcement operations. The concrete portion of the cask is constructed by placing concrete between a reusable, exterior form and the steel liner. Reinforcing bars are used near the inner and outer concrete surfaces to provide structural integrity. The structural steel liner and base are shop fabricated. The dimensions of three different types of over-pack for MAGNASTOR storage system are provided in Table 2-1.

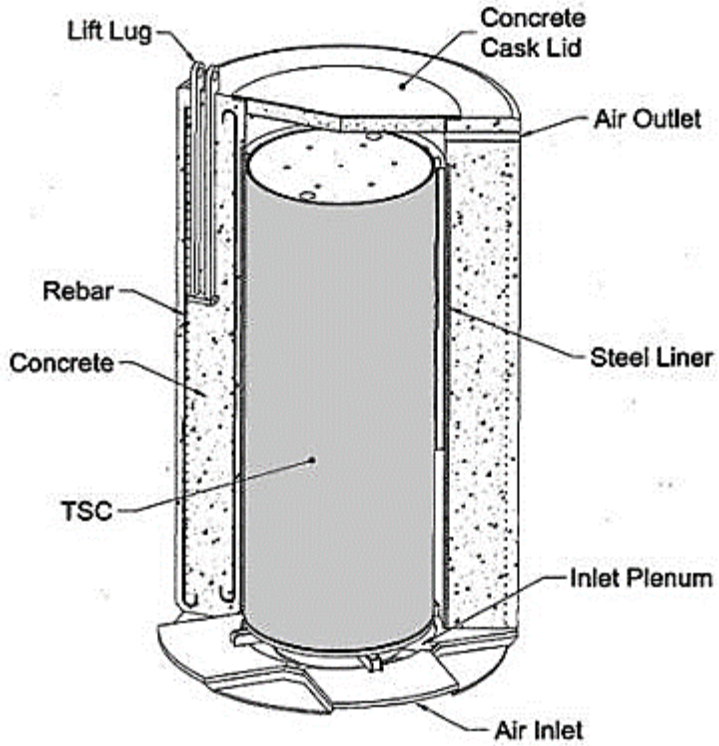

Figure 2-7 MAGNASTOR (NAC, 2011).

Table 2-1 Three MAGNASTOR Designs.

Cask Types	Height (mm)	Concrete Inner Diameter (mm)	Concrete Outer Diameter (mm)	Concrete Thickness (mm)	Liner Height (mm)	Lid Inner Diameter (mm)	Liner Thickness (mm)	Lid Plate Diameter (mm)	Lid Thickness (mm)
CC1[1]	5723	2108	3454	673	5558	2019	44.5	2235	173
CC2	5723	2108	3454	673	5558	2019	44.5	2235	173
CC3	5545	2108	3454	643	5380	1956	76.2	2324	325

[1]Concrete Cask (CC and CC3 are the standard versions; CC2 has segmented design. The systems are also different in height and shielding level).

2.3. SELECTION OF A CASK DESIGN FOR DETAILED INVESTIGATION

2.3.1. Cask Geometry and Similitude

A review of the most commonly used casks in the United States was performed as presented in a summary above. Typical values were chosen for the weight and dimensions of the cask models. The scaled dimensions used in the physical model casks are provided in Table 2-2.

Table 2-2 Main Dimensions of Most Common Vertical Concrete Casks in the United States.

Vertical Concrete Cask	Vendor	Height (mm)	Outer Diameter (mm)	Liner Thickness (mm)	Concrete Thickness (mm)
MAGNASTOR, CC1 and CC2[1]	NAC International	5723	3454	44.5	673
MAGNASTOR CC3	NAC International	5545	3454	76.2	643
VSC-24[2]	BNG Fuel Solutions Corporation	5718, 5410, 5000	3353	44.5	737
HI-STORM[3]	Holtec International	5867	3353	51	699
NAC-UMS	NAC International	5309-5740	3454	63.5	711
VSC-17[2]	BNG Fuel Solutions Corporation	5740	2667	89	508
Average	-	5607	3416	56	692
Scaled Average	-	1979	1206	19.8	244
Physical Model	-	2030	1220	16	238

[1]Different configuration of the Concrete Cask based on fuel type
[2]Ventilated Storage Cask
[3]Holtec International Storage Module (In HI-STORM, the concrete is sandwiched between two steel liners).

More realistic behavior of the structure may be obtained from full-scale tests; however, the specimen dimensions and weight are in most cases limited due to the cost of fabrication and capabilities of the testing facility. Reduced-scale models are commonly used for experimental investigation of large structures. The main objective of the scaling procedure is to reduce the size and weight of the specimen without losing the main structural characteristics. Therefore, a scaling factor of 2.83 was chosen in this study. The similitude requirements for a structural model may be determined using the Buckingham pi-theorem (Dove and Bennett 1986). If the scaled model (replica) satisfies all the similarity equations, it is called a true model. In a true model, the following are satisfied: the geometry, stress-strain relationship, mass, gravity forces, and the initial and boundary conditions. However, most often it is not possible to satisfy all the required relations between the model and prototype due to its size, shape, material properties and boundary conditions (Balawi et al, 2015). For example, if the prototype material is used for fabrication of the model, a true reproduction is impossible. Therefore, a distorted model should be developed and artificial mass should be added to the model. There are several approaches including direct, strength and dynamic model to develop the replica depending on whether

testing is in the elastic regime or ultimate capacity and a failure will be reached. The dynamic similitude (also called artificial mass simulation) is time dependent and one of the most popular methods for shake table experiments where the material is the same in the prototype and the replica. In this method, artificially added mass is needed without affecting the structural stiffness. Therefore, the two major scaling requirements for structural problems (see Table 2-3) Froude and Cauchy are satisfied (Severn, 1997). This condition provides the most accurate results.

Table 2-3 Cauchy and Froude Similitude Requirements (Bursi and Wagg, 2009). $\alpha=L_p/L_m$ for Length and $e=E_p/E_m$ for Modulus of Elasticity and $\rho=\rho_p/\rho_m$ for the Specific Mass Ratio. *P* Stands for Prototype and *m* for Model.

Quantity	Symbol	Cauchy	Froude
Length	L	α	α
Modulus of Elasticity	E	e	e
Specific Mass	ρ	ρ	ρ
Area	A	α^2	α^2
Volume	V	α^3	α^3
Mass	M	$\rho\alpha^3$	$\rho\alpha^3$
Velocity	v	$e^{0.5}\rho^{0.5}$	$\alpha^{0.5}$
Acceleration	a	$e\rho^{-1}\alpha^{-1}$	1
Force	F	$e\alpha^2$	$\rho\alpha^3$
Stress	σ	$e\alpha^3$	$\rho\alpha^4$
Strain	ε	e	$\rho\lambda$
Time	t	$e^{-0.5}\rho^{0.5}\alpha$	$\alpha^{0.5}$
Frequency	f	$e^{0.5}\rho^{-0.5}\alpha^{-0.5}$	$\alpha^{-0.5}$

However, when the addition of extra mass to the specimen is not possible, one of the two methods should be utilized independently based on nature of the test. In this study, to follow the dynamic method, the required weight of the replica, considering a scaling factor of 2.83, would be about 19 tons for a typical cask design. Although the cask was completely filled with steel (simulated fuel), this weight could not be reached. Figure 2-8 shows the required weight of the replica with respect to the scaling factor for the current study.

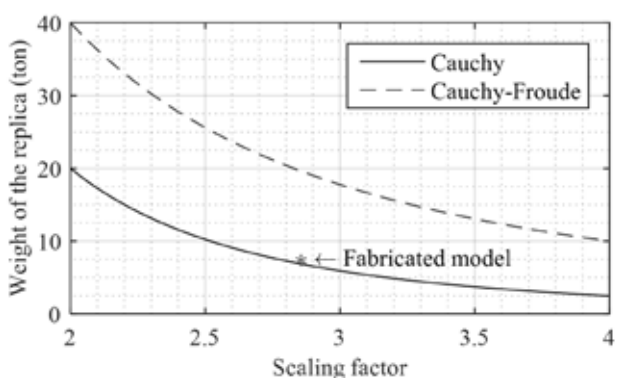

Figure 2-8 Required weight for the specimen based on the scaling factor for the current study.

Since the weight requirement using the dynamic model could not be satisfied (Figure 2-8), the Cauchy method was selected for the current study which can be used when the restoring force is derived from the stress-strain constitutive relationship. One of the major reason for this choice is application of the strain gages for strain measurement. In this case, the measured strain could be used without scaling. This type of scaling is called partial similarity and the model is called distorted model (Balawi, Shahid, and Al Mulla 2015). Note that the dimensionless Cauchy number, C_n, is the ratio between the dynamic inertia force and the elastic restoring force (Williams and Blakeborough 2001, du Beton 1996) according to

$$C_n = \frac{(r L^3 v^2 / L)}{E L^2} = \frac{r u^2}{E} \qquad 2.1$$

Where, ρ is the density of the material, v is the velocity and E is the Young's modulus. These values should be the same both in the model and the prototype. Using this method, the scaling factor for each of the parameters was obtained and presented in Table 2-4.

Table 2-4 Scaling Factors for Dynamic Testing.

Variable	Scaling Factor	Variable	Scaling Factor	Variable	Scaling Factor
Length (L)	α	Time (t)	α	Strain (ε)	1
Mass (M)	α^3	Velocity (V)	1	Acceleration (A)	$1/\alpha$
Stress (σ)	1	Displacement (δ)	α	Strain Rate ($\dot{\varepsilon}$)	$1/\alpha$

2.3.2. Fabrication of the Scaled Cask Models

Using the similitude procedure described in the previous section and the general dimension of the commercial casks summarized in Table 2-2, the following dimensions in Table 2-5 were considered for the fabrication of the scaled model. The detailed fabrication drawings of the specimens are provided in Appendix B. Standard material test based on ASTM codes were performed on the concrete, steel plate and reinforcement to obtain material properties. The results are described in Chapter 3.

Table 2-5 Dimensions of the Model Components.

Model Part	Prototype Size (mm)	Scaled Model Size (mm)
Cask Length	5723	2030
Cask Outer Diameter	3454	1220
Concrete Thickness	673	238
Liner Length	5558	1969
Liner Inner Diameter	2019	710
Liner Thickness	44	16
Lid Plate Diameter	2019	830
Lid Plate Thickness	19	6
Base Plate Thickness	76	19
Base Total Diameter	3454	1220
Air Vents	114 x 1300	47 x 457

In order to represent the SNF canister inside the cask, an assembly of eight solid steel rods packed inside a steel tube was used (see Figure 2-9). The fabrication process of the scaled physical cask models is shown in Figure 2-10. The dimensions for each component of the model are summarized in Table 2-5. The lid was fixed in place using six high strength bolts anchored to the concrete overpack. A concrete cover of 40 mm was provided according to ACI 318-14 (2014) and #10 rebar (9.5 mm diameter) was used as both vertical and horizontal reinforcement. The yield strength of the rebar was found to be 551.4 MPa (for further details, see Section 3.2.1.g). The rebar was placed with center to center spacing of 75 mm and 130 mm in vertical and circumferential direction, respectively. The rebar were fabricated at a precast concrete plant and shipped to the University of Houston Structural Research Laboratory. They were placed around the steel liner in the laboratory as it shown in Figure 2-10(b).

The three concrete mixtures, two identical SCC mixtures with 25% fly ash replacement of cement and one SCC mixture with no fly ash replacement of cement, were delivered separately in three ready-mix trucks. NaOH powder was added to the fresh SCC mixture with no fly ash to accelerate ASR and mixed inside the truck for 15 min before casting. The concrete mixtures for the cask were provided along with the first phase concrete. Similarly, $CaCl_2$ flakes were added to one of the SCC mixtures with fly ash to accelerate corrosion. Thereafter, casks were poured and formwork (see Figure 2-10(c)) was sealed with plywood and plastic sheets to prevent rapid loss of moisture. After 28 days of casting, the formwork was removed (see Figure 2-10(d)). The properties of these three concrete mixtures are shown in Table 2-6. Series of specimens also casted along with the cask preparation which is described in detail in Chapter 3.

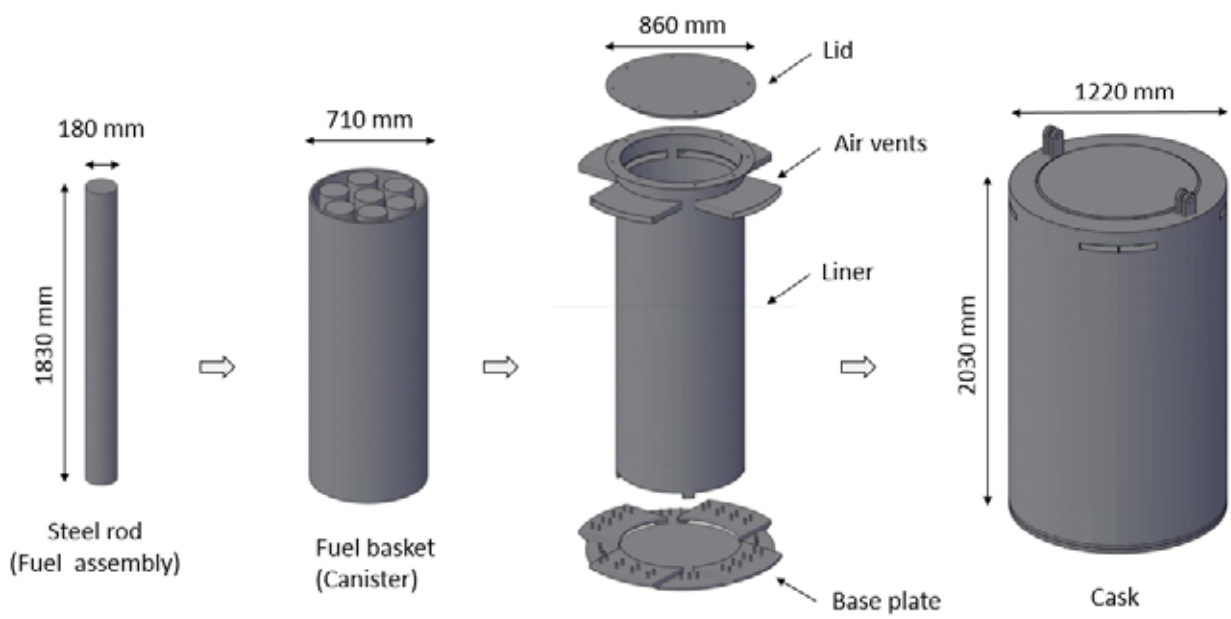

Figure 2-9 Components of the tested physical cask models.

Figure 2-10 Fabrication of the specimens (a) steel parts (b) reinforcement (c) concrete casting (d) fabricated casks.

Table 2-6 Properties of Concrete Mixtures.

Material	Unit	SCC	NaOH-4	$CaCl_2$-4
Cement	kg/m^3	323.80	431.55	323.80
Fly Ash	kg/m^3	107.55	-	107.55
Pea Gravel	kg/m^3	1227.54	1227.54	1227.54
Sand River	kg/m^3	1086.99	1086.99	1086.99
Water	kg/m^3	213.10	213.10	213.10
Admix #1*	ml/m^3	1155	1155	1155
Admix #2**	ml/m^3	2320	2320	2320
Add. NaOH	kg/m^3	-	3.67	-
Add. $CaCl_2$	kg/m^3	-	-	19.68

Weight of the each component and total weight of the specimens are estimated and presented in Table 2-7.

Table 2-7 Weight of Each Cask Component.

Parts	Weight (kg)
Steel Parts (Liner, Base, Vents)	832
Concrete Segment Overpack	3640
Lid Assembly	87
Canister Assembly	3260
Total	7819

2.4. CONCLUSIONS

A comprehensive review was performed on the existing commercial dry storage systems. The vertical concrete configuration with a steel liner inside was considered for the aging and tip-over study due to its high vulnerability with the exposed concrete. A generic cask design was developed based on this review. Fabrication drawings were developed and three scaled specimens were constructed, two for environmental aging and one as control. Two aging mechanisms, corrosion and alkali-silica reactivity (ASR) of concrete were considered. Chemical agents were added to the concrete mixture of two casks to initiate the aging process from the first day of casting. The casks were monitored for aging close to two years prior to the tip-over testing using non-destructive tests as well as material experiments. The tip-over test results are discussed in Chapter 5.

2.5. REFERENCES

ACI (2014). *Building code requirements for structural concrete (ACI 318-14) and commentary (ACI 318-14R)*, A. C. I. (ACI), Farmington Hills, MI.

Balawi, S., Shahid, O., & Al Mulla, M. (2015). "Similitude and Scaling Laws-Static and Dynamic Behaviour Beams and Plates". Procedia Engineering, 114

BNG. (2005). *Final Safety Analysis for The VSC-24 Ventilated Storage Cask System*. prepared by BNG Fuel Solutions Corporation, Campbell, CA.

Bursi, Oreste S, and David Wagg. (2009). *Modern testing techniques for structural systems: dynamics and control*. Vol. 502: Springer Science & Business Media.

Dove, R., & Bennett, J. (1986). *Scale modeling of reinforced concrete category i structures subjected to seismic loading*. prepared by Los Alamos National Lab., NM (USA).

du Beton, Comite Euro-Internationale. (1996). "RC frames under earthquake loading: state of the art report." *Tomas Telford, London, UK*.

Holtec. (2012). *Final Safety Analysis Report on The HI-STORM FW System*. prepared by Holtec International, 555 Lincoln Drive West, Marlton, NJ.

Greene, S., Medford, J. and Macy, S. (2013). *Storage and transport cask data for used commercial nuclear fuel,* ATI-TR-13047, Oak Ridge, TN.

Kim, D.-H., Seo, K.-S., Lee, J.-C., Cho, C.-H., Jang, H.-K., & Choi, B.-I. (2006). "A Test for Verifying a Tip-Over Analysis of a Dry Storage Cask". Journal of the Korean Radioactive Waste Society, 4(3)

NAC. (2011). *Final Safety Analysis Report*. prepared by NAC International, 3930 East Jones Bridge Road, Norcross, GA.

NUREG. (2000). *Standard Review Plan for Spent Fuel Dry Storage Facilities, NUREG-1567*. prepared by U.S. Nuclear Regulatory Commission, Washington, D.C.

Pennington, Charles W. (2013). "NAC Technology and Experience: 2012 in Review." INMM Spent Fuel Management Seminar, Washington, DC.

Severn, Roy T. (1997). *Structural Response Prediction Using Experimental Data: The sixth Mallet-Milne lecture*. Vol. 6: CRC Press.

Shappert, L. (1970). *CASK DESIGNERS GUIDE: A GUIDE FOR THE DESIGN, FABRICATION, AND OPERATION OF SHIPPING CASKS FOR NUCLEAR APPLICATIONS*. prepared by Oak Ridge National Lab, Oak Ridge, TN.

Shappert, L., & Ludwig, S. (2004). "44 years of testing radioactive materials packages at ORNL". *The 14th international symposium on the packaging and transportation of radioactive materials.*,September 20-24, 2004, Berlin, Germany.

Shimizu, M., & Hoshikawa, T. (2004). "Dual-purpose Transport and Storage Dry-type Metal Casks for Spent Nuclear Fuel". Hitachi Review, 53(3)

U.S.NRC. "Dry Cask Storage." Accessed 12 Dec. https://www.nrc.gov/waste/spent-fuel-storage/dry-cask-storage.html.

Vecchio, F. J., & Sato, J. A. (1988). "Drop, Fire, and Thermal Testing of a Nuclear Fuel Container". Structural Journal, 85(4)

Williams, M., & Blakeborough, A. (2001). "Laboratory testing of structures under dynamic loads: an introductory review". Philosophical Transactions of the Royal Society of London A: Mathematical, Physical and Engineering Sciences, 359(1786)

CHAPTER 3

ACCELERATED AGING AND MATERIALS STUDIES

3.1. INTRODUCTION

Deterioration in concrete structures is due to a combination of various physical, thermal, chemical, biological or mechanical processes. This time-dependent deterioration of concrete is called aging. The changes in concrete start with cement hydration and continue with the crystallization of amorphous constituents and reactions between cement, aggregate and reinforcing steel. Concrete may also deteriorate because of its interaction with the environment and exhibit distress due to shrinkage, creep, corrosion of reinforcing steel and ASR of aggregates. The aging of concrete structures may continue to the point that the structure cannot meet its functional and performance requirements any longer. This study investigates two aging effects, ASR and corrosion. Each of these effects are briefly explained below.

3.1.1. Alkali-Silica Reactivity in Concrete

ASR is a pathogenic and progressive reaction in cement composites (Mladenovic et al. 2009, Cusatis, Alnaggar, and Rezakhani 2014) and it is one of the most common damage mechanisms in concrete structures. Necessary elements for initiation of this reaction are reactive silica, sufficient alkali and sufficient moisture. Pesavento and Gawin (2012) explained ASR as the reaction of the hydroxyl ion (OH^-) of the alkalis (sodium and potassium) from hydraulic cement or other sources with the silanol groups (Si-O) and breaking of the siloxane bonds. Pan et al. (2012) expressed this reaction

$$Si\text{-}O\text{-}S_i^{\circ} + Na^+(K^+) + OH^- \rightarrow {}^{\circ}Si\text{-}O\text{-}Na(K) + H\text{-}O\text{-}Si^{\circ} \qquad 3.1$$

Where, the silonal groups react with hydroxyl ions and produce a weak acid on the surface of the aggregate. This silicic acid immediately reacts with further hydroxyl ions and liberates more water according to (Pan et al. 2012)

$${}^{\circ}Si\text{-}O\text{-}H + Na^+(K^+) + OH^- \rightarrow {}^{\circ}Si\text{-}O\text{-}Na(K) + H_2O \qquad 3.2$$

where the cations of the pore solution are attracted to Si-O- molecules and bind to form Si-O-Na, which comprises the alkali-silica gel. Na^+, K^+ and Ca_2^+ diffuse into the gel in sufficient numbers to balance the negatively charged groups. After reaching the saturation point, a gel consisting of silica, alkalis, water and other ions is created. The reactions are shown below (Bahadure and Naik 2013, Farny and Kosmatka 1997)

$$SiO_2 + 2NaOH + H_2O \rightarrow Na_2SiO_3 \times 2H_2O \qquad 3.3$$

$$SiO_2 + 2KOH + H_2O \rightarrow K_2SiO_3 \times 2H_2O \qquad 3.4$$

$$SiO_2 + Ca(OH)_2 \rightarrow CaO \times SiO_2 \times H_2O \qquad 3.5$$

In this process, alkalis from the cement or from an external source (sodium, potassium or calcium) penetrate into the siliceous particle and react with free silica present in the aggregate, thus forming alkali hydroxide and loosening the lattice structure (Sarkar et al. 2004). The product of this reaction is a hydrophilic alkali-silica gel, which has a high tendency to absorb water from its environment such as pore solution, and expand. Since the gel is surrounding mortar, an osmotic pressure is generated by the swelling. When the pressure from this gel exceeds the tensile strength of concrete, cracks occur to relieve the pressure; more water migrates inside the concrete, and the gel swells even more (ACI Committee 221 1998). This cracking may eventually cause the failure of the concrete (Anantharaman 2008). According to previous studies, gel can be formed at different relative humidity levels, although for it to swell, relative humidity (RH) must be higher than 80% (Figg 1983, Ferraris 1995). Temperature can also influence the speed of this reaction; however, it cannot be easily interpreted, since higher temperature causes not only quicker reaction but also reduced viscosity of the gel, which can make the gel enter the concrete pores with a reduction of its expansive potential (Pignatelli 2012). The width of alkali-silica macro-cracks at the exposed surface of concrete element is usually between 0.1 mm to over 10 mm. The ASR effect on properties of concrete becomes significant after cracks become visible on the surface of the concrete. This effect reduces compressive inelastic secant stiffness (and hence the resonant frequency), flexural and tensile strength, and Young's modulus of concrete (Fan and Hanson, 1998a; Monette and Gardner, 2002; Jones and Clark, 1998; Attoh-Okine and Atique, 2006; Rezakhani et al., 2016). However, the influence of ASR on compressive strength is unclear because of contradictory results obtained by different researchers (Fan and Hanson, 1998b; Monette and Gardner, 2002; Attoh-Okine and Atique, 2006).

3.1.2. Corrosion in Reinforced Concrete

As fresh concrete is placed around the steel in reinforced concrete structures, the mix solution penetrates through the rust pores on the steel and forms hydrated calcium ferrite ($4.CaO.Fe_2O_3.13H_2O$). Additionally, a thin passive layer of iron and calcium hydroxides [$Fe(OH)_2$ and $Ca(OH)_2$] with thicknesses from 1 nm to 100 nm is formed. These products in the vicinity of the steel raise the pH of the concrete pore solution to about 13 (CEFRACOR 2014). This layer is a dense and impenetrable film. When the pH of concrete becomes less than 11.5, it indicates that the pore solution is becoming acidified and the passive layer will degrade (Holder 1999). In the presence of chloride ions or due to carbonation, the alkalinity of the concrete will reduce to pH levels of 9 (Bargaheiser and Butalia 2007) and 8 (Parrott 1987), respectively. The passive layer will be damaged and corrosion will start. This process reduces the cross-sectional area of the rebar and the load bearing capacity of the structure. If corrosion reaches a certain level, it also reduces the bond strength (Almusallam et al. 1996), and degrade the reliability of the adjacent concrete (Jaffer and Hansson 2009). The temperature and relative humidity (RH) have effect on the corrosion. Below freezing point, the pore water will freeze and stop the corrosion. Additionally, tests indicate that the corrosion rate is maximum when the RH is around 90-95% (Tuutti 1982). When concrete is completely saturated, oxygen starvation slows down the corrosion (Broomfield 1997). The chloride-induced corrosion process is described in the following equations (Bentur, Diamond, and Berke 1997):

$$Fe^{2+} + 2Cl^{-} \rightarrow FeCl_2 \quad 3.6$$

$$Fe \rightarrow Fe^{2+} + 2e^{-} \quad 3.7$$

$$\frac{1}{2}O_2 + H_2O + 2e^{-} \rightarrow OH^{-} \quad 3.8$$

$$FeCl_2 + 2H_2O \rightarrow Fe(OH)_2 + HCl \quad 3.9$$

$$Fe^{2+} + 2OH^{-} \rightarrow Fe(OH)_2 \quad 3.10$$

$$2Fe(OH)_2 + \frac{1}{2}O_2 + H_2O \rightarrow Fe(OH)_3 \rightarrow Fe_2O_3 \times 3H_2O \quad 3.11$$

In these reactions, when the chloride ion reaches to the rebar, it activates the surface of the bar to form an anode; two electrons released in this reaction must be consumed elsewhere to preserve electrical neutrality (Broomfield 1997). Therefore, the stable passivized surface film acts as a cathode, and the decomposition of the passive layer starts. After oxidation of the steel, hydroxide forms that leads to corrosion where ferrous hydroxide becomes ferric hydroxide and then hydrated ferric oxide (rust). This reaction happens during a time period in the service life of structure and different factors can alter the rate of corrosion. In Figure 3-1, curve 1 shows regular corrosion due to chloride ion penetration or carbonation induced corrosion; however, if a crack is induced on the surface of the concrete, the initiation period will decrease and follow curve 2 (Jung, Yoon, and Sohn 2003). The initial period shows depassivation and is the time required for the protective layer of the alkaline hydrated cement matrix to be destroyed. The second slope shows the propagation phase, the time when corrosion products form and apply enough stress to the surrounding concrete that the concrete cracks. The service life is reached when the reliability of the structure is impaired (Schiessl 1988).

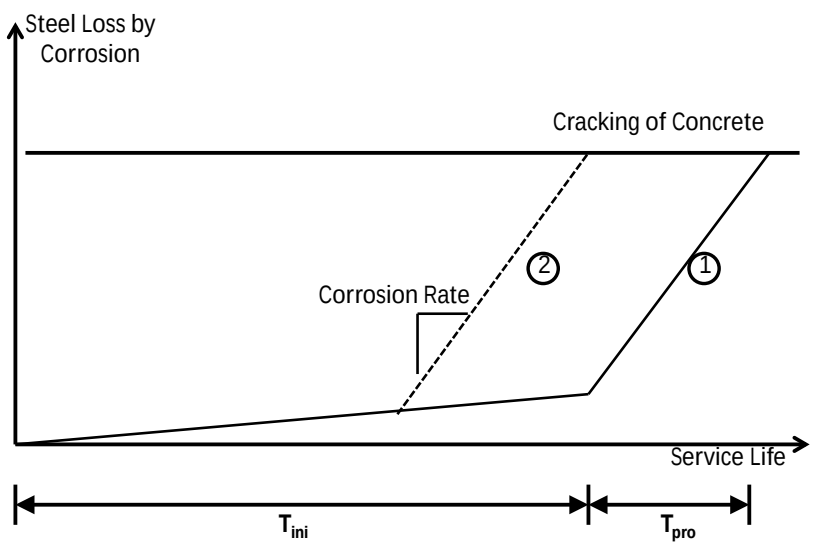

Figure 3-1 Steel corrosion according to time (reprinted from Jung et al. (2003)).

Furthermore, the presence of chloride ion in the concrete changes the chemical composition of the cement paste (Brown and Doerr 2000). It can have a positive effect, such as reduction in bleeding of concrete (Lamond and Pielert 2006), and accelerate some of the concrete properties at early age, but adverse effects are observed in the long term. Increasing the percentage of chloride in concrete or in curing medium causes mechanical properties of concrete such as strength and dynamic modulus to deteriorate (Attar 2016, Attar et al. 2016).

Chloride ions may be present in the mixture due to two reasons: intentional or unintentional addition into the fresh mix and ingress from outside in the hardened state:

- *Addition of chloride in the fresh mix.* Concrete may be contaminated with chloride because of using seawater or brackish water. Portland cement may also contain a small amount of chloride. Or chlorides may be added deliberately as inorganic accelerators; this method was widely used until the mid-1970s (Broomfield 1997). Similarly, other additives in concrete such as ground granulated blast furnace slag may have significant chloride content (Neville 1995). This case can causes immediate corrosion reactions (Schiessl 1988). To reduce the effects of chloride in concrete, different standards recommended different limits on the chloride content. For example, BS 8110 (2005) and EN 206 (2000) permit a chloride ion concentration of 0.2%-0.4% by mass of binder for reinforced concrete. ACI 318 (2011) permits 0.15% water-soluble chloride by weight of cement; ACI 222 (2001) limits this amount to 0.2%.
- *Ingress of chlorides.* Chloride ions may also ingress from outside. This is mostly a concern for structures that are located in or close to a marine environment because of sea salt spray or sea water wetting, or in cold regions, structures are subjected to deicing salt such as NaCl, $CaCl_2$ and $MgCl_2$ where the cycles of wetting and drying repeat with different concentrations of ions.

3.1.3. Accelerated Aging

ASTM E632-82 (1996) defines accelerated aging tests as ones in which the degradation of building materials is intentionally accelerated over the conditions expected in service. In other words, if the aging process of concrete and its degradation is accelerated by means of different chemical or physical processes, it is called accelerated aging. This specific exposure condition provokes the degradation reaction to occur more rapidly than would normally happen in the service environment. In this testing method, it is assumed that the accelerated sample behaves the same way as an in-service structure and a control specimen can measure the changes in properties due to acceleration (Pommersheim and Clifton 1985). It should be noted that there are some limitation in accelerated tests, which Pommersheim (1985) summarized as follows: methods for correlating laboratory results with in-service results are rarely provided; provisions are usually not made for taking different applications into account; the concrete specimens tested in the laboratory have substantially different configurations compared to real-life structures; the factors affecting service life and the degradation mechanics are complex, not well understood and difficult to quantify; sensitive detection methods are needed since changes may be small under normal conditions; results need to be extrapolated, often for exposure periods hundreds or thousands of times longer than the measurement period. It is important to remember that

acceleration can change the mechanism of aging and the performance may not correlate well with the real structure. Regardless of all the limitations, the accelerated testing method is usually the best solution to overcome the long waiting periods extending to several decades when aging is to be observed under normal service conditions.

The following methods are used individually or sometimes together to accelerate aging of concrete due to ASR and corrosion:

- Creating a corrosion cell with or without impressed current through the rebar
- Adding chemicals to the mixture
- Subjecting to high temperatures
- Subjecting to high humidity and wet-dry cycles
- Subjecting to high levels of chemical solutions

There are different studies on the acceleration of alkali-silica reactivity in the lab and mostly two methods are being used. In the first method, ASR was accelerated by immersing the specimens inside the alkaline solutions at different temperatures (Parsons and Insley 1944, Fournier and Bérubé 1993, Mukhopadhyay et al. 2009, Gillott and Soles 1993, Harrisson, Varma, and Winter 1987). In some other cases, a high-alkali content cement was also used (Stanton 1943b, Jones and Tarleton 1958b, Davis and Oberholster 1988). The other method that is frequently used is adding sodium hydroxide or other alkali hydroxide to the mixing water or concrete paste, and keeping the specimens at different temperatures (Diamond and Ong 1994, Smaoui et al. 2005, Poole 2007, Temuujin, Williams, and Riessen 2009, Nuruddin et al. 2011, Garci Juenger and Jennings 2011, Memon et al. 2013, Gao et al. 2013, Kupwade-Patil and Allouche 2013, Bahadure and Naik 2013). Adding NaOH to the mixing water mostly increases the pH in the pore solution, and mixing it to the concrete paste increases the internal alkali content of the mixture (Poole 2007). Immersing in solution is a practical approach for small specimens in a laboratory environment. However, for real-size structures, immersion is not easily achievable and the second method is more practical.

Some studies investigated the effect of fly ash and its type on ASR (Shehata and Thomas 2000, Thomas et al. 2011). Fly ash in the concrete reduces the ASR gel expansion (Blackwell et al. 1992, Nagataki, Ohga, and Inquel 1991). This reduction is due to three different mechanisms: dilatation of the cement alkalis by mixing the cement with fly ash, low availability of calcium to react with the expansive gel, and lower permeability to water and low diffusivity of alkalis from outside (Shehata and Thomas 2000, Thomas et al. 2011, Detwiler 1997).

For accelerating corrosion, in most studies, a corrosion cell is created and the corrosion is driven by passing a direct current through the reinforcement. To create the corrosion cell, a wet sponge (Silva 2013, Hansson, Poursaee, and Laurent 2006, Jung, Yoon, and Sohn 2003, Ortega et al. 2011) or direct immersion inside a saline solution was adopted (Yu et al. 2010, Johnson 2010, Okba, El-Dieb, and Reda 1997, Shayanfar and Ghalehnovi 2007). Passing current is an effective approach for accelerating corrosion; however, it comes with various challenges for real-size structures related to creating the electrochemical cell and achieving uniform corrosion in reinforcement distributed throughout the structure. Adding salts directly to the mixture is another method that

was used previously and showed good results in accelerating corrosion (Al-Attar and Abdul-Kareem 2011, Jang, Iwasaki, and Weiblen 1995). The effect of adding different salts such as KCl, NaCl and $CaCl_2$ to the concrete mixture with different percentages from 0 to 2.0% chloride by weight of cement on the corrosion of rebar has been studied. Researchers looked at the pH, electrical conductivity and corrosion rate in concrete containing these salts. Some studies also looked at the values of chloride to hydroxyl concentration. The importance of this value is that when it exceeds 0.6, the chloride ion starts to break down the passive layer; this amount is approximately equal to a concentration of 0.4% chloride by weight of cement if chloride salts are cast into concrete and 0.2% if they diffuse into it (Broomfield 2007, Hausmann 1967). This ratio is also related to the pH of the pore water and the amount of chloride in the pore water (Holder 1999).

Diamond (1986) studied the effect of adding $CaCl_2$ and NaCl to concrete mixtures and measured the values of Cl^-/OH^- in the pore solution. No difference was observed between $CaCl_2$ and NaCl. However Pruckner and Gjørv (2004) showed that adding NaCl to the mix as a source of chloride results in a higher pH and lower Cl^-/OH^- ratio compared with $CaCl_2$. There have been other studies that made similar investigations and came to the conclusion that the corrosive effect of NaCl is significantly less than that of $CaCl_2$ (Helmuth et al. 1993, Jang, Iwasaki, and Weiblen 1995, Kelestemur and Yildiz 2006, Pakshir and Esmaili 1998, Pruckner and Gjørv 2004). They also found that concrete containing calcium chloride has more open pore structures and lower pH compared to the other salts (Hansson, Frølund, and Markussen 1985). However, the impacts of this approach on various properties of the concrete mixture have not been studied in detail before.

There have been a handful of studies in the literature on accelerated aging of structural members for ASR and corrosion (Folliard et al., 2006; Deschenes et al., 2009; Talley et al., 2016). However, in almost all of these studies aging was accelerated through application of heat and/or higher exposure to chemicals from the environment. These techniques are not easily applicable at the structural scale; therefore, in this study, to accelerate aging due to ASR and corrosion, the addition of alkalis and chloride was investigated as a practical method at the structural scale.

3.2. EXPERIMENTAL PROGRAM

3.2.1. Design of Concrete Mixtures

3.2.1.a. Fine and coarse aggregates

In order to deliberately accelerate ASR for laboratory trials, a reactive fine aggregate (silica sand from the Brazos River near Houston, TX) was used. The coarse aggregate was regular and non-reactive. The gradations of coarse and fine aggregates are presented in Figure 3-2 (see also Table A-1 and Table A-2 in the appendix).

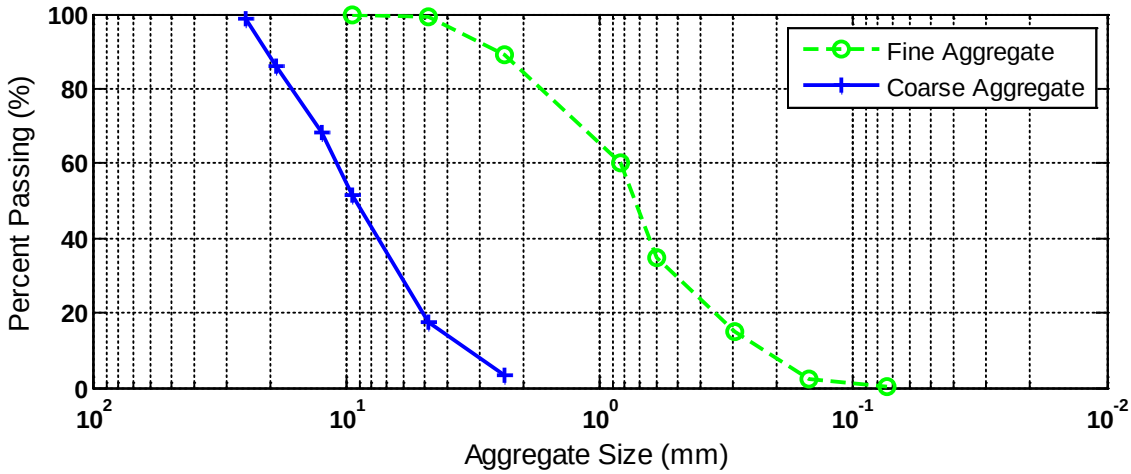

Figure 3-2 Gradations of aggregate used in preparing concrete specimens.

For certain tests on hardened concrete, it is necessary to know the density, relative density and absorption of fine and coarse aggregate. Therefore these properties are measured based on ASTM C127-12 (2012d) and ASTM C128-12 (2012e) for coarse and fine aggregate, respectively. The results of these tests are shown in Table 3-1.

Table 3-1 Density of Fine and Coarse Aggregate.

Aggregate	Relative density (OD[1])	Relative density (SSD[2])	Density (OD) kg/m^3	Density (SSD) kg/m^3	Apparent density
Fine	2.40	2.42	2395	2410	2430
Coarse	1.62	1.64	1620	1635	1645

[1]OD: oven dry, [2]SSD: saturated surface dry

3.2.1.b. Potential alkali reactivity of fine aggregate

A mortar bar test was performed on two different mixes. One of the mixes was prepared following the recommendations of ASTM C1260 (2007) to measure the potential for deleterious ASR of fine aggregate. The dimensions of the specimen are shown in Figure 3-3. Note that the reactivity of fine aggregate is tested here and these specimens were not prepared during the main casting but at a later date using the same mixture ingredients. Figure 3-4 show the expansion of this mix up to 90 days.

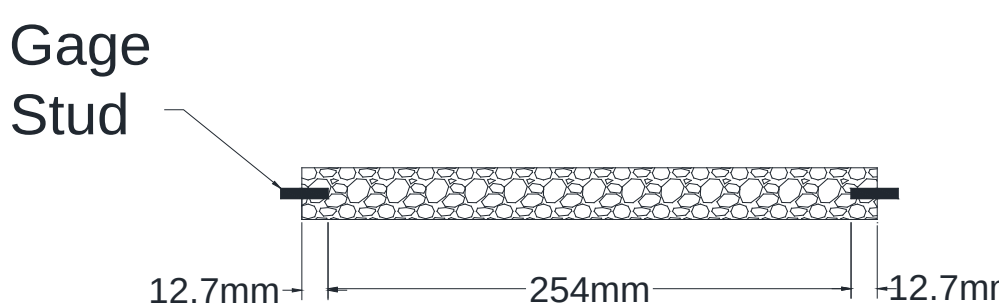

Figure 3-3 Specimen dimension for ASR expansion tests based on ASTM C1260 (2007).

At 14 days, if the expansion is less than 0.1%, the aggregate is characterized as non-reactive. On the other hand, when the expansion is over 0.2%, it means that the aggregate is reactive. If expansion falls between 0.1% and 0.2%, the test is inconclusive regarding the reactivity of the aggregate. From Figure 3-4, it is seen that the expansion is about 0.202%, which shows that the aggregates are reactive.

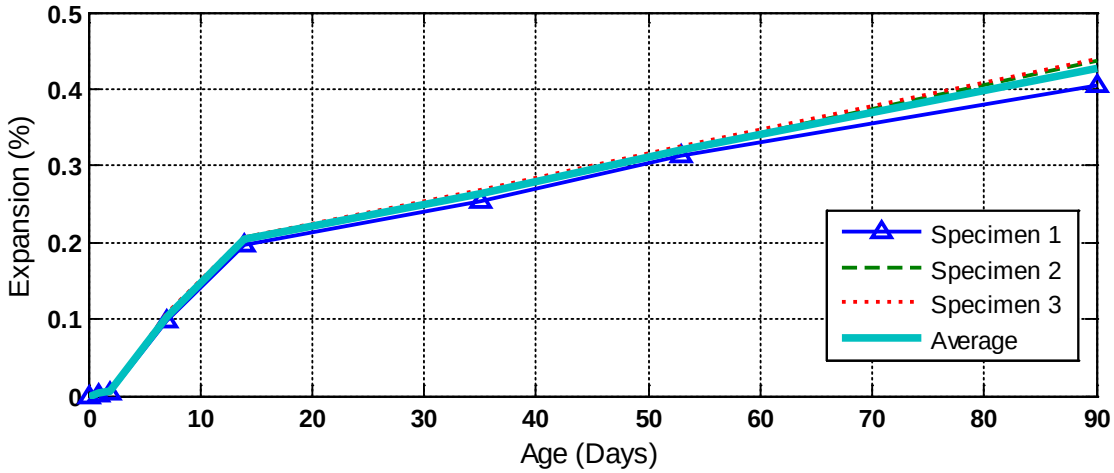

Figure 3-4 Expansion of regular mortar mix.

3.2.1.c. Potential alkali reactivity of coarse aggregate

The reactivity of coarse aggregate was also measured using the proposed accelerated concrete prism method (Berube and Fournier 1993) by increasing the temperature to 80°C and immersing the specimens in 1N NaOH. However, it should be noted that this test procedure is too severe compared to the method presented in ASTM C1293 (2008b) for finding the reactivity of coarse aggregate in long-term testing. The limit suggested for this test was 0.04% at 4 weeks. Since the reactivity of coarse aggregate was intended to be measured, non-reactive fine aggregate was used in the specimens' preparation. Figure 3-5 shows the dimensions of specimen prepared for this test. The results of this test are shown in Figure 3-6. According to the result, shown in Figure 3-6, the coarse aggregate used was not reactive.

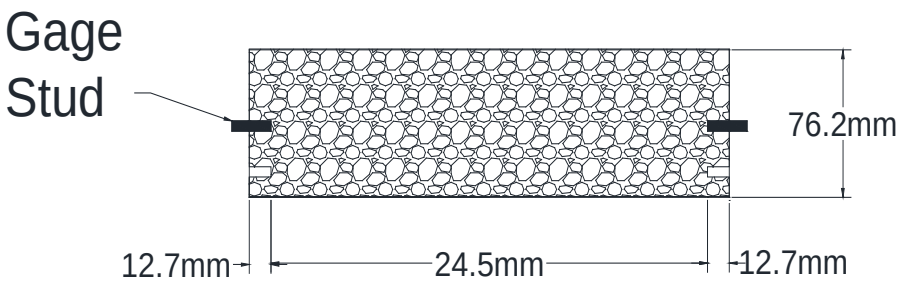

Figure 3-5 Specimen dimension for ASR expansion tests based on ASTM C1293 (2008b).

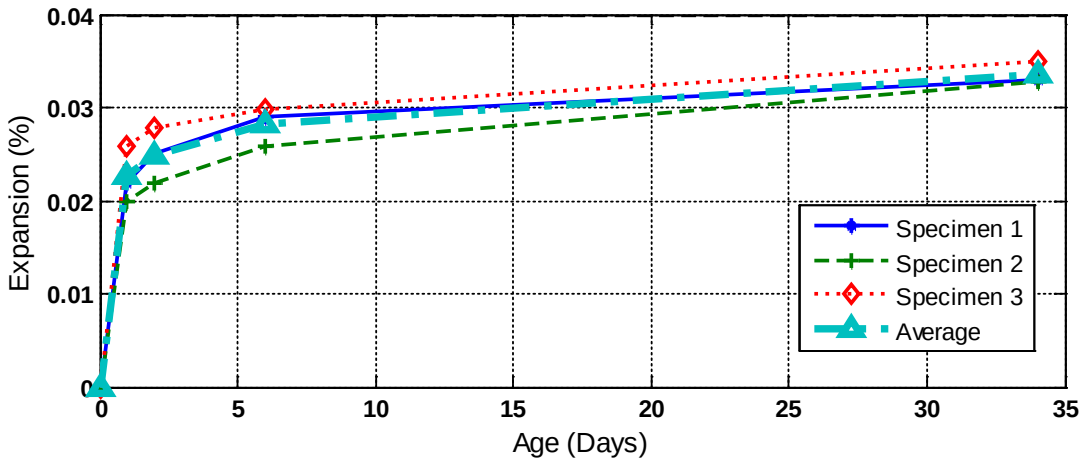

Figure 3-6 Expansion of coarse aggregate concrete mix.

3.2.1.d. Portland cement

Based on ASTM C150 (2012b), there are ten types of Portland cement, I through V, air-entraining type IA, IIA, IIIA, and moderate heat of hydration II(MH), II(MH)A. In this study, type I/II Portland cement was used, which satisfies requirements for both Type I and Type II. In this cement, the strength requirements meet those for Type I, and composition requirements meet those for Type II. The chemical composition of the cement is given in Table 3-2. Physical properties of the cement reported by the manufacturer are provided in Table 3-3. The cement was tested based on ASTM C150 (2012b).The Na_2O equivalent in weight percent of cement was 0.49.

Table 3-2 Chemical Composition of Cement.

Compound	Oxide (%)							Compounds (%)		
	SiO_2	Al_2O_3	Fe_2O_3	CaO	MgO	SO_3	Na_2O_{eq}	C_3S	C_2S	C_3A
Percentage	21.11	4.43	3.87	63.96	1.54	2.48	0.49	58	17	5

Table 3-3 Physical and Mechanical Property Test Results on Cement.

Physical Item	Spec. Limit	Test Result
Air content of mortar (volume %)	12 max	9
Fineness (cm^2/g) (Air permeability)	2800 min	3993
# 325 Fineness, % pass	Not Applicable	97
Autoclave expansion (%)	0.80 max	-0.01
Compressive strength (MPa)		
1 Day	Not Applicable	13.5
3 Days	12.0	22.0
7 Days	19.0	32.4
28 Days	Not Applicable	Not Applicable
Setting time (minutes) (Vicat)		
Initial	Not less than 45	84
Final	Not more than 375	210
False set (%)	Not Applicable	Not Applicable

3.2.1.e. Fly ash

Fly ash is the finely divided residue that results from the process of combustion of ground or powdered coal. Fly ash is classified in three different types: Class N, Class F, and Class C. Class N fly ash is from raw or calcined natural pozzolans; Class F is produced from burning anthracite or bituminous coal; and Class C is produced from burning lignite or subbituminous coal. For this study, Class F fly ash was used. The chemical composition of fly ash is shown in Table 3-4. The Na_2O equivalent in fly ash was 0.84 weight percent. Physical properties of fly ash as reported by the manufacturer are provided in Table 3-5. The fly ash was tested based on ASTM C618 (2012a).

Table 3-4 Chemical Component of Fly Ash.

Compound	SiO_2	Al_2O_3	Fe_2O_3	CaO	MgO	SO_3	Na_2O	K_2O	Na_2O_{eq}
Percentage	58.21	24.06	4.13	8.12	1.96	0.29	0.2	0.97	0.84

Table 3-5 Physical Property Test Results on Fly Ash.

Physical Tests	Results	ASTM C618 (2012a) Class F/C	AASHTO M 295 (2011) Class F/C
Moisture Content, %	0.01	3.0 max.	3.0 max.
Loss on Ignition, %	0.44	6.0 max.	5.0 max.
Amount Retained on No. 325 Sieve, %	30.72	34 max.	34 max.
Specific Gravity	2.22		
Autoclave Soundness, %	-0.03	0.8 max.	0.8 max.
Strength Activity Index with Portland Cement at 7 days, % of Control	75	75 min.	75 min.
Strength Activity Index with Portland Cement at 28 days, % of Control	87.2	75 min.	75 min.
Water Required, % of Control	96.7	105 max.	105 max.
Loose Bulk Density, kg/m^3	1081.2		

3.2.1.f. Chemical admixtures

Chemical admixtures are the ingredients in concrete that help enhance the properties of hardened concrete during the process of preparation and mixing, transportation, placement and curing. Different types of these admixtures are used based on the necessary function for the concrete mixture: water-reducing admixtures, retarding admixtures, accelerating admixtures, superplasticizers, corrosion inhibition admixtures, workability enhancement, etc. For the self-consolidated mixture prepared for this study, two types of admixtures are used, MasterGlenium as superplasticizer and MasterPozzolith as normal plasticizer; both of which have water-reducing function. The latter was also used to control the setting time.

3.2.1.g. Reinforcing bars

In the design of prototype casks, threaded rebar #19 is used, and #10 bar size conforms to the final scaled cask design. Therefore, tensile testing is performed on #10 and #19 rebar based on

ASTM A370 (2012f) to characterize the stress-strain behavior. The results are shown in Figure 3-7 and Figure 3-8 for #10 and #19 rebar, respectively. The yield strengths of #10 and #19 rebar were found as 551.4 MPa and 429.5 MPa, respectively. Other properties of the rebar are provided in Table 3-6. It is noted here that the yield strength of the bars vary depending on the manufacturer and batch of steel. Both rebar sizes tested here had acceptable yield strength.

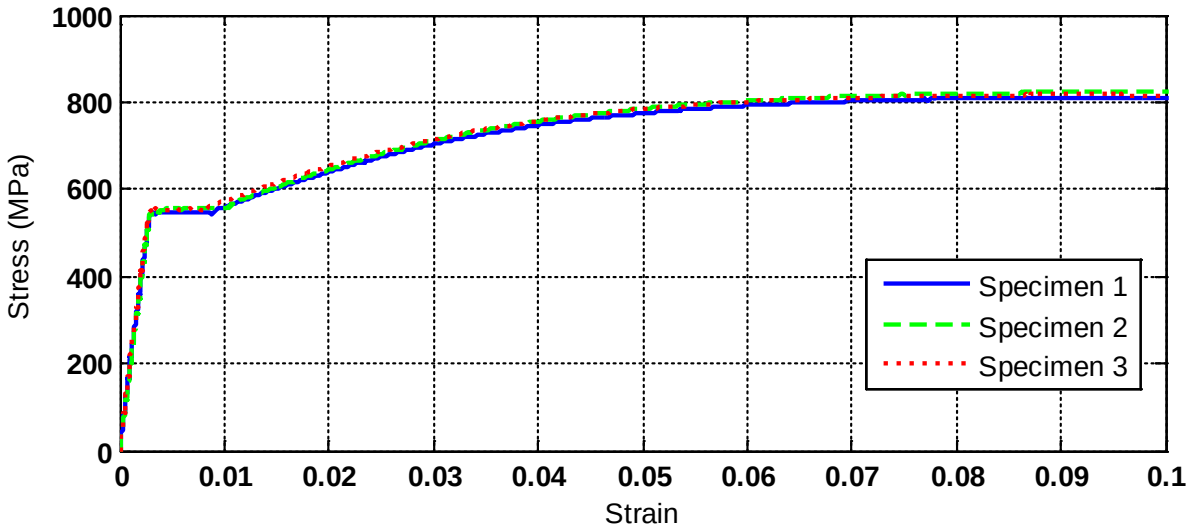

Figure 3-7 Tensile stress-strain behavior of #10 rebar.

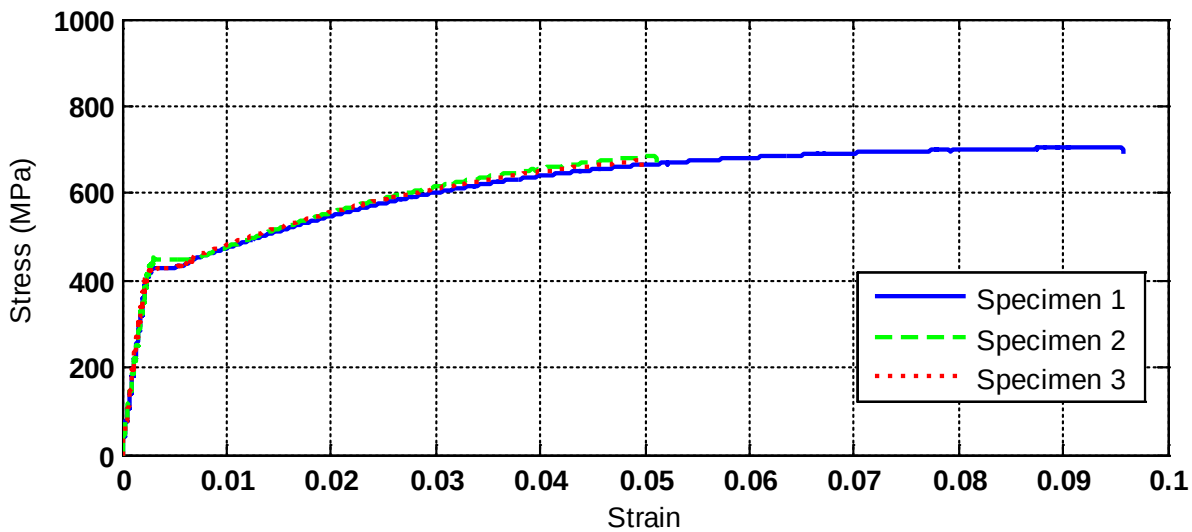

Figure 3-8 Tensile stress-strain behavior of #19 rebar.

Table 3-6 Properties of Rebar.

Rebar Size	Yield Stress (MPa)	Ultimate Stress (MPa)	Modulus of Elasticity (GPa)
#10	551.41	817.66	190.98
#19	429.54	728.78	175.37

3.2.2. Design of Concrete Mixtures

To understand the effects of NaOH and $CaCl_2$, which were used as aging accelerators, on the fresh and hardened properties of concrete (such as slump, which is an indicator of workability of concrete, setting time and compressive strength), and to choose the maximum practical mixing amounts before the complete set of specimens were prepared, four different mixtures were studied. The first mix was prepared as a control without any additional $CaCl_2$ or NaOH. Sodium hydroxide was added to the second mix and the other two mixtures were prepared by adding calcium chloride. Table 3-7 shows the mixed proportions.

As explained above, using fly ash replacement of cement is one of the most effective ways to reduce ASR in concrete. Therefore, based on a literature review (Stanton 1943a, Jones and Tarleton 1958a, Ferraris 1995, Smaoui et al. 2005, Bahadure and Naik 2013), to get a higher expansion rate in a shorter period, fly ash was omitted from the second mix and 0.8% NaOH by weight of cement as an extra alkaline was added to the mixture. To accelerate corrosion, additional chloride ions (Cl^-) as $CaCl_2$ flakes were added in mixtures three and four, amounting to 4% and 7%, respectively, by weight of concrete. It should be noted that the amount of water for these mixes was adjusted based on the moisture content of coarse and fine aggregates. The percentage of evaporable moisture in a sample of aggregate was determined by drying both surface moisture and moisture in the pores based on ASTM C566 (2013d). The results of this test are provided in Table 3-8. Two tests were performed for each of the fine and coarse aggregates to obtain the results shown in Table 3-8.

Table 3-7 Proportions of Concrete Mixtures for Phase 1.

Material	Unit	Mixture 1	Mixture 2	Mixture 3	Mixture 4
Cement (~0.57% alkali content)	Kg	12.84	37.70	12.84	12.84
Type F Fly Ash	Kg	4.26	0.00	4.26	4.26
3/8" Pea Gravel (~0.3% expansion)	Kg	48.67	48.67	48.67	48.67
Sand River (~0.3% expansion)	Kg	43.09	43.09	43.09	43.09
Water	Kg	5.72	5.72	5.72	5.72
Admix #1 (Pozzolith 200N)	Ml	45.84	45.84	45.84	45.84
Admix #2 (Glenium 7500N)	Ml	91.97	91.97	91.97	91.97
Additional Alkali (NaOH)	Kg	-	0.15	-	-
Additional Chloride (CaCl2)	Kg	-	-	0.78	1.36

Table 3-8 Moisture Contents of Aggregates in Phase 1.

Aggregate	Mass of original sample (g)	Mass of dried sample (g)	Moisture content (%)
Pea Gravel #1	828	804	2.99
Pea Gravel #2	884	860	2.79
Sand #1	427	403	5.96
Sand #2	417	390	5.84

Figure 3-9 shows different tests performed on the fresh concrete. The results of these tests for the four mixes are shown in Table 3-9. Adding chemicals especially calcium chloride, noticeably reduced the workability of the concrete. Adding 7% chloride by weight of concrete resulted in a slump of zero for this mix. The added chemicals considerably changed the setting time of the concrete as well. The effect of calcium chloride was substantially more than that of sodium hydroxide; in particular mixture no. 4 set in about 15 minutes, which was considered unacceptable.

Figure 3-9 Tests on fresh concrete: (a) mix temperature (b) slump (c) sieving the concrete for setting time test.

Table 3-9 Fresh Properties of Concrete Mixtures.

Mix No.	Ambient Temp. (˚F)	Fresh Concrete		
		Mix Temp. (˚F)	Slump (mm)	Setting Time (min)
1	24	24.4	254	285
2	23	24.4	190.5	240
3	25.5	24.4	203.2	180
4	27.6	29.4	0	15

A compression test was performed on 101.6 x 203.2 mm cylinders at ages of 1, 7 and 28 days. The results of these tests are provided in Figure 3-10. As mentioned above, the last mix set in 15 min; therefore, no testing for hardened properties was performed for mixture no. 4. Based on these findings, 4% chloride by weight of cement was deemed suitable for the accelerated corrosion mixture design and mixture no. 2 was used to accelerate ASR. Furthermore, the results indicate that the addition of chloride higher than 4% will reduce the workability to an unacceptable level. Therefore, for the second phase of the research, to better understand the effect of the addition of these chemicals, different amounts between 0% to 4% chloride by weight of cement and 0% to 0.8% sodium hydroxide by weight of cement were chosen and studied.

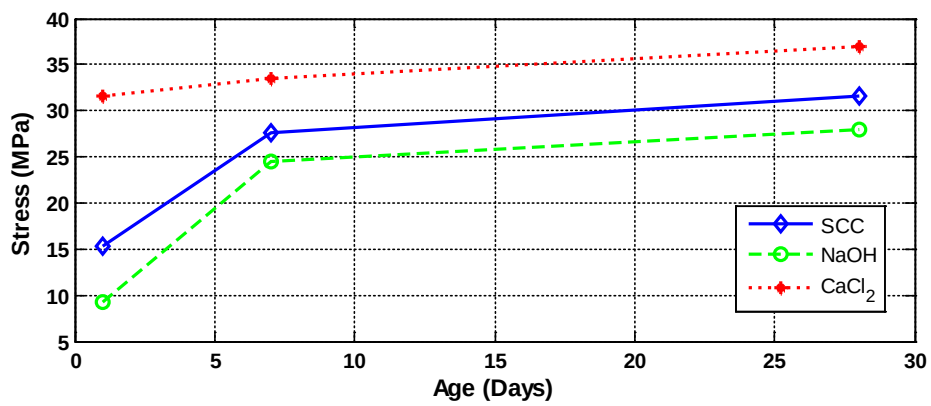

Figure 3-10 Compressive strength of concrete mixtures.

Once the molds and test setups were prepared, the first phase of the project proceeded and the specimens were cast alongside the three scaled physical models of the casks with the mixtures designed as mentioned in the previous sections. Each mixture was prepared separately. These specimens were kept outside close to the casks and they were demolded at 7 days.

The second phase of the project was performed on 8 other mixtures with different amounts of NaOH and $CaCl_2$. The first four were prepared with 0%, 0.2%, 0.4% and 0.8% of NaOH by weight of cement and the second four were prepared with 0%, 1%, 2% and 4% of chloride ion by weight of cement. The mixture proportions for these concretes are shown in Table 3-10. In this table Admix #1 is Pozzolith 200N and Admix #2 is Glenium 7500N. These series of specimens were kept inside the lab for their first 28 days then were moved to the outside environment to go through the environmental cycles of temperature and humidity.

The naming of these mixtures in the texts are as follows: NaOH-0, NaOH-2, NaOH-4 and NaOH-8 for mixture with 0%, 0.2%, 0.4% and 0.8% of NaOH by weight of cement, respectively. Similarly, four $CaCl_2$ mixtures, $CaCl_2$-0, $CaCl_2$-1, $CaCl_2$-2, $CaCl_2$-4 were used for mixtures with addition of 0%, 1%, 2% and 4% chloride ion into the mixture, respectively. Between phases 1 and 2, a total of 880 specimens were prepared for this study.

Table 3-10 Proportions of Concrete Mixtures for Phase 2.

Material	Unit	NaOH-0	NaOH-1	NaOH-2	NaOH-4	$CaCl_2$-0	$CaCl_2$-1	$CaCl_2$-2	$CaCl_2$-4
Cement	kg/m^3	431.6	431.6	431.6	431.6	323.8	323.8	323.8	323.8
Fly Ash	kg/m^3	-	-	-	-	107.6	107.6	107.6	107.6
Pea Gravel	kg/m^3	1227.5	1227.5	1227.5	1227.5	1227.5	1227.5	1227.5	1227.5
Sand River	kg/m^3	1087.0	1087.0	1087.0	1087.0	1087.0	1087.0	1087.	1087.0
Water	kg/m^3	213.1	213.1	213.1	213.1	213.1	213.1	213.1	213.1
Admix #1*	ml/m^3	1155	1155	1155	1155	1155	1155	1155	1155
Admix #2**	ml/m^3	2320	2320	2320	2320	2320	2320	2320	2320
Add. NaOH	kg/m^3	-	0.92	1.84	3.67	-	-	-	-
Add. $CaCl_2$	kg/m^3	-	-	-	-	-	4.92	9.84	19.68

3.2.3. Testing Plan for First Phase of Specimens

As mentioned previously, three different concrete mixtures are considered. The first mixture is regular self-consolidating concrete (SCC) (control) following the requirements of temperature and radiation shielding for dry casks as obtained from the literature and relates to the case study application. The second mixture accelerates ASR. This was achieved by increasing the alkalinity of the concrete mixture through sodium hydroxide (NaOH) addition and by replacing the fine aggregates with reactive ones. The third mixture design is a corrosive mixture, which was

achieved by adding chloride ions (in the form of $CaCl_2$) to the fresh concrete. The specimens from these mixtures were prepared along with the casks. To plan the material testing, a comprehensive list of properties related to reinforced concrete was prepared as shown in Table 3-11. Among these properties, a selection was made considering the available knowledge in the literature and the objectives of this research. The selected properties to be measured are shown in bold font.

Table 3-11 Concrete Properties for Material Testing.

Category	Property
Mix Properties	Aggregate content, mixing water content, water-to-cement ratio
Fresh Concrete	**Density, setting time, slump**, filling ability, passing ability, segregation resistance, air content
Mechanical	**Static elastic modulus, static Poisson's ratio**, dynamic elastic modulus, dynamic Poisson's ratio, **tensile strength**, **compressive strength**, flexural strength, tensile ductility, compressive ductility, fracture energy, creep function, shrinkage function, shear strength, dynamic shear modulus, bond strength, slip behavior
Physical	Concrete cover, air Content, acidity, **density**, **porosity**, chemical composition (Scanning Electron Microscopy/ Energy-dispersive X-ray spectroscopy (SEM/EDS)), **chloride content**, sorptivity, **absorption**, carbonation, leaching, pH, **cracking,** honeycombing, moisture content, sulfate resistance
Thermal	Conductivity, diffusivity, capacity, expansion/contraction
Transport	Chloride diffusivity
Other	Alkali silica reactivity, alkali carbonation reaction, corrosion potential, elongation

Material testing was mainly based on American Society for Testing and Materials (ASTM) and some European standardized tests. These tests were performed on fresh and hardened concrete. For fresh concrete setting time, horizontal free flow and density of concrete were measured. Tests for hardened concrete were density, absorption, and void (physical properties); compressive, splitting tensile and flexural (mechanical properties); chloride penetration rate, and ASR mortar bar expansion (other properties). The test plans are shown in Table 3-12.

Table 3-12 Test Plan for Concrete Mixtures in Phase 1.

Temperature (ºC)	Room Temperature
Standards/ References	ASTM C39 (2012), ASTM C496 (2011), ASTM C78 (2010), ASTM C1260 (2007), ASTM C1293 (2008), ASTM G1-03 (2011), NT (Nordtest)-build 208 (1996), NT-build 443 (1995)
Specimen type	Cylinders for compressive and split tensile strength (101.6 x 203.2 mm)
	Cylinders for density, absorption and void (76.2 x 152.4 mm)
	Un-notched prisms for flexural strength (101.6 x 101.6 x 355.6 mm)
	Chloride penetration specimens (for SCC and NaOH mixes) Diameter at least 75 mm and not more than 3 times the maximum aggregate size, and length should be minimum 100 mm for Nordtest
	Lollipop specimen for mass loss measurement 76.2x 254 mm cylinder, having #10 bar in the middle 127x 254 mm cylinder, having #19 bar in the middle
	Mortar-bar specimen for ASR (for SCC only) 25.4 x 25.4 x 285.75 mm prisms having 254 mm gauge length for reactivity of fine aggregate 76.2 x 76.2 x 285.75 mm prisms, having 254 mm gauge length for reactivity of coarse aggregate
Property measured	Compressive strength, splitting tensile strength, flexural strength, fracture energy, bond strength, alkali reactivity, density, absorption and void, pH
Test ages	Compressive and splitting tensile strength tests: 1, 3, 7 and 28 days, 6 and 12 Other tests: 28 days, 6 and 12 months

3.2.4. Testing Plan for Second Phase of Specimens

To test the effect of different amounts of NaOH and $CaCl_2$ on the concrete mixture and to determine the optimum amounts of chemicals to add for accelerating the aging process in the concrete structures, additional specimens were prepared as mentioned previously. Four different mixtures with 0%, 0.2%, 0.4% and 0.8% NaOH by weight of cement were considered. The fly ash was removed from these mixes and replaced with cement in order to accelerate ASR. Four other mixtures with 0%, 1%, 2% and 4% chloride ion by weight of cement have also been prepared. Table 3-13 shows the testing program for NaOH and $CaCl_2$ mixtures.

Table 3-13 Test Plan for Concrete Mixtures Containing Different Levels of NaOH and $CaCl_2$.

	NaOH	$CaCl_2$
Standards/ References	ASTM C39 (2012), ASTM C496 (2011), ASTM C78 (2010), ASTM C469 (2014), ASTM C805 (2013)	ASTM C39 (2012), ASTM C496 (2011), ASTM C78 (2010), ASTM C469 (2014), ASTM G1-03 (2011), ASTM C805 (2013)
Specimen type	Cylinders for compressive and split tensile strength (101.6 x 203.2 mm)	
	Cylinders for density, absorption and void (76.2 x 152.4 mm)	
	Un-notched prisms for flexural strength and measuring the length change (101.6 x 101.6 x 355.6 mm)	
	Rapid chloride penetration specimens Cutting 50.8 mm height of 101.6 x 203.2 mm Cylinders	Lollipop specimen for mass loss and half-cell potential measurement 76.2 x 254 mm cylinder, having #3 bar in the middle
Property measured	Compressive strength, splitting tensile strength, flexural strength, static modulus of elasticity, static Poisson's ratio, rapid chloride permeability, density, absorption and void, ultrasonic pulse velocity (UPV), surface resistivity, length change	Compressive strength, splitting tensile strength, flexural strength, static modulus of elasticity, static Poisson's ratio, rapid chloride permeability, density, absorption and void, UPV, surface resistivity, half-cell potential, corrosion (mass loss)
Test ages	**Flexural test:** 28 days and 6 months Density, absorption and void: 28 days **Other tests:** 7 and 28 days, 3 and 6months	
Specimen number	A minimum of 3 specimens will be tested at each age and for each test	

3.2.5. Testing Plan for Already Aged Specimens Obtained from a Research Nuclear Reactor

TRIGA (Training, Research, Isotopes, and General Atomics) is a class of small reactors which are designed and built for scientific institutions and universities. Specimens from the thirty-eight-year-old research reactor TRIGA MARK II, located inside a building at the campus of University of Illinois at Urbana Champaign (UIUC), which was decommissioned in 2012, were secured for testing and analysis in this study. Specimens 203 mm in diameter and 457 mm in length were obtained. These specimens were used for material characterization at the University of Houston (UH). All the samples were shipped to UH from UIUC.

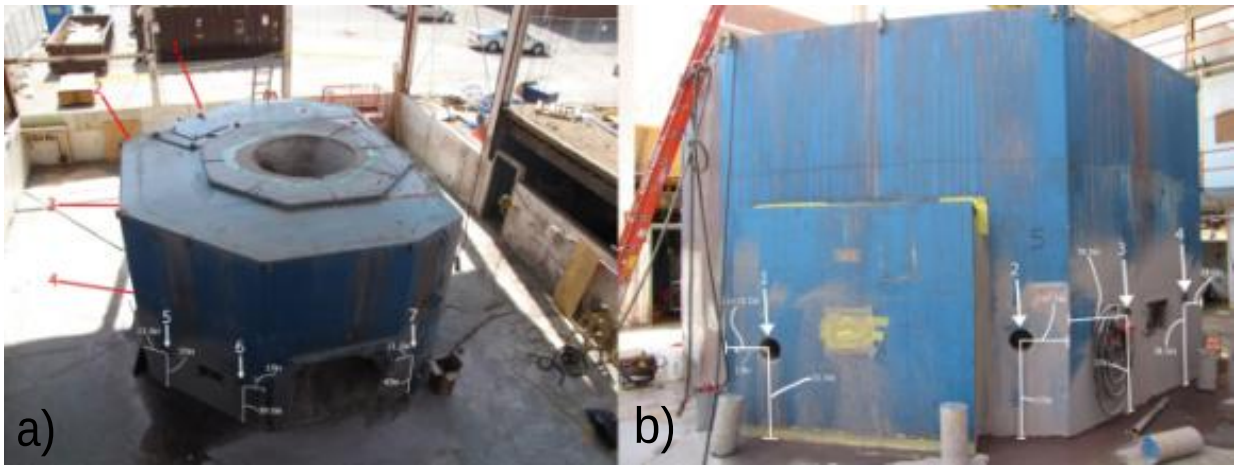

Figure 3-11 (a) Picture of the biological shielding wall of the decommissioned UIUC TRIGA reactor. (b) Numbered holes show the locations from where the concrete samples were taken. Cylindrical shaped samples in front of the holes can also be seen.

Figure 3-12 Picture of the seven samples.

The testing plan considered for these specimens is presented in Table 3-14. To perform mechanical testing on these concrete samples, it was required to drill smaller cores taken from the TRIGA Reactor.

Table 3-14 Test Plan for TRIGA Specimens.

Standards/ References	ASTM C39-12 (2012c), ASTM C496-11 (2011b), ASTM C642-13 (2013b), NT-build 208 (1996), NT-build 443 (1995), SEM test
Specimen type	Cylinders for compression testing (Diameter: max [94 mm, at least two times the nominal maximum size of the coarse aggregate]. Length: between 1.9 to 2.1 of diameter)
	Chloride Penetration Specimens Diameter at least 75 mm and not more than 3 times maximum aggregate size and length should be minimum 100 mm for ***Nordtest*** (NT-build 1995)
Property measured	Compressive strength, splitting tensile strength, chloride amount, chloride permeability, alkali reactivity, density, absorption and void, carbonation depth

3.3. RESULTS

3.3.1. Fresh Properties of Concrete

Addition of different amounts of sodium hydroxide and calcium chloride affects the fresh properties of concrete such as setting time, density and slump. These are discussed in this section.

3.3.1.a. Setting time

The degree of stiffening of a mixture is measured based on ASTM C403 (2008a) and using the penetration resistance apparatus. After the concrete is mixed, it is sieved through the 4.75 mm sieve; thereafter, the mortar obtained is mixed thoroughly and placed inside a cylindrical container with a size of 76.2 x 76.2 mm. Prior to making a penetration test, the bleeding is removed using a pipette. The force for penetrating the needle 25 mm into the mortar is measured every hour.

Calcium chloride is one of the inorganic accelerators that is being used in the construction of concrete structures to decrease the setting time (or increase the hardening rate). In this study, the addition of 4% chloride in the concrete mixture decreased the setting time from 285 minutes to 180 minutes, which is about 37% reduction. The results of addition of $CaCl_2$ and NaOH to the mixtures and their effect on setting time are shown in Table 3-15. It was seen that the setting time decreased substantially for the $CaCl_2$ mixture. The effect of NaOH on the setting time was less drastic. Different studies investigated the effect of alkali on these two properties (Hewlett 2004, Allahverdi and Ghorbani 2006, Memon et al. 2013). Their results indicate the reduction in setting time of concrete is in accordance with the results of this study.

Table 3-15 Setting Time of Fresh Concrete, Phase 1.

Mix	Setting Time (min)
SCC_PH1*	285
NaOH-8_PH1	240
$CaCl_2$-4_PH1	180

*PH1 indicates phase 1 experiments

3.3.1.b. Density

Density measurements on fresh concrete based on the gravimetric method of ASTM C1611 (2009b) were performed. The results are provided in Table 3-16 through Table 3-18. The density of fresh concrete in all mixtures was found to be approximately the same and these chemicals do not have a significant effect on density.

Table 3-16 Density of Fresh Concrete, Phase 1.

Mix	Average Density (g/cm^3)
SCC_PH1	2.325
NaOH-8_PH1	2.319
$CaCl_2$-4_PH1	2.347

Table 3-17 Density of Fresh Concrete, NaOH Mixtures, Phase 2.

Mix	Average Density (g/cm^3)
NaOH-0_PH2*	2.36
NaOH-2_PH2	2.41
NaOH-4_PH2	2.42
NaOH-8_PH2	2.38

*PH2 indicates phase 2 experiments

Table 3-18 Density of Fresh Concrete, $CaCl_2$ Mixtures, Phase 2.

Mix	Average Density (g/cm^3)
$CaCl_2$_0_PH2	2.31
$CaCl_2$_1_PH2	2.36
$CaCl_2$_2_PH2	2.33
$CaCl_2$_4_PH2	2.30

3.3.1.c. Horizontal free flow (slump)

A horizontal free flow test is performed on fresh concrete and passing abilities of the concrete mixtures were measured based on ASTM C1688 (2013a). This test measures the behavior of a compacted inverted cone of concrete under gravity as shown in Figure 3-13.

Figure 3-13 Slump test.

The results are also provided in Table 3-19, Table 3-20 and Table 3-21. The slump was found to be very similar in each series of the mixtures. However, the addition of chloride, especially when the chloride amount is in higher concentration decreased the workability and slump of the concrete mixture. The difference between the measured slump for each series and in different phases is due to the differences in the volumes of the mix in each phase. The volume of concrete in the first phase was 2.3 m^3 and this volume for the second phase for each mix was about 3.5

ft^3. Furthermore, different temperatures at the time of pouring concrete and casting the specimens is another source of difference.

Table 3-19 Slump Test Results, Phase 1.

Mix	Average Slump (mm)
SCC_PH1	271.8
NaOH-8_PH1	228.6
$CaCl_2$-4_PH1	275.1

Table 3-20 Slump Test Results, NaOH Mixtures, Phase 2.

Mix	Average Slump (mm)
NaOH-0_PH2	19.1
NaOH-2_PH2	25.4
NaOH-4_PH2	25.4
NaOH-8_PH2	25.4

Table 3-21 Slump Test Results, $CaCl_2$ Mixtures, Phase 2.

Mix	Average Slump (mm)
$CaCl_2$_0_PH2	254.0
$CaCl_2$_1_PH2	254.0
$CaCl_2$_2_PH2	215.9
$CaCl_2$_4_PH2	203.2

3.3.2. Physical Properties of Hardened Concrete

3.3.2.a. Density, absorption and void

Density, absorption and voids in hardened concrete are measured according to ASTM C642 (2013b) and based on the conversion between mass and volume. The weight of concrete is measured under different conditions: after drying in an oven for more than 24 hours at a temperature of 110˚C, after immersing in water until it is completely saturated, after boiling in water for 5 hours, and finally when immersed inside water and hanging with a wire to determine the apparent mass. Boiling and immersion of concrete is shown in Figure 3-14. After determining the mass of concrete specimens in these procedures, bulk density and absorption in different conditions as well as void space were calculated using the following equations

$$Absorption\ after\ immersion, \% = \frac{B - A'}{A} 100 \qquad 3.12$$

$$Absorption\ after\ immersion\ and\ boiling, \% = \frac{C - A'}{A} 100 \qquad 3.13$$

$$Bulk\ density,\ dry = (\frac{A}{C - D})r = g_1 \quad 3.14$$

$$Bulk\ density\ after\ immersion = (\frac{B}{C - D})r \quad 3.15$$

$$Bulk\ density\ after\ immersion\ and\ boiling = (\frac{C}{C - D})r \quad 3.16$$

$$Apparent\ density = (\frac{A}{A - D})r = g_2 \quad 3.17$$

$$Volume\ of\ permeable\ pore\ space\ (voids),\ \% = \frac{g_2 - g_1}{g_2} \times 100 \quad 3.18$$

where, *A* is the mass of the oven-dried sample in air (g), *B* is mass of the surface-dry sample in air after immersion (g), *C* is mass of the surface-dry sample in air after immersion and boiling (g), *D* is the apparent mass of sample in water after immersion and boiling (g), g_1 is the bulk density dry (Mg/m^3), g_2 is apparent density, (Mg/m^3), and ρ is the density of water (1 g/cm^3).

Figure 3-14 (a) Boiling the specimens in water (b) measuring the weight of the specimens immersed in water.

Density, absorption and voids in hardened concrete of all 8 mixtures in the second phase were measured at 28 days; see Figure 3-15 and Figure 3-16 (see also Table A-7 to Table A-10 in the appendix). Different amounts of NaOH and $CaCl_2$ did not have significant effects on the density, void and absorption of the concrete mixture. These properties were also measured on the specimens of the first phase (SCC, NaOH-8 and $CaCl_2$-4 concrete mixtures) at three different ages of 28, 210 and 365 days. The average results of two measurements of each property are provided in Table 3-22 and Table 3-23 and it is clear that these properties do not vary substantially with time.

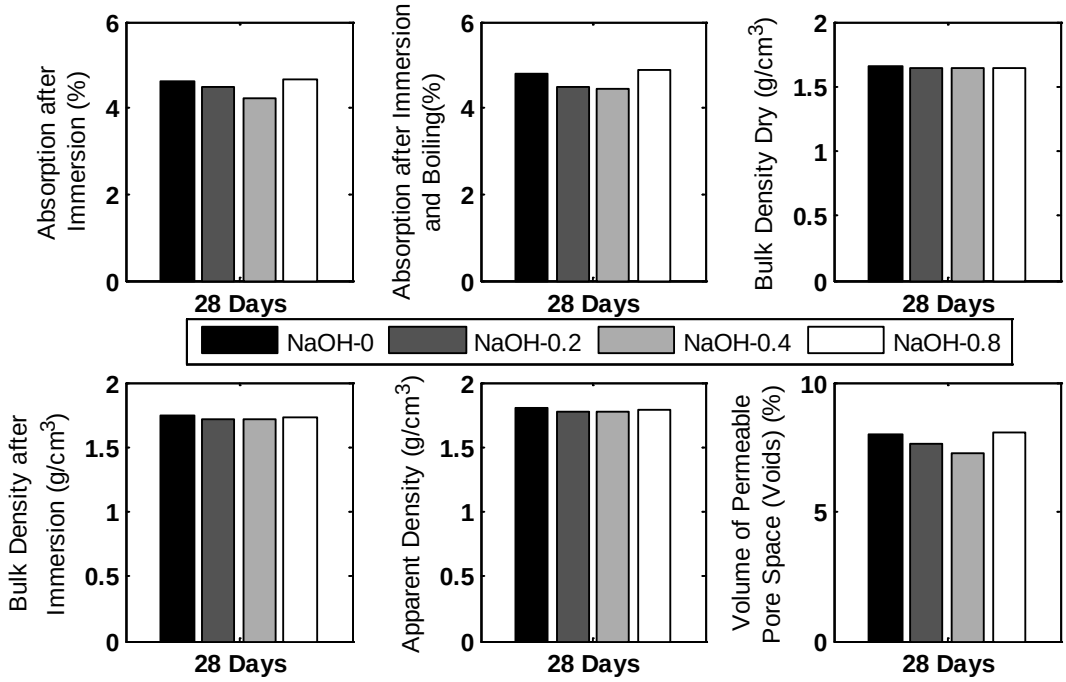

Figure 3-15 NaOH mixture (a) absorption after immersion (b) absorption after immersion and boiling (c) bulk density dry (d) bulk density after immersion (e) apparent density (f) volume of permeable pore space (voids).

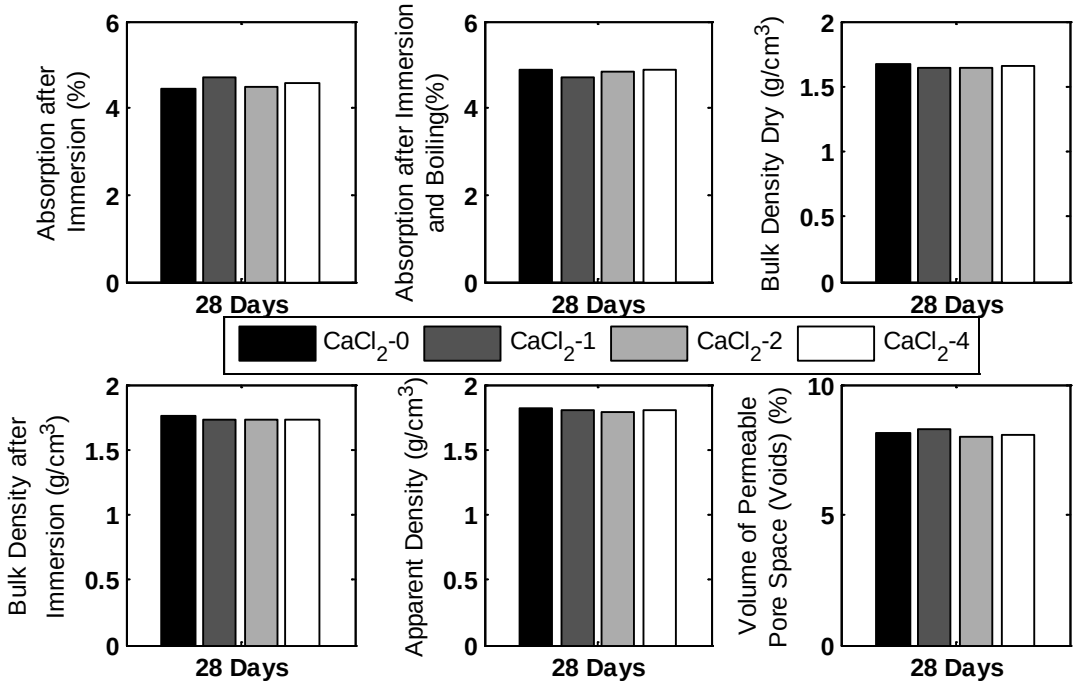

Figure 3-16 $CaCl_2$ mixture (a) absorption after immersion (b) absorption after immersion and boiling (c) bulk density dry (d) bulk density after immersion (e) apparent density (f) volume of permeable pore space (voids).

Table 3-22 Density of Hardened Concrete, Phase 1.

Mix	Bulk Density, Dry (g/cm^3)			Bulk Density after Immersion (g/cm^3)			Apparent Density (g/cm^3)		
	28 day	210 day	365 day	28 day	210 day	365 day	28 day	210 day	365 day
SCC_PH1	1.66	1.68	1.65	1.76	1.78	1.75	1.85	1.87	1.83
NaOH-8_PH1	1.65	1.59	1.63	1.75	1.71	1.75	1.84	1.79	1.84
$CaCl_2$-4_PH1	1.65	1.63	1.63	1.76	1.76	1.74	1.85	1.87	1.84

Table 3-23 Absorption and Voids of Hardened Concrete, Phase 1.

Mix	Absorption after Immersion (%)			Absorption after Immersion and Boiling (%)			Volume of permeable pore space (voids) (%)		
	28 day	210 day	365 day	28 day	210 day	365 day	28 day	210 day	365 day
SCC_PH1	5.5	5.6	5.4	6.0	6.2	5.9	10.0	10.4	9.7
NaOH-8_PH1	5.7	6.1	6.5	6.2	6.8	7.3	10.2	10.9	11.9
$CaCl_2$-4_PH1	6.5	6.7	6.6	6.8	7.5	7.2	11.1	12.3	11.6

These properties were also measured on already aged specimens of TRIGA reactors. The average density of aged specimens as the specimens received at the lab was found to be 2.71 g/cm^3. The results of gravimetrical measurement on these specimens are shown in Table 3-24 and Table 3-25. These properties, density, absorption and void, measured from the TRIGA reactor specimens are similar to the concretes that were prepared in the lab.

Table 3-24 Density of TRIGA Specimens.

No.	Bulk Density, Dry (g/cm^3)	Average	Bulk Density after Immersion (g/cm^3)	Average	Apparent Density (g/cm^3)	Average
1	1.50	1.49	1.60	1.58	1.66	1.64
2	1.49		1.58		1.64	
3	1.48		1.58		1.64	

Table 3-25 Absorption and Voids of TRIGA Specimens.

No.	Absorption after Immersion (%)	Average	Absorption after Immersion and Boiling (%)	Average	Volume of permeable pore space (voids) (%)	Average
1	5.8	5.8	6.3	6.4	9.4	9.4
2	5.7		6.2		9.2	
3	5.9		6.6		9.8	

3.3.2.b. Chloride content

Chloride content tests were performed on all the mixtures in the first phase. Figure 3-17 shows various steps of the NT-build 208 (1996) test used for measuring the chloride content. Figure 3-17(a) shows the concrete powder obtained from cylinders made with different mixtures and kept inside the oven for two hours at 105˚C; in Figure 3-17(b) distilled water and nitric acid were added to the concrete powder to dissolve the chloride in the solution; the solution containing ions of chloride is added to an excess of silver nitrate. The chlorides precipitate as silver nitrate. Figure 3-17(c) shows the last step when the color of the solution changes to bright red when just enough silver nitrate and ammonium thiocyanate is added to the solution to titrate the Cl^-. In this reaction, the excess of thiocyanate ions is indicated by the formation of a red iron(III)-complex. The amount of chlorides (Cl^-) is calculated according to the formula:

$$Weight\text{-}\ \%Cl^- = 3.45\frac{V_1N_1 - V_2N_2}{m} \qquad 3.19$$

where, V_1 is the added amount of silver nitrate solution (ml), N_1 is the normality of the silver nitrate solution, V_2 is the amount of ammonium thiocyanate solution added during the titration (ml), N_2 is the normality of ammonium thiocyanate solution and m is the weight of the sample (g).

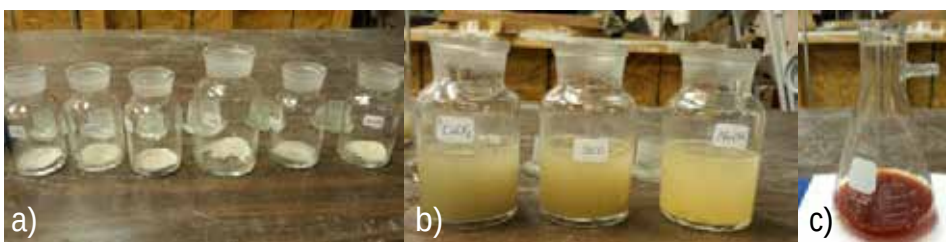

Figure 3-17 (a) concrete powder (b) concrete dissolved in solution (c) changing the color of solution because of indicator.

The chloride content of each mixture from phase 1 is shown in Table 3-26. As expected, there was a negligible amount of chloride in SCC and NaOH-8 mixes and the amount of chloride in the $CaCl_2$-4 mixture was consistent with what was intended.

Table 3-26 Chloride Content of Concrete Mixtures, Phase 1.

Mix	Percent Cl^-	Average weight percent Cl^- of the weight of concrete
SCC_PH1	0.0143	0.01
NaOH-8_PH1	0.0215	0.02
$CaCl_2$-4_PH1	0.6112	0.60
	0.5932	
	0.6069	
	0.6040	

3.3.2.c. Chloride penetration

Chloride ion penetration in concrete indirectly measures the permeability of concrete as a characteristic parameter of durability and its resistance to corrosion. The permeability of concrete and diffusion of the chloride ion is strongly influenced by the type of cement, and the type and proportions of blending materials such as fly ash (Roy, Malek, and Licastro 1987). To measure this parameter NT build 443 (1995) is used. To perform this test, the concrete specimens should be at least 28 days old. After the concrete reaches this age, the specimen is cut in half and immersed in calcium hydroxide solution until it reaches a weight that does not change more than 0.1% within a 24 hour period. After that, three sides of the specimens are sealed with epoxy to create a 1-D diffusion case and the specimen is placed inside the NaCl solution for at least 35 days; the concrete powder is collected from different depths and the amount of chloride is measured in these depths at desired ages. Figure 3-18(a) shows the specimens inside the $Ca(OH)_2$ solution and Figure 3-18 (b) shows them inside the NaCl solution.

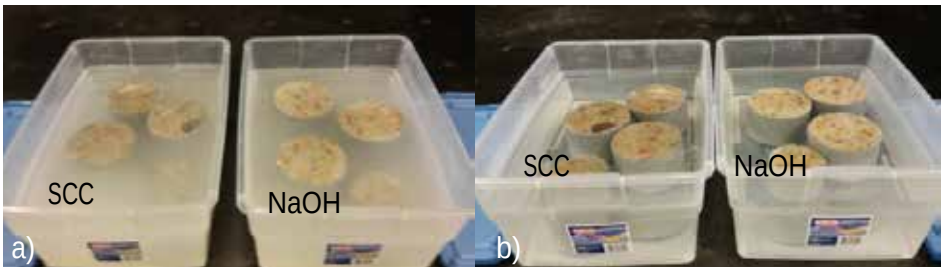

Figure 3-18 Concrete specimens in (a) $Ca(OH)_2$ solution (b) NaCl solution.

After ponding the specimens, the general form of Fick's second law was used to calculate effective chloride transport coefficient and the boundary condition of the chloride profile at the exposed surface. It should be noted that chloride resistance of the concrete is presented in terms of effective chloride transport coefficient.

This bulk diffusivity test was performed on SCC and NaOH-8 mixtures from first phase, as well as on the already aged specimens of the TRIGA Reactor. The results of these tests are shown in Figure 3-19 and Figure 3-20. It is seen that for the concrete with fly ash and no NaOH addition (i.e., SCC mixture), the diffusivity is significantly lower than the mix without fly ash and 8% NaOH addition. This difference is attributed to the presence of NaOH but more importantly to the reduced diffusivity of the SCC mixture due to the presence of fly ash (Bilodeau and Malhotral 1992, Naik, Ramme, and Tews 1995, Naik, Singh, and Hossain 1994). As shown in Table 3-27, the diffusivity of the SCC mixture remained more or less the same over time; while for the NaOH mixture, the diffusivity increased by 30% at 365 days in comparison to 28 days measurement. Most of these changes was between 210 days 365 days. This increase is related to the increased interconnectivity of micro-cracks due to ASR gel expansion.

The average of effective chloride transport coefficient measured after 35 days immersion in NaCl solution for TRIGA specimens was 3.85e-12 m^2/sec, which was closer to the coefficient measured for the SCC mixture at 365 days.

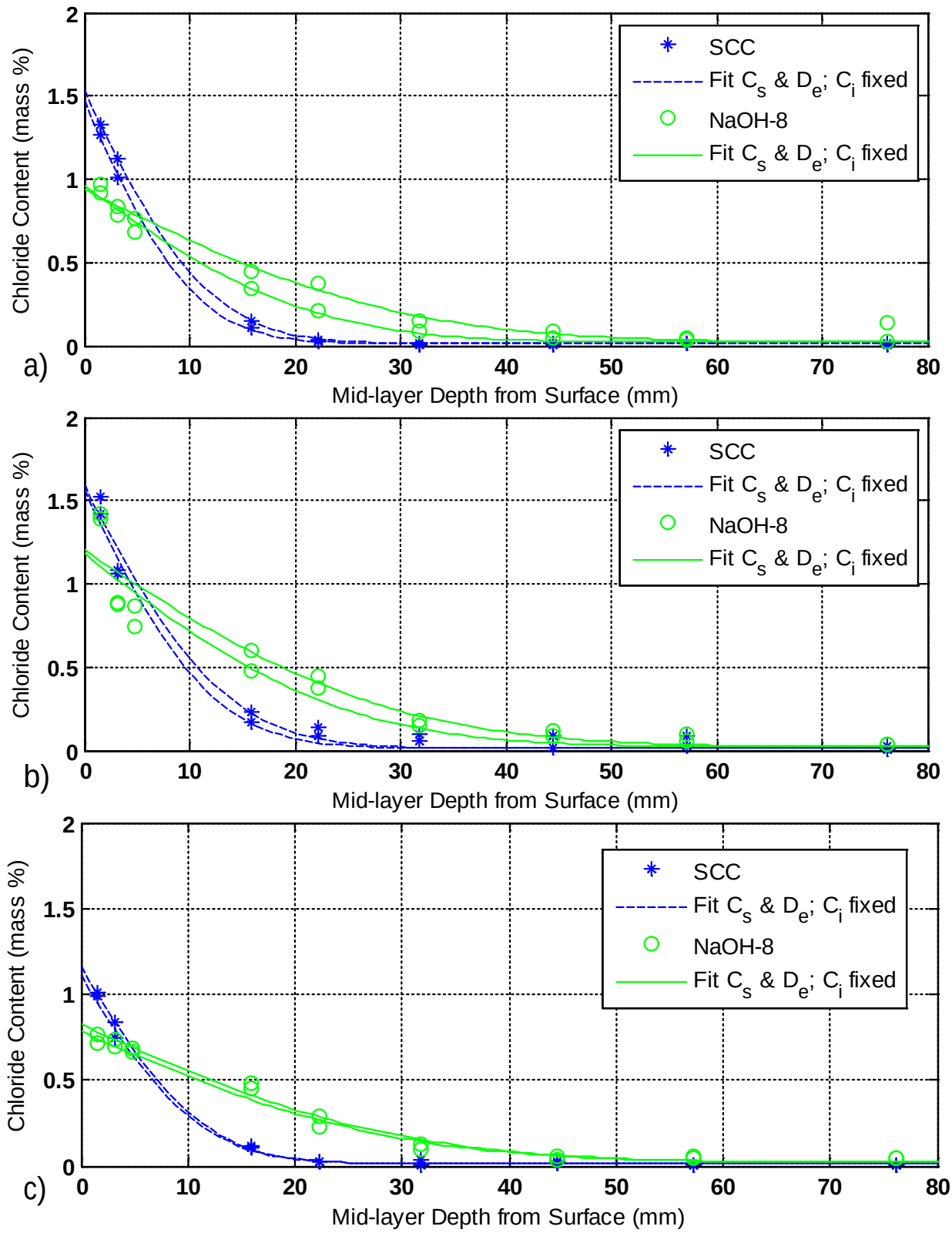

Figure 3-19 Accelerated chloride test on SCC and NaOH-8 concrete specimens at (a) 28 days (b) 210 days (c) 365 days.

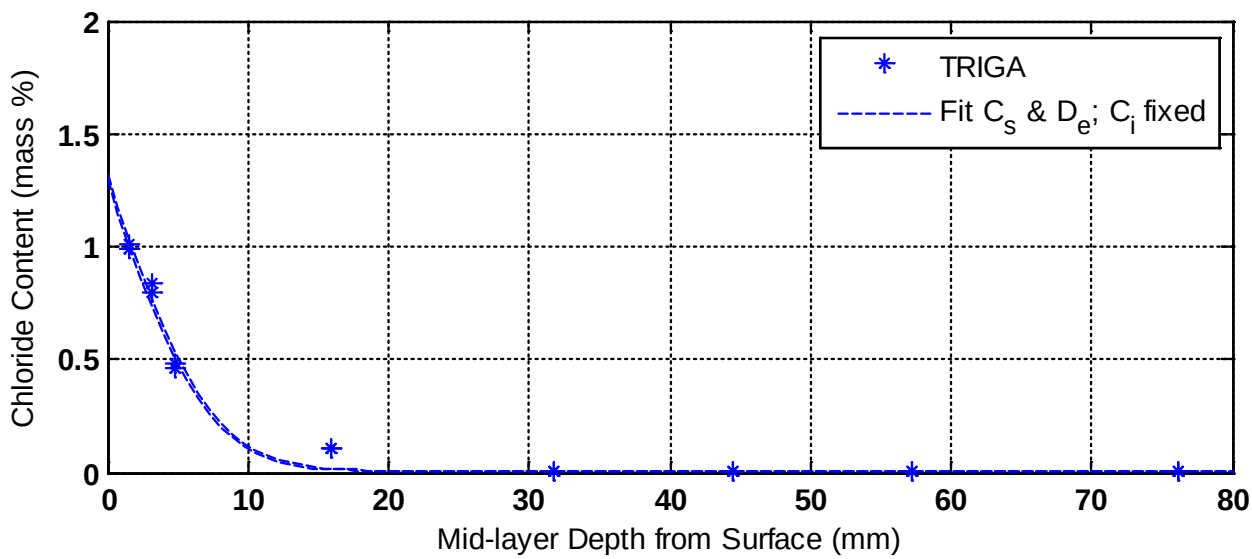

Figure 3-20 Chloride penetration test on TRIGA specimen after 35 days of immersion.

Table 3-27 Average Effective Chloride Transport Coefficient, Phase 1.

Mix	28 Days	210 Days	365 Days
	D_e (m^2/sec)	D_e (m^2/sec)	D_e (m^2/sec)
SCC_PH1	9.55E-12	1.09E-11	1.10E-11
NaOH-8_PH1	5.01E-11	5.10E-11	7.27E-11

3.3.2.d. pH of concrete

Determining the pH is important since it is an indicator of corrosion or carbonation. The average pH of regular concrete is approximately 12; however, when it is carbonated, the pH reduces to about 8. Once pH falls below 10, the potential for corrosion increases. The pH of concrete is measured using a pH indicator paper as shown in Figure 3-21.

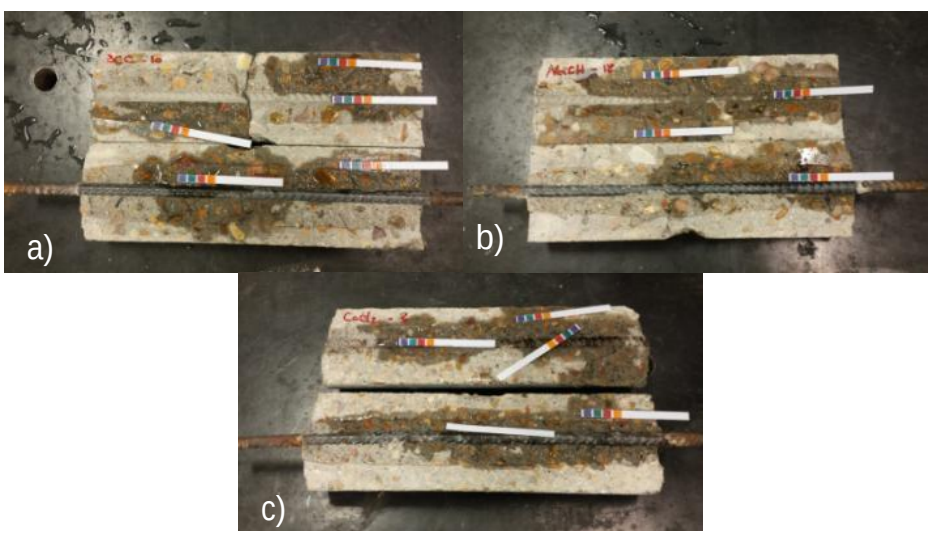

Figure 3-21 (a) pH of concrete in SCC specimen (b) pH of concrete in NaOH specimen (c) pH of concrete in $CaCl_2$ specimen.

The results are shown in Table 3-28. The pH was measured at three different ages of 28, 210 and 365 days, and the results were similar. However, when the pH around the rebar is measured, a significant drop was observed in the presence of $CaCl_2$-4.

Table 3-28 pH of Concrete.

Mix	pH of concrete	pH around the rebar
SCC_PH1	12	11
NaOH-8_PH1	12	11
$CaCl_2$-4_PH1	12	6

When calcium bearing phases present in the concrete are attacked by carbon dioxide of the air, conversion to calcium carbonate (i.e., carbonation) occurs. This chemical process lowers the pH of concrete to about 7, which is a value below the passivization threshold of steel. To determine the carbonation, there are different methods that can be used. The first method is visual inspection of the concrete and checking the discoloration of concrete, the second method is through optical microscope by detecting the presence of calcite crystals and absence of calcium hydroxide, ettringite and un-hydrated cement grains. The third method is using phenolphthalein. To determine the depth of carbonation, 0.2% solution of phenolphthalein is sprayed on concrete as a pH indicator on a freshly cut or broken concrete sample. The depth can be estimated based on the change in the color of the specimen, as shown in Figure 3-22.

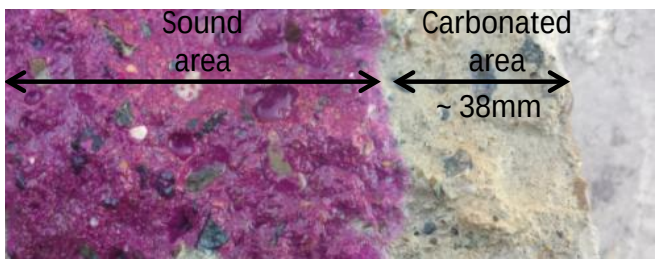

Figure 3-22 Determining the depth of carbonation.

The TRIGA reactor was kept indoors and in controlled temperature and humidity; therefore, changes in these parameters had no effect on the concrete compared to a regular reinforced concrete structure exposed to outdoor environmental conditions. Three concrete cores from the surface of the reactor were broken to have a fresh surface and carbonation was measured. The depth of carbonation from the surface was determined to be 38 mm. It should be noted that no significant carbonation was observed on the specimens prepared in the first and second phases.

3.3.3. Mechanical Properties of Concrete

3.3.3.a. Compressive strength

The compressive strength test was performed based on ASTM C39 (2012c). Stress and strain of the concrete during the compression test was measured using axial averaging extensometer. The test setup for the compression test is shown in Figure 3-23.

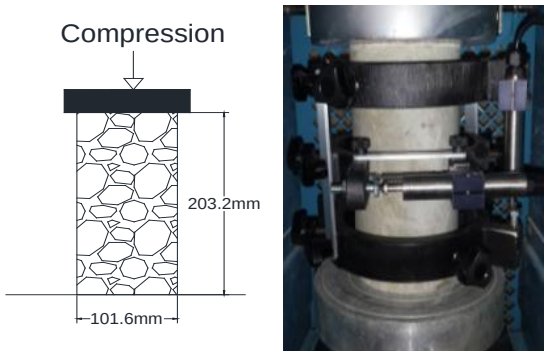

Figure 3-23 Compression test setup.

The compressive strength was measured at 1 day, 3 days, 7 days, 28 days, 210 days and 365 days for the three concrete mixtures (the complete results of measurements are provided in Appendix A). Figure 3-24 shows the comparison of concrete strength for the different mixes at the five testing days. SCC and NaOH-8 from the first phase exhibited similar 1-day strength; however, a lower strength was obtained from NaOH-8 for most of the testing days. In this phase, $CaCl_2$-4 exhibited higher strength compared to the other two mixtures at the early age, which is due to increase in hydration in the concrete due to calcium chloride. However, in the long term and more mature concrete, SCC mixtures showed higher strength.

For NaOH and $CaCl_2$ concrete mixtures in the second phase, the compressive strength was measured at 7 days, 28 days and 180 days (see Figure A-7 to Figure A-22, also

Table A-11 and Table A-12). These results are compared at different ages as shown in Figure 3-25 for NaOH and $CaCl_2$ mixtures. Before the chemicals were added to the mixtures, 3 cylinders were taken and compared at 28 days for consistency among the 8 mixtures prepared. The results indicate the similarity of the mixtures prepared in each batch to each other and the mixtures prepared in first phase before mixing any chemicals. The complete test results are provided in Figure A-23 and Figure A-24 in Appendix A.

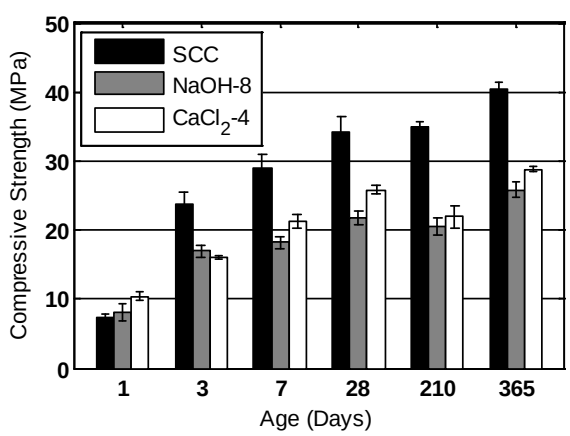

Figure 3-24 Concrete strength at different ages, phase 1.

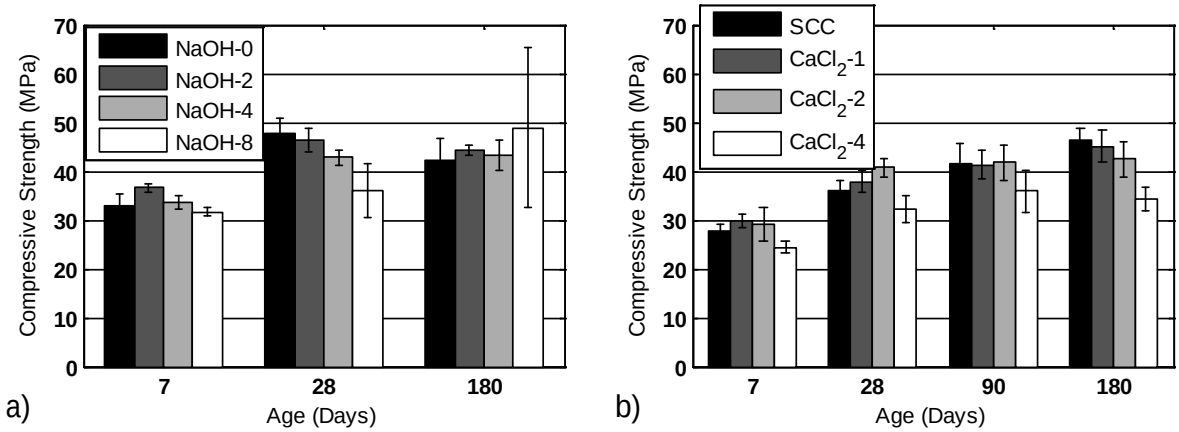

Figure 3-25 Strength at different ages, (a) NaOH concrete mixtures phase 2, (b) $CaCl_2$ concrete mixtures phase 2.

It is seen from second phase test results that the addition of 0.2% sodium hydroxide to the mixture increases the strength of the concrete on the first day due to increased rate of hydration compared to the regular concrete. However, further addition (NaOH-4 and NaOH-8) was not beneficial in this regard. NaOH-4 yielded very similar 1-day strength as the control mixture, while NaOH-8 had slightly lower compressive strength. At 28 days, the control mixture with no NaOH had the highest strength and the strength was gradually lower at higher NaOH levels. At 180 days, NaOH-2 and NaOH-4 yielded slightly higher compressive strengths than the control. While, NaOH-8 resulted in a delayed strength gain and a considerable strength development was obtained at a later age. As a result, the highest compressive strength (which is 13% higher than that of NaOH-0 on average) at 180 days was observed from NaOH-8. A drop in the strength of NaOH and NaOH-2 specimens were observed from 28 days to 180 days, which were within the intra-mixture variability at different ages. One of the reasons for difference in strength between the NaOH-0 and SCC mixtures is the replacement of 25% of the cement with fly ash in SCC mixtures, which reduces the strength of concrete. The reason for the difference in strengths of NaOH-8 specimens prepared in the first and second phases is potentially due to the differences in the water contents of these mixtures. A significantly larger volume of concrete, approximately 2000 liters was prepared for the first series and the accompanying material specimens, while only 100 liters of concrete was cast for each of the NaOH mixtures, which allowed a significantly better control of the mixture proportions in the latter.

Adding different amounts of calcium chloride to the concrete mixture resulted in different compressive strengths. It is seen that the addition of one or two percent chloride increases the early strength of concrete compared to SCC and $CaCl_2$-4 mixtures, however, at later ages, the strength gain of the mix without $CaCl_2$ is much higher than those of the other mixtures. The overall strength of $CaCl_2$-4 is the lowest among all mixtures.

Additionally, the results for specimens obtained from the TRIGA reactor are shown in Table 3-29 (see also Figure A-25 and Figure A-26). Unconfined compressive strength of concrete in nuclear power plants (NPP) is typically in the range of 13 MPa to 55 MPa, with 28 MPa being most common (Naus, Oland, and Ellingwood 1996). Here compressive tests results show an average

strength of 40.53 MPa, which is higher than the average concrete strength in NPP. Furthermore, the initial strength of concrete mixture can be estimated on the basis of this strength test. Concrete exposed to a temperature of 90°C (similar to the NPP conditions) may lose up to 10% of its room temperature strength (Naus, Oland, and Ellingwood 1996, Freskakis 1979).

Table 3-29 Compressive Strength of TRIGA Specimens.

Specimen	Compressive Strength (MPa)	Average
TRIGA	43.7	40.5
	37.5	
	40.4	

Along with the compressive strength, modulus of elasticity and Poisson's ratio was measured. In the first phase, the modulus of elasticity was measured at the ages of 210 days and 365 days. The results are shown in Figure 3-26 (see also

Table A-13). The results of the test indicate that the modulus of elasticity in SCC and $CaCl_2$-4 mixture is similar at these two testing ages. However, for NaOH-8 mixture, this property is lower. This difference can be explained because of the increase in the density of cracks that leads to softening of concrete and decrease the modulus of elasticity.

In the second phase, the modulus of elasticity for NaOH and $CaCl_2$ mixtures were also measured at the ages shown in Figure 3-27 (see also Table A-14 and Table A-15). It is clear that the modulus of elasticity in NaOH mixtures at early ages does not show differences between different amounts of sodium hydroxide additive, however, looking at this property in the first phase specimens at 210 days and 365 days shows that adding 0.8% NaOH decreases the modulus of elasticity. This decrease is due to the increase in the crack density and softening of concrete. For $CaCl_2$ mixtures this property decreases with addition of the salts; for 1% and 2%, the measurement is similar and higher than 4% $CaCl_2$ addition.

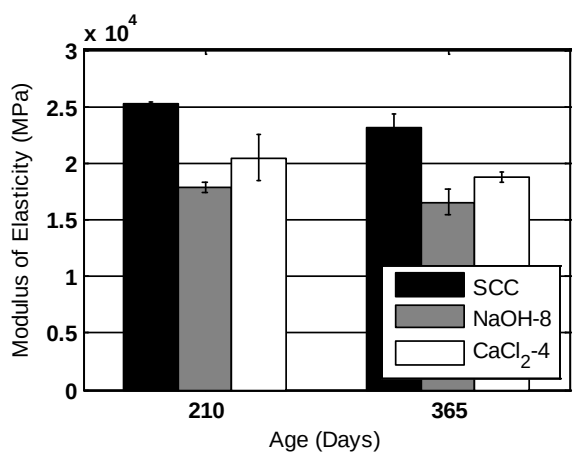

Figure 3-26 Modulus of elasticity of concrete mixtures, phase 1.

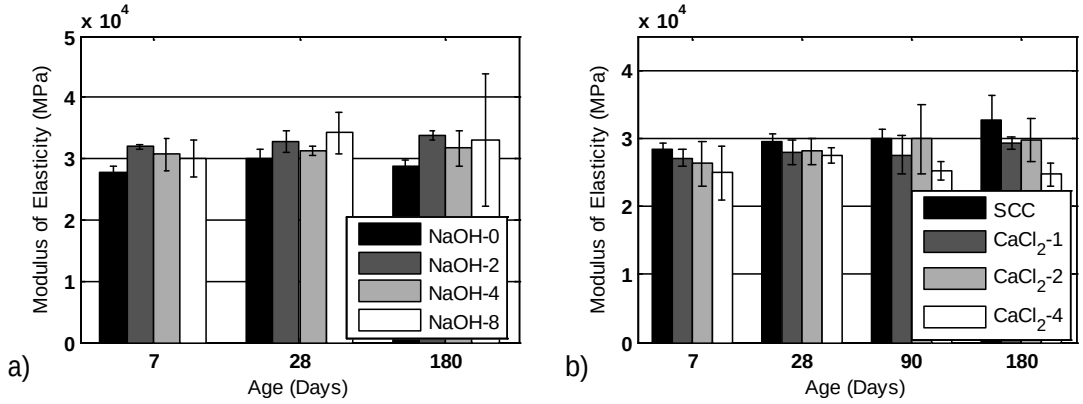

Figure 3-27 Modulus of elasticity (a) NaOH concrete mixture, phase 2 (b) $CaCl_2$ concrete mixture, phase 2.

Poisson's ratio was also measured at the same time as the modulus of elasticity, at 210 days and 365 days for first phase concrete mixtures. In the second phase, this property was measured at 7 days, 28 days and 180 days for NaOH mixtures and at 7 days, 28 days, 90 days and 180 days for $CaCl_2$ mixtures. The results are shown in Figure 3-28 and Figure 3-29 (see also Table A-16 to Table A-18). The results indicate the same trends as the modulus of elasticity.

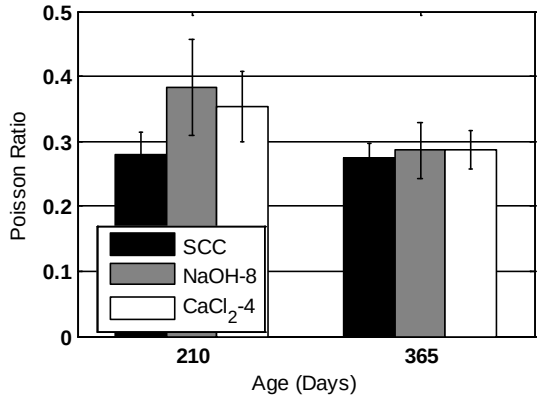

Figure 3-28 Poisson's ratio of concrete mixtures, phase 1.

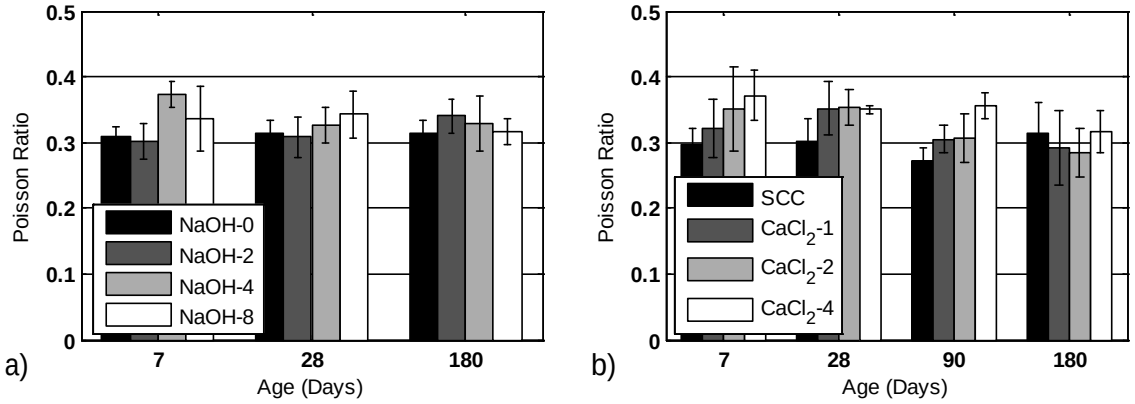

Figure 3-29 Poisson's ratio (a) NaOH concrete mixtures, phase 2 (b) $CaCl_2$ concrete mixtures, phase 2.

The modulus of elasticity of TRIGA specimens is shown in Table 3-29. The results were similar to those of the SCC mixture prepared in the first phase of this study, see Figure 3-26. Poisson's ratio of concrete specimens from the TRIGA reactor concrete was also measured; see Table 3-30. This parameter was 25% higher than the SCC mixture in the first phase of this study. It has been hypothesized that changes in Poisson's ratio at the elevated temperature of NPP are very small and are about the same as at room temperature (Naus 2010).

Table 3-30 Modulus of Elasticity and Poisson's Ratio of TRIGA Specimens.

Test	MOE (MPa)	Average	Poisson's Ratio	Average
TRIGA	23516	24781	0.39	0.39
	27632		0.38	
	23195		0.41	

3.3.3.b. Splitting tensile strength

ACI 349 (2013) eliminated the splitting tensile strength requirement for nuclear structures; however, finding the splitting tensile strength for a structure that might have alkali silica reactions in the long term is important, since this property is sensitive to microcracking and decreases due to this effect (Fan and Hanson 1998b, Deschenes, Bayrak, and Folliard 2009). Moreover, this test is important because of the tensile mode of failure of the concrete. The test is performed based on ASTM C496 (2011b). The details of the splitting tensile test is shown in Figure 3-30. Since the dimension of the upper and lower bearing face is less than the length of the cylinder, two steel plates having dimensions of 279.4 x 50.8 x 19.05 mm (L x W x H) were used. Plywood bearing strips, 3.175 mm thick, were also placed at the top and bottom between the specimen and the steel plates.

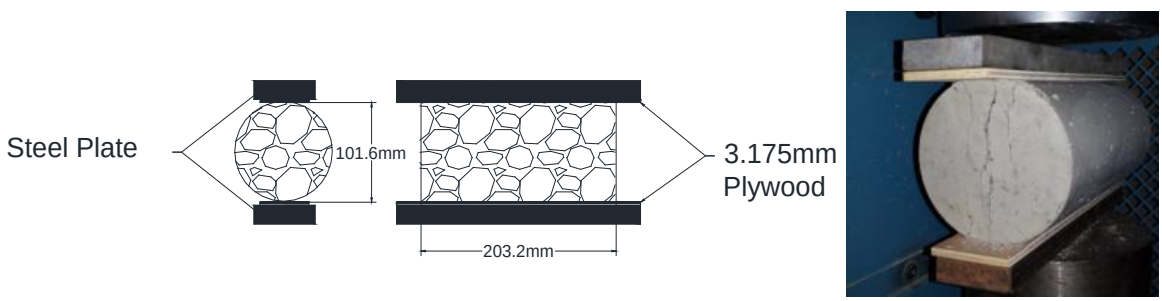

Figure 3-30 Splitting tensile strength test setup.

The results of splitting tensile strength tests at 1 day, 3 days, 7 days, 28 days, 210 days and 365 days for the three concrete mixtures of first phase are provided in Figure 3-31. The results show that the NaOH-8 mixture's strength is considerably less than that of SCC and after 28 days the strength was almost constant. The $CaCl_2$-4 mixture in this phase has lower strength than the NaOH-8 at an early age and higher strength that later ages and lower strength than SCC at all ages. The difference between $CaCl_2$ and NaOH addition at early age is due to the difference in hydration rates with the addition of chemicals. The results of splitting tensile strength tests for the NaOH and $CaCl_2$ concrete mixtures of the second phase are provided in Figure 3-32. The observations for split tensile strength were similar to those of the compressive strength tests in

the NaOH mixtures of the second phase, a lower strength at early age and a delayed strength development. The 180 day strength of all the mixtures was similar, ranging from 4.54 MPa to 5.32 MPa. Again this difference between the NaOH-8 specimens for the first and second phases might be attributed to the differences in water content of the mixtures. The development of tensile strength of the concretes with different levels of chloride shows a good agreement with that of the compressive strength. The 7-day splitting tensile strengths of $CaCl_2$-1 and $CaCl_2$-2 mixtures were higher than that of SCC; however, the further addition of chloride (i.e., 4%) results in a significant decrease of early age strength. At 28 days, the average splitting tensile strength of SCC mix was the highest, and $CaCl_2$-4 showed the lowest splitting tensile strength. However at 180 days considering the deviation in the results, the results from all four mixtures were comparable.

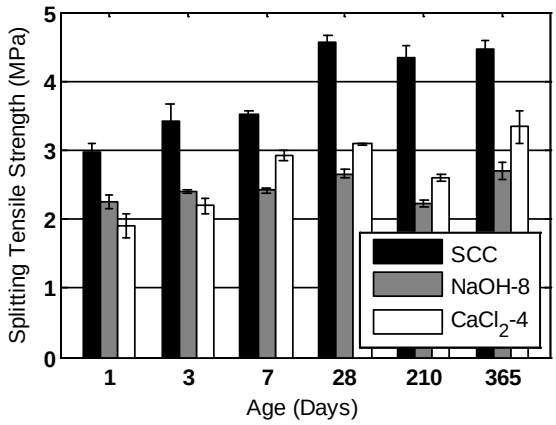

Figure 3-31 Split tensile test result at different ages, phase 1.

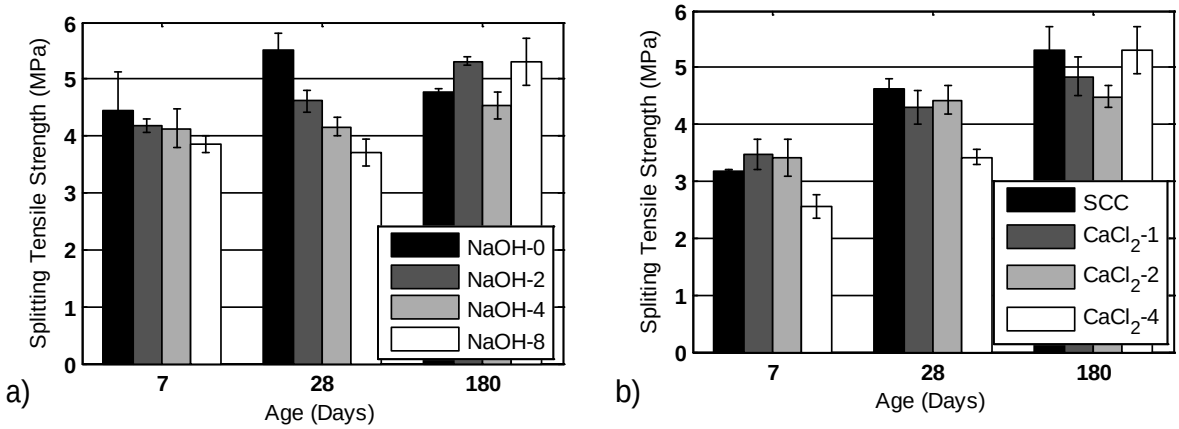

Figure 3-32 Split tensile test result at different ages, (a) NaOH concrete mixtures, phase 2, (b) $CaCl_2$ concrete mixtures, phase 2.

The tensile strength of TRIGA reactor specimens was also measured, see Table 3-31. In the high temperature of reactors and in the presence of nuclear radiation, there can be up to 5% reduction in the splitting tensile strength (Naus 2007). This strength is usually considered to be one-tenth to one-fifth of its compressive strength (Naus 2007). The results of the tensile strength test confirm that the tensile strength of the concrete is still in an acceptable range. The tensile

strength of TRIGA reactor specimens are 15% less than SCC specimens prepared in the first phase. It is 27% and 13% higher than accelerated aged specimens for ASR and corrosion of first phase specimens, respectively.

Table 3-31 Tensile Strength of TRIGA Specimens.

Test	Tensile Strength (MPa)	Average
TRIGA	3.96	3.74
	3.56	
	3.70	

3.3.3.c. Flexural strength

To find the flexural strength of concrete, there are two commonly used tests, 3-point and 4-point bending. In the latter, since the volume under stress is larger, the probability of finding a longer crack is higher and it yields a more accurate strength estimation (Nordson 2014). Therefore, a 4-point bending test was chosen for measuring flexural strength. Figure 3-33 shows the flexural test setup. The specimens had dimensions of 101.6 x 101.6 x 355.6 mm.

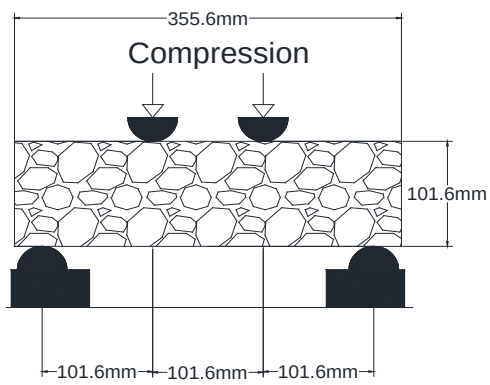

Figure 3-33 Flexural strength test setup.

Knowing the dimensions of the specimens and the maximum load applied to the specimen during the flexural tests, the modulus of rupture can be found. Since all the fractures in the specimens tested here initiate in the middle third of the span length, the modulus of rupture is calculated using the following equation:

$$R = \frac{PL}{bd^2} \qquad 3.20$$

where *R* is modulus of rupture (MPa), *P* is maximum applied load (N), *L* is the span length (mm), *b* is the average width of specimen (mm) and *d* is the average depth of specimen (mm).

Flexural strength in the first phase was measured at three ages: 28 days, 365 days and 455 days. The average results are provided in Figure 3-34; 6 beams were tested for each mixture at 28 days and 3 beams each at 365 days and 455 days of age (see Table A-19). The modulus of rupture of NaOH and $CaCl_2$ mixtures was obtained at 28 days and the results are provided in Figure 3-35.

At 28 days, the addition of sodium hydroxide reduced the modulus of rupture of the specimens and this reduction was greater in the mixture with 0.4% NaOH per weight of cement. For $CaCl_2$ mixtures, the flexural strength increased with the addition of 2% chloride ion by weight of cement to the mixture, which is due to acceleration in the hydration rate. However, increasing the amount of chloride ion, decreased strength noticeably, since high concentrations of $CaCl_2$ decrease the extent of cement hydration (Kishar et al. 2013). Overall, the SCC specimens had the highest modulus of rupture while that of the NaOH samples was the lowest.

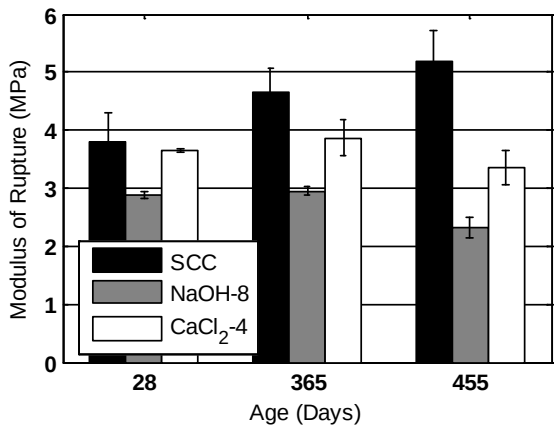

Figure 3-34 Modulus of rupture of concrete mixtures, phase 1.

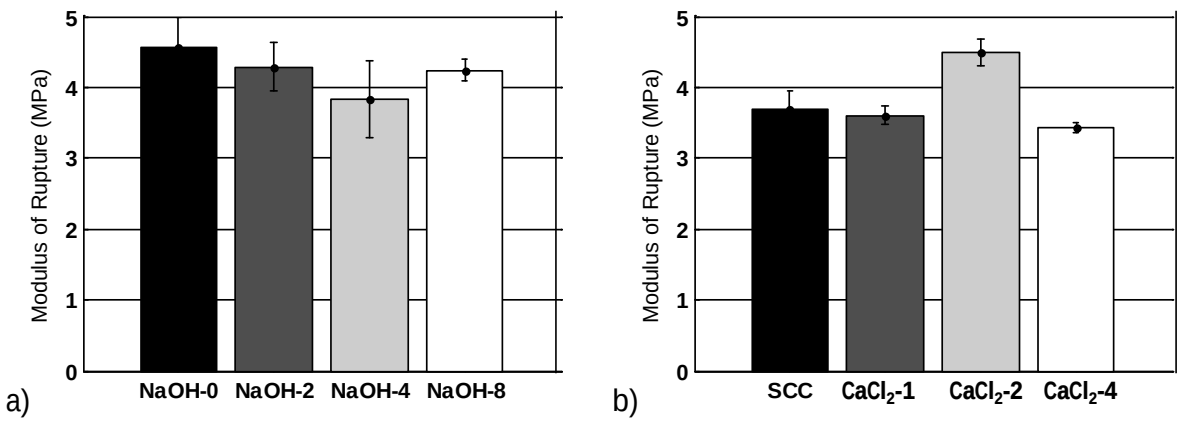

Figure 3-35 Modulus of rupture (a) NaOH concrete mixtures, phase 2 (b) $CaCl_2$ concrete mixtures, phase 2.

3.3.4. Non-Destructive Testing

3.3.4.a. Crack mapping

One of the methods to check the soundness of concrete is visual inspection. When the corrosion progresses and applies pressure on the concrete, the surface will crack and the cracks will grow over time. The crack growth with time indicates that the amount of corrosion product increased and the rebar has corroded further. Similarly, when ASR gel starts to expand and cracks the surface of the concrete, the ASR progression can be measured from crack growth or crack density. To measure crack widths, a magnifier with a scale, as shown in Figure 3-36 was used. To

document the crack growth and propagation, a grid was drawn on the surface of the specimens. A grid and crack width measurement on ASR specimens using a magnifier is shown in Figure 3-37.

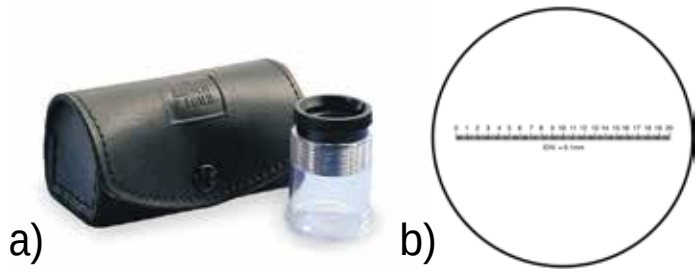

Figure 3-36 (a) Magnifier, (b) 0.1 mm scale (Grainger, 2014).

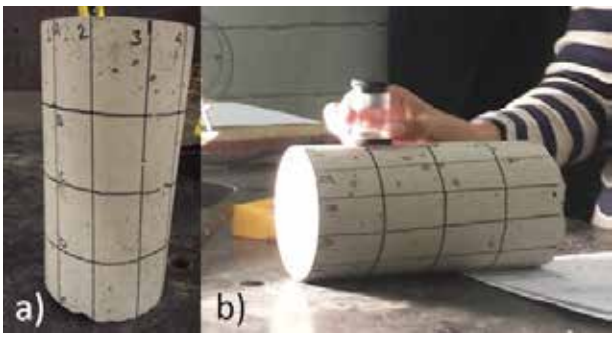

Figure 3-37 (a) Grid on a specimen, (b) crack width measurement using magnifier.

In ASR accelerated specimens, when the internal pressure due to the ASR gel expansion exceeded concrete tensile strength, it caused crack formation on the surface of concrete. The cracks were mostly in the form of three branches (Triskele) and increased with age due to the expansion of gel through the time and transformed into honeycomb cracks when they started interconnecting. After three months, cracks were visible in both specimen sizes (75 x 150 mm and 100 x 200 mm cylinders of the NaOH mixture prepared during the first phase). Figure 3-38 and Figure 3-39 show this crack formation for seven different times (at 114 days, 171 days, 225 days, 276 days, 342 days, 432 days and 492 days after casting) through the lifetime of two cylinders with dimensions of 75 x 150 mm and 100 x 200 mm. The specimens were prepared with 0.8% NaOH by weight of cement in the mix from the first phase. The comparison of the cracks in the different specimen sizes indicates that geometry plays an important role in the amount of cracking, and the smaller specimen showed more cracks on the surface. The crack width was almost constant and varied from 0.05 mm to 0.1 mm; however, the amount of cracks increased with aging of the concrete.

Cracks were also observed on the corrosion accelerated specimens. The crack width increased with increasing expansion and eventually resulted in the spalling of the cover concrete. The lollipop shaped specimens with single embedded rebar with rebar #10 and #19 were prepared for this test. The diameter of the concrete cylinders is chosen based on actual concrete cover inside the dry cask storages. #10 rebar had a cover of 38.1 mm and it is for the scaled down cask tests presented later in this report. #19 rebar had a cover of 63.5 mm and represents the prototype cask. The length of all the lollipop specimens is the same and equal to 254 mm. The dimensions of the specimens are shown in Figure 3-40. Cracks on lollipop specimens with #10

rebar, containing 4% chloride ion per weight of cement cracked after approximately three months in the outdoor environmental conditions. The results from monitoring the crack widths over a fourteen-month period are provided in Figure 3-41 and Figure 3-42 for two separate specimens with #10 rebar and in Figure 3-43 and Figure 3-44 for two separate specimens with #19 rebar. The crack growth continued during the aging process and the width of some of these cracks increased from 0.1 mm to 0.4 mm; in some cases, spalling could be seen on these specimens (the crack widths for these specimens are shown in Table A-22 and Table A-23).

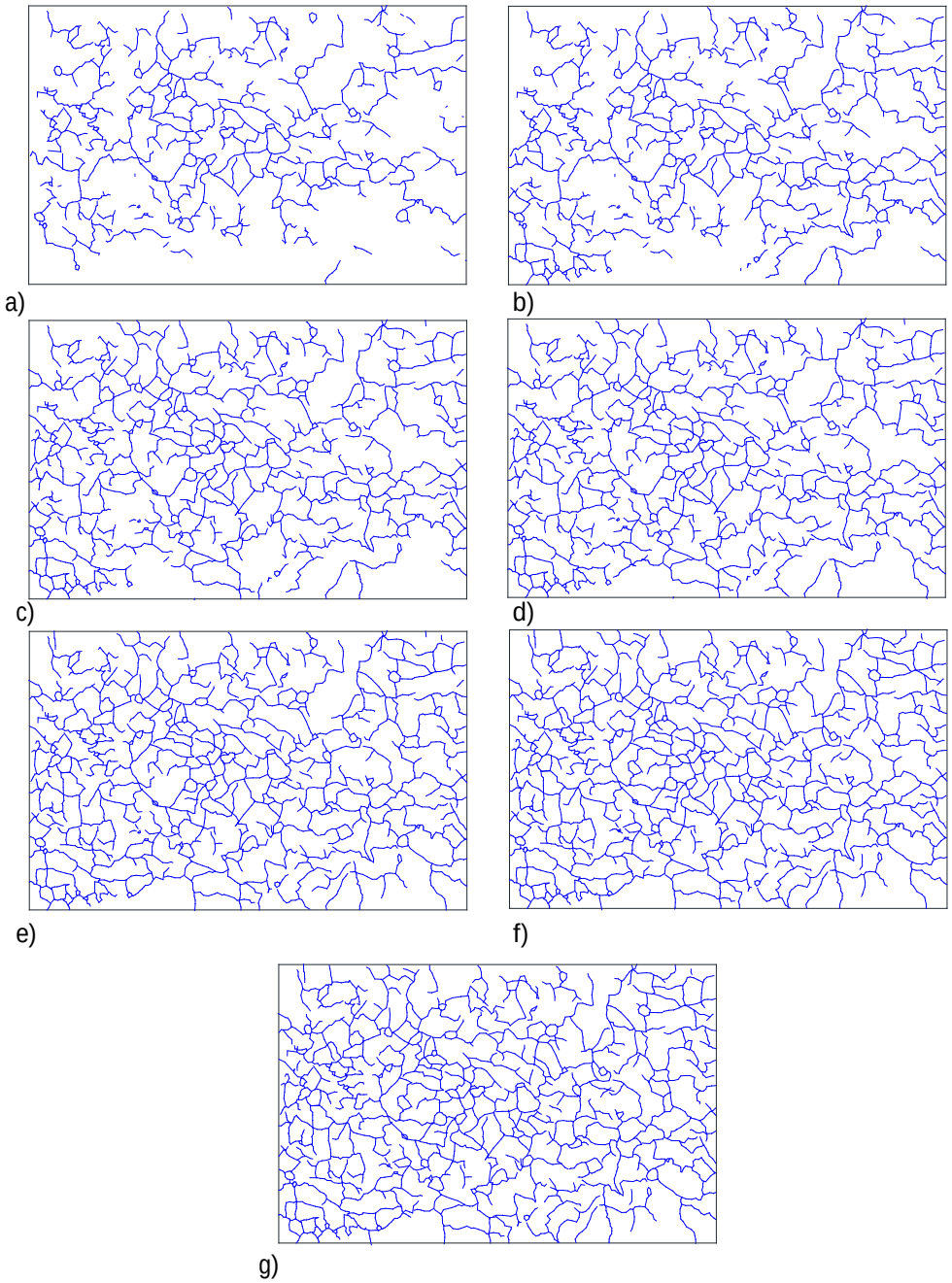

Figure 3-38 ASR crack mapping on a 75 x 150 mm specimen (a) 117 days (b) 171 days (c) 225 days (d) 276 days (e) 342 days (f) 432 days, and (g) 492 days.

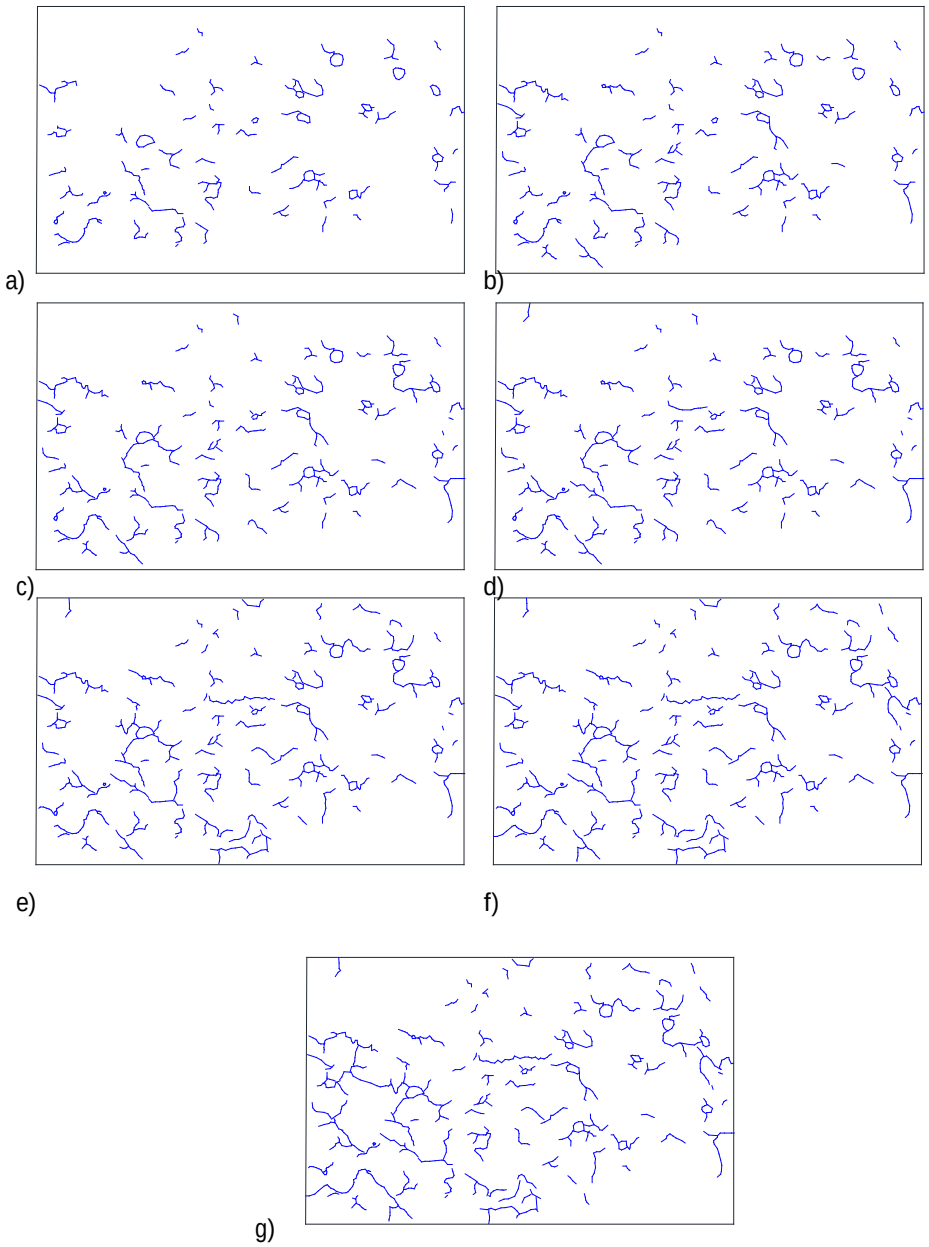

Figure 3-39 ASR crack mapping on a 100 x 200 mm specimen (a) 117 days (b) 171 days (c) 225 days (d) 276 days (e) 342 days (f) 432 days, and (g) 492 days.

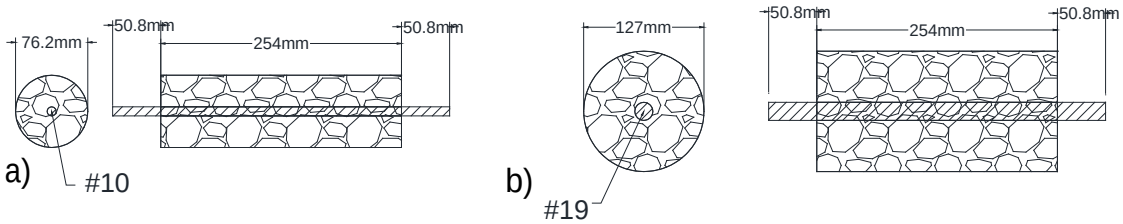

Figure 3-40 Corrosion/mass loss specimen dimension, (a) bar #10 (corresponds to #3 in US system) (b) bar #19 (corresponds to #6 in US system).

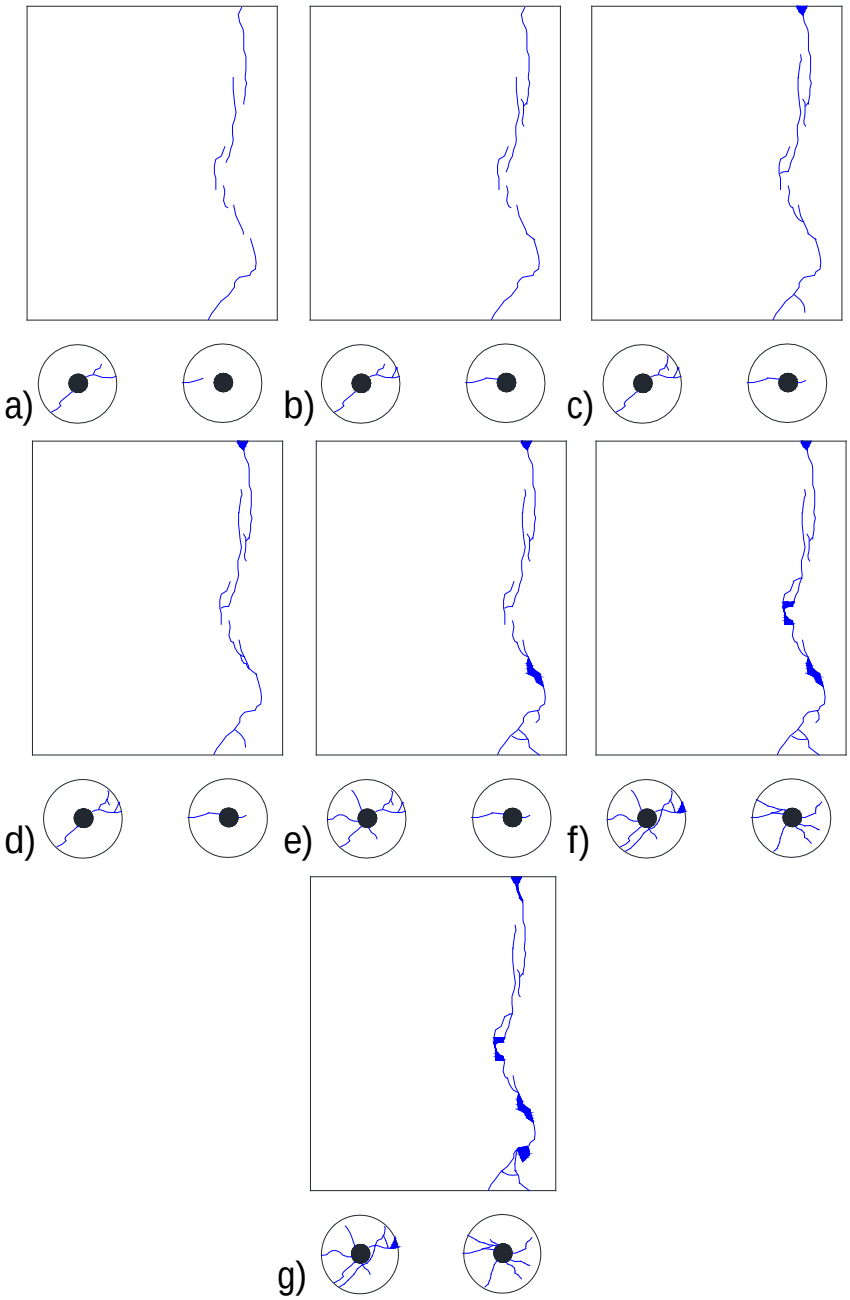

Figure 3-41 Crack maps on lollipop specimen no. 4 with #10 rebar at (a) 117 days (b) 171 days (c) 225 days (d) 276 days (e) 342 days (f) 432 days (g) 492 days.

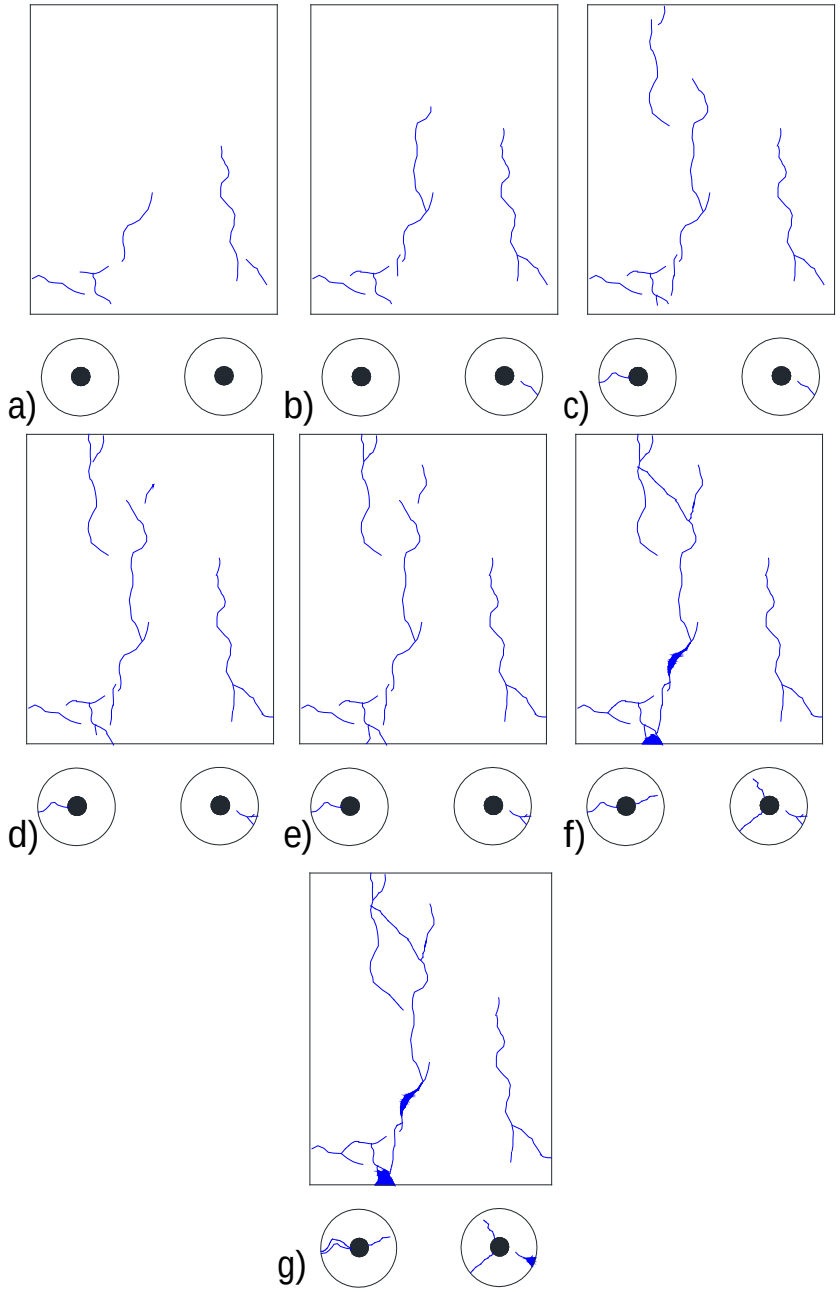

Figure 3-42 Crack maps on lollipop specimen no. 5 with #10 rebar at (a) 117 days (b) 171 days (c) 225 days (d) 276 days (e) 342 days (f) 432 days (g) 492 days.

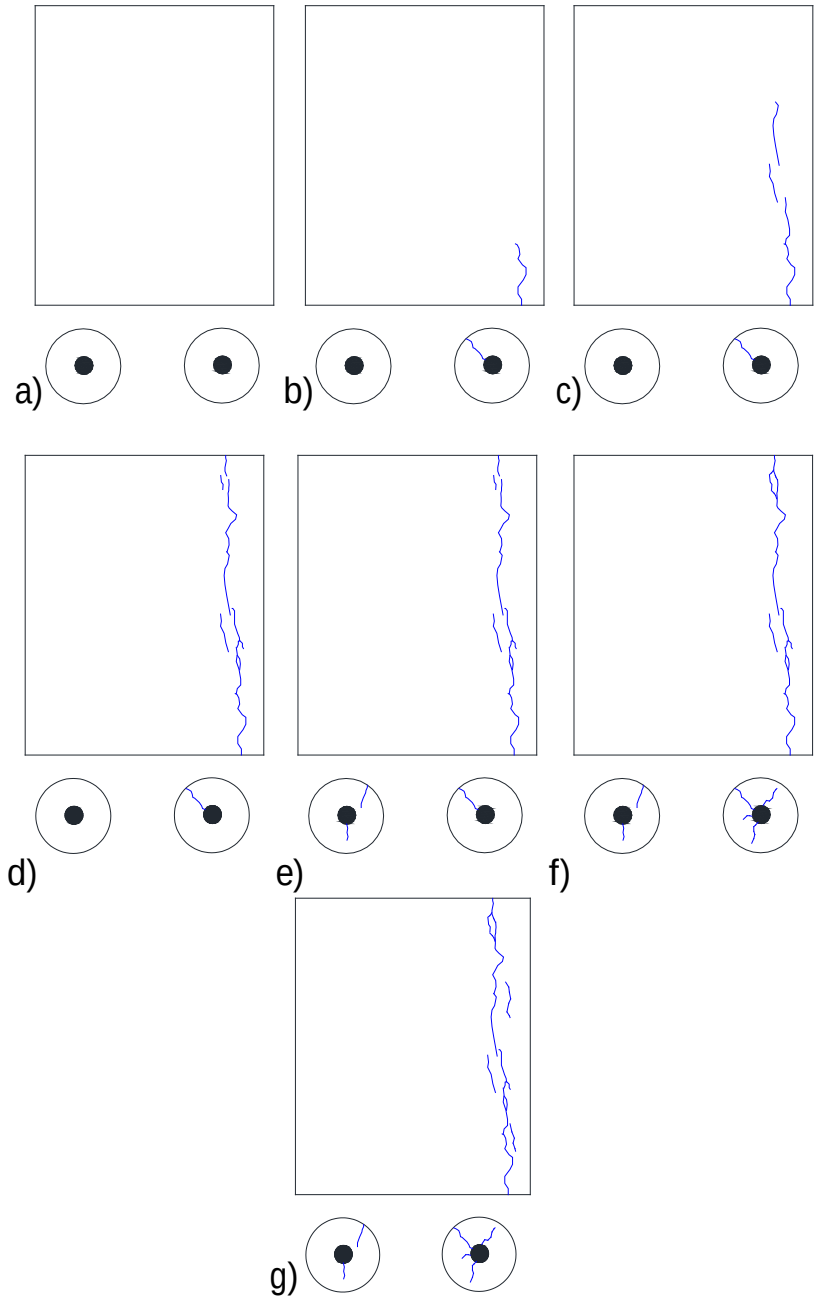

Figure 3-43 Crack maps on lollipop specimen no. 14 with #19 rebar at (a) 117 days (b) 171 days (c) 225 days (d) 276 days (e) 342 days (f) 432 days (g) 492 days.

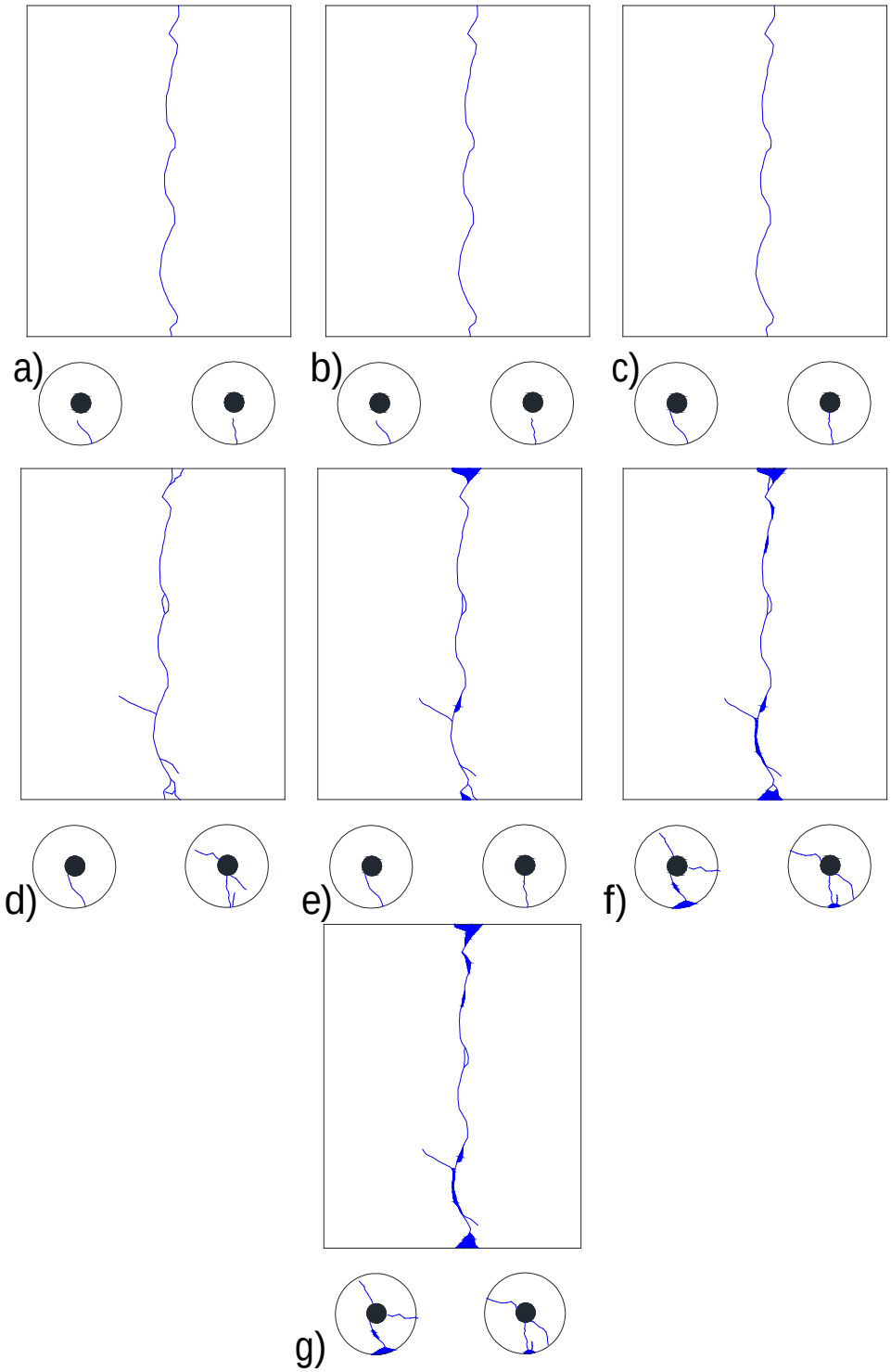

Figure 3-44 Crack maps on lollipop specimen no. 17 with #19 rebar at (a) 117 days (b) 171 days (c) 225 days (d) 276 days (e) 342 days (f) 432 days (g) 492 days.

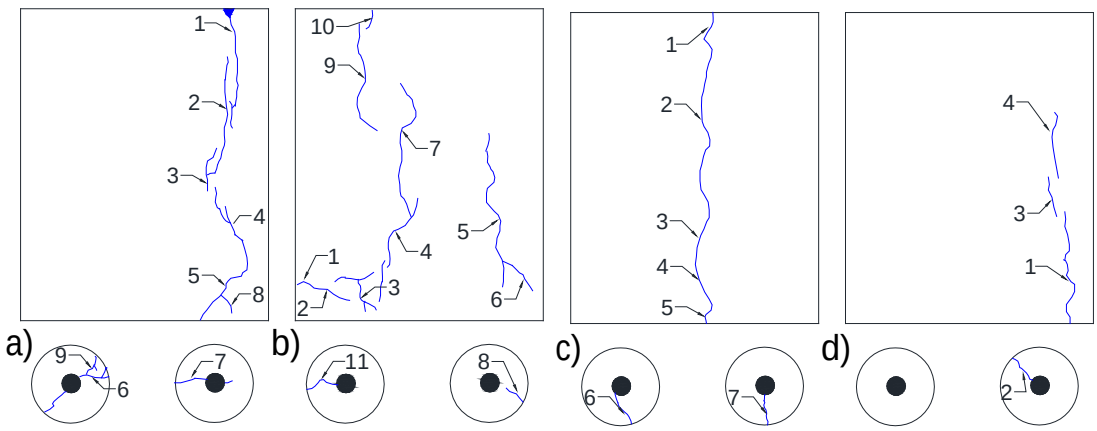

Figure 3-45 Crack numbers on (a) bar #10, No.4 (b) bar #10, No.5 (c) bar #19, No. 17, (d) bar #19, No. 14.

3.3.4.b. Electrochemical tests

The effect of the addition of chloride ions was investigated by means of electrochemical monitoring of concrete and the corrosion behavior of steel embedded in concrete through two different tests: half-cell potential and surface resistivity.

Half-cell potential measurements

Half-cell potential measurement is one of the non-destructive methods that helps understand the progress of corrosion with time. The device, as shown in Figure 3-46, measures the potentials on the surface of the concrete with respect to an arbitrary reference point on the reinforcement. The measured value is dependent on several factors such as temperature, type of reference electrode, pre-wetting time, cover thickness concrete carbonation, oxygen and chloride content. Since concrete cover and chloride content are the same, the other four parameters, temperature, moisture, oxygen content and carbonation, should be considered during the measurement. Moisture and oxygen content are related to each other; when the moisture content of the specimens increases, the oxygen content decreases. If carbonation is observed, a note should be made for the measurement and the recording should be corrected accordingly. In this study, since the carbonation was not observed on the specimens, the temperature and humidity of the specimens are recorded alongside the half-cell potential. The half-cell potential measurements were repeated once a month.

Figure 3-46 Half cell potential device (Giatec, 2014).

Table 3-32 shows the relationship between the potential values and corrosion probability based on ASTM C876 (2009a). Three points were measured and averaged.

Table 3-32 Relationship between the Potential Values and Corrosion Probability Based on ASTM C876 (2009a). Note: CSE is Copper Sulfate Electrode.

Measured Potential (mV/CSE)	Probability of Steel Corrosion Activity
> -200	Less than 10%
-200 to -350	Uncertain
< -350	More than 90%

The dimensions of the test specimens are shown in Figure 3-40. The measurement was performed at three different locations along the length of the rebar embedded in the concrete. The temperature effect was considered in these measurements and the value was converted to measurement at 25˚C based on the JSCE-E 601-2000 (2002) using the following equation for the copper/copper sulfate electrode

$$P = 0.9' \ (T - 25) + P_0 \qquad 3.21$$

where P is the potential after correction, T is the temperature measured in Celsius and P_0 is the initial potential.

Figure 3-47 and Figure 3-48 show the potential measurement in specimens of first phase with #10 rebar and #19 rebar, respectively (see also Table A-24 and Table A-25). Potential values more than -200mV/CSE indicate the probability of steel corrosion is less than 10%; when this value is less than -350mV/CSE, the probability of corrosion is more than 90%. It is clear from these results that for both rebar sizes in SCC and NaOH mixtures, the half-cell potential is higher than -200mV/CSE, which indicates little to no corrosion in these specimens. But in $CaCl_2$ mixtures, there is a high corrosion potential. It is also observed that specimens with #10 rebar have a higher amount of corrosion compared to the specimens with #19 rebar.

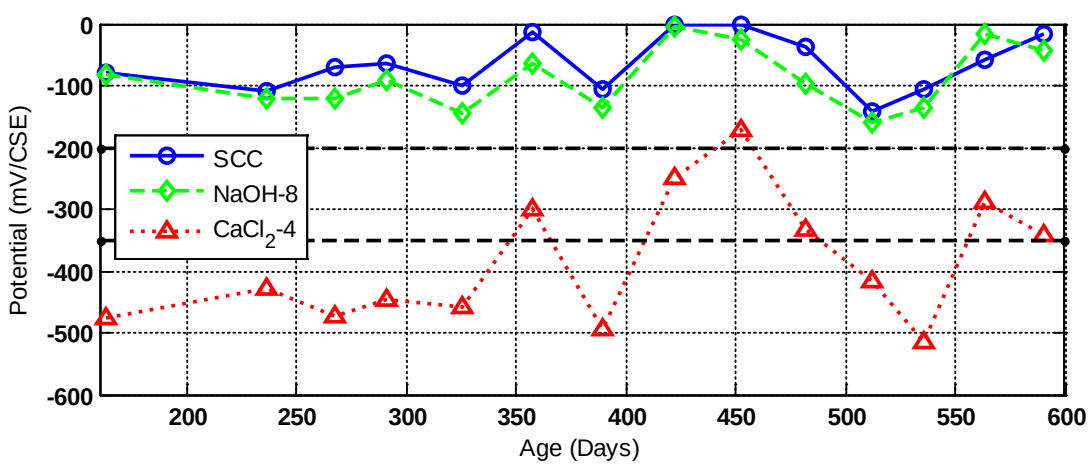

Figure 3-47 Half-cell potential measurements in specimens with #10 rebar (corresponds to #3 in the US system), phase 1.

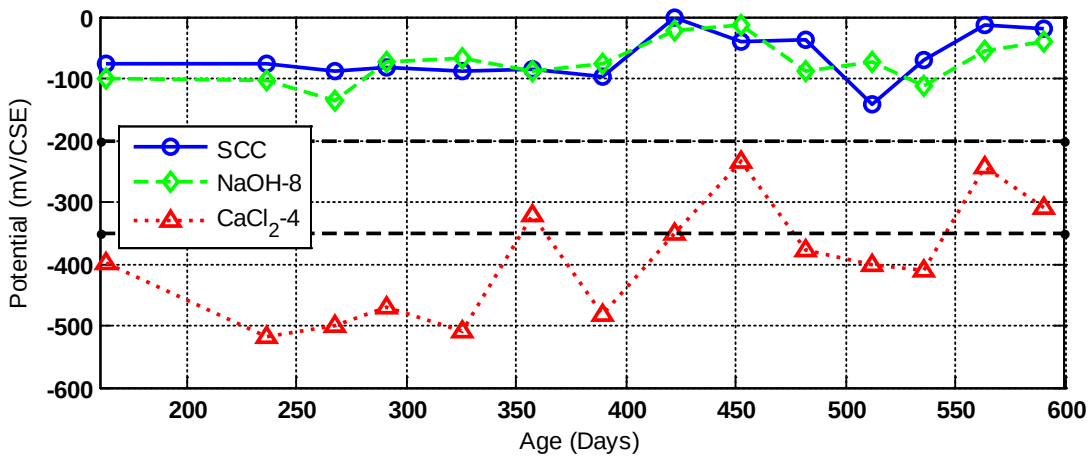

Figure 3-48 Half-cell potential measurements in specimens with #19 rebar (corresponds to #6 in the US system), phase 1.

The specimens from the second phase with addition of different percentage of $CaCl_2$ showed a similar trend. Figure 3-49 shows that the probability of steel corrosion increased with the increasing amount of chloride (also see Table A-26). It was also found that the effect of adding 1% and 2% chloride ion by weight of cement to the mixture was almost the same. However, 4% chloride drastically increased the probability of corrosion to more than 90%.

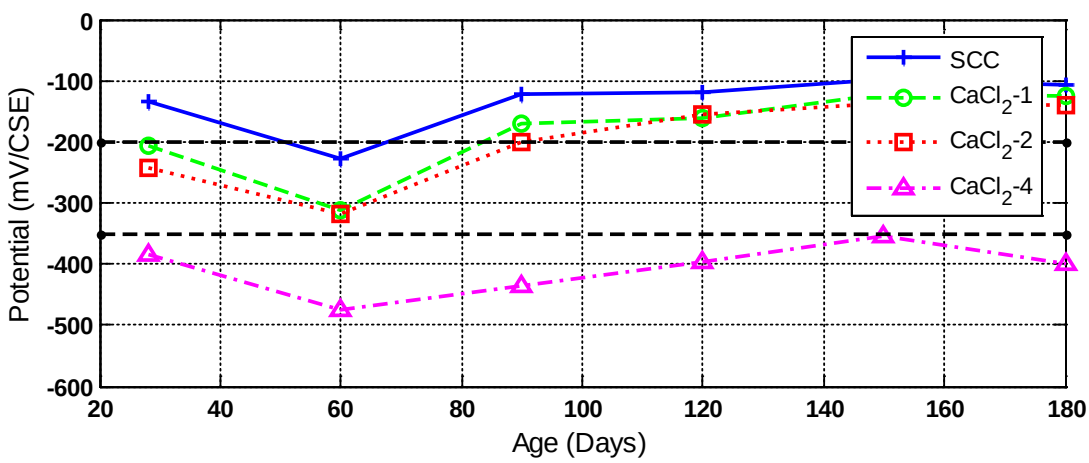

Figure 3-49 Half-cell potential measurements in $CaCl_2$ specimens with #10 rebar (corresponds to #3 in the US system), phase 2.

Surface resistivity

Surface resistivity is a noninvasive and non-destructive test that gives information regarding concrete's ability to resist chloride ion diffusivity, permeability, and properties of its pore water solution in water-saturated conditions (Morris, Moreno, and Sagues 1996, Streicher and Alexander 1995). This test is performed directly on the surface of the structure. According to previous studies (Kessler et al. 2008, Rupnow and Icenogle 2011, Ardani 2012, Ghosh and Tran 2015), this test has a good correlation with bulk diffusivity and rapid chloride penetration test

(RCPT) and can be a reliable replacement for these tests. The measurement of concrete resistivity varies based on different factors such as humidity content, temperature, chloride content, carbonation, type of cement and aggregate as well as porosity of concrete (NEA 2002). To reduce these effects and obtain similar conditions of specimens, the electrical resistivity of water-saturated concrete is measured based on AASHTO TP 95 (2014). To obtain the saturated concrete cylinders, specimens must remain in a 100% humidity condition for at least 7 days before testing; therefore, the specimens of all three mixtures were immersed in water and kept inside the lab during this time period. Additionally, to see the difference and make sure that the specimens with NaOH and $CaCl_2$ content were not losing some of their free ions because of immersion, they were also stored in solutions with 1.3 g/l NaOH and 6.85 g/l $CaCl_2$ respectively as shown in Figure 3-50. After the specimens were removed from the water, the excess water was blotted off and they were placed inside the surface resistivity measurement device as shown in Figure 3-51. This test repeated once a month.

Figure 3-50 Immersing specimens inside water, NaOH or $CaCl_2$ solutions.

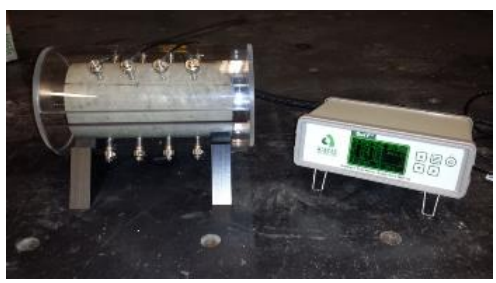

Figure 3-51 surface resistivity measurement device.

AASHTO TP 95-14 (2014) present a table that shows the chloride ion penetrability based on the surface resistivity test, shown in Table 3-33 for 100 x 200 mm cylinder specimens.

Table 3-33 Relationship between the Surface Resistivity and Chloride Ion Penetrability Based on AASHTO TP 95-14 (2014).

Chloride Ion Penetrability	Surface Resistivity Test
	100 x 200 mm Cylinder (kOhm-cm)
High	< 12
Moderate	12 -21
Low	21- 37
Very Low	37 – 254
Negligible	> 254

Results of surface resistivity measurements on first phase specimens are shown in Figure 3-52 (see also Table A-27). The results indicate that SCC has moderate chloride ion permeability and the other two mixtures (NaOH and $CaCl_2$) have high chloride ion permeability based on AASHTO TP 95-14 (2014). Figure 3-53 (see also Table A-33) show the surface resistivity for NaOH specimens, in the second phase. The specimens without sodium hydroxide showed the lowest surface resistivity and the specimens with the highest amounts of sodium hydroxide (0.8%) showed the highest resistivity. The other two mixtures have almost the same resistivity. The resistivity in all cases increased with aging. Figure 3-54 (see also Table A-29) shows the surface resistivity for $CaCl_2$ mixtures. In this series of specimens, the addition of calcium chloride decreased the resistivity, except in the case of addition of 2% chloride ion to the mixture. The surface resistivity of already aged specimens of the TRIGA reactor was measured using the same method and the results are shown in Table 3-34 These results show high chloride ion permeability for this aged concrete which can lead to corrosion of rebars inside the concrete and decrease the serviceability of the structure. The surface resistivity of TRIGA specimens was 75%, 41%, and 58% less than SCC, NaOH-8 and $CaCl_2$-4 specimens from the first phase, respectively.

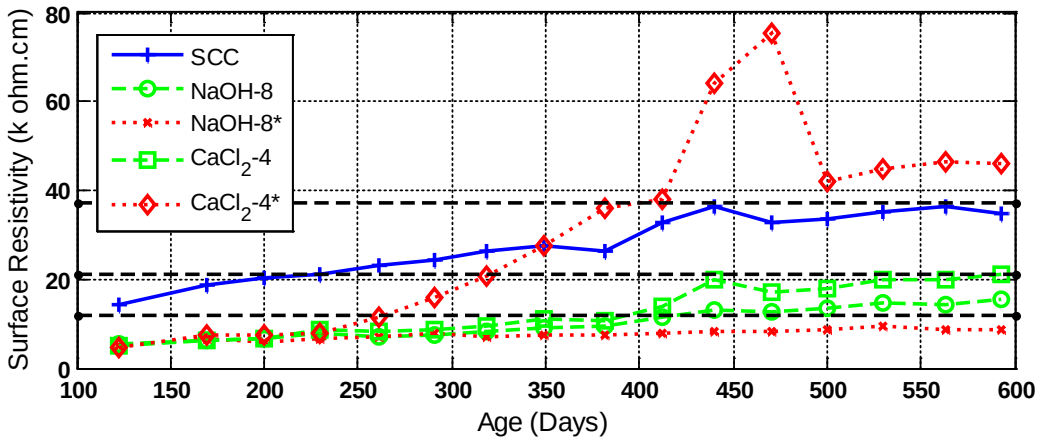

Figure 3-52 Surface resistivity of three concrete mixtures at different ages (* indicates specimens in solution NaOH-8 in 1.3 g/l NaOH solution and $CaCl_2$-4 in 6.85 g/l $CaCl_2$ solution), phase 1.

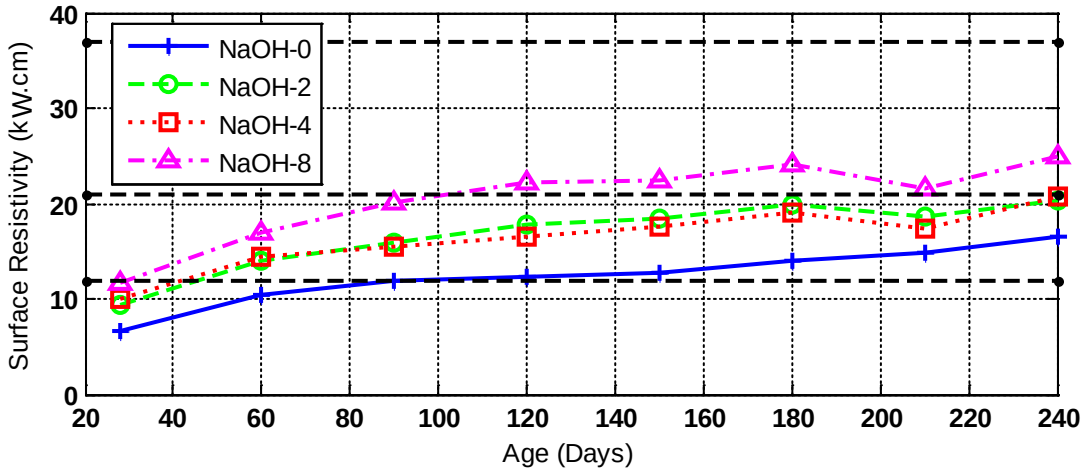

Figure 3-53 Surface resistivity of NaOH mixtures at different ages, phase 2.

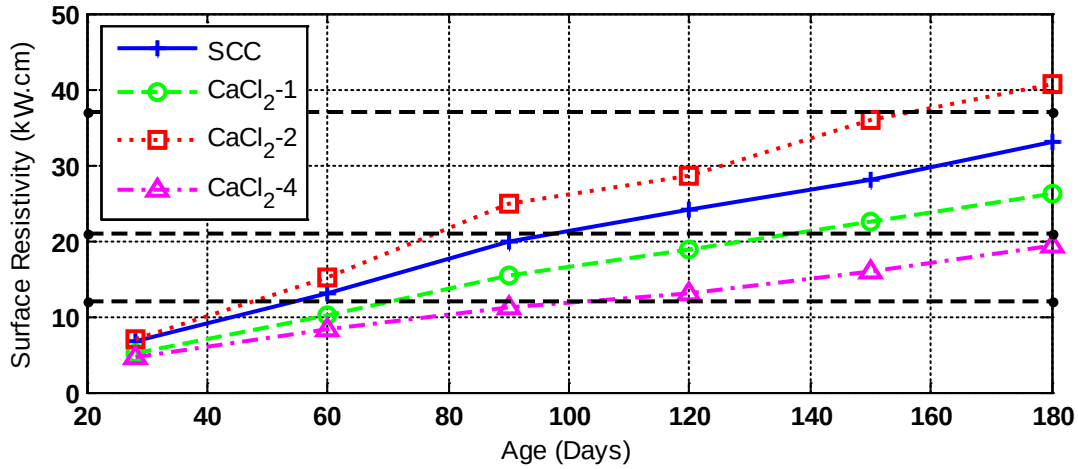

Figure 3-54 Surface resistivity of $CaCl_2$ mixtures at different ages, phase 2.

Table 3-34 Surface Resistivity of TRIGA Specimens.

No.	ρ (KΩ.com)
1	9.8
2	9.8
3	7.5

Ultrasonic pulse velocity (UPV)

UPV is a non-destructive test to estimate flaws and non-uniformity inside the concrete by measuring the propagation velocity of an ultrasonic pulse that travels through the material (Ohdaira and Masazawa 2000). The velocity primarily depends on the elastic properties of the materials and is almost independent of the geometry. For concrete, because of the high scattering that occurs at matrix/aggregate interfaces as well as at micro cracks, the velocity is measured using through-transmission techniques (Bungey and Millard 1996). UPV can give information regarding quality of concrete. Higher velocities are obtained when density, homogeneity and uniformity are good and low velocity indicates poor quality. Based on this knowledge, BS 1881 (1983) classifies the concrete quality based on UPV as shown in Table 3-35. Therefore, UPV not only can be used for quality control, such as identification of cracks and voids, but also allows the evaluation of aging and deterioration of reinforced concrete structures.

Table 3-35 Quality of Concrete Based on BS 1881 (2005).

UPV (m/s)	Concrete Quality
Above 4500	Excellent
3500 to 4500	Good
3000 to 3500	Medium
Below 3000	Doubtful

The wave velocity inside the specimens was measured by using a UPV system based on ASTM C597M (1997); see Figure 3-55. The ultrasonic equipment consists of a pair of transducers, one

is for transmitting and the other one for receiving the ultrasonic pulses. To perform this test, a conductive gel is applied on the surface of the transducers (here, 54 kHz transducers that measure P-waves were used). Afterwards, they are placed on the sides of the specimens along the same line and the wave velocity is recorded. There are three basic ways in which the transducers may be arranged, opposite faces (direct transmission), adjacent faces (semi-direct transmission) and same face (indirect transmission), as shown in Figure 3-56. The most reliable method is the direct reading and the least reliable method is the indirect reading since the received signal amplitude might be less than 3% of that for a comparable direct transmission (Bungey and Millard 1996). For this study the direct reading is used for the material level tests.

Figure 3-55 Ultrasonic pulse velocity system.

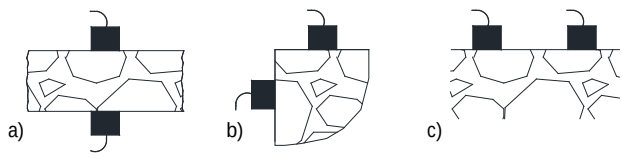

Figure 3-56 Types of reading (a) direct (b) semi-direct (c) indirect.

The velocity of sound is calculated according the following formula

$$V = \frac{L}{t} \qquad 3.22$$

where V is wave velocity (m/s), L is length of specimen (m), and t is the transit time (s). The UPV measurement was repeated once a month.

The UPV was measured on 100 x 200 mm cylinders. Figure 3-57 (see also Table A-27) shows the velocity measurements in NaOH and SCC specimens of first phase at different ages. The temperature and relative humidity of the storage environment are also included in Figure 3-57. The higher UPV measurements between 129 days and 261 days is due to an increase in the water content of specimens and lower temperatures, which reduce the loss of moisture. This is in accordance with the findings of Ohdaira and Masazwa (2000) and Panzera et al. (2011) that UPV increases with an increase in the specimen's water content. UPV is also related to the strength of concrete; therefore, when temperature and relative humidity are almost the same, it can be said that according to the results, the compressive strength did not change substantially. UPV was also measured on the mixtures prepared in the second phase of the project. The results are shown in Figure 3-58. It is shown that among NaOH concrete mixtures, the control mix which did not contain fly ash or NaOH had the lowest UPV and adding sodium hydroxide to the mix

increased the UPV value. However, among the $CaCl_2$ mixtures, SCC (as the control mixture) showed the highest UPV and adding chloride ion to the mix decreased the UPV. It should be noted that 1% and 2% addition of chloride ion to the mix had similar results but increasing the percentage of chloride ion to 4% drastically decreased the UPV in this mix series.

UPV was measured on the cores taken from TRIGA reactor. These cores did not contain rebar and the direct measurement was performed in a manner similar to the method used for specimens in the first and second phases of the project. Table 3-36 shows the UPV measurement on six different concrete specimens from this structure. The average UPV measurement shows that the quality of concrete after 33 years is good and in the acceptable range. The results from these specimens were close to the mixtures prepared in the lab. The difference can be explained by the water content of specimens at the time of testing as well as the type of aggregate used in TRIGA. TRIGA specimens were completely dry during the testing; therefore, moisture content had little to no effect on the results. Furthermore, magnetite was mixed with concrete of the TRIGA reactor to provide extra shielding, which can affect the wave speed inside the concrete matrix.

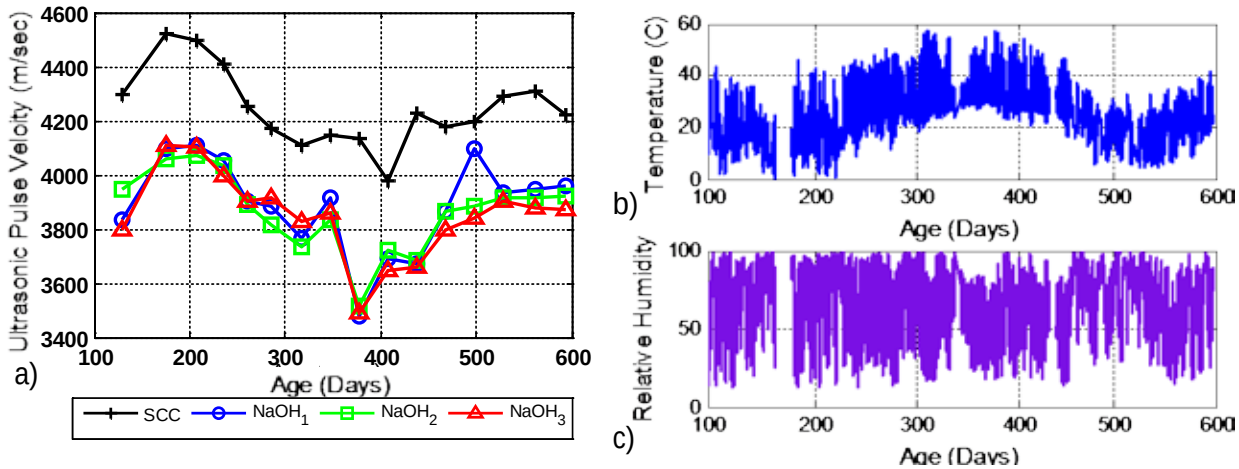

Figure 3-57 (a) UPV measurement of specimens in phase 1 (b) ambient temperature from 100 to 600 days (c) relative humidity from 100 to 600 days.

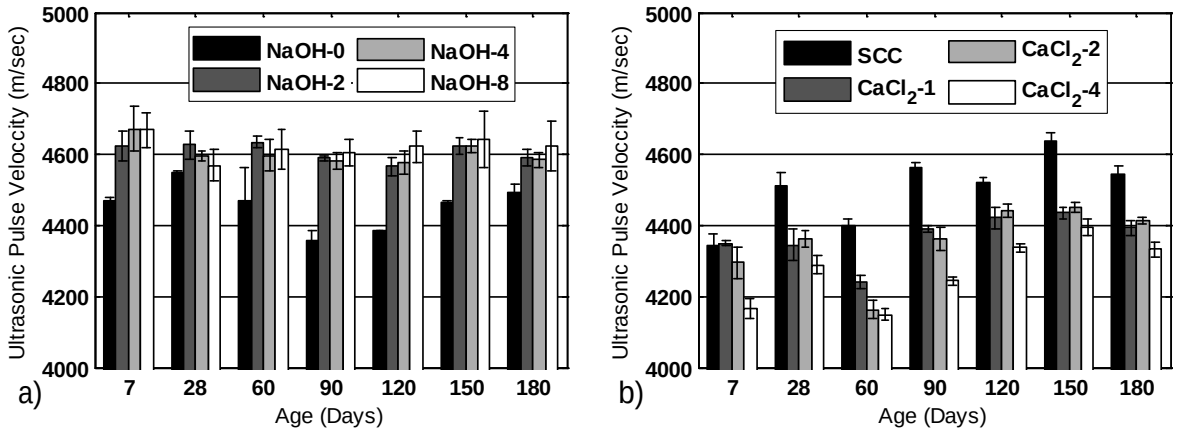

Figure 3-58 UPV measurement (a) NaOH concrete mixture, phase 2 (b) $CaCl_2$ concrete mixture, phase 2.

Table 3-36 UPV Measurement Results of TRIGA Specimens.

No.	V_{avg} (m/sec)	Average
1	4027	3962
2	4352	
3	4100	
4	3909	
5	3771	
6	3612	

3.3.4.c. Schmidt hammer

Schmidt hammer is one of the non-destructive testing methods used to estimate the relative strength of concrete in structures. However, it can provide only an estimate of strength; it cannot be considered a substitute for a compressive strength test. According to ASTM C805 (2013c), the concrete members for this test shall be at least 100 mm thick and the distance between each impact point shall be at least 25 mm. Also this test should not be performed on frozen concrete. In this study, Schmidt rebound hammer is used on the specimens of NaOH and $CaCl_2$ mixtures prepared in the second phase at ages of 7 days, 28 days, 90 days and 180 days. The results of these tests are shown in Figure 3-59 (see also Table A-33 and Table A-34).

The results indicate an increase in the strength of NaOH concrete mixtures of phase 2 until 28 days; at later ages, the strength is almost similar in all the mixtures. It should be noted that a high percentage of sodium hydroxide (NaOH-8) reduces the concrete strength at both early ages and later ages. The results of $CaCl_2$ addition to the second phase showed a higher strength for concrete with 2% percent ($CaCl_2$-2) due to the higher hydration amount and lower strength in $CaCl_2$-4 mixtures caused by the excessive amount of calcium chloride inside the mixture. The results of testing on all the specimens in the second phase are similar to compressive strength obtained from destructive testing.

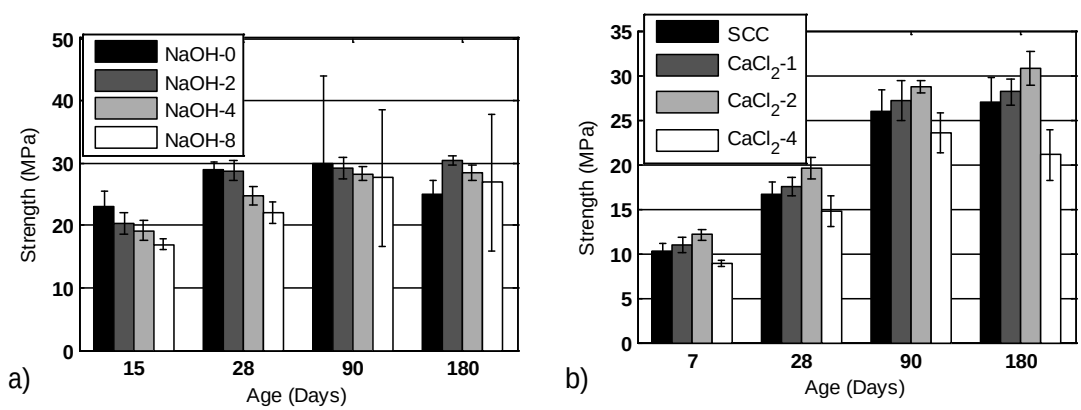

Figure 3-59 Schmidt hammer (a) NaOH concrete mixture, phase 2 (b) $CaCl_2$ concrete mixture, phase 2.

3.3.5. Other Measurements

3.3.5.a. Mass loss

Corrosion (through half-cell potential) and mass loss, as a function of age, are measured for both #10 and #19 rebar. The dimensions of these specimens are shown Figure 3-40. To measure the mass loss, the rebar is cleaned with the use of a soft brush in a solution that contains hydrochloric acid, antimony trioxide and stannous chloride. After the rebar is cleaned, the mass loss is measured using a gravimetric method and through a direct comparison to the mass that was measured and recorded prior to the rebar being placed inside the concrete cylinders. The results of tests at 28 days, 210 days and 365 days are shown in Table 3-37. From the results it is seen that the mass loss of $CaCl_2$ specimens with both #10 and #19 rebar increased with the age of the concrete. Additionally, the corrosion rate at 28 days was higher than at the later age, which indicates that the rate of corrosion is higher at the beginning and it decreases with aging.

Table 3-37 Mass Loss and Corrosion Rate of Lollipop Specimens of Phase 1.

Bar Size	Mix	28 Days		210 Days		365 Days	
		Mass loss (%)	Corrosion rate (mm/year)	Mass loss (%)	Corrosion rate (mm/year)	Mass loss (%)	Corrosion rate (mm/year)
#10	SCC-PH1	0.51	0.076	0.51	0.009	0	0
	NaOH-8-PH1	0.51	0.076	0.26	0.005	0	0
	$CaCl_2$-4-PH1	1.27	0.19	1.27	0.023	2.02	0.036
#19	SCC-PH1	0.132	0.037	0.26	0.009	0.13	0.004
	NaOH--PH1	0	0	0.13	0.004	0.13	0.004
	$CaCl_2$-4-PH1	0.652	0.185	1.81	0.039	1.19	0.037

3.4. CONCLUSIONS

Using reactive fine aggregate, not using fly ash and adding alkalis in the form of NaOH directly into the fresh concrete paste was found to be an effective method for accelerating alkali-silica reactivity (ASR) of specimens kept in ambient outdoor conditions. 0.2% and 0.4% addition of NaOH by weight of cement were found to result in acceptable changes in mechanical properties of concrete, while the changes were more drastic for 0.8% NaOH addition and the ensuing concrete mixture may not be considered a good representation of the original concrete design. The following summarize the key findings.

- The first ASR cracks on specimens with 8% NaOH addition by weight of cement were observed after around 90 days and the crack intensity increased over time during the 432

days measurement period. While the crack intensity on the surface increased and the cracks coalesced, the crack widths remained between 0.05 mm and 0.1 mm throughout.

- Similarly, the addition of chloride to the fresh concrete paste in the form of $CaCl_2$ flakes substantially accelerated the rebar corrosion. Addition of 1% and 2% chloride by weight of cement resulted in acceptable differences in the physical and mechanical properties of the concretes, while the effects of 4% chloride addition were more drastic and deemed not representative of the control mixture.
- Cracks due to corrosion on specimens with 4% chloride by weight of cement were first observed after approximately 90 days of casting. The crack lengths and widths increased during the course of measurements. The average crack width increased by about 82% within a year and spalling was seen occasionally. Approximately 2% mass loss of rebar was observed within one year.
- Adding NaOH to the concrete mixture, removing any supplementary cementitious materials with ASR suppression characteristics (e.g., fly ash) and using reactive fine aggregate could be used as an effective method to accelerate ASR at the structural level. A 0.8% addition of NaOH by weight of cement into the fresh concrete reduced the time to first observation of ASR distress from tens of years to approximately 90 days. However, the concrete strength with this special mixture reduced by approximately 36% at 28 days compared to the control self-consolidating concrete (SCC).
- Similarly, it was observed that the direct addition of $CaCl_2$ is an effective way of accelerating the corrosion-induced aging. In this study, corrosion cracks were observed at approximately 120 days of age with 4% addition of $CaCl_2$ by weight of cement into the fresh concrete. However, it was seen that the concrete strength reduced by 24% at 28 days in comparison to the control SCC mixture. The $CaCl_2$ and SCC mixtures were identical except for the addition of chloride; therefore, all of this reduction was due to the presence of chloride.
- Adding chloride and alkali to the mixture decreased the setting time of the concrete by 37% and 16%, respectively. Addition of chloride also increased the hydration temperature by 5%.

3.5. REFERENCES

AASHTO (2011). *Standard Specification for Coal Fly Ash and Raw or Calcined Natural Pozzolan for Use in Concrete,* AASHTO M 295, American Association of State Highway and Transportation Officials (AASHTO), Washington, DC.

AASHTO (2014). *Standard Method of Test for Surface Resistivity Indication of Concrete's Ability to Resist Chloride Ion Penetration,* AASHTO TP 95-14, American Assocition of State Highway and Transportation Officials (AASHTO), Washington, DC.

ACI Committee 221 (1998). *Report on Alkali-Aggregate Reactivity,* ACI 221.1R, American Concrete Institute, Farmington Hills, MI.

ACI Committee 222 (2001). *Protection of metals in Concrete Against Corrosion,* ACI 222-01, American Concrete Institute, Farmington Hills, MI.

ACI Committee 318 (2011). *Building Code Requirements for Structural Concrete and Commentary (ACI 318-11)*, American Concrete Institute, Farmington Hills, MI.

ACI Committee 349 (2013). *Code Requirements for Nuclear Safety-Related Concrete Structures and Commentary (ACI 349-13)*, American Concrete Institute, Farmington Hills, MI.

Al-Attar, T. S. and Abdul-Kareem, M. S. (2011). "Effect of Chloride Ions Source on Corrosion of Reinforced Normal and High Performance Concrete," Buletinul AGIR, 2, 107-112.

Allahverdi, A. and Ghorbani, J. (2006). "Chemical Activation and Set Acceleration of Lime-Natural Pozzolan Cement," Ceramics-Silikaty, 50(4), 193-199.

Almusallam, A. A., Al-Gahtani, A. S., Aziz, A. R. and Rasheeduzzafar (1996). "Effect of Reinforcement Corrosion on Bond Strength," Construction and Building Materials, 10(2), 123-129.

Anantharaman, S. (2008). "Sulfate and Alkali Silica Resistance of Class C & F Fly Ash Replaced Blended Cements," School of Sustainable Engneering and Built Environment, Arizona State University, Tuscon, AZ.

Ardani, A. (2012). *Surface Resistivity Test Evaluation as an Indicator of the Chloride Permeability of Concrete,* FHWA-HRT-13-024, US Department of Transportation, Federal Highway Administration (FHWA), McLean, VA.

ASTM (1996). *Standard Practice for Developing Accelerated Tests to Aid Prediction of the Serice Life of Building Componenets and Materials (Withdrawn 2005),* ASTM E632-82, American Society of Testing and Materials Academic & Science (ASTM), West Conshohocken, PA.

ASTM (1997). *Standard Test Method for Pulse Velocity Through Concrete,* ASTM C597-97, American Society of Testing and Materials Academic & Science (ASTM), West Conshohocken, PA.

ASTM (2007). *Standard Test Methods for Potential Alkali Reactivity of Aggregates,* ASTM C1260-07, American Society of Testing and Materials Academic & Science (ASTM), West Conshohocken, PA.

ASTM (2008a). *Standard Test Method for Time of Setting of Concrete Mixtures by Penetration Resistance,* ASTM C403/C403M-08, American Society of Testing and Materials Academic & Science (ASTM), West Conshohocken, PA.

ASTM (2008b). *Standard Test Methods for Determination of Length Change of Concrete Due to Alkali-Silica Reaction,* ASTM C1293-08b, American Society of Testing and Materials Academic & Science (ASTM), West Conshohocken, PA.

ASTM (2009a). *Standard Test Method for Corrosion Potentials of Uncoated Reinforcing Steel in Concrete,* ASTM C876-09, American Society of Testing and Materials Academic & Science (ASTM), West Conshohocken, PA.

ASTM (2009b). *Standard Test Method for Slump Flow of Self-Consolidating Concrete,* ASTM C1611/C1611M-09b, American Society of Testing and Materials Academic & Science (ASTM), West Conshohocken, PA.

ASTM (2010). *Standard Test Method for Flexural Strength of Concrete (Using Simple Beam with Third-Point Loading,* ASTM C78-10, American Society of Testing and Materials Academic & Science (ASTM), West Conshohocken, PA.

ASTM (2011a). *Standard Practice for Preparing, Cleaning, and Evaluating Corrosion Test Specimens,* ASTM G1-03, American Society of Testing and Materials Academic & Science (ASTM), West Conshohocken, PA.

ASTM (2011b). *Standard Test Method for Splitting Tensile Strength of Cylindrical Concrete Specimens,* ASTM C496-11, American Society of Testing and Materials Academic & Science (ASTM), West Conshohocken, PA.

ASTM (2012a). *Standard Specification for Coal Fly Ash and Raw or Calcined Natural Pozzolan for Use in Concrete,* ASTM C618, American Society of Testing and Materials Academic & Science (ASTM), West Conshohocken, PA.

ASTM (2012b). *Standard Specification for Portland Cement,* ASTM C150/C150M, American Society of Testing and Materials Academic & Science (ASTM), West Conshohocken, PA.

ASTM (2012c). *Standard Test Method for Compressive Strength of Cylindrical Concrete Specimens,* ASTM C39-12, American Society of Testing and Materials Academic & Science (ASTM), West Conshohocken, PA.

ASTM (2012d). *Standard Test Method for Density, Relative Density (Specific Gravity), and Absorption of Coarse Aggregate,* ASTM C127-12, American Society of Testing and Materials Academic & Science (ASTM), West Conshohocken, PA.

ASTM (2012e). *Standard Test Method for Density, Relative Density (Specific Gravity), and Absorption of Fine Aggregate1,* ASTM C128-12, American Society of Testing and Materials Academic & Science (ASTM), West Conshohocken, PA.

ASTM (2012f). *Standard Test Methods and Definitions for Mechanical Testing of Steel Products,* ASTM A370-12, American Society of Testing and Materials Academic & Science (ASTM), West Conshohocken, PA.

ASTM (2013a). *Density and Void Content of Freshly Mixed Pervious Concrete,* ASTM C1688/C1688M-13, American Society of Testing and Materials Academic & Science (ASTM), West Conshohocken, PA.

ASTM (2013b). *Standard Test Method for Density, Absorption, and Voids in Hardened Concrete,* ASTM C642, American Society of Testing and Materials Academic & Science (ASTM), West Conshohocken, PA.

ASTM (2013c). *Standard Test Method for Rebound Number of Hardened Concrete,* ASTM C805/C805M-13a, American Society of Testing and Materials Academic & Science (ASTM), West Conshohocken, PA.

ASTM (2013d). *Standard Test Method for Total Evaporable Moisture Content of Aggregate by Dryin,* ASTM C566, American Society of Testing and Materials Academic & Science (ASTM), West Conshohocken, PA.

ASTM (2014). *Standard Test Method for Static Modulus of Elasticity and Poisson's Ratio of Concrete in Compression,* ASTM C469/C469M - 14, American Society of Testing and Materials Academic & Science (ASTM), West Conshohocken, PA.

Attar, A. (2016). "Accelerated Alkali-Silica Reaction and Corrosion of Reinforcing Steel in Concrete: Application on Dry Casks," Civil Engineering, University of Houston, Houston, TX.

Attar, A., Gencturk, B., Hanifehzadeh, M. and Willam, K. (2016). "Accelerated Aging of Concrete Dry Cask Storage System for Nuclear Waste," Journal of Adanced Concrete Technology, 14, 299-310.

Attoh-Okine, N. and Atique, F. (2006). *Service Life Assessment of Concrete with ASR and Possible Mitigation,* DCT 172, Delaware Center for Transportation, Newark, Delaware.

Bahadure, B. M. and Naik, N. S. (2013). "Effect of Alkaline Activator on Workability and Compressive Strength of Cement Concrete with RHA " International Journal of Computational Engineering Research, 3(5), 15-20.

Bargaheiser, K. and Butalia, T. S. (2007). *Prevention of Corrosion in Concrete Using Fly Ash Concrete Mixes*.

Bentur, A., Diamond, S. and Berke, N. S. (1997). *Steel Corrosion in Concrete*, E & FN Spon, New York, NY.

Berube, M.-A. and Fournier, B. (1993). "Canadian Experience with Testing for Alkali-Aggregate Reactiity in Concrete," Cement & Concrete Composites, 15(1-2), 27-47.

Bilodeau, A. and Malhotral, V. M. (1992). "Concretes Incorporating High Volume of ASTM Class F Fly Ashes: Mechanical Properties and Resistance to De-icing Salt Scaling and to Chloride-ion Penetration." *Fourth International Conference on the Use of Fly Ash, Silica Fume, Slag and Natural Pozzolans in Concrete*, ed Malhotra, V. M., May 1, Istanbul, Turkey, SP-132, 319-349.

Blackwell, B. Q., Thomas, M. D. A., Nixon, P. J. and Pettifer, K. (1992). "The Use of Fly Ash to Suppress Deleterious Expansion due to AAR in Concrete Containing Greywacke Aggregates." *9th International Conference on AAR in Concrete*, July 27-31, London, UK, 102-109.

Broomfield, J. P. (1997). *Corrosion of Steel in Concrete, Understanding, Investigation and Repair*, E & FN Spon, London, UK.

Broomfield, J. P. (2007). *Corrosion of Steel in Concrete, Understanding, Investigation and Repair*, Taylor & Francis, New York, NY.

Brown, P. W. and Doerr, A. (2000). "Chemical Changes in Concrete Due To the Ingress of Aggressive Species," Cement and Concrete Research, 30(3), 411-418.

BSI (1983). *Method for Determination of Compressive Strength of Concrete Cubes* BS 1881: Part 116, British Standards Institution (BSI), London,UK.

BSI (2000). *Concrete Specification, Performance, Production and Conformity,* BS EN-206, British Standards Institute (BSI), London,UK.

BSI (2005). *Structural Use of Concrete,* BS 8110, British Standards Institute (BSI), London, UK.

Bungey, J. H. and Millard, S. G. (1996). *Testing of Concrete in Structures*, Blackie Academic & Professional, London, UK.

CEFRACOR (2014). *Steel in the Sound Concrete,* Available from: http://www.concretecorrosion.net/html_en/mecanism/cadre.htm, Accessed on November 20, 2014.

Cusatis, G., Alnaggar, M. and Rezakhani, R. (2014). *Multiscale Modeling of Alkali Silica Reaction Degradation of Concrete*, Beijing, China.

Davis, G. and Oberholster, R. E. (1988). "Alkali-Silica Reaction Products and Their Development," Cement and Concrete Research, 18(4), 621-635, DOI: 10.1016/0008-8846(88)90055-5.

Deschenes, D. J., Bayrak, O. and Folliard, K. J. (2009). *ASR/DEF-Damaged Bent Caps: Shear Tests and Field Implications,* Report No. 12-8XXIA006, Texas Department of Transportation (TxDOT), Austin, TX.

Detwiler, R. (1997). *The Role of Fly Ash Composition in Reducing Alkali-Silica Reaction,* Report No. 2092, Portland Cement Association (PCA), Skokie, Illinois.

Diamond, S. (1986). "Chloride Concentrations in Concrete Pore Solutions Resulting from Calcium and Sodium Chloride Admixtures," Cement, Concrete and Aggregates, 8(2), 97-102.

Diamond, S. and Ong, S. (1994). "Effects of Added Alkali Hydroxides in Mix Water on Long-Term SO_4^{2-} Concentration in Pore Solution," Cement & Concrete Composites, 16(3), 219-226, DOI: 10.1016/0958-9465(94)90019-1.

Fan, S. and Hanson, J. M. (1998a). "Effect of Alkali Silica Reaction Expansion and Cracking on Structural Behavior of Reinforced Concrete Beams," Structural Journal, 95(5), 498-505, DOI: 10.14359/564.

Fan, S. and Hanson, J. M. (1998b). "Length Expansion and Cracking of Plain and Reinforced Concrete Prisms Due to Alkali-Silica Reaction," ACI Materials Journal, 95(5), 480-487.

Farny, J. A. and Kosmatka, S. H. (1997). *Diagnosis and Control of Alkali-Aggregate Reactions in Concrete* Portland Cement Association.

Ferraris, C. F. (1995). *Alkali-Silica Reaction and High Performance Concrete,* NISTIR 5742, National Institute of Standards and Technology (NIST), Gaithersburg, MD.

Figg, J. (1983). *An Attempt to Provide an Explanation for Engineers of the Expansive Reaction between Alkalis and Siliceous Aggregates in Concrete*, Copenhagen, Denmark.

Fournier, B. and Bérubé, M. A. (1993). "Recent Applications of a Modified Gel Pat Test to Determine the Potential Alkali-Silica Reactivity of Carbonate Aggregates," Cement & Concrete Composits, 15(1-2), 49-73, DOI: 10.1016/0958-9465(93)90038-B.

Freskakis, G. N. (1979). "Strength Properties of Concrete at Elevated Temperature." *Civil Engineering Nuclear Power*, April 12th, 1979, Boston, MA, 1.

Gao, X. X., Multon, S., Cyr, M. and Sellier, A. (2013). "Alkali-Silica Reaction (ASR) Expansion: Pessimum Effect versus Scale Effect," Cement and Concrete Research, 44, 25-33.

Garci Juenger, M. C. and Jennings, H. M. (2011). "Effects of High Alkalinity on Cement Pastes," ACI Materials Journal, 98(3), 251-255.

Ghosh, P. and Tran, Q. (2015). "Correlation between Bulk and Surface Resistivity of Concrete," International Journal of Concrete Structures and Materials, 9(1), 119-132.

Gillott, J. E. and Soles, J. A. (1993). "Petrography of Concrete Cores from New Brunswick, Relating to the Durability Problem," Cement and Concrete Composits, 15(1-2), 101-114, DOI: 10.1016/0958-9465(93)90041-7.

Hansson, C. M., Frølund, T. and Markussen, J. B. (1985). "The Effect of Chloride Cation Type on the Corrosion of Steel in Concrete by Chloride Salts," Cement and Concrete Research, 15(1), 65-73.

Hansson, C. M., Poursaee, A. and Laurent, A. (2006). "Macrocell and Microcell Corrosion of Steel in Ordinary Portland Cement and High Performance Concrete," Cement and Concrete Research, 36(11), 2098-2102, DOI: 10.1016/j.cemconres.2006.07.005.

Harrisson, A. M., Varma, S. P. and Winter, N. B. (1987). "Alkali-Silica Gel Formation at an Early Age through Solution," ACI Special Publication, SP 100-89, 1743-1758.

Hausmann, D. A. (1967). "Steel Corrosion in Concrete; How Does It Occur?," Materials Protection, 6(11), 19-23.

Helmuth, R., Stark, D., Diamond, S. and Moranville-Regourd, M. (1993). *Alikali-Silica Reactivity: An Overview of Research,* SHRP-C-342, Strategic Highway Research Program (SHRP), Washington, DC.

Hewlett, P. C. (2004). *Lea's Chemistry of Cement and Concrete*, Elsevier Science & Technology Books.

Holder, T. B. (1999). "The Deterioration of Chloride Threshold Concentrations Using Different Supplementary Cementing Materials in Steel-Reinforced Concrete," Department of Civil Engineering, University of Toronto, Toronto, Canada.

Jaffer, S. J. and Hansson, C. M. (2009). "Chloride-Induced Corrosion Products of Steel in Cracked-Concrete Subjected to Different Loading Conditions," Cement and Concrete Reseach, 39(2), 116-125.

Jang, J.-W., Iwasaki, Iwao and Weiblen, P. (1995). *Effect of Salt Additives on Concrete Degradation (Phase II),* MN/RC-96/10, Minnesota Department of Transportation (MnDOT), St. Paul, Minnesota.

Johnson, J. B. (2010). "Bond Strength of Corrosion Resistant Steel Reinforcement in Concrete," Department of Civil and Environmental Engineering, Virginia Polytechnic Institute and State University, Charlottesville, Virginia.

Jones, A. E. K. and Clark, L. A. (1998). "The Effects of ASR on the Properties of Concrete and the Implications for Assessment," Engineering Structures, 20(9), 785-791.

Jones, F. E. and Tarleton, R. D. (1958a). *Reaction between Aggregates and Cements, Parts I-IV*, DSIR National Building Studies Research, HMSO, London, UK.

Jones, F. E. and Tarleton, R. D. (1958b). *Reaction between Aggregates and Cements, Parts I-IV*, DSIR National Building Studies Research, HMSO, London, UK.

Jung, W.-Y., Yoon, Y.-S. and Sohn, Y.-M. (2003). "Predicting the Remaining Service Life of Land Concrete by Steel Corrosion," Cement and Concrete Research, 33(5), 663-677.

Kelestemur, O. and Yildiz, S. (2006). "Effect of Various NaCl Concentration on Corrosion of Steel in Concrete Produced by Addition of Styrofoam," Gazi University Journal of Science, 19(3), 163-172.

Kessler, R. J., Powers, R. G., Vivas, E., Paredes, M. A. and Virmani, P. Y. (2008). "Surface Resistivity as an Indicator of Concrete Chloride Penetration Resistance." *Concrete Bridge Conference*, May 4-7, St. Louis, MO.

Kishar, E. A., Ahmed, D. A., Mohammed, M. R. and Noury, R. (2013). "Effect of Caclium Chloride on the Hydration Characteristics of Ground Clay Bricks Cement Pastes," Bein-Suef University Journal of Basic and Applied Sciences, 2(1), 20-30.

Kupwade-Patil, K. and Allouche, E. (2013). "Impact of Alkali Silica Reaction on Fly Ash-Based Geopolymer Concrete," Journal of Materials in Civil Engineering, 25(1), 131-139.

Lamond, J. F. and Pielert, J. H. (2006). *Significance of Tests and Properties of Concrete and Concrete-Making Materials,* STP 169D, ASTM International, West Conschohocken, PA.

Memon, F. A., Nuruddin, M. F., Khan, S., Shafiq, N. and Ayub, T. (2013). "Effect of Sodium Hydroxide Concentration on Fresh Properties and Compressive Strength of Self-Compacting Geopolymer Concrete," Journal of Engineering Science and Technology, 8(1), 44-56.

Mladenovic, A., Šturm, S., Mirtic, B. and Šuput, J. S. (2009). "Alkali Silica Reaction in Mortars Made from Aggregates Having Different Degrees of Crystalinity," Ceramics – Silikáty, 53(1), 31-41.

Monette, L. J. and Gardner, N. J. (2002). "Residual Strength of Reinforced Concrete Beams Damaged by Alkali-Silica Reaction - Examination of Damage Rating Index Method," ACI Material Journal, 99(1), 42-50.

Morris, W., Moreno, E. I. and Sagues, A. A. (1996). "Practical Evaluation of Resistivity of Concrete in Test Cylinders Using a Wenner Array Probe," Cement and Concrete Research, 26(12), 1779-1787.

Mukhopadhyay, A. K., Ghanem, H., Shon, C.-S., Gress, D. and Hooton, D. (2009). *Mitigation of ASR in Concrete Pavement - Combined Materials Testing,* IPRF-01-G-002-03-2, Innovative Pavement Research Foundation (IPRF), Skokie, Illinois.

Nagataki, S., Ohga, H. and Inquel, T. (1991). "Evaluation of Fly Ash for Controlling Alkali-Aggregate Reaction." *2nd International Conference on Durability of Concrete* June 13-15, Montreal, Canada, 126, 955-972.

Naik, T. R., Ramme, B. W. and Tews, J. H. (1995). "Pavement Construction with High-Volume Class C and Class F Fly Ash Concrete," ACI Materials Journal, 92(2), 200-210.

Naik, T. R., Singh, S. S. and Hossain, M. M. (1994). "Permeability of Concrete Containing Large Amount of Fly Ash," Cement & Concrete Research, 24(5), 913-922.

Naus, D. J. (2007). *Primer of Durability of Nuclear Power Plant Reinforced Concrete Structures - A Review of Pertinent Factors,* NUREG/CR-6927, ORNL/TM-2006/529, Oak Ridge National Laboratory (ONRL), Washington, DC.

Naus, D. J. (2010). *A Compilation of Elevated Temperature Concrete Material Property Data and Information for Use in Assessments of Nuclear Power Plant Reinforced Concrete Structures,* NUREG/CR-7031, ORNL/TM-2009-175, Oak Ridge National Laboratory (ORNL)

United States Nuclear Regulatory Commision (U.S. NRC), Oak Ridge, TN.

Naus, D. J., Oland, C. B. and Ellingwood, B. R. (1996). *Report on Aging of Nuclear Power Plant Reinforced Concrete Structures* NUREG/CR-6424, BNL-NUREG-13148, Oak Ridge National Laboratory (ONRL), Oak Ridge, TN.

NEA (2002). *Electrochemical Techniques to Detect Corrosion in Concrete Structures in Nuclear Installations - Technical Note,* NEA-CSNI-R-2002-21, Nuclear Energy Agency of the OECD (NEA), Paris, France.

Neville, A. (1995). "Chloride Attack of Reinforced Concrete: an Overview," Materials and Structures, 28, 63-70.

Nordson, D. (2014). *3 and 4 Point Flexural Testing, Application Note*

NT-build (1995). *Concrete, Hardened: Accelerated Chloride Penetration,* NT build 443, Nordtest, Esbo, Finland.

NT-build (1996). *Concrete, Hardened: Chloride Content by Volhard Titration,* NT build 208, Nordtest, Esbo, Finland.

Nuruddin, M. F., Demie, S., Ahmed, M. F. and Shafiq, N. (2011). "Effect of Superplasticizer and NaOH Molarity on Workability, Compressive Strength and Microstructure Properties of Self-Compacting Geopolymer Concrete " World Academy of Science, Engineering and Technology, 5(3), 187-194.

Ohdaira, E. and Masazawa, N. (2000). "Water Content and Its Effect on Ultrasound Propagation in Concrete - the Possibility of NDE," Ultrasonics, 38(1-8), 546-552.

Okba, S. H., El-Dieb, A. S. and Reda, M. M. (1997). "Evaluation of the Corrosion Resistance of Latex Modified Concrete (LMC)," Cement and Concrete Research, 27(6), 861-868.

Ortega, N. F., Rivas, I. E., Aveldaño, R. R. and Peralta, M. H. (2011). "Beams Affected by Corrosion Influence of Reinforcement Placement in The Cracking," Structural Engineering and Mechanics, 37(2), 163-175.

Pakshir, M. and Esmaili, S. (1998). "The Effect of Chloride Ion Concentration on the Corrosion of Concrete," Scientia Iranica, 4(4), 201-205.

Pan, J. W., Feng, Y. T., Wang, J. T., Sun, Q. C., Zhang, C. H. and Owen, D. R. (2012). "Modeling of Alkali-Silica Reaction in Concrete: A Review," Frontiers of Structures and Civil Engineering, 6(1), 1-18.

Parrott, L. J. (1987). *A Review of Carbonation in Reinforced Concrete*, Cement and Concrete Association, Slough, UK.

Parsons, W. H. and Insley, H. (1944). "Alkali Etching Tests on Concrete Aggregates," Journal of American Concrete Institute, 40, 229-244.

Pesavento, F., Gawin, D., Wyrzykowski, M., Schrefler, B. A. and Simoni, L. (2012). "Modeling alkali-silica reaction in non-isothermal, partially saturated cement based materials," Computer Methods in Applied Mechanics and Engineering, 225-228, 95-115.

Pignatelli, R. (2012). "Modeling of Degradation Induced by Alkali-Silica Reaction in Concrete Structures," Structural Engineering, Politecnico di Milano, Milan, Italy.

Pommersheim, J. and Clifton, J. (1985). "Prediction of Concrete Service-Life," Materials and Structures, 18(1), 21-30.

Poole, J. L. (2007). "Modeling Temperature Sensitivity and Heat Evolution of Concrete," Graduate School, The University of Texas at Austin, Austin, TX.

Pruckner, F. and Gjørv, O. E. (2004). "Effect of $CaCl_2$ and NaCl Additions on Concrete Corrosivity," Cement and Concrete Research, 34(7), 1209-1217.

Rezakhani, R., Alnaggar, M. and Cusatis, G. (2016). *Multiscale Homogenization Modeling of Alkali-Silica-Reaction Damage in Concrete*, Berkeley, CA.

Roy, D., Malek, R. and Licastro, P. (1987). "Chloride Permeability of Fly Ash-Cement Pastes and Mortars," in *Concrete Durability,* ed Scanlon, J. M., American Concrete Institute (ACI), 100, 1459-1476.

Rupnow, T. D. and Icenogle, P. (2011). *Evaluation of Surface Resistivity Measurements as an Alternative to the Rapid Chloride Permeability Test from Quality Assurance and Acceptance,* FHWA/LA.11/479, Louisiana Department of Transportation and Development (LaDOT), Baton Rouge, LA.

Sarkar, S. L., Zollinger, D. G., Mukhopadhyay, A. K., Seungwook, L. and Shon, C.-S. (2004). *Handbook for Identification of Alkali-Silica Reactivity in Airfield Pavement,* 150/5380-8, US Department of Transportation, Federal Aviation Administration (FAA), College Station, Texas.

Schiessl, P. (1988). *Corrosion of Steel in Concrete*, Reunion Internationale des Laboratoires et Experts des Materiaux (RILEM), New York, NY.

Shayanfar, M. A. and Ghalehnovi, M. (2007). "Corrosion Effects on Tension Stiffening Behavior of Reinforced Concrete," Computers and Concrete, 4(5), 403-424.

Shehata, M. H. and Thomas, M. D. A. (2000). "The Effect of Fly Ash Composition on the Expansion of Concrete Due to Alkali-Silica Reacting," Cement and Concrete Reseach, 30(7), 1063-1072, DOI: http://dx.doi.org/10.1016/S0008-8846(01)00680-9.

Silva, N. (2013). "Chloride Induced Corrosion of Reinforcement Steel in Concrete," Department of Civil and Environmental Engineering, Chalmers University of Technology, Göteborg, Sweden

Smaoui, N., Bérubé, M. A., Fournier, B., Bissonnette, B. and Durand, B. (2005). "Effects of Alkali Addition on the Mechanical Properties and Durability of Concrete," Cement and Concrete Research, 35(2), 203-212.

Stanton, T. E. (1943a). "Studies to Develop an Accelerated Test Procedure for The Detection Of Adversely Reactive Cement-Aggregate Combination." *American Society of Testing and Materials Proceeding*, 43, 875-893.

Stanton, T. E. (1943b). "Studies to Develop an Accelerated Test Procedure for the Detection of Adversley Reactive Cement-Aggregate Combination." *American Society of Testing and Materials Proceeding*, 43, 875-893.

Streicher, P. E. and Alexander, M. G. (1995). "A chloride Conduction Test for Concrete," Cement and Concrete Research, 25(6), 1284-1294, DOI: http://dx.doi.org/10.1016/0008-8846(95)00121-R.

Temuujin, J., Williams, R. P. and Riessen, A. v. (2009). "Effect of Mechanical Activation of Fly Ash On The Properties Of Geopolymer Cured at Ambient Temperature," Journal of Materials Processing Technology, 209(12-13), 5726-5280.

Thomas, M., Dunster, A., Nixon, P. and Blackwell, B. (2011). "Effect of Fly Ash on the Expansion of Concrete due to Alkali-Silica Reaction – Exposure Site Studies," Cement & Concrete Composites, 33(3), 359-367.

Tuutti, K. (1982). *Corrosion of Steel in Concrete*, Swedish Cement and Concrete Research Institute, Stockholm, Sweden.

Yu, H., Shi, X., Hartt, W. H. and Lu, B. (2010). "laboratory Investigation of Reinforcement Corrosion Initiation and Chloride Threshold Content for Self-Compacting Concrete," Cement and Concrete Research, 40(10), 1507-1516.

CHAPTER 4

THERMAL ANALYSIS OF DRY CASKS

4.1. INTRODUCTION

In this chapter, the heat transfer in the concrete cask is analyzed to determine the thermal state of the concrete cask. The temperature distributions were first computed for full-scale model and was further analyzed for a scaled model (based on scaling analysis). The effects of thermal radiation, laminar/turbulence models, summer and winter operation conditions were also analyzed and discussed in the following sections.

4.2. THERMAL LOADING OF DRY CASKS

There are various designs of dry casks, like VSC-17, Castor V/21, MC-10, REA-2023, TN-24P (see Figure 4-1). The VSC-17 is a concrete-shielded spent nuclear fuel (SNF) storage cask system, which contains 17 pressurized water reactor (PWR) fuel assemblies (Morton et al., 2006) (see also Section 2.2.2.b). VSC-17 design is adopted to develop the benchmark calculation of temperature distribution inside the dry cask. The dimensions and heat source terms are taken from the report titled, "Performance Testing and Analyses of the VSC-17 Ventilated Concrete Cask" (McKinnon et al., 1992). This cask consists of a Ventilated Concrete Cask (VCC) and a Multi-Assembly Sealed Basket (MSB) with annular flow cooling the outside of the MSB and the inside of the VCC. The VCC includes a reinforced concrete body, inner steel liner and a weather cover (lid), see Figure 4-2 Design of VSC-17 cask (McKinnon et al., 1992). The total fuel rod decay heat is approximately 14.9 kW predicted by ORIGEN2 (McKinnon et al., 1992). The fuel assemblies had cooling times of 9 years to 15 years. Standard calculations were first carried out to determine the temperature distributions in next section.

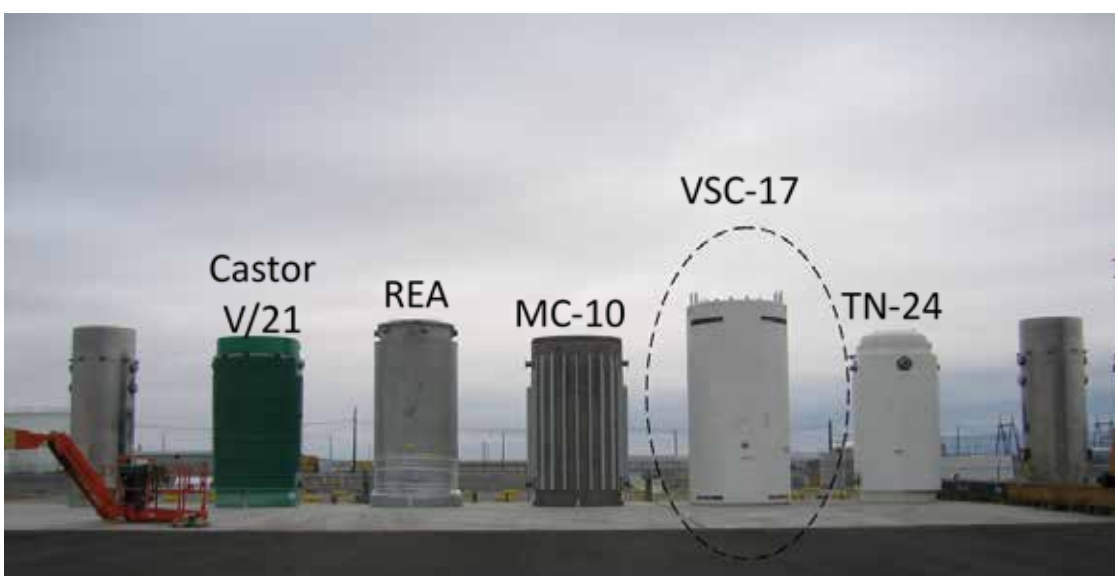

Figure 4-1 Different types of dry casks (Morton et al.,2006).

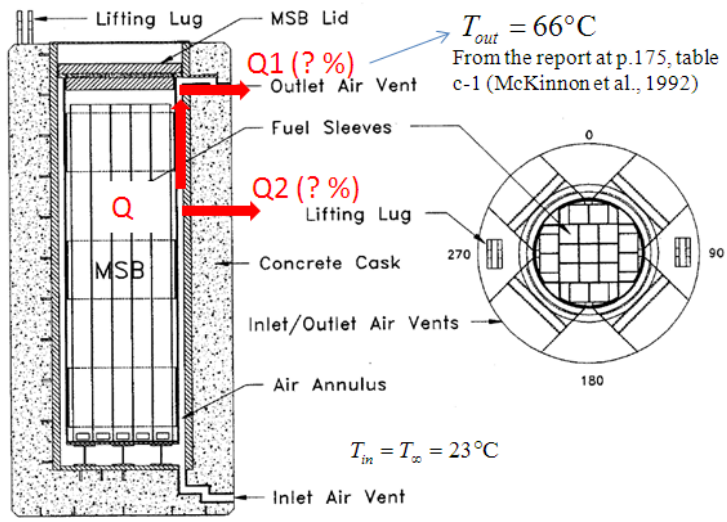

Figure 4-2 Design of VSC-17 cask (McKinnon et al., 1992).

4.3. ESTIMATION OF TEMPERATURE DISTRIBUTION IN DRY CASKS

4.3.1. Evaluation of Temperature Distribution in Concrete

4.3.1.a. Heat transfer coefficient determination (air, outside of the dry cask)

For vertical plate (Incropera et al., 2006)

$$Nu = \left\{ 0.825 + \frac{0.387 Ra^{1/6}}{[1+(0.492/\Pr)^{(9/16)}]^{8/27}} \right\}^2 \qquad 4.1$$

The results can be applied to the vertical cylinder under the following condition

$$\frac{D}{H} \geq \frac{35}{Gr^{1/4}} \qquad 4.2$$

In this case

$$\frac{D}{H} = \frac{1.3335m}{3.658m} = 0.3645, \quad \frac{35}{Gr^{1/4}} = 0.0508, \quad Gr = 2.2567 \times 10^{11},$$

which satisfies Eq. 4.2. Using Eqn. 4.1, Nusselt number is found to be *Nu*=610.6. The corresponding heat transfer coefficient of air at surface of the cask, *h*

$$h = \frac{Nu \times k}{H} = 4.39 \text{ W/m}^2\text{-K} \qquad 4.3$$

From the report: Computational Fluid Dynamics Best Practice Guidelines for Dry Cask Applications (Zigh & Solis, 2013), the heat transfer coefficients used in the calculation are:

- heat-transfer coefficient of **5** W/m^2-K on the top and side of the VCC
- heat-transfer coefficient of **10** W/m^2-K on the top of the VCC weather cover

The value calculated here is close to that applied in the CFD simulation.

4.3.1.b. Estimation of surface temperature

Case a) if all the decay heat is transferred all the way through the cask surface:

From the VSC-17 cask design: decay heat Q=14.9 kW

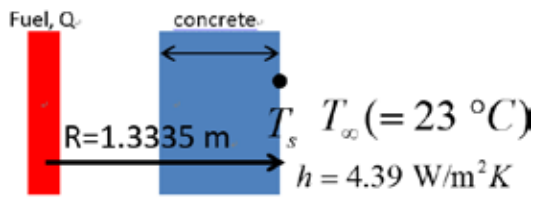

$$h\,(T_s - T_\infty)\,A = Q = 14.9\ kW \qquad 4.4$$

$$A = 2\rho RH,\ H = 3.658\ m$$

$$\Rightarrow T_s = T_\infty + \frac{Q}{hA} \qquad 4.5$$

$$\Rightarrow T_s(°C) = T_\infty + 133.75$$

Under these conditions, the surface temperature is found to be very high.

Case b) Considering the impact of the annular air channel between MSB and VCC:

In VSC-17 cask, natural circulation allows annular airflow to cool the outside of MSB and inside of VCC. Thus, at the outside surface of MSB, the decay heat can be transmitted to the environment through two ways:

1. Natural circulation in annular channel (outside of MSB; inside of VCC): Q1
2. Outer surface of VCC: Q2

To determine the temperature distribution, we need to first find out the percentage of total decay heat that is carried through each mechanism. From the report by McKinnon et al. (1992), the average temperature at the exit of the annular channel is $66°C$. Using this we can calculate Q1 and Q2 (Figure 4-2 and Figure 4-3).

The velocity in the annular channel is approximately 2 ft/s (McKinnon et al., 1992, p.137).

$$V = 2\ \mathrm{ft/s} = 0.6096\ \mathrm{m/s} \qquad 4.6$$

$$A_{annulus} = p(R_2^2 - R_1^2) = 0.356885\ m^2 \qquad 4.7$$

$$\begin{aligned} Q1 &= rVACp(T_{out} - T_{in}) \\ &= 1.0782 \times 0.6096 \times 0.356885 \times 1.008 \times (66 - 23) \\ &= 10.167kW\ (68.2\%) \end{aligned} \qquad 4.8$$

$$Q2 = Q - Q1 = 4.733kW\ (31.8\%) \qquad 4.9$$

This shows that about 70% of decay heat is removed by natural circulation. From Eq. 4.5

$$T_s = T_\infty + \frac{Q2}{hA} = 23 + \frac{4.733 \times 10^3}{4.39 \times 2p \times 1.3335 \times 3.658} = 58.2\ °C = 331\ K \qquad 4.10$$

Using the heat conduction equation $(1/r)(d/dr)(k \cdot r \cdot dT/dr) = 0$, the analytical solution for temperature in the concrete region (layer 4, Figure 4-4) is

$$T(r) = C_1 \ln(r) + C_2 \qquad 4.11$$

Applying the boundary conditions at R3 and R4,

$BC1$:

$$\begin{aligned} & -k_{concrete} \left.\frac{dT}{dr}\right|_{r=R3=0.86m} \times A = Q2 \\ & \Rightarrow -k_{concrete} \left.\frac{C_1}{r}\right|_{r=R3=0.86m} = \frac{Q2}{A} \\ & \Rightarrow C1 = -\frac{R3 \times Q2}{k_{concrete} \times A} \\ & \quad = -\frac{0.86 \times 4733}{1.47 \times 2p \times 0.86 \times 3.658} \\ & \quad = -22.295 \end{aligned} \qquad 4.12$$

$BC2$:

$$\begin{aligned} & T(r = R4 = 1.3335m) = 58.2\ °C \\ & \Rightarrow -22.295 \times \ln(1.3335) + C_2 = 58.2 \\ & \Rightarrow C_2 = 64.617 \end{aligned} \qquad 4.13$$

Therefore,

$$T(r) = -22.295 \ln(r) + 64.617 \qquad 4.14$$

$$T(r = R3 = 0.86m) = 67.98\ °C \qquad 4.15$$

Figure 4-4 shows the temperature distribution in the concrete shell.

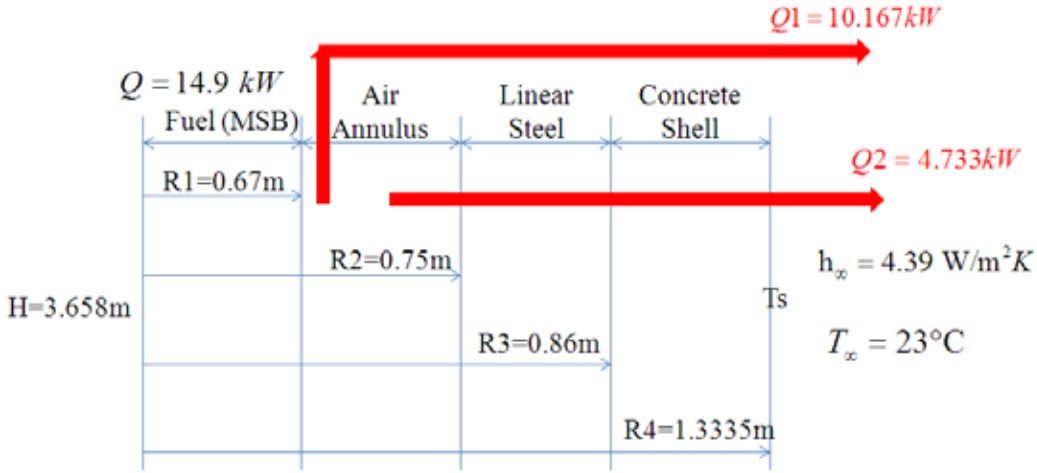

Figure 4-3 Dimensions of four layers of VSC-17 cask (not to scale).

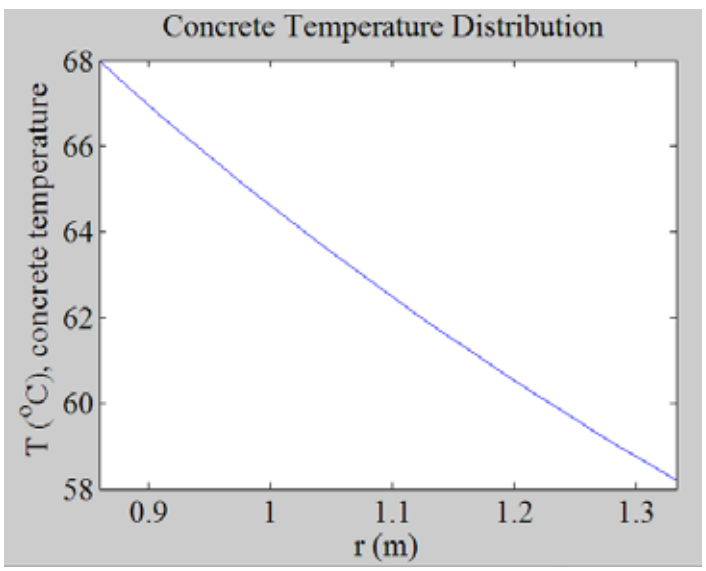

Figure 4-4 Temperature distribution in concrete shell.

4.3.2. Consideration of Volumetric Heat Source in the Concrete Layer.

Radiative capture reactions will emit γ rays and deposit part of the energy in concrete. To evaluate this volumetric heat source, we need to calculate the attenuation and absorption coefficients for steel and concrete, for the energy level of incoming γ rays. Thermal neutrons absorbed by hydrogen atoms emit 2.22 MeV gamma photon. 2.22 MeV is used to compute the corresponding coefficients for steel and concrete.

4.3.2.a. <u>For steel</u>

The attenuation coefficient is calculated to determine the fraction of gamma rays that penetrate the steel layer all the way, and enter the concrete cask.

Table 4-1 Mass Coefficients (cm^2/g) for Natural Iron with a Density of 7.874 g/cm^3. Read Entry 1.234-5 as 1.235 x10^{-5} (Kenneth and Faw, 2002).

				Attenuation	Energy Transfer	Energy Absorption
	Iron (Z = 26)					
E (MeV)	μ_c/ρ	μ_{ph}/ρ	μ_{pp}/ρ	μ/ρ	μ_{tr}/ρ	μ_{en}/ρ
0.0010	8.776−3	9.080+3		9.080+3	9.052+3	9.052+3
0.0015	1.530−2	3.395+3		3.395+3	3.388+3	3.388+3
0.0020	2.124−2	1.622+3		1.622+3	1.620+3	1.620+3
0.0030	3.206−2	5.542+2		5.543+2	5.536+2	5.535+2
0.0040	4.212−2	2.538+2		2.539+2	2.536+2	2.536+2
0.0050	5.133−2	1.373+2		1.374+2	1.372+2	1.372+2
0.0060	5.966−2	8.272+1		8.278+1	8.268+1	8.265+1
2.00	4.107−2	1.003−4	1.364−3	4.254−2	2.258−2	2.199−2
3.00	3.232−2	5.448−5	3.792−3	3.616−2	2.122−2	2.042−2
4.00	2.697−2	3.669−5	6.085−3	3.309−2	2.094−2	1.990−2

Table 4-2 Mass Coefficients (cm^2/g) for ANSI/ANS-6.4.3 Standard Concrete of Density of2.3 g/cm^3. Composition by Weight Fraction: H 0.005599, O 0.498250, Na 0.017098, Mg 0.002400, Al 0.045595, Si 0.315768, S 0.001200, K 0.019198, Ca 0.082592, Fe 0.012299. Read Entry 1.234-5 as 1.235 x10^{-5} (Kenneth and Faw, 2002).

				Attenuation	Energy Transfer	Energy Absorption
	Concrete					
E (MeV)	μ_c/ρ	μ_{ph}/ρ	μ_{pp}/ρ	μ/ρ	μ_{tr}/ρ	μ_{en}/ρ
0.00100	1.117−2	3.443+3		3.443+3	3.436+3	3.436+3
0.00104	2.098−2	3.144+3		3.144+3	3.138+3	3.138+3
0.00107	1.249−2	2.871+3		2.871+3	2.865+3	2.865+3
0.00107K	1.249−2	2.972+3		2.972+3	2.964+3	2.964+3
0.00118	3.115−2	2.300+3		2.300+3	2.295+3	2.295+3
0.00131	1.701−2	1.775+3		1.775+3	1.771+3	1.771+3
2.00	4.416−2	9.586−6	6.212−4	4.480−2	2.376−2	2.353−2
3.00	3.474−2	5.267−6	1.775−3	3.652−2	2.124−2	2.091−2
4.00	2.898−2	3.576−6	2.899−3	3.189−2	1.975−2	1.934−2

From (the table for natural iron is used), for 2.22 MeV gamma ray:

$$\frac{m}{r} = 0.0411364 \ \frac{cm^2}{g}$$

$$r = 7.874 \ \frac{g}{cm^3} \qquad 4.16$$

$$m = 0.323908 \ \text{cm}^{-1}$$

$$= 32.4 \ \text{m}^{-1}$$

Thickness of steel r = 0.11 m.

$$\frac{I}{I_0} = e^{-mr} = 2.8\% \qquad 4.17$$

Therefore, only about 3% of the (gamma ray) energy is expected to enter the concrete, and will constitute the volumetric heat source.

4.3.2.b. <u>For concrete</u>

The absorption coefficient is computed to examine the volumetric heat source distribution due to the absorption of gamma ray. From Table 4-2, for 2.22 MeV gamma ray:

$$\frac{\mu_{en}}{\rho} = 0.0229536 \ \frac{cm^2}{g}$$

$$\rho = 2.3 \ \frac{g}{cm^3} \qquad 4.18$$

$$\mu = \mu_{en} = 0.0527933 \text{ cm}^{-1}$$

$$= 5.279 \text{ m}^{-1}$$

Solving the heat conduction equation with volumetric heat source in concrete, the governing equation:

$$\frac{1}{r}\frac{d}{dr}(k \times r\frac{dT}{dr}) + g_0 e^{-\mu(r-R3)} = 0 \ , \ \text{let g} = \frac{g_0}{k}$$

$$\Rightarrow \frac{1}{r}\frac{d}{dr}(r\frac{dT}{dr}) + g e^{-\mu(r-R3)} = 0 \qquad 4.19$$

Boundary conditions:

$$-k\left.\frac{dT}{dr}\right|_{r=R3=0.86m} \times A = 0.972 \times Q2$$

$$\Rightarrow \left.\frac{dT}{dr}\right|_{r=R3=0.86m} = -\frac{0.972 \times Q2}{kA} = -\frac{4600.48}{1.47 \times 2\pi \times 0.86 \times 3.658} = -159.633 \qquad 4.20$$

$$\Rightarrow BC1: \ \left.\frac{dT}{dr}\right|_{r=R3=0.86m} = -158.33 \qquad 4.21$$

$$BC2: \ T(r = 1.3335m) = 58.2°\text{C} \qquad 4.22$$

Determination of g_0 and g, assume 2.8% of gamma ray energy becomes volumetric heat source in concrete:

$$Q2 \times 2.8\% = \int_{R3=0.86m}^{R4=1.3335m} (g_0 e^{-\mu(r-R3)}) \times 2\pi r dr \times H$$

$$\Rightarrow 4733 \times 2.8\% = \int_{0.86m}^{1.3335m} (g_0 e^{-5.279(r-0.86)}) \times 2\pi r dr \times 3.658 \qquad 4.23$$

$$g_0 = 48.4054$$

$$g = 32.9288$$

To solve Eq. 4.19, apply Taylor series to expand the source term $ge^{-m(r-R3)}$ (keeping 30 terms, which provides sufficient accuracy for this case, μ = 5.279).

$$q_{dot} = ge^{-m(r-R3)} = 5.52251\,\acute{}\,10^{-8} r^{30} - 3.13838\,\acute{}\,10^{-7} r^{29} + ¼ - 16285.4r + 3084.94 \qquad 4.24$$

Solving Eq. 4.19 and applying the two BCs:

$$\mathrm{T}(\mathrm{r}) = -5.39302\,\acute{}\,10^{-11} r^{32} + 3.26573\,\acute{}\,10^{-10} r^{31} + ¼ + 237.077 \qquad 4.25$$

Figure 4-5 compares the temperature distributions with and without volumetric heat source. The temperatures at the inner surface of concrete with and without the effects of volumetric heat source differ by less than 0.01 °C (because the steel layer stops most of gamma rays and only 2.8% enters the concrete region). Therefore, the volumetric heat source term can be ignored in this calculation.

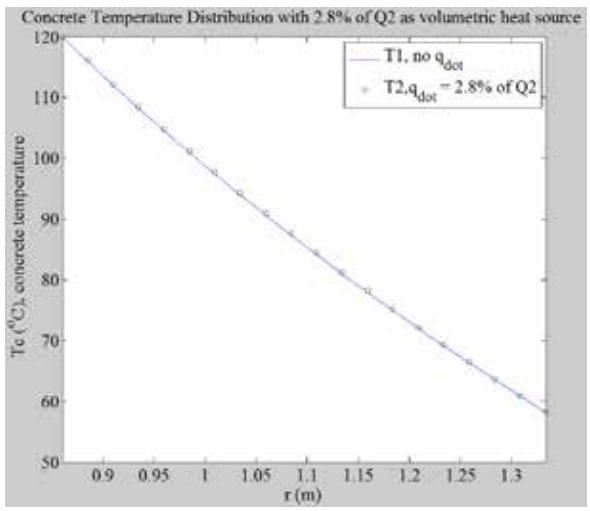

Figure 4-5 Temperature distribution in concrete shell with 2.8 % of Q2 as heat source.

The following parameters are used for the calculations above:

Nu: Nusselt number

Ra: Rayleigh number, $Ra = Gr \times \mathrm{Pr}$

Pr: Prandtl number, $\mathrm{Pr} = 0.707$ (air)

D: diameter of the cask, D=1.3335 m

H: active fuel length, H=3.658 m

Gr: Grashof number, $Gr = \dfrac{g\,b(T_s - T_¥)H^3}{n^2}$

g: acceleration of gravity, $g = 9.8\ \mathrm{m/s^2}$

β: thermal expansion coefficient, $b = \frac{1}{T_{¥}}$

$T_{¥}$: environmental temperature, $T_{¥} = 296\ \mathrm{K}$

T_s : surface temperature of the cask, $T_s = 331\ \mathrm{K}$

n: kinematic viscosity, $n = 1.589 \times 10^{-5}\ m^2 / s$

k: thermal conductivity, k=0.0263 W/m-K (air) =1.47 W/m-K (Concrete)

4.4. COMPUTATIONAL FLUID DYNAMICS OF DRY CASKS

The code STARCCM+ (CD-adapco, 2016) is used for the fluid dynamics and heat transfer analysis. The solid concrete cask model developed for the fabrication of the test specimen is investigated and meshed to simulate the natural convection flow through the air vent. The dimensions of the scaled cask are 80 inches (2.03 m) for VCC length, 48 inches (1.22 m) for VCC outer diameter, and 9.375 inches (23.8 cm) for concrete thickness. CFD analysis is important to have an accurate estimate of the concrete temperature, and hence a better understanding of the design.

4.4.1. Mesh Generation

The solid and fluid models are presented in Figure 4-6. Figure 4-7 shows the general mesh configuration of the model and a cutting plane, which were used to present the mesh models to conduct grid independence tests.

(a) (b)

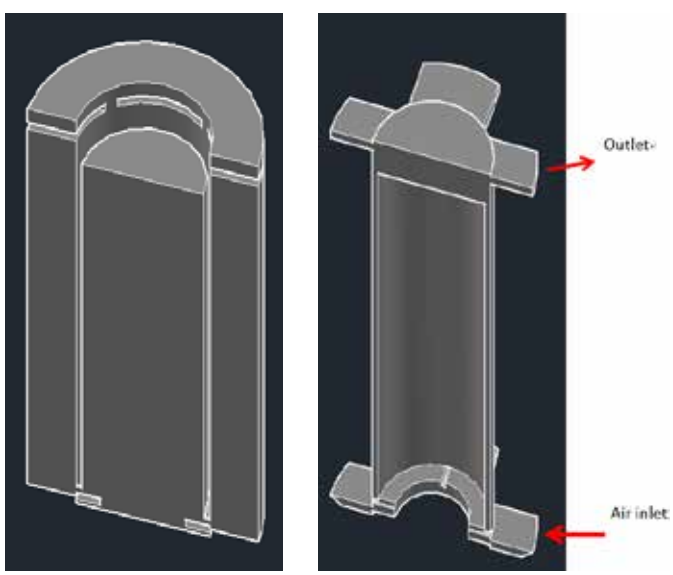

Figure 4-6 (a) Half model of solid region (b) half model of fluid region (for CFD simulation).

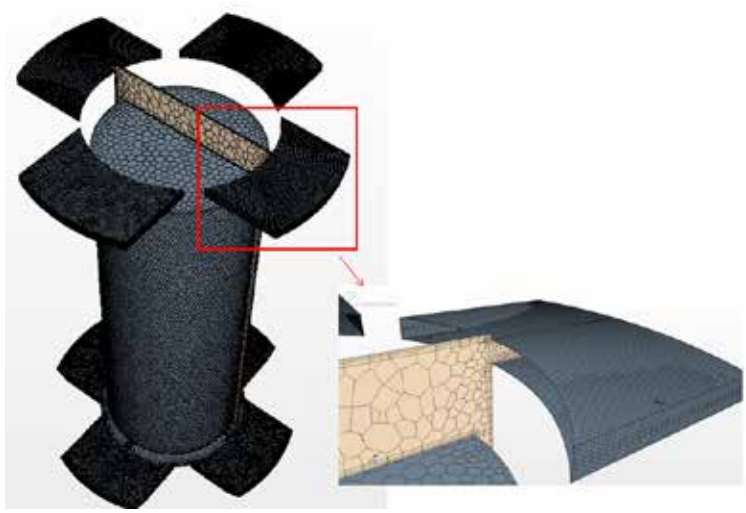

Figure 4-7 Mesh and cutting plane diagram.

4.4.2. Boundary Conditions

Figure 4-8 shows the boundary conditions. In reality, the convection condition is imposed on the outer wall of concrete to transfer heat to the environment. However, in this analysis we did not include the concrete (solid region) part in our model. Therefore, the convection boundary condition was (temporarily) replaced by adiabatic condition. The heat load was 342 W/m^2.

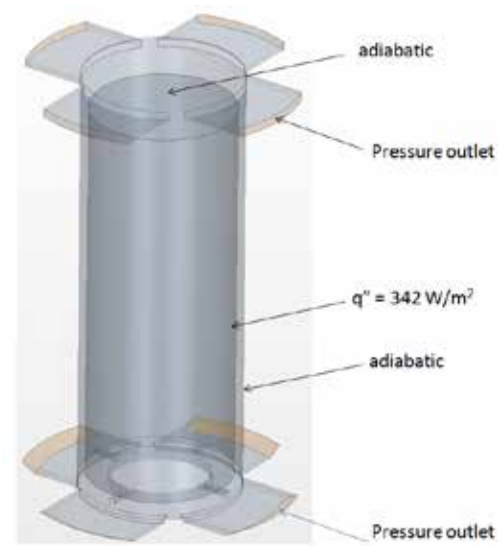

Figure 4-8 Boundary conditions.

4.4.3. Grid Independence Studies

Three mesh configurations were analyzed and the outer surface convection boundary condition was temporarily changed to adiabatic boundary condition to check the energy balance. Note that the convection boundary condition will be included when both the solid and fluid regions are

considered. Considering the scaling factor, 2.83, between the real and simulated models, the applied heat flux is lowered to 342 W/m^2 from 964 W/m^2.

It can be seen in Figure 4-10 that the hot fluid close to the heated wall moves up and directly flows out from the air vent. Figure 4-11 presents temperature contours near the outlet vent. The average temperature at the inner wall of the concrete cask and average outlet temperature for different mesh configurations are shown in Figure 4-12. The difference between the results obtained for 2.4 and 2.9 million meshes is small. Therefore, 2.4 million mesh case is considered sufficiently fine for the fluid region.

The total heat Q is 837 W corresponding to the heat flux of 342 W/m^2. The specific heat C_p of air is 1003.62 J/kg-K, average mass flow rate in the channel is 0.0061 kg/s and inlet temperature is 300 K. A simple energy balance based on $Q = \dot{m} \times C_p \times \Delta T$, leads to an average outlet temperature of 436.7 K. However, the average outlet temperature right at the exit of air vent shown in Figure 4-12 and Figure 4-13 is around 394 K. The reason that the outlet temperature is lower than expected is due to a recirculation region inside the vent where the ambient air from the outside (300 K) is sucked in. If the average temperature is calculated at the vent exit (a plane that includes the recirculation flow from the ambient), it leads to a high error in the energy balance (average temperature of 394 K, and an error of nearly 9.8% in the energy balance). The above calculation shows that considering energy balance between inlet and outlet of air vents could be misleading in this simulation since the average outlet temperature is affected by both decay heat and cooler temperature from the environment (recirculation region shown in Figure 4-13). A much appropriate way to verify the energy balance in this simulation is to calculate the average temperature between inlet plane and a plane (average temperature at this plane is about 436.2 K) away from the recirculation region inside outlet vent, which shows that the energy conservation calculation has an error of only 0.1%. Figure 4-13 shows the energy balance between the inlet and a plane in the interior of the outlet vent where the average temperature is unaffected by the ambient air.

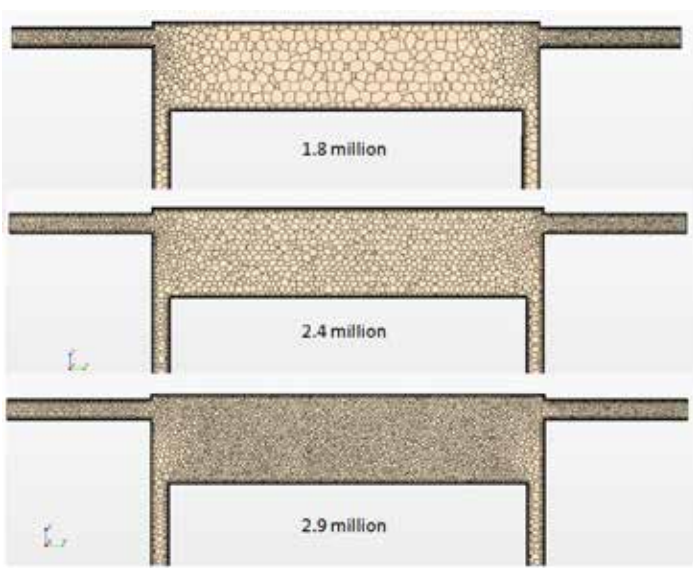

Figure 4-9 Tested mesh configurations.

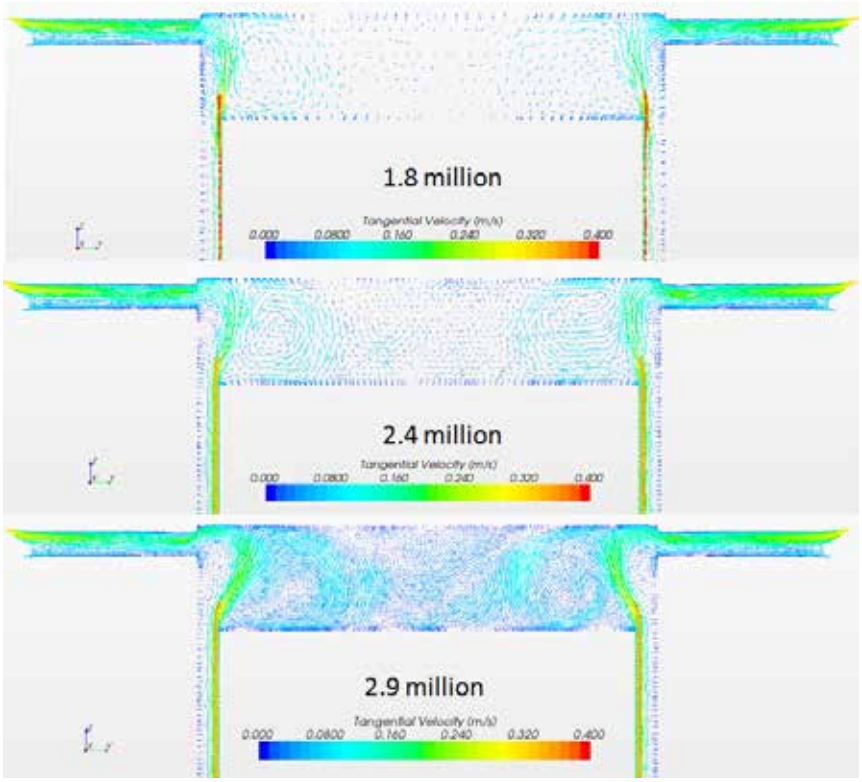

Figure 4-10 Velocity vector plots.

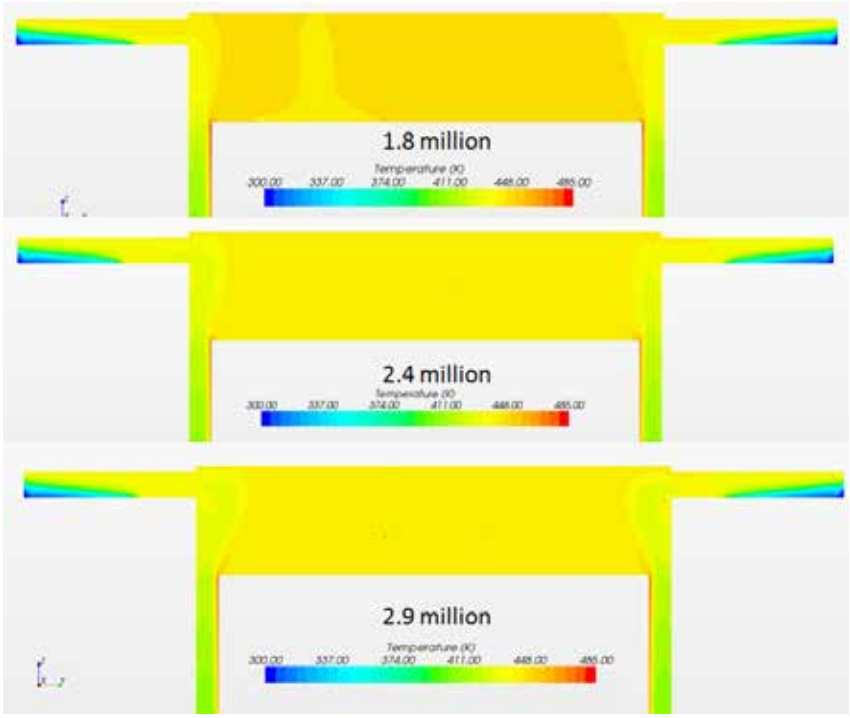

Figure 4-11 Temperature contours.

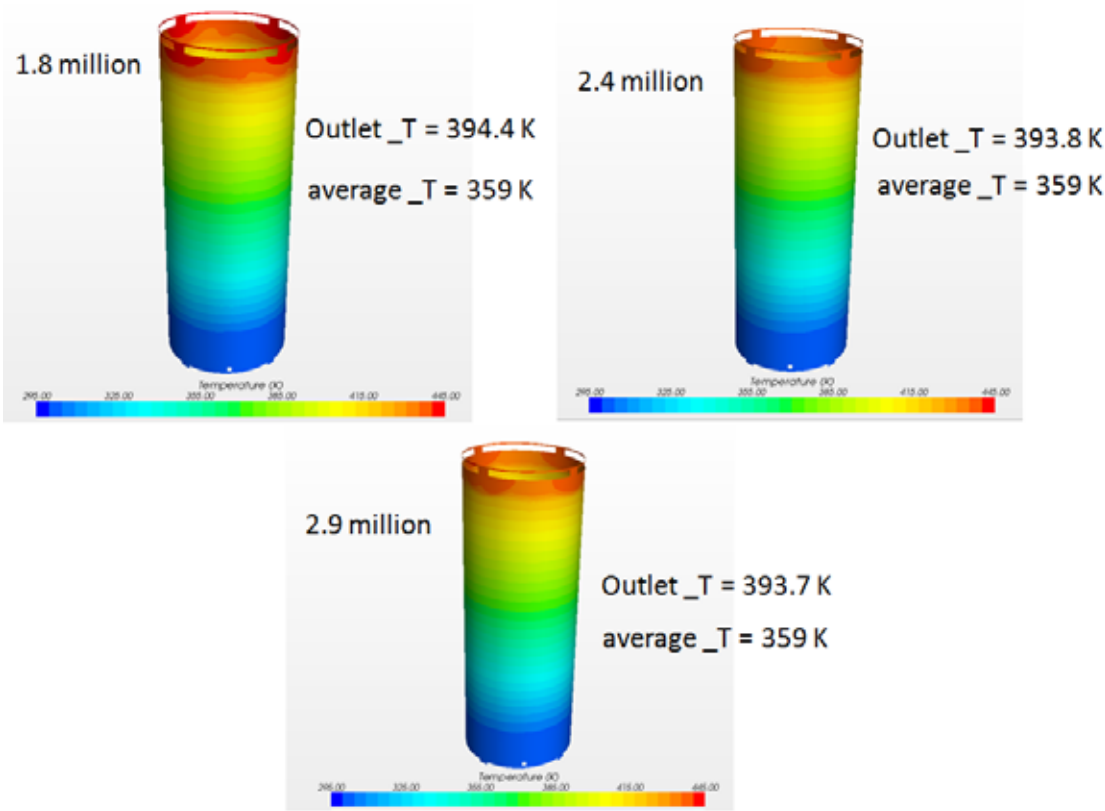

Figure 4-12 Temperature distributions at the inner wall of the concrete cask.

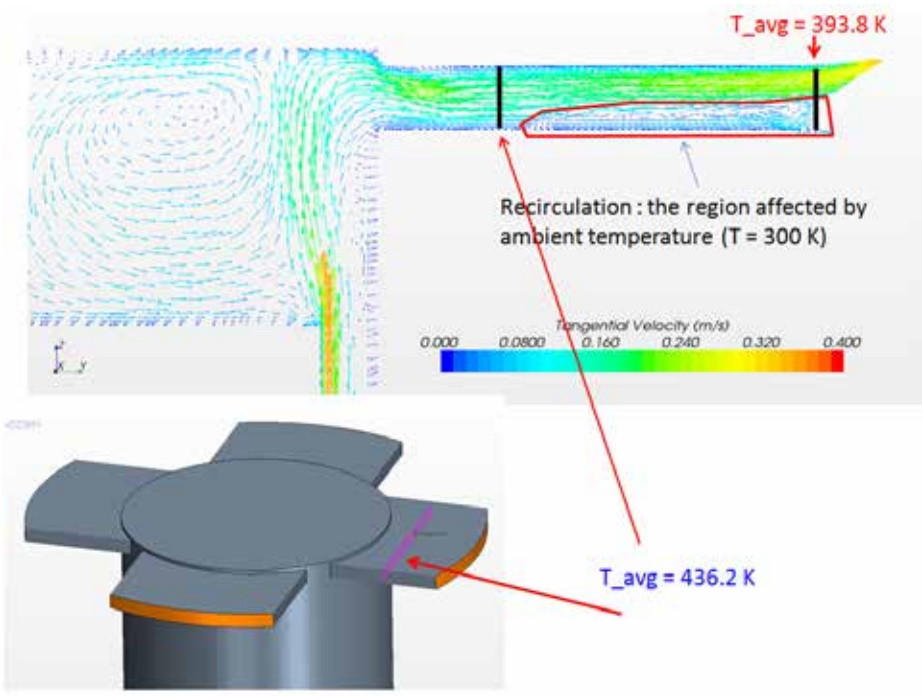

Figure 4-13 Energy balance between the inlet and a plane in the interior of the outlet vent where the average temperature is unaffected by the ambient air.

4.4.3.a. Conjugate heat transfer problem

In this section, the importance of conjugate heat transfer in CFD simulations is discussed. Heat convection condition with heat transfer coefficients (4.9 W/m-K) was applied (Figure 4-14). A quarter-symmetry CFD model with two different mesh configurations (Figure 4-15 and Figure 4-16) was prepared to reduce the mesh size and manage computing time. Figure 4-17 through Figure 4-19 show the preliminary results for temperature, density, and velocity distributions. Apparently, no natural circulation phenomenon is observed. Lower temperature and higher density at top and higher temperature and lower density at bottom indicate that air goes in form top of the concrete cask, flows downward, and flows out at the bottom. The flow pattern can be observed in Figure 4-19. However, normal, upward natural circulation was observed in the model that contains fluid region only. To identify potential problems in the current quarter model (considering both fluid and solid), a simple test model containing both fluid and solid regions is created to study the conjugate heat transfer problem since the results can easily be verified through hand calculations.

Figure 4-20 shows the simple model and related dimensions, thermal properties, boundary conditions, and the hand calculation results. With 1W heat input and 0.1 m/s air velocity, the calculated outlet temperature should be 394 K. Four cases, one with only the fluid region, and the others with different thermal conductivities of the solid region, were studied. Since the walls at top, bottom, and outer layer are all adiabatic, to conserve the energy released from the volumetric heat source, the outlet temperatures in all four cases should be 394 K. The outlet temperatures and temperature distributions are presented in Figure 4-21. The outlet temperature (T) in Figure 4-21(a) is 394K, which is identical to the temperature from hand calculation (fluid only). Figure 4-21(b) is the case with Al's thermal conductivity (237 W/m-K) for the solid part. The outlet T in this case is reduced to 383 K. Outlet temperature in Case C (Figure 4-21 (c)) drops to 391.6 K (solid's conductivity is 2 W/m-K). When a solid with a very low thermal conductivity (Figure 4-21(d)) is used (air's thermal conductivity; 0.026 W/m-K), the outlet T is correctly predicted by the CFD simulations (394 K). It seems that the simulations with high thermal conductivity of solid in the conjugate heat transfer problem do not conserve energy. This problem is further investigated in next section.

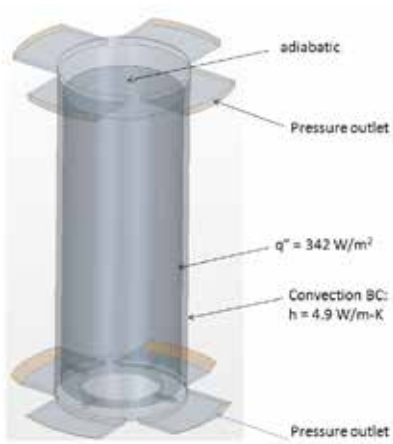

Figure 4-14 Boundary conditions.

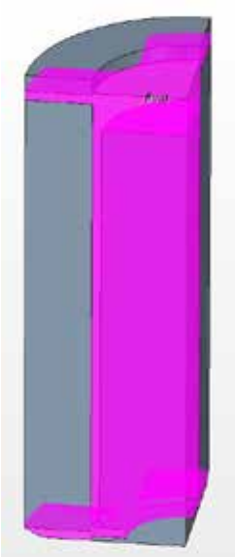

Figure 4-15 CFD quarter model (solid and fluid regions).

(a) (b)

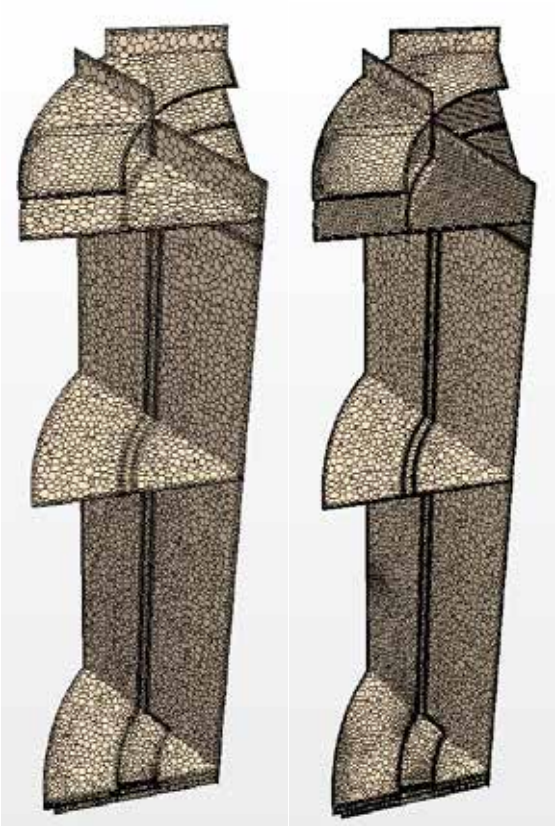

Figure 4-16 Two generated meshes for quarter model, (a) 0.25 million, (b) 0.5 million.

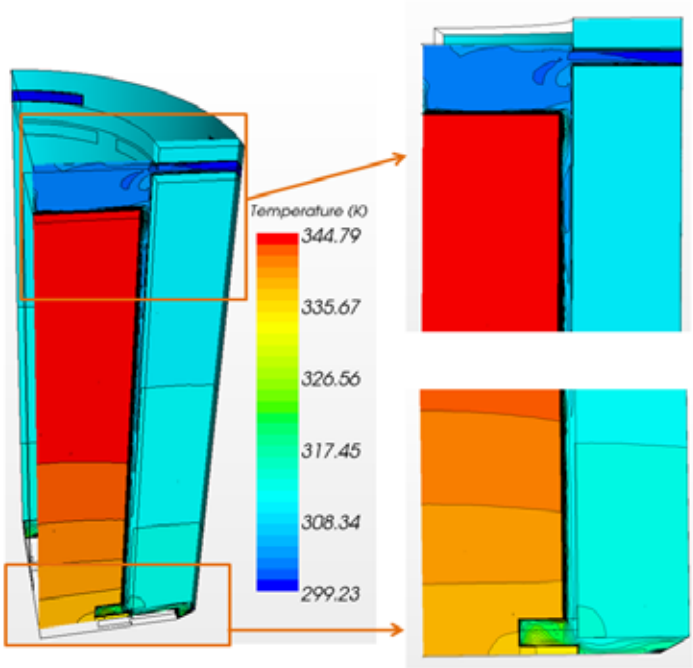

Figure 4-17 Temperature distribution (preliminary result).

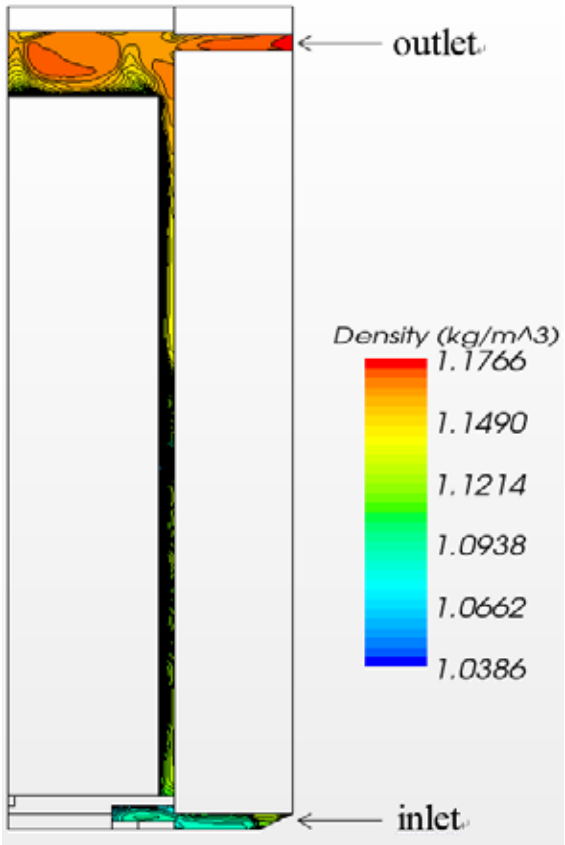

Figure 4-18 Density distribution (preliminary result).

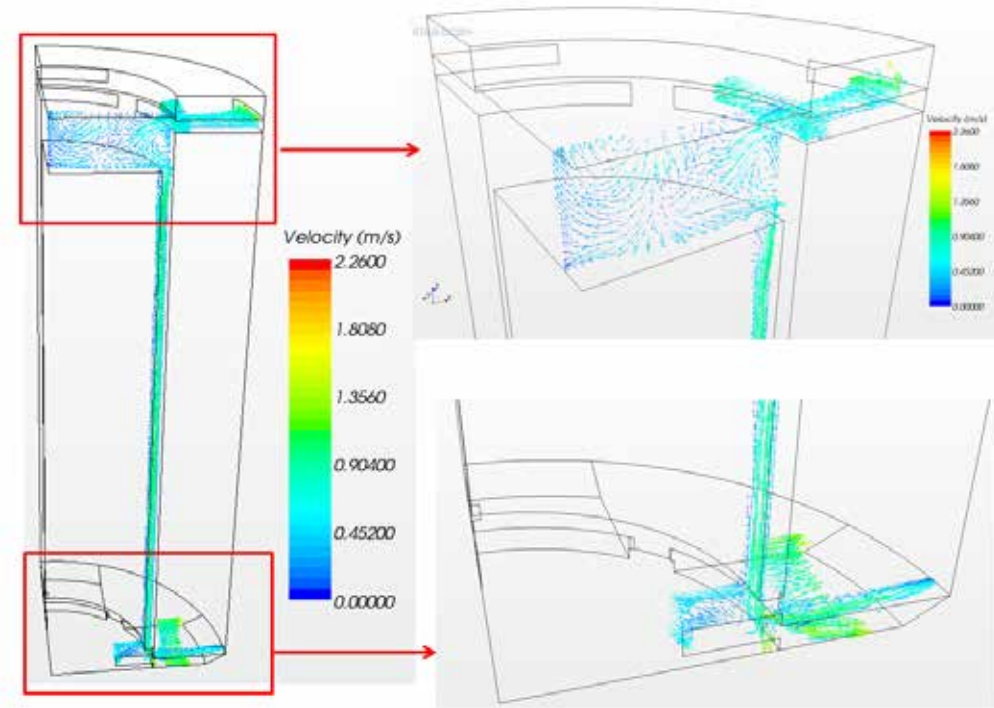

Figure 4-19 Velocity vector plot (preliminary result).

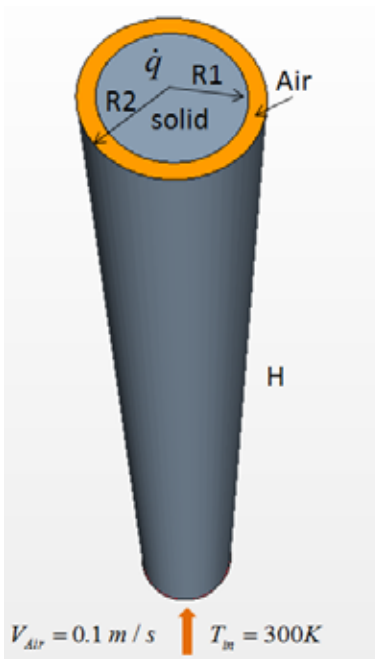

R1	0.008 m
R2	0.01 m
H	0.2 m
rho	0.94 kg/m^3 (air density)
Cp	1003.62 J/kg-K (air specific heat)
A_{air}	$\pi(R2^2 - R1^2) = 1.13 * 10^{-4}$ m^2
V_{air}	0.1 m/s
$\dot{m}$	rho*V_{air}*A_{air} = $1.06 * 10^{-5}$ kg/s
T_{in}	300 K
$\dot{q}$	25000 W/m^3 (volumetric heat)
Total Q	$\dot{q} \times \pi R1^2 H = 1$ W
T_{out}	$T_{in} + \dot{q} \times \pi R1^2 H / (\dot{m} \times Cp) = 394$ K

Figure 4-20 A simple test model.

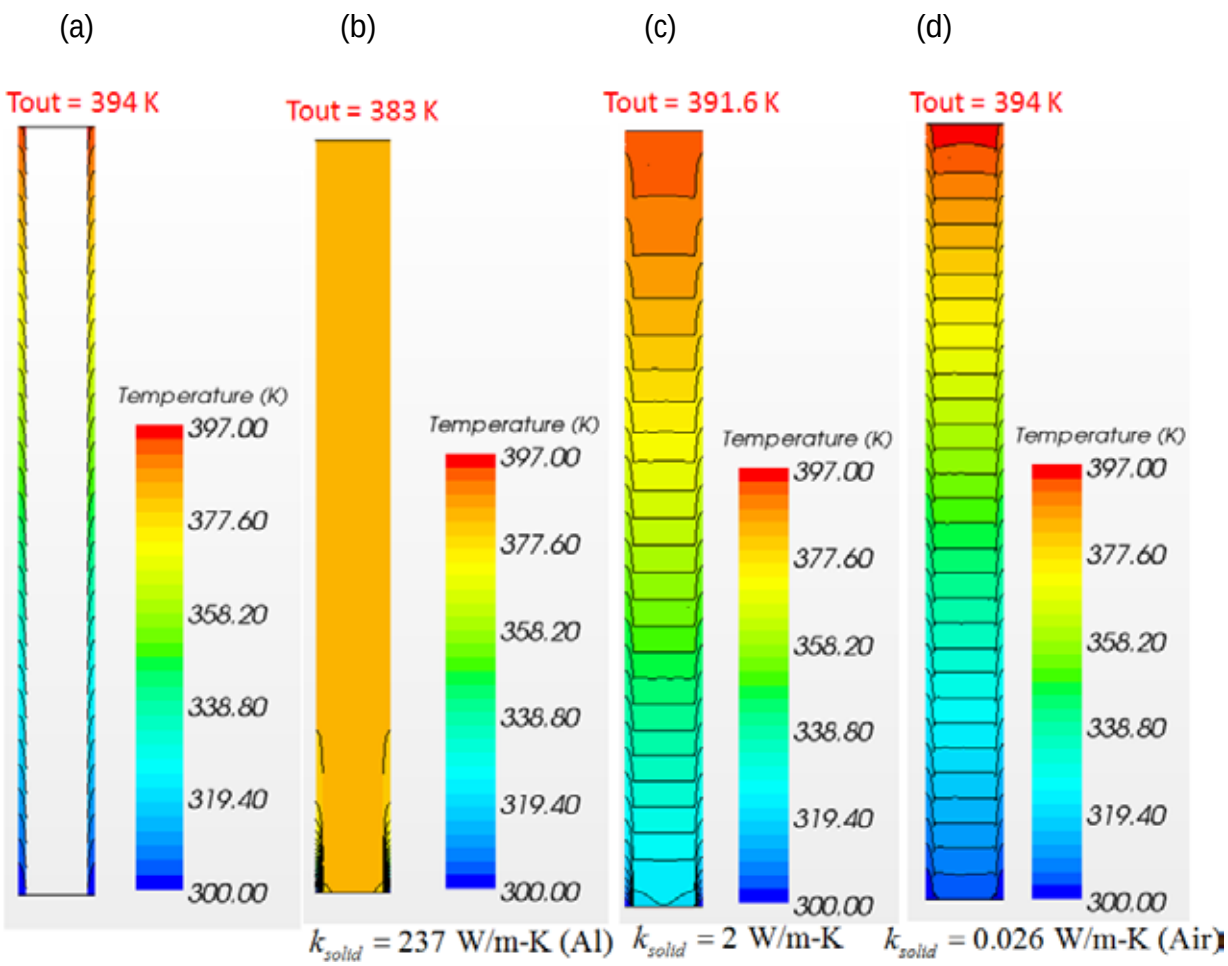

Figure 4-21 Relationship between solid conductivity and outlet temperature.

4.4.3.b. Thermal modeling and analysis

In the previous section, a simple circular model was built to identify the potential challenges in conjugate heat transfer problem in STAR-CCM+. Four cases, one with only the fluid region, and the others with different thermal conductivities of the solid region, were studied. Energy balance dictates the outlet temperature to be 394 K. However, the CFD simulations showed that the outlet temperatures for the cases with higher thermal conductivities of solids were lower than the expected result (Figure 4-21).

Figure 4-21 (b) shows that very high temperature gradient occurs at the inlet region with high thermal conductivity for the solid. The heat flux vector at solid and fluid interface for Al case (high thermal conductivity) is shown in Figure 4-22. Figure 4-22 shows that most of the total heat is transferred to the fluid region at the inlet due to the high solid thermal conductivity. Average fluid temperatures along the flow direction are shown in Figure 4-23. As shown in Figure 4-23(a), the temperature distribution for the model without the solid region varies linearly. However, for the case with high thermal conductivity of solid, the average fluid temperature increases to a high value in a region close to the inlet region (Figure 4-23(b)). High temperature gradient indicates that part of the heat was transported out of the system at the inlet, which is the reason

why the outlet temperature for this case (383 K) is much lower than 394 K (expected value if all the energy is to be transferred to the fluid leaving the exit).

Figure 4-24 shows the temperature distribution of quarter concrete model. The calculated outlet temperature is 431 K, which is much higher than 333 K (60°C), the value in the report titled, "Performance Testing and Analyses of the VSC-17 Ventilated Concrete Cask" (McKinnon et al., 1992). The area of air annulus in this report (McKinnon et al., 1992) is 0.357 m^2 (Figure 4-25); however, the area of air annulus in our dry cask design is only 0.07 m^2, which is 5 times smaller (Figure 4-26). Smaller flow area implies smaller mean velocity and flow rate in the air channel. Therefore, less coolant is allowed to remove the decay heat and causes high outlet temperature.

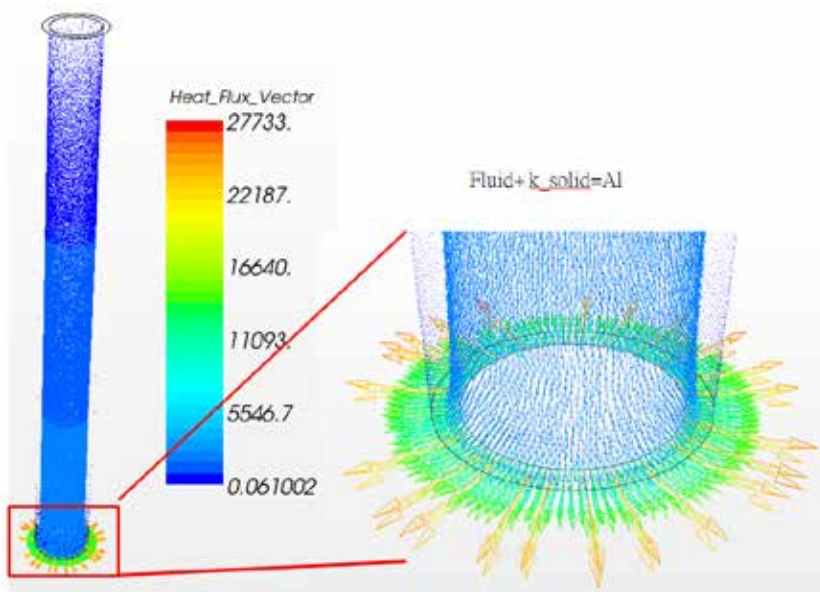

Figure 4-22 Heat flux vector for Al solid case.

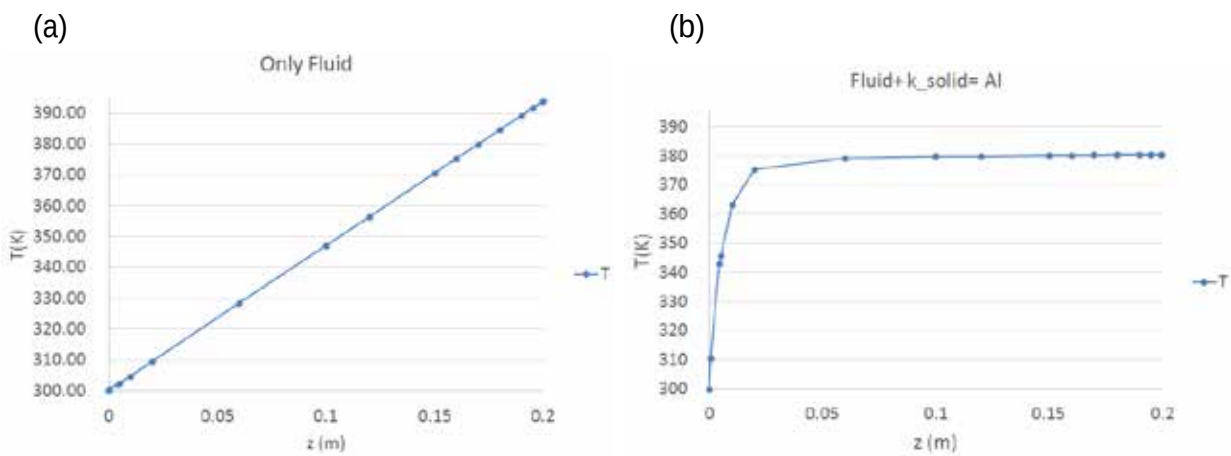

Figure 4-23 Average fluid temperature (a) for fluid-only case, (b) for k_solid = Al case. Note that *z* (m) is the elevation along flor direction show in Figure 4-20.

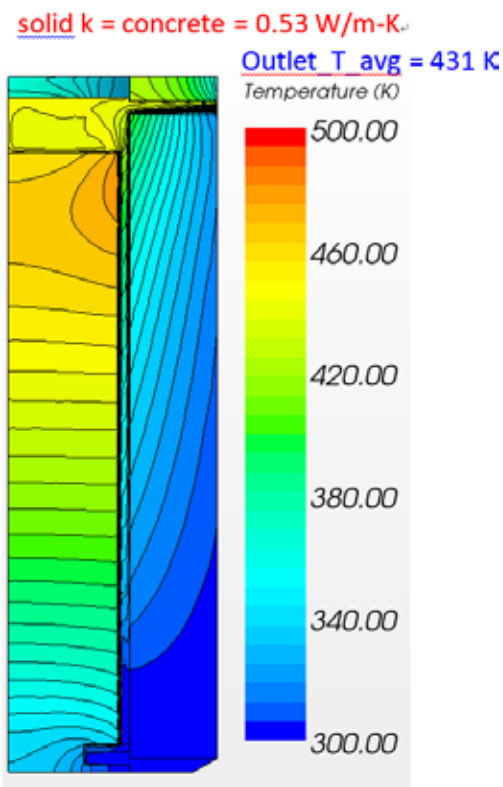

Figure 4-24 Temperature distribution of quarter cask model.

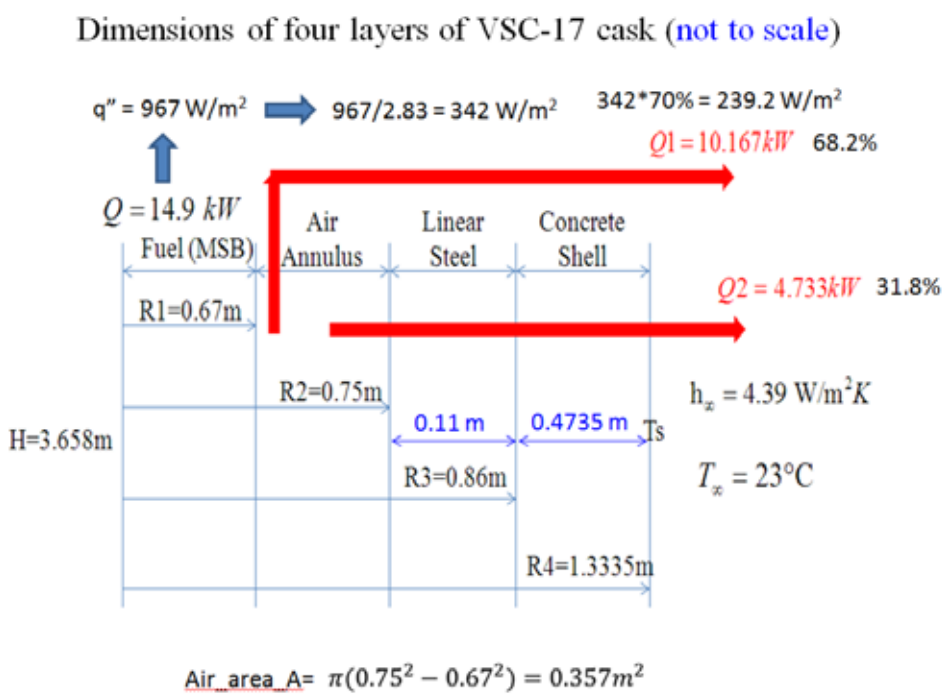

Figure 4-25 Thermal analysis using the data from the report "Performance Testing and Analyses of the VSC-17 Ventilated Concrete Cask" (McKinnon et al., 1992).

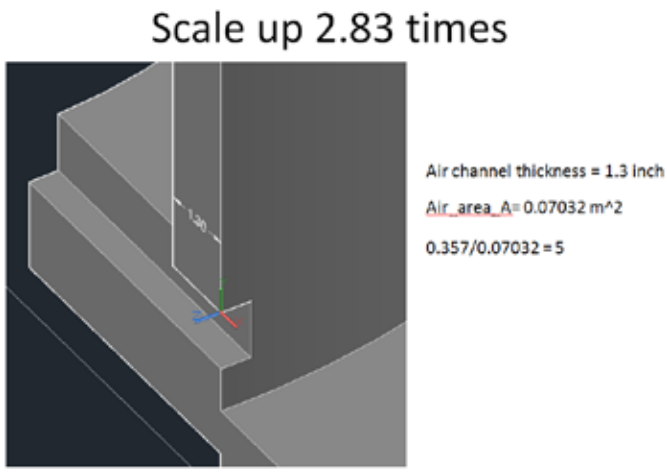

Figure 4-26 Area of air annulus for original dry case design.

The results presented in Figure 4-24 was with scaled geometry (scaling factor = 2.83), with reduced heat flux, 342 W/m^2 (based on the geometry scaling factor = 2.83), and without considering the effects lid plate by which heat can also be transported out through conduction and convection. However, the heat flux used in this simulation may not be appropriate to preserve important heat parameter like the temperature difference between inlet and outlet in full scale model (the prototype). The applied heat flux on reduce-scale model should be calculated based on scaling analysis, instead of using the scaling factor (2.83) directly. The results based on scaling analysis can be found in next section.

4.4.4. CFD Results for Dry Cask under Normal, Summer and Winter Conditions

4.4.4.a. Normal conditions (ambient temperature = 300 K)

Full scale model without the lid plate and without thermal radiation model

The number of meshes for full scale model is around 2.9 million and the mesh configuration is presented in Figure 4-27. Figure 4-28 to Figure 4-31 show the temperature and velocity distributions. The outlet temperature predicted by this full scale model is 436 K (163 °C), still very high. As shown in Figure 4-29, the average temperature on concrete outer wall is 307 K (= 34 °C). The temperature near the outlet duct is 382 K (= 109 °C). The effects of lid plate, thermal radiation, and turbulent flow model are included into the simulations step by step in the following sections.

Reduced model (scaling factor = 2.83) with the heat flux based on scaling analysis, without the lid plate and without thermal radiation model

To determine the appropriate heat flux used in reduced model, Kim et al. (2014) performed scaling analysis for natural convection in concrete cask air path. In the analysis, the quantity θ represents physical variables. The ration of θ between the prototype and small scale model is defined below:

$$[q]_{Ratio} = \frac{q_{\mathrm{m}}}{q_{\mathrm{p}}} \qquad 4.26$$

where the prototype and the scaled model are denoted by subscripts p and m respectively.

The temperature difference between outlet and inlet is ΔT. The objective of this scaling analysis is to preserve the ΔT in full scale (prototype) and reduced model. Based on this criterion

$$[\Delta T]_{Ratio} = \frac{\Delta T_{\mathrm{m}}}{\Delta T_{\mathrm{p}}} = 1 \qquad 4.27$$

Kim et al. (2014) had the following conclusions:

Heat source scaling:

$$[q''']_{Radio} = \left[L^{-1/2}\right]_{Ratio} \qquad 4.28$$

Heat flux scaling:

$$[q'']_{Radio} = \left[L^{1/2}\right]_{Ratio} \qquad 4.29$$

Total heat scaling:

$$[\dot{Q}]_{Radio} = \left[L^{5/2}\right]_{Ratio} \qquad 4.30$$

Mass flow rate scaling:

$$[\dot{m}]_{Radio} = \left[L^{5/2}\right]_{Ratio} \qquad 4.31$$

Average velocity scaling:

$$[u]_{Radio} = \left[L^{1/2}\right]_{Ratio} \qquad 4.32$$

where L is the characteristic length scale.

In our simulations with scaling factor 2.83, we have

$$[L]_{Radio} = \frac{L_{\mathrm{m}}}{L_{\mathrm{p}}} = \frac{1}{2.83} \qquad 4.33$$

Therefore,

$$\frac{q''_{\mathrm{m}}}{q''_{\mathrm{p}}} = [L]_{Ratio}^{\frac{1}{2}} \quad \text{è} \quad q''_{\mathrm{m}} = q''_{\mathrm{p}} \times [L]_{Ratio}^{\frac{1}{2}}$$

$$\text{è } q''_{\mathrm{m}} = 967 \times \left(\frac{1}{2.83}\right)^{\frac{1}{2}} = 574.82 \text{ W/m}^2 \qquad 4.34$$

Figure 4-32 shows the temperature distribution with appropriate scaled heat flux (= 574.82 W/m^2), and the outlet temperature is 429 K. Since the outlet temperature for full scale model is 436 K, the error is (436-429)/436 = 1.6 %. Figure 4-33 shows the temperature distributions at concrete inner wall for reduced and full scale model and the error of maximum temperature (at outlet duct) is (447-433)/447 = 3.1 %.

Full scale model with lid plate and turbulent k-ε model and without thermal radiation model

In previous model, the effect of the lid plate was not considered. The lid plate is added here to apply the heat convection condition at this boundary. The heat transfer coefficient is calculated as follows (Incropera et al., 2007).

The characteristic length L_{c} is defined by

$$L_c = \frac{D}{4} = \frac{3.45}{4} = 0.8625\,m \qquad 4.35$$

where *D* is the outer diameter of VCC. The surface temperature T_{s} is assumed to be 370 K and the air (environment) temperature T_{a} is 300 K. Therefore, the average temperature T_{avg} is

$$T_{avg} = \frac{T_s + T_a}{2} = 335 \text{ K} \qquad 4.36$$

The thermal expansion coefficient β is

$$b = \frac{1}{T_{avg}} \qquad 4.37$$

The Rayleigh number at the top surface (lid plate) of concrete cask is calculated from

$$Ra_{top} = \frac{g\,b\,L_c^3 (T_s - T_a)}{a_a v_a} \qquad 4.38$$

where g is acceleration due to gravity, α_{a} is thermal diffusivity of air and ν_{a} is the kinetic viscosity of air. The relationship between the Nusselt number Nu and Rayleigh number Ra_{top} at the top surface of concrete cask is

$$Nu = 0.54 Ra_{top}^{\frac{1}{4}} \quad 4.39$$

The heat transfer coefficient h for the lid plate can be calculated from the formula

$$h = \frac{Nuk_a}{L_c} = 4 \text{ W/m}^2 \text{ - } K \quad 4.40$$

where k_a is the thermal conductivity of air. Figure 4-35 presents the temperature distribution of this model. Key temperatures of this model are listed below:

- Average outlet temperature = 432 K = 159 °C
- Average concrete outer wall temperature = 306 K = 33 °C
- Average lid plate temperature = 334 K = 61 °C
- Average canister wall temperature = 524 K = 251 °C

The average outlet temperature drops form 436 K (without lid plate, adiabatic BC) to 432 K (with lid plate, heat convection BC). The difference is (436-432)/436 = 0.9%, which is actually ignorable.

4.4.4.b. Effects of transmissivity on temperature Fields

Full scale model with lid plate and the thermal radiation model but using laminar flow model

The materials for transportable storage canister (TSC) and concrete in the MAGNASTOR System are stainless steel 304L and Type II Portland cement (Subiry, 2013). The emissivities for stainless steel and cement are 0.6 and 0.9. The Kirchhoff's Law requires that for each boundary or interface, the sum of emissivity (α), reflectivity (ρ), and transmissivity (τ) equals unity. To get a convergent result, this simulation was run with laminar flow model. The results are used as initial conditions for turbulent flow model in the following sections. Figure 4-36 shows the settings of thermal radiation properties for each surface. For this simulation, transmissivity for almost all surfaces is set to be zero. Appropriate values will be determined in a later section by comparing the temperature distribution of the concrete cask in the literature. It is observed from Figure 4-35 and Figure 4-37 that the temperature distribution is affected by the thermal radiation model significantly. Some temperature results for this simulation are shown below:

- Average outlet temperature = 398 K = 125 °C
- Average concrete outer wall temperature = 347 K = 74 °C
- Average lid plate temperature = 348 K = 75 °C
- Average canister wall temperature = 443 K = 170 °C

With the inclusion of thermal radiation model and switching form turbulent k-ε to laminar model, the average outlet temperature drops from 432 K (=159 °C) to 398 K (= 125 °C) but the average concrete outer wall temperature increases from 306 K (= 33 °C) to 347 K (= 74 °C). The increase of the outer wall temperature is due to the thermal radiation. Without considering thermal radiation, the decay heat is transported to the outer wall purely by thermal conduction; with inclusion of thermal radiation model, the outer wall is also heated by the thermal radiation.

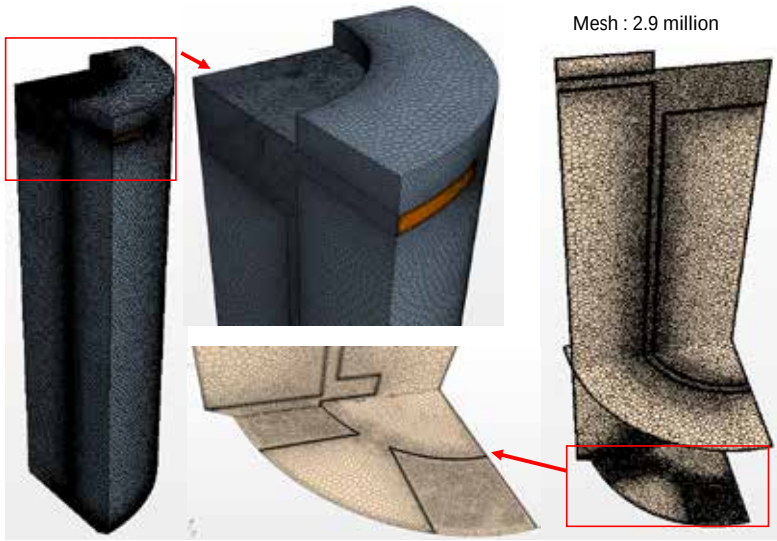

Figure 4-27 Mesh configuration for full scale model.

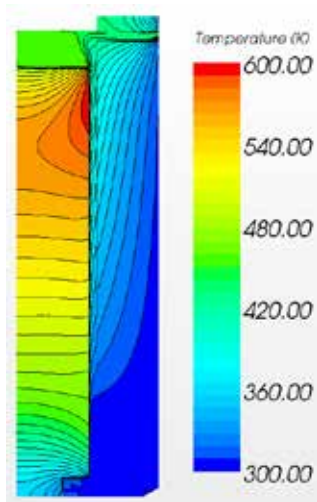

Figure 4-28 Full scale, temperature distribution with q" = 967 W/m^2.

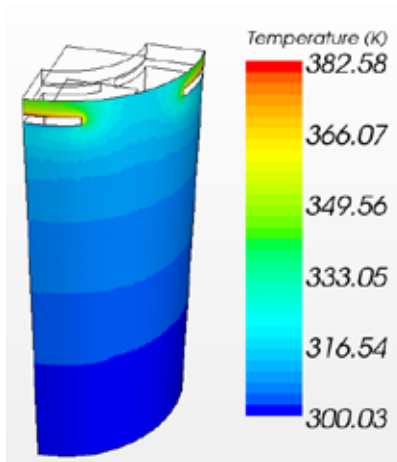

Figure 4-29 Full scale, temperature distribution on concrete outer wall.

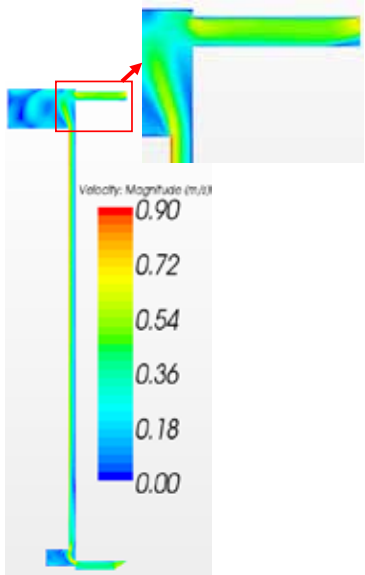

Figure 4-30 Full scale, velocity distribution.

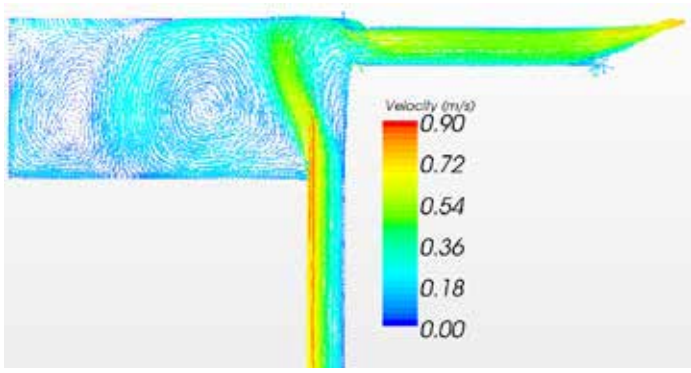

Figure 4-31 Full scale, Velocity vector near the outlet.

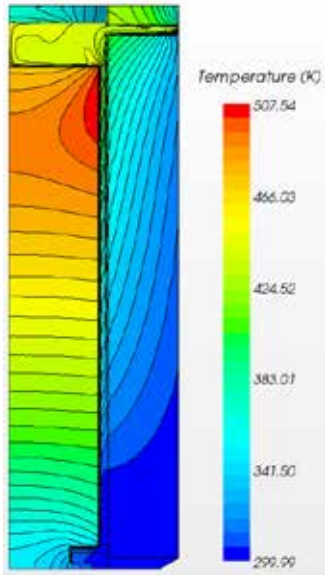

Figure 4-32 Reduced model, temperature distribution with q" = 574.82 W/m^2.

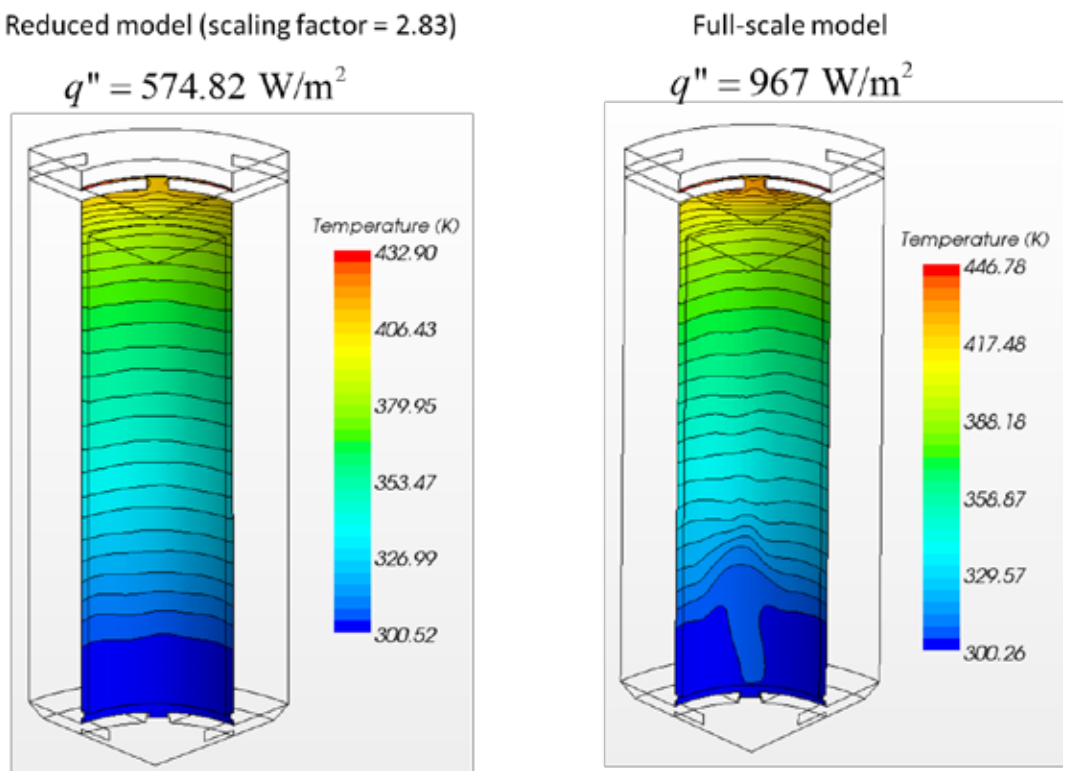

Figure 4-33 Comparison of temperature distributions at concrete inner wall between reduced and full scale model.

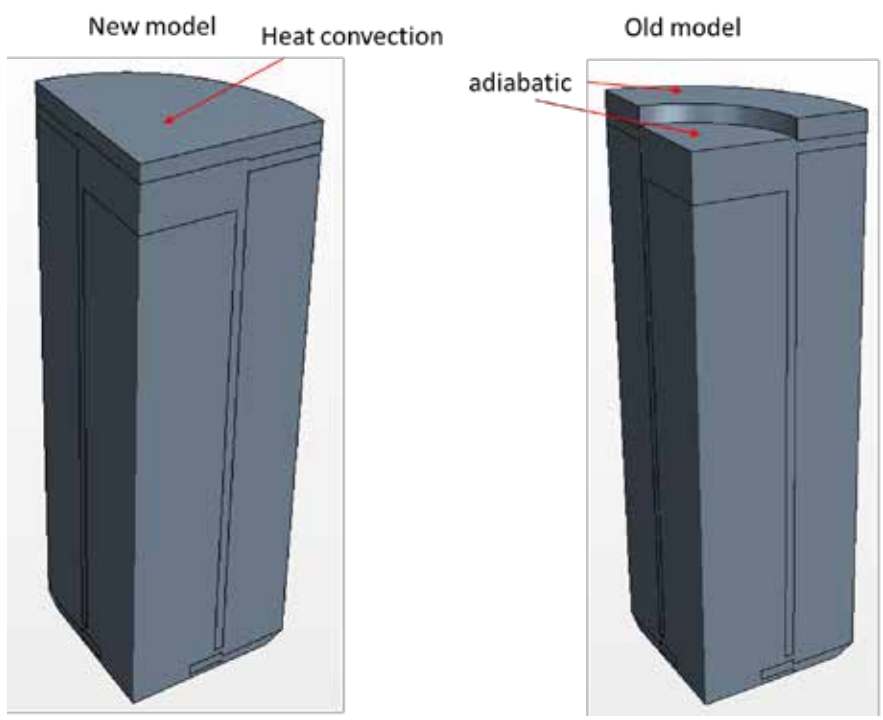

Figure 4-34 Comparison between new (with lid plate) and old models.

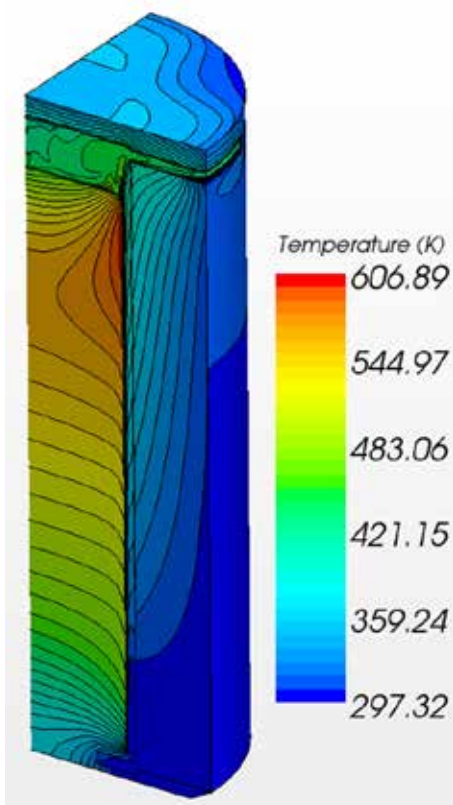

Figure 4-35 Full scale, temperature distribution, with lid plate, with turbulent k-ε model, without thermal radiation.

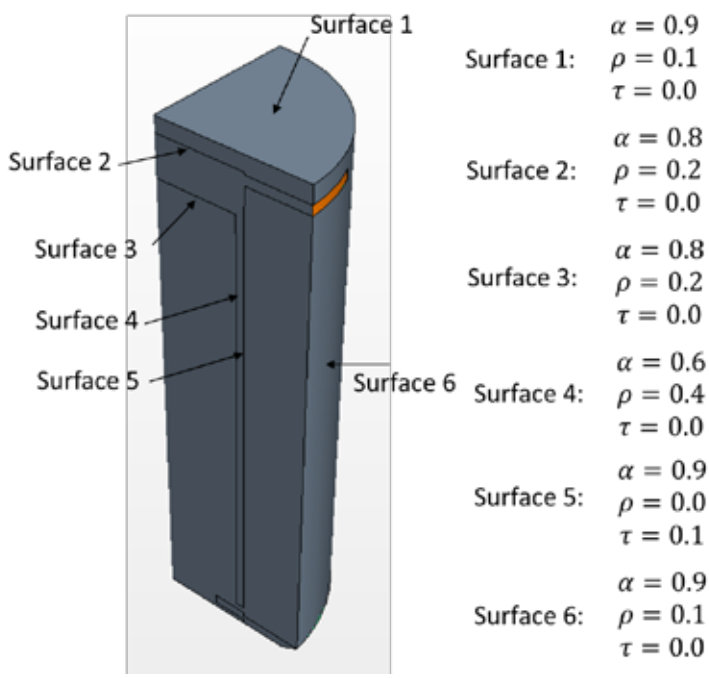

Figure 4-36 Full scale, settings for thermal radiation model based on Kirchhoff's Law.

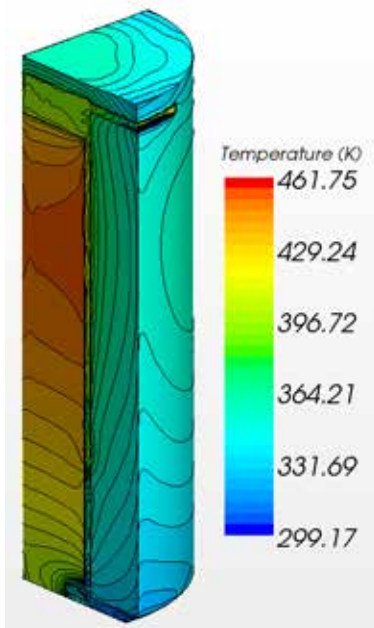

Figure 4-37 Full scale, temperature distribution with thermal radiation and laminar flow model.

Full scale model with different fluid dynamics models with transmissivity = 0 for most surfaces

For full scale model, the heat flux applied on the canister wall is 967 W/m^2. Table 4-3 compares the temperature fields between laminar and turbulence k-ε model with transmissivity = 0 for most surfaces. As expected, the turbulence model predicts better heat transfer. The temperatures predicted by turbulence k-ε model are 5°C to 10°C lower than laminar model. The comparison of temperature distributions between two models is shown in Figure 4-38.

Table 4-3 Comparison of Temperatures between Laminar and Turbulence Model.

Full scale, with lid plate, with thermal radiation model, transmissivity = 0 for most surfaces		
Fluid dynamics model	Laminar model	Turbulence k-ε model
Average outlet temperature	398 K (125 °C)	391 K (118 °C)
Average outer wall temperature	347 K (74 °C)	342 K (69 °C)
Average lid plate temperature	348 K (75 °C)	343 K (70 °C)

Effects of transmissivity on temperature fields

In thermal radiation simulation, the key parameter is the emissivity and the value is around 0.6 - 0.8 in the dry storage system simulation (Brewster et al., 2012; Kim et al., 2014). The Kirchhoff's Law requires that for each boundary or interface, the sum of emissivity (α), reflectivity (ρ), and transmissivity (τ) equals unity. However, the value of transmissivity was not mentioned or was set to zero in the literature of CFD simulations in dry storage systems. In this section, the simulations of transmissivity = 0 for most surfaces (the transmissivity on interior surface of

concrete is set to 0.1; the rest surfaces have a transmissivity value of 0) and transmissivity = 0.1 for all surfaces were performed. The comparisons are shown in Table 4-4 and Figure 4-39. In general, the transmissivity enhances the heat transfer and the temperature differences between transmissivity = 0 and transmissivity = 0.1 are around 3°C ~ 6°C, which confirms that the key parameter in thermal radiation simulation is not the value of transmissivity.

Table 4-4 Comparison of Temperatures between Different Transmissivity Settings.

Full scale, with lid plate, with thermal radiation and turbulence k-ε models		
transmissivity	transmissivity = 0 for most surfaces	transmissivity = 0.1 for all surfaces
Average outlet temperature	391 K (118 °C)	388 K (115 °C)
Average outer wall temperature	342 K (69 °C)	338 K (65 °C)
Average lid plate temperature	343 K (70 °C)	338 K (65 °C)
Average canister wall temperature	433 K (160 °C)	427 K (154 °C)

Comparison of temperature field in the literature

Herranz et al. (2015) applied CFD analysis on the HI-STORM (Holtec International Storage and Transfer Operation Reinforced Module) dry storage system, which contains a concrete cask with similar dimensions of MAGNASTOR System (HI-STORM cask: height = 6.1 m, outer diameter = 3.36 m, concrete thickness = 0.7 m; MAGNASTOR cask: height = 5.7.m, outer diameter = 3.45 m, concrete thickness = 0.67 m). In the CFD analysis (Herranz et al., 2015), it was found that the air outlet temperature of HI-STORM was 382 K (109 °C), close to the value of 386 K (113 °C) from the report Holtec International (2010). The two air outlet temperatures (109 °C and 113 °C) in the literature are very close to our simulation result (115 °C). The k-ω SST turbulence model was utilized by Herranz et al. (2015). The same model was also used in our model for comparison. The results are shown in Figure 4-5 and Figure 4-40.

Table 4-5 Comparison of Temperatures between Two Turbulence Models.

Full scale, with lid plate, with thermal radiation, turbulence models, transmissivity = 0.1 for all surfaces		
turbulence model	k-ε model	k-ω SST model
Average outlet temperature	388 K (115 °C)	388 K (115 °C)
Average outer wall temperature	338 K (65 °C)	337 K (64 °C)
Average lid plate temperature	338 K (65 °C)	339 K (66 °C)
Average canister wall temperature	427 K (154 °C)	425 K (152 °C)

Reduced-scale model (scaling factor = 2.83) with thermal radiation and transmissivity = 0.1 for all surfaces

For reduced-scale model (scaling factor = 2.83), the scaled heat flux based on scaling analysis is 574.82 W/m^2. Laminar and turbulence k-ε models were used for this reduced-scale geometry and the transmissivity for all surfaces was 0.1. The differences in temperature fields between two model are only 1°C ~ 2 °C (Table 4-6 and Figure 4-41).

Table 4-6 Comparison of Temperature Distributions of Reduced-Scale Model between Laminar and Turbulence k-ε Model with Transmissivity = 0.1 for All Surfaces.

Reduced-scale, with lid plate, with thermal radiation, transmissivity = 0.1 for all surfaces		
Fluid dynamics model	Laminar model	Turbulence k-ε model
Average outlet temperature	371 K (98 °C)	370 K (97 °C)
Average outer wall temperature	329 K (56 °C)	329 K (56 °C)
Average lid plate temperature	334 K (61 °C)	333 K (60 °C)
Average canister wall temperature	397 K (124 °C)	395 K (122 °C)

(a) (b)

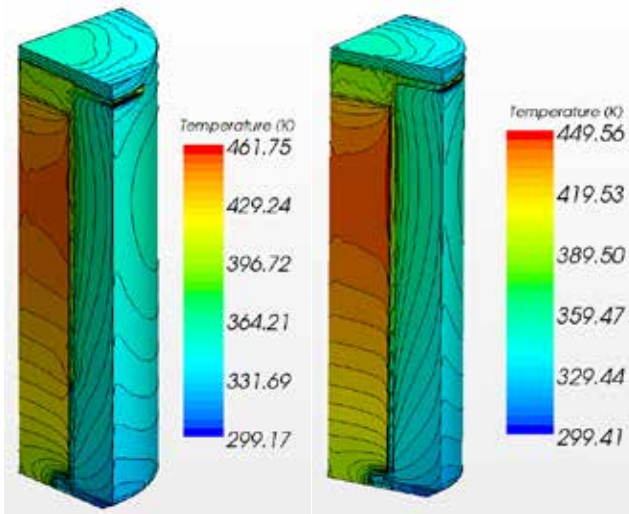

Figure 4-38 Full scale, temperature distribution with thermal radiation, (a) laminar model (b) turbulence k-ε model.

(a) (b)

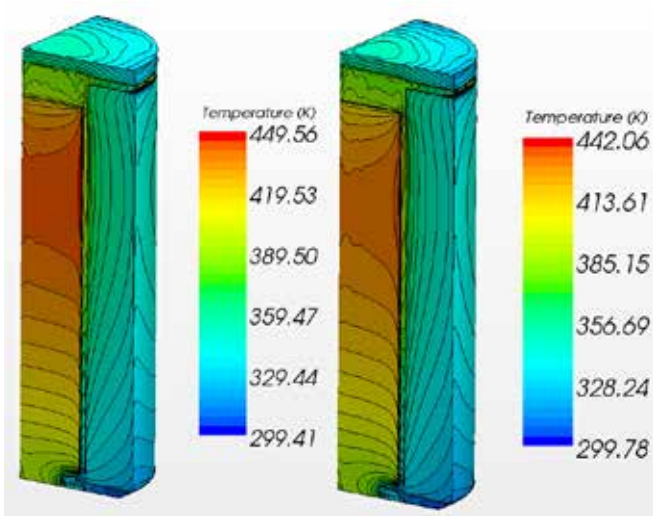

Figure 4-39 Full scale, temperature distribution with thermal radiation and turbulence k-ε model (a) transmissivity = 0 for most surfaces (b) transmissivity = 0.1 for all surfaces.

(a) (b)

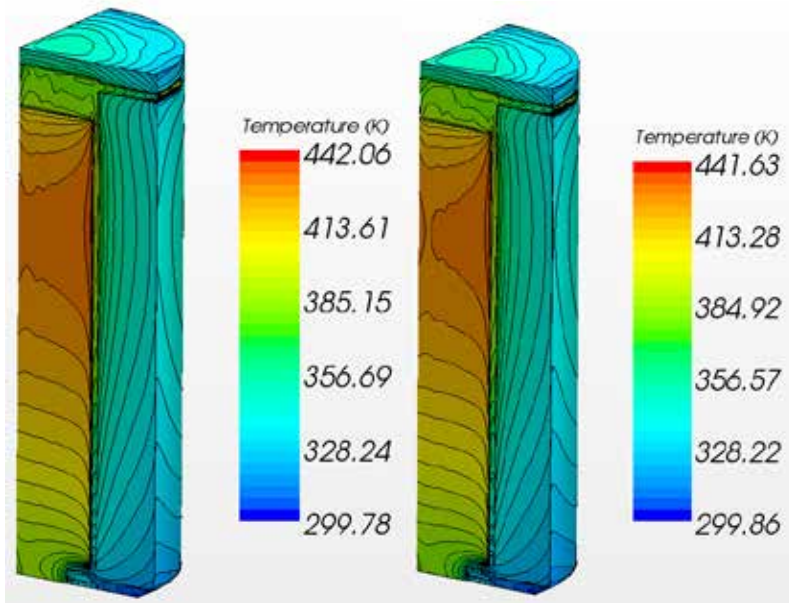

Figure 4-40 Full scale, temperature distribution with thermal radiation and transmissivity = 0.1 for all surfaces (a) turbulence k-ε model (b) k-ω SST model.

(a) (b)

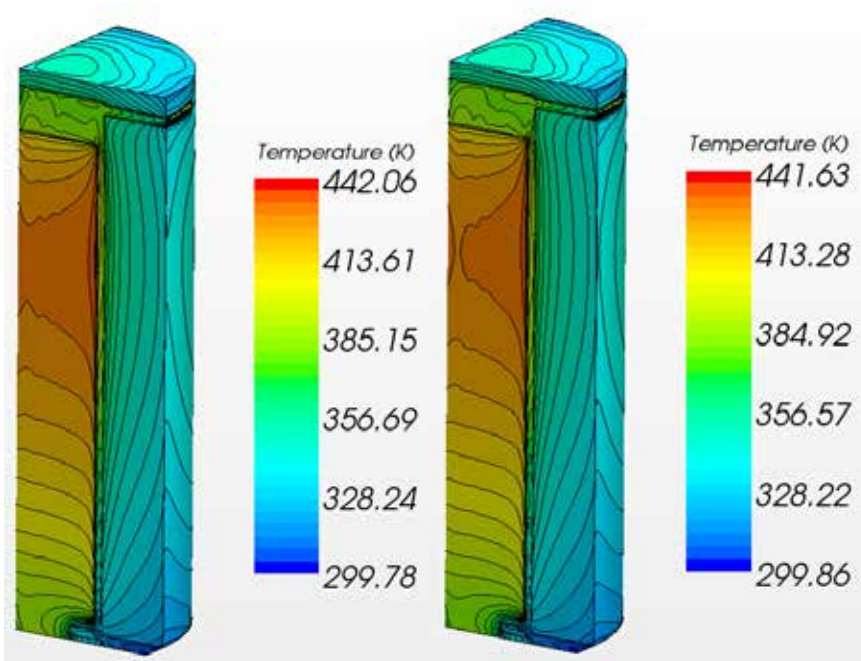

Figure 4-41 Reduced-scale model, temperature distributions with thermal radiation and transmissivity = 0.1 for all surfaces (a) laminar model (b) turbulence k-ε model.

4.4.4.c. Summer conditions for full-scale cask

Full scale model with summer conditions

For the summer conditions the ambient temperature is considered as 311 K (38˚C). Accordingly, the heat transfer coefficient was calculated for the air on the outside surface of cask and top surface, which were found to be 3.604 W/m^2 and 3.827 W/m^2, respectively. The model which uses the above heat transfer coefficients is referred as "modified heat transfer coefficient" model.

Another model is also considered retaining the previous heat transfer coefficients which were calculated at an ambient temperature of 300 K (27˚C). Though the heat transfer coefficients were calculated at 300 K, the ambient temperature of the air outside is taken as 311 K for this model. This model is referred as "unmodified heat transfer coefficient" model.

A comparison is carried out between the model with the modified heat transfer coefficient and the model with unmodified heat transfer coefficient. It was found that the change in the heat transfer coefficient did not cause an appreciable change in the temperature. The comparison is shown in Table 4-7. It can be seen that the difference between the temperatures for the two models is just 1˚C ~ 2˚C.

It is to be noted that for both the model k-ε turbulence model is used.

Table 4-7 Comparison of Temperature Distributions of Full-Scale Models with Modified Heat Transfer Coefficients and Unmodified Heat Transfer Coefficients.

Full-scale, with lid plate, with no thermal radiation and ambient temperature at 311 K (summer condition)		
Fluid dynamics model	Modified heat transfer coefficient model	Unmodified heat transfer coefficient model
Average outlet temperature	421.8 K (148.8 °C)	421.7 K (148.7 °C)
Average outer wall temperature	317.4 K (44.4 °C)	316 K (43 °C)
Average lid plate temperature	341.6 K (68.6 °C)	340 K (67 °C)
Average canister wall temperature	525.9 K (252.9 °C)	525.7 K (252.7 °C)

The maximum temperature observed in the cask for both the models was around 596 K (323˚C), this can be seen in the Figure 4-42. This brings us to the conclusion that thermal radiation model should be included to get a more accurate temperature distribution.

Figure 4-43 shows the temperature distribution of the canister wall. It can be seen that both the models have a similar temperature distribution.

(a) (b)

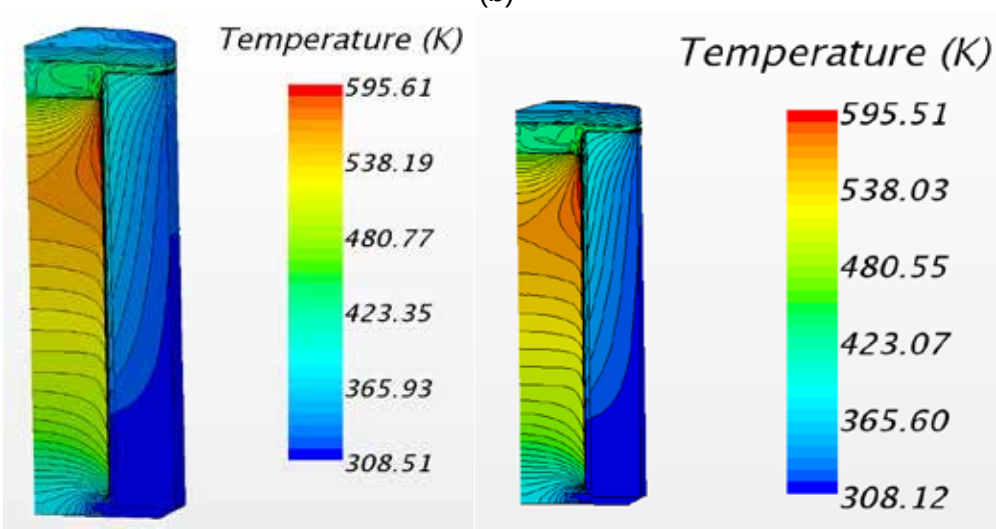

Figure 4-42 Full-scale model, temperature distributions for summer conditions (a) modified heat transfer coefficients model (b) unmodified heat transfer coefficients model.

(a) (b)

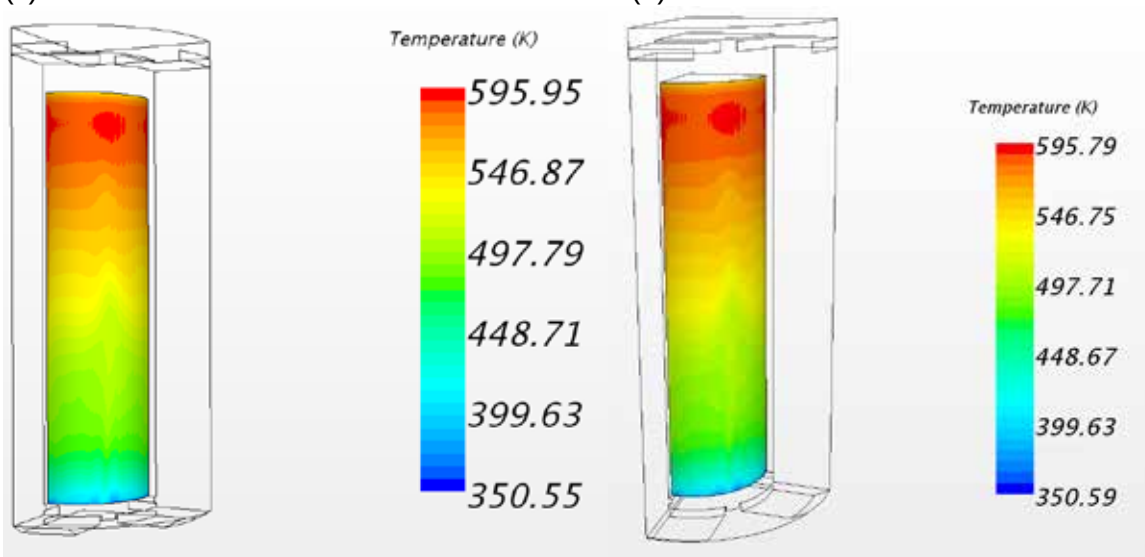

Figure 4-43 Full-scale model, temperature distributions for summer conditions on the canister wall surface (a) modified heat transfer coefficients model (b) unmodified heat transfer coefficients model.

Full-scale model with thermal radiation and transmissivity (= 0.1) for all surfaces under summer conditions

The ambient temperature for the summer conditions is considered to be 311 K (38˚C) as mentioned before, and the heat transfer coefficient is calculated previously for the outside surface of cask and top surface, which were found to be 3.604 W/m^2 and 3.827 W/m^2, respectively. Due to high temperatures, radiation mode of heat transfer is also considered in this

simulation to obtain a more accurate temperature distribution. The key parameter in thermal radiation simulation is the emissivity, and its value is around 0.6 - 0.8 for the dry storage system (Brewster et al., 2012; Kim et al., 2014).

Table 4-8 Comparison of Temperatures between Models with and without Radiative Heat Transfer.

Full scale, with lid plate , turbulence k-ε models, summer conditions		
Radiative Heat transfer mode	No	Yes (transmissivity = 0.1 for all surfaces)
Average outlet temperature	422 K (149 °C)	360 K (87 °C)
Average outer wall temperature	317 K (44 °C)	338 K (65 °C)
Average lid plate temperature	342 K (69 °C)	338 K (65 °C)
Average canister wall temperature	526 K (253 °C)	427 K (154 °C)

It can be seen from Table 4-8 that accounting for radiation as a mode of heat transfer considerably reduces the average canister wall temperature, but increases the outer wall temperature by a small amount. This indicates that heat transfer by radiation should also be taken into account as the contribution by this mode of heat transfer is no longer negligible for our model.

Figure 4-46 gives the velocity distribution of air, and it can be seen that the higher velocity of air is observed at regions closer to the canister wall and also at the inlet.

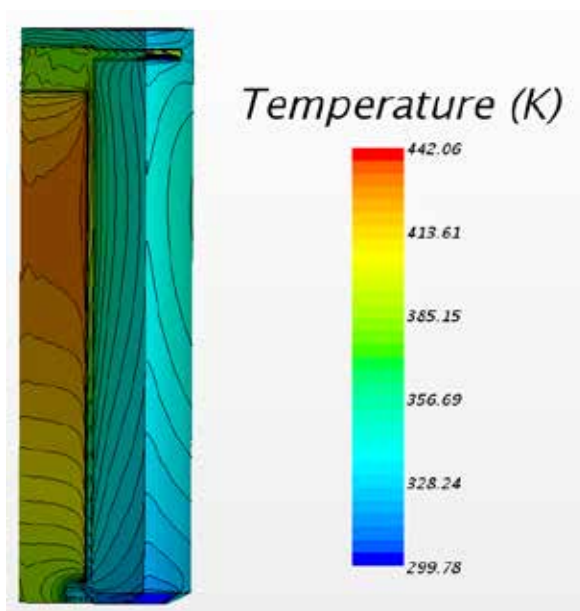

Figure 4-44 Full-scale model, temperature distributions under summer conditions including the radiative mode of heat transfer.

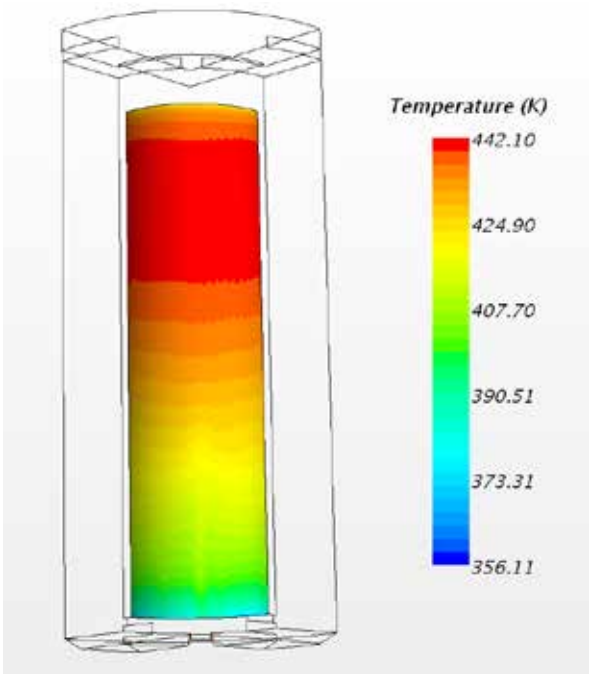

Figure 4-45 Temperature distribution on the canister surface under summer conditions including radiative mode of heat transfer.

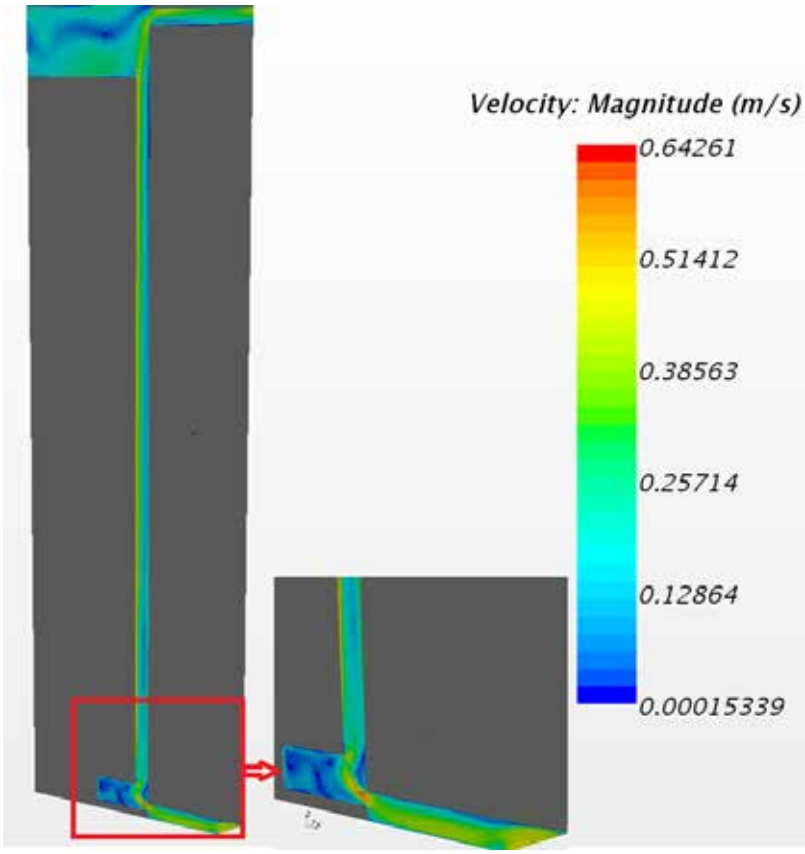

Figure 4-46 Velocity distribution in a planar section under summer conditions including radiative mode of heat transfer.

4.4.4.d. Winter conditions

Full-scale model with thermal radiation and transmissivity = 0.1 for all surfaces in winter conditions

In previous section, the thermal analysis for summer condition with the inclusion of radiative heat transfer model was carried out. A similar analysis has been carried out for winter conditions in this section. The ambient temperature for the winter conditions is taken to be 283 K (10˚C) and the heat transfer coefficient was calculated accordingly for the air on the radial and top surface of cask, which were found to be 4.26 W/m^2 and 5 W/m^2, respectively. The emissivity, which is around 0.6 - 0.8 in the dry storage system (Brewster et al., 2012; Kim et al., 2014) are the same values used in the previous case for summer conditions.

Table 4-9 lists the average temperatures of various surfaces for summer and winter ambient conditions, respectively.

Table 4-9 Comparison of Cask Temperatures for Summer and Winter Ambient Conditions (with Radiative Heat Transfer).

Full scale, with lid plate, turbulence k-ε models		
Ambient Conditions	Summer	Winter
Ambient Temperature	311 K (38 °C)	283 K (10 °C)
Heat transfer coefficient	h(top)=3.8 W/m^2-k h(outer wall)=3.6W/m^2-k	h(top)=5 W/m^2-k h(outer wall)=4.26 W/m^2-k
Radiative Heat transfer mode	Yes, transmissivity = 0.1 for all surfaces	Yes, transmissivity = 0.1 for all surfaces
Average outlet temperature	381 K (108 °C)	366 K (93 °C)
Average temperature difference between inlet and outlet	70°C	83°C
Average outer wall temperature	352 K (79 °C)	325 K (52 °C)
Average lid plate temperature	347 K (74 °C)	323 K (50 °C)
Average canister wall temperature	431 K (158 °C)	424 K (151 °C)

It can be seen from Table 4-9 that in summer less amount of heat is removed by the air as the change in the temperature of the air is lesser in summer when compared to winter. This causes heat to be lost from the outer and top surfaces of the cask to increase which results in the high temperatures of the outer wall and lid plate temperature.

Figure 4-47 shows the temperature distribution for both summer and winter conditions respectively. It can be seen that the peak temperature of the canister does not vary much, only 3 K difference. Figure 4-48 shows the canister interface temperature distributions for both ambient conditions. The temperature distributions are similar for both conditions; this indicates that the ambient temperature has little effect on the peak temperature and canister surface temperatures.

Figure 4-49 shows the temperature distribution in a plane which only cuts across the concrete region of the geometry. It can be seen that the peak temperature in the concrete is higher than in winter.

Figure 4-50 shows the velocity distribution of planar region for both the cases.

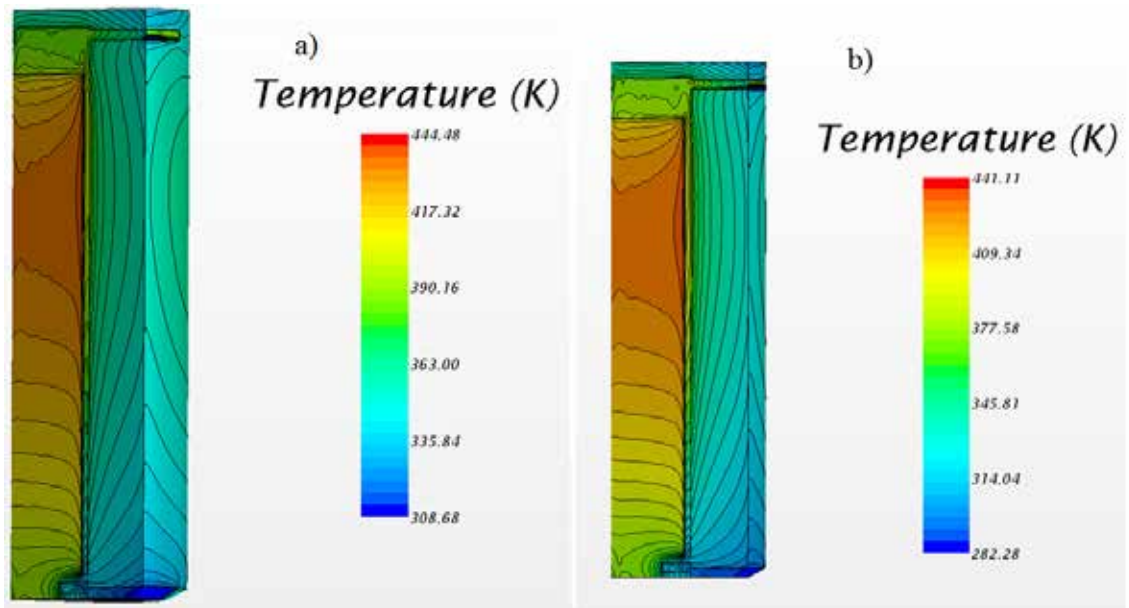

Figure 4-47 Temperature distribution in full scale models for (a) summer and (b) winter conditions.

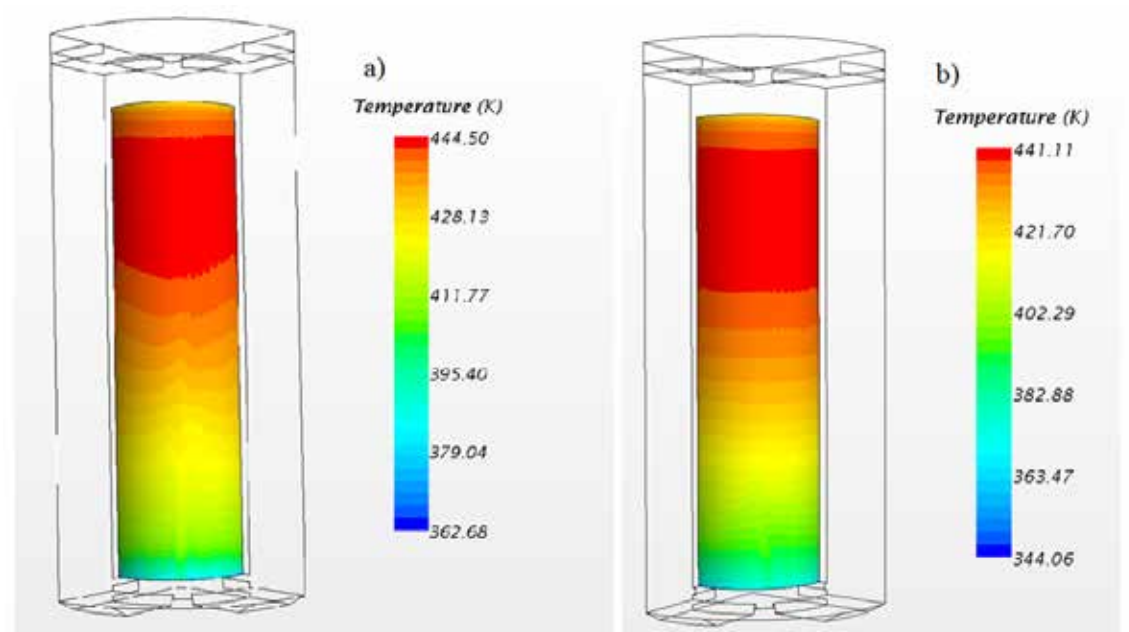

Figure 4-48 Temperature distribution on the canister interface for (a) summer and (b) winter conditions.

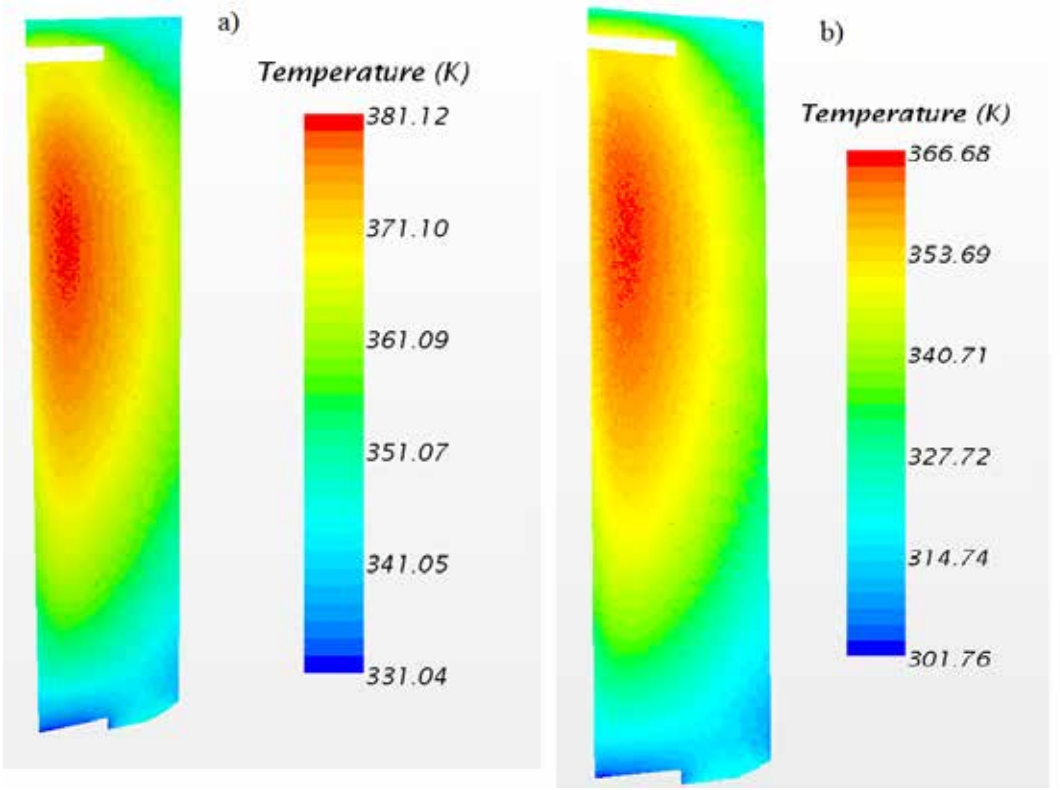

Figure 4-49 Temperature distribution on the plane through concrete for a) summer and b) winter conditions.

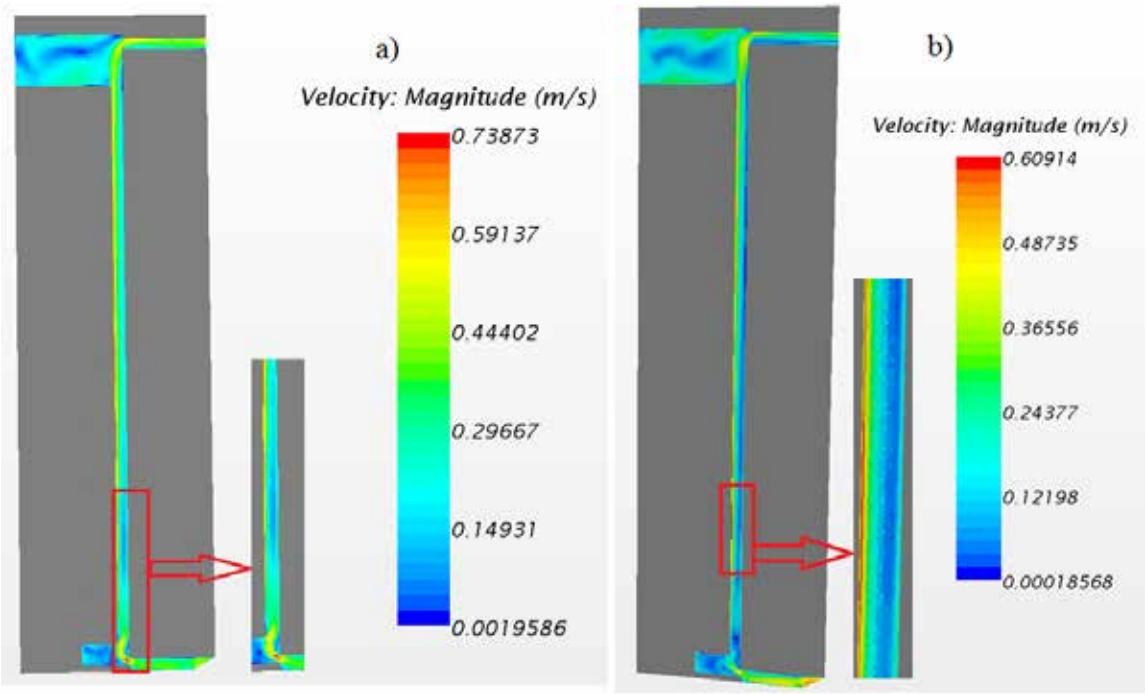

Figure 4-50 Velocity distributions in planar section for a) summer and b) winter conditions.

4.5. CONCLUSIONS

It has been shown that the conjugate heat transfer, and the effects of thermal radiation model should both be considered in the CFD simulation to predict comparable and reasonable temperature distributions as those in the literature for normal ambient temperature (300K). Summer (ambient temperature = 38 °C) and winter (ambient temperature = 10 °C) conditions are also investigated to identify the effects of the ambient temperature on the temperature distributions in the dry cask. The important temperature fields are summarized in Table 4-10. It can be observed that the temperature differences between inlet and outlet air vents are around 70 ~ 88 °C, and the temperature differences across the concrete cask (interior/exterior surfaces) are around 22 ~ 39 °C. Under summer condition, the temperature difference between inlet and outlet of the dry cask is 70°C, which is much lower than the temperature difference in winter, 83°C. Part of the reason is due to higher average air velocity when the cask is operated in summer condition. As expected, the outer concrete wall temperature is 78 °C in summer, which is 27 °C higher than in winter condition. The heat flux used in scaled model was determined through scaling analysis (Kim et al.,2014) and works properly to preserve temperature difference between inlet and outlet (see Section 4.4.4.a) in full scale and reduced-scale models (error of 1.6% for outlet temperature) if the effects of thermal radiation are not considered. With inclusion of thermal radiation model in simulation, the error of outlet temperature between full scale and reduced-scale model is (388-370)/388*100% = 4.6%, which is still acceptable for the purposes of this research. However, the absolute values of temperatures on interior surface of concrete cask are 97 °C and 78 °C for full scale and scaled model respectively, which has 19 °C difference and can have significant effect on the integrity of the concrete cask. Therefore, a more sophisticated scaling analysis method should be developed to include thermal radiation effect and to preserve important temperature field in different scales of models.

Table 4-10 Summary of Important Temperature Metrics.

	Normal Condition		Summer Condition	Winter Condition
	Full-scale	Reduced-scale	Full-scale	Full-scale
Ambient temp. (outside of cask), inlet temp.	300 K (27 °C)	300 K (27 °C)	311 K (38 °C)	283 K (10 °C)
Ave. outlet temp.	388 K (115 °C)	370 K (97 °C)	381 K (108 °C)	366 K (93 °C)
Ave. temp. on canister surface	427 K (154 °C)	395 K (122 °C)	431 K (158 °C)	424 K (151 °C)
Ave. temp. on interior surface of concrete cask	370 K (97 °C)	351 K (78 °C)	377 K (104 °C)	364 K (91 °C)
Ave. temp. on exterior surface of concrete cask	338 K (65 °C)	329 K (56 °C)	352 K (79 °C)	325 K (52 °C)
Ave. temp. difference between inlet/outlet	88 °C	70 °C	70 °C	83 °C
Ave. temp. difference between interior/exterior surface	32 °C	22 °C	25 °C	39 °C

4.6. REFERENCES

Brewster, R.A., Baglietto, E., Volpenhein, E. and Bajwa, C.S. (2012). "CFD analyses of the TN-24P PWR spent fuel storage cask." *ASME 2012 Pressure Vessels and Piping Conference, PVP 2012*, July 15-19 Toronto, ON; Canada.

CD-adapco (2016). *STAR-CCM+,* Available from: http://mdx.plm.automation.siemens.com/star-ccm-plus , Accessed on December 23, 2016.

Herranz, L. E., Penalva, J. and Feria, F. (2015). "CFD analysis of a cask for spent fuel dry storage: Model fundamentals and sensitivity studies," Annals of Nuclear Energy, 76, 54-62.

Holtec International. (2010). *FSAR, Final Safety Analysis Report for the HI-STORM 100 Cask System.* Holtec Report No. HI-2002444, Rev. 8.

Incropera, F., DeWitt, D., Bergman, T., & Lavine, A. (2007). *Fundamentals of heat and mass transfer*, John Wiley and Sons, New York.

Kim, H. M., No, H. C., Bang, K. S., Seo, K. S. and Lee, S. H. (2014). "Development of scaling laws of heat removal and CFD assessment in concrete cask air path," Nuclear Engineering & Design, 278, 7-16.

McKinnon, M. A., Dodge, R. E., Schmitt, R. C., Eslinger, L. E., and Dineen, G. (1992). *Performance testing and analyses of the vsc-17 ventilated concrete cask,* Final Report, prepared Pacific Northwest Laboratory and Idaho National Engineering Laboratory.

Morton, S., Carlson, A., Hoffman, C., Rivera, J., Winston, P., Shirai, K., Takahashi, S., and Tanaka, M. (2006). *Nondestructive evaluation of the vsc-17 cask,* Idaho National Laboratory (INL), United States.

Shultis, J. K. and Faw, R. E. (2002). *Fundamentals of nuclear science and engineering (2nd ed.)*, Marcel Dekker, New York.

Subiry, J (2013). *MAGNASTOR System,* Available from: http://www.iaea.org/OurWork/ST/NE/NEFW/Technical-Areas/NFC/documents/spent-fuel/TM-45455/Agenda-24-USA-Evolution_to_ultra-high_capacity_spent_fuel_storage_systems.pdf , Accessed on July 3, 2013.

Zigh, G., & Solis, J. (2013). *Computational fluid dynamics best practice guidelines for dry cask applications,* Final Report, prepared by United States Nuclear Regulatory Commission, Office of Nuclear Regulatory Research, Office of Nuclear Material Safety and Safeguards, Washington, District of Columbia, USA.

CHAPTER 5

DURABILITY AND IMPACT TESTING OF CASKS

5.1. INTRODUCTION

The objective of this chapter is to investigate the multi-hazard performance of scaled cask models fabricated as a part of this project. The three physical models of the casks were monitored for a period of two years for signs of corrosion and ASR cracking. Following the monitoring periods, the casks were subjected to end-drop and side impact tests to investigate the structural integrity of casks under such loading scenarios and in aged conditions. The same tests were repeated on a control (unaged) cask to compare the performance.

5.2. MONITORING OF AGING

A series of non-destructive testing, such as ultrasonic pulse velocity (UPV), half-cell potential, visual inspection and Schmidt hammer, was performed on the three casks, self-consolidating concrete (SCC), NaOH-8, and $CaCl_2$-4, to monitor the aging effect. The results are presented in the following sections.

5.2.1. Schmidt Hammer Test Results

Schmidt hammer was used to estimate the compressive strength distribution of the casks along their height at 370 days. The Schmidt hammer measurements were calibrated using the actual compressive strengths obtained from material testing such that the mean value along the height was the same as the average of the material test results at 365 days. The strength was measured using a Schmidt hammer at ten equally spaced locations along the height of the cask. Ten measurements were collected around each location and averaged. The results of these measurements are shown in Figure 5-1. Before calibration, the SCC cask showed the highest strength and the NaOH-8 cask showed the lowest strength, which was in line with the material tests. In all three casks, the strength was found to decrease along the height of the casks from bottom to top. This is attributed to the settlement of the coarse aggregate towards the bottom of the casks, since the casting was done from the top. Although some variation along the height is observed, the strengths at the bottom were approximately 17%, 28% and 30% higher than those at the top for the SCC, NaOH-8 and $CaCl_2$-4 casks, respectively.

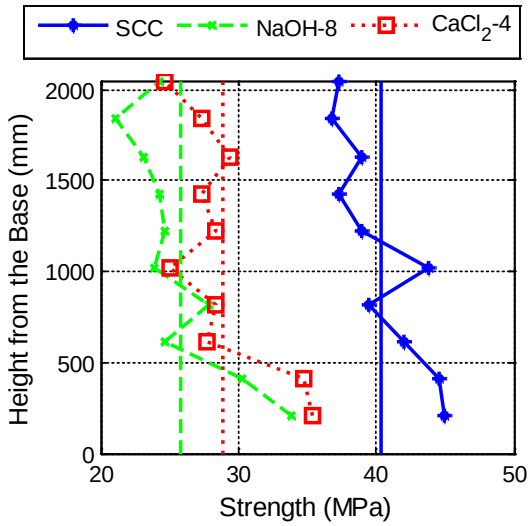

Height from the base (mm)	SCC Cask (MPa)	NaOH-8 Cask (MPa)	$CaCl_2$-4 Cask (MPa)
2042	37.3	24.3	24.7
1838	36.8	21.1	27.4
1634	38.9	23.1	29.4
1430	37.3	24.3	27.4
1225	38.9	24.7	28.4
1021	43.8	23.9	25.0
817	39.5	27.9	28.4
613	42.0	24.7	27.7
408	44.6	30.3	34.7
204	45.0	33.9	35.4
Avg.	40.42	25.82	28.9

Figure 5-1 Schmidt hammer measurement. Note that the vertical dashed lines in the figure shows the average compressive strength measurements at 365 days from material tests.

5.2.2. Visual Inspection

Cracks were observed in the NaOH cask approximately 90 days after casting. This indicates that the alkali silica reactivity (ASR) process was accelerated considerably, given that in regular structures it takes approximately 10 years until the first appearance of cracks (IStructE 2010). The crack maps for ASR accelerated casks at 517 days and 591 days are shown in Figure 5-2(a) and (b), respectively. Comparing the time of appearance of cracks on the casks and small NaOH-8 specimens prepared in phase 1 of material testing, it is clear that ASR cracks were observed around the same time at both levels; however, the density of the cracks was different due to the differences in geometry and internal reinforcement. The density of cracking increased with time and higher crack density was observed towards the top of the cask, potentially due to lower concrete strength in that region as explained above. Similar to the results of material specimens, the crack widths remained between 0.05 mm and 0.1 mm over the measurement period.

On the $CaCl_2$-4 cask, the first cracks were visually observed at around 120 days. Comparing the time frame of the appearance of cracks on the surface of the specimens at the material level prepared in the first phase, there is a one month period difference, which shows the effect of geometry and internal reinforcement of structure on the occurrence and propagation of cracks. The crack propagation over time on the $CaCl_2$-4 cask is shown in Figure 5-3. After less than a year, there was extensive cracking on the casks and several of the cracks had coalesced. The crack width was measured at 23 randomly chosen points on the casks, and the change over time in the average crack width is shown in Figure 5-4 (see also Table A-35). It is seen that at 569 days (i.e., the last measurement) the cracks were 0.33 mm wide on average with the smallest and largest measurements being 0.1 mm and 1.0 mm, respectively.

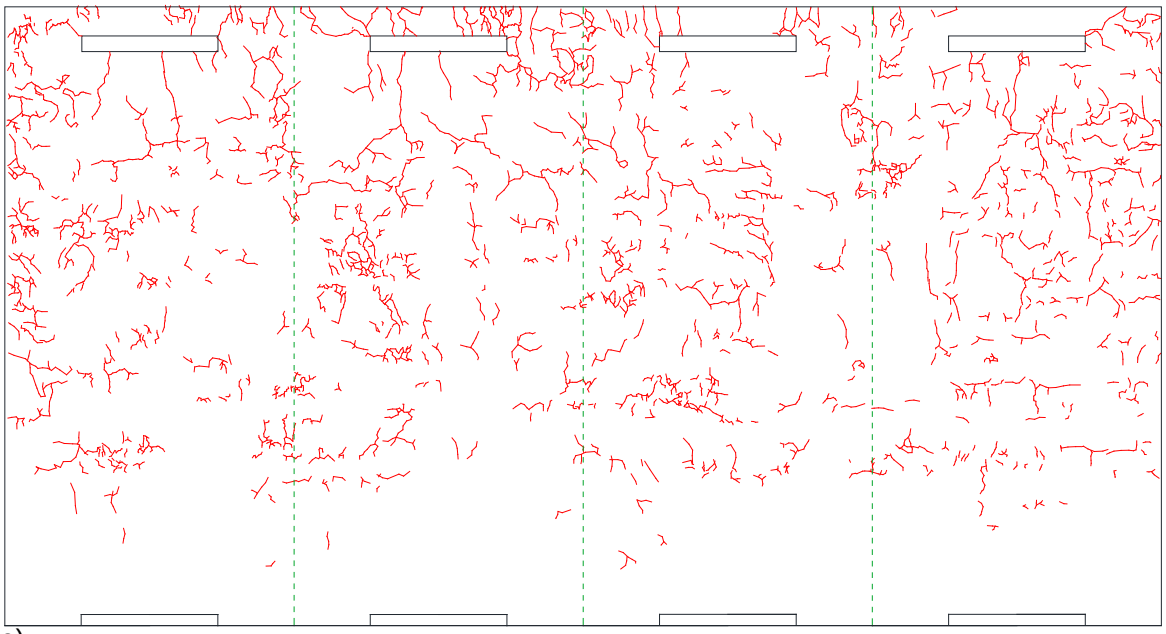

a)

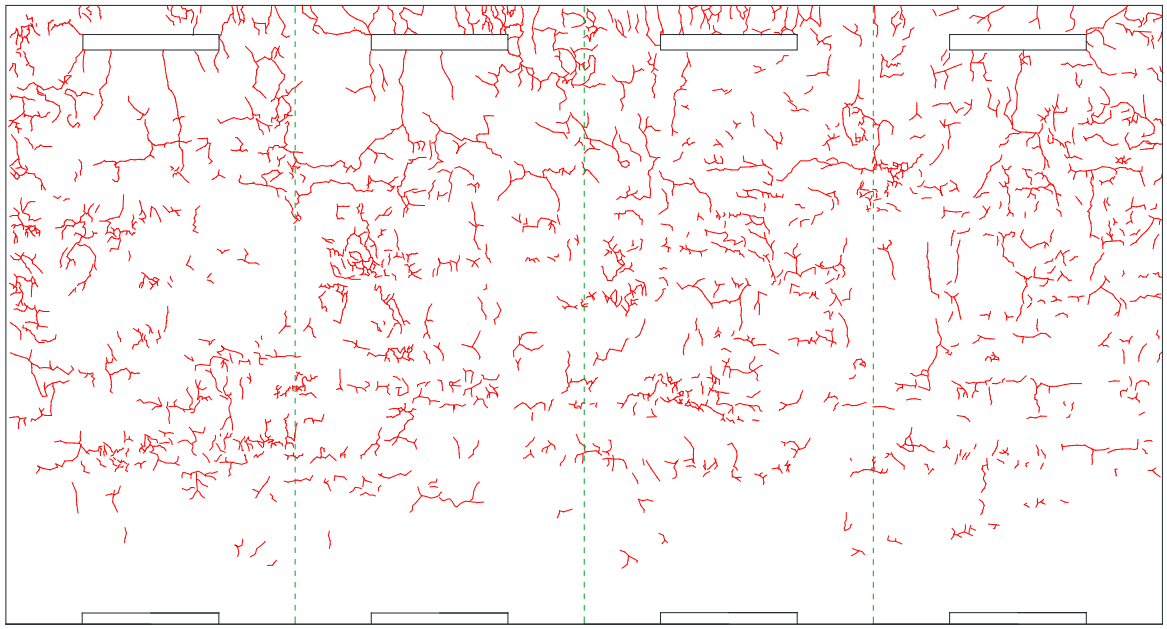

b)

Figure 5-2 Crack propagation on cask with NaOH-8 mixture (a) 517 days (b) 591 days.

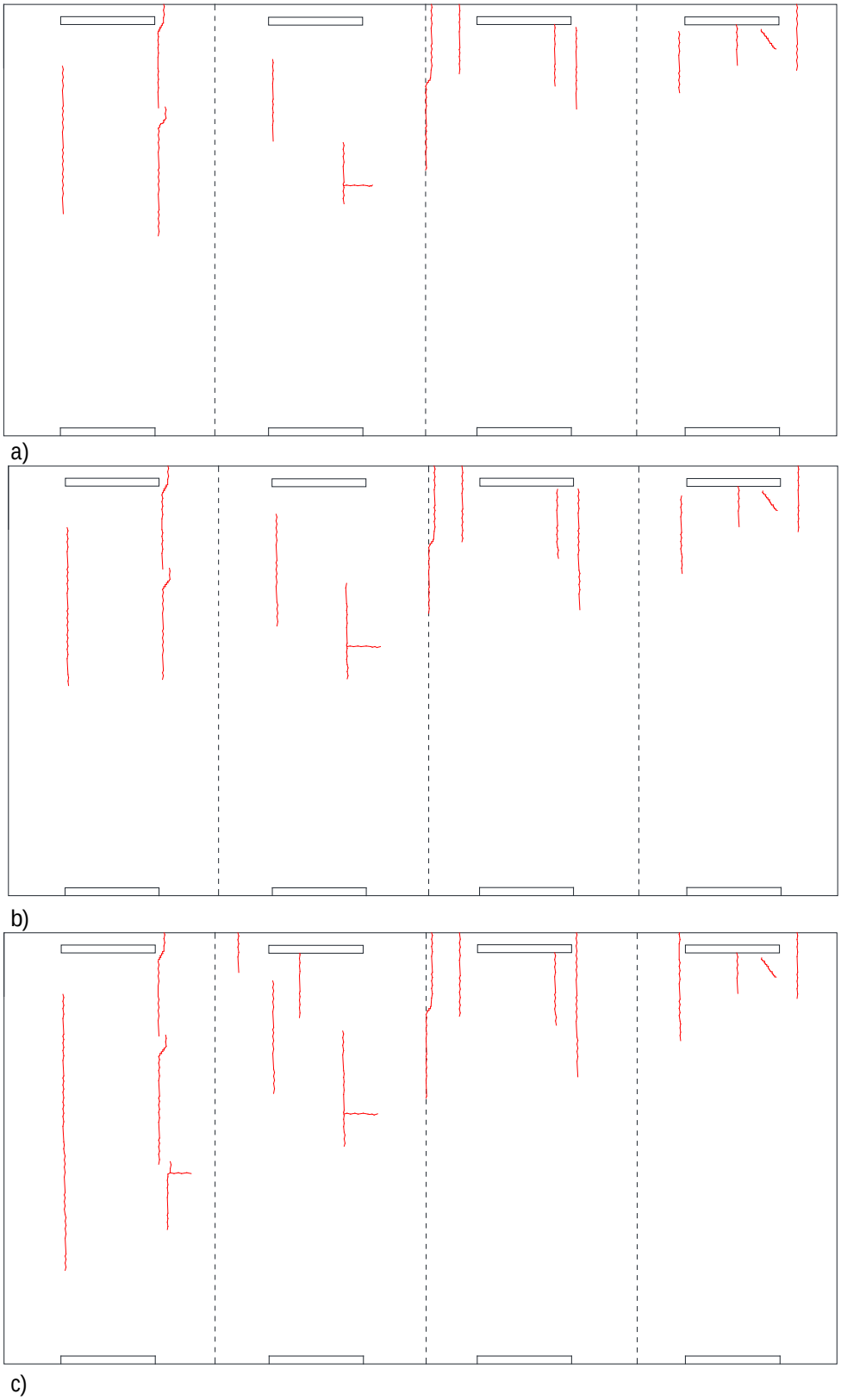

Figure 5-3 Crack propagation on cask with $CaCl_2$-4 mixture (a) 163 days (b) 186 days (c) 225 days (d) 295 days (e) 512 days (f) 569 days.

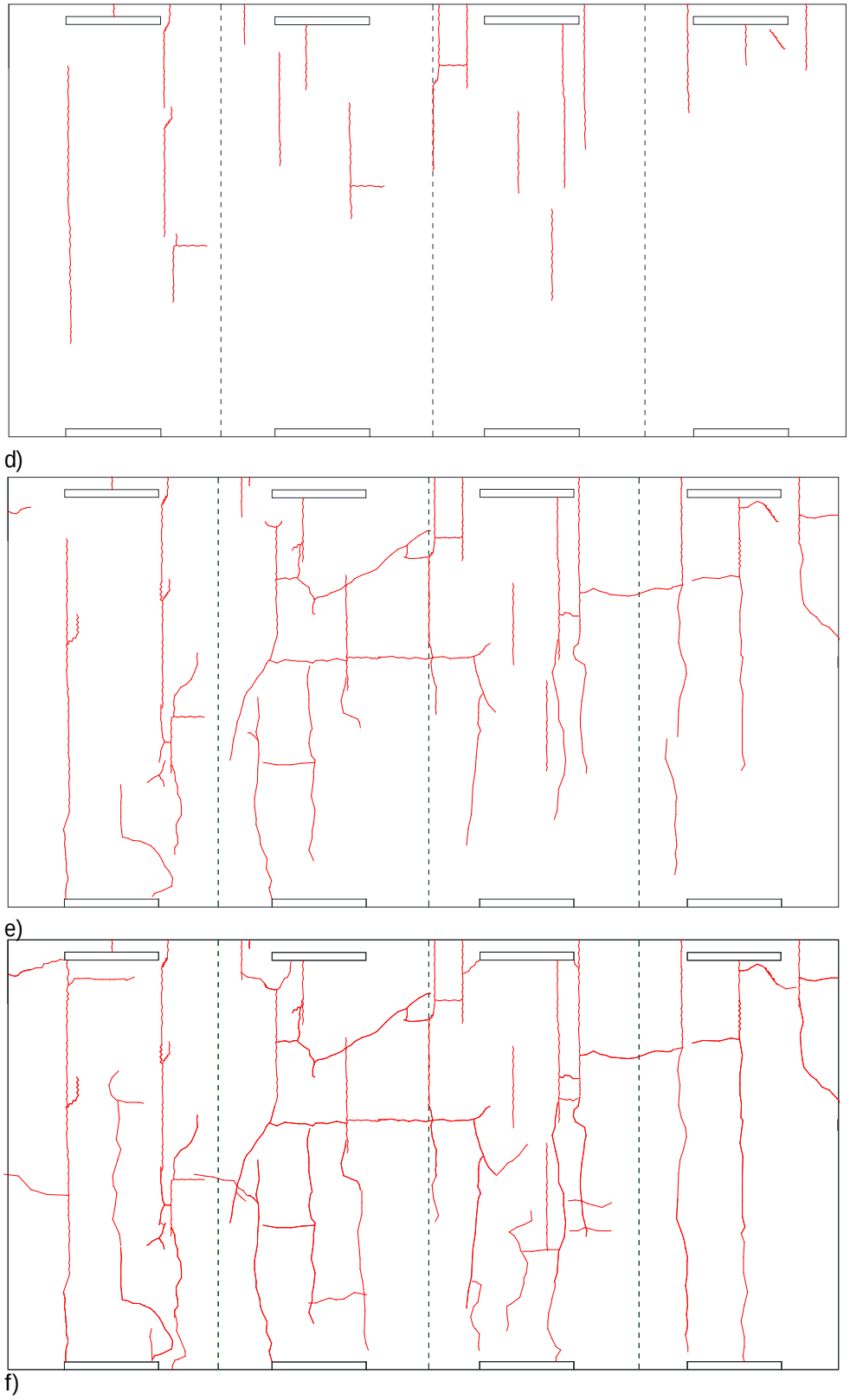

Figure 5-3 (continued) Crack propagation on cask with $CaCl_2$-4 mixture (a) 163 days (b) 186 days (c) 225 days (d) 295 days (e) 512 days (f) 569 days.

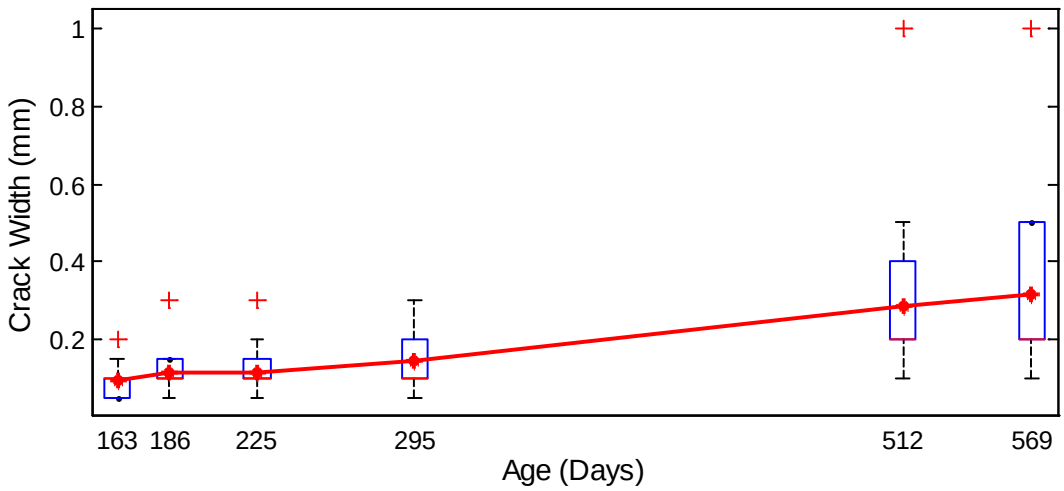

Figure 5-4 Crack width growth on $CaCl_2$ cask.

5.2.3. Ultrasonic Pulse Velocity Test Results

The UPV was measured at three different levels and on two sides of each cask as shown in Figure 5-5. Since it was not possible to measure the UPV on the casks by the direct method, a series of readings were performed with a fixed transmitter and incremental movement of the receiver as shown in Figure 5-5. The average of UPV measurements over time is shown in Figure 5-6. These results indicated a higher velocity in the SCC cask compared to NaOH-8 and $CaCl_2$-4 casks, which had similar UPV values. Small differences in the measured values between material testing and the structural level can be explained due to the existence of rebar inside the casks as well as not being able to measure the UPV with the direct method. Contrary to what was initially thought, the UPV results were not able to capture any degradation in concrete properties due to aging at this scale because of their sensitivity to moisture content, temperature and the presence of rebar and other minor defects inside the concrete around the measurement locations.

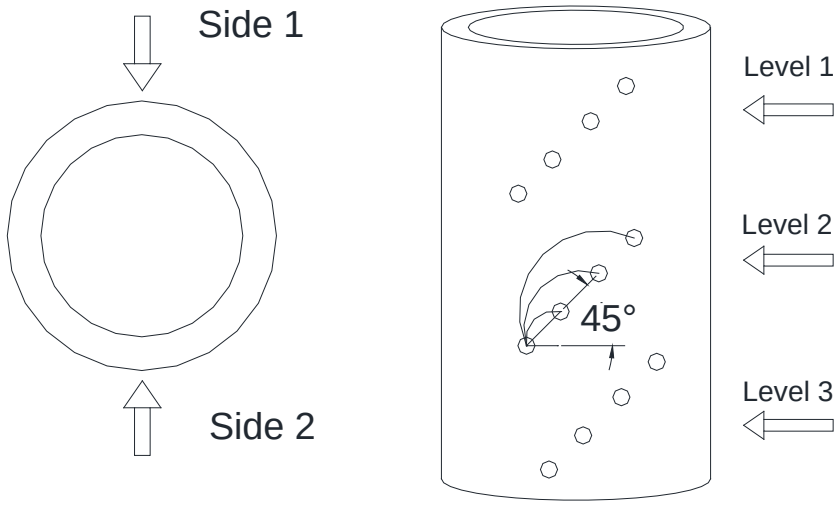

Figure 5-5 Level of UPV measurement on casks.

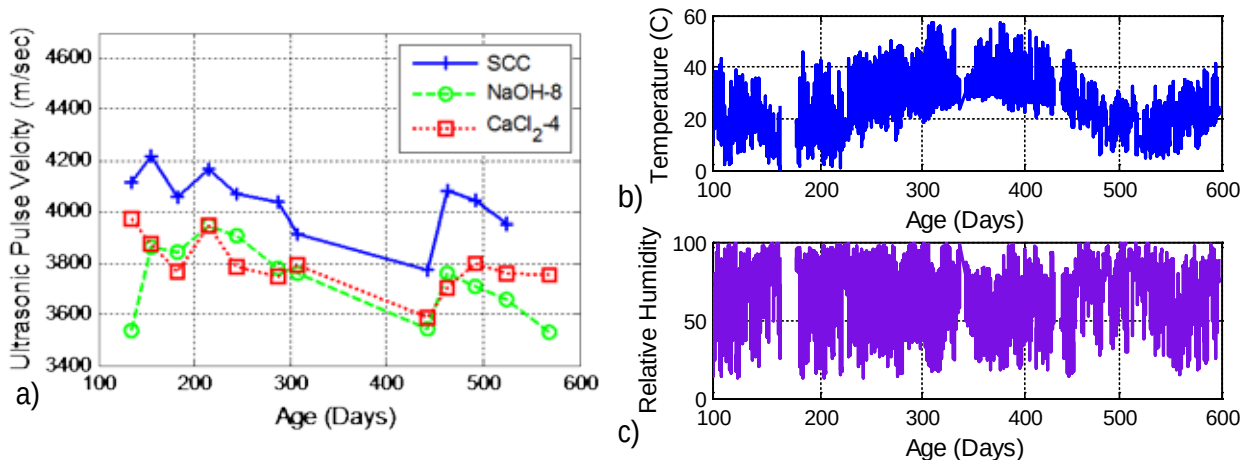

Figure 5-6 (a) UPV measurement on casks (b) temperature from 100 days to 600 days (c) relative humidity from 100 days to 600 days.

5.2.4. Half-Cell Potential Test Results

The half-cell potential was measured to evaluate the probability of corrosion in each of the casks. At each measurement date, more than 150 points were read on one half of the cask along a grid of lines. The measurements were consistent at different locations on the casks; therefore, in Figure 5-7, only the average of these measurements in an eighteen-month period is shown. Half-cell potentials in SCC and NaOH-8 casks were similar and always higher than -100mV/CSE, which indicates that the probability of corrosion is less than 10%. On the other hand, the measurement for $CaCl_2$-4 cask was always lower than -350mV/CSE, which shows that the probability of corrosion is more than 90%. As an overall trend, the half-cell potential decreased over time, which is an indicator of increased corrosion activity in the $CaCl_2$-4 cask. The measurement on the casks was similar to the measurement at the material level specimens of first phase.

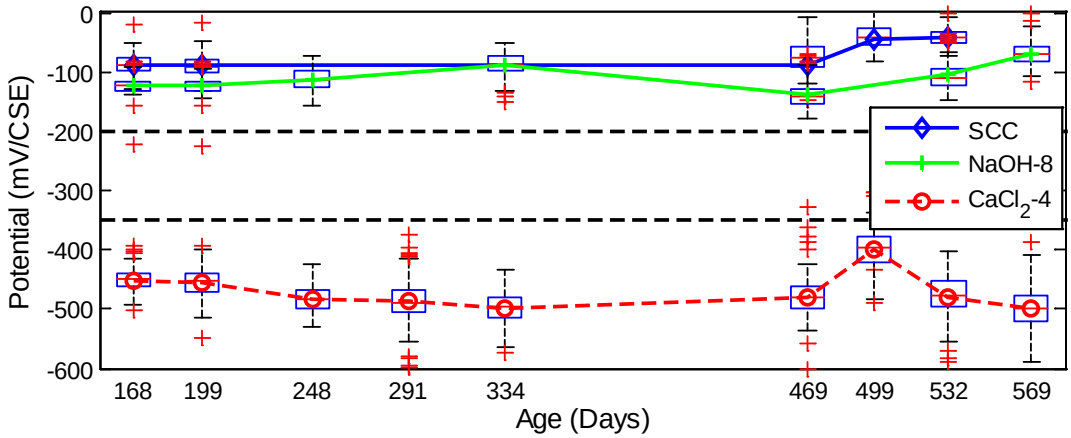

Figure 5-7 Half-cell potential in three casks.

5.3. EXPERIMENTAL PROGRAM FOR IMPACT TESTING

The main focus of this section is evaluation of tip-over accident for the storage casks, however; according to the hypothetical accidents defined by United States Nuclear Regulatory Commission (NRC), three different impact tests were considered for the specimens: end drop, tip-over and side drop. The test plan was developed in a way that the specimens remain elastic during the end drop tests. Based on the finite element (FE) simulations the maximum drop height that does not induce damage in the specimens was approximately estimated and several tests were performed from different drop heights in order to develop a relationship between the drop height and maximum deceleration. The side drop tests were performed after the tip-over tests to evaluate the ultimate strength of the casks. The tests on SCC and $CaCl_2$ casks were performed on the dates presented in Table 5-1.

Table 5-1 History of the Tip-Over Tests.

Cask	Type	Test #	Date	Impact Side
SCC	End drop	1	11/24/2015	-
	End drop	2	1/5/2016	-
	End drop	3	1/20/2016	-
SCC	Tip-over	1	1/29/2016	1
	Tip-over	2	5/2/2016	1
	Tip-over	3	12/2/2016	2
$CaCl_2$	Tip-over	1	3/28/2016	1
	Tip-over	2	1/4/2016	1
	Tip-over	3	4/8/2016	2
NaOH	Tip-over	1	4/29/2016	1
	Tip-over	2	5/5/2016	1
	Tip-over	3	5/17/2016	2

5.3.1. Test Setup

The test setup as shown in Figure 5-8 consists of a gantry frame, positioned transversely along with the guard frame on top of the pad. A hydraulic release hook was purchased and paired with a hydraulic pump. The capacity of both the release system and the gantry crane is 10 tons so the loaded cask could be lifted with a single attachment point. With the current configuration the cask could be released immediately without having to exert any physical effort through hydraulic pressure. A detail of the release system is shown in Figure 5-9.

Figure 5-8 Test setup

Figure 5-9 Ten tons hydraulic release system

5.3.2. Sensors and Instrumentation

A CompactDAQ (NI 9188) data acquisition system from National Instruments (2013) equipped with NI 9237 and NI 9234 analog input modules for strain and acceleration measurements, respectively, with 50kS/s sampling rate was used for data collection. Based on a review of previous experiments and computational studies (Kim et al. 2006), the duration of the tip-over impact was estimated to be approximately 5 milliseconds. With the mentioned system setup, in 5 milliseconds acquisition window, about 250 data points could be recorded, which was deemed

enough for extracting the dynamic response of the specimens. Eight uniaxial accelerometers (analog, type 42A, sensitivity equal to 10 mV/g, and range up to 500 g) were used during a given test. Figure 5-10 shows the locations of the accelerometers mounted on the cask.

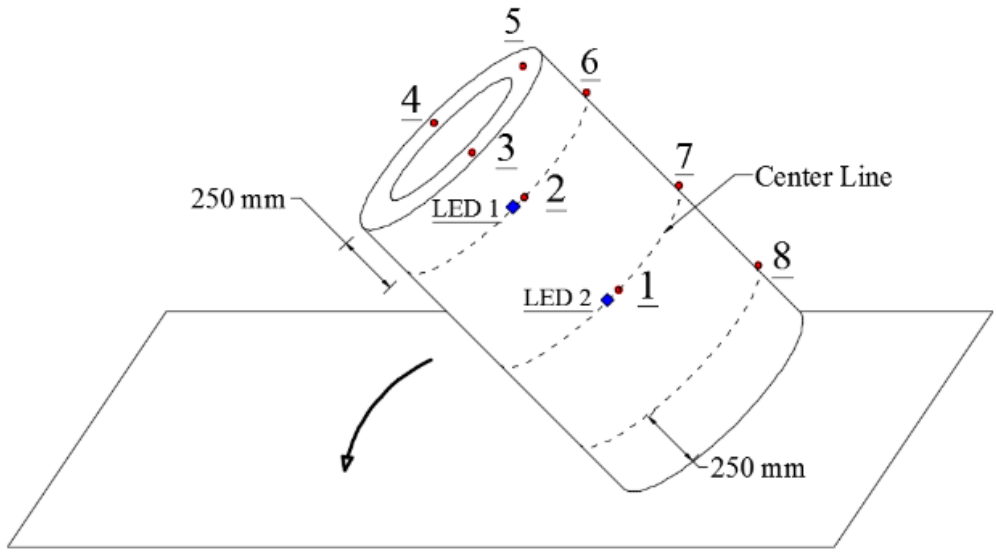

Figure 5-10 Acceleration sensor locations (accelerometers are shown with circle and LEDs with square symbols).

A Krypton K610 non-contact dynamic measurement system (Nikon, 2016) was used to for recording the displacement at two locations on the cask as a redundant measurement. The system consisted of three cameras, a controller and light-emitting diodes (LEDs) which were attached to the desired measurement locations. The displacement of the LEDs was tracked with a measurement accuracy of up to $60\ \mu m$ during the tests. A sampling frequency of 750 Hz was used. Two LEDs on the top and mid-height of the cask were installed as shown in Figure 5-10.

Twenty-six strain gages including surface gages from Kyowa (120 ohms, quarter bridge, weldable, waterproof) and rebar gage from HPI (120 ohms, quarter bridge, weldable, waterproof) were used in the vertical and circumferential reinforcement and on the surface of the lid, liner, and base plate as shown in Figure 5-11. Due to the limitation in number of data acquisition channels, only twenty four gages were sampled for each test. Based on the geometry of the model cask, two impact scenarios were considered. The two impact sides were different due to the presence of the air inlets and outlets on the first impact side. Hence, two tip-over tests on each of the model casks were conducted to investigate the potential difference in the structural performance with changing impact sides.

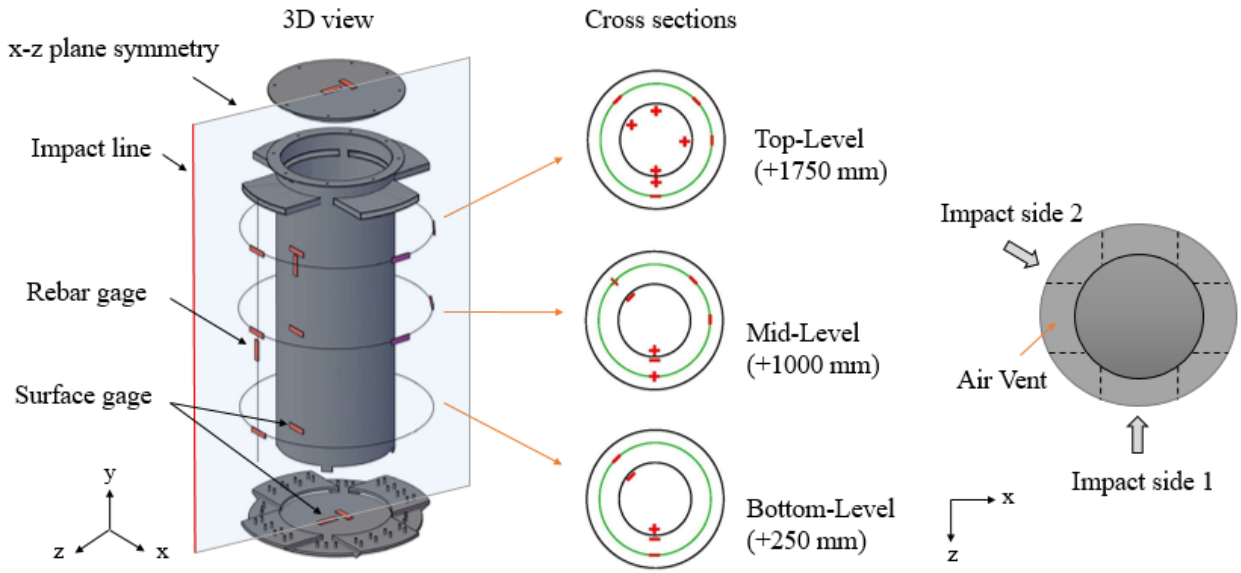

Figure 5-11 Schematic layout of strain gages for the specimens (note: cross symbols mean gages positioned both in vertical and horizontal directions).

Rebar gages were positioned at three different elevations along the height of the cask as shown in Figure 5-12(a). Theoretically, three strain gages are needed in order to obtain surface strain components at a specific location. However, due to the symmetry of the model cask about to the plane passing through the impact line and the absence of shear at the installation locations, two perpendicular strain gages are installed to obtain principal strains Figure 5-12(b).

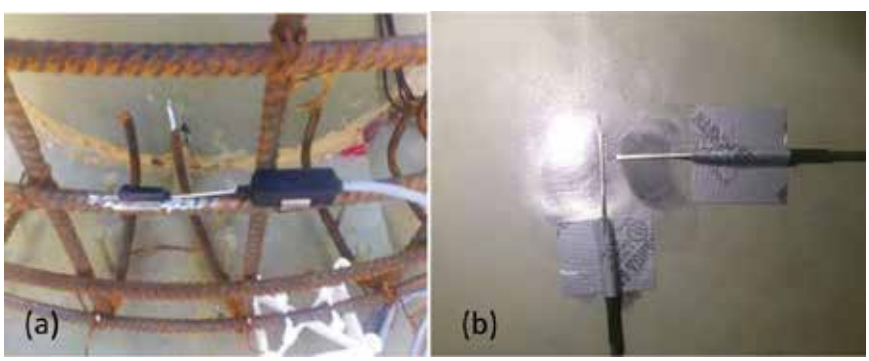

Figure 5-12 (a) Rebar gages (b) perpendicular welded surface gages.

Concrete embedded strain gages were used for strain measurement in concrete (see Figure 5-13). For the tip-over tests, the concrete is exposed to aging. Considering the accelerated situation, the surface of the concrete might be deteriorated after the aging period. Therefore, using ordinary gages on the surface of the concrete especially with presence of cracks will not yield the desired results. Hence, use of embedded gages is considered as a potential solution. By putting adequate number of embedded gages, especially near the impact area, beneficial information about the behavior of concrete during impact can be obtained. The embedded gages can measure the strain in one direction; therefore, by using several gages in orthogonal directions

and by knowing the modulus of elasticity, one can approximate the stresses in all directions. The data could then be compared with results obtained from finite element models.

Figure 5-13 Sample concrete embedment strain gages from Geokon (Geokon, 2015).

In order to obtain consistent results with the other strain gages, it was decided to fabricate custom embedded strain gages using the same type of weldable surface strain gages used on other parts of the cask as described above. Figure 5-14 shows the fabrication of these embedded concrete strain gages.

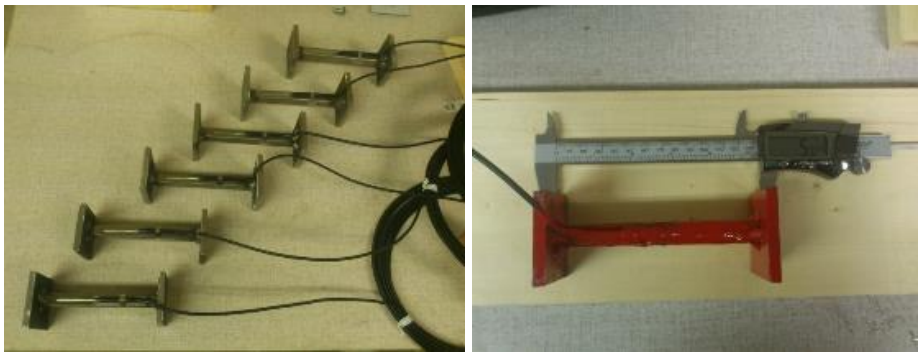

Figure 5-14 Fabrication of concrete embedded strain gages.

All the weldable sensors were covered with M-Coat J from Vishay which provides protection against chemical attacks and mechanical damage (see Figure 5-15).

Figure 5-15 Polysulfide protective coating for weldable strain gages.

The measurement systems for the tip-over and end drop test is shown in Figure 5-16.

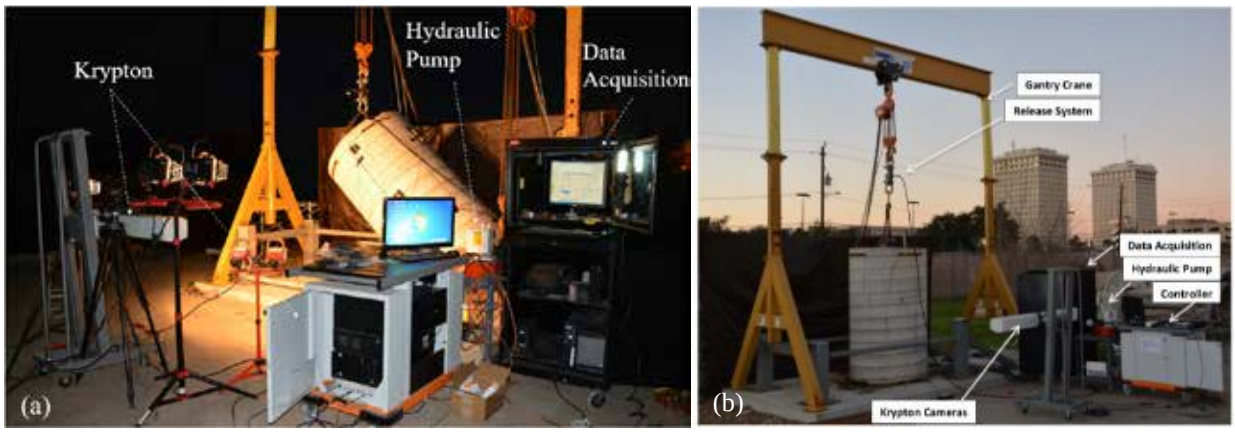

Figure 5-16 Instrumentation (a) tip-over test (b) end drop test.

5.4. IMPACT TEST RESULTS

5.4.1. End-Drop Tests

Eight end drop tests were performed in total with different drop heights ranging from 25 mm to 100 mm. One of the main purposes of this exercise is to verify the functionality of all the measurement systems. Triggering and synchronizing the systems was a challenging task since the duration of the test is only a few milliseconds. Furthermore, the end drop test is one of the hypothetical impact accidents which may happens during transportation. The results help develop a relationship between the drop height and the maximum deceleration due to the impact which is the critical parameter for the safety of the canister. Considering heavy weight of the cask, it is very difficult to level the cask while hanging so that during the impact the whole bottom surface of the cask touch the pad at the same time. In most of the cases, one side of the bottom touches the pad first and a few milliseconds later other side of the bottom hits the pad. This phenomenon causes some lateral movement of the cask. Furthermore; the sensors located on the side which hit the pad first have higher initial amplitude than the ones on the other side. Here, the maximum amplitude of the sensors is considered for the post processing which is associated with the upper limit of the applied load.

5.4.1.a. Signal processing

As explained earlier, eight accelerometers were used in the impact tests as shown in Figure 5-10. As expected, three of the sensors (3, 4, and 5) measured the highest decelerations during the test. Sensor 2 and 6 are important since they are at the same level as the canister top and therefore give an estimate of the maximum deceleration experienced by the canister. The sensor measurements include a range of frequencies and the peak acceleration is not a direct indication of the applied load on the specimen. The signal contains free vibration and resonance of the cask in different modes with relatively high frequencies as well as measurement noise. To remove the unwanted frequency content, a Butterworth filter (see Figure 5-17) was applied on all of the acceleration time histories.

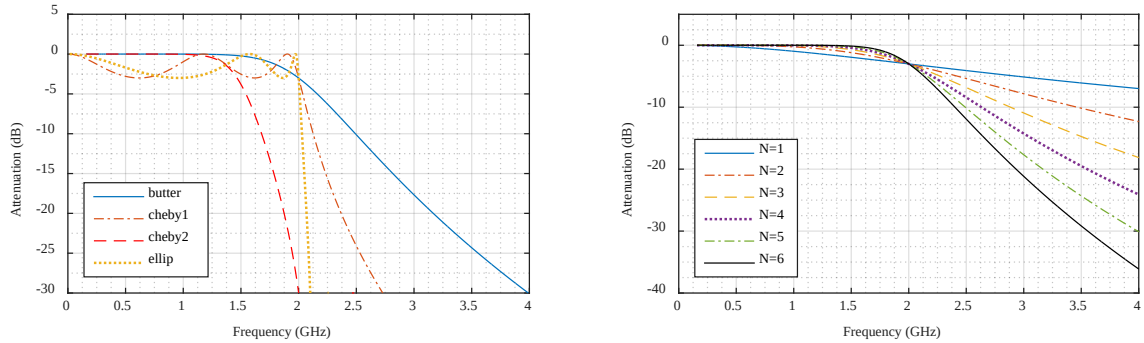

Figure 5-17 (a) Various filtering functions (b) low-pass Butterworth filter function.

Note that higher cutoff frequencies cause less distortion; however, they result in a lower signal-to-noise ratio. Therefore, identification of an optimal cut-off frequency and filter parameters is an important issue. Fast Fourier transform (FFT) is applied to the results to identify a suitable cut off frequency. Figure 5-18 shows that most of the recorded data with high Fourier amplitude are in the range from 0 Hz to 200 Hz, and there is no significant frequency content beyond 10 kHz. According to the Nyquist-Shannon theorem, the required sampling rate is at least twice of the highest frequency in the signal. Therefore, 50 kHz sampling rate and 200 Hz cutoff frequency were found to yield an accurate representation of the cask accelerations.

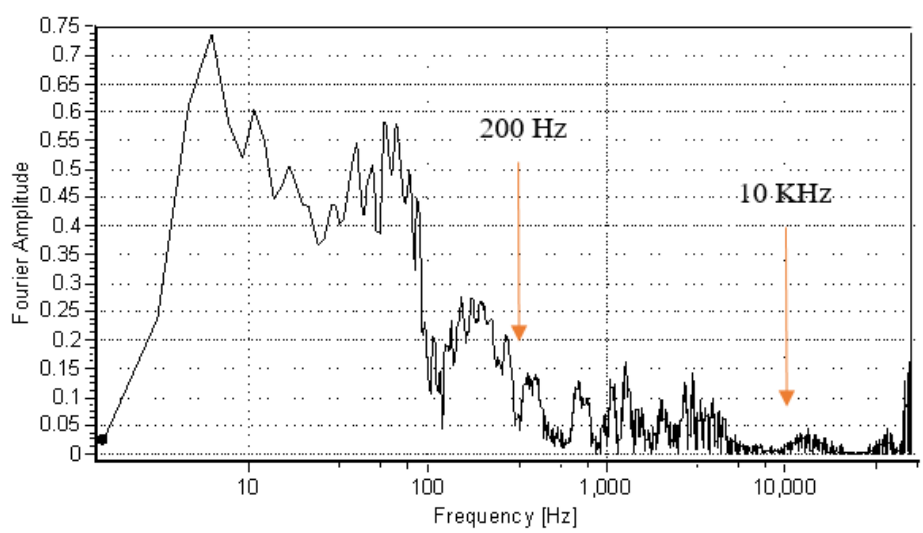

Figure 5-18 Fourier response of control specimen, test 1, Sensor 7.

A 6th order low-pass Butterworth filter with 200 Hz cut off frequency was used to identify the peak acceleration. The filtered and unfiltered measured data for sensor no. 7 are presented in Figure 5-19. The filtering is only applied on the acceleration record. The non-contact measurement system does not require filtering.

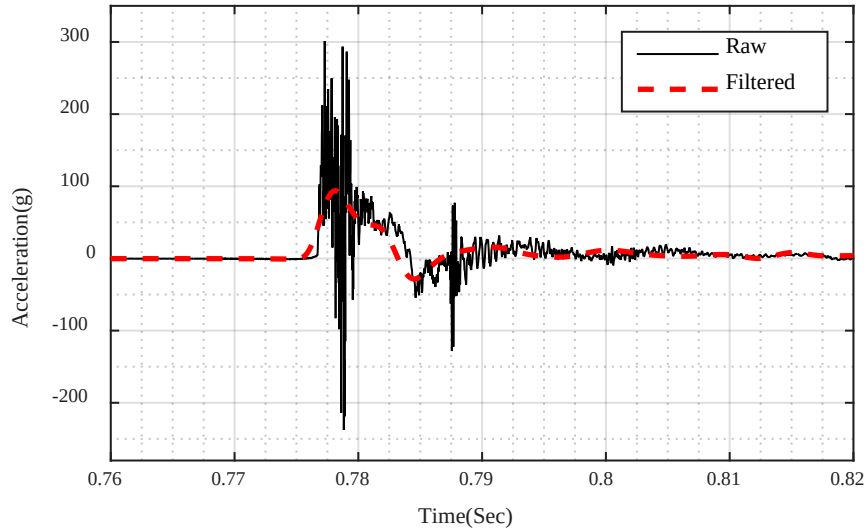

Figure 5-19 Raw and filtered (dashed-red) acceleration, SCC, sensor 1.

5.4.1.b. Accelerometer results

Figure 5-20 shows the recorded acceleration from all eight sensors for the 25 mm end drop test. The filtered data for accelerometer no. 2 attached on top of the cask is presented in Figure 5-21 which is considerably less than peak raw acceleration.

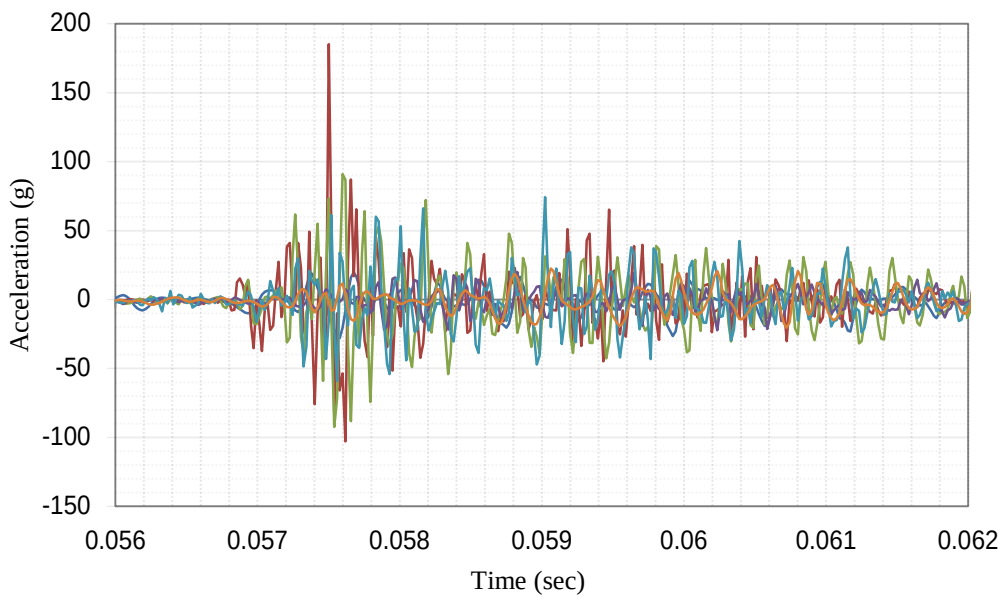

Figure 5-20 Acceleration time history obtained from accelerometers for 25.4 mm drop test.

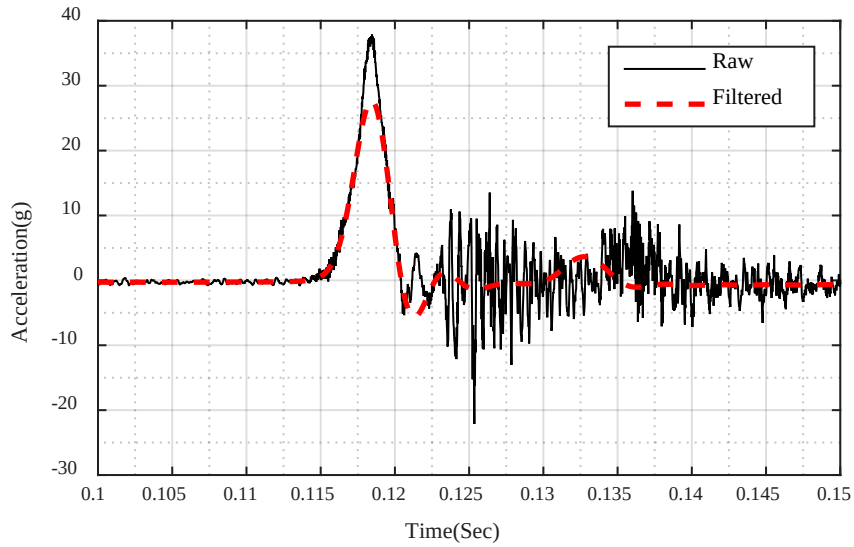

Figure 5-21 Filtered acceleration, 25.4 mm drop test

5.4.1.c. Non-contact measurement system results

For a correct measurement using the non-contact displacement measurement system, it is first necessary to define the coordinate axis for the system. For this purpose, first a horizontal plane is defined which is parallel to the surface of the pad, then one point is defined out of the plane to specify the vertical axis. In this case, the measured value in vertical direction is used for calculation of the impact velocity and acceleration. The system records the position of the LED with respect to the time. For calculation of velocity and acceleration, it is sufficient to take the first and second derivative with respect to the time, respectively. Considering 775 Hz sampling rate for each LED, the time step is $\Delta t = \frac{1}{775} = 1.29 \text{ millisec}$. In addition, an accurate drop height could be calculated from initial and final location of the LEDs as shown in Figure 5-22.

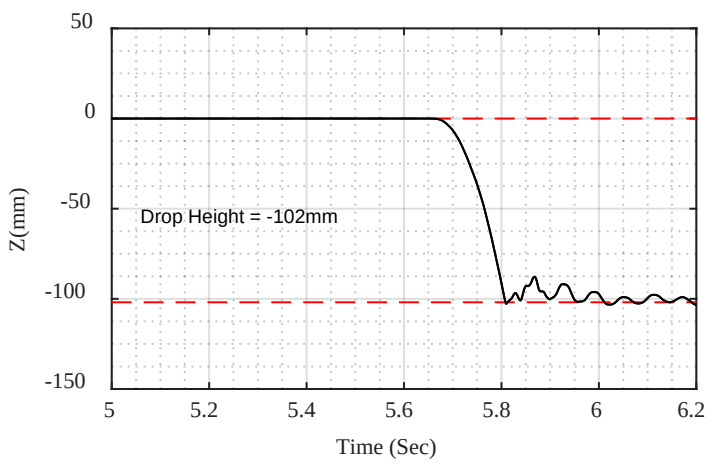

Figure 5-22 Calculation of the real drop height in z direction.

Furthermore, the impact velocity could be measured using the non-contact measurement system and compared with the analytical values obtained from the following equations

$$mgh = \frac{1}{2}mv^2 \qquad 5.1$$

$$v = \sqrt{2gh_1} \qquad 5.2$$

where h_1 is the drop height, m is the mass of the cask, g is gravitational acceleration and v is impact velocity. The actual drop height, measured and calculated velocity for the eight end drop tests are presented in Table 5-2 and Figure 5-23.

Table 5-2 Measured Dynamic Parameters from Non-Contact Measurement System.

Test #	Expected Height (mm)	Actual Drop Height (mm)	Analytical Velocity (mm/Sec)	Measured Velocity (mm/Sec)		Average Velocity (mm/Sec)	Measured Acceleration (mm/Sec^2)		Average Acceleration (mm/Sec^2)
				LED1	LED2		LED1	LED2	
1	25.4	26.7	724	697	702	700	25	27.4	26.2
2	25.4	25.6	709	678	685	682	28.5	31.1	29.8
3	50.8	50.7	997	1013	1009	1011	48.7	54.7	51.7
4	50.8	49.5	985	1017	1043	1030	45.2	52.3	48.7
5	50.8	51.1	1001	955	958	957	33.9	34.7	34.3
6	76.2	74	1205	1244	1248	1246	55.7	58.2	56.9
7	76.2	75.3	1215	1234	1236	1235	58.2	65.1	61.6
8	101.6	101.9	1414	1319	1323	1321	57.9	62.9	60.4

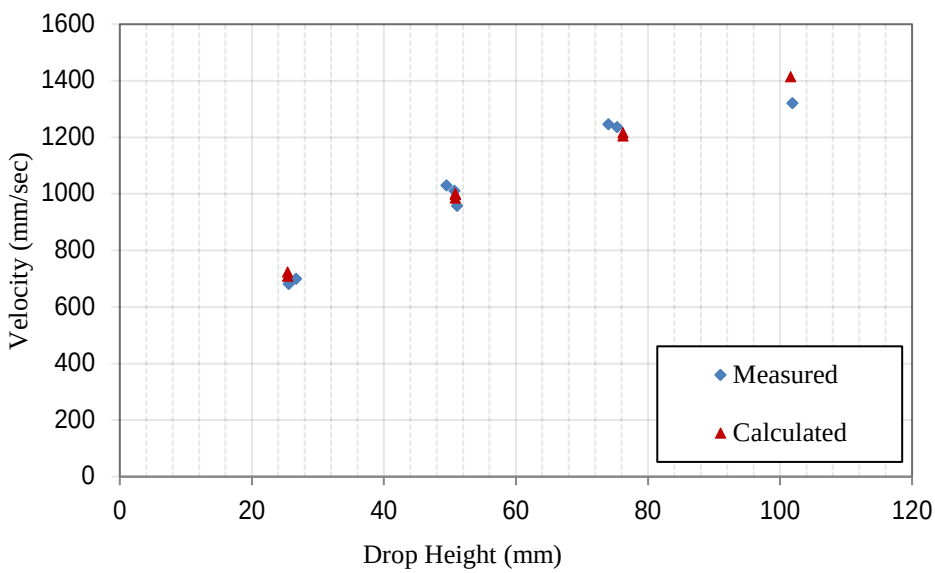

Figure 5-23 Measured versus calculated impact velocity.

As an example, the dynamic measurements of the LED1 and LED2 for 100 mm drop height are presented in Figure 5-24, Figure 5-25 and Figure 5-26.

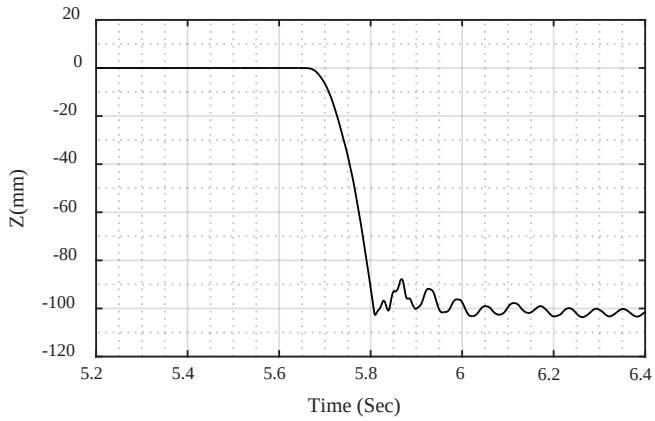

Figure 5-24 Displacement time-history for 100 mm drop.

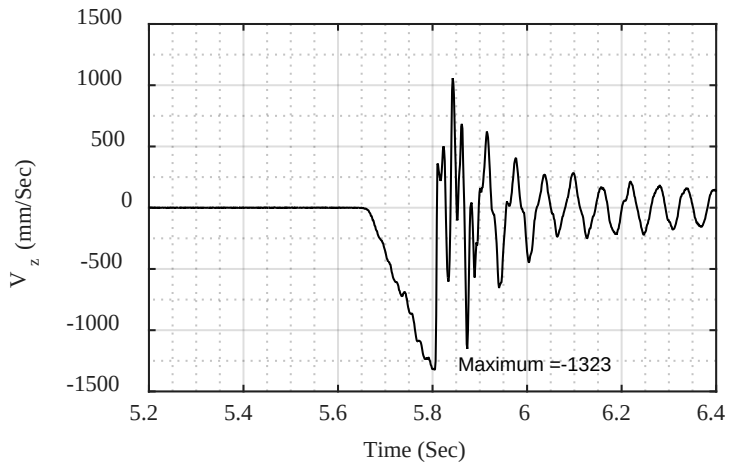

Figure 5-25 Velocity time-history for 100 mm drop.

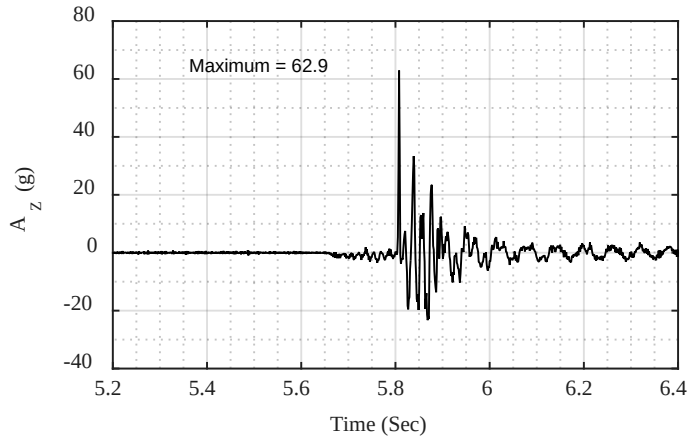

Figure 5-26 Acceleration time-history for 100 mm drop.

5.4.2. Side-Drop Tests

Three tip-over tests were performed on each cask including two on the first impact side and one test on the second impact side.

5.4.2.a. Accelerometer results

A summary of the filtered peak deceleration from accelerometers and the non-contact measurement system are presented in Figure 5-20. In some tests, the data from certain sensors could not be measured. In Figure 5-20, the average of the acceleration measurements from available data is presented for each location.

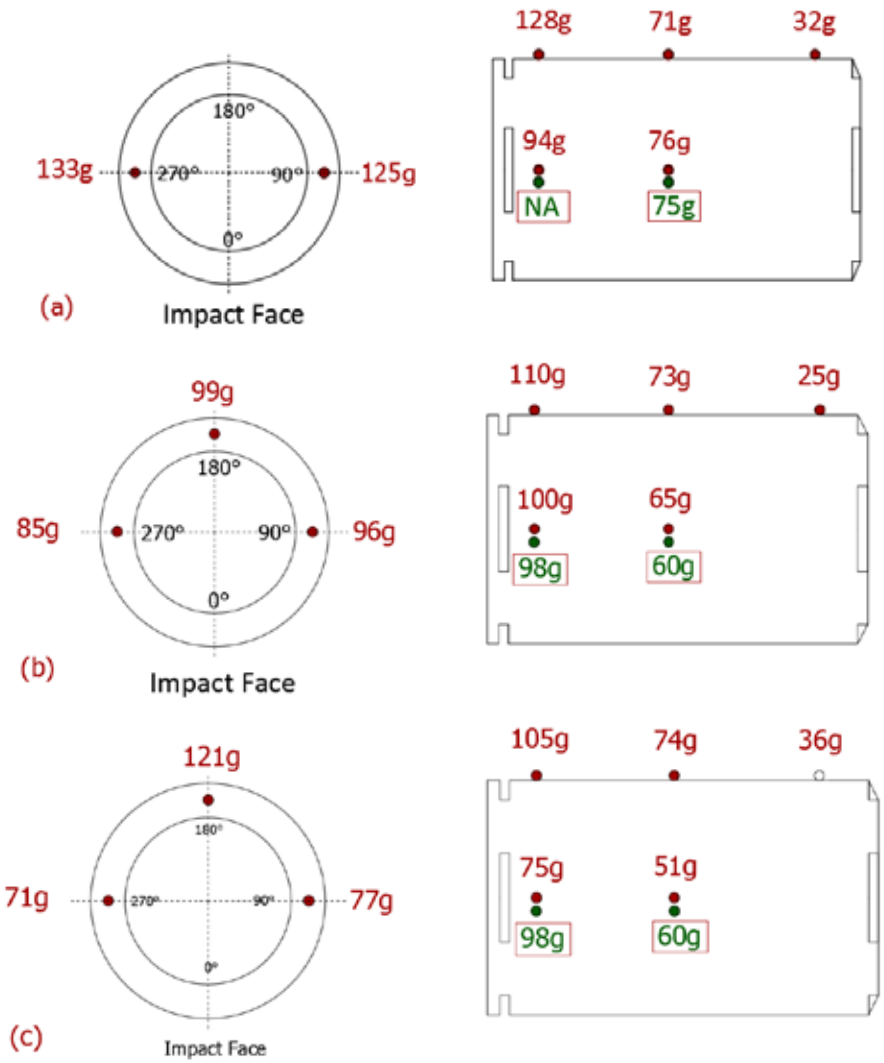

Figure 5-27 Average of filtered peak acceleration (a) SCC (b) $CaCl_2$ (c) NaOH (boxed: non-contact measurement data, unboxed: accelerometer data).

5.4.2.b. Non-contact measurement system results

The results obtained from non-contact measurement system including displacement, velocity and acceleration are presented in Figure 5-28. Note that the system measures only the displacement, and the velocity and acceleration were obtained by numerical differentiation of the vertical displacement with respect to time. A sampling rate of 775 Hz was used in non-contact measurements.

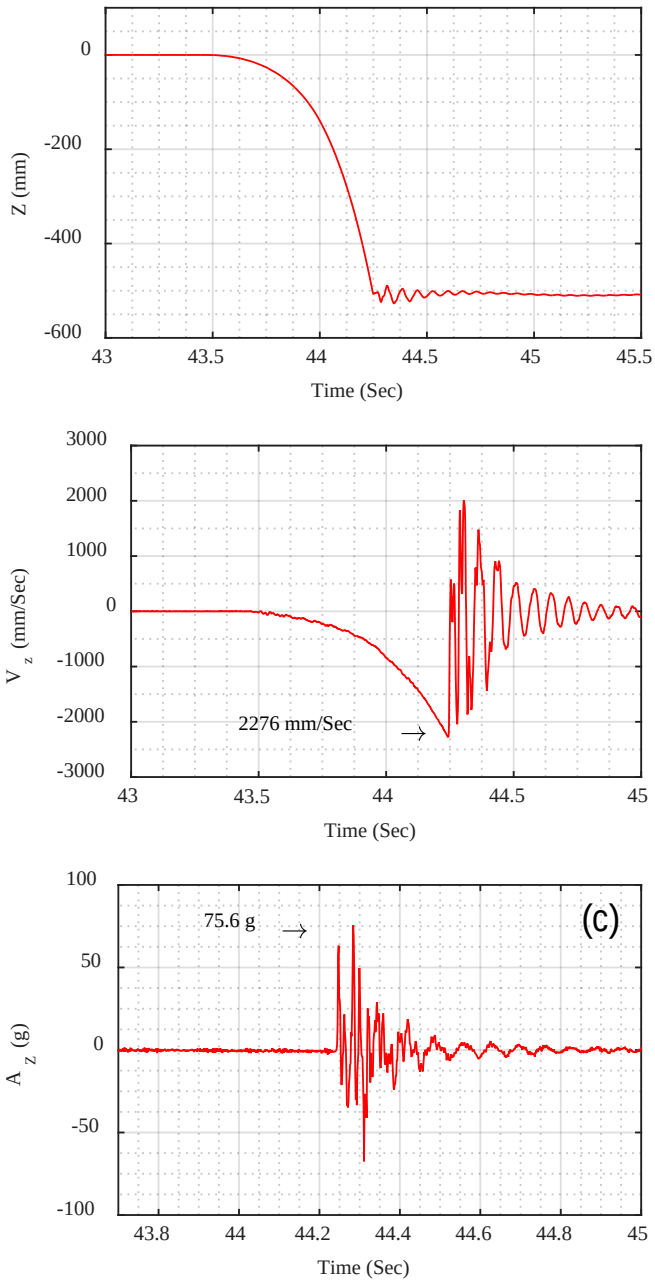

Figure 5-28 Dynamic parameters of the SCC, test 1 (a) displacement (b) velocity (c) acceleration.

The tip-over impact consists of multiple impacts due to bouncing of the cask. The most important impact is the first one which has the highest amplitude. The consequent impacts are due to rebound and elastoplastic behavior of the material, and due to material damping and other sources of energy dissipation, they have lower amplitudes with respect to the first impact. The duration of the first impact could be measured using the velocity time history. It is equal to twice the time period between the occurrence of maximum velocity and the subsequent first zero crossing of velocity. As presented in Figure 5-29, the impact duration is calculated as Δt=2x7.7=15.4 ms, Δt=2x9=18 ms and Δt=2x9.2=18.4 ms for the SCC , CaCl2 and NaOH casks, respectively. The results are from Test 1 for each cask at LED2 location.

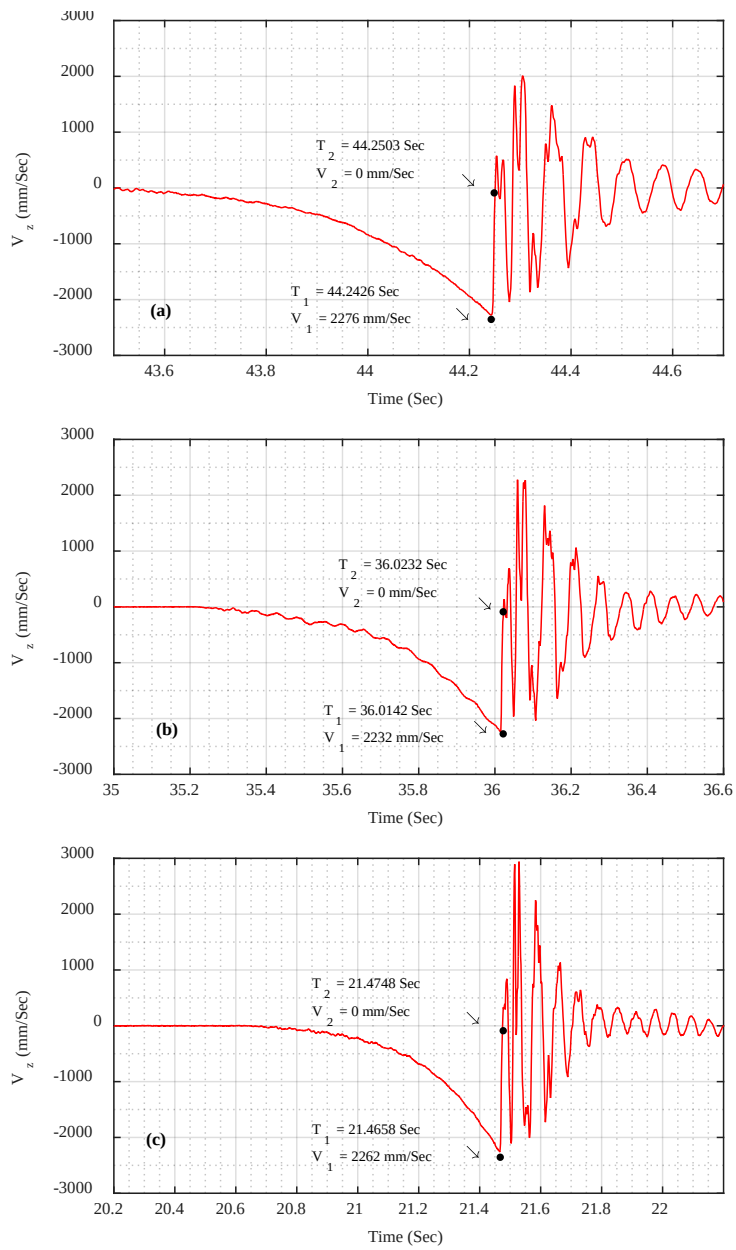

Figure 5-29 Estimation of the impact duration from velocity time-history for test 1 (a) SCC (b) $CaCl_2$ (c) NaOH.

5.4.2.c. Strain measurement results

As described above, strains were measured at several locations including liner, base plate and the lid. Rebar gages were also used to measure the strain in the circumferential reinforcement at three levels along the height of the cask. In order to evaluate the results obtained from the strain gages, it is necessary to define a yield criterion. The von Mises yield criteria is used to determine the yield behavior of steel. It is based on second invariant of deviatoric component of stress tensor and reads as follow:

$$F(s,k) = s_{dev} - s_y \pounds 0 \qquad 5.3$$

where σ_{dev} is the deviatoric stress and σ_y is the yield stress, κ is a parameter which describes hardening behavior of steel. The von Misses stress in uniaxial yield condition under tension or compression in one direction is

$$s_{dev} = |s_{11}|, \quad F(s,k) = |s_{11}| - s_y \pounds 0 \qquad 5.4$$

Where, σ_{11} is the current uniaxial stress. In the case of plane stress condition, generalized form of Hook's law will take the form of Eqs. 5.5, 5.6 and 5.7.

$$s_{11} = \frac{E}{1-v^2}[e_{11} - v(e_{22} + e_{33})] \qquad 5.5$$

$$s_{22} = \frac{E}{1-v^2}[e_{22} - v(e_{11} + e_{33})] \qquad 5.6$$

$$s_{33} = 0 = \frac{E}{1-v^2}[e_{33} - v(e_{11} + e_{22})], \quad e_{33} = v(e_{11} + e_{22}) \qquad 5.7$$

where σ_{11}, σ_{22} and σ_{33} represent the stress values in *x,y,z* directions, respectively. ε_{11}, ε_{22} and ε_{33} are the strains corresponding to these stresses. *E, v* are the Young's modulus and Poisson's ratio, respectively. These equations are valid for plain stress conditions where $\sigma_{13} = \sigma_{23} = \sigma_{33} = 0$. In the general plane stress case, Eq. 5.4 will be re-written in the form

$$\sqrt{s_{11}^2 - s_{11}s_{22} + s_{22}^2 + 3s_{12}^2} \pounds s_Y \qquad 5.8$$

To evaluate the potenitial yielding in the reinforcement, Eq. 5.4 was used due to uniaxial conditions, while for the stresses on the steel surfaces where plain stress assumtion is valid, Eq. 5.8 was considered. The von Misses strain was calculated using the measured strain obtained from two prependicular strain gages attached to the lid. The maximum stress for the SCC and $CaCl_2$ was found as 75 MPa and 53.5 MPa, respectively, which are about 10% of the yield strength of the steel. From the observed results, it can be concluded that the yielding in steel has not been achieved and the equations of plane stress condition are valid for this type of experiments and can be used to calculate the stress value in different directions in the lid.

Figure 5-31 shows the calculated stresses. The measurements at different locations along the liner height on the impact side shows that yielding occurred in all the specimens.

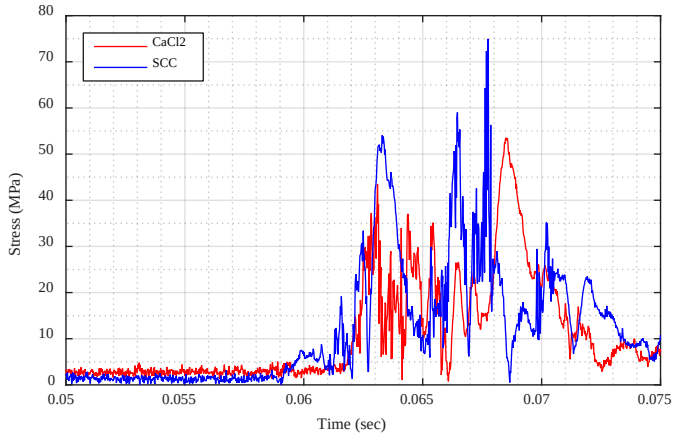

Figure 5-30 von Misses stress on lid center.

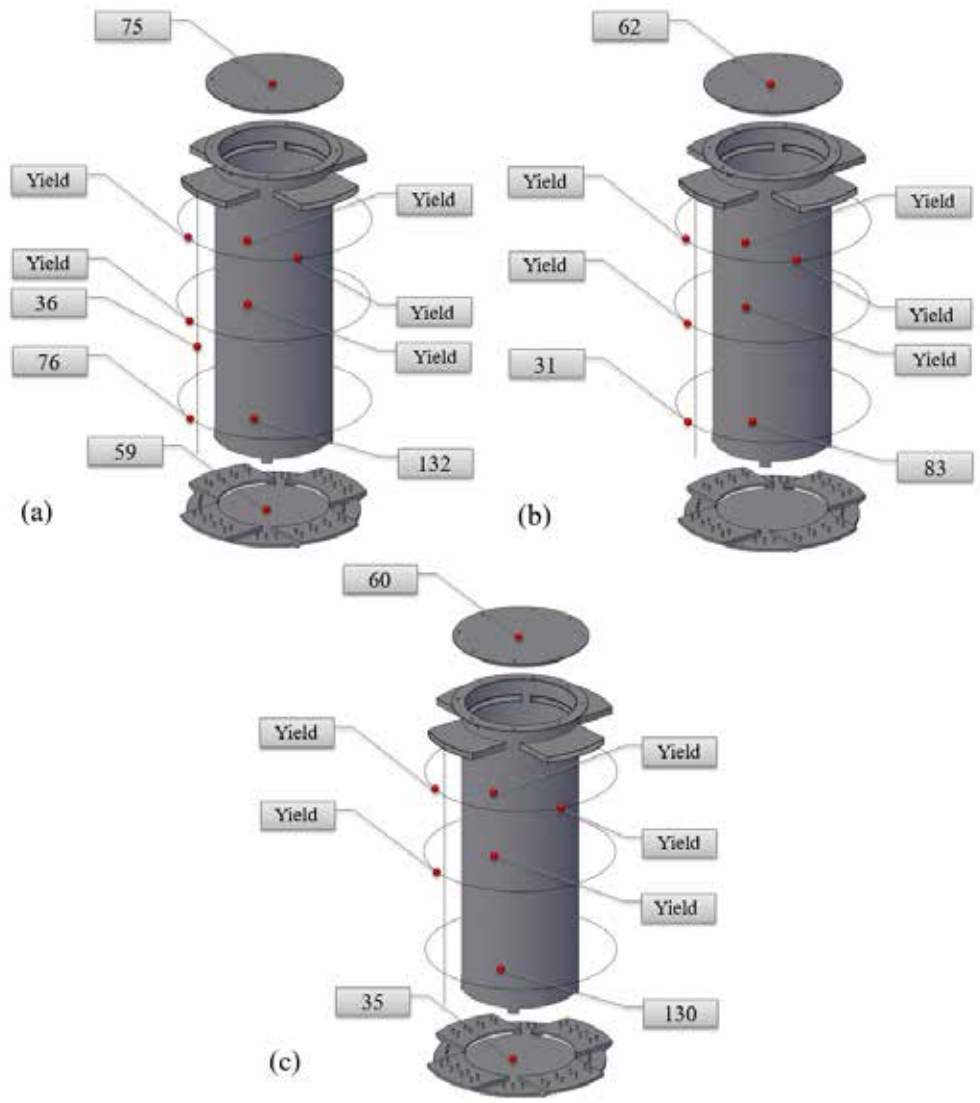

Figure 5-31 Measured stresses (a) SCC (b) $CaCl_2$ (C) NaOH (all units are in MPa)

The embedded concrete gages were also recorded for the three specimens. Due to the permanent damage and plastic deformation, only the results from the first test for each specimen was available. The recorded strains for three specimens are provided in Figure 5-32.

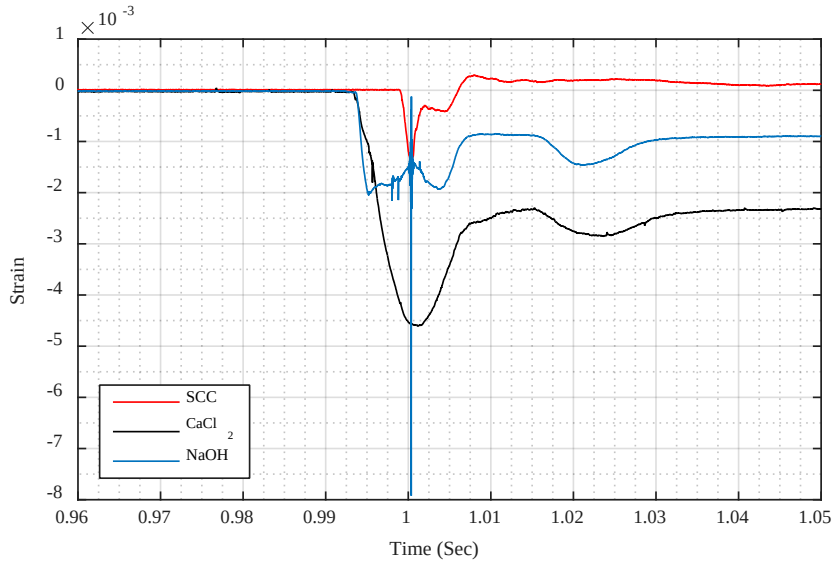

Figure 5-32 Recorded strains from concrete embedded gages (test 1).

5.4.2.d. Damage evaluation

Pre-existing damage of $CaCl_2$ cask due to corrosion

As presented previously, extensive cracking was observed on the surface of the aged cask after two years of accelerated aging (see Figure 5-33). The first crack was observed approximately after 120 days after casting. The crack pattern is influenced by cover thickness and steel bar position (Cabrera, 1996). On the surface of the cask, the cracks were mostly formed in the same direction with the circumferential and longitudinal reinforcement. Prior to impact testing, the crack width varied from 0.1 mm to 1.0 mm and the average was 0.33 mm. Note that according to ACI the recommended maximum crack width in seawater exposure condition is 0.15 mm (ACI, 2003). The crack width measured and recorded on the predefined points throughout the aging process using a 10X gaged magnifier. The half-cell potential measurement was also performed on the entire surface of the cask in accordance with ASTM C876 (2015) prior to the test. Comparing the average value of -500mV/CSE with the threshold value of -350 mV/CSE, indicates the probability of corrosion was more than 90%.

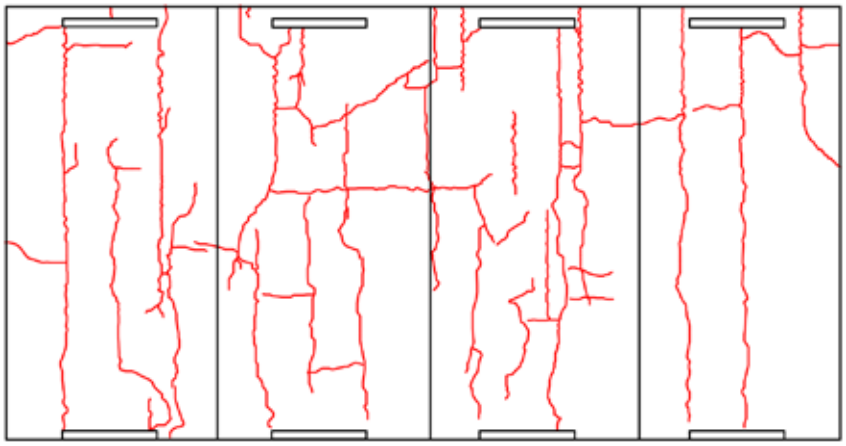

Figure 5-33 Crack pattern due to corrosion prior to impact testing.

Visual damage

A high-speed camera was used to record the impact in most of the tests. The frame captures from the high-speed camera are presented in Figure 5-34 to Figure 5-38. As shown in the figures, local fracture and damage occurred on the impact side as well as inclined cracking.

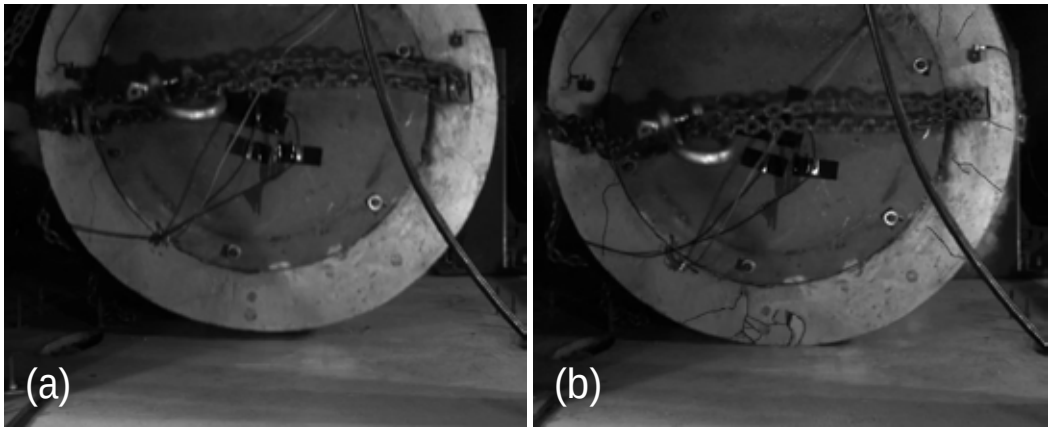

Figure 5-34 Cask condition (a) before and (b) after the impact (SCC, Test 2).

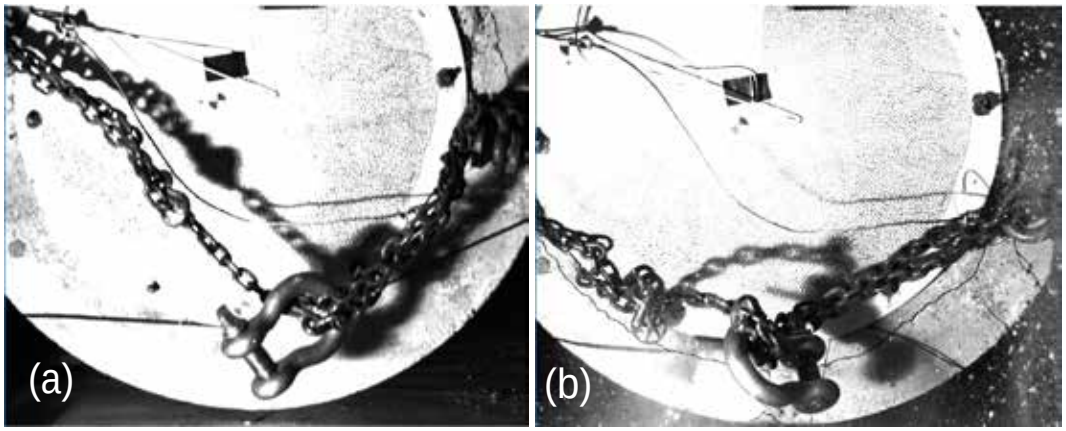

Figure 5-35 Cask condition (a) before and (b) after the impact ($CaCl_2$, Test 3).

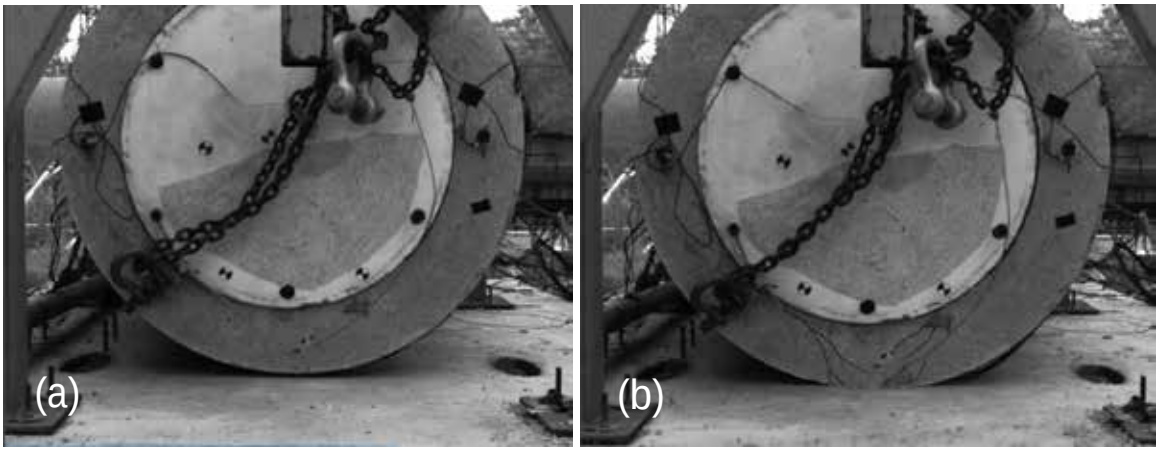

Figure 5-36 Cask condition (a) before and (b) after the impact (NaOH, Test 1).

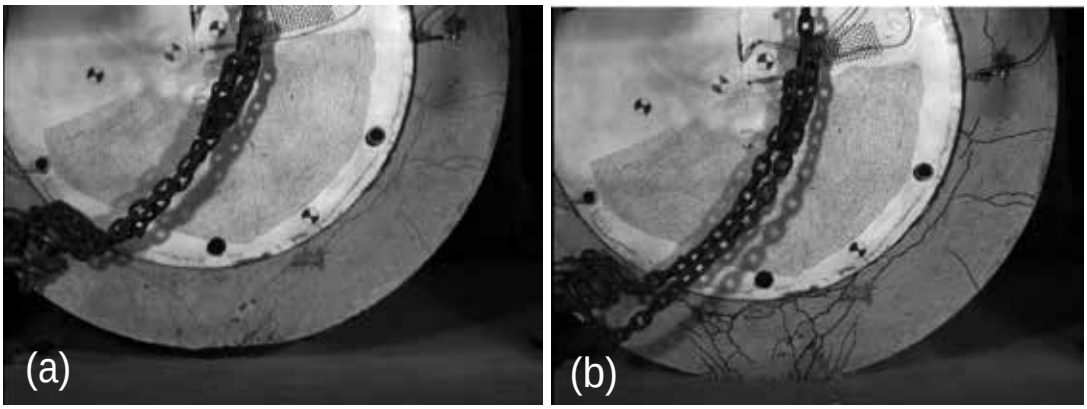

Figure 5-37 Cask condition (a) before and (b) after the impact (NaOH, Test 2).

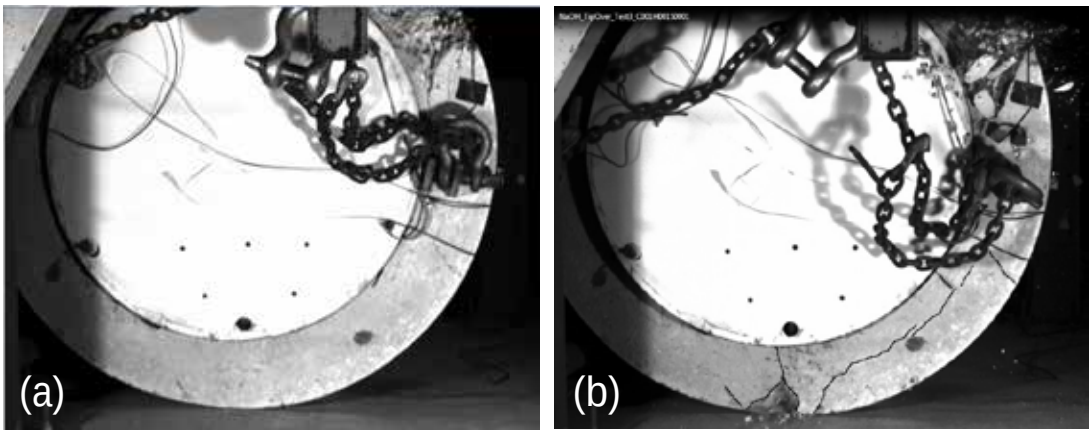

Figure 5-38 Cask condition (a) before and (b) after the impact (NaOH, Test 3).

The typical patterns of the cracks on the concrete surface including radial and inclined type are provided in Figure 5-39 and Figure 5-40.

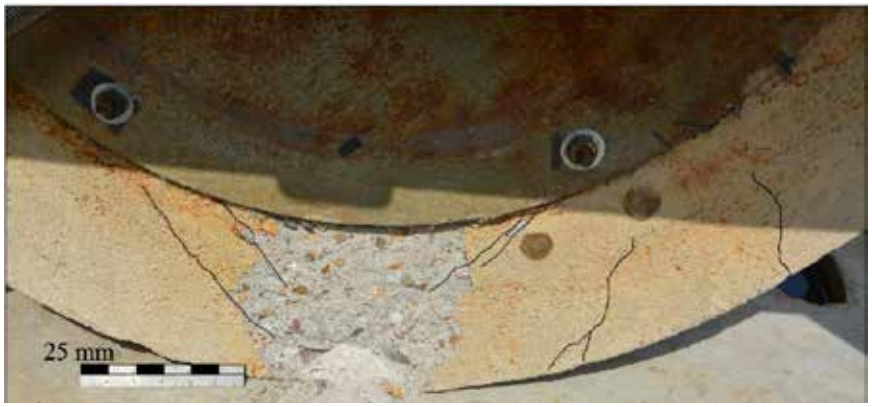

Figure 5-39 Radial cracks on concrete formed on top (SCC, test 1).

Figure 5-40 Inclined cracks formed on surface of the SCC cask after the first tip-over test.

A maximum crack width of 0.9 mm was observed for the control cask (SCC) while the maximum crack width for the aged cask was 2.65 mm ($CaCl_2$). In order to evaluate the level of damage, the cracks were marked and recorded after each test. Severe damage and spalling were observed in the aged cask as shown in Figure 5-41. In addition to inclined shear and radial cracks for the $CaCl_2$ cask, the third mode of observed damage is the spalling of the top part. Due to the impact force the concrete cover on the top cracked and a large portion of concrete on the top fell off. In addition, the steel rods simulating the weight of the nuclear fuel hit the lid from the inside and caused failure of the anchorage bolts during the third test. The lid was fixed in place using eight high strength bolts that were inserted into drilled holes in the concrete on top of the cask with high strength expansive cement. In the control cask, the anchors sustained the impact loads and the lid remained fixed in the place. However in the $CaCl_2$ specimen, due to loss of bond between the anchorage and concrete because of corrosion, six of eight anchors failed as shown in Figure 5-41(a). It is recommended to study this mode of failure in the future modeling and experimental studies. Figure 5-42 through Figure 5-44 provide additional information on the condition of the casks.

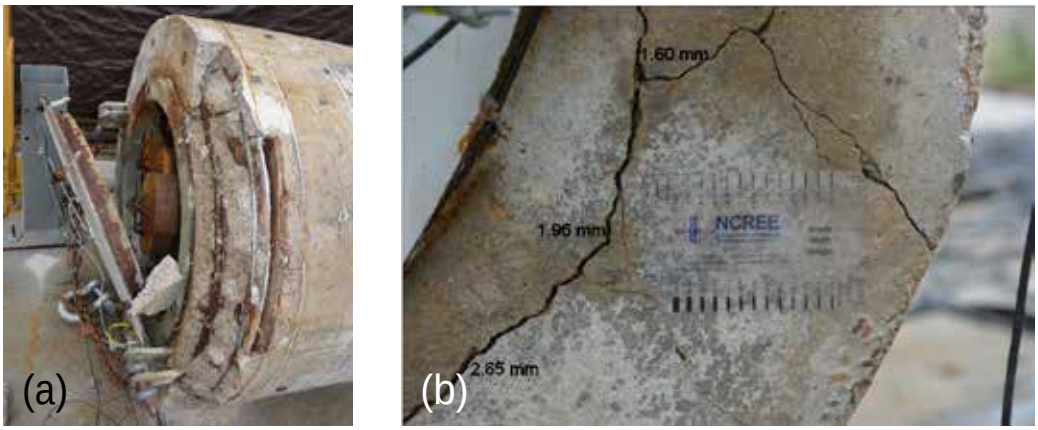

Figure 5-41 Cracks and concrete spalling of the $CaCl_2$ cask.

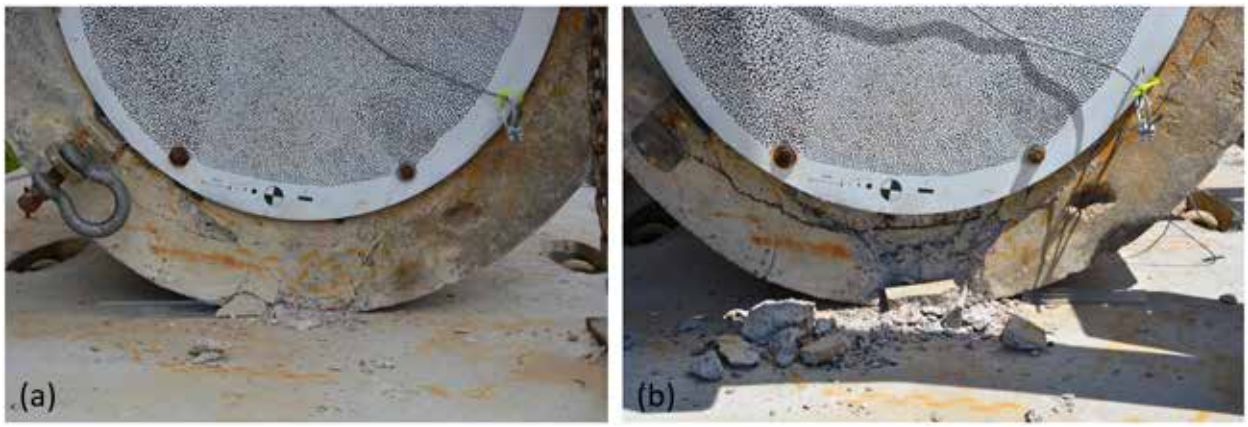

Figure 5-42 Top cracking damage of $CaCl_2$ cask after (a) Test 1 and (b) Test 2.

Figure 5-43 Cracks and concrete spalling of the $CaCl_2$ cask (a) after the test (b) impact moment ($CaCl_2$, Test 3).

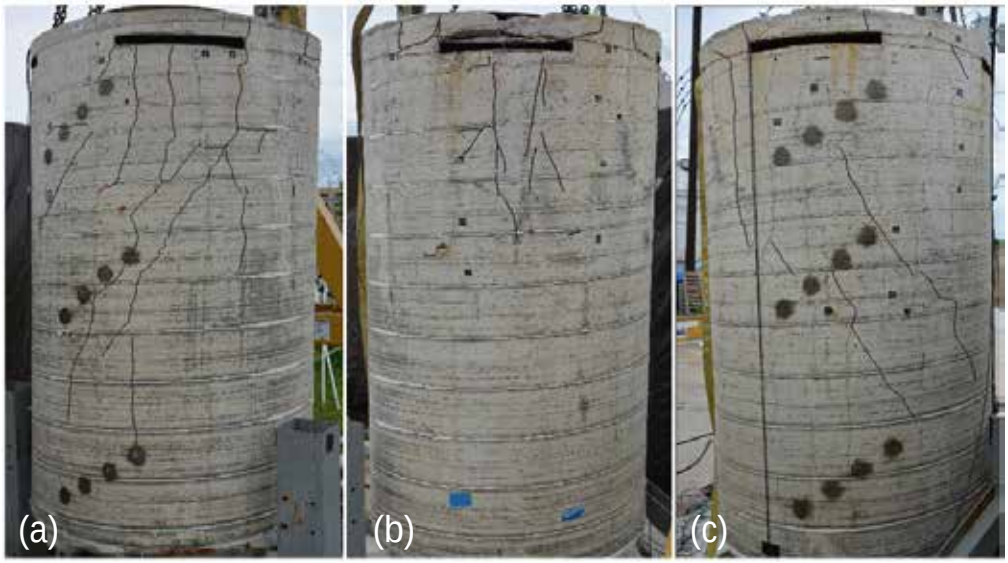

Figure 5-44 Crack patterns on the $CaCl_2$ cask (a-c) pictures from three different sides.

In order to evaluate the level of damage, the cracks were marked and recorded after each test. Crack patterns were mapped manually from photos for each specimen after the first tip over test as presented in Figure 5-45.

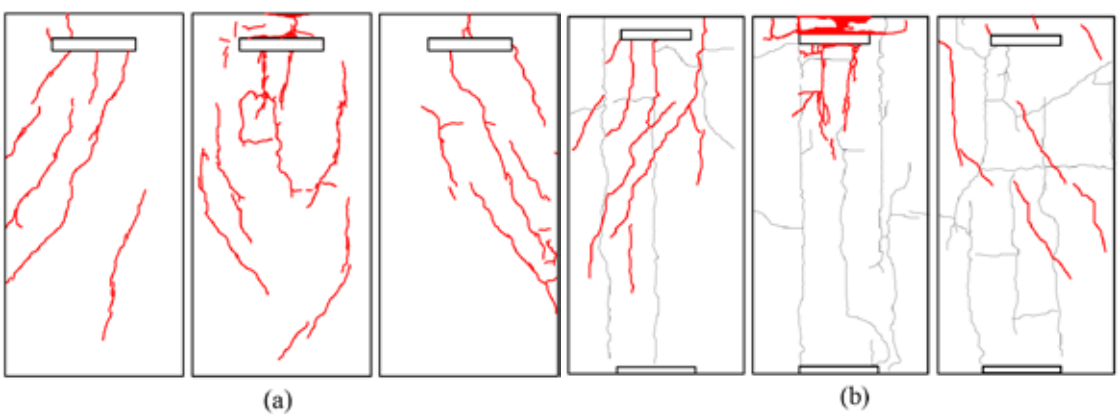

Figure 5-45 Residual crack patterns due to tip over on the (a) SCC (b) $CaCl_2$ cask.

5.4.3. Analytical Results and Comparisons with Experimental Data

The center of gravity is approximately located at the mid-height of the model (see Figure 5-46). The mass of the specimen is 7900 kg and the mass moment of inertia with respect to an axis passing through pivot of the cylindrical shape is given by

$$I = \frac{mr^2}{4} + \frac{mh^2}{12} \qquad 5.9$$

where, m is the mass of the cask, r is the cask radius and h is the cask height. The calculated moment of inertia in the above equation is around the axis passing through the middle of the

cask. By using the parallel axis theorem, the moment of inertia about the pivot (the base of the casks), is calculated as:

$$I_{pivot} = I + mR^2 \qquad 5.10$$

where R is the distance between the parallel axes. Angular velocity of the cask right before impact is then calculated as:

$$mg\Delta h = \frac{1}{2} I_{pivot} w^2 \qquad 5.11$$

Using Eqs. 5.3 and 5.5 we have

$$w = \sqrt{\frac{2mg\Delta h}{I_{pivot}}} = \sqrt{\frac{2g\Delta h}{\frac{r^2}{4} + \frac{h^2}{12} + R^2}} = 2.398 \ rad/\sec \qquad 5.12$$

where, g is the gravitational acceleration and Δh is the displacement of the cask center of gravity from tilted to impact position. Note that according to the equations above, the angular velocity is independent of the weight. The vertical velocity *v* along a line passing through the center line of the cask is calculated as $v=r\times\omega\times\cos(\theta)$, where *r* is the distance from the pivot point (see Figure 5-46).

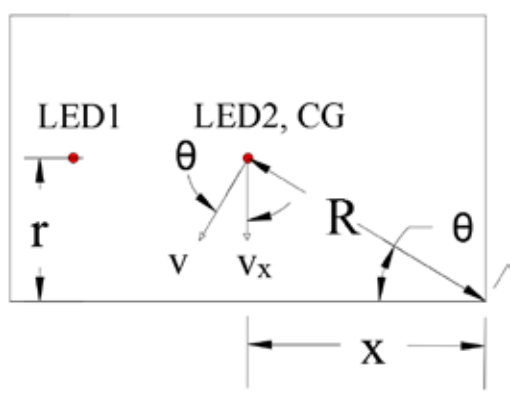

Figure 5-46 Geometry of the cask (CG is center of gravity).

Considering $\cos\theta=x/r$, the vertical velocity along the center line of the cask is $v=\omega \times x$. Using Eq. 5.12, the vertical velocities of the cask at the location of LED1 and LED2 are estimated to be 4474 mm/sec and 2551 mm/sec, respectively. The measured velocity was found comparable with the non-contact measurement as shown in Table 5-3 with a better match at the center of gravity of the cask.

Table 5-3 Comparison of the Measured and Calculated Velocity (Test 1).

Velocity (mm/sec)	SCC	$CaCl_2$	Analytical solution
LED1	4153	4082	4268
LED2, CG	2276	2232	2434

The cask is stable up 32 degrees of rotation from vertical position after which the tip-over event initiates under zero initial angular velocity (see Figure 5-47).

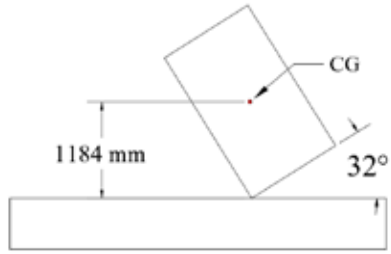

Figure 5-47 Ultimate stable condition.

In this situation, the CG is 1184 mm higher compared to the regular standing position of the cask. Therefore, the required energy (*W*) for tilting the cask up to this tipping-over point is

$$W = mg\Delta h = 7900 \times 9.81 \times (1.184 - 1.030) = 11935 \text{ kJ} \qquad 5.13$$

where *m* is the weight of the loaded cask, *g* is the gravitational constant and *Δh* is the vertical displacement of center of gravity (see Figure 5-48). This value is useful to evaluate the possibility of tip-over due to impact of a projectile with known weight and velocity. Hence, the minimum initial angular velocity to induce a tip-over event is

$$w = \sqrt{\frac{2g\Delta h}{\frac{r^2}{4} + \frac{h^2}{12} + R^2}} = 1.19 \text{ rad/sec} \qquad 5.14$$

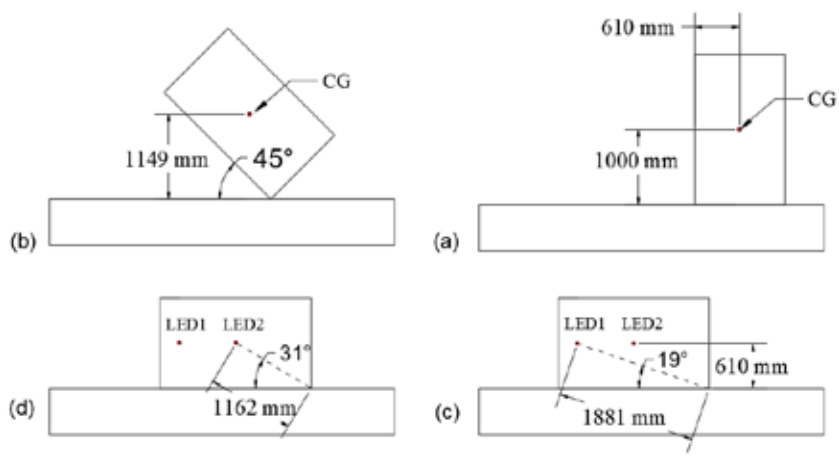

Figure 5-48 Center of the gravity in various positions (a) standing (b) initial (c) and (d) final.

5.5. SERVICE-LIFE PREDICTION

ASTM E632-82 (1996) defines the service life of the structure as the period of the time after installation during which all properties exceed the minimum acceptable values when routinely maintained. To be able to predict the service life, certain information from the actual structure

is needed, such as the initial and exposure conditions. Here corrosion is considered as the main effect. By the time the earliest visible signs of corrosion become apparent on the concrete, the structure may be severely damaged; therefore, it is important to be able to predict the service life of concrete structures susceptible to corrosion. Predicting the service life of a reinforced concrete structure is a complex task because of the large influence of the environmental conditions and concrete properties. Furthermore, the tolerated extent of damage may vary with the intended use of the structure and can affect the service life prediction (Lopez, Gonzalez, and Andrade 1993). There are different methods to predict the service life such as the time crack appears on the surface and using time shift method. The latter is mostly used to predict the age of concrete when changes in the concrete changes the degree of hydration over a time and is mostly used to predict the creep over time. Therefore, first method was chosen for this study. It should be noted that in the modeling procedures, there is always some limitation with regard to the complexity of the reaction, as the models do not consider all relevant factors. For these reasons, it is customary to make various assumptions and rely on empirical formulations.

To correlate the rate of deterioration and service life of the structure under accelerated conditions and compare to the real field conditions, the environmental exposure should be considered. Based on the location, the environmental parameters that affect the speed of this process vary substantially. For this study, three locations around the United States are considered: Seabrook Station in New Hampshire, St. Lucie Power Plant in Florida, and Rancho Seco Nuclear Generating Station in California. These locations were chosen based on the locations of the existing nuclear power plants (NPP) accommodating concrete dry cask storage and the amount of chloride ion deposition in that area. Since most of the independent spent fuel storage installations (ISFSIs) are located near a marine setting, most of the salts and chloride ions in dust and aerosols originate from sea water (Enos, Bryan, and Norman 2013). Figure 5-43 shows the three chosen locations in addition to the chloride ion concentration in different areas of the US as taken from the National Atmospheric Deposition Program/National Trends Network (NADP 2016).

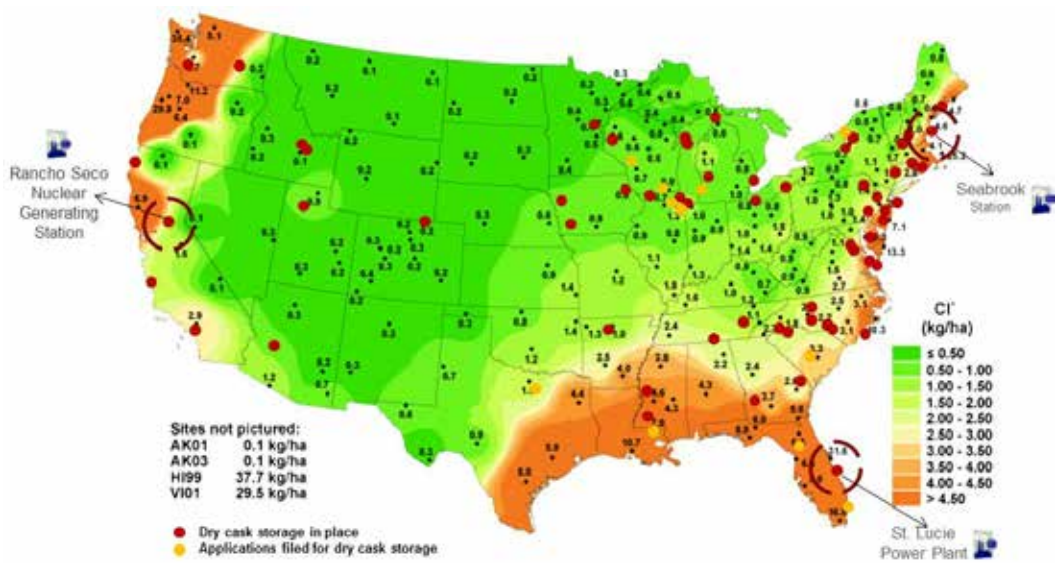

Figure 5-49 Location of the chosen dry cask sites (NAPD, 2016).

As was summarized in Table 4-10, the highest temperature in concrete close to the fuel basket was found to be equal to 154 °C and on the surface to be equal to 65°C. However, under normal conditions this temperature is lower and considering that the temperature of the fuel basket decreases over the years, the temperature of the concrete was assumed to be 60°C on the inside surface. Furthermore, since the basket located inside the dry cask is the source of heat and the temperature is higher than the ambient temperature, it is considered that the temperature on the inside surface in all three locations is the same regardless of the physical location of the dry cask.

The chloride concentration on the surface of casks in these locations was chosen based on extrapolation of the results taken from Shill (2014) and based on the average of chloride ion amounts in these locations. Shill (2014) measured the chloride concentration on the surface of concrete specimens placed close to Dania Beach, FL, for over a year; these results are shown in Table 5-4. The chloride concentration on the surface of the casks in each station was estimated by extrapolating these data based on chloride ion concentration at Dania Beach. Based on a proportional scaling using the data in Figure 5-49, and each of these three stations; the results shown in Figure 5-50 were found. A linear relationship between the chloride concentration and time was assumed.

Table 5-4 Chloride Concentration at Surface of Specimens Close to Dania Beach, FL (Shill, 2014).

C_s (% weight of cement)				
Time	6 months	10 months	18 months	24 months
Spec01	0.679%	1.752%	0.996%	1.233%
Spec02	1.005%	0.909%	1.483%	1.233%
Spec03	0.574%	0.606%	0.782%	0.939%
Spec04	1.199%	0.545%	1.139%	1.087%
Spec05	0.863%	0.684%	0.848%	1.188%
Spec06	0.714%	0.643%	0.863%	1.509%
Spec07	0.762%	0.534%	0.493%	0.819%
Avg.	0.828%	0.810%	0.943%	1.144%

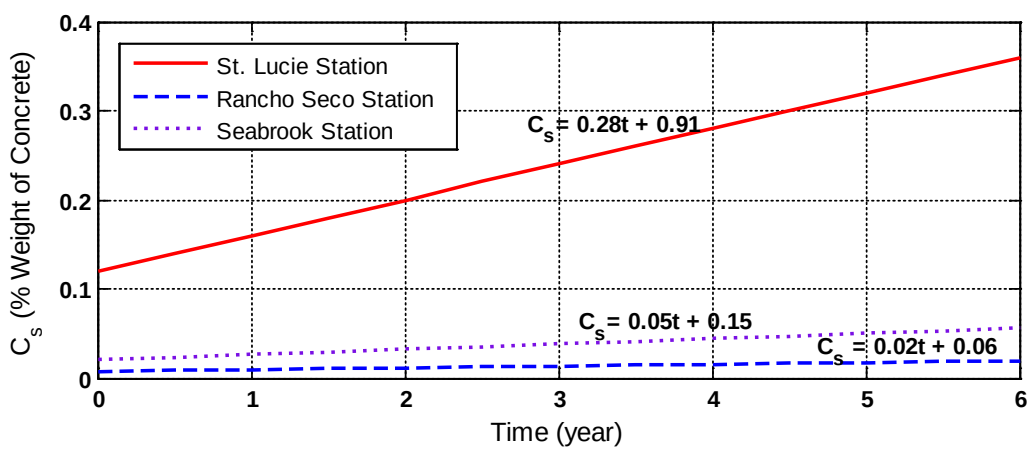

Figure 5-50 Assumed chloride concentration on the surface of DCSS.

With these data, corrosion initiation can be found by solving the one dimensional equation for Fick's second law of diffusion. It should be noted that the length of this stage may vary greatly from one reinforced concrete to another, depending on many factors such as thickness of the concrete cover, the permeability of concrete, and the environmental conditions. In general this stage is the longest stage during the life span of concrete structures (Suwito and Xi 2003).

$$\frac{\P C}{\P t} = D_e(\frac{\P^2 C}{\P x^2}) \qquad 5.15$$

where C is chloride ion concentration, t is time and D_e is the diffusion coefficient. In this model, the diffusion coefficient was considered constant. The well-known analytical solution for this equation is

$$C(x,t) = C_i + (C_s - C_i) erf(\frac{x}{\sqrt{4tD_e}}) \qquad 5.16$$

Where, $C(x,t)$ is the chloride concentration inside the concrete (mass %), C_s is the surface chloride concentration (mass %), C_i is the initial chloride concentration measured on the concrete (mass %), x is the depth below the exposed surface (m), D_e is the effective chloride transport coefficient (m^2/sec), t is the exposure time (sec) and *erf* is the error function. Based on this equation the corrosion initiation time can be estimated as follows:

$$T_i = \frac{x_{cr}^2}{4D_e}[erf^{-1}(\frac{C_s - C_{cr}}{C_s - C_i})]^{-2} \qquad 5.17$$

where, x_{cr} is concrete cover depth, D_e is the effective chloride transport coefficient (m^2/sec), C_s is the surface chloride concentration (mass %), C_i is the initial chloride concentration measured on the concrete (mass %), and C_{cr} is the threshold chloride content. In this model, the chloride content of the exposed concrete surface is constant.

Table 5-5 summarizes the values assigned to the parameters used in this calculation. The concrete cover was considered to be equal to 38.1 mm, similar to the scaled cask concrete cover. The effective chloride transport coefficient used in this equation was equal to the average of measured values for SCC specimens in the first phase of the project (see Section 3.3.2) and equal to 1.048e-11 m^2/sec. Initial chloride content was considered similar to the value of SCC mixture prepared in first phase and equal to 0.0143% weight of concrete. Critical chloride concentration was chosen based on the value presented in the previous study of DuraCrete (1998). The results of calculations are presented in Table 5-6. The high chloride concentration at the St. Lucie station area, which led to the highest value of chloride concentration on the surface of the cask in this region, led to having the shortest time span compared to the other two locations for initiation of corrosion. The low chloride concentration also leads to the longest time period for corrosion initiation in the cask located in the Rancho Seco station area.

Table 5-5 Assumed Parameter for Corrosion Initiation Measurement.

Parameter	Value
x_{cr}: Concrete cover (mm)	38.1
D_i: Diameter of steel bar (mm)	9.5
D_e: Diffusion coefficient (m^2/sec)	1.048e-11
C_{cr}: Critical chloride concentration (% weight of concrete)	0.1
C_i: Initial chloride content (% weight of concrete)	0.0143

Table 5-6 Corrosion Initiation Time at Different Locations.

Station	Corrosion Initiation Time (years)
St. Lucie	2.92
Rancho Seco	56.60
Seabrook	18.59

After corrosion initiation, it will only take a few years until the concrete starts to crack and reach the end of its service life. To estimate this time, different studies developed mathematical models. Beaton and Stratfull (1963) proposed an empirical model which later became the Stratfull formula

$$T_{cr} = 1011' \frac{10^{0.0442C_0} C_0^{0.717} C^{1.22}}{K_0^{0.42} W_m^{1.17}} \qquad 5.18$$

where, T_{cr} is years to cracking of concrete, C_0 is sacks of cement per cubic yard of concrete, C is concrete cover (in), K_0 is the chloride concentration of water (ppm),and W_m is the mixing water in percent of concrete volume. Later, Clear and Hay (1976), modified the Stratfull formula to

$$T_{cr} = \frac{129C^{1.22}}{K_0^{0.42} P} \qquad 5.19$$

where C is concrete cover (in), K_0 is the chloride concentration of water (ppm), and P is the water-cement ratio. The formula can also be rewritten as (Purvis et al. 1994)

$$T_{cr} = \left[\frac{2.695C^{1.22}t^{0.21}}{C_s^{0.42} P}\right]^{\frac{1}{1.21}} \qquad 5.20$$

where C is concrete cover (in), C_s is the surface chloride concentration (mass %), t is the time at which C_s was measured, and P is the water-cement ratio. Another empirical model was later proposed by Morinaga (1990) with the assumption that cracking of concrete happens when corrosion products on reinforcing steel reach to a certain level. The amount is divided by the instantaneous corrosion rate to get the time for cracking as

$$T_{cr} = \frac{0.602(1+\frac{2C}{D_i})^{0.85} D_i}{J_r} \qquad 5.21$$

$$J_r = (\frac{W}{F}) i_{corr} \qquad 5.22$$

where, D_i is the diameter of steel bar (mm), C is the thickness of concrete cover (mm), i_{corr} is the corrosion current density (μA/cm^2), J_r is the instantaneous corrosion rate, W=27.925 g, and F is Faraday's constant (96487 Coulombs/mol).

The empirical models presented above do not account for the mechanical properties of concrete which have significant effects on the time to corrosion cracking. Later, other researchers worked on mathematical models to account for more parameters. Some of these studies are discussed below.

Bažant (1979) proposed a physics-based model for prediction of corrosion of steel and time to corrosion cracking of concrete cover for marine structures. In this model, the basic assumption is that the oxygen and chloride ion transports through concrete occur in one dimension and are quasi-stationary. Additionally, in this model, the volume expansion due to hydrated red rust, ($Fe(OH)_3$), was introduced as a prescribed displacement at the surface of the bars. This process causes an increase in the diameter of the bars and applies stresses to the cover which lead to cracking. By combining all these assumptions, the time to cracking of concrete can estimated from

$$r_r = \frac{r_{st}}{4} \qquad 5.23$$

$$r_{cor} = \frac{p}{2}[(\frac{1}{r_r}) - (\frac{0.583}{r_{st}})]^{-1} \qquad 5.24$$

$$d_{pp} = [\frac{D_i(1+j_c)}{E_c}]\left\{(1+v_c) + d^2[\frac{2}{S^2} + \frac{1}{4C(1+D_i)}]\right\} \qquad 5.25$$

$$\Delta D = 2 f_t \frac{C}{D_i} d_{pp} \qquad 5.26$$

$$T_{cr} = r_{cor} \frac{D_i \Delta D}{S J_r} \qquad 5.27$$

where ρ_r is the mass density of $Fe(OH)_3$, ρ_{st} is the mass density of steel, φ_c is the creep coefficient (typically about 2.0), E_c is the elastic modulus of concrete, υ_c is the Poisson ratio of concrete, C is the thickness of concrete cover (mm), f_t is the tensile strength of concrete, D_i is the diameter of steel bar (mm), and S is the bar spacing. The critical value of ΔD here was brought for inclined cracks emanating from a single bar and for the conditions where the rebar spacing is

less than $6D_i$. This model relates the time of cracking to corrosion rate, cover depth, spacing, and some properties of concrete such as tensile strength, Poisson's ratio, elastic modulus and creep coefficient.

Liu (1996) proposed a simplified methodology for characterizing the dynamic corrosion process based on the chloride content, temperature, resistance of concrete, and corrosion time after initiation. In this model, three stages were considered: free expansion, stress initiation and cracking. Free expansion is related to the porous zone around the steel/concrete interface, which gradually gets filled with the corrosion products. The next stage is after the porous zone gets filled and corrosion products start to apply expansive pressure, and when this pressure exceeds the tensile strain of concrete, the crack initiates. The critical amount of rust and the time of cracking are defined as follows:

$$R_i = \frac{D_i + 2d_0}{2}, \qquad R_0 = C + \frac{D_i + 2d_0}{2} \tag{5.28}$$

$$W_{st} = \alpha \times W_{crit} \tag{5.29}$$

$$K_p = 2.59 \times 10^{-6} \left(\frac{1}{\alpha}\right) \rho D_i i_{corr} \tag{5.30}$$

$$E_{ef} = \frac{E_c}{1+\varphi_c} \tag{5.31}$$

$$W_{crit} = \rho_{rust} \left\{ \rho \left[\frac{Cf_t}{E_{cf}} \left(\frac{R_i^2 + R_0^2}{R_0^2 - R_i^2} + \nu_c \right) + d_0 \right] D_i + \frac{W_{st}}{\rho_{st}} \right\} \tag{5.32}$$

$$T_{cr} = \frac{W_{crit}^2}{2k_p} \tag{5.33}$$

where D_i is the diameter of the steel bar (mm), C is the thickness of concrete cover (mm), ρ_{rust} is the mass density of rust, d_0 is the thickness of the porous zone, W_{st} is the mass of corroded steel, α is the molecular weight of steel or corrosion products, φ_c is the creep coefficient (typically about 2.0), E_c is the elastic modulus of concrete, ρ_{rust} is the mass density of rust, and f_t is the tensile strength of steel.

Bhargava et al (2006) in their analytical model followed similar assumptions to Bažant and Liu. The solutions presented considering a simple two-zone model for the cover concrete, cracked and uncracked zone. The time until cracking can be found from the following equations when R_c is equal to R_0,

$$u_c = d_c \left\{ \frac{E_{ef1}[(1-\nu_{c2})R_c^2 + (1+\nu_{c2})R_0^2](2R_iR_c)}{E_{ef1}[(1-\nu_{c2})R_c^2 + (1+\nu_{c2})R_0^2][(1+\nu_{c1})R_c^2 + (1-\nu_{c2})R_i^2] - E_{ef2}(R_c^2 - R_0^2)(1-\nu_{c1}^2)} \right\} \tag{5.34}$$

$$R_c = \sqrt{\frac{1}{\frac{f_t(1+v_{c2})}{E_{ef2}[\frac{(1+v_{c2})u_c R_c R_0^2}{(1+v_{c2})R_0^2+(1-v_{c2})R_c^2}]} - \frac{1}{R_0^2}}} \quad 5.35$$

$$r_{rust} = \frac{r_{st}}{aa_1} \quad 5.36$$

$$D_2 = \frac{2(R_i + d_c)}{1 - \frac{d_c}{R_i}[\frac{E_{ef1}(1-v_s)}{E_s(\frac{R_0^2+R_i^2}{R_0^2+R_i^2}+v_{c1})}]} \quad 5.37$$

$$a_1 = 10.60138 - 12.67876a + 1.50424a^2 \quad 5.38$$

$$W_r = \frac{p}{4} r_{rust} a_1 (\frac{D_2^2 - D_i^3}{a_1 - 1}) \quad 5.39$$

$$k_p = A_p p D_i i_{corr} \quad 5.40$$

$$T_{cr} = \frac{W_r^2}{2k_p} \quad 5.41$$

where, R_c is the radius of the crack front, R_0 is the outer radius of a thick concrete cylinder, u_c is the radial displacement at R_c, v_c is the Poisson ratio of concrete, D_i is the diameter of the steel bar (mm), E_{ef} is the effective modulus of elasticity of concrete, C is the thickness of concrete cover (mm), d_0 is the thickness of the porous zone, W_{st} is the mass of corroded steel, α is the molecular weight of steel or corrosion products, φ_c is the creep coefficient (typically about 2.0), E_c is the elastic modulus of concrete, ρ_{rust} is the mass density of rust, f_t is the tensile strength of steel, E_s is the Young modulus of steel, α_1 is the volume expansion ratio for the expansive corrosion products, i_{corr} is the annual mean corrosion rate and A_p is a constant.

Maaddawy (2007) presented a mathematical model to predict the time from corrosion to cracking. The concrete ring is assumed to crack when the tensile stresses in the circumferential direction at every part of the ring have reached the tensile strength of concrete. The time of cracking can be found from the following equation:

$$D' = D + 2d_0 \quad 5.42$$

$$y = \frac{D'^2}{2C}(C + D') \quad 5.43$$

$$T_{cr} = [\frac{7117.5(D+2d_0)(1+v_c+y)}{iE_{ef}}][\frac{2cf_{ct}}{D} - \frac{2d_0E_{ef}}{(1+v_c+y)(D+2d_0)}] \quad 5.44$$

where D_i is the diameter of steel bar (mm), d_0 is the thickness of porous zone, C is the thickness of concrete cover (mm), v_c is the Poisson ratio of concrete, E_{ef} is the effective modulus of elasticity of concrete, i is the current density, f_{ct} is the tensile strength of concrete, ψ is a factor that depends on D_i, C and d_0. The parameters needed for estimating the concrete cover cracking using equations presented above is shown in Table 5-7. These parameters were chosen based on parameters measured in this study such as concrete cover, diameter of steel bar, modulus of elasticity of concrete, compressive and tensile strength of concrete, water-cement ratio as well as bar spacing in the casks. The time from corrosion to concrete cover cracking estimated using the equations presented above and the results are shown in Table 5 9.

Table 5-7 Assumed Parameter for Concrete Cover Cracking Measurement.

Parameter	Value
C: Concrete cover (mm)	38.1
D_i: Diameter of steel bar (mm)	9.5
d_0: Porous zone around the steel-concrete interface (mm)	1.048e-11
φ_c: creep coefficient	0.2
E_c: Elastic modulus of concrete (MPa)	23503.39
E_s: Young modulus of steel (MPa)	210000
v_c: Poisson ratio of concrete	0.29
v_s: Poisson ratio of steel	0.3
f_c: Compressive strength of concrete (MPa)	40.42
f_t: Tensile strength of concrete (MPa)	4.38
S: Bar spacing (mm)	106
ρ_{st}: Mass density of steel (kg/m^3)	7850
α is the molecular weight corrosion products	Between 0.523 and 0.622; here 0.5725
α_1: Volume expansion ratio	0.3
R_c: Resistivity of Concrete (Ohm)	1450
w/c: water cement ratio	0.5
T: Temperature on steel (˚K)	331
t: Time when chloride concentration measured (years)	1

Table 5-8 Time from Corrosion to Concrete Cover Cracking at Different Locations.

	Time from Corrosion to Concrete Cover Cracking (years)		
Model	St. Lucie	Rancho Seco	Seabrook
Beaton and Stratfull (1963)	1.41	3.60	2.62
Clear and Hay (1976)	1.51	4.71	3.20
Morinaga (1990)	0.05	0.28	0.23
Bazant (1979)	0.03	0.14	0.11
Liu (1996)	2.83	15.20	12.65
Bhargva et al (2006)	2.20	11.78	9.80
Maaddawy (2007)	6.19	33.19	27.63

The results show the wide range of estimation for different locations. The differences in the results of each model are due to the different parameters considered in the modeling. The empirical modeling of Beaton and Straful (1963), Clear and Hay (1976) and Morinaga (1990) were based on limited test data and do not consider all the parameters. In mathematical modeling it is true that all of the models presented here used elastic mechanics and a thick walled cylinder model; however, only one model, Bhargava (2006), considers the rust, and the models have other differences in their assumptions and modeling, which results in different estimated values. However, similar to corrosion initiation, the specimens located in the St. Lucie station showed a shorter time span until the concrete cover cracking and Rancho Seco Station showed the highest interval. Among the seven presented models, the results of two models, Liu (1996) and Bhargva et al. (2006), were close to each other. The time averages of these models were chosen as the time from corrosion to concrete cover cracking at these three stations as shown in Table 5-9.

Table 5-9 Average Time from Corrosion to Concrete Cover Cracking at Different Locations.

Station	Time from Corrosion to Concrete Cover Cracking (years)
St. Lucie	2.52
Rancho Seco	13.49
Seabrook	11.22

Service life of a structure is defined from the time it was built until concrete cover cracks, meaning that it is the summation of corrosion initiation time and time from corrosion to concrete cover cracking. The range of service life of the cask can be estimated as shown in Table 5-10. Considering cracks were observed on the corrosion accelerated cask at 4 months (0.33 year), the acceleration factor compared to real life can be estimated as shown in Table 5-10. Having a high percentage of chloride on the surface of the structure in the St. Lucie station as well as having only 38.1 mm of concrete cover led to the very short life span for the cask located in this area. The acceleration factor in each station compared to the corrosion accelerated cask is 16.5, 213.4, and 90.3 years for St. Luce, Rancho Seco, and Seabrook station, respectively. It should be noted that the service lives for casks with real dimension are higher, since the concrete cover is 3 times larger, and this delays corrosion initiation time considerably (increases the time by 71%, 24%, 42% for St. Lucie, Rancho Seco and Seabrook station, respectively as shown in Table 5-10).

Table 5-10 Service Life of Casks at Three Locations.

Station	Scaled Casks		Prototype Casks
	Service life (years)	Acceleration factor	Service life (years)
St. Lucie	5.4	16.5	72.3
Rancho Seco	70.1	213.4	294.9
Seabrook	29.8	90.3	195.6

5.6. CONCLUSIONS

Adding NaOH to the concrete mixture, removing any supplementary cementitious materials with ASR suppression characteristic and using reactive fine aggregate effectively accelerated the

corrosion at the structural level and the cracks were observed on the surface of the specimens after 90 days. Although, the crack width remained between 0.1 mm to 1 mm throughout the aging process, the density of cracks increased significantly. Similarly, it was observed that the direct addition of $CaCl_2$ to the concrete accelerated the corrosion process and the half-cell potential measurements clearly showed the difference between corrosion cask, and SCC and NaOH casks as significant differences in the probability of corrosion. Furthermore, corrosion cracks were observed on the surface of the cask after 120 days and both density and width of cracks increased during the aging process.

Nine tip-over tests were performed on the three specimen including two aged specimen affected by ASR and $CaCl_2$ accelerated aging and one control specimen. The dynamic parameters were recorded using contact and non-contact measurement systems. The level of damage and spalling in the $CaCl_2$ cask was the highest specially on the top surface. The impact increased the width of preliminary vertical cracks which happened due to corrosion and also made inclined shear cracks. As discussed earlier major damage was observed after the third test which was due to spalling of the cover on the top. Overall, the damage in the CaCl2 cask seemed to be unrepairable. The level of damage was less in NaOH cask. Inclined cracks formed after the impacts. The cracks width was smaller with higher density in comparison with the $CaCl_2$ cask. The SCC cask experienced the least damage. No major structural damage was observed on the SCC cask even after performing three tests except the inclined cracks on each side. The strain records show yielding in the liner and lid for all three specimens however the damage was not visually noticeable and the canister space was maintained well. Large deformation was observed on the air outlet plates when the specimens hit the pad on the vent side.

Comparing the predicted service life of dry cask storage for three different locations in the United States indicated the strong effect of salt exposure on service life and corrosion initiation. The results indicated that the corrosion in laboratory experiments were accelerated by factor of 16.5, 213.4 and 90.3 for St. Lucie, Rancho Seco, and Seabrook stations, respectively. The predicted lives of the scaled casks varied from 5 years to 70 years while the same for the prototype casks was from 72 years to 295 years.

5.7. REFERENCES

American Concrete Institute. (2003). ACI 224R-01, Control of Cracking of Concrete Structures. Farmington Hills, MI.

ASTM (1996). *Standard Practice for Developing Accelerated Tests to Aid Prediction of the Serice Life of Building Componenets and Materials (Withdrawn 2005),* ASTM E632-82, American Society of Testing and Materials Academic & Science (ASTM), West Conshohocken, PA.

Bažant, Z. P. (1979). "Physical Model for Steel Corrosion in Concrete Sea Structures - Application," Journal of the Structural Division, ASCE, 105(ST6), 1155-1166.

Beaton, J. L. and Stratfull, R. F. (1963). *Environmental Influence on Corrosion of Reinforcing in Concrete Bridge Substructures,* HRR 14 HRB, Concrete Bridge Decks and Pavement Surfaces, Washington, DC.

Bhargava, K., Ghosh, A. K., Mori, Y. and Ramanujam, S. (2006). "Model for Cover Cracking due to Rebar Corrosion in RC Structures," Engineering Structures, 28(8), 1093-1109.

Cabrera, JG. 1996. "Deterioration of concrete due to reinforcement steel corrosion." *Cement and concrete Composites* 18 (1):47-59.

Childress, P., Matheson, J. and McGuinn, E. (1989). *Constar-A Family of Concrete Spent Fuel Dry Storage Casks,* 1.

Clear, K. C. and Hay, R. E. (1976). *Time-to-Corrosion of Reinforcing Steel in Concrete Slabs,* FHWA-RD-76-70, Federal Highway Administration (FHWA), Washington, DC.

COWI, DuraCrete and Brite EuRam III (1998). *Mini-Project Chloride Induced Corrosion: DuraCrete, Performance Based Durability Design of Concrete Structures,* BRPR-CT95-0132, Project BE95-1347, The European Union Brite EuRam III, Gouda, Netherlands.

Enos, D. G., Bryan, C. R. and Norman, K. M. (2013). *Data Report on Corrosion Testing of Stainless Steel SNF Storage Canisters,* FCRD-UFD-2013-000324, SAND2013-8314P, Sandia National Laboratory (SNL), US Department of Energy Used Fuel Disposition Campaign, Albuquerque, NM.

Geokon. "Embeded strain gage manufacturer." Accessed on 26 Dec. 2016. Available from: http://www.geokon.com/Strain-Gages.

HITEC PRODUCTS INC. "Strain Gage Manufacturer." Accessed on 26 Dec. 2016. Available from: http://www.hitecprod.com/.

IStructE (2010). *Addendum*, The Institution of Structural Engineers, London, UK.

Kim, D.-H., Seo, K.-S., Lee, J.-C., Cho, C.-H., Jang, H.-K., & Choi, B.-I. (2006). "A Test for Verifying a Tip-Over Analysis of a Dry Storage Cask". Journal of the Korean Radioactive Waste Society, 4(3):245-253.

Kyowa (2016). Strain Gage Manufacturer, Available from: http://www.kyowa-ei.com/ Accessed on December 21 2016.

Liu, Y. (1996). "Modeling the Time-to-Corrosion Cracking of the Cover Concrete in Chloride Contaminated Reinforced Concrete Structures," Department of Civil Engineering, Virginia Polytechnic Institute and State University, Blacksbourg, VA.

Lopez, W., Gonzalez, J. A. and Andrade, C. (1993). "Influence of Temperature on the Service Life of Rebars," Cement & Concrete Research, 23(5), 1130-1140.

Maaddawy, T. E. and Soudki, K. (2007). "A Model for Prediction of Time from Corrosion Initiation to Corrosion Cracking," Cement & Concrete Composites, 29(3), 168-175.

Morinaga, S. (1990). "Prediction of Service Lives of Reinforced Concrete Buildings Based on the Corrosion rate of Reinforcing Steel." *5th International Conference on Durability of Building Materials and Components*, Nov. 7-9, Brighton, UK, 5-16.

NADP (2016). *Chloride Ion Wet Deposition,* National Atmospheric Deposition Program/National Trends Network (NADP), Available from: http://nadp.sws.uiuc.edu, Accessed on May 15, 2016.

Nikon. Non-Contact Measurement System Manufacturer, Available from: http://www.nikonmetrology.com/en_US/Products/Portable-Measuring/Optical-CMM/K-Series-Optical-CMM Accessed on December 21 2016.

Purvis, R. L., Babaei, K., Clear, K. C. and Markow, M. J. (1994). *Life-Cycle Cost Analysis for Protection and Rehbilitation of Concrete Bridges Relative to Reinforcement Corrosion,* SHRP-S-377, Strategic Highway Research Program (SHRP), Washington, DC.

Shill, S. T. (2014). "Chloride Penetration into Concrete Structures Exposed to the Marine Atmosphere," Engineering and Computer Science, Florida Atlantic University, Boca Raton, FL.

Suwito, A. and Xi, Y. (2003). "Service Life of Reinforced Concrete Structures with Corrosion Damage due to Chloride Attack," in *Life-Cycle Performance of Deteriorating Structures: Assessment, Design, and Management,* eds. Frangopol, D. M., Bruhwiler, E., Faber, M. H. and Adey, B., American Society of Civil Engineers (ASCE), Reston, VA, 207-218.

Vishay Precision Group Inc. "Strain gage and coating manufacturer." Accessed on 26 Dec. 2016. Available from: http://www.vishaypg.com/micro-measurements/.

CHAPTER 6

DURABILITY MODELING AND IMPACT SIMULATION OF CASKS

6.1. INTRODUCTION

The concrete outerpack may degrade due to different reasons including creep, shrinkage and alkali silica reactivity (ASR). The effects of creep and shrinkage were studied using B4 model (RILEM, 2014) for concrete and Norton-Bailey law (Betten, 2008) for metal creep. These rules werer implemented in COMSOL (COMSOL Multiphysics, 2015) which is capable to perform hygro-thermal-chemo-mechanical analysis. Detailed information about managing the effects of ASR can be found in Saouma and Hariri-Ardebili (2014). The first order kinetic approach was used to model ASR in concrete. Additionally, the chemical hydration process was performed by educational FORTRAN codes named "CEMHYD3D" developed by the National Institute of Standards and Technology (NIST). The result of this study was incorporated in the commercial code LS-DYNA version 970 (Hallquist, 2006) to assess the tip-over crash-induced impact of the dry cask structure.

The outline of this chapter is as follows: creep and shrinkage model is explained in Section 6.2. A hygro-thermo model is introduced and implemented for simulation of a dry cask structure in Section 6.3. ASR model is summarized in Section 6.4; and the tip-over scenario for young and aged concrete is investigated in Section 6.5. This chapter concluded with some remarks in Section 6.6.

6.2. CREEP AND SHRINKAGE MODELING OF CASKS

6.2.1. Introduction

At constant temperature, two different phases may cause time-dependent deformations of concrete. One of these phases is independent from loading called shrinkage and the other is a load dependent part, called creep. Shrinkage in concrete is due to the changes of pore water content due to drying and it causes a volume of the concrete. In other words, shrinkage is a change of strain in time due to moisture withdrawal without applying any loads; creep is a change of strain in time due to stress. Shrinkage is generally divided to two parts: autogenous and drying shrinkage. The Japan Concrete Institute, JCI, (Tazawa et al., 1999) defined autogenous shrinkage as "the macroscopic volume reduction of cementitious materials when cement hydrates after initial setting. Autogenous shrinkage does not include the volume change due to loss or ingress of substances, temperature variation, application of an external force and restraint". The autogenous shrinkage is a concern where concrete has a water-to-cement ratio less than 0.42 (Holt, 2001). Drying shrinkage is due to the loss of the water from the concrete pores. As the water evaporates to the outside, concrete shrinks. Drying shrinkage is similar to the autogenous shrinkage where both occur due to loss of water. For drying shrinkage, the water is transferred to the outside, whereas for autogenous shrinkage the water is transferred within the pore structure. It is necessary to distinguish between the components of creep of concrete under conditions of no moisture movement (ambient medium) called basic creep, and the component

caused by the concurrent drying process called drying creep. The idea of drying creep was introduced by Pickett to explain the observed excess of total creep at drying over basic creep. Concrete creep (ε_c) is commonly modeled in terms of a basic creep component (ε_{bc}) which is independent of concrete drying, and a drying creep component: $\varepsilon_c = \varepsilon_{bc}+\varepsilon_{dc}$. The calcium silicate hydrates (C-S-H) are the main cause of the creep in the hardened Portland cement and it happens at all stress levels and when the pore water content is constant, is a linear stress dependent value. Usually researchers use a compliance function $J(t,t`)$ to separate shrinkage from creep. The compliance function is defined as the stress-produced strain caused at time of the measurement by a unit sustained uniaxial stress applied at age $t`$ and is measured as the strain difference between the loaded and load-free specimens, which separates the shrinkage strain from the creep strain.

Saegusa, et al (1996) provided an experimental study to model the creep behavior of the cask structures. ACI committee 209 (1972, 2008), Brooks (2005), CEB-FIP (1990), Harboe, et al (1958), Jirasek and Bazant (1975), RILEM (1988), Troxell, et al (1958), Wittmann (1982), and Bazant and Yu (2012) introduced some approaches to describe the behavior of the creep and shrinkage in concrete. Recently published methodology by RILEM committee is described here and has been implemented to model the time-dependent behavior of dry cask structures.

6.2.2. Evaluating the Creep and Shrinkage Based on B4 Model

In response to the continuously advancing concrete technology, a new prediction model for creep and shrinkage is used. This model, named B4, as shown in Figure 6-1, builds on the theoretically justified model B3, which is a RILEM recommendation from 1996 (RILEM, 1996). Improvements to the model allow for enhanced multi-decade prediction, distinguishing between the drying and autogenous shrinkage, and introduction of new equations and parameters to capture the effects of various admixtures and aggregate types. As it is seen in Figure 6-1(a), with increasing thickness of the specimens, the shrinkage strain decreases during the time of loading while the relative humidity is constant. Figure 6-1(b) shows that the shrinkage strain decreases when the relative humidity increases for a specific specimen during the time of loading. Figure 6-1(c) and Figure 6-1(d) show that with increasing the age at the start of environmental exposure, the creep compliance decreases significantly. Figure 6-2 shows the flow chart of calculation procedure for the B4 model.

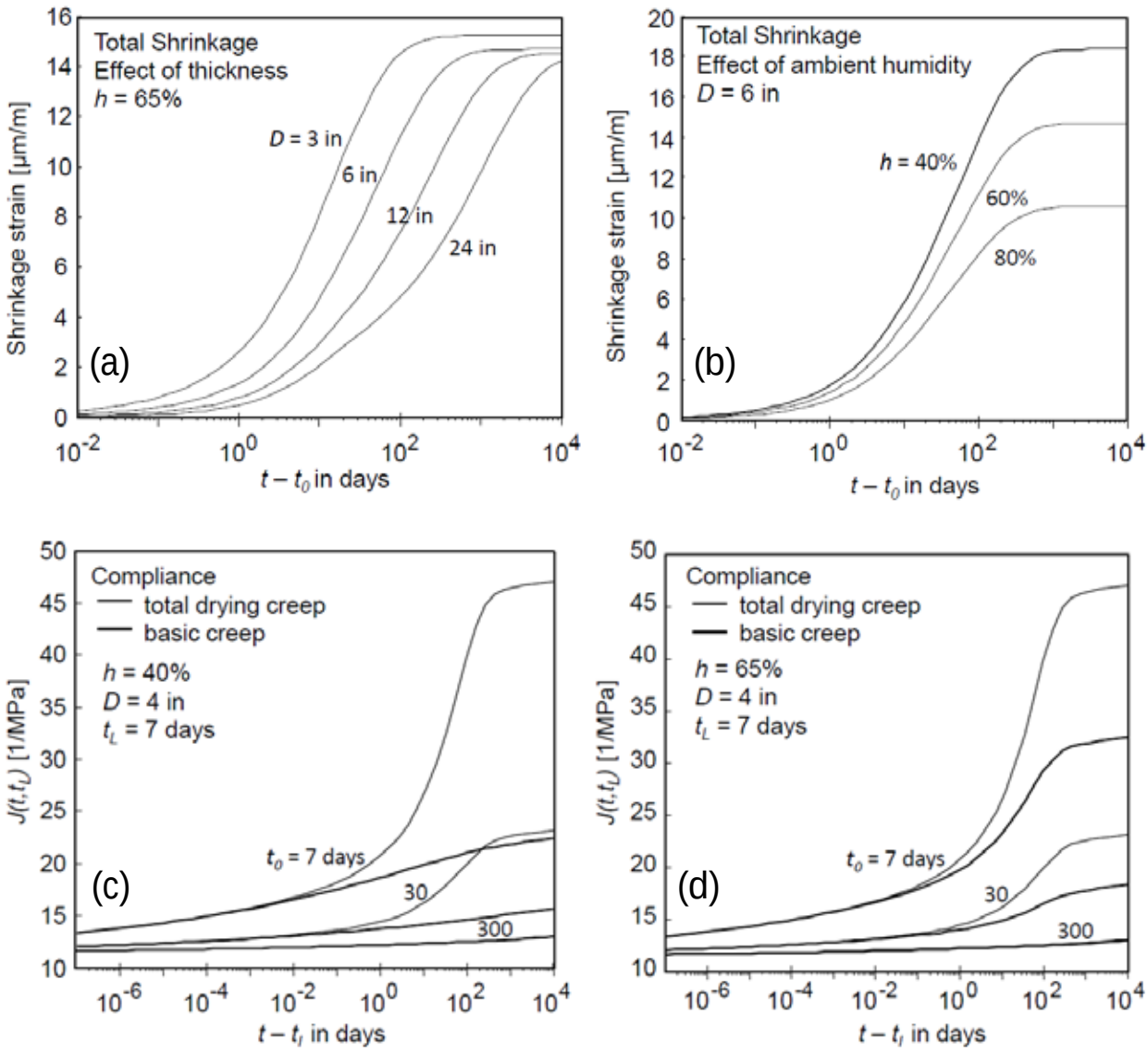

Figure 6-1 Typical creep and shrinkage curves of the B4 model (RILEM, 2014).

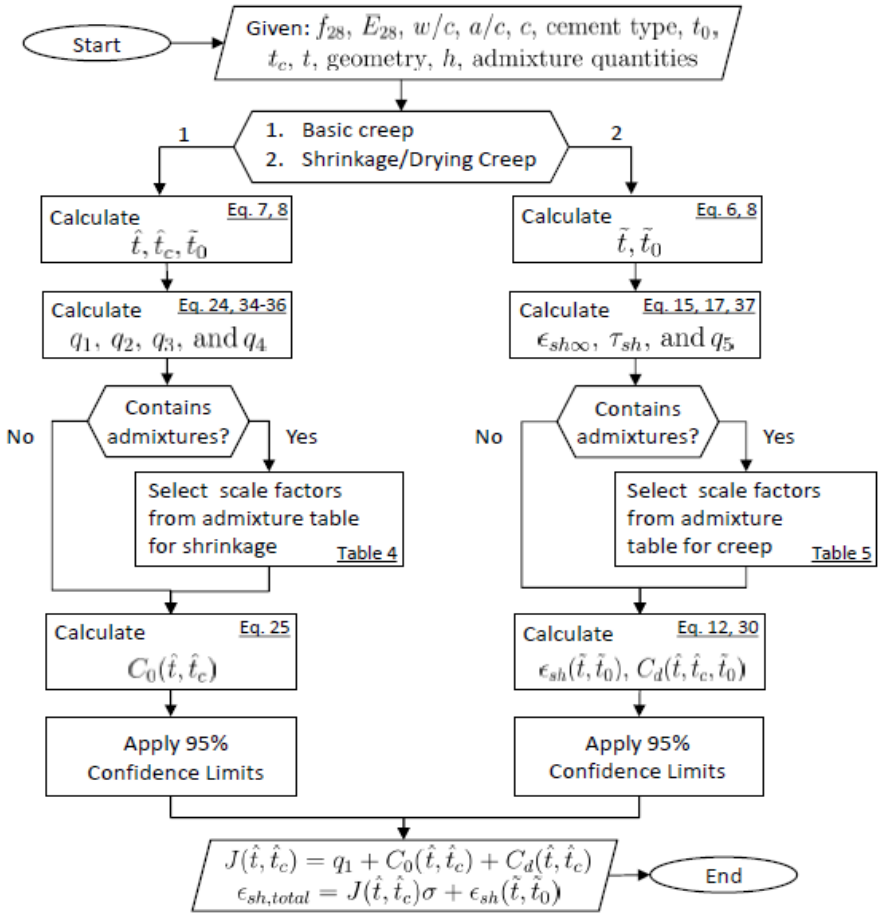

Figure 6-2 Flow chart showing the calculation procedure for the B4 model (RILEM,2014).

The latest recommendation of RILEM committee (B4 model) (RILEM, 2014) has been used to capture the long term behavior of the cask under creep. Based on that formulation creep compliance can be calculated as

$$J(\hat{t},\hat{t}') = q_1 + R_T C_0(\hat{t},\hat{t}') + C_d(\hat{t},\hat{t}',\bar{t}_0) \qquad 6.1$$

where q_1 is the instantaneous compliance (compliance extrapolated from compliance curves between 0.1 s and 1 hour to zero load duration, which is approximately independent of the age t' at loading of the compliance curve); $C_0(\hat{t},\widehat{t'})$ is the compliance function for basic creep (i.e., creep at constant moisture content and no moisture movement through the material); and $C_d(\hat{t},\widehat{t'},\bar{t}_0)$ is the additional compliance due to simultaneous drying.

Creep behavior of steel parts is described by the nonlinear Norton-Bailey formulation as shown below (Betten, 2008):

$$\frac{\partial e_c}{\partial t} = A\left(\frac{s_{eff}}{s_{ref}}\right)^n m\left(\frac{t+t_{shift}}{t_{ref}}\right)^{m-1} n^D, \quad n^D = \frac{3}{2}\frac{dev(s)}{s_{eff}} \qquad 6.2$$

where *A* is creep rate coefficient equal to *3.125E-14 1/hr*, *n* is the stress exponent equal to *5.0*, and *m* is the time hardening exponent equal to *0.5*. Strain hardening approach is chosen for computation of the creep and temperature dependency of steel for this analysis.

Assumptions with regard to our problem:

- Cement Type I;
- Age of loading: 28 days ($t' = t_c = 28\ days$);
- Age when drying begins: ($t_0 = 28\ days$);
- Constant relative humidity: ($h = 80\%$);
- Max cylinder compressive strength: ($f_c' = 27.6MPa$);
- Volume to surface ration of cask: ($\frac{V}{S} = 192.18mm$);
- Cement content: ($C = 219.3\frac{Kg}{m^3}$);
- Water-cement ratio: ($\frac{\omega}{c} = 0.6$);
- Aggregate-cement ratio: ($\frac{a}{c} = 7.0$);
- Iso-thermal condition: ($T = 20^{\circ}C$).

Figure 6-3 shows the creep compliance for 40 years under constant humidity.

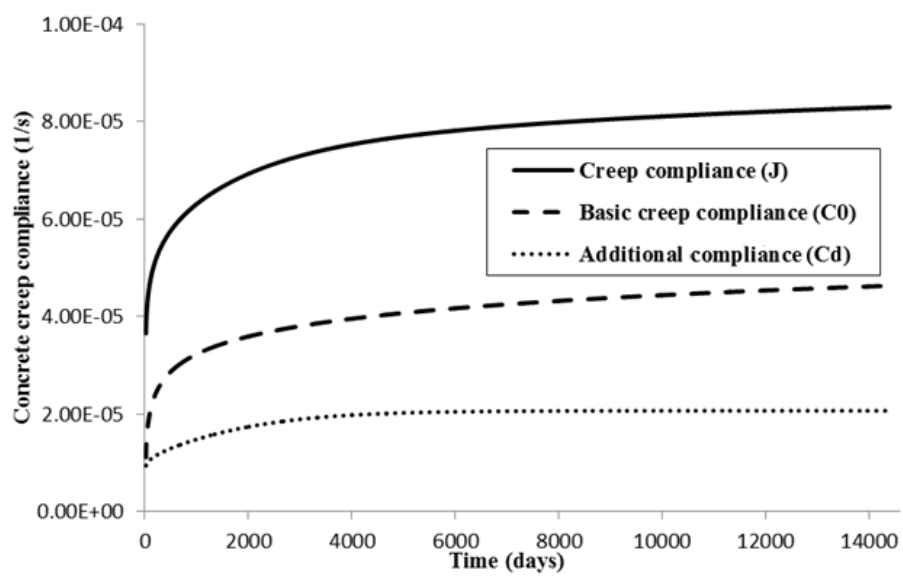

Figure 6-3 Concrete creep compliance of dry cask structures for 40 years.

The latest formulation of RILEM committee, B4 model (RILEM, 2014) has been used to model the shrinkage behavior of the cask. Based on that model, the total shrinkage strain is calculated according to

$$e_{sh,total}(\bar{t},\bar{t}_0) = e_{sh}(\bar{t},\bar{t}_0) + e_{au}(\bar{t},\bar{t}_0) \quad 6.3$$

where, ε_{sh} is the drying shrinkage, ε_{au} is the autogenous shrinkage. $\bar{t}$ is the equivalent exposure duration in days (temperature corrected), and $\bar{t}_0$ is the equivalent time in days, temperature corrected age at exposure. The final autogenous shrinkage is calculated as

$$e_{au\infty} = -\, e_{au,cem}\left(\frac{a/c}{6}\right)^{r_{ea}}\left(\frac{w/c}{0.38}\right)^{r_{ew}} \quad 6.4$$

where, $\varepsilon_{au,cem}$ is autogenous shrinkage in cement, $\frac{\omega}{c}$ is water-to-cement ratio in the mix (by weight) and $\frac{a}{c}$ is aggregate-to-cement ratio in the mix (by weight). Drying shrinkage is calculated according to:

$$e_{sh}(\bar{t},\bar{t}_0) = e_{sh\infty}(\bar{t}_0)K_h S(\bar{t}) \quad 6.5$$

where, $\varepsilon_{sh\infty}(\bar{t}_0)$ is the ultimate shrinkage strain, $S(\bar{t})$ defines the time variation of shrinkage, and K_h is dependent on RH.

Shrinkage strain is calculated and shown in Figure 6-4 for examination of the long term behavior with constant relative humidity.

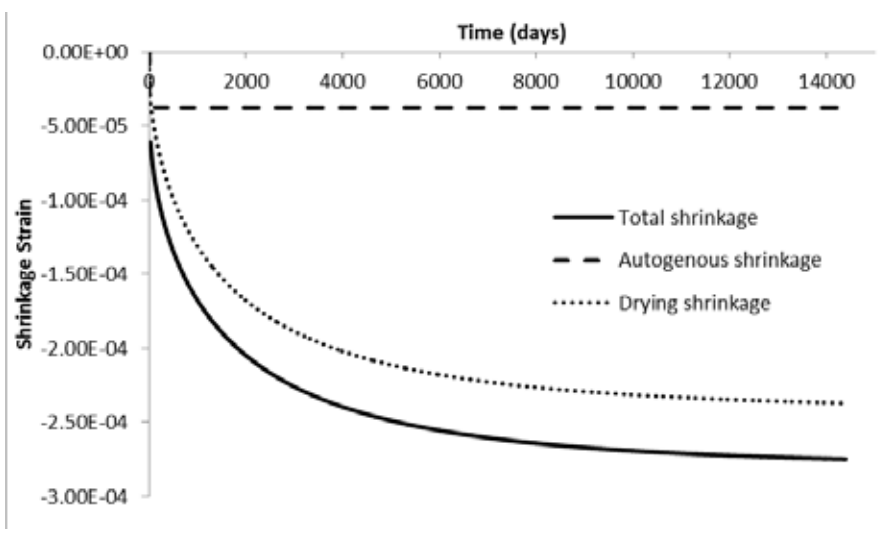

Figure 6-4 Concrete shrinkage strain of Dry cask structures for 40 years.

To illustrate the stress dependency of creep, the total strain including shrinkage strain and creep compliance during a year will be:

$$e_{sh,total} = e_{sh} + e_{au} = -\,(88.49 + 37.70)\times 10^{-6} = -\,126.19\times 10^{-6} \quad 6.6$$

$$e = J(\hat{t}',\hat{t})s + e_{sh,total} = 85.81\times 10^{-6}s - 126.19\times 10^{-6} \quad 6.7$$

6.2.3. Creep and Shrinkage Modeling of Dry Cask Structure

Seven different cases are considered here to investigate the behavior of cask structure including creep, shrinkage and thermal effects. These cases are:

1) Stationary analysis of cask under gravity (dead load);
2) Time dependent analysis of cask under volumetric effect of creep;
3) Time dependent analysis of cask under deviatoric effect of creep;
4) Time dependent analysis of cask under shrinkage with constant relative humidity;
5) Coupling between total effects of creep and shrinkage;
6) Stationary analysis of thermal effects of cask including the gravity load;
7) Coupling between creep, shrinkage, gravity and thermal effects.

The dry cask structure is modeled as 2-D axisymmetric composite solid. The concrete cask, base plate, lid assembly, canister and steel liner are modeled as shown in Figure 6-5 in COMSOL (COMSOL Multiphysics, 2015). The geometric properties are summarized in Table 6-1. The model cask is 2.83 times smaller than the prototype cask. Weight of the scaled canister with fuel is 5.7 ton and this weight is added to the canister bottom (r9) part during these simulations.

Table 6-1 Dimensions Used in Simulating the Degradation of Concrete Scale Cask Model.

Part	Height (mm)	Internal radius (mm)	External radius (mm)	Thickness (mm)
Concrete model cask (r1)	1962.2	371.5	609.6	238.1
Steel liner (r2)	1962.2	355.6	371.5	15.9
Base plate (r3)	-	-	609.6	63.5
Canister (r4)	1905.0	-	352.4	352.4
Lid-Top (r5)	-	-	431.8	6.4
Concrete Lid (r6)	50.8	-	349.3	349.3
Lid-Rib (r7)	50.8	349.3	352.4	3.2
Lid-Bottom (r8)	-	-	352.4	3.2
Canister bottom (r9)	3.2	-	349.3	349.3

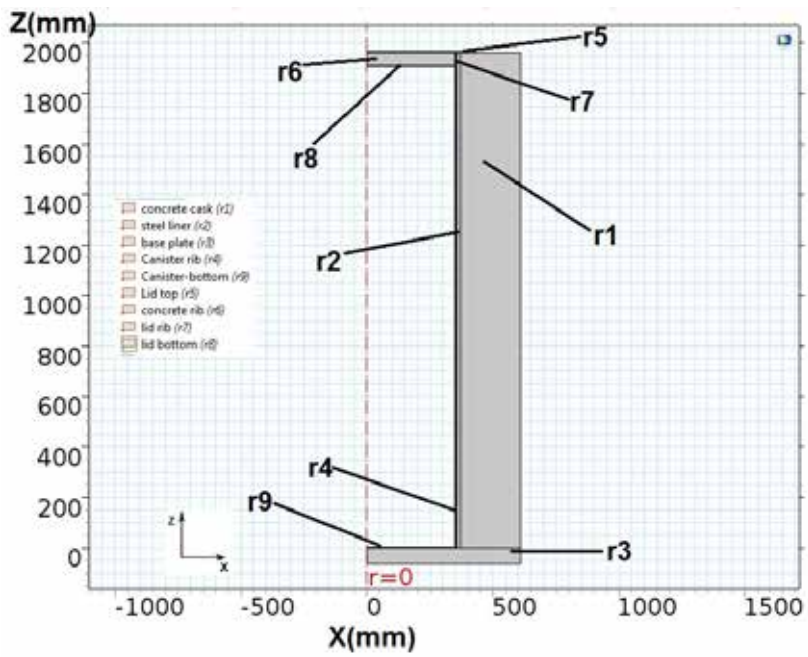

Figure 6-5 Model of dry cask structures in COMSOL Multiphysics software.

The bottom surface of the base plate is constrained in the vertical direction to remove rigid body translation. Gravity force is considered in all parts. Figure 6-6 shows the assumed mesh of this composite structure. Linear elastic material behavior is assumed for the concrete part and elastic-perfectly plastic model is considered for the steel parts. These parameters for steel and concrete are described in Table 6-2 and Table 6-3, respectively. Additional mass (8500 kg) due to similitude is also applied to the concrete cask.

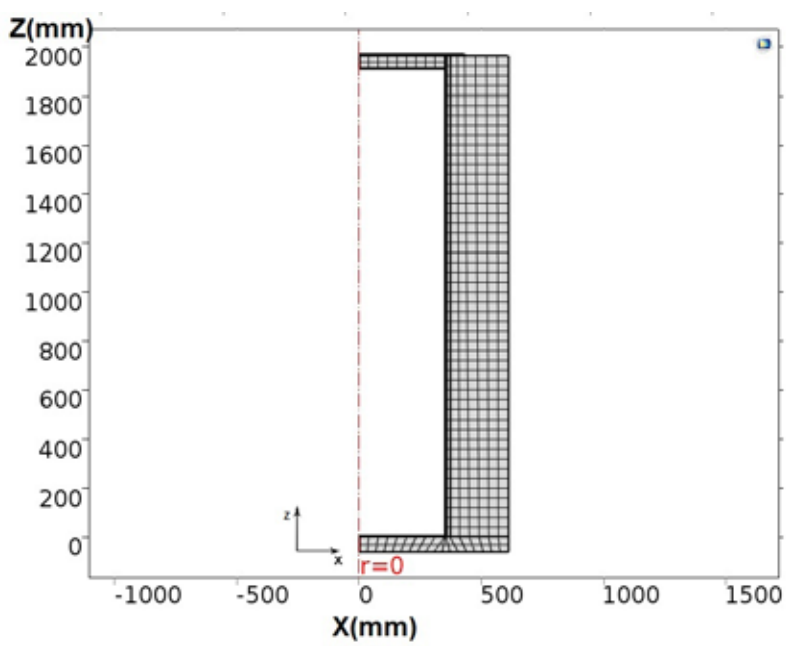

Figure 6-6: Mesh of dry cask structure.

Table 6-2 Structural Steel Properties.

Property	Value
Heat capacity at constant pressure	475 [J/(kg*K)]
Thermal conductivity	44.5 [W/(m*K)]
Coefficient of thermal expansion	12.3e-6 [1/K]
Density	7850 [kg/m^3]
Young's modulus	200e9 [Pa]
Poisson's ratio	0.33
Initial yield stress	220 [MPa]
Lamé parameter λ	1.5e11[Pa]
Lamé parameter μ	7.5e10[Pa]

Table 6-3 Concrete Properties.

Property	Value
Coefficient of thermal expansion	10e-6 [1/K]
Density	2450 [kg/m^3]
Thermal conductivity	1.8 [W/(m*K)]
Heat capacity at constant pressure	880 [J/(kg*K)]
Young's modulus	25e9 [Pa]
Poisson's ratio	0.15
Uniaxial tensile strength	3.5 [MPa]
Uniaxial compressive strength	30 [MPa]
Biaxial compressive strength	35 [MPa]

6.2.3.a. Case 1: Stationary analysis of cask under gravity (dead load) only

In this case a stationary analysis is performed and the performance of dry cask structure is investigated under the gravity load of parts, canister fuel and added mass due to similitude. Figure 6-7 and Figure 6-8 show the contour plots of von-Mises stress, volumetric stress and deformed shape of the cask structures in this case. It is noted that a large scale factor was used to illustrate the deformations. The deformations were otherwise negligible. The von-Mises stress along the bottom surface and top surface of the cask is plotted in Figure 6-9.

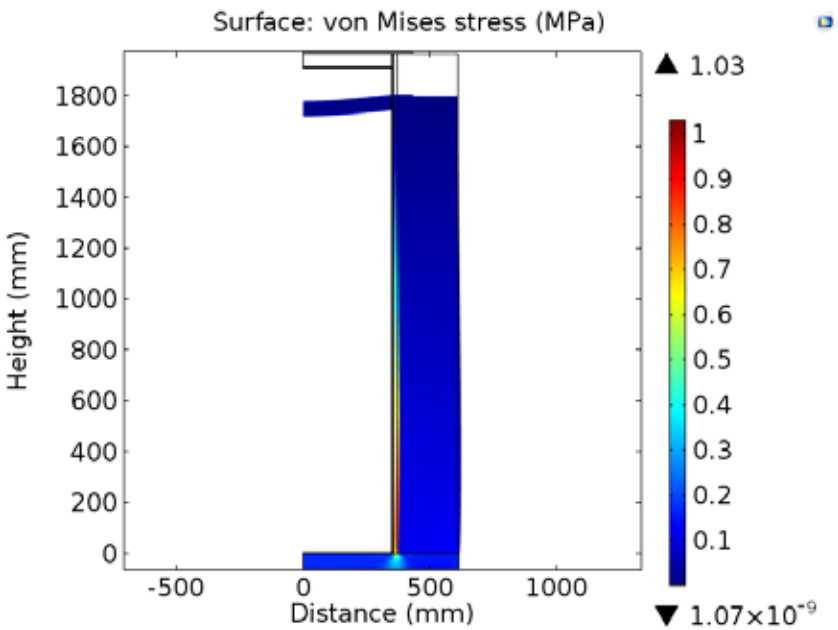

Figure 6-7 von-Mises stress in the cask due to the gravity load.

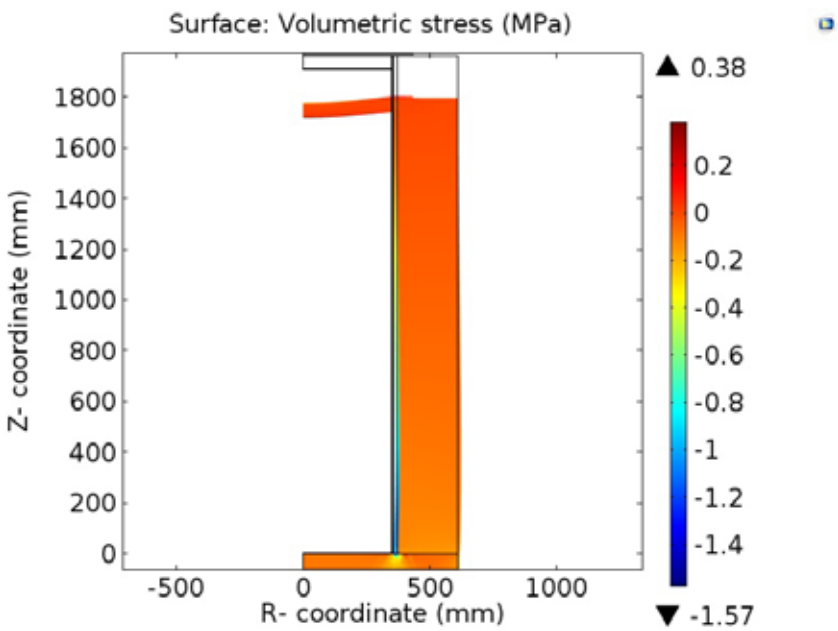

Figure 6-8 Volumetric stress in the cask due to the gravity load.

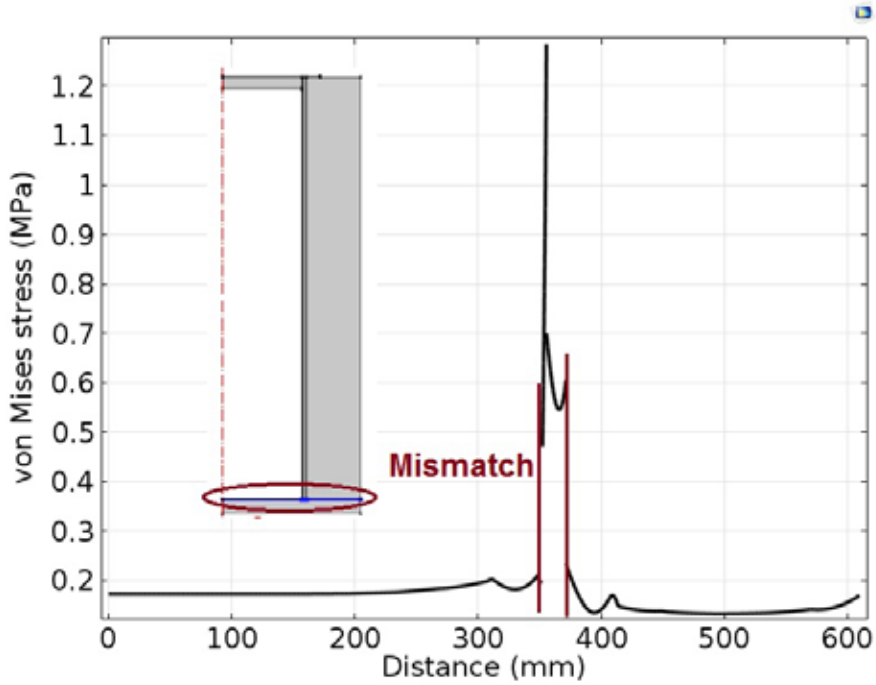

(a) von-Mises stress along the bottom surface of the concrete cask and steel liner

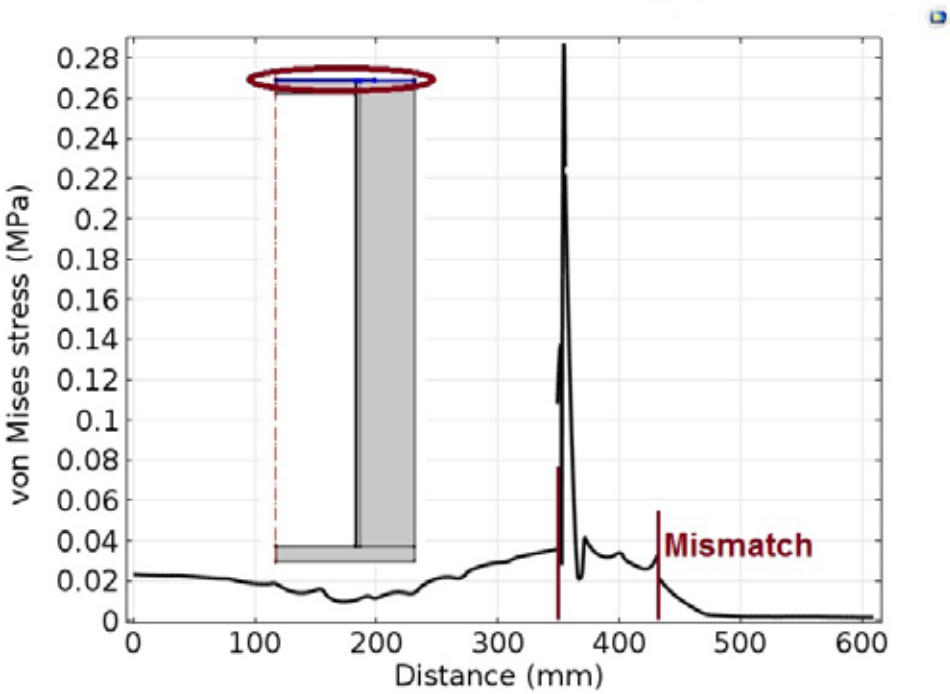

(b) von-Mises stress along the upper surface of the concrete cask and steel liner

Figure 6-9 von-Mises stress along the radial direction due to the gravity load.

As it can be seen, the mismatch is negligible for this case and the gravity force does not induce large von-Mises and volumetric stresses.

6.2.3.b. Case 2: Time dependent analysis of cask under volumetric effect of creep

Creep compliance is calculated earlier and is plotted in Figure 6-3 under constant relative humidity. COMSOL has a capability to consider the volumetric and deviatoric effects of creep separately. A time dependent study is performed for the cask structure over a duration of 40 years by applying the creep model of RILEM (2014) for concrete and Norton-Bailey creep formulation for steel parts. If the creep formulation is written in an incremental format, the incremental creep strain can be written as

$$\Delta e_{cr}(t_n) = \frac{1}{E(t_0)} \sigma(t_n)[f(t_{n+1}, t_0) - f(t_n, t_0)] \qquad 6.8$$

In the above equation Ø is creep coefficient and it is equal

$$f(t, t_0) = E(t_0) J(t, t_0) - 1 \qquad 6.9$$

For volumetric creep, a parameter called "F_{cr}" needs to be inputted in COMSOL such that:

$$\frac{\partial e_{cr}}{\partial t} = \frac{1}{3} F_{cr} I \qquad 6.10$$

$\boldsymbol{I}$ is the identity matrix. "F_{cr}" is creep rate and its unit is 1/sec. This parameter is calculated as follows:

$$\frac{\partial e_{cr}}{\partial t} \approx \frac{\Delta e_{cr}}{\Delta t} = \frac{1}{\Delta t} \frac{\Delta f(t, t_0)}{E(t_0)} \sigma(t_n) \approx F_{cr} = [J(t_{n+1}, t_0) - J(t_n, t_0)] \frac{t_r(\sigma)}{\Delta t} \qquad 6.11$$

Contours of von-Mises stress and volumetric stress after 40 years are plotted in Figure 6-10. It is clear that von-Mises stress and volumetric stress do not change much with respect to volumetric effect of creep. The von-Mises stress along the bottom and top surface is the same as the previous case, so we can say the volumetric effect of creep is not dominant. Contours of axial, radial, and hoop strain are shown in Figure 6-11.

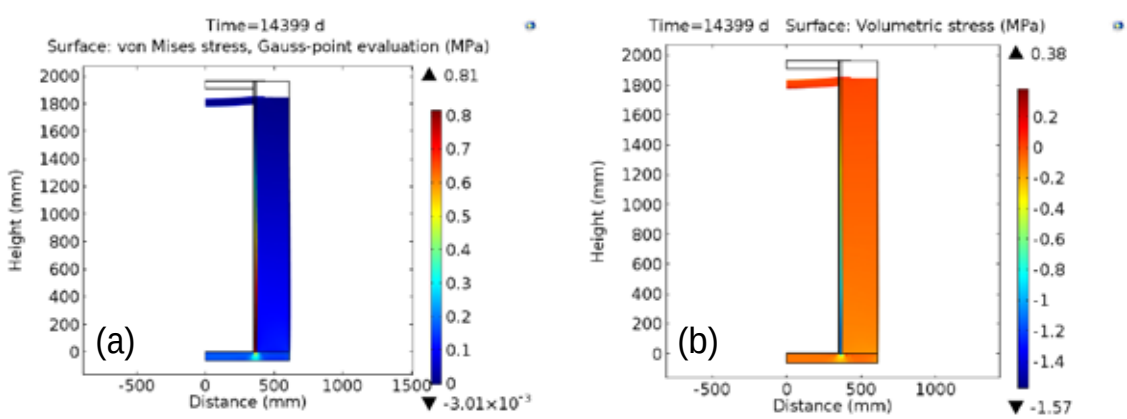

Figure 6-10 von-Mises stress (a) and volumetric stress (b) in the cask due to the volumetric creep after 40 years.

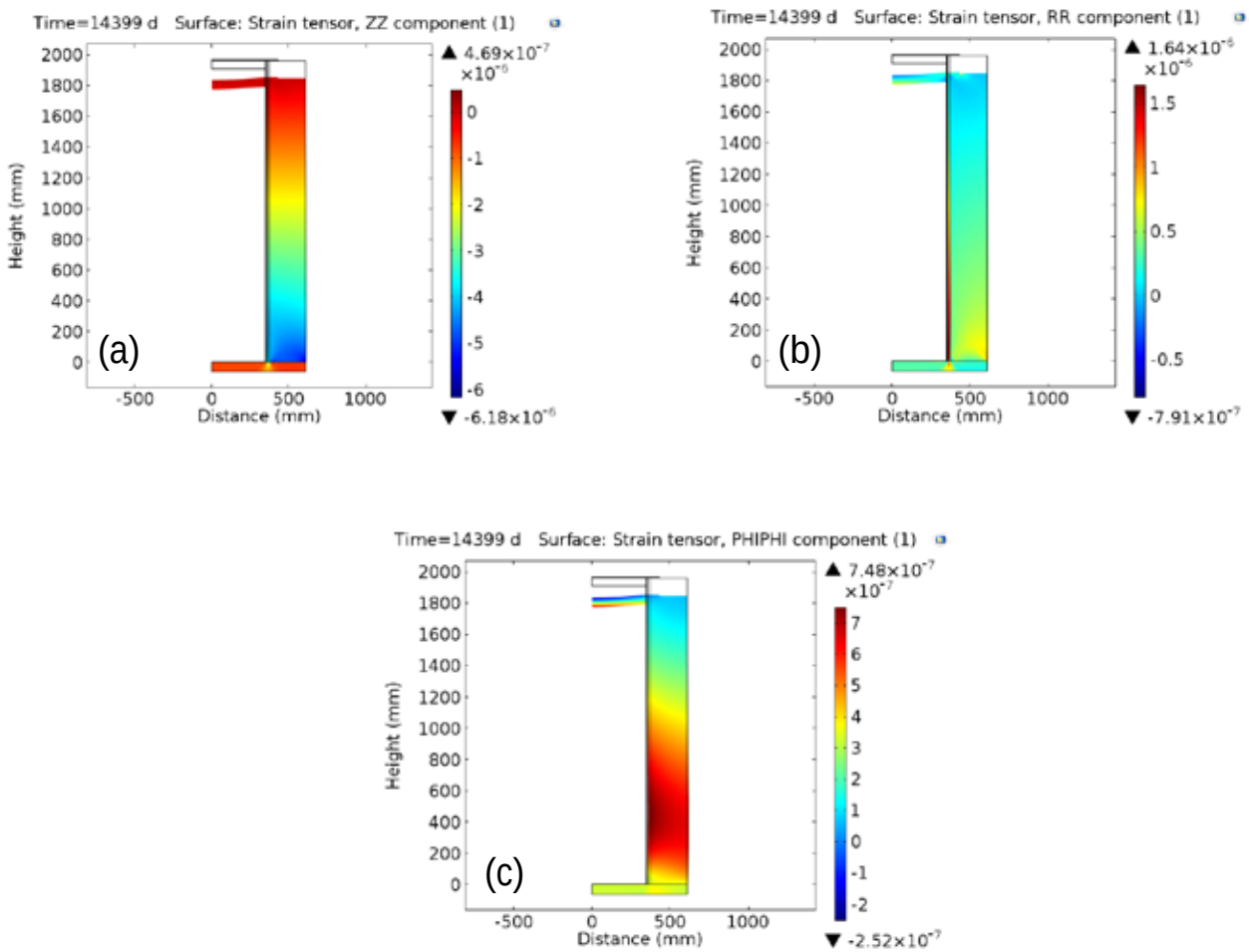

Figure 6-11 Axial (a), radial (b) and hoop (c) strain in the cask due to volumetric creep after 40 years.

6.2.3.c. Case 3: Time dependent analysis of cask under deviatoric effect of creep

Similar to the previous case, only the deviatoric effect of creep is considered here for concrete parts and Norton-Bailey formulation is implemented for steel parts.

For deviatoric creep, a parameter called "F_{cr}" needs to be input in COMSOL such that

$$\frac{\partial e_{cr}}{\partial t} = \frac{3}{2}\frac{dev(s)}{s_{eff}} F_{cf} \qquad 6.12$$

"F_{cr}" is creep rate and its unit is 1/sec. This parameter is calculted as follows

$$\frac{\partial e_{cr}}{\partial t} \approx \frac{\Delta e_{cr}}{\Delta t} = \frac{1}{\Delta t}\frac{\Delta f(t,t_0)}{E(t_0)} dev s(t_n) \Rightarrow F_{cr} = \frac{2}{3}[J(t_{n+1},t_0) - J(t_n,t_0)]\frac{s_{eff}}{\Delta t} \qquad 6.13$$

In this case, contours and plots are similar to those shown for case 2.

6.2.3.d. Case 4: Time dependent analysis of cask under shrinkage with constant relative humidity

Shrinkage strain is calculated earlier and is plotted in Figure 6-4 with constant relative humidity. A time dependent study is performed by applying the shrinkage model of RILEM (2014) for concrete. Since shrinkage has a volumetric effect on concrete component of the cask, we have:

$$\frac{\partial e_{sh}}{\partial t} \approx \frac{\Delta e_{sh}}{\Delta t} = \frac{1}{3} F_{cr} I \otimes F_{cr} \approx [e_{sh}(t_{n+1}, t_0) - e_{sh}(t_n, t_0)] \frac{3}{\Delta t} \qquad 6.14$$

The result of COMSOL model shows that shrinkage strain does not change the behavior of the cask structure significantly.

6.2.3.e. Case 5: Coupling between total effects of creep and shrinkage

In this case, volumetric, and deviatoric effects of creep, effect of shrinkage on concrete cask, and creep of steel parts are considered. The results are similar to those of the previous cases.

6.2.3.f. Case 6: Stationary analysis of thermal-mechanical effects on the cask structure

Different level of temperature inside and outside of the cask will cause some thermal stress on the structure and may increase the aging process of the cask. This factor is investigated in this section separately. Outside temperature is considered 20 °C and inside temperature is considered 80 °C. Figure 6-12 through Figure 6-15 show different plots for this case. It is seen that the stress in the liner is much higher than in the concrete. A large stress difference appears between these cask parts. This stress difference did not result in damage to the interface between the steel liner and the concrete cask.

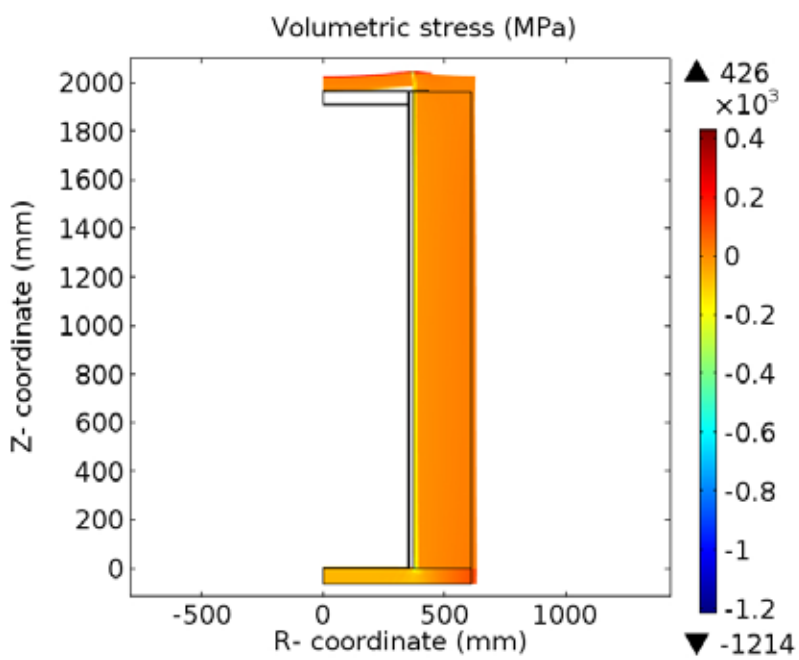

Figure 6-12 Volumetric stress in the cask for case 6.

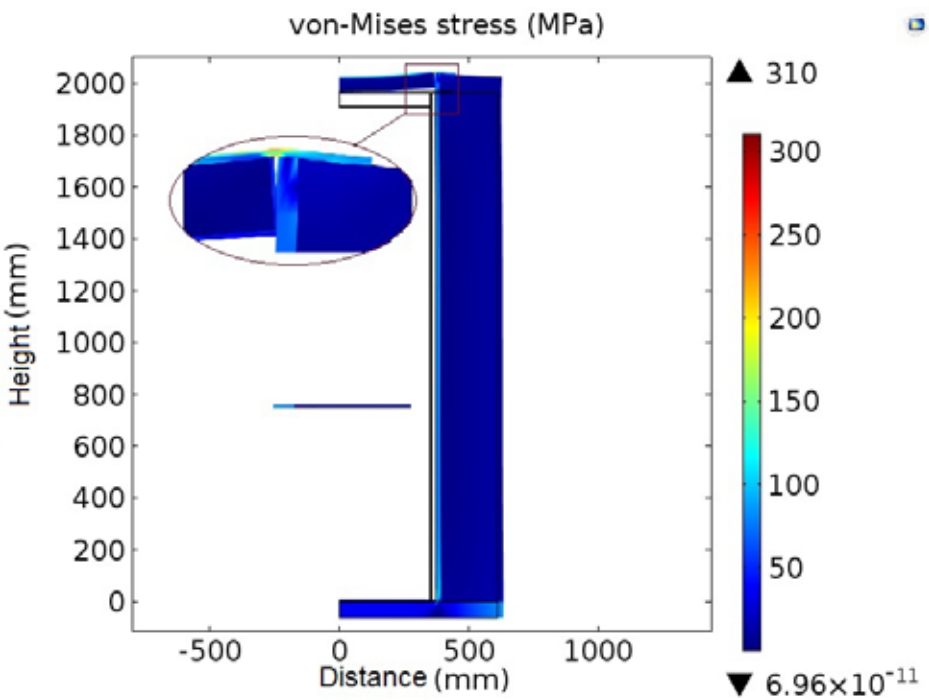

Figure 6-13 von-Mises stress in the cask for case 6.

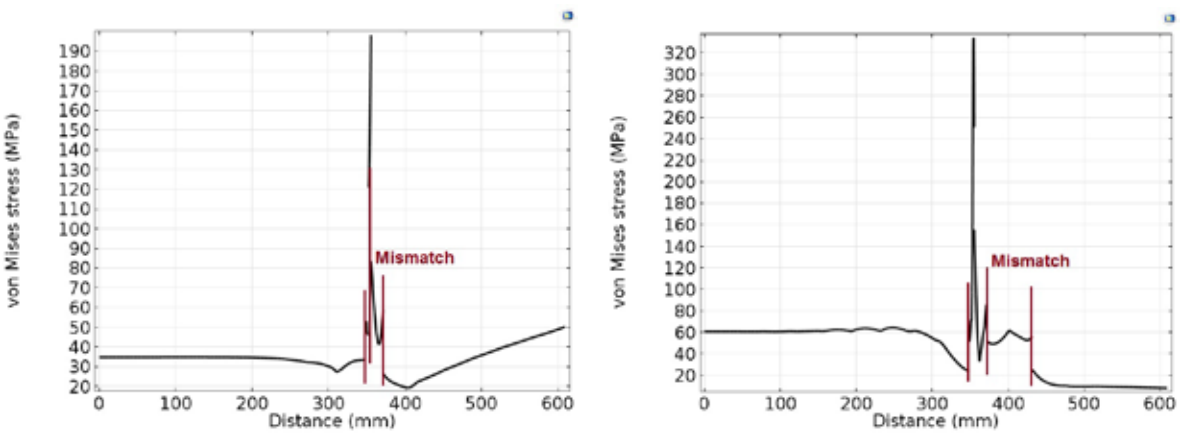

(a) along the bottom surface of the cask (b) along the upper surface of the cask

Figure 6-14 Plot of von-Mises stress for case 6.

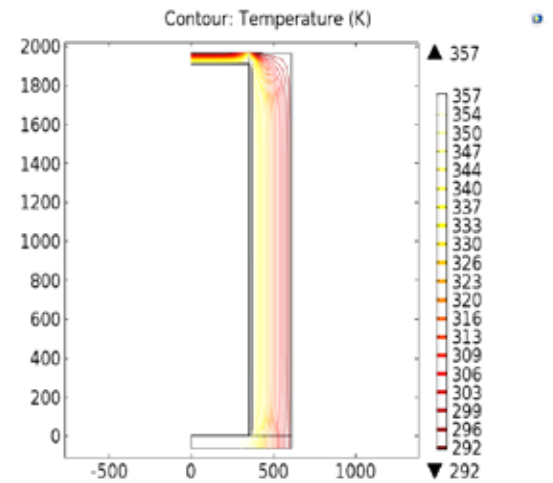

(a) Isothermal profile

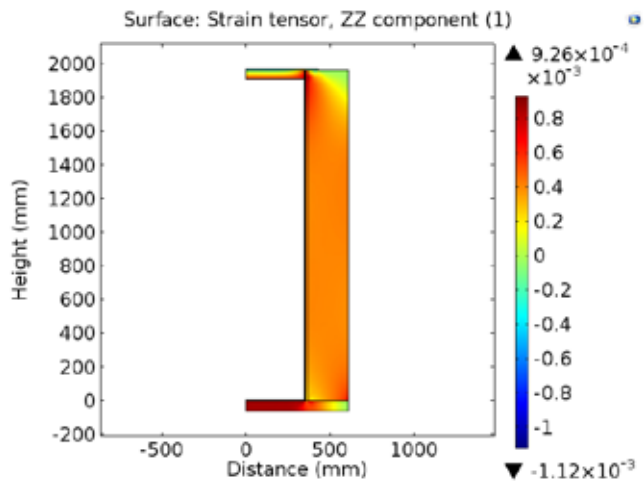

(b) Axial strain

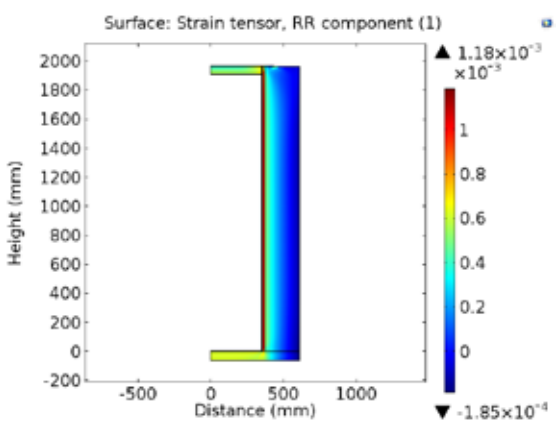

(c) Radial strain

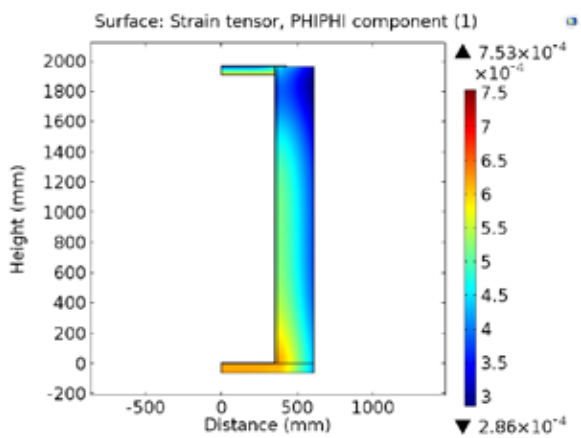

(d) Hoop strain

Figure 6-15 Temperature profile, and contours of cylindrical strains for case 6.

6.2.3.g. Case 7: Coupling between creep, shrinkage and thermal effects.

A time dependent study considers the effect of creep and shrinkage coupling with temperature for a 40 years' time period. Results are shown in Figure 6-16 and show that coupling between temperature, creep and shrinkage does not change the performance of the structure significantly when compared to the temperature effect only.

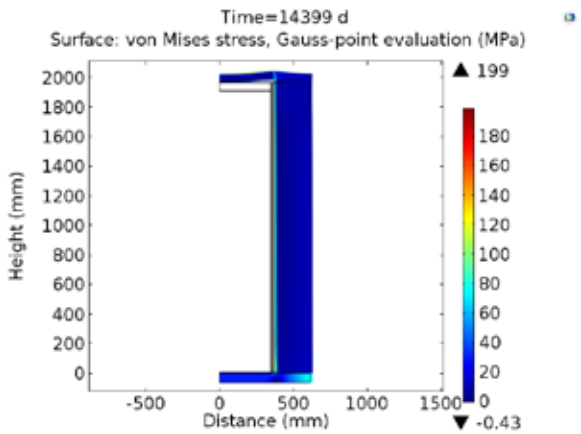

(a) von-Mises stress

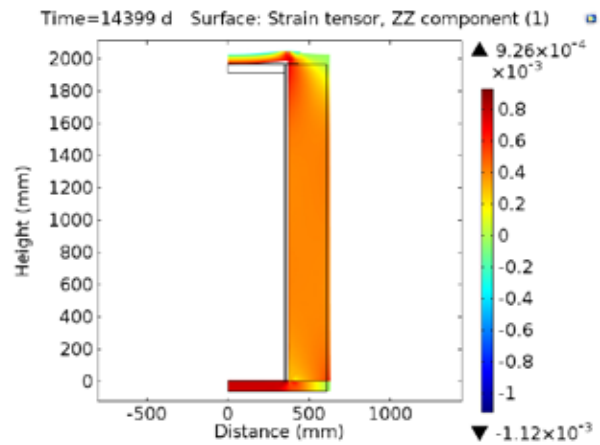

(b) Axial strain

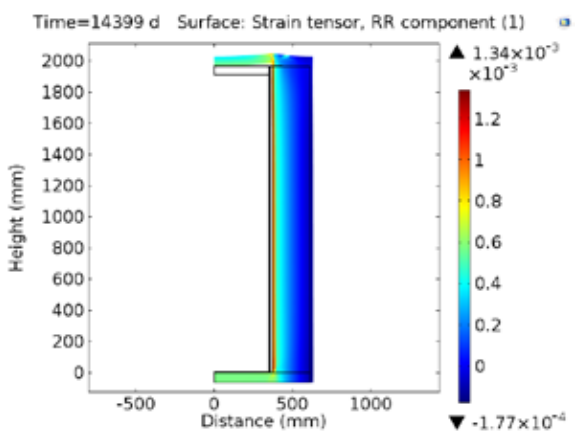

(c) Radial strain

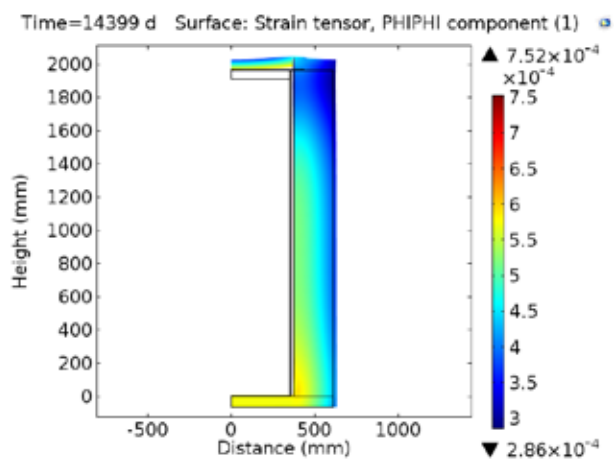

(d) Hoop strain

Figure 6-16 Contours of stresses and strains for case 7.

6.2.4. Conclusions

Since the only active load on the dry structures is gravity load and it does not change over the life of the cask structure, creep and shrinkage do not affect this structure significantly. The results of thermo-mechanical study illustrate the mismatch of deformations and residual stresses in the steel liner and contiguous concrete considering full bond in order to assess progressive damage at the interface of the two materials. The concomitant shear transfer between the steel liner and the concrete cask does not induce significant damage in the interfacial region of the two cask components.

The swelling strain due to the chemical reaction of alkali-silica interaction is added to this analysis in the following sections in order to account for the chemical effect of ASR at future stages of the life-cycle behavior of the casks.

6.3. THERMO-HYGRO MODEL

Until now, the behavior of concrete component is investigated with respect to creep, shrinkage and temperature. All these physics were taken into account under isothermal and constant relative humidity conditions where it was assumed that the temperature and relative humidity are considered as independent of time during the life of concrete structure, which may not be a correct assumption. Here, a rigorous methodology is introduced to model concrete structures under heat transfer and moisture diffusion based on concrete specifications.

6.3.1. Modeling of Heat transfer in Porous Media

The governing equation for heat transfer in porous media is represented as

$$\rho C \frac{\partial T}{\partial t} = \nabla(k \nabla T) + Q \qquad 6.15$$

where t is time in sec, and T is temperature in K, ρ is the mass density of concrete in $\frac{kg}{m^3}$ and C is the specific heat of concrete in $\frac{J}{kg^\circ K}$ which are temperature dependent and can be calculated based on different standards. ASCE (1992) suggests the following to calculate the mass density and specific heat for siliceous aggregate concrete:

$$\rho C = \begin{cases} 0.005T + 1.7 & 20^\circ C \le T \le 200^\circ C \\ 2.7 & 200^\circ C \le T \le 400^\circ C \\ 0.005T + 1.7 & 400^\circ C \le T \le 500^\circ C \\ 0.005T + 1.7 & 500^\circ C \le T \le 600^\circ C \\ 2.7 & T \ge 200^\circ C \end{cases} \quad (\text{MJ}/(\text{m}^3{}^\circ\text{C})) \qquad 6.16$$

where temperature is in °C and should be converted to K in order to use it in Eq. 6.15. k is the thermal conductivity of concrete in $\frac{W}{m^\circ K}$ which is temperature dependent and based on ASCE (1992), it can be expressed for siliceous aggregate concrete as

$$k = \begin{cases} -0.000625T + 1.5 & 20^\circ C \le T \le 800^\circ C \\ 1.0 & T \ge 800^\circ C \end{cases} \quad (\text{W}/(\text{m}^\circ\text{C})) \qquad 6.17$$

where Q is rate of heat per unit volume generated within the body ($\frac{W}{m^3}$). Saouma et al. (2015) showed that the heat transfer in concrete is moisture dependent and moisture diffusivity should be taken into account based on Bazant's experiments (1979; 1982). Here, the moisture dependency is treated as rate of heat and this term is

$$Q = -c_w J \nabla T + C_a \frac{\partial w}{\partial f} \frac{\partial f}{\partial w} + Q_f \qquad 6.18$$

where C_w is the mass density and isobaric (constant pressure) heat capacity of liquid water and can be calculated as

$$C_w = C_{water}\, r_{water} \qquad 6.19$$

Where

$$r_{water} = 314.4 + 685.6\left[1 - \left(\frac{(T - 273.15)}{374.14}\right)^{\frac{1}{0.55}}\right]^{0.55}\left(\frac{kg}{m^3}\right) \qquad 6.20$$

and the heat capacity of water is

$$C_{water} = 4185.5\left(\frac{J}{kg\,^0K}\right) \qquad 6.21$$

where J is the moisture flux ($J = -D_h \nabla \emptyset$), D_h is the moisture diffusivity and can be calculated based on Section 6.3.2; and $\emptyset$ is the relative humidity. C_a is the heat absorption of free water in ($\frac{J}{kg}$) and can be neglected or its influence is minimal based on recommendations of Bazant et al. (1982). For simplicity, it is considered that $C_a = 0.001 C_{water}$ (Bazant et al. 1982), ω is the total water content (g/g) (for unit volume of concrete, cm^3) and Q_f is an extra rate of heat conducted in concrete which is calculated based on experiments.

6.3.2. Modeling of Moisture Transfer in Porous Media

The general format of moisture diffusion (Fick's law) in porous media is

$$x\frac{\partial f}{\partial t} = \nabla \times (F) + G \qquad 6.22$$

Where

$$x = \frac{\partial w}{\partial f} \qquad 6.23$$

and ω is moisture storage function in $\frac{kg}{m^3}$; $F = \xi D_w \nabla \emptyset + \delta_p \nabla(\emptyset \rho_{sat})$, D_w is moisture diffusivity in $\frac{m^2}{s}$, δ_p is the vapor permeability in sec, and ρ_{sat} is the saturated mass density of concrete.

Based on Saouma et al (2015), Eq. 6.22 can be rewritten as follows. δ_p can be assumed zero, and as a result, its associated term can be neglected. g function should be rewritten in order to consider the effect of heat transfer as

$$F = D_h \nabla f + D_{ht} \nabla T \qquad 6.24$$

Based on Bazant et al. (1982), the coupling term of the thermal gradient (D_{ht}) can be neglected. The source term (G) can be considered as follows:

$$G = \frac{\partial w_d}{\partial t} \tag{6.25}$$

where, ω_{d} is the total mass of free evaporable water released into the pores by dehydration of the cement paste.

Based on Saouma et al (2015), there are three unknowns

1) Moisture storage function (ω)

Based on Bazant et al (1979), moisture storage function follows the following relationship

$$w = \frac{CKV_m f}{(1 - Kf)[1 + (C - 1)Kf]} \tag{6.26}$$

where, $C = \exp\left(\frac{855}{T}\right)$, and temperature is expressed in Kelvin units.

Relative humidity can be treated as pore vapor pressure and follows from the following equation

$$f = \frac{P_v}{P_{vs}} \tag{6.27}$$

where, P_{vs} denotes the saturated vapor pressure at a given temperature, T and can be calculated based on Eq. 6.8

$$P_{vs} = P_{atm} \exp(4871.3 \frac{T - 100}{373.15T}) \tag{6.28}$$

In Eq. 6.26, V_m is the monolayer capacity that can be defined as mass of adsorbate required to cover the surface of the adsorbent with a single molecular layer. V_m and K should be calculated separately for cement paste and aggregate. V_m for cement paste is

$$V_m = V_t(t) V_w \left(\frac{w}{c}\right) V_{ct}(ct) V_T(T) \tag{6.29}$$

Where, V_t accounts for the effect of time, V_ω accounts for the effect of water to cement ratio, V_{ct} is a constant based on the cement type and V_T changes with temperature.

$$V_t(t) = \begin{cases} 0.068 - \frac{0.22}{t} & t > 5 days \\ V_t(5) & t \leq 5 days \end{cases} \tag{6.30}$$

$$V_w\left(\frac{w}{c}\right) = \begin{cases} 0.85 + 0.45\frac{w}{c} & 0.3 < \frac{w}{c} < 0.7 \\ V_w(0.3) & 0.3 \le \frac{w}{c} \end{cases} \qquad 6.31$$

$$V_{ct} = \begin{cases} 0.9 & \text{Cement type I} \\ 1.0 & \text{Cement type II} \\ 0.85 & \text{Cement type III} \\ 0.6 & \text{Cement type IV} \end{cases} \qquad 6.32$$

$$V_T(T) = 1 \qquad 6.33$$

V_m for cement paste is calculated based on Eq. 6.29 as follows:

$$V_m = 0.0064 V_{agg} \qquad 6.34$$

Where, V_{agg} depends on the pore structure of various aggregates as follows:

$$V_{agg} = \begin{cases} 0.05 - 0.1 & \text{dense} \\ 0.04 - 0.1 & \text{porous} \end{cases} \qquad 6.35$$

K is empirical constant and can be calculated based on

$$K = \frac{\left(1 - \frac{1}{n}\right)C - 1}{C - 1} \qquad 6.36$$

Where, n is number of adsorbed layers of molecules, and should be calculated for cement paste and aggregate separately.

For cement paste, n is determined according to Bazant et al (1979)

$$n = N_t(t)\, N_w\left(\frac{w}{c}\right) N_{ct}(ct)\, N_T(T) \qquad 6.37$$

where, the N functions are defined as follows:

$$N_t(t) = \begin{cases} 2.5 + \frac{15}{t} & t > 5\,\text{days} \\ N_t(5) & t \le 5\,\text{days} \end{cases} \qquad 6.38$$

$$N_w\left(\frac{w}{c}\right)=\begin{cases}0.33+2.2\frac{w}{c} & 0.3<\frac{w}{c}<0.7\\ N_w(0.3) & 0.3\le\frac{w}{c}\end{cases} \qquad 6.39$$

$$V_{ct}(ct)=\begin{cases}1.1 & \textit{Cement type I}\\ 1.0 & \textit{Cement type II}\\ 1.15 & \textit{Cement type III}\\ 1.5 & \textit{Cement type IV}\end{cases} \qquad 6.40$$

$$N_T(T)=1 \qquad 6.41$$

For aggregates, n is calculated

$$n=4.603n_{agg} \qquad 6.42$$

where, n_{agg} depends on the pore structure of various aggregates as follows:

$$n_{agg}=\begin{cases}1.0-1.5 & \textit{dense}\\ 1.7-2.0 & \textit{porous}\end{cases} \qquad 6.43$$

Based on Eq. 6.26, $\xi|_{CP;agg}$ can calculated as

$$x\Big|_{CP;agg}=\frac{\partial w}{\partial f}\Big|_{CP;agg}=\frac{CKV_m+wK[1+(C-1)Kf]-wK(1-Kf)(C-1)}{(1-Kf)[1+(C-1)Kf]} \qquad 6.44$$

Based on weight percentage of cement paste and aggregate, the final value of ξ is calculated as follows

$$x=\frac{\partial w}{\partial f}=f_{agg}\left(\frac{\partial w}{\partial f}\right)_{agg}+f_{CP}\left(\frac{\partial w}{\partial f}\right)_{CP} \qquad 6.45$$

where, f_{agg} is weight percentage of aggregates and f_{CP} is weight percentage of cement paste in concrete.

2) Moisture diffusivity (D_h)

Moisture diffusivity (D_h) can be calculated based on Bazant et al. (1982) in $\frac{m^2}{s}$ as

$$D_h=\begin{cases}D_{h,0}f_1(T) & T\le 95^0C\\ D_{h,0}f_1(95^0C)f_2(T) & T>95^0C\end{cases} \qquad 6.46$$

where

$$D_{h,0} = 3.10 \times 10^{-10} f_H \qquad 6.47$$

$$f_H = \begin{cases} \alpha_D + \dfrac{1-\alpha_D}{1+\left(\dfrac{1-f}{1-0.75}\right)^n} & T \le 95^0C \\ 1 & T > 95^0C \end{cases} \qquad 6.48$$

where $\alpha_D = \frac{1}{1+\frac{19(95-T)}{70}}$ and $n \in [6:16]$.

$f_1(T)$ and $f_2(T)$ are calculated as follows

$$f_1(T) = \exp\left(\frac{Q}{R}\left(\frac{1}{T_{ref}} - \frac{1}{T}\right)\right) \qquad 6.49$$

$$f_2(T) = \exp\left(\frac{T-95}{0.881+0.217(T-95)}\right) \qquad 6.50$$

where, Q is the activation energy for water migration along the adsorption layers in the necks (between layers of aggregate and cement paste), and R is the gas constant. It can be assumed that $\frac{Q}{R} = 2700K$ (Bazant et al., 1982).

3) Total mass of free evaporable water (ω_d)

A source term in the moisture diffusion governing equation is the amount of dehydrated water ω_d (in units g water/g material per 1 cm^3 volume of material), and represents the water molecules released into concrete pores due to dehydration of hydrated minerals within cement paste as the temperature in concrete increases. ω_d, based on Bazant et al. (1979), is given by

$$w_d = w_H^{105} f_d(T) \qquad 6.51$$

where ω_H^{105} is the hydrated water content (in units of g water/g material per 1 cm^3 volume of material) at 105°C, and $f_d(T)$ is a function of the weight loss of the concrete due to heat. Dehydration of hydrated minerals within cement paste typically begins at about 120 °C where

$$w_H^{105}(t_e) = 0.21c\left(\frac{t_e}{t_e + t_e}\right), \quad t_e = 23 days \qquad 6.52$$

where c is the mass of cement per cm^3 of concrete and t_e is the equivalent hydration period which is calculated as follows

$$t_e = \int b_{Æ} b_T dt \qquad 6.53$$

where

$$b_{Æ}(f) = \frac{1}{1 + (3.5 - 3.5f)^4} \qquad 6.54$$

$$b_T(T) = \exp\left[\frac{Q}{R}\left(\frac{1}{T_{ref}} - \frac{1}{T}\right)\right] \qquad 6.55$$

Finally, typical values of $f_d(T)$ are plotted by Harmathy and Allen (1973) and it is assumed that $f_d(T) = \frac{0.05T}{600}$.

6.3.3. A Validation for Coupled Moisture/Thermal Model

The developed approach for the coupled moisture transport and heat transfer is implemented into a MATLAB code and was coupled with COMSOL Multiphysics. In order to verify the model, an experimental study has been chosen which is a large-scale reinforced concrete (MAQBETH mock-up) performed by the French Atomic Energy Commission (Ranc et al, 2003). The MAQBETH mock-up is a reinforced hollow concrete cylinder with inner and outer diameters of 1.0 m and 2.2 m, respectively, and a height of 3 m, as shown in Figure 6-17 and Figure 6-18. This structure was heated to 200 °C from the inside of the hollow cylinder and maintained at 200 ° C for several hundred hours. The outside surface of the concrete cylinder was cooled by convective heat transfer to the air, as shown in Figure 6-17, which produced a significant thermal gradient in the radial direction. Several sensors were placed at a number of radial positions inside the structure to measure the spatial and temporal evolution of temperature, gas pressure and relative humidity.

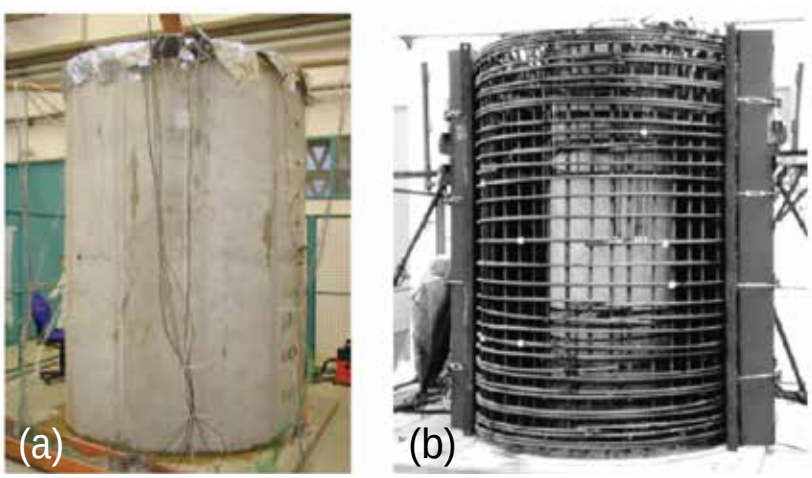

Figure 6-17 General view of MAQBETH mock-up (a) and cylindrical steel reinforcement (b) (Ranc et al, 2003).

Since the geometry and thermal and moisture boundary conditions are axisymmetric, it's convenient to model this problem as a 2D axisymmetric. Figure 6-19 shows the initial and boundary conditions of the 2D axial symmetric model used in the simulation. The initial temperature and relative humidity are assumed to be 20 °C and 0.96, respectively, as in Bary et al. (2012). A vapor pressure of 2,500 Pa which defines the relative humidity is implemented into the inner and outer surfaces for moisture diffusion. The bottom and top of concrete cylinder are insulated for both physics. A heat flux of h=10 W/m^2°C is considered in the outer surface of concrete cylinder with a constant air temperature of 20 °C as shown in Figure 6-19. A prescribed temperature profile is applied to the inner surface of cylinder as shown in Figure 6-19.

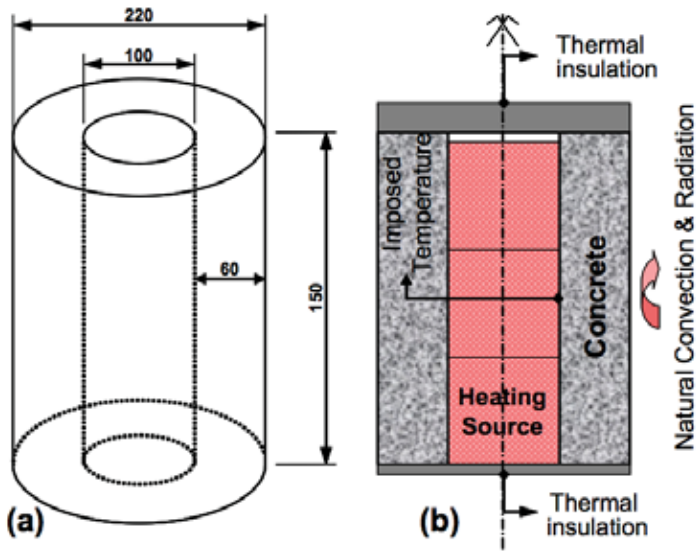

Figure 6-18 (a) Geometric characteristics of MAQBETH mock-up concrete hollow cylinder (Ranc et al, 2013) and (b) schematic description of the experiment (Bary et al, 2012).

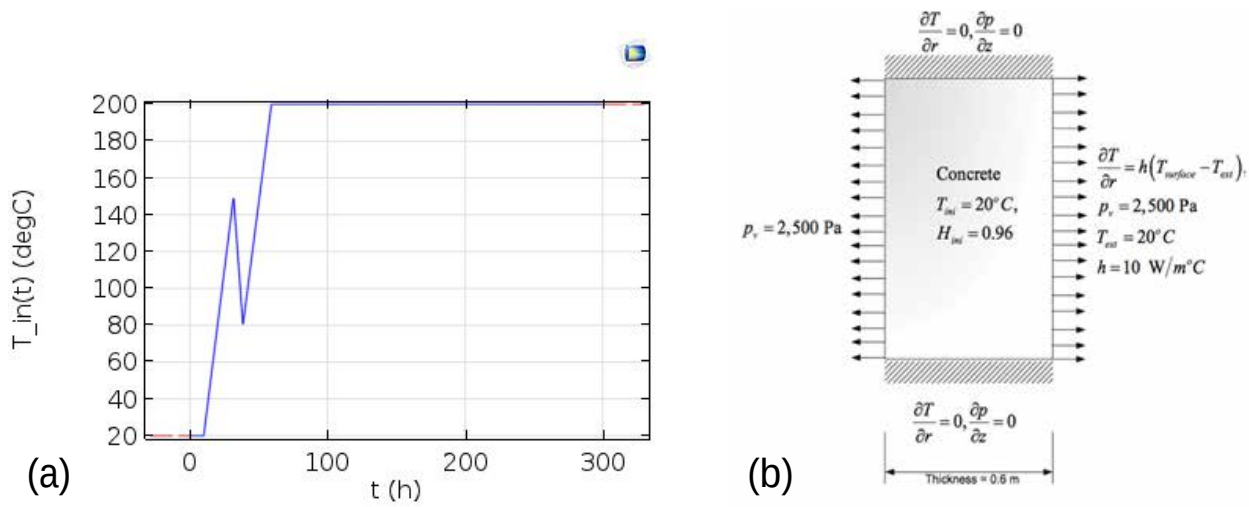

Figure 6-19 (a) The thermal loading history on the inner surface, (b) initial conditions and time history of boundary conditions applied to the 2D axial symmetric model (Saouma et al, 2015).

The concrete composition and characteristics of the MAQBETH mock-up are listed in Figure 6-4. This information is used to calculate moisture capacity function and dehydrated water term. In this simulation, due to the small total volumetric fraction of reinforcing steel bars in the structure, the effect of steel reinforcing bars on the thermal and moisture diffusion processes was ignored.

Figure 6-20 shows the 2D axial symmetric finite element mesh used in the simulation, and contours of the simulated temperature and relative humidity fields at the time 250 hours after the heating started, are presented in Figure 6-21 and Figure 6-22 for both 2D and 3D representation. To resolve the steep gradients of the relative humidity near both the inner and outer surfaces, the mesh was refined in the radial direction near both surfaces. It is obvious that the heating near the inner surface dries up the adjacent concrete and leads to the reduction of pore relative humidity (i.e., the reduction of moisture content). It is noted that because of the low moisture diffusivity of the concrete, the simulated relative humidity field exhibits steep gradients near both the inner and outer surfaces of the hollow concrete cylinder.

Time history of temperature and relative humidity are compared with the experimental data and the developed model is in a good agreement with experimental results which validates the model. These quantitative comparisons are shown in Figure 6-23 and Figure 6-24.

Table 6-4 Composition of Concrete in MAQBETH Experiment (Bary et al, 2012).

Data	Value
Cement mass (m_c) (CEM I 52,5 Lafarge)	354 kg/m^3
Aggregate mass (m_a)	1877 kg/m^3
Calcium-siliceous gravel 5-20 mm	715 kg/m^3
Fine calcium-siliceous gravel 5-14 mm	402 kg/m^3
Siliceous sand 0-5mm	760 kg/m^3
Mix water (m_w)	154 kg/m^3
Water/cement ratio	0.43
Hydrated water (d_0)	0.9*0.21*m_c kg/m^3

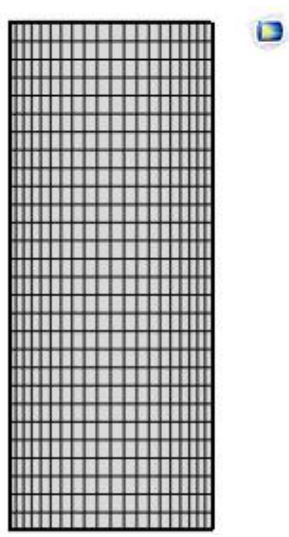

Figure 6-20 2-D Finite element mesh (finer around edges).

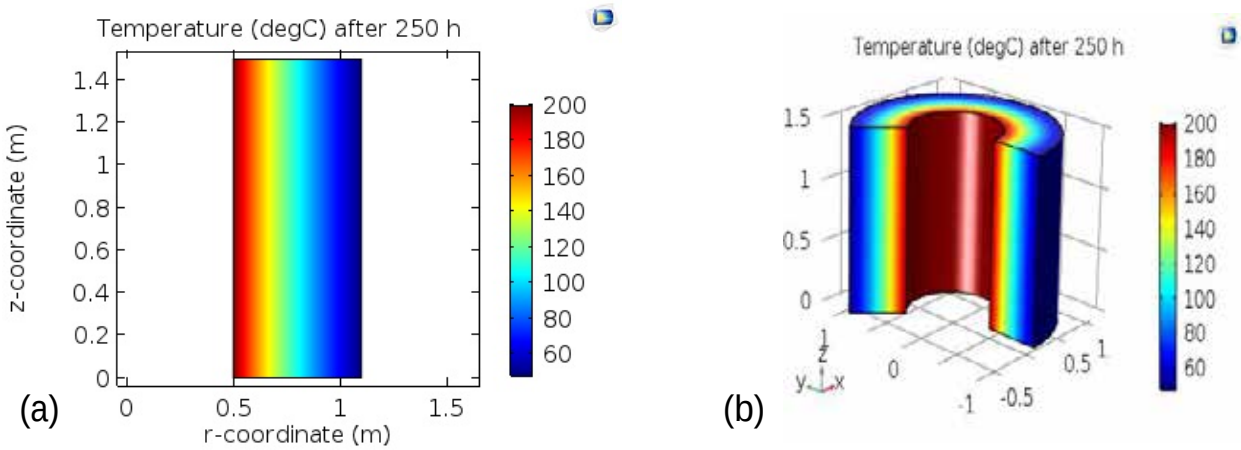

Figure 6-21 Simulated temperature field in 2D (a) and 3D representation (b) at the time 250 hours after the heating started.

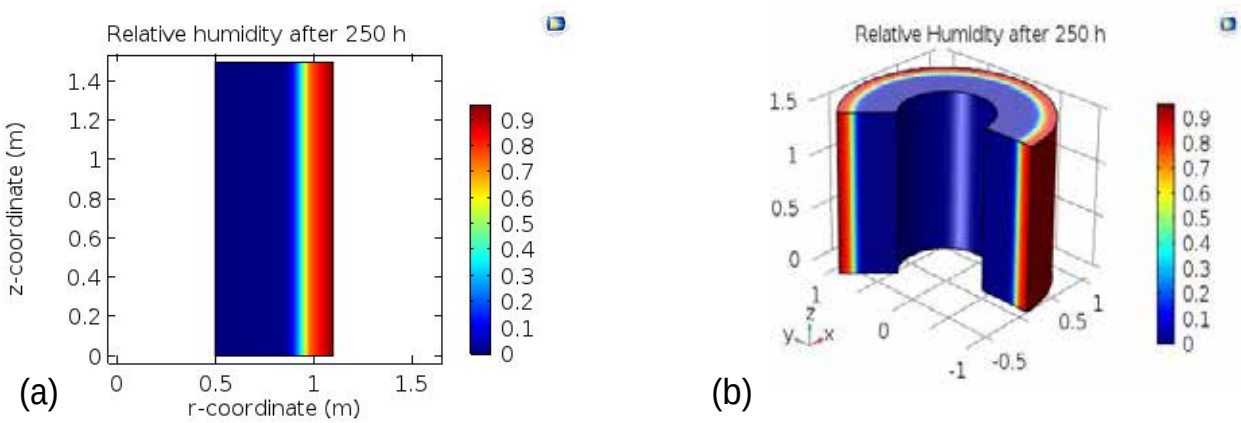

Figure 6-22 Simulated relative humidity field in 2D (a) and 3D representation (b) at the time 250 hours after the heating started.

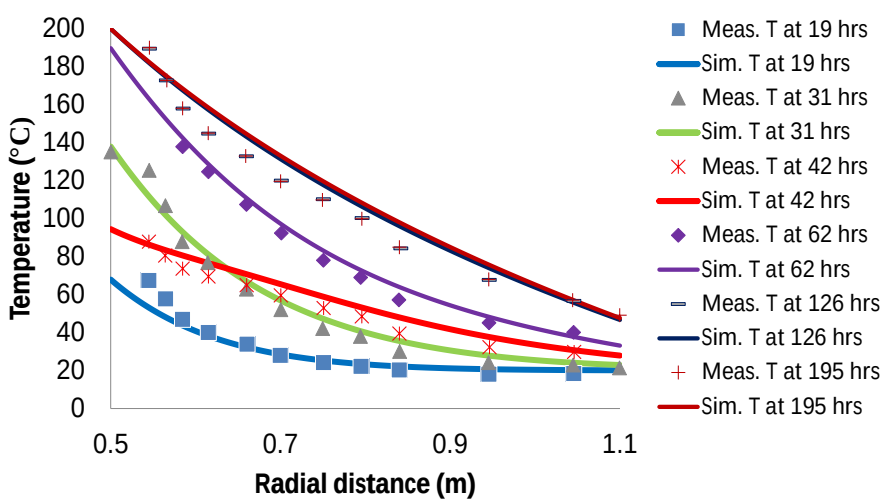

Figure 6-23 Comparisons of radial temperature profiles at various times between the simulation (lines) and experimental measurements (symbols).

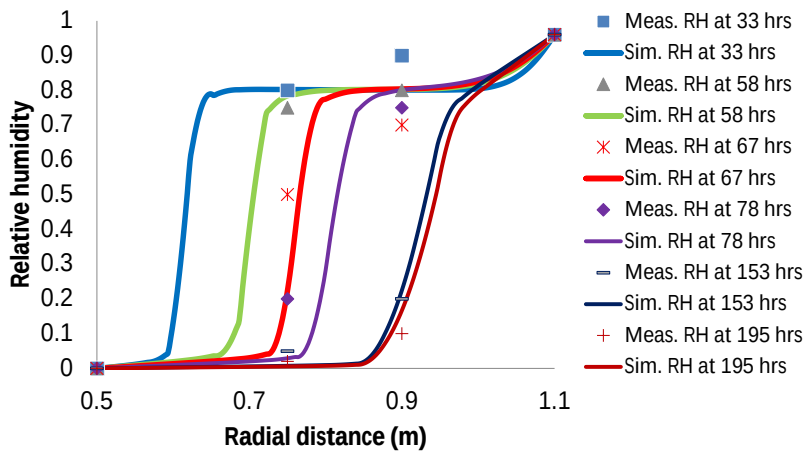

Figure 6-24 Comparisons of radial relative humidity profiles at various times between the simulation (lines) and experimental measurements (symbols).

Figure 6-25 and Figure 6-26 show the spatial distributions of the humidity (moisture) diffusivity (D_h) and moisture capacity ($\partial\omega/\partial\emptyset$) within the concrete structure at the time 250 hours after the start of heating. The whole concrete structure starts with constant values of D_h and $\partial\omega/\partial\emptyset$ before heating. Due to the strong dependency of these two moisture transport properties on the temperature and relative humidity, strong spatial variations in D_h and $\partial\omega/\partial\emptyset$ appear as they evolve with the transient temperature and relative humidity fields. This demonstrates the necessity of a fully coupled solution strategy for a coupled thermal/moisture diffusion model.

It is worthwhile to mention that this problem is a challenging benchmark model and it is not easy to converge and some challenges are faced up with some convergence errors such as singularity error and threshold. Different techniques were used to perform this modeling due to high dependency of two physics as well as highly nonlinear boundary conditions which are chosen for this benchmark problem. Here, with an appropriate stabilization method, nonlinear Newton approach, and increasing the number of iterations in each time step, proper solutions could be obtained for this highly nonlinear challenging problem.

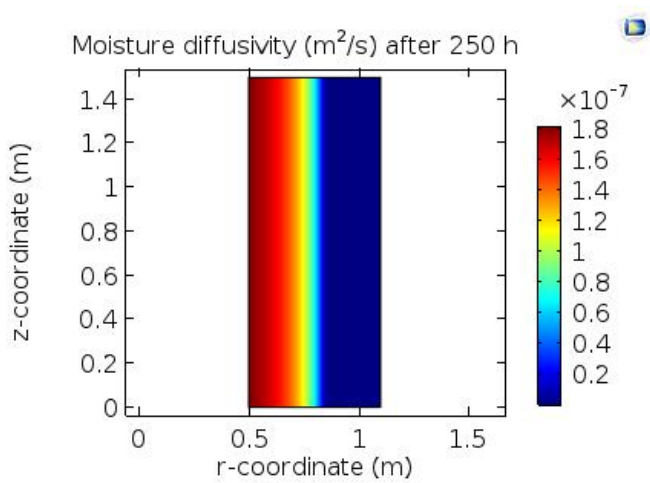

Figure 6-25 Spatial distributions of the humidity diffusivity (D_h) at 250 hours.

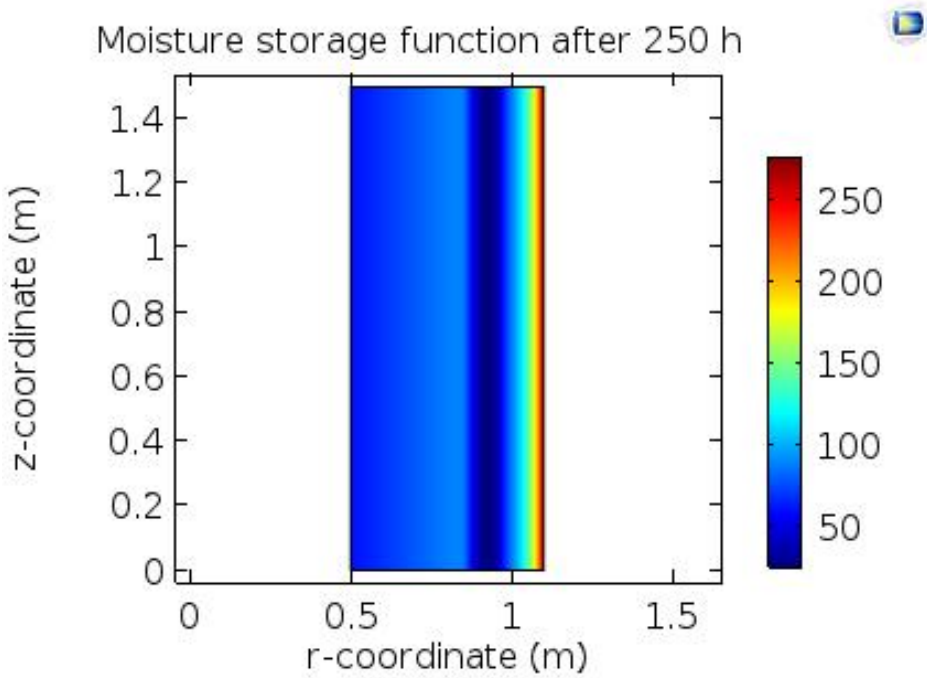

Figure 6-26 Spatial distributions of the moisture capacity $\partial\omega/\partial\emptyset$ at 250 hours.

6.3.4. Thermo-Hygro Modeling of Dry Cask Structure

This verified hygro-thermal model is used to evaluate the behavior of the dry cask structure. Steel parts are not considered in this study and just the concrete outerpack is modeled. As a boundary condition for heat transfer, it is assumed that the internal edge of the concrete outerpack is *80°C* and the external edge which is in the vicinity of the environment and temperature is assumed to be *20°C.* The external edge of the concrete outerpack has a relative humidity of 0.96 and the internal part is insulated as moisture transfer boundary conditions. The behavior of the concrete outerpack in investigated during 3 years of the performance and similar mesh size as same as the previous section is assumed.

Contours of the simulated temperature and relative humidity fields at the time 3 years after the heating started, are presented in Figure 6-27 and Figure 6-28 for both 2D and 3D representation. Here, it can be seen that relative humidity is reduced near the internal edge since the heating dries up the adjacent concrete.

Time history of temperature and Relative humidity are shown in Figure 6-29 and Figure 6-30 for the bottom edge of the concrete outerpack. The temperature history shows an uniform behavior during different time steps, but the relative humidity is different until the first year and after that it doesn't change significantly.

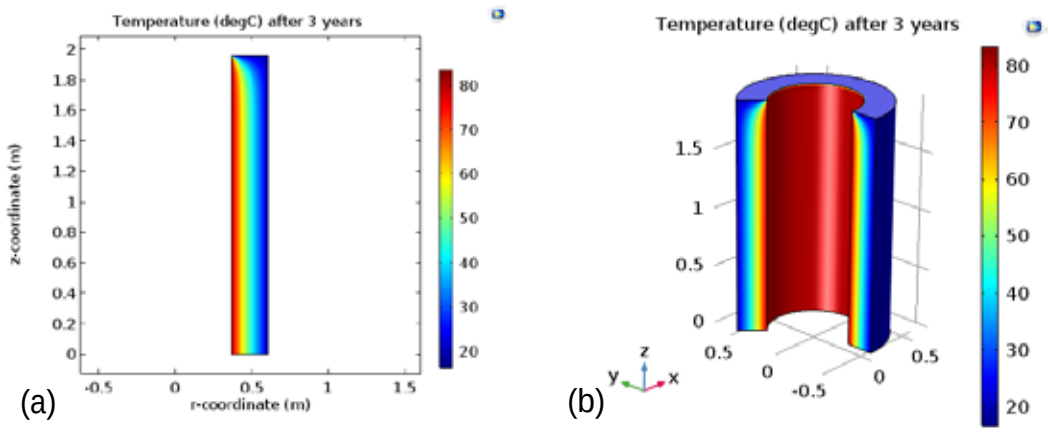

Figure 6-27 Simulated temperature field in 2D (a) and 3D representation (b) at the time 3 years after the heating started for dry cask structure.

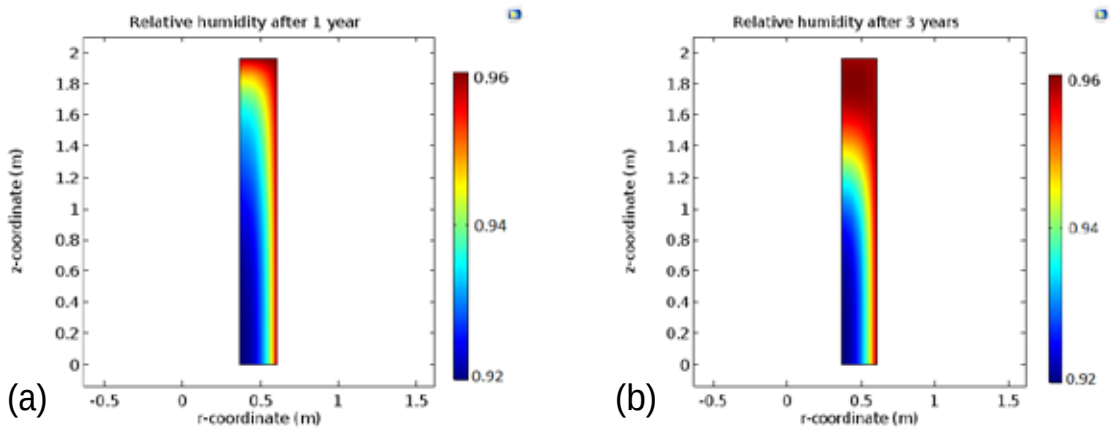

Figure 6-28 Simulated relative humidity field after 1 year (a) and 3 years (b) for dry cask structure.

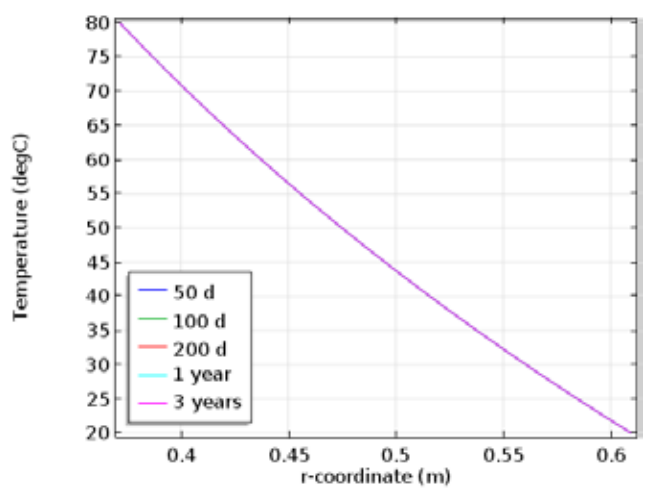

Figure 6-29 Comparisons of radial temperature profiles at various times between the simulation for dry cask structure.

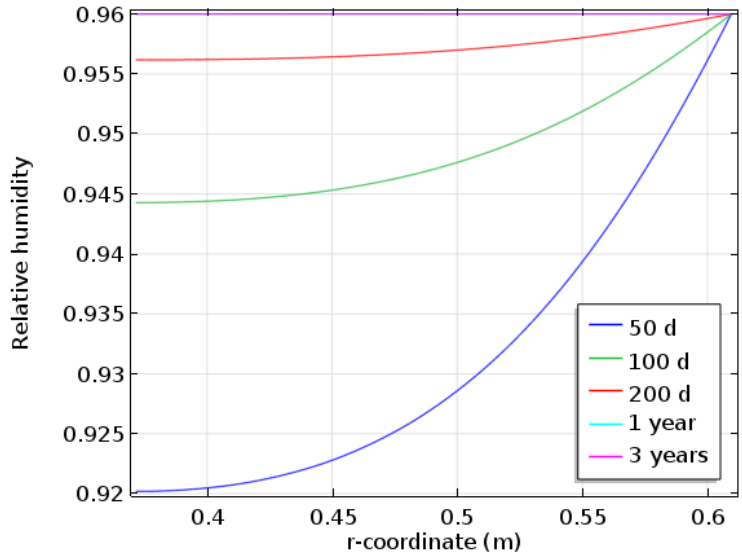

Figure 6-30 Comparisons of radial relative humidity profiles at various times between the simulation for dry cask structure.

Figure 6-31 and Figure 6-32 show the spatial distributions of the humidity (moisture) diffusivity (D_h) and moisture capacity ($\partial\omega/\partial\emptyset$) within the concrete outerpack at the time 3 years after the start of heating. The entire concrete structure starts with constant values of D_h and $\partial\omega/\partial\emptyset$ before heating. The strong dependency of the moisture diffusivity and moisture storage function on the temperature are seen here.

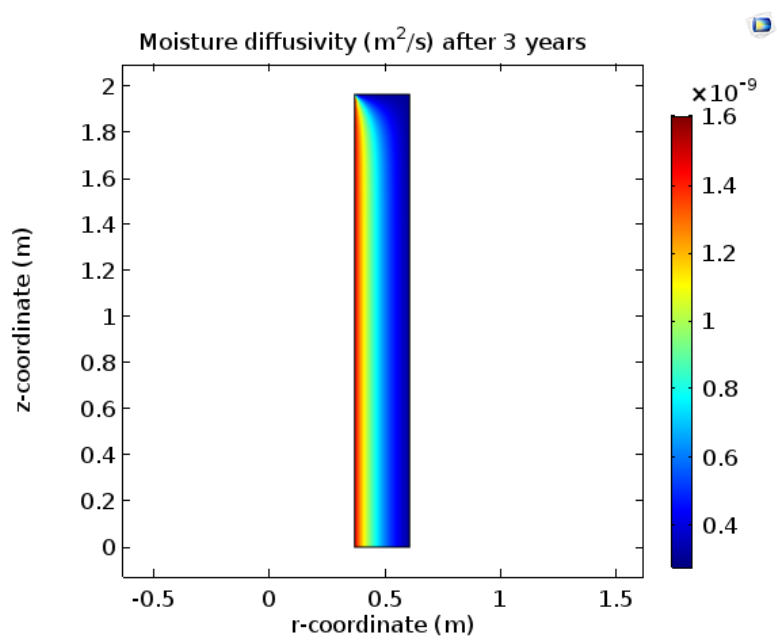

Figure 6-31 Spatial distributions of the humidity diffusivity (D_h) after 3 years for dry cask structure.

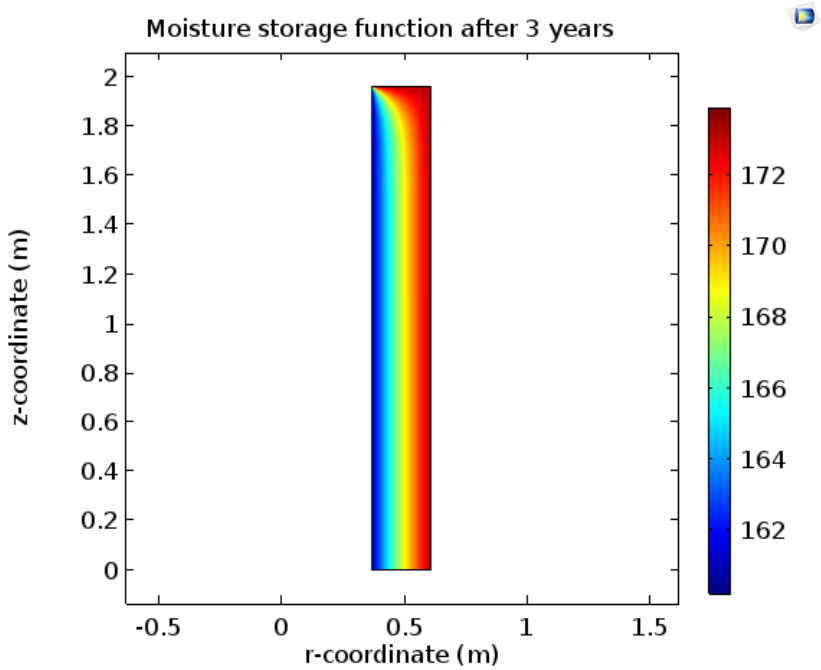

Figure 6-32 Spatial distributions of the moisture capacity $\partial\omega/\partial\emptyset$ at 3 years for dry cask structure.

Solid mechanics can be coupled to the proposed thermal-hygro model to capture induced stresses and strains within the concrete outerpack through the thermal coefficient of concrete. Figure 6-33 shows the contour of first principal stress and von-Mises stress for the concrete outerpack. The stress level reaches to 12 MPa near the outside surface of the concrete cask.

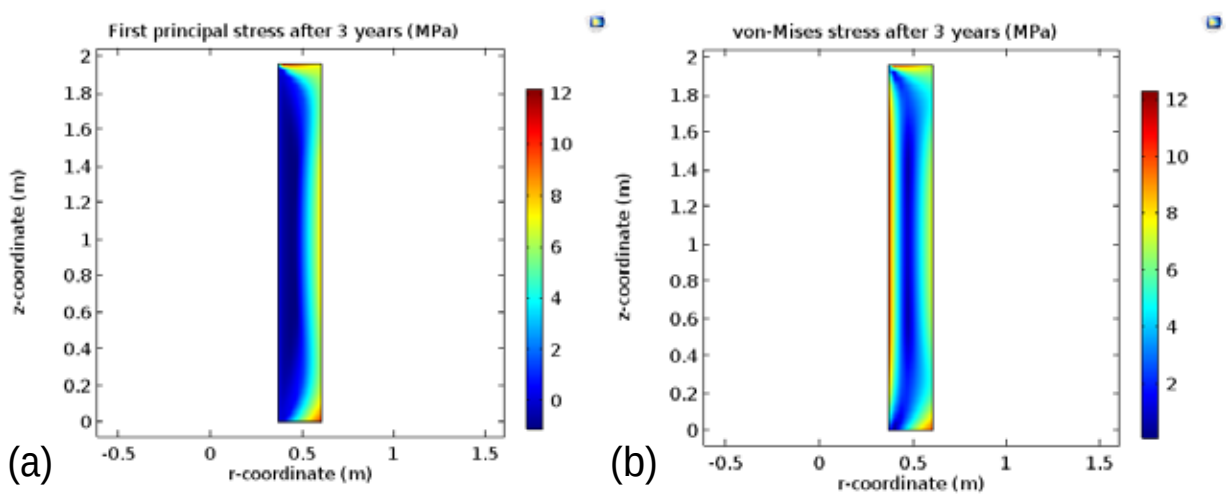

Figure 6-33 Major principal stress (a) and von-Mises stress (b) at the time 3 years after the heating started for dry cask structure.

Figure 6-34 show the contours of first principal strain and volumetric strain for the concrete outerpack. The coupling between moisture and temperature induces a higher strain on the internal surface of the concrete cask.

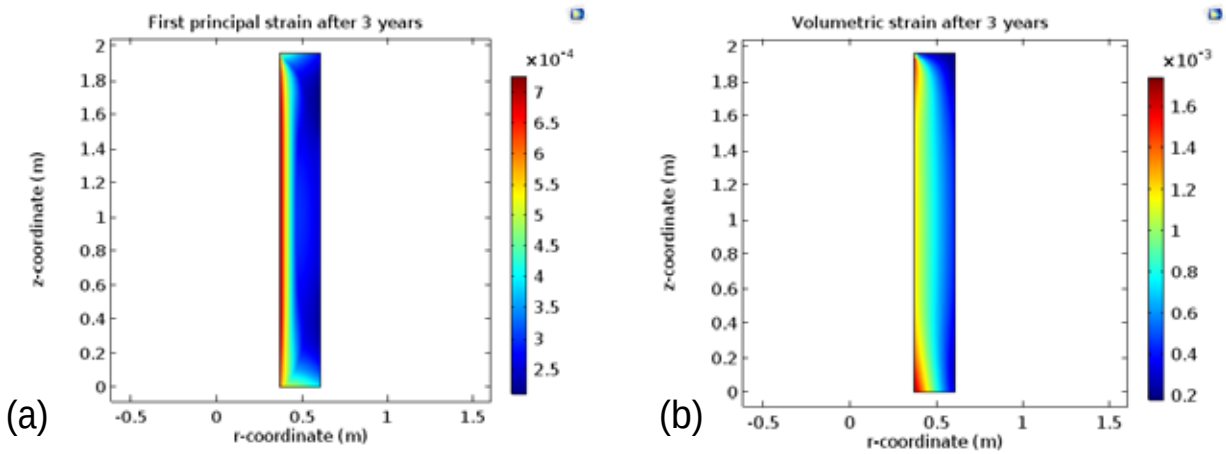

Figure 6-34 Major principal strain (a) and volumetric strain (b) at the time 3 years after the heating started for dry cask structure.

6.4. ALKALI-SILICA REACTION (ASR) SWELLING MODEL

In this section, the hydration process of two different mixtures which are utilized in the University of Houston, are compared to each other. One mixture is the reference concrete called the self-consolidated concrete (SCC), and the other one is Alkali mixture which is developing ASR (NaOH). As a result of this section, different concentrations of different species are computed using Scanning Electron Microscopy (SEM) methodology implemented in the CEMHYD3D code (Bentz 2012, 2001, 2000, and 1997) developed at the National Institute of Standards and Technology (NIST) and then mechanical properties of the early age of concrete are assigned.

There are many numerical models available for modeling of ASR in concrete. Among them, Ulm et al. (2000) developed a coupled thermo-hydro-mechanical-chemical (THMC) model which is thermodynamically consistent based on the extensive experimental work by Larive (1998). This model does not consider the effect of stress state on the reaction kinetics and volumetric swelling and only considers isotropic swelling. Later on, Saouma and Perotti (2006) developed a coupled THMC model for ASR swelling which is based on the model by Ulm et al. (2000), where they considered the effect of stress on both the ASR reaction kinetics and the anisotropic volumetric expansion. Saouma and Perotti (2006) showed that this ASR strain is a strain tensor, which is temperature dependent. In the following, sections these models are introduced briefly, and then benchmark problems, which are taken from Multon and Toutlemonde (2006), are studied using COMSOL Multiphysics (2015). Later, the verified model has been implemented to the model concrete cask to capture the long term behavior under ASR.

6.4.1. A Comparison between the Hydration Process

6.4.1.a. Introduction

Two concrete mixtures were prepared at the University of Houston as shown in Table 6-5, which are the reference concrete SCC, and the NaOH mixture in order to accelerate the ASR process (see also Section 2.3).

Table 6-5 Composition of Concrete Mixtures (Volume of Each Mixture is 2.294m^3)

Material	Unit	SCC	NaOH
Cement	kg	12.84	17.10
Type F Fly Ash	kg	4.26	0.00
3/8" Pea Gravel	kg	48.67	48.67
Sand River	kg	43.09	43.09
Water	kg	5.72	5.72
Admix #1 (Pozzolith 200N)	ml	45.84	45.84
Admix #2 (Glenium 7500N)	ml	91.97	91.97
Additional NaOH (NaOH)	kg	-	0.15
Additional Chloride ($CaCl_2$)	kg	-	-

To simulate the ASR effects on concrete, it is necessary to investigate the hydration process of the cement paste. Simulating the hydration process of these two mixtures helps to define the steady state of initial concentrations of solid phases. Later on, the result of this hydration process will be implemented into ASR modeling.

The NIST developed the FORTRAN code named "CEMHYD3D" to simulate the hydration process of cement paste, and to determine transport and mechanical properties of concrete (Bentz, 2000). CEMHYD3D is a three-dimensional computer model for creating a microstructure and simulating the Portland cement hydration. First, the particle size distribution (PSD) of cement is measured, and a set of two-dimensional Scanning Electron Microscopy (SEM) backscattered electron and X-ray microanalysis image of the cement of interest are obtained. Based on analysis of these images and the measured PSD, three-dimensional microstructures of various water-to-cement ratios are created using CEMHYD3D with matching the phase volume fractions and surface area fractions of the two-dimensional images. Cellular-automata rules are applied into the microstructure to model the chemical reactions for all of the major phases during the evolving hydration process. Bentz (1997) stated that the dissolution cycles used in the model have been calibrated to real time using a single set of parameters for two cements at three different water-to-cement ratios. He validated the proposed model with experimental measurements for degree of hydration, heat release (ASTM C186, 2005), and chemical shrinkage based on this calibration. The degree of hydration is evaluated to predict the compressive strength of mortar cubes (ASTM C109, 2007) for the two mixtures. The effects of temperature were examined by performing hydration experiments at 15°C, 25°C, and 35°C and applying a maturity-type relationship to determine a single degree of hydration. Bentz (2000) also considered the effects of saturated and sealed condition of curing and implemented it into the code. Figure 6-35 shows the microstructure presentation of hydration process as an example. For more information refer to Bentz (2012, 2001, 2000, and 1997).

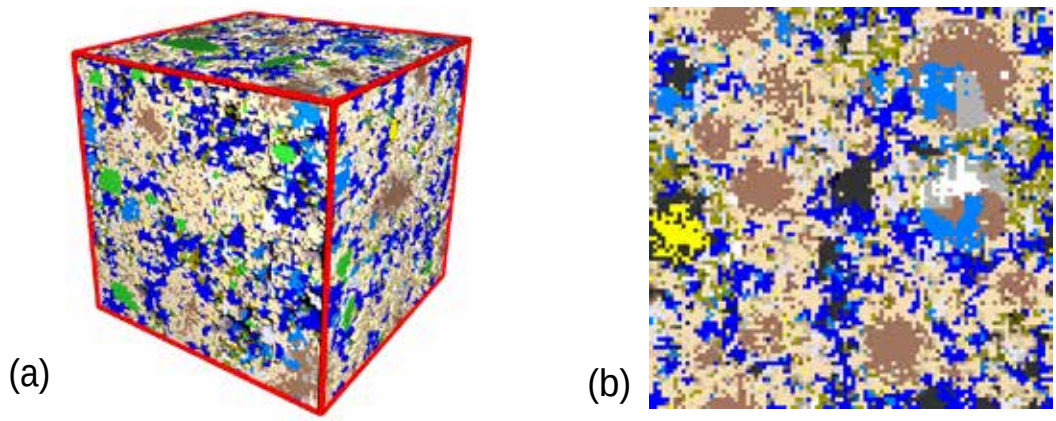

Figure 6-35 3-D (a) and 2-D (b) representation of microstructure during the hydration process in CEMHYD3D.

To process the input SEM/X-ray images and to determine the distribution of phases, a decision tree is traversed for each pixel location in the images. An example of a decision tree for a typical cement powder is shown in Figure 6-36. In Figure 6-36, X* represents a critical threshold grey level value. Pixels having a grey level greater than the value of X* are considered to contain the element of interest and those with a grey level below X* are classified as not containing the element (Bentz et al., 2000). For an isotropic system, the area fraction of a phase present in a 2-D image will directly correspond to its volume fraction in three dimensions (Bentz et al., 2000).

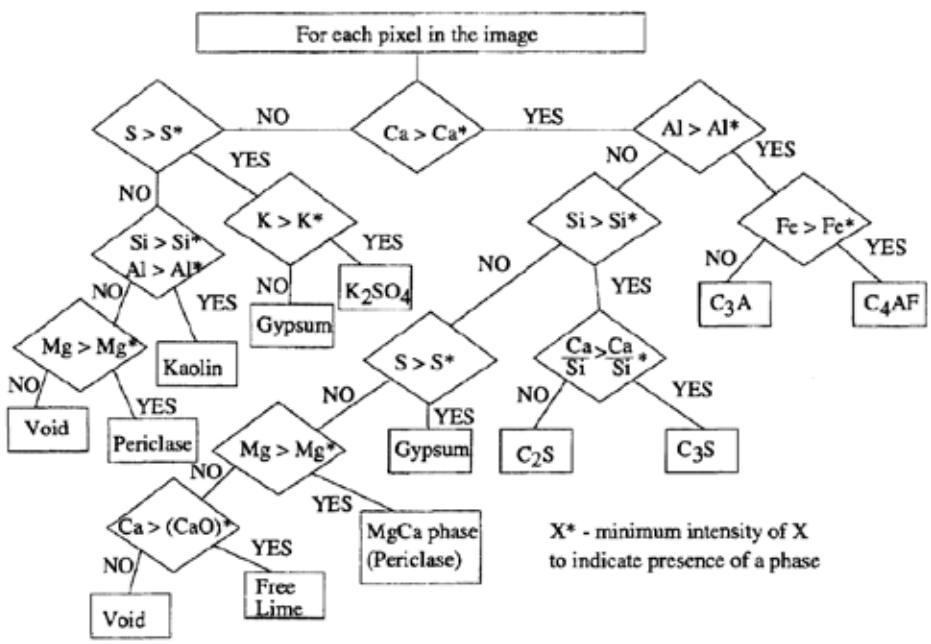

Figure 6-36 Segmentation algorithm for separating Portland cement into its components (Bentz et al., 2000).

A finite element FORTRAN code called elas3d.f which is available inside of CEMHYD3D program is used for computing the elastic moduli of composite materials. The program takes a 3-D digital image of the microstructure, assigns elastic moduli tensors to each pixel according to what

material phase is present, and then computes the effective composite linear elastic moduli of the material (Bentz, 2001).

As a result of this study, initial concentration of solid phases in cement paste are determined as well as transport and mechanical properties.

6.4.1.b. Input parameters

PSDs of cement, aggregate, fly ash, slag, and filler are important parameters, which can be input into this software. Portland cement with the microstructure image shown in Figure 6-37 is considered in the hydration process for both SCC and NaOH mixtures. The PSDs of Portland cement Type I is available by in NIST (2012). Volume fraction of each cement component is also presented in Figure 6-37. For SCC, cement and fly ash with a specific gravity of 2.22 has been considered in the simulation. PSD of fly ash was assumed to be the same as those of Portland cement Type I.

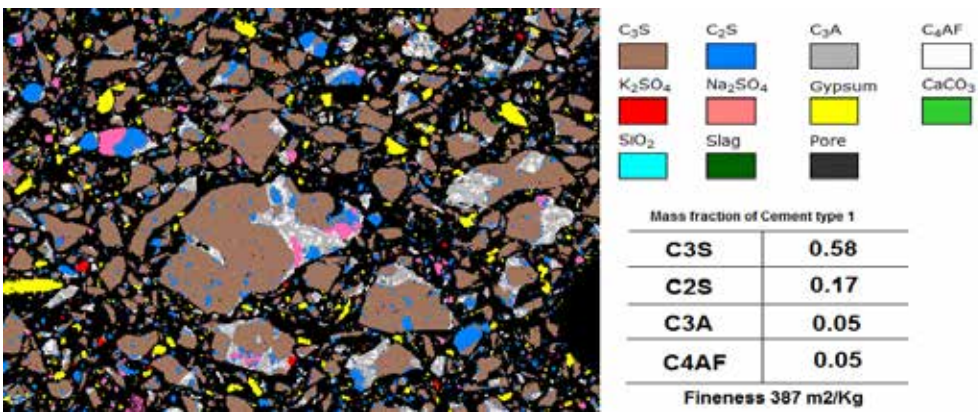

Figure 6-37 2-D representation of U.S. cement Type 1 with considered volume fraction in CEMHYD3D code (Bentz et al., 2000).

Grading of the aggregate should be determined and inputted into the code. The mechanical and geometry properties of coarse and fine aggregate, respectively, are presented in Figure 6-38 and Figure 6-39.

Figure 6-38 Description of coarse aggregate in CEMHYD3D code (Bentz et al., 2000).

Figure 6-39 Description of fine aggregate in CEMHYD3D code (Bentz et al., 2000).

Based on the information presented in Table 6-5, the water-to-cement ratio is equal to 0.344 for the NaOH mixture and 0.445 for the SCC mixture. Figure 6-40 shows the microstructure of the two mixes.

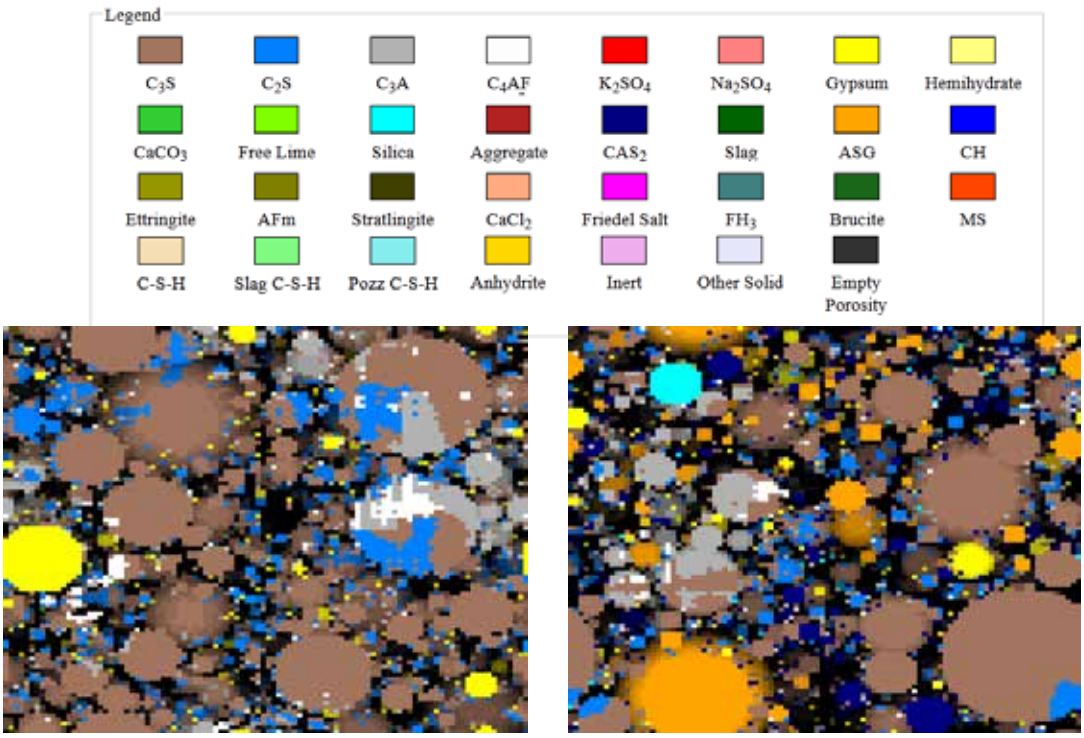

(a) NaOH microstructure (b) SCC microstructure

Figure 6-40 Microstructure of mixtures by CEMHYD3D code.

Mass fraction or volume fraction of each component should be input into the code. This information is sufficient to perform the mixing. The next process is the hydration and some additional information such as reaction activation energies, hydration behavior options, surface deactivation, C-S-H nucleation seeding, curing conditions, aging parameters, chemical shrinkage, saturation conditions, and simulation parameters including: percolation of porosity time, percolation of total solids time, individual particle hydration time, and hydrating microstructure time, should be input in the code.

6.4.1.c. Hydration results

CEMHYD code is implemented to capture the behavior of cement hydration in 28 days. System size for the binder is 100 microns in each direction and for concrete is 50 millimeters in each direction with a resolution of 1.90 millimeters/pixel. Figure 6-41 compares the different behavior of SCC and NaOH mixture. The results are presented by evaluating degree of hydration, porosity, PH of solution, heat release rate, chemical shrinkage, solution conductivity, volume fraction of solid phases and components, and concentration and activity of components.

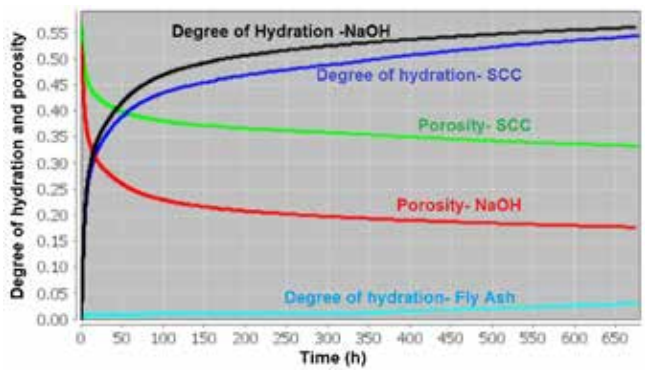

(a) degree of hydration and porosity

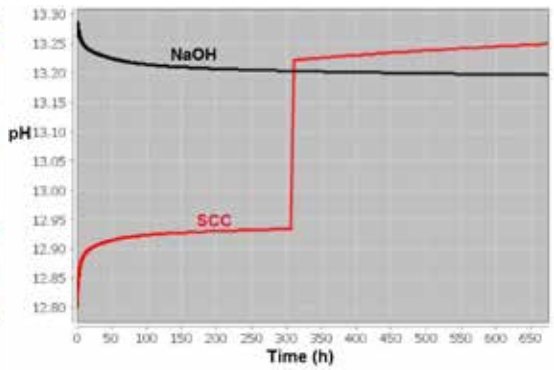

(b) PH of solution

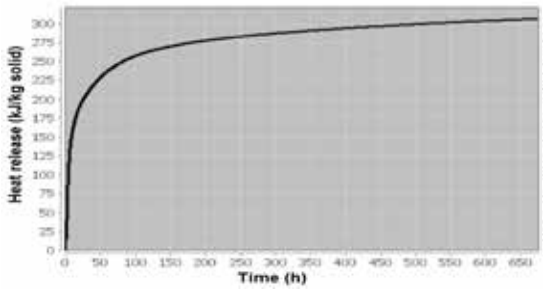

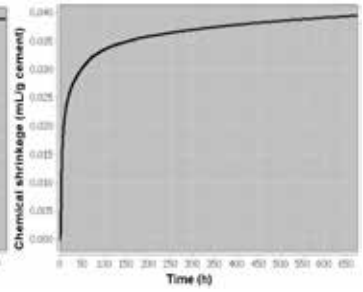

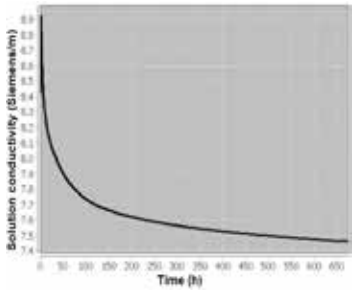

(c) heat release rate (d) Chemical shrinkage (e) Solution conductivity

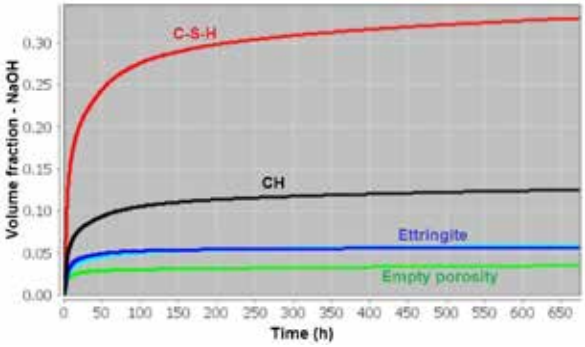

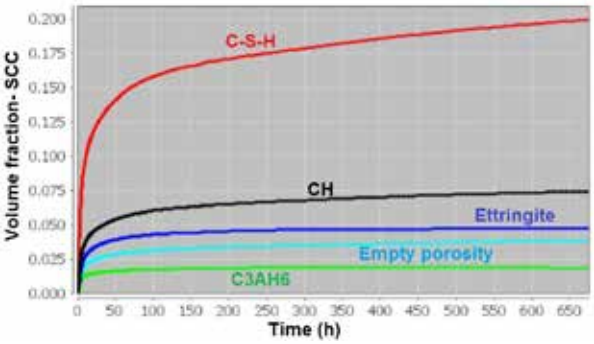

(f) Volume fraction of NaOH solid phases (g) Volume fraction of SCC solid phases

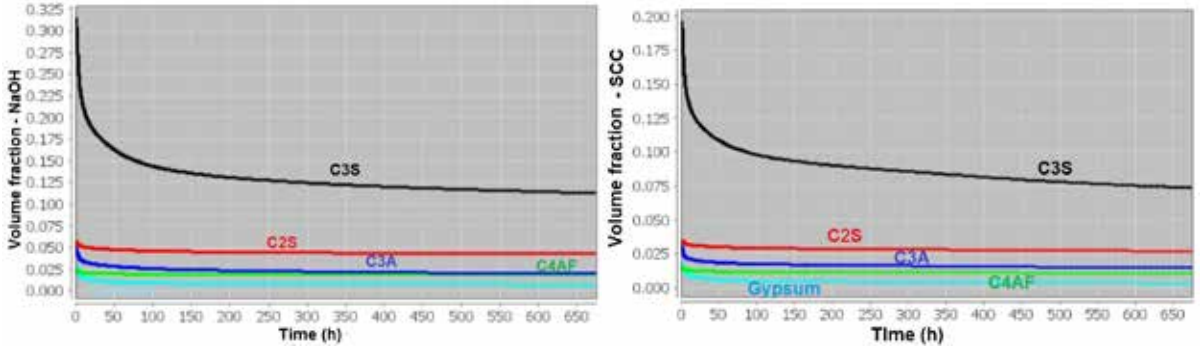

(h) Volume fraction of NaOH components (i) Volume fraction of SCC components

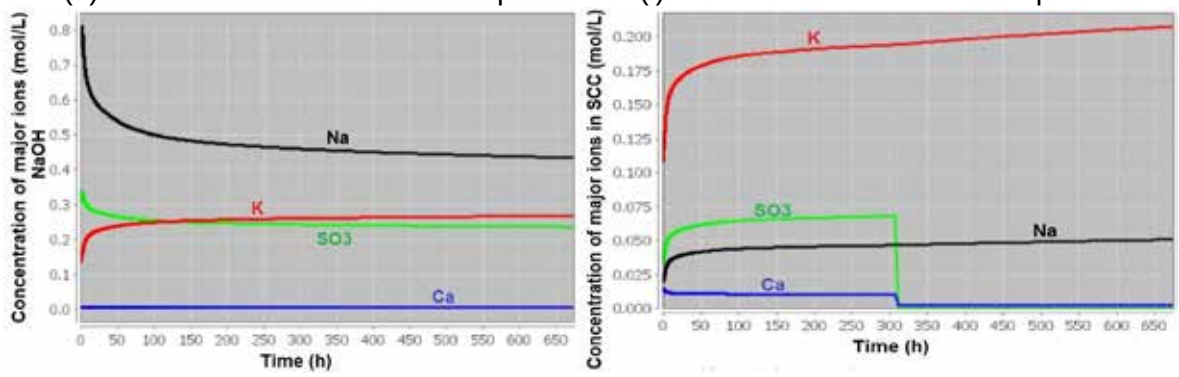

(j) Concentration of NaOH ions (k) Concentration of SCC components

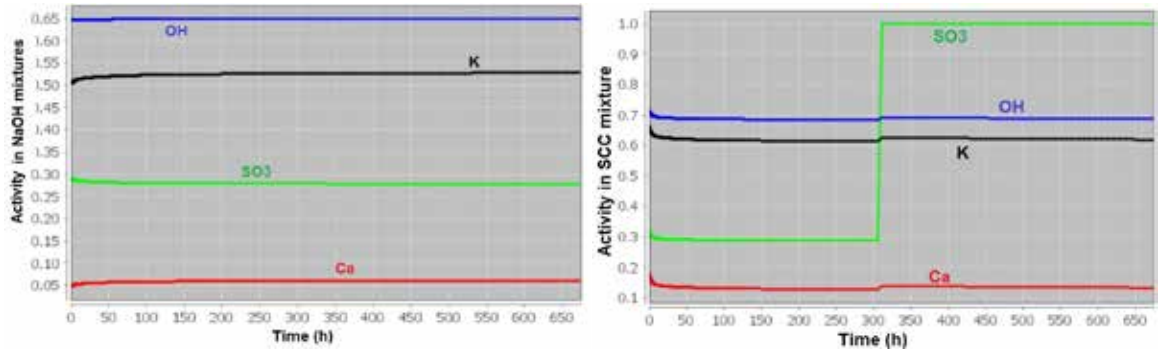

(l) Activity of NaOH components (m) Activity of SCC components

Figure 6-41 Comparison of the hydration process for SCC and NaOH solution.

As seen in Figure 6-41, volume fraction of each solid phase and component is different for these two mixtures and it can be stated that the additional NaOH changes the properties of cement paste and concrete significantly. Fly ash changes the pH of SCC mixture as shown in figure which diffuses certain chemical components after 300 hours. The steady state volume fraction of components will give us the concentration of each solid phase. Finally, Figure 6-42 shows the microstructure of hydration process after 28 days for NaOH and SCC mixtures, which is another capability of the CEMHYD3D code.

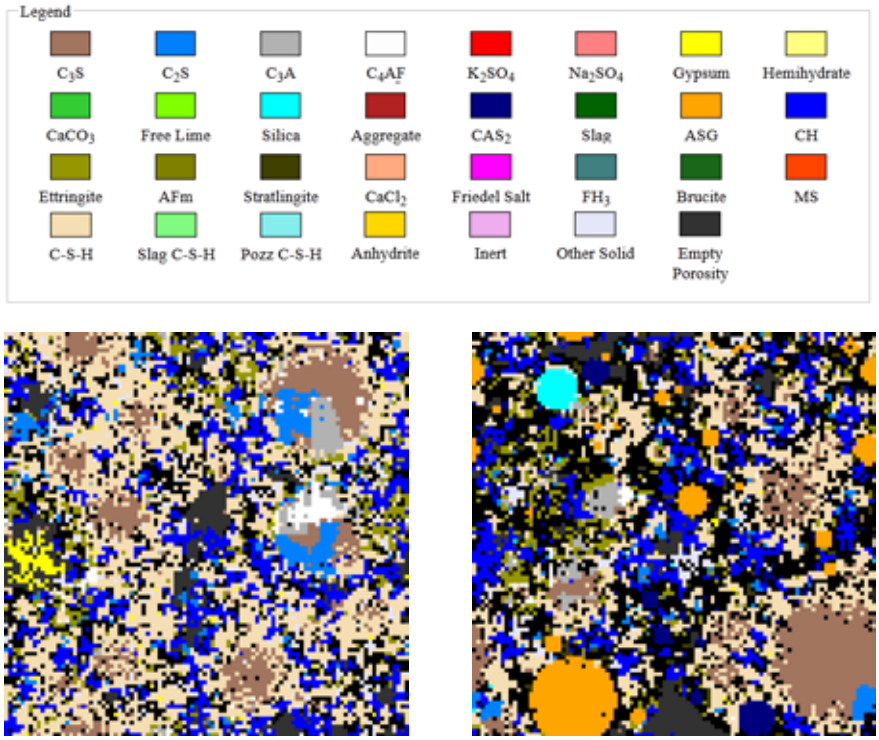

(a) NaOH mixture (b) SCC mixture

Figure 6-42 Microstructure of the hydrated concrete at 28 days.

As stated before, CEMHYD3D code has a capability to calculate mechanical properties of cement paste and concrete mixtures. Table 6-6 shows computed mechanical properties for 28 days.

Table 6-6 Mechanical properties of Alkali specimen (Elastic modulus is in GPa and strength is in MPa).

	Property	1 day	4day	7day	10day	13day	16day	19day	22day	25day	28day
Cement paste	Bulk modulus	13.15	13.71	13.92	14.03	14.12	14.19	14.25	14.30	14.34	14.30
	Shear modulus	7.19	7.53	7.67	7.73	7.79	7.84	7.88	7.91	7.94	7.95
	Young's modulus	18.25	19.11	19.44	19.59	19.75	19.86	19.97	20.04	20.12	20.12
	Poisson's ratio	0.268	0.268	0.267	0.267	0.267	0.267	0.266	0.266	0.266	0.265
Concrete	Effective Young mod	38.23	38.76	38.96	39.066	39.16	39.22	39.29	39.33	39.38	39.38
	Effective shear modulus	15.46	15.68	15.76	15.80	15.84	15.87	15.89	15.91	15.93	15.93
	Effective bulk modulus	24.15	24.47	24.59	24.65	24.71	24.74	24.78	24.81	24.83	24.81
	Concrete cube compressive strength	34.60	36.09	36.66	36.95	37.23	37.42	37.60	37.74	37.89	37.87

6.4.1.d. Discussion

For the solid phase chemistry of the concrete, it is needed to run a hydration model like Gem (Kulik et al., 2013) and CEMHYD3D or some empirical approaches such as that proposed by Parrot and Killoh (1984) should be used. CEMHYD3D was used to model the hydration process of the mixtures. These multiple FORTRAN codes are widely used in the literature and they were validated with experimental studies several times. Cement, fly ash, and aggregate properties were input in this codes and pH, volume fraction of each solid phase and ion activity were measured.

First it was seen the NaOH can change the properties of concrete significantly. Different concentration values can be seen for NaOH and SCC mixtures. Then a study was performed to see if the hydration process is complete after 28 days or not and also to see how water-to-cement ratio can change the behavior of cement hydration. If the results of 90 days vs. 28 days are compared, the concentrations of cement clinkers are in the same order of magnitude. Therefore, for boundary conditions and initial solid phase assemblage for the domain, we can neglect the remaining C3S, C2S, C3A and C4AF (assuming they are no longer reactive).

6.4.2. 1st-Order ASR Reaction Kinetics

In order to investigate the long term effects of ASR expansion on concrete specimens, ASR should be modeled for the same duration and the changes in the degradation of concrete strength should be calculated. Until now, different models were developed to determine the ASR effect on concrete. Between these models Ulm et al. (2000) introduced a 1st order kinetics model based on extensive experimental works of Larive (1998). Ulm et al. (2000) stated that the first order ASR reaction kinetics is represented as:

$$1 - x = t_c(x,q)\frac{dx}{dt} \qquad 6.56$$

in which ξ is extent of the ASR reaction ranging from 0 (initial state) to 1 (fully developed), θ is the temperature, and t_c is the characteristic time of the reaction.

With some minor manipulations of Ulm et al. (2000) model, Saouma and Perotti (2006) showed that the ASR expansion is dependent on both the temperature and the first invariant of the stress tensor $\boldsymbol{\sigma}$ as:

$$t_c(x,q) = t_c(q)/(x,q) \qquad 6.57$$

$$/(x,q) = \frac{1+\exp[-\frac{t_L(q,I_s,f_c')}{t_c(q)}]}{x+\exp[-\frac{t_L(q,I_s,f_c')}{t_c(q)}]} \qquad 6.58$$

Where, I_σ is the first invariant of the stress tensor, $f_c^{'}$ is the compressive strength of concrete, and $\tau_L(\theta, I_\sigma, f_c^{'})$ and $\tau_c(\theta)$ are two time constants of the ASR kinetics, and can be calculated based on the following equations:

$$t_c(q) = t_c(q_0)\exp[U_c(\frac{1}{q} - \frac{1}{q_0})] \qquad 6.59$$

$$t_L(q, I_s, f_c^{'}) = f(I_s, f_c^{'})t_L(q_0)\exp[U_L(\frac{1}{q} - \frac{1}{q_0})] \qquad 6.60$$

in which θ_0 is the reference temperature. Using the Arrhenius equation, the slopes U_C and U_L can be considered as activation energy constants of the characteristic time τ_c and the latency time τ_L, respectively, and Larive (1998) proposed values based on their experimental studies

$$U_C = 5400 \pm 500K \qquad 6.61$$

$$U_L = 9400 \pm 500K \qquad 6.62$$

The function $f(I_\sigma, f_c^{'})$ represents the effect of compressive stress on the ASR reaction kinetics and can be calculated as:

$$f(I_s, f_c^{'}) = \begin{cases} 1 & if \;\; I_s > 0 \\ 1 + a\dfrac{I_s}{3f_c^{'}} & if \;\; I_s < 0 \end{cases} \quad where \; I_s = s_I + s_{II} + s_{III} \qquad 6.63$$

Saouma and Perotti (2006) investigated the effect of volumetric stress on the parameter α and suggested a value of 4/3 based on experimental data. The above equation shows that when we have a tensile stress state, there is no effect of tensile stress on the reaction kinetics.

Eq. 6.56 is a nonlinear ordinary differential equation (ODE) that can be solved implicitly using Newton-Raphson iteration of Euler backward integration:

$$j = x_{n+1} - x_n - \frac{\Delta t}{t_c(q_{n+1})}\frac{1 - x_{n+1}}{l(x_{n+1}, q_{n+1})} = 0 \qquad 6.64$$

where, ξ_n and ξ_{n+1} denote the ASR extent at time t_n and $t_{n+1} = t_n + \Delta t$.

After defining the increment of ASR extension ($\Delta\xi$), we can calculate the ASR volumetric strain at each state based on the following equation:

$$\Delta e_{vol}^{ASR} = G_t(f_t^{'}, s_1 | COD)G_c(f_c^{'}, \bar{s})g(H)\Delta x e^{x} |_{q=q_0} \qquad 6.65$$

where, $f_t^{'}$ denotes the tensile strength of the concrete, and σ_1 is the major principal stress (the positive one is the tensile stress), COD is the crack opening displacement, $\bar{\sigma}$ is the ratio between

the hydrostatic stress and compressive strength of concrete, and ε^{∞} is the laboratory-determined maximum free volumetric expansion at the reference temperature θ_0 which is $\varepsilon^{\infty} = 0.00262$ according to Larive (1998). The function g(H) is a function of relative humidity and usually follows this relationship:

$$g(H) = H^m \qquad 6.66$$

The exponent m is an empirical constant and H is the relative humidity in concrete. $g(H)$ has a value between 0 to 1, and here for simplicity we assumed that it is equal to 1. The symbol | represents "or" and indicates whether if we are using linear elasticity or a smeared crack approach.

The function $\Gamma_t(f_t', \sigma_I | COD)$ defines the reduction of ASR expansion due to tensile cracking and equals to:

$$\Gamma_t = \begin{cases} \text{Elasticity}: & \begin{cases} 1 & \text{if } \sigma_I \le \gamma_t f_t' \\ \Gamma_r + (1-\Gamma_r)\dfrac{\gamma_t f_t'}{\sigma_1} & \text{if } \sigma_I > \gamma_t f_t' \end{cases} \\ \text{Smeared crack} & \begin{cases} 1 & \text{if } COD_{max} \le \gamma_t w_c \\ \Gamma_r + (1-\Gamma_r)\dfrac{\gamma_t w_c}{COD_{max}} & \text{if } COD_{max} > \gamma_t w_c \end{cases} \end{cases} \qquad 6.67$$

where γ_t is the fraction of the tensile strength beyond which gel is adsorbed by cracks and is a user input parameter in the simulation. Here, it's assumed that γ_t is equal to 0.5. Γ_r is a residual ASR expansion retention factor for ASR under tension and has a value of 0.5 in this report. COD_{max} is the maximum crack opening displacement at the current Gauss point, and ω_c is the maximum crack opening displacement in the tensile softening curve. Γ_c in Eq. 6.65 accounts for the reduction in ASR volumetric expansion under compressive stresses and equals to

$$\Gamma_c = \begin{cases} 1 & \text{if } \bar{\sigma} \le 0 \text{ tension} \\ 1 - \dfrac{e^{\beta}\bar{\sigma}}{1+\left(e^{\beta}-1\right)\bar{\sigma}} & \text{if } \bar{\sigma} > 0 \text{ compression} \end{cases}, \quad \bar{\sigma} = \frac{\sigma_I + \sigma_{II} + \sigma_{III}}{3 f_c'} \qquad 6.68$$

where, β is an empirical constant (between -2 and 2 according to Samoua and Perroti (2006)). Here β is equal to 0. Later we adjust this parameter based on experimental data.

The ASR volumetric strain with the reported equations and data. Saouma and Perotti (2006) introduced a factorization method (weight of stresses in principal directions) to redistribute this volumetric strain in the principal directions. The details of this distribution method is introduced assuming the stress state is known beforehand.

Given the full stress tensor (in Cartesian coordinates) on a quadrature point within an element, principal stresses $\sigma_k, \sigma_l, \sigma_m$ and associated eigenvectors for the directions of principal stresses R_k, R_l, R_mcan be calculated.

Considering $f_c^{'}$, $f_t^{'}$, and σ_{u} (compressive stress beyond which no further gel expansion can occur, Saouma and Perotti (2006) proposed a value of -10 MPa based on some experimental studies), one can draw the Figure 6-43, which has nine divided quadrants of the stress space with 16 points. A pair of principal stresses (let us say σ_l, σ_m) are considered, then this stress state is located in Figure 6-43. Later, this proposed method is reused for the two other pairs. For instance, assuming that our stress state is located between nodes of 1, 2, 3, 4 as shown in Figure 6-43.

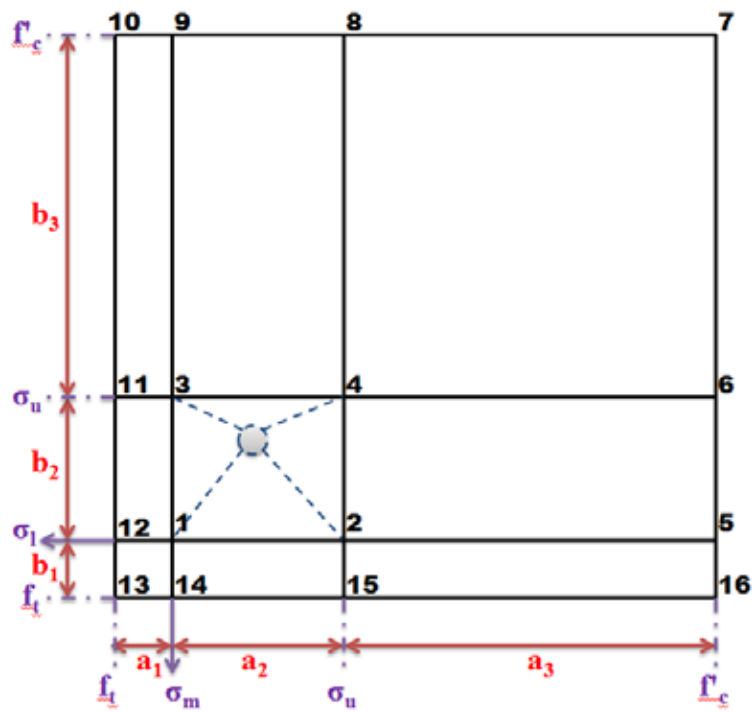

Figure 6-43 Weight regions.

Using Table 6-7, the weights of the neighboring nodes can be determined with proper linear interpolation of σ_{k} from the last 3 columns in the corresponding rows.

Then the weight can be computed using

$$W_k(s_k, s_l, s_m) = \sum_{i=1}^{4} N_i(s_l, s_m) W_i(s_k) \qquad 6.69$$

Where, N_i denotes the usual bilinear shape functions used in finite element and is given by:

$$N(s_l, s_m) = \frac{1}{ab}\left[(a - s_l)(b - s_m),\ s_l(b - s_m),\ s_l s_m,\ (a - s_l)s_m\right] \qquad 6.70$$

$$W(s_k) = \left[W_1(s_k), W_2(s_k), W_3(s_k), W_4(s_k)\right]^T \qquad 6.71$$

$$a = (a_1 \mid a_2 \mid a_3); \quad b = (b_1 \mid b_2 \mid b_3) \tag{6.72}$$

$$s_l = (s_l \mid s_l - s_u); \quad s_m = (s_m \mid s_m - s_u) \tag{6.73}$$

In Eq. 6.72, it is clear that the value of *a* and *b* depends on which quadrant the stress state is located in, so that the corresponding value for *a* and *b* can be picked. However, in Eq. 6.73 it's not clear when the user should take σ_l or $\sigma_l - \sigma_u$. Also it is not specified by Saouma and Perotti (2006). It was found that when $\sigma_l \leq \sigma_u$, then $\sigma_l = \sigma_l - \sigma_u$.

Table 6-7 Triaxial Weights.

$Pointgeometry$			$Weightdirectionk$		
$Point$	σ_l	σ_m	$\sigma_k \leq 0$	$\sigma_k = \sigma_u$	$\sigma_k = f_c'$
1	0	0	1/3	0	0
2	σ_u	0	1/2	0	0
3	σ_u	σ_u	1	1/3	0
4	0	σ_u	1/2	0	0
5	f_c'	0	1/2	0	0
6	f_c'	0	1	1/2	0
7	f_c'	f_c'	1	1	1/3
8	σ_u	f_c'	1	1/2	0
9	0	f_c'	1/2	0	0
10	f_t'	f_c'	1/2	0	0
11	f_t'	σ_u	1/2	0	0
12	f_t'	0	1/3	0	0
13	f_t'	f_t'	1/3	0	0
14	0	f_t'	1/3	0	0
15	σ_u	f_t'	1/2	0	0
16	f_c'	f_t'	1/2	0	0

The previous steps are repeated for calculating the ASR expansion weights along the other two principal directions $W_l(\sigma_k, \sigma_l, \sigma_m)$ and $W_m(\sigma_k, \sigma_l, \sigma_m)$. The summation of W_k, W_l, W_m equals to 1. The individual incremental ASR strains along the principal directions are then obtained using these relative weights by the following equation

$$De_i^{ASR} = W_i De_V^{ASR} \quad i = 1,\ 2,\ 3 \tag{6.74}$$

The ASR expansion-induced incremental strain tensor $\Delta\varepsilon^{ASR}$ on quadrature points is calculated by rotating $\Delta\epsilon_i^{ASR}$ into the current coordinates via

$$De^{ASR} = R\left\{ \mathbb{D} De_i^{ASR} \right\} R^T \tag{6.75}$$

in which $\Delta\varepsilon^{ASR}$ is the chemically imposed incremental strain tensor at each quadrature point.

According to this procedure, degradation of the modulus elasticity and tensile strength can be computed based on the following equations

$$E(t,q) = E_0[1 - (1 - b_E)x(t,q)] \tag{6.76}$$

$$f_t(t,q) = f_{t,0}[1 - (1 - b_f)x(t,q)] \tag{6.77}$$

Where, E_0 and $f_{t,0}$ are the initial elastic modulus and tensile strength, respectively, and β_E and β_f are the corresponding residual fractional values when the concrete has fully reacted. Here these values are equal to 0.5.

A simple example for weight determination is shown below. Assuming that the principal stresses are given by $(\sigma_k, \sigma_l, \sigma_m) = (-5.0, -8.0, -5.0)MPa$, and that f_c', f_t', and σ_u are equal to -30.0, 2.0, and -10.0 MPa, respectively. The stress tensor is placed in the quadrant defined by nodes 1-2-3-4.

One can calculate that when a and b are both equal to -10 MPa. The weights are equal to:

$$W_1 = \frac{1}{2}\left(\frac{1}{3}\right) = \frac{1}{6}; W_2 = \frac{1}{2}\left(\frac{1}{2}\right) = \frac{1}{4}; W_3 = \frac{1}{3} + \frac{1}{2}\left(1.0 - \frac{1}{3}\right) = \frac{2}{3}; W_4 = \frac{1}{2}\left(\frac{1}{2}\right) = \frac{1}{4} \tag{6.78}$$

$$N_1 = \frac{1}{100}\left[(-10+5)(-10+8)\right] = \frac{1}{10} \tag{6.79}$$

$$N_2 = \frac{1}{100}\left[(-5)(-10+8)\right] = \frac{1}{10} \tag{6.80}$$

$$N_3 = \frac{1}{100}\left[(-5)(-8)\right] = \frac{4}{10} \tag{6.81}$$

$$N_4 = \frac{1}{100}\left[(-8)(-10+5)\right] = \frac{4}{10} \tag{6.82}$$

Therefore,

$$W_k = \frac{1}{10}\left(\frac{1}{6}\right) + \frac{1}{10}\left(\frac{1}{4}\right) + \frac{4}{10}\left(\frac{2}{3}\right) + \frac{4}{10}\left(\frac{1}{4}\right) = 0.40833 \tag{6.83}$$

6.4.3. Benchmark Problems of the ASR Model

The introduced methodology has been implemented in a Matlab code which is linked to COMSOL Multiphysics (2015) to study some benchmark problems.

Multon and Toutlemonde (2006) investigated the behavior of concrete specimens subjected to ASR swelling under different confinement and stress states.

The specimen is a concrete cylinder with 120 mm diameter and 240 mm height including a steel rings outside of the specimen. Material properties and ASR parameters are summarized in Table 6-8. Now, the behavior of these two cases is investigated.

Table 6-8 General Parameters of the ASR Model.

Characteristics	Symbol	Unit	Value
Characteristic time at test temperature	τ_c	day	68.9
Latency time at test temperature	τ_L	day	110.0
Activation energy associated with τ_c	U_C	K	5,400
Activation energy associated with τ_L	U_L	K	9,400
Tensile strength	f_t'	MPa	3.2
Compressive strength	f_c'	MPa	-31
Concrete Young's modulus	E_0	GPa	37.3
Concrete Poisson's ratio	ν	-	0.22

6.4.3.a. ASR expansion without steel ring confinement

In this case, there is no lateral confinement and various axial stresses (0 MPa, 10 MPa, 20 MPa, and 30 MPa) are applied to the specimen. Due to symmetry, this cylinder was modeled by using a 2D axisymmetric model of half of the height of the specimen. As a boundary condition, there is a roller support on the bottom. Figure 6-44 shows the boundary conditions of the model of finite element mesh which has been used for this simulation. Since there is no confinement, the applied load imply in a uniform stress state, ASR reaction extent and associated ASR induced strain, however the extent of ASR reaction and ASR strain are different under different loading conditions.

Figure 6-45 compares the ASR reaction extent, the ASR-induced volumetric strain, and the ASR strains in the axial and lateral directions for four different loadings. Figure 6-45(a) shows that ASR reaction is retarded by axial loads and caused a reduction of the ASR volumetric strain as shown in Figure 6-45(b). Additionally, as the axial loading stress increased from 0 MPa to 10 MPa, despite the small reduction of total ASR volumetric strain, the lateral ASR strain increases as shown in Figure 6-45(c). One can say that when the axial loading stress increased, the compressive stress along the axial direction suppressed the axial ASR strain, and redistributed the ASR volumetric strain to the lateral direction along which the stress is zero since there is no lateral confinement. Higher ASR strain is observed in the lateral direction at 10 MPa axial load in Figure 6-45(c). However, when the axial load is increased further to 20 MPa and 30 MPa, the lateral ASR strain decreases below that of the 10 MPa axial load case. This is due to the further reduction of the total ASR volumetric strain when the axial load increased from 10 MPa to 20 MPa and 30 MPa. Figure 6-45(d) shows that when the compressive load is equal or higher than σ_{u}, there is no axial strain. Additionally, it is important to mention that with no axial stress, both the axial and lateral ASR strains are the same, verifying isotropic swelling. The results are consistent with experimental observations which are stated by Multon and Toutlemonde (2006).

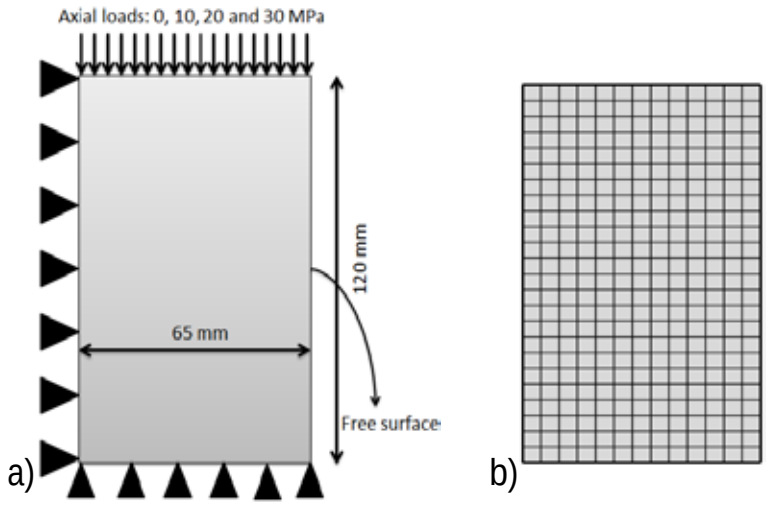

Figure 6-44 (a) Schematic description of geometry and boundary conditions of the 2D axis symmetric model and (b) the finite element mesh in COMSOL Multiphysics.

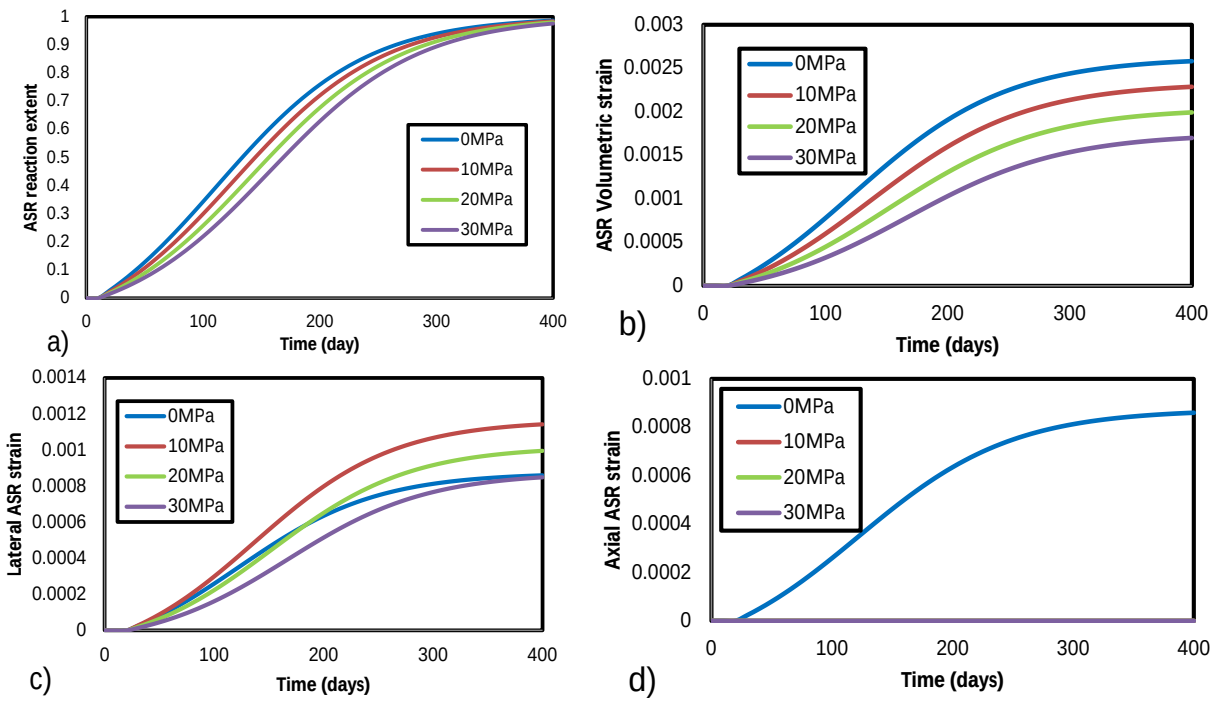

Figure 6-45 Comparison of ASR parameters for four axial loading stresses 0, 10, 20, 30 MPa (a) Temporal evolution of the ASR reaction extent (b) Temporal evolution of the ASR volumetric strain (c) Temporal evolution of the ASR strain in lateral direction (d) Temporal evolution of the ASR strain in axial direction.

Figure 6-46 shows the comparisons of the axial and lateral displacements for all three loading stresses.

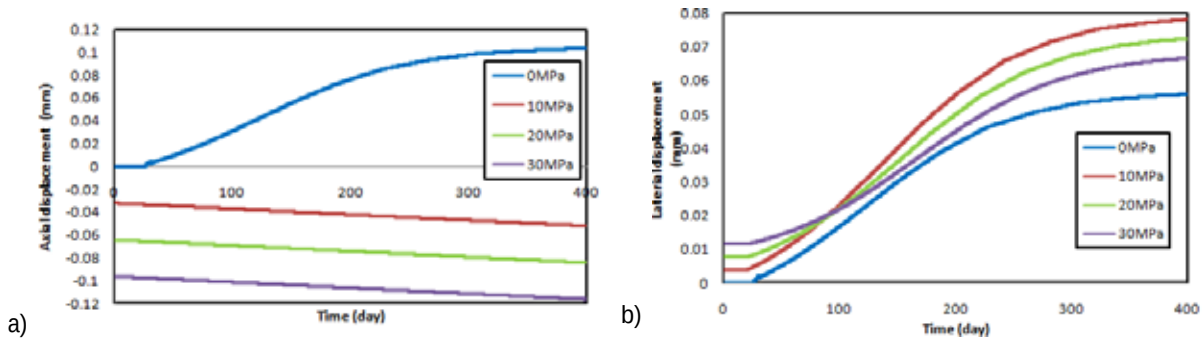

Figure 6-46 Comparisons of the displacements in axial (a) and lateral (b) directions for three axial loads, 0, 10 and 20 MPa.

Figure 6-47 shows the comparisons between the simulated (lines) and measured (symbols) lateral strains from Multon and Toutlemonde (2006) for all three loading stresses. Since the ASR model parameters were calibrated against the data measured from specimens under no axial stress, the simulated lateral strain under no axial stress agrees well with the measurements. The simulated lateral strain under 20 MPa, axial load agrees reasonably well with the measurements by using the same set of calibrated ASR model parameters. However, the match between the measured and simulated lateral strains for 10 MPa axial load case is also satisfactory by using the same set of calibrated ASR model parameters. Some further investigations are necessary to provide more accurate approach using the experimental results. For example, these simulations clearly show the instantaneous lateral strains at 10 MPa and 20 MPa loads, however, the experimental data does not show such instantaneous lateral strain due to axial loads.

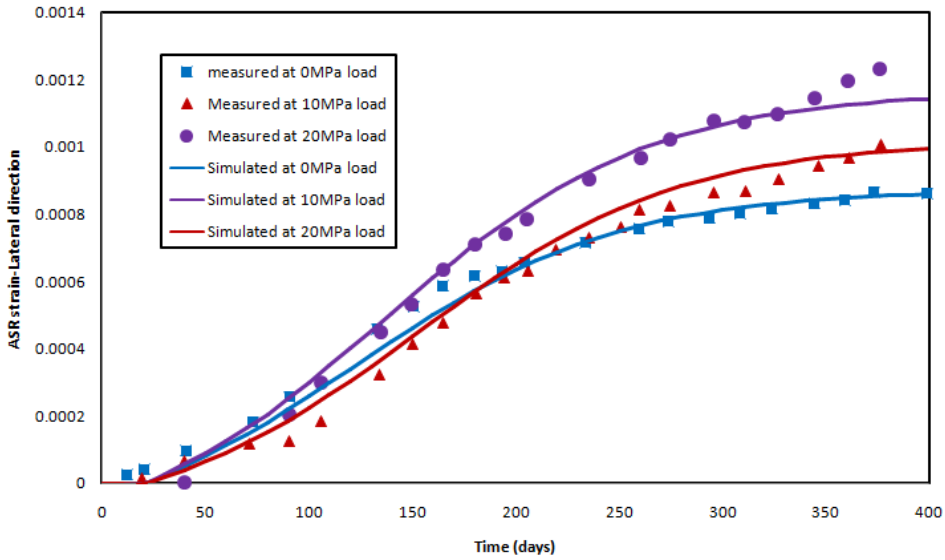

Figure 6-47 Comparisons of the measured and simulated lateral strains of specimens without confinement under three axial loads, 0 MPa, 10 MPa and 20 MPa.

6.4.3.b. ASR expansion with steel ring confinement

In this section, a 3 mm-thick steel ring confinement is attached to the previous benchmark problem as investigated by Multon and Toutlemonde (2006). Figure 6-48 shows the geometry, boundary conditions and finite element mesh of this 2D axisymmetric problem. The steel ring is assigned a Young's modulus of 193 GPa, Poisson's ratio of 0.3 and yield stress of 206 MPa. The steel ring is not connected to the specimen, so it's not constraining the axial movement of the specimen. A frictionless contact model has been implemented in COMSOL to represent the interaction between this steel ring and concrete specimen. The results are provided for the case of 10 MPa axial stress. ASR parameters which are used in the previous case, are implemented in this case as well. Figure 6-49 shows the simulated axial and lateral stress fields at a time of 400 days. The axial stress in the specimen is 10 MPa, as expected, to be equal to the applied load, and is uniform everywhere. The lateral stress in the specimen is about -3 MPa, smaller than the axial stress and is uniform everywhere within the specimen due to the confinement of different Poisson's ratio. Additionally, the axial stress in the steel ring is zero, which represents the frictionless contact.

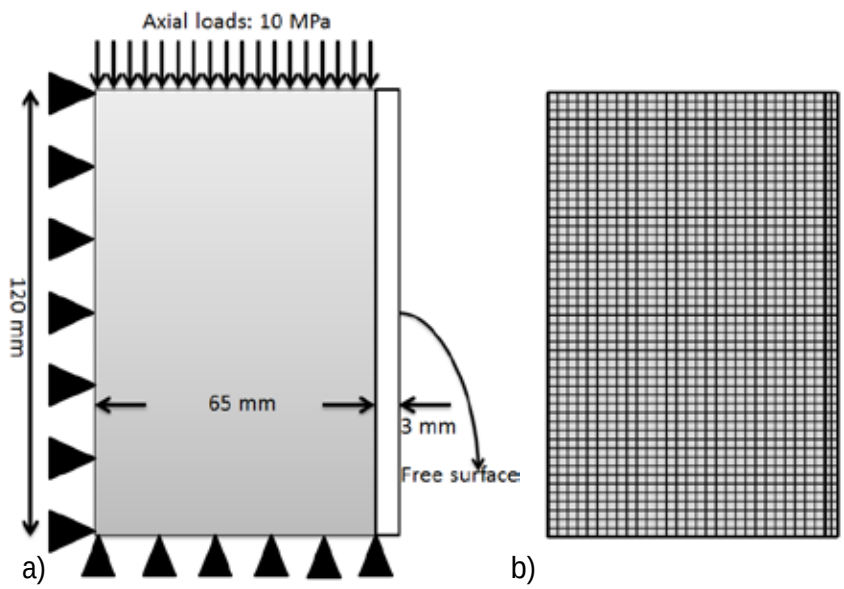

Figure 6-48 (a) schematic description of geometry and boundary conditions of the 2D axis symmetric model and (b) the finite element mesh in COMSOL Multiphysics with steel ring confinement.

Figure 6-50 shows the axial and lateral displacement fields at a time of 400 days. Axial ASR strain is uniform everywhere in concrete and it is equal to $\epsilon_{zz} = 5.2e^{-5}m$, and the lateral ASR strain is equal to $\epsilon_{zz} = 6.02e^{-4}m$. There is a discontinuity between the concrete and steel ring in the axial displacement due to the frictionless contact, while the lateral displacement is continuous across the concrete and steel ring. The results of this problem are also consistent with experimental observations which are stated by Multon and Toutlemonde (2006) but they differ slightly because of implementation of the contact algorithm in COMSOL Multiphysics.

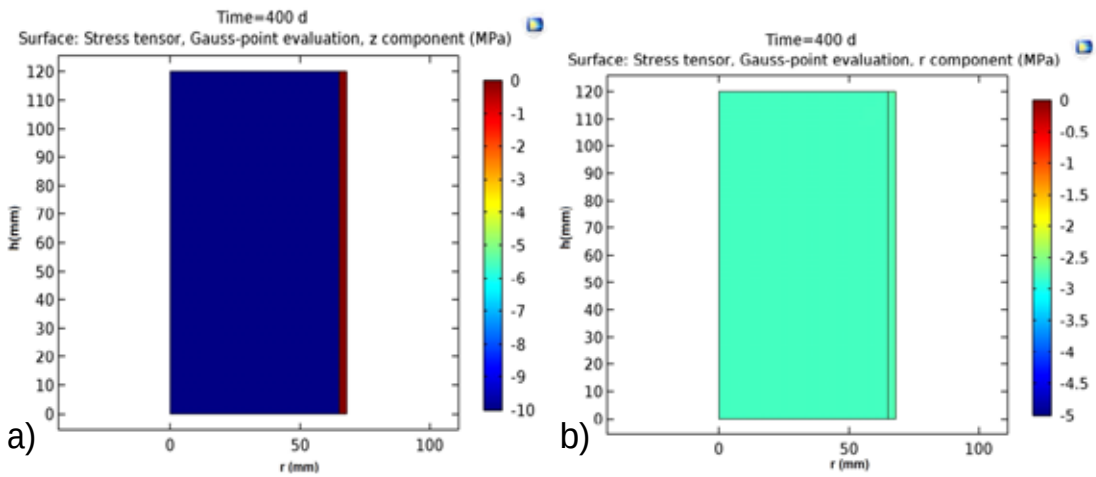

Figure 6-49 (a) The axial (b) lateral stresses of 400 days.

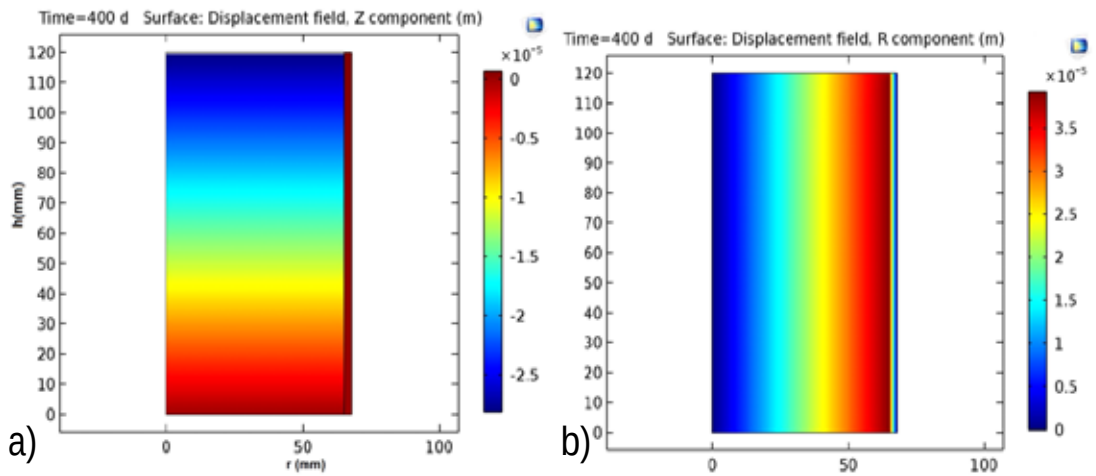

Figure 6-50 (a) The axial and (b) lateral displacements at time of 400 days.

Figure 6-51 compares the simulated results with the measure data by Multon (2006) for the confined specimen subjected to 10 MPa and 20 MPa axial load stresses. It should be mentioned that the simulated data using 10 MPa load stress is calibrated with the measured data and it was found that α should be 4.3 and β should be 1.5. With these parameters, we can see a good agreement for 20 MPa loading stress as depicted in Figure 6-51. Saouma and Perotti (2006) proposed a value of 0.5 for β, but they did not explain the details of the modeling as well as the contact and the effect of confining steel rings.

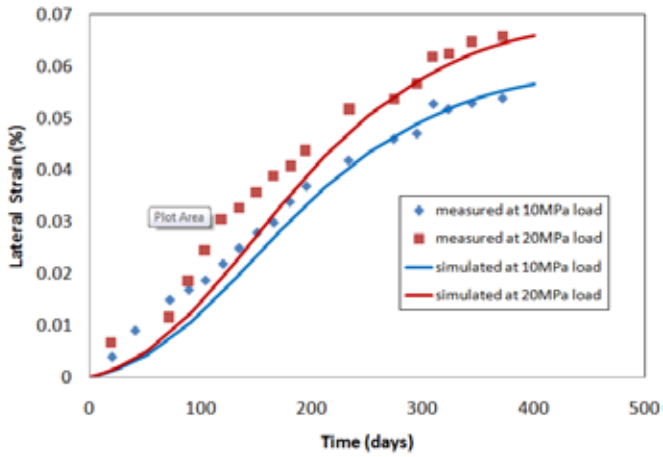

Figure 6-51 The simulated and measured lateral strains for confined specimens.

6.4.4. ASR model of Dry Cask Structure

This verified model is considered to model ASR in the dry cask structure. For this, the concrete outerpack and the steel liner are considered where the concrete outerpack confines the steel liner. A 2-D axissymmeric model is considered for this study. Friction is considered between these two parts and a value of 0.6 which is considered in the next section for tip-over simulation, is considered. A time dependent study is performed for behavior of the dry cask structure up to 500 days. Those parameters were introduced in Section 6.4.2 to model ASR, are simply considered in this study. Some experimental studies are necessary to validate those parameters in this study, which are mainly activation energy parameters and triaxial effects of ASR on concrete mixture in order to calibrate α in Eq. 6.63 and β in Eq. 6.68.

The entire model is free of loading and outer and upper surfaces of the concrete outerpack are free, therefore, initially the stress and strain are zero. But ASR induces some strains into the concrete part, and because of the confinement, one may have stress in the model. Figure 6-52 shows the volumetric strain of ASR reaction, ASR axial strain, and ASR radial strain in the concrete part of dry cask structure. Figure 6-53 shows the temporal evolution of the ASR reaction extent for the concrete outerpack.

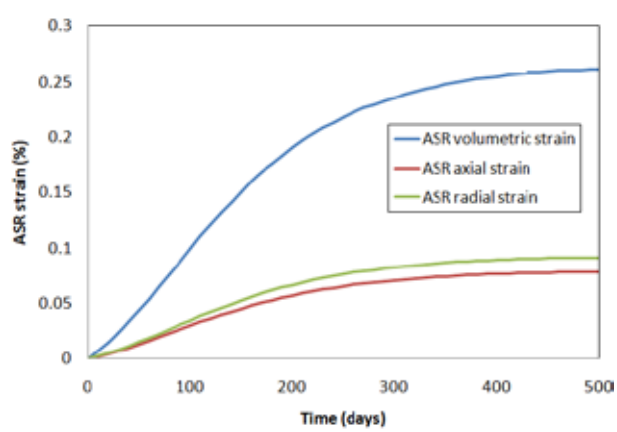

Figure 6-52 ASR strains in the concrete outerpack for dry cask structure.

As it is seen, the axial ASR strain and ASR radial strain have almost the same magnitude. Contours of axial and radial stresses, and axial and radial displacement fields of the concrete outerpack in presented in Figure 6-54 and Figure 6-55.

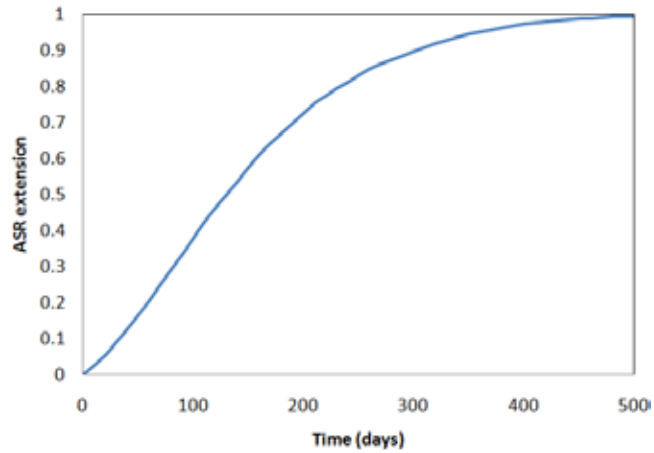

Figure 6-53 Temporal evolution of the ASR reaction extent in the concrete outerpack for dry cask structure.

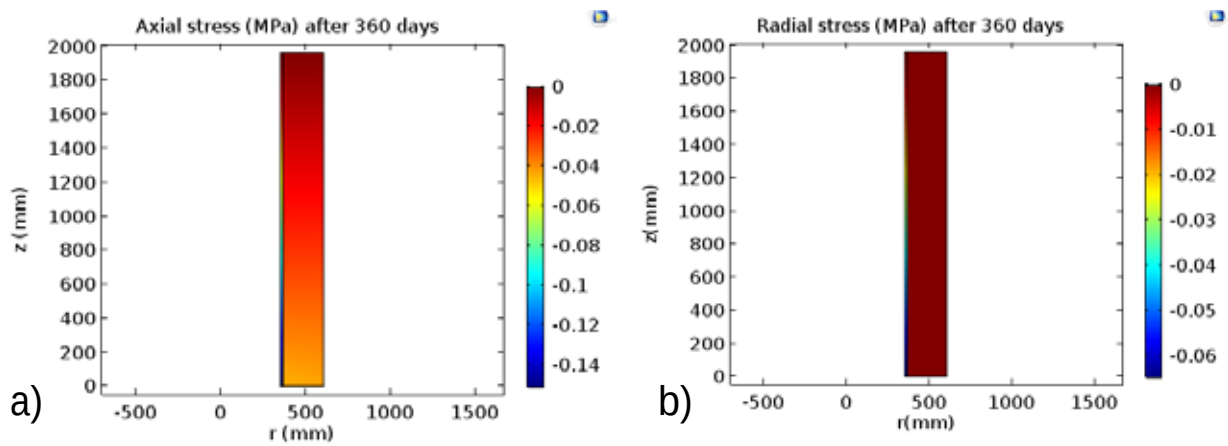

Figure 6-54 Axial (a) and radial (b) stresses after 360 days in the dry cask structure.

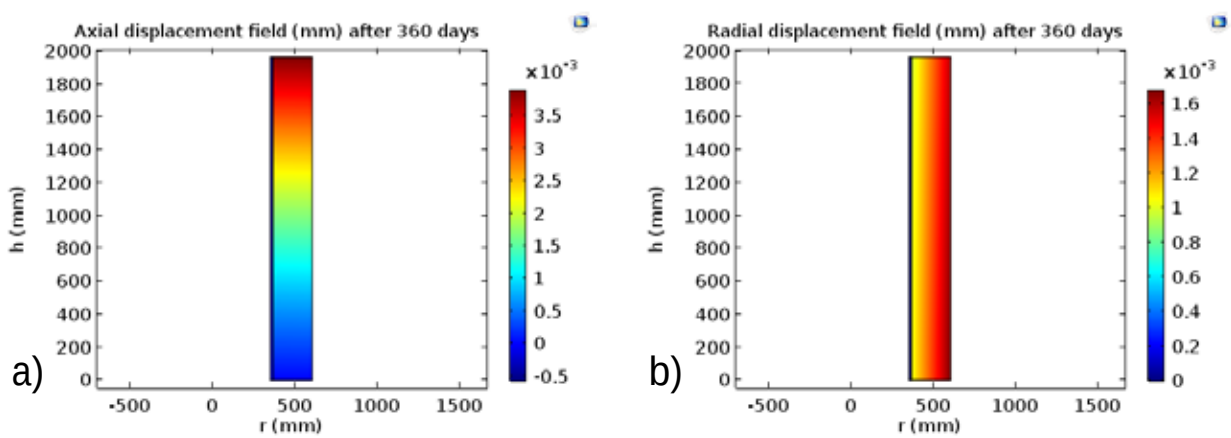

Figure 6-55 Axial (a) and radial (b) displacements after 360 days in the dry cask structure.

Degradation of the modulus elasticity and tensile strength of the concrete cask is calculated based on the following equations after a year:

$$E(t,q) = E_0 \left[1 - (1 - b_E)x(t,q)\right] = 29.2\left[1 - (1 - 0.5) \times 0.94\right] = 15.5\,GPa \qquad 6.84$$

$$f_t(t,q) = f_{t,0}\left[1 - (1 - b_f)x(t,q)\right] = 4.1\left[1 - (1 - 0.5) \times 0.94\right] = 2.173\,MPa \qquad 6.85$$

Where, E_0 is assumed to be *29.2 GPa* and $f_{t,0}$ is *4.1 MP.* β_E and β_f are the corresponding residual fractional values when the concrete has fully reacted. Here we consider that these values are equal to 0.5 corresponding to Saouma and Perotti (2006). These values are considered in the next section for modeling of tip-over scenario for the dry cask structure.

Discussion: Since the cask is self-weighted structure and there is no external load, it is clear that it shows a volumetric behavior and the level of strain is almost same in all directions. The anisotropic behavior of the model can be captured when at least one axis reaches to σ_u (compressive stress beyond which no further gel expansion can occur), which is about 10 MPa experimentally. Here, the stress level does not reach to that stress level and the anisotropic behavior is not significant.

6.5. CRASH ANALYSIS OF DRY CASK STRUCTURE IN LS-DYNA

6.5.1. Constitutive Behavior of Concrete Material Model in LS-DYNA

6.5.1.a. Selection of the concrete material models

Many concrete material models are available in LS-DYNA where they consider damage and plasticity (Brannon and Leelavinchkul). Karagozian and Case model or concrete damage model-Management Aptitude Test (MAT)-72 (Malvar et al., 1997), the Riedel-Hiermaier-Thoma model-RHT, MAT-272 (Hansson and Skoglund, 2002; Borrvall and Riedel, 2011), the Brannon-Fossum model-BF1 (Fossum and Brannon, 2004), and Continuous surface cap model (CSCM), MAT-159 (Murray, 2007) are some of those. Among these, CSCM material has many applications in the literature (Champiri et al., 2015a, 2015b; Brannon and Leelavanichkul, 2004; Bermejo et al., 2011), because this material uses two parameters including uniaxial compressive strength and maximum size of aggregate in the simplest version for concrete structures, while other material models need many inputs. This material model uses the Duvaut-Lions formulation (Simo, 1988) and its constitutive model will be addressed in the next section. In this model, the user can apply parameters such as maximum strain increment for sub-incrementation, and pre-existing damage factor.

Three concrete models are initially selected to perform some benchmark loading scenarios to choose the best one. MAT-16 (Pseudo tensor material model), MAT-72 (Karagozian and Case model), and MAT-159 (Continuous surface material model) are compared to each other here in case of uniaxial compression, tension and simple shear).

Figure 6-56 shows the prediction of the three concrete models under uniaxial compression using a single brick element of plain concrete with compressive strength of 30 MPa. MAT_72 shows very brittle behavior in comparison with other models. In contrast, MAT_159 exhibits a more ductile softening behavior. All of three material models have the same compressive strength.

For the tension test, a tensile strength of 3 MPa (1/10 of compressive strength) is expected. The results are shown in Figure 6-57. The tensile strain capacity of MAT_16 is negligible in comparison with MAT_72 and MAT_159, and it exhibits a larger tensile strength (f_t=3.6 MPa) than the other two concrete models. MAT_159 exhibits more ductile softening behavior than MAT_72 and a lower tensile strength of f_t=2.4 MPa.

The post peak response of the three material models in simple shear in Figure 6-58 shows very different behavior of peak shear capacity and softening. The large discrepancy is based on the entered material parameters, which are taken from literature. Based on this figures, MAT_72 and MAT_16 show very brittle post peak behavior for simple shear and MAT_159 shows high shear capacity and more ductile behavior and energy dissipation in simple shear.

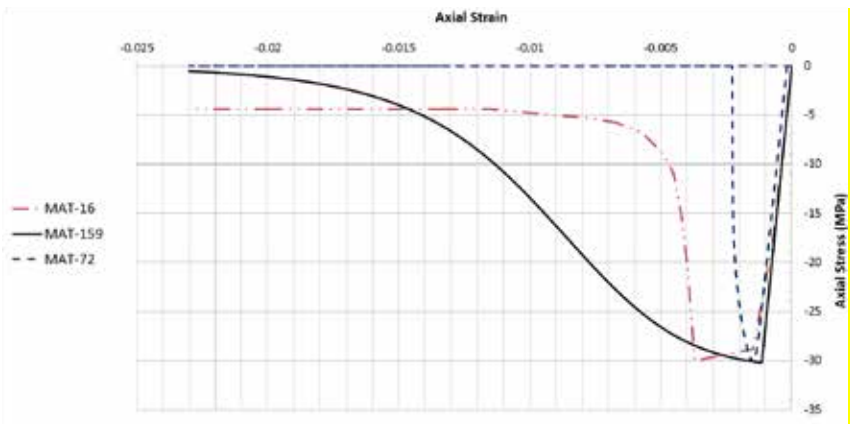

Figure 6-56 Comparison the compression predictions of three material models in compression.

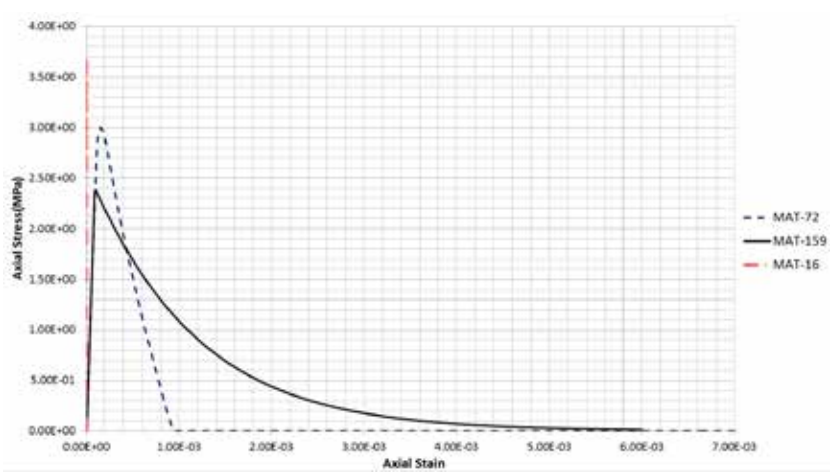

Figure 6-57 Comparison the tensile predictions of three material models.

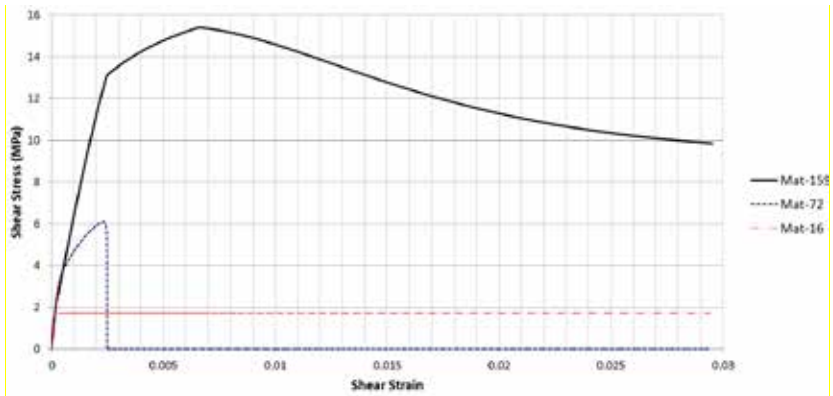

Figure 6-58 Comparison the simple shear prediction of material models.

After observing these three results, the CSCM (MAT_159) concrete model was used, because its behavior is more realistic and can exhibit more ductile behavior in compression.

6.5.1.b. Constitutive formulation of CSCM model (MAT-159)

CSCM is an enhanced version of the concrete model that has been successfully used and further developed since 1990 on defense contracts to analyze the response behavior under dynamic loading of reinforced concrete structures (Hallquist, 2006). This material model was empirically developed to simulate concrete behavior in the National Cooperative Highway Research Program (NCHRP 350, 1993) for safety hardware testing program. This model needs 40 coefficients in the General format and about 3 coefficients (compressive strength, maximum aggregate size, and mass density) for the simple calibration format. CSCM model is a cap model with a smooth or continuous intersection between the failure surface and hardening cap. The yield surface uses a multiplicative formulation to combine the shear (failure) surface with the hardening compaction surface (cap) smoothly and continuously. The smooth intersection eliminates the numerical complexity of treating a compressive corner region between the failure surface and cap. This type of model is often referred to as a smooth cap model or as a CSCM. Additionally, the rate effects are modeled using visco-plasticity. The yield function for this material model reads as (Murray, 2007):

$$f_{CSCM}\left(I_1, J_2, J_3, k\right) = J_2 - \hat{A}^2 F_f^{\,2} F_c \qquad 6.86$$

in which $F_f(I_1), F_c(I_1, \kappa), \Re(J_2, J_3)$ are functions which are defined using shear surface, cap region and Rubin scaling factor, respectively.

Tensile and low confining pressure regimes define the strength of concrete in the shear surface. The shear surface F_f is defined along the compression meridian

$$F_f\left(I_1\right) = a - I e^{-b_0 I_1} + q I_1 \qquad 6.87$$

α, β, λ, and θ are calculated with TXC tests by fitting the model surface to strength measurements. Cap failure surface function is calculated by

$$F_c\left(I_1,k\right) = \begin{cases} 1 - \dfrac{\left(I_1 - k\right)^2}{\left(X - k\right)^2} & : I_1 \geq k_0 \\ 1 & : \text{otherwise} \end{cases} \qquad 6.88$$

where κ is cap hardening parameter, and X represent the current cap location. The intersection of the cap with the I_1 axis is at $I_1 = \mathrm{X}(\kappa)$. Rubin scaling function can be calculated using the following expression:

$$\hat{A}\left(J_2,J_3\right) = \frac{-b_1 + \sqrt{b_1^2 - 4b_1b_0}}{2b_2} \qquad 6.89$$

Rubin function internal parameters can be calculated using

$$b_0 = -\frac{3 + b - a^2}{4} \qquad 6.90$$

$$b_1 = a\left(\cos b - a\sin b\right) \qquad 6.91$$

$$b_2 = \left(\cos b - a\sin b\right)^2 + b\sin^2 b \qquad 6.92$$

$$b = \left(2Q_1 + a\right)^2 - 3 \qquad 6.93$$

$$a = \frac{-a_1 + \sqrt{a_1^2 - 4a_2a_0}}{2a_2} \qquad 6.94$$

$$a_0 = 2Q_1^2\left(Q_2 - 1\right) \qquad 6.95$$

$$a_1 = \sqrt{3}Q_2 + 2Q_1\left(Q_2 - 1\right) \qquad 6.96$$

$$a_2 = Q_2 \qquad 6.97$$

$$\sin 3\hat{b} = \frac{3\sqrt{3}J_3}{2J_2^{3/2}} \qquad 6.98$$

where $\hat{\beta}$ is angle in deviatoric plane (invariant). Q_1 and Q_2 are the parameters which determine the yield surface parameters that we want to fit. As a generalized form

$$\begin{aligned} Q_1 &= a_1 - l_1 e^{-b_1 I_1} + q_1 I_1 \\ Q_2 &= a_2 - l_2 e^{-b_2 I_1} + q_2 I_1 \end{aligned} \qquad 6.99$$

These values depend on the state of stress through the angle, and on experimentally determined values (fits to data) for Q_1 and Q_2 as functions of pressure. Strength in TOR is modeled as $Q_1 F_f$. Strength in TXE is modeled as $Q_2 F_f$. Finally current cap location can calculated using following:

$$L(k) = \begin{cases} k & : k > k_0 \\ k_0 & : k \leq k_0 \end{cases} \tag{6.100}$$

$$X(k) = L(k) + R_0 F_f\left(L(k)\right) \tag{6.101}$$

In formulation for material CSCM, the softening is modeled using damage formulation for tensile and in the case of compression with moderate confinement. It means that the softening is not activated unless damage formulation is activated. Softening behavior and stiffness degradation (modulus reduction) are in direct correlation with each other. The scalar damage parameter is categorized into two different categories: brittle damage, which happens when stress state is tensile and ductile damage, in which, the stress state is compressive. The ductile and brittle damage evolution functions, are

$$\begin{aligned} d(t_b) &= \frac{0.999}{D}\left(\frac{1+D}{1+De^{-C(t_b - r_{0b})}} - 1\right) \\ d(t_d) &= \frac{d_{max}}{B}\left(\frac{1+B}{1+Be^{-A(t_d - r_{0d})}} - 1\right) \end{aligned} \tag{6.102}$$

in which, d is scalar damage parameter, τ_b, τ_d are strain energy corresponding to current strain state and r_{0b}, r_{0d} are initial damage threshold for brittle and ductile damage, respectively. A, B, C, D are softening parameters for compression (A, B) and tension (C, D), respectively. d_{max} is maximum damage parameter which can be defined. (Recommended to take $d_{max} < 1$ and is usually taken $d_{max} > 0.99$). The fracture energy is calculated from

$$G_f = \int_0^{u_0} (1 - d) f' dx \tag{6.103}$$

in which, u_0 is displacement corresponding to the peak strength value. By putting Eq. 6.102 into Eq. 6.103, relationship between fracture energy and softening parameters for brittle damage is calculated as

$$G_f = r_{0b} L \left(\frac{1+D}{CD}\right) \tag{6.104}$$

Based on Eq. 6.104, a parameter reduction can be done by eliminating parameter C from the brittle damage evolution Eq. 6.102

$$C = r_{0b} L\left(\frac{1+D}{G_f D}\right)\log(1+D) \tag{6.105}$$

Parameter reduction for ductile damage is obtained from the following equation

$$G_f = 2r_{0d}L\left(\frac{1+B}{AB}\right)\log\left(1+B\right) + 2L\left(\frac{1+B}{A^2}\right)\int_0^{\infty}\frac{ye^{-y}dy}{1+Be^{-y}} \qquad 6.106$$

in which, $y = -A(\sqrt{u} - \sqrt{u_0})\sqrt{\frac{f_t}{L}}$. The integral for equation above does not have a closed form solution. It is calculated numerically and the value is shown as $dilog$. By re-arranging Eq. 6.106, the parameter A is obtained as following

$$A = \frac{-b + \sqrt{b^2 - 4c}}{2} \qquad 6.107$$

$$b = \frac{-2\left(1+B\right)\log\left(1+B\right)Lr_{0d}}{BG_f} \qquad 6.108$$

$$c = \frac{-2L\left(1+B\right)di\log}{G_f} \qquad 6.109$$

Based on equations above after parameter reduction, the parameter that determines compressive behavior of concrete in the post peak regime, in addition to compressive fracture energy is B. Similarly, the parameter which shapes the post peak behavior of concrete under tensile loading condition is D along with tensile fracture energy. The discussion about these parameters and values of each parameter are shown in the next section.

6.5.1.c. Behavior of CSCM material models under different loading scenarios

The set of inputs for CSCM material are as shown in Table 6-9. The material model has been assigned to a single cube element with displacement boundary conditions at one top side and symmetric boundary conditions in two perpendicular sides. The roller supports restraining bottom of the element from moving along load direction has been applied to the model. The analysis has been implemented in LS-DYNA in the case of uniaxial compression, cyclic uniaxial compression, uniaxial tension and simple shear, and the results are compared in terms of stress vs. strain in Figure 6-59. Concrete shows strain hardening before reaches the maximum strength in compression. Hardening parameters which are mainly N_H and C_H are not clearly investigated for CSCM material model. After calibrating this material model, some values are suggested for these two parameters as mentioned in Table 6-9.

Table 6-9 CSCM Parameters Used under Different Loading Scenarios (Units are MPa, mm, N).

α	β_0	λ	θ	α_1	β_1	λ_1	θ_1
14.2	0.01929	10.51	0.2965	0.7473	7.25e-2	0.17	1.204e-3
α_2	β_2	λ_2	θ_2	f'_c	Aggregate size	G	K
0.66	7.25e-2	0.16	1.45e-3	28	16	1.15×10^4	1.26×10^4
R	X_0	D_1	D_2	W	G_c	G_T	G_s
5	90	2.5×10^{-4}	3.5×10^{-7}	0.05	10	0.1	0.1
B	D	N_H	C_H				
$10-500$	$0.05-10$	0.7	999				

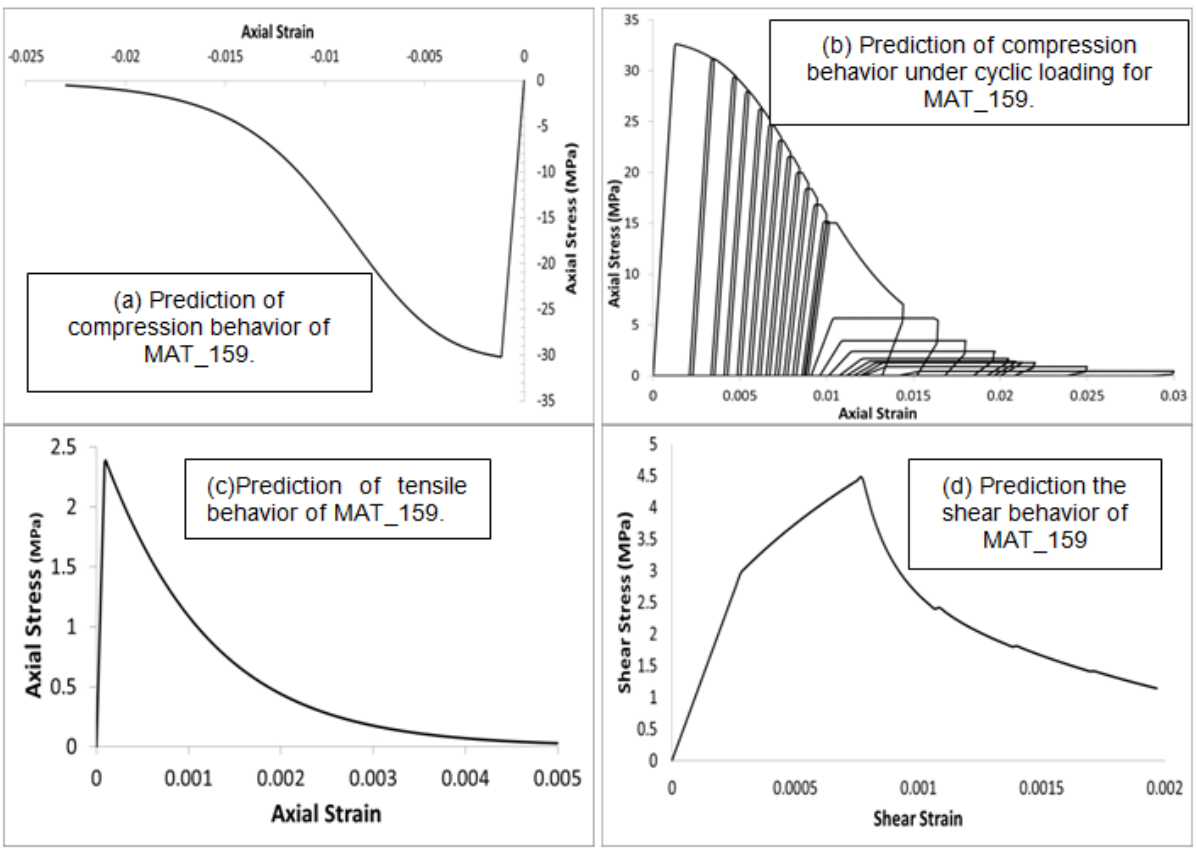

Figure 6-59 Behavior of MAT_159 under different loading scenarios.

Figure 6-59(a) shows the behavior of this model under monotonic compression loading for a single unit cubic element with compressive strength of *30* MPa. Figure 6-59(b) shows the compression behavior under cyclic loading. As seen, the compressive strength is larger than 30 MPa because of the rate effects, which also changes the slope of unloading/reloading after peak

because of the effect of ductile damage that introduces a reduction of the stiffness under cyclic loading. In this material model, rate effects apply to the plasticity surface, damage surface and fracture energy which is based on Simo et al. (1988). Figure 6-59(c) shows the behavior of this material under uniaxial tensile stress. Simple shear is applied to this material model and Figure 6-59(d) shows the shear response. As seen, the shear strength is between the compressive strength. There is a kink at a stress of 3 MPa due to transfer from elastic to strain hardening.

A study was done in order to capture the influence of size effects with applying CSCM model. Four different sizes including 2.54 mm, 25.4 mm, 100 mm, and 254 mm were selected and uniaxial compression test and uniaxial tension test were done on these sizes to evaluate how CSCM behave under different sizes (see Figure 6-60). Based on the area under stress-displacement curve, fracture energy of softening part was calculated and the results are shown in Table 6-10.

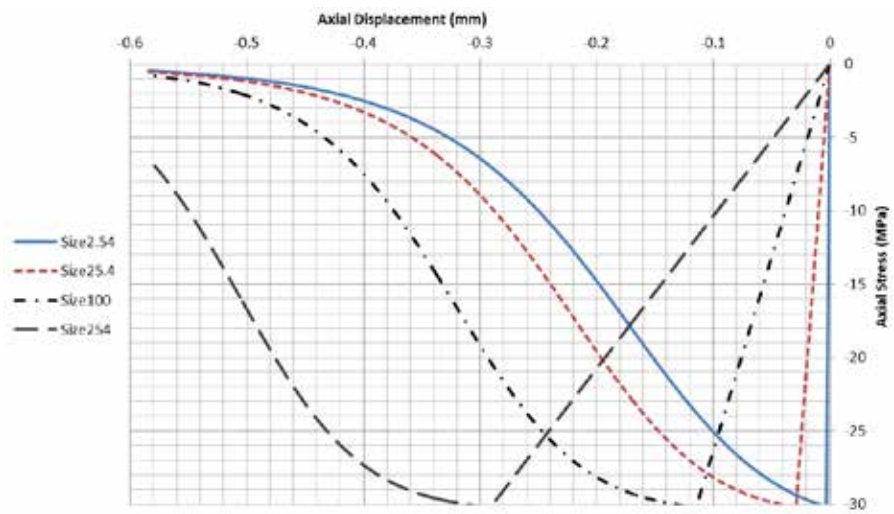

Figure 6-60 Prediction of compression behavior under monotonic loading for CSCM model with different sizes.

Table 6-10 Fracture Energy of Softening Part for Uniaxial Compression Test.

Size of Element (mm)	Fracture energy of softening part (MPa.mm)
2.54	6.388163
25.4	6.764928
100	6.700571
254	6.401343

Figure 6-61 and Table 6-11 show similar results for uniaxial tension test.

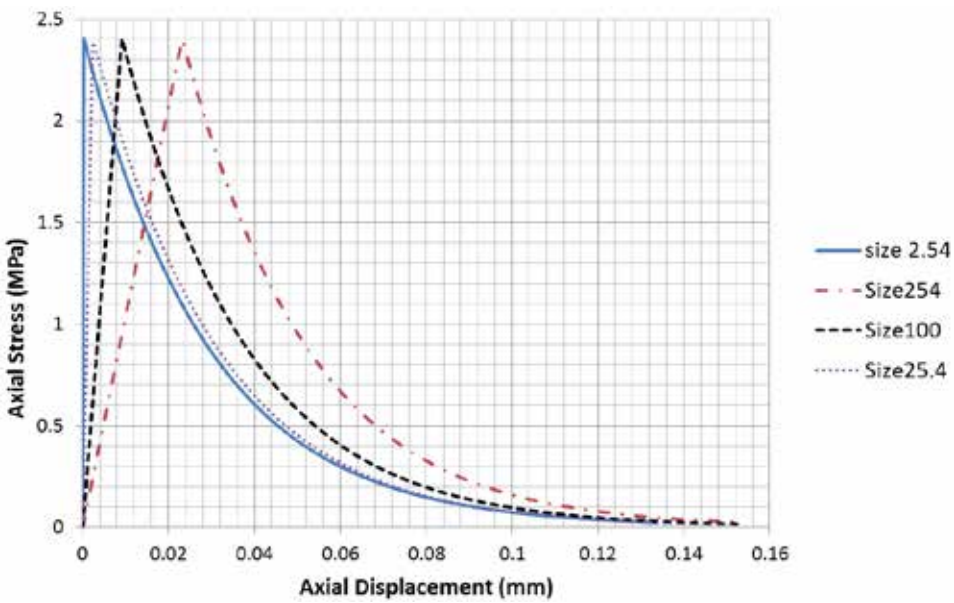

Figure 6-61 Prediction of tensile behavior under monotonic loading for MAT_159 with different sizes.

Table 6-11 Fracture Energy of Softening Part for Uniaxial Tension Test.

Size of element	Fracture energy
2.54 mm	0.068468
25.4 mm	0.067842
100 mm	0.068271293
254 mm	0.068289

The influence of *B* parameter on post peak behavior of CSCM material under uniaxial compression test can be seen in Figure 6-62, Figure 6-63 and Figure 6-64. It is clearly shown that lateral strains are longer than axial strains. Because of using associate flow rule in CSCM model, it is expected to observe higher value of lateral expansion in this material which has been confirmed with the analysis results.

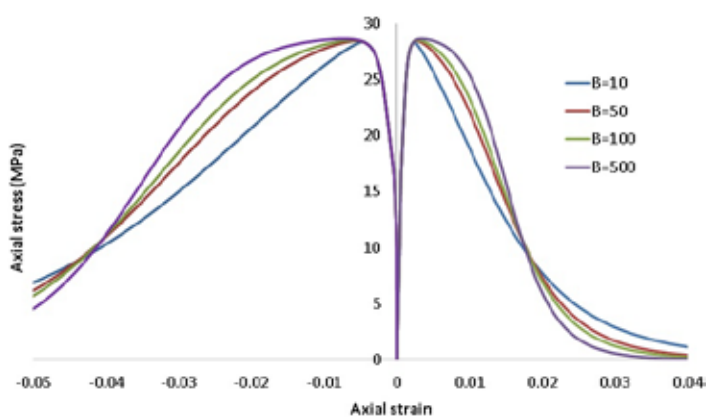

Figure 6-62 Effect of *B* parameter on axial and lateral strains in uniaxial compression test.

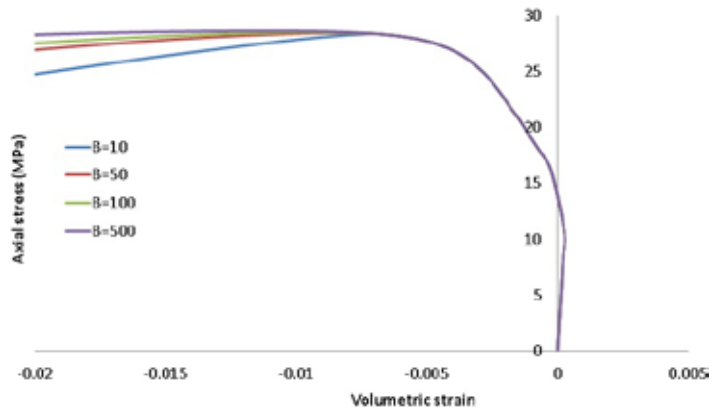

Figure 6-63 Effect of *B* parameter on volumetric strain in uniaxial compression test.

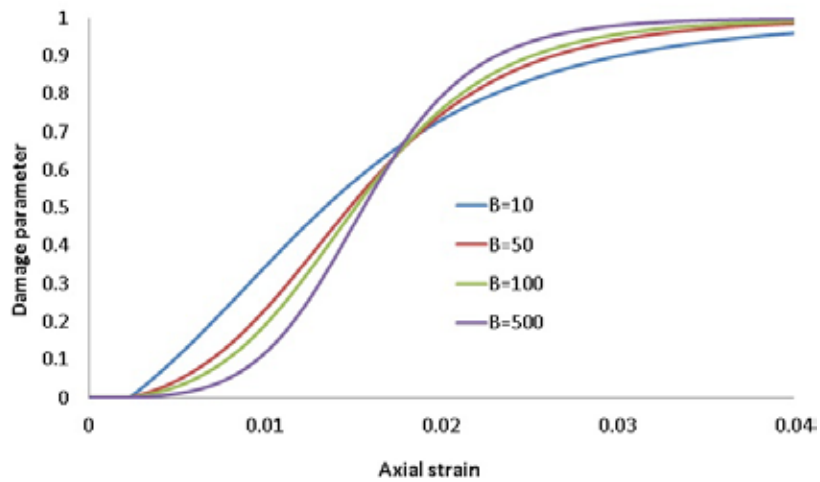

Figure 6-64 Effect of *B* parameter on damage parameter in uniaxial compression test.

Figure 6-65 and Figure 6-66 show the effect of *D* parameter on behavior of CSCM model under uniaxial tension test.

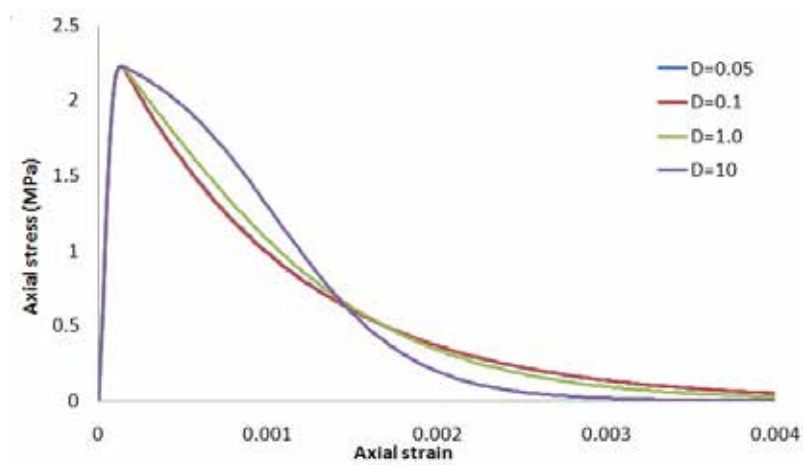

Figure 6-65 Effect of *D* parameter on axial strains in uniaxial tension test.

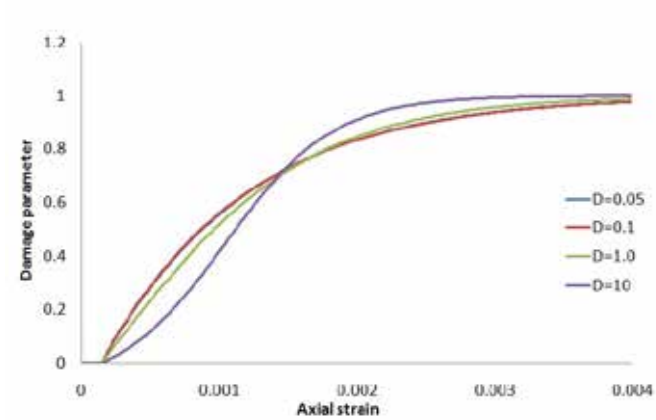

Figure 6-66 Effect of *D* parameter on damage parameter in uniaxial tension test.

For a detail overview of this material model under different confinements, rainbow plot of these materials are presented here. CSCM model look reasonable in stress-strain behavior in different confinements as shown in Figure 6-67, but under higher confinements this material does not show a proper Compaction to Extension behavior as depicted in Figure 6-68.

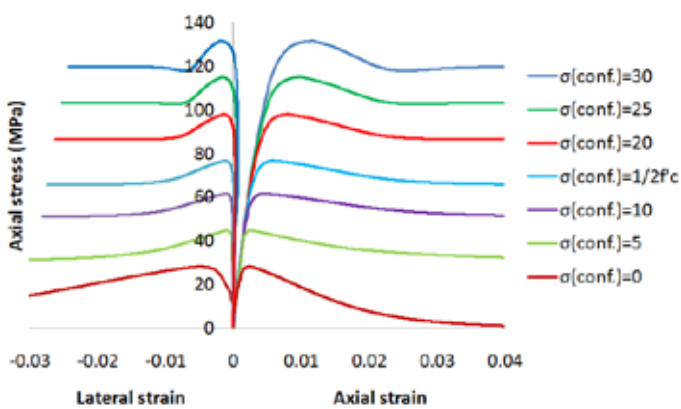

Figure 6-67 Rainbow plot of CSCM model under different confinements (applied confinements are in MPa).

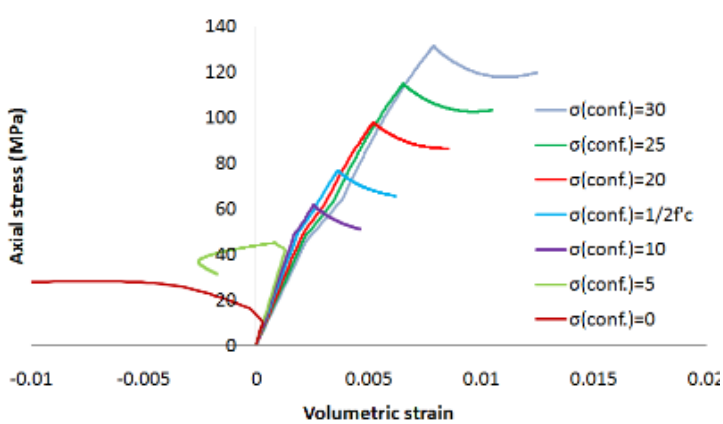

Figure 6-68 Compaction to Extension behavior of CSCM model under different confinements (applied confinements are in MPa).

6.5.2. Drop Test of a Thick-Walled Concrete Cylinder subjected to Shrinkage and Expansion

6.5.2.a. Introduction

Degradation of concrete limits the service life of structures. Shrinkage due to moisture transfer in the early age of concrete and expansion due to thermal effect and ASR may degrade the concrete properties. Thick-walled cylinders are widely used for nuclear containment and the U.S Nuclear Regulatory Commission (NRC) provided some regulations to perform a drop test which are mainly for steel structures (NRC; Dilger et al., 2012; Halstead, Dilger, 2006). A long-thick-walled cylinder is selected to perform some drop tests. Shrinkage strain is calculated based on the latest model of RILEM called "B4" (RILEM, 2014) which considers the autogenous shrinkage and drying shrinkage separately. Expansion of ASR gel between aggregate and cement paste reduces the stiffness and strength of concrete and may cause cracking (Champiri et al., 2012). Substantial experimental work was performed by Larive (1998) to evaluate the ASR expansion in concrete and a 0.2% strain after one year was proposed for concrete cylinder specimens.

Many researchers worked on hypothetical events including drop test and free drop test of thick-walled cylinders with different geometries. Gupta (1997) proposed a mathematical approach for tip-over simulation. He considered some simple assumptions such as a rigid pad and a single degree of freedom mass–spring system. For better results, researchers used finite element method which is now extensively applied for crash simulations. Since implicit time integration is not capable of simulating this contact-impact problem due to the convergence issues with regard to the large deformations and rotations and high nonlinearity, explicit time integration is generally used. Teng et al. (2003) used a dynamic explicit FEA code, named DYNTRAN for impact analysis of a cask. Elfahal (2003) performed an experimental and numerical study to investigate the size effect in normal and high strength concrete cylinders subjected to static and dynamic axial compressive loads. Lee et al. (2005) simulated the drop impact of a cask using LS-DYNA and ABAQUS. Kim et al. [18] studied shock-absorption of a pad of a cask using ABAQUS explicit. Champiri et al. (2015a; 2015b) investigated the behavior of a thick-walled degraded concrete cylinder structure under a tip-over event using LS-DYNA.

6.5.2.b. Geometry and material properties

For this study, a thick-walled cylinder which is about one-third of a prototype structure has been selected with an external radius of *635* mm, a thickness of *254* mm and a height of *2032* mm. The friction-less contact happens on a rigid pad in order to minimize the complexity of this scenario.

For the drop test, unconfined compressive strength of concrete is selected 5.5 ksi (38 MPa), A Young's modulus of 4192 ksi (28.9 GPa) and a Poisson's ratio 0.15 is used.

6.5.2.c. Equivalent temperature due to shrinkage and expansion

The behavior of this thick-walled cylinder is investigated under shrinkage and expansion. The outer and inner surfaces of the concrete are subjected to negative strains due to shrinkage and positive strains due to expansion of concrete while the other elements are in self-equilibrium.

Shrinkage

Shrinkage strain is calculated based on the B4 model as described in section 6.2.2. This model has been applied to the thick walled cylinder. Figure 6-69 shows the behavior of shrinkage strain for *2* years. The following parameters are considered: cement type I, age of loading: 28 days ($t'=t_c=28$ days), age when drying begins: ($t_0=28$ days), relative humidity: ($h=80\%$), volume to surface ratio of cask (V/S = 113 mm), cement content: (C = 219.3 kg/m^3), water-to-cement ratio (w/c = 0.6), aggregate-to-cement ratio (a/c = 0.7).

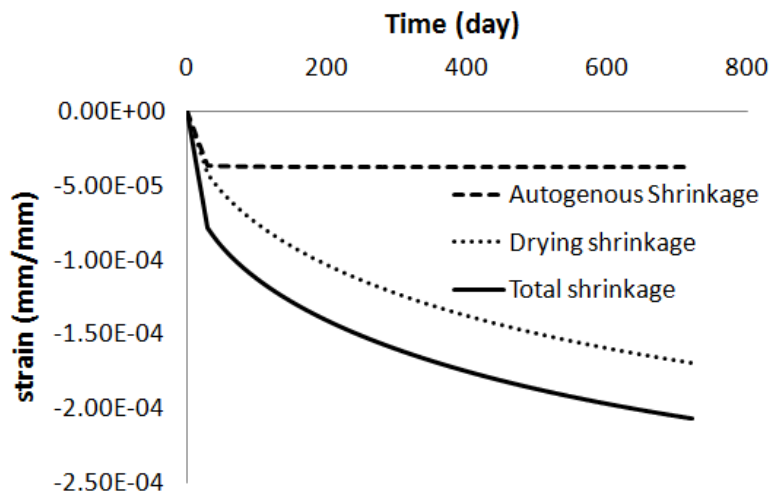

Figure 6-69 Shrinkage strain within 2 years.

Expansion

ASR is one of the chemical attacks that may happen in concrete structures. ASR may cause cracking of the concrete when the ASR gel between the aggregate and cement paste expands. Larive (1998) showed that ASR strain can reach to *0.2%* at under different temperature and humidity conditions as shown in Figure 6-70.

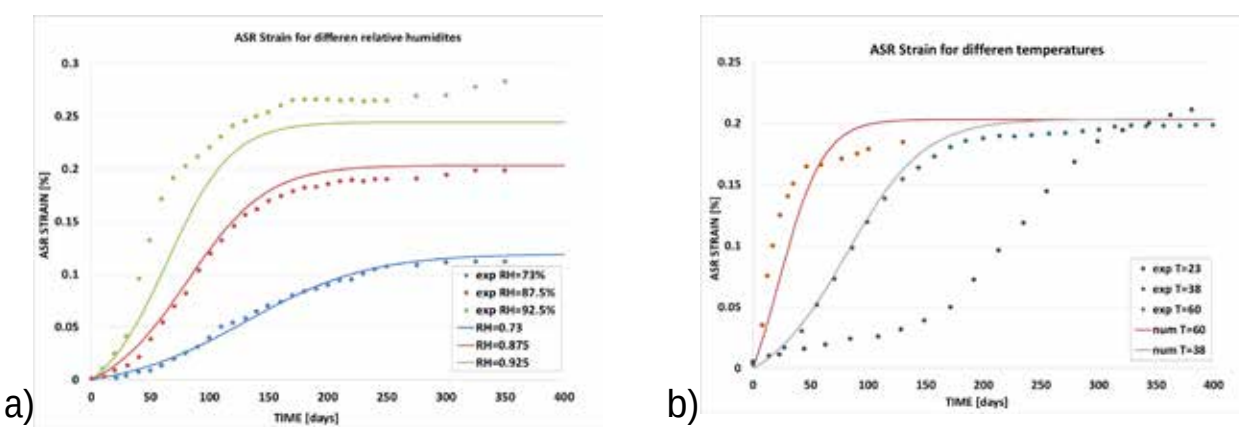

Figure 6-70 ASR strain at different temperature and humidity suggested by Larive (1998).

6.5.2.d. Modeling parameters

Boundary conditions

In the finite element simulations, only half of the cylinder was considered due to symmetry. The displacement component in the circumferential direction of the nodes in the plane of symmetry (X–Z plane) was restrained. The rigid wall was modeled as a frictionless contact to the state of impact.

Other parameters

In order to simulate the drop test, a 3 meter free drop of the cask onto a flat surface was applied. This height is an arbitrary number to see the effects of a high velocity impact. The model has about 20,000 elements and about 23,000 nodes.

Total energy reported in LS-DYNA is the sum of: internal energy, kinetic energy, contact (sliding) energy, hourglass energy and system damping energy. In LS-DYNA, internal energy includes elastic strain energy and work done in permanent deformation. External work includes the work done by applied forces and pressures as well as work done by velocity, displacement or acceleration boundary conditions.

Hourglass stabilization was considered in this model by using Belytschko-Bindeman (1993) (assumed strain co-rotational stiffness form for 2D and 3D solid elements) since one integration point was implemented to evaluate the 8-node brick elements of the 3-D model. This form is available for explicit problems.

Hourglass energy, which is the work done by the forces calculated to resist hourglass modes, takes away from physical energy of the system. Hourglass energy is considered reasonable when it is less than 10% of total energy, so this can be another check point of the accuracy of the model.

Rate effect is another important issue during contact type problems. If rate effect is not taking into account, the response may be different. Rate sensitivity of material was considered for concrete materials during this problem and can be activated directly from MAT-159.

Gravity load was applied to the model as a body load. Internal pressure was implemented as segment load to the internal elements. Shrinkage and ASR strains were imposed to the model in the form of a temperature gradient. To achieve this, a coefficient of thermal expansion (which is assumed here as $\alpha = 1 \times 10^{-5}$ was introduced and a corresponding thermal load was applied in the form of a temperature curve. Shrinkage strain was calculated about $\varepsilon_{\mathrm{sh}} = -2 \times 10^{-4}$, therefore, the temperature gradient is from 0 to -20 degrees. ASR strain was calculated as $\varepsilon_{\mathrm{ASR}} = 2 \times 10^{-3}$, which indicates that the temperature is increasing about 200 degrees.

6.5.2.e. Results

Five different cases were considered with regards to material models and for shrinkage, expansion and internal pressure. Energy-time histories, hour-glass force and von-Mises stress

contour plots of these cases are compared. The time corresponding to the maximum hour-glass force is selected to present the stress contours in the contact state.

Case 1: linear elastic material model

In this case, linear elastic material is considered for the thick-walled cylinder. This case is a benchmark problem and other cases are compared to this case. Figure 6-71 shows the contour of von-Mises stress in the contact state. Effective stress reaches to 90 MPa in the lower level of cylinder where the contact happens.

Time histories of total energy, kinetic energy, and internal energy, are presented in Figure 6-72. It is noted that internal energy suddenly increases at t=1.15 sec because of contact between the pad and cask. After impact, kinetic energy decreases because of deceleration during contact.

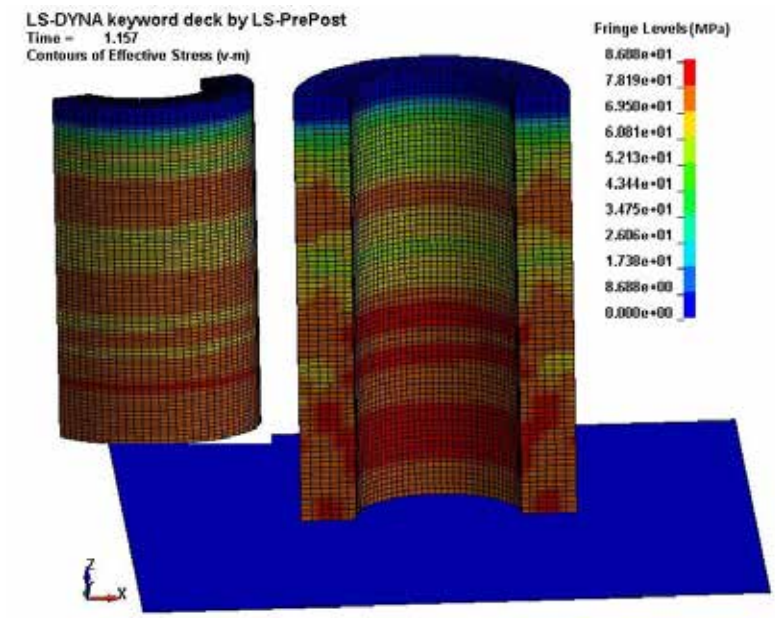

Figure 6-71 von-Mises stress (MPa) contour for case 1.

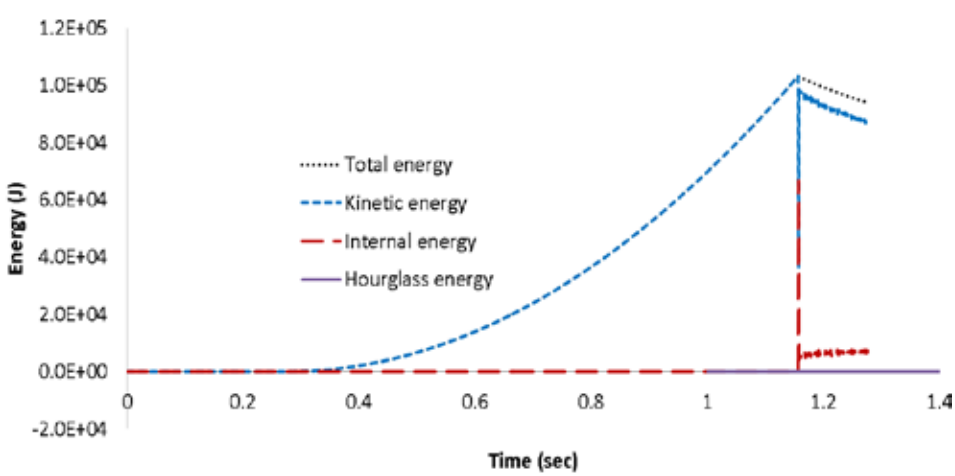

Figure 6-72 Energy time history for case 1.

Case 2: non-linear material model

CSCM model was implemented for thick-walled cylinder and its behavior was investigated without internal pressure. As shown in Figure 6-73, von-Mises stress is reduced to 41 MPa during the impact.

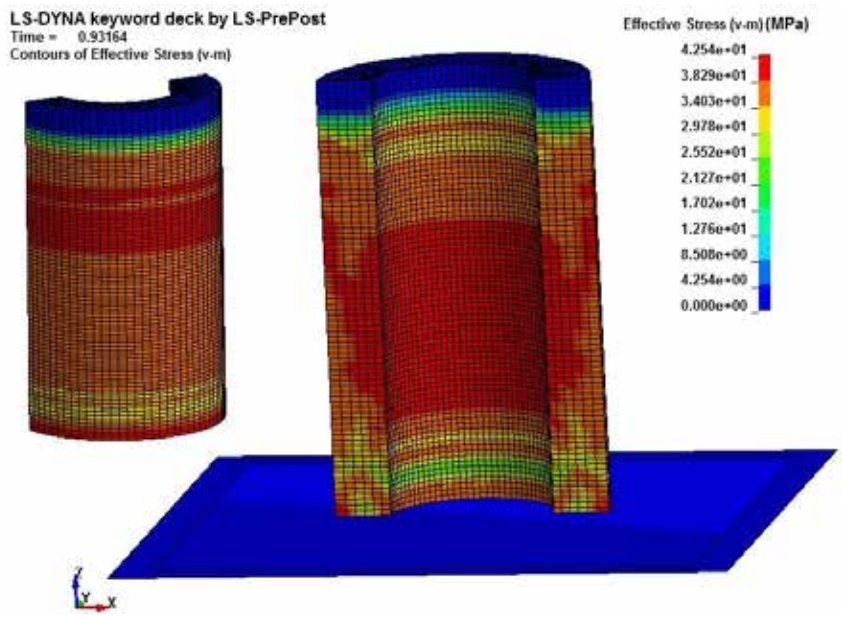

Figure 6-73 von-Mises stress (MPa) contour for case 2.

Time histories of kinetic energy, internal energy and hourglass energy are presented in Figure 6-74. Hourglass energy is less than 10 percent of total energy.

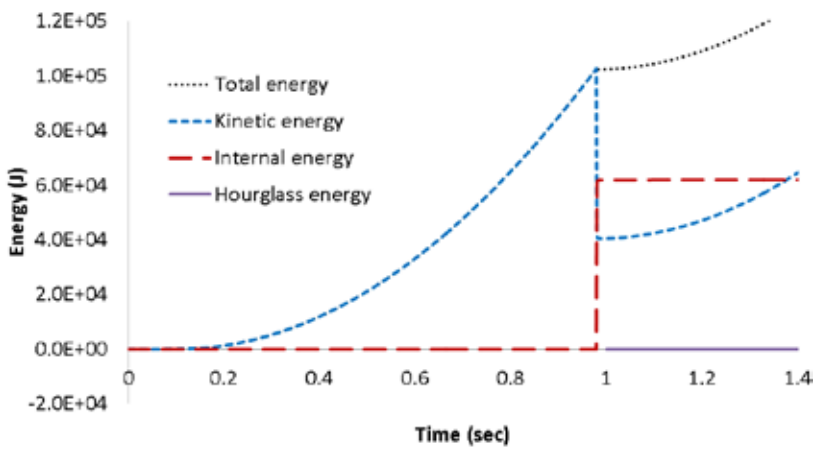

Figure 6-74 Energy time history for case 3.

Case 3: non-linear material model with shrinkage strain

Shrinkage strain is calculated and implemented in the inner and outer layer of the part as described above. The behavior of the cylinder is investigated considering MAT-159 in case of no

internal pressure. As shown in Figure 6-75, von-Mises stress is reduced to 27.5 MPa during the impact. It may be said that the concrete sees less damage in comparison to previous cases.

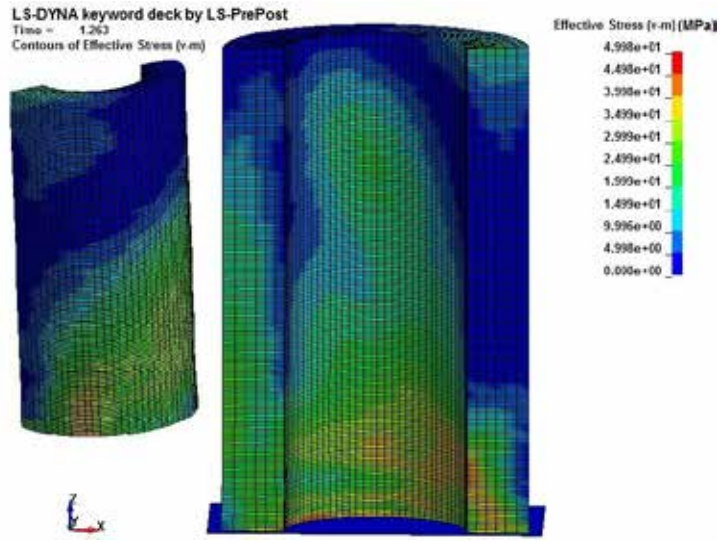

Figure 6-75 von-Mises stress (MPa) contour for case 5.

Case 5: non-linear material model with expansion

ASR strain is calculated as described above. The behavior of the cylinder is investigated considering MAT-159 without internal pressure. As shown in Figure 6-76, von-Mises stress reduces to less than 17 MPa during impact. Additionally, the energy time histories are plotted in Figure 6-77.

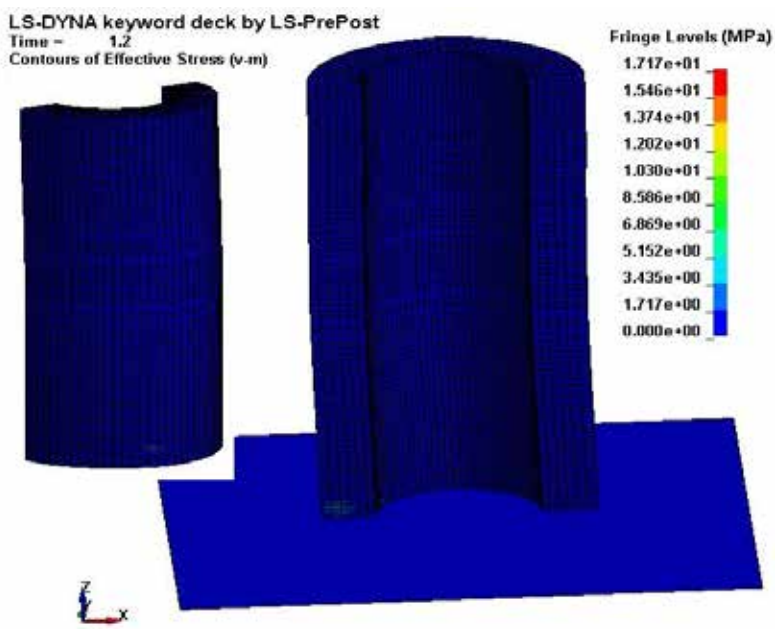

Figure 6-76 von-Mises stress (MPa) contour for case 6.

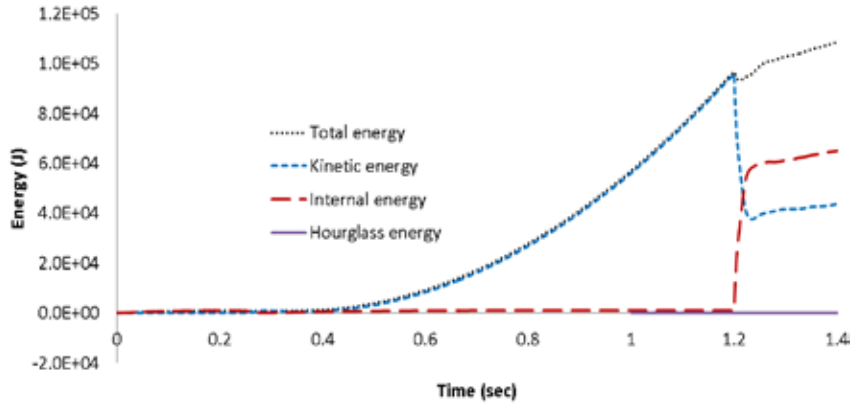

Figure 6-77 Energy time history for case 6.

Case 6: failure mode during impact

In this case, failure modes of the thick-walled cylinder are investigated. Elements can be deleted in LS-DYNA when they reach a failure criterion. Different failure criteria can be used in LS-DYNA and they are explained in section 6.5.3.d.

It was found that using only the maximum compressive strength as an erosion criterion is not a good approach because the stiffness of the structure is highly decreased when the element is deleted, in other words, the stiffness of elements in the softening part is neglected. Therefore, damage based criterion was used. A damage parameter of 0.99 was used. However, it was seen that this criterion cannot capture the shear bond and shear cracks correctly. Therefore, a combination of damage and maximum shear strain was used. Selecting a value for maximum shear strain is not straightforward and it is highly dependent on the material model. A value between 0.1 to 0.9 is widely used in the literature (Islam et al., 2011; Shi et al., 2010; Tang and Hao, 2010; Wu et al., 2011). It was concluded that 0.1 can better describe this criterion for CSCM model. Figure 6-78 show the failure modes of the concrete after impact. As seen in the Figure 6-78, the dominant failure modes is concrete crushing. Additionally, several micro-macro cracks are seen.

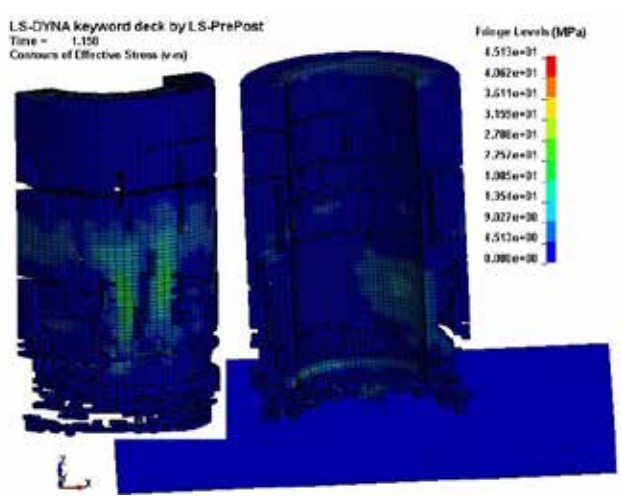

Figure 6-78 von-Mises stress (MPa) contour for case 7.

6.5.2.f. Conclusions

It is necessary to investigate the behavior of concrete containment structures with degraded material properties to predict their long term behavior. Here, different cases of impact of a concrete cask were studied using finite element modeling and analyses with linear and non-linear material, internal pressure, and shrinkage and expansion strains. The results are presented in the form of von-Mises stress and energy-time histories. It is shown that low rate internal pressure does not change the behavior of structure significantly during impact. Additionally, shrinkage and expansion strain reduce the level of stress during impact. Energy level does not change significantly under different cases while the hourglass energy should be accounted for. Failure modes of the concrete structure are also investigated due to impact and it is found that concrete crushing and shear bond are the most dominant failures for tip-over impact events.

6.5.3. Tip-Over Simulation of Model Dry Cask Structure Using the Reference Concrete

6.5.3.a. Finite element model

In the FE simulation, only half of model cask is considered due to symmetry. The geometric properties are summarized in Table 6-12. The model cask is 2.83 times smaller than the prototype cask.

Table 6-12 Dimensions for Simulating the Impact Problem for 1:3 Scale Cask Model.

Part	Height (mm)	Length (mm)	Width (mm)	Internal radius (mm)	External radius (mm)	Thickness (mm)
Rectangular concrete pad	381.0	3810.0	3810.0	-	-	-
Subgrade soil	2540.0 (var.)	7620.0	7620.0	-	-	-
Steel liner	1962.2	-	-	355.6	371.5	15.9
Concrete model cask	1962.2	-	-	371.5	609.6	238.1
Lid-Top	-	-	-	-	431.8	6.4
Lid-Bottom	-	-	-	-	352.4	3.2
Lid-Rib	50.8	-	-	349.3	352.4	3.2
Concrete Lid	50.8	-	-	-	349.3	349.3
Base plate	-	-	-	-	609.6	63.5
Canister	1905.0	-	-	349.3	352.4	3.2

The assumptions of this study are:

- Air outlet and inlet are not considered in this study. Some detailed investigation should be made for these opening effects.
- Base plate is modeled as a solid cylinder. Equivalent mass density of this cylinder is calculated based on the weight of the actual base plate.

- Extra weight for dynamic similitude has been added to the concrete cask part. An equivalent mass density of concrete has been considered to come up with this extra mass.
- Canister is modeled as a rigid part.
- All of cask parts are connected by using master-slave type contact (penalty method).

Isotropic elastic plastic material model is assumed for steel part. Concrete cap surface material model (CSCM_159) is used for mechanical behavior of cask and pad as described in Table 6-13. Elastic material behavior is considered for soil with ρ=1.5 gr/cm^3 $E = 34,474\,MPa$, and n=0.3. Figure 6-79 shows different parts of the cask structure in this simulation.

Table 6-13 Material Properties for Tip-Over Simulation.

Structural Steel properties		Concrete properties	
Name	Value	Name	Value
Density	7850 [kg/m^3]	Density	2450 [kg/m^3]
Poisson's ratio	0.26	Poisson's ratio	0.15
Young's modulus	206E+9 [Pa]	Young's modulus	29.2E+9 [Pa]
Initial yield stress	250 [MPa]	Uniaxial tensile strength	4.14 [MPa]
Tangent Modulus	2E+9[Pa]	Uniaxial compressive strength-Cask	41.4 [MPa]
		Uniaxial compressive strength- Pad	55 [MPa]

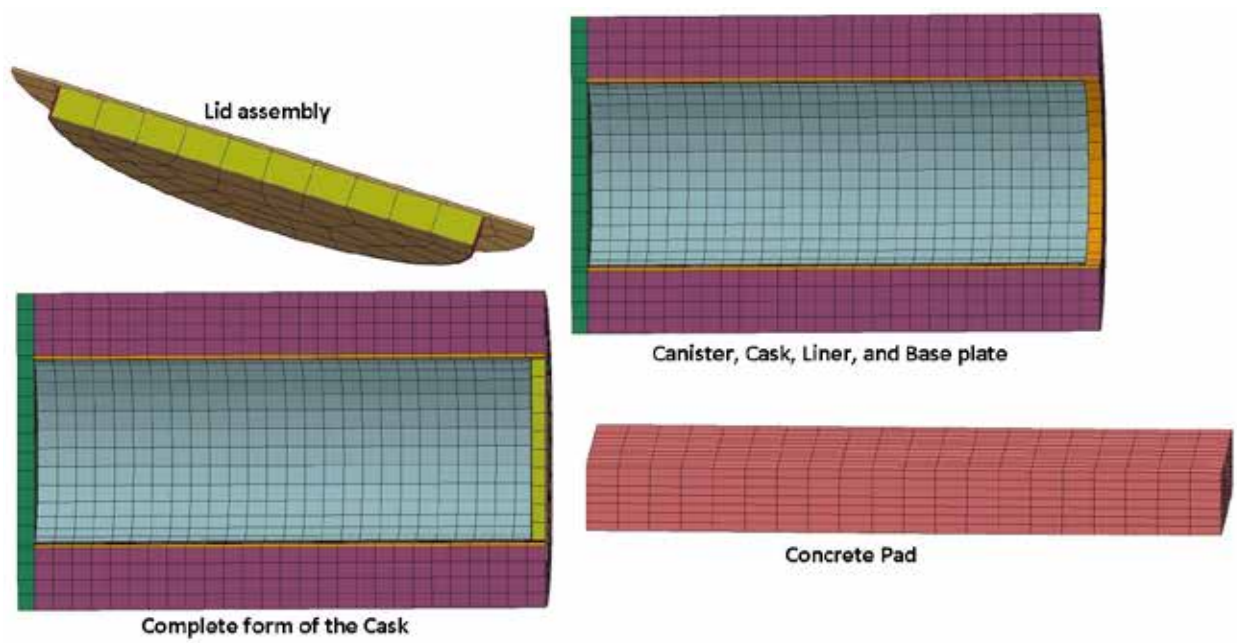

Figure 6-79 Different parts of the cask structures.

Boundary conditions: the displacement component in the circumferential direction of the nodes in the plane of symmetry (X–Z plane) is restrained due to the symmetry of the entire cask. During tip-over event, only the responses within near field of the soil foundation are of interest and stress waves should not be reflected. Thus, the absorbing boundary conditions are imposed on the surfaces of the soil foundation.

The cask is tilted to 35 degree as an initial condition (see Figure 6-80). Surface to surface contact is used for concrete cask-pad, pad-soil, base plate-pad, canister-base, and canister-liner interfaces. Static and dynamic friction coefficients in the contact surface are considered equal to μ=0.25. For Contact between the cask, steel liner and the lid, tied contact surface to surface offset is used to activate penalty method instead of constraint method (tied contact surface to surface is a constraint method contact). Penalty method shows better behavior in most cases than constraint method while both of them have same computational cost.

Hourglass mode has been considered in this model by using Belytschko-Bindeman (1993) (assumed strain co-rotational stiffness form for 2D and 3D solid elements) since one integration point has been implemented in this study. This form is available for explicit problems. Hourglass energy, which is work done by the forces calculated to resist hourglass modes, is taken away from physical energy of the system. Hourglass energy is reasonable when it is less than 10% of total energy, so this can be another point to check the accuracy of this model.

Sliding interface energy or contact energy is another important issue in this problem. This energy should not be less than zero to satisfy the definition of the contact. In addition, it is recommended that this number be around 10%.

Rate effect is another important issue during contact type problems. If rate effect is not taken into account, the response will be completely different. Rate sensitivity of material has been considered for concrete materials.

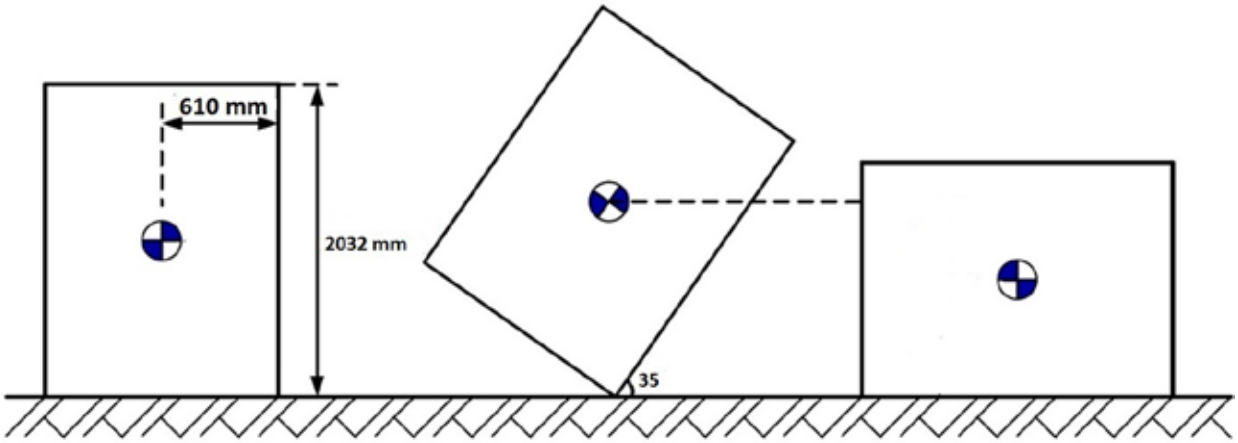

Figure 6-80 Inclined 1:3 scale cask for Tip Over analysis.

6.5.3.b. Analysis results

The internal time step of this analysis is 4.45E-08 sec. This small number is chosen by LS-DYNA software because of explicit time integration of two–body contact and to properly apply penalty method for convergence. This simulation takes 6 hours to complete using 8 processors in parallel. Contact happened at time equal to 1.0146 sec (corresponding to the maximum acceleration at tip of the cask) after starting tip-over simulation from initial condition. Figure 6-81 and Figure 6-82 show the simulation at initial state and after impact, respectively, by LS-DYNA software.

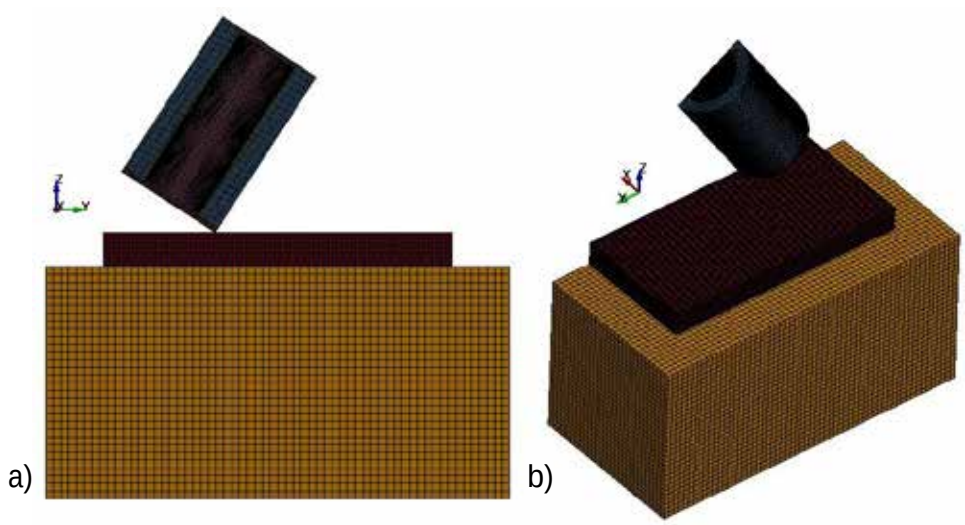

Figure 6-81 Initial condition of tip-over simulation (1:3 scale cask) (Num_{ele}= 266,830 and Num_{nod} =304,329), (a) side view, (b) isometric view.

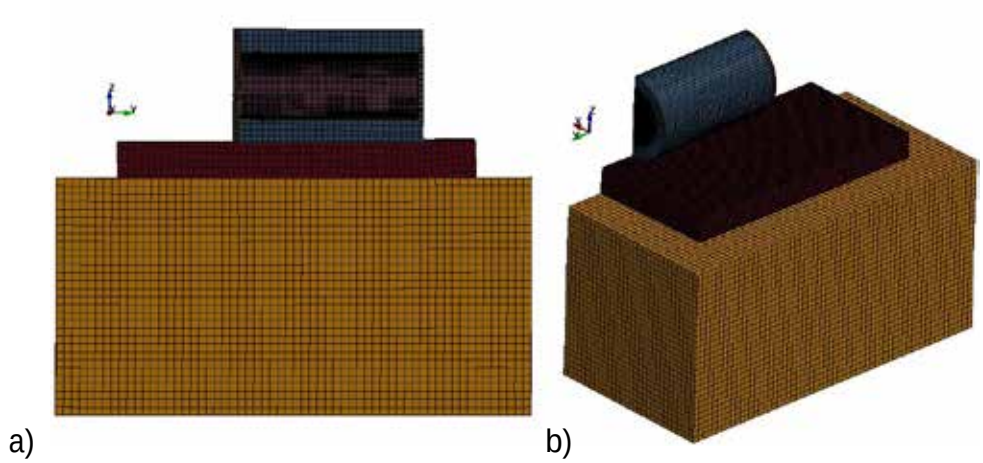

Figure 6-82 Impact state of tip-Over simulation for 1:3 scale cask, (a) side view, (b) isometric view.

Effective plastic strain is a monotonically increasing scalar value which is calculated incrementally as a function of $(Dp)_{ij}$, the plastic component of the rate of deformation tensor. In tensorial notation, this is expressed as

$$epspl = \int_t \sqrt{\frac{2}{3}(DP)_{ij}(DP)_{ij}}\, d\,t \qquad 6.110$$

Effective plastic strain grows whenever the material is actively yielding, i.e., whenever the state of stress is on the yield surface. Figure 6-83 shows ductile damage contours due to compressive stress in different regions of the 1:3 scale cask. Figure 6-84 shows brittle damage contour due to tensile stress in different regions of 1:3 scale cask. Figure 6-85 shows the contours of von-Mises stress.

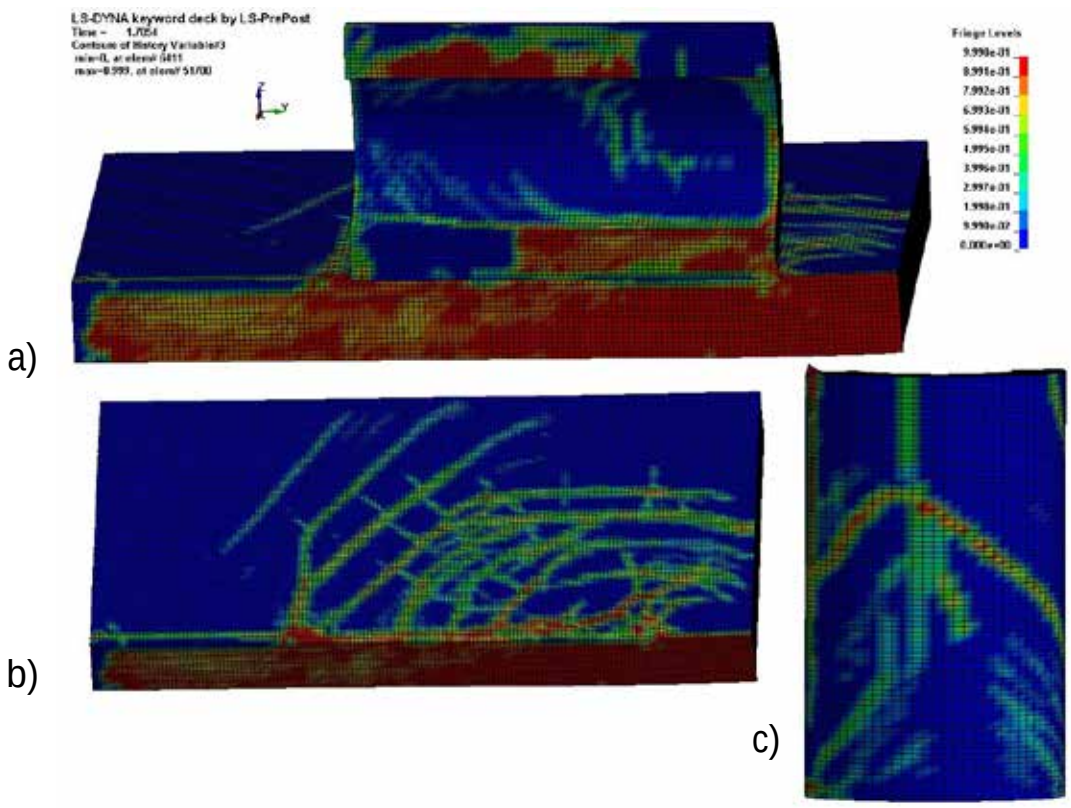

Figure 6-83 Contours of ductile damage at t=1.7054 sec (a) side view, (b) pad, (c) elevation view.

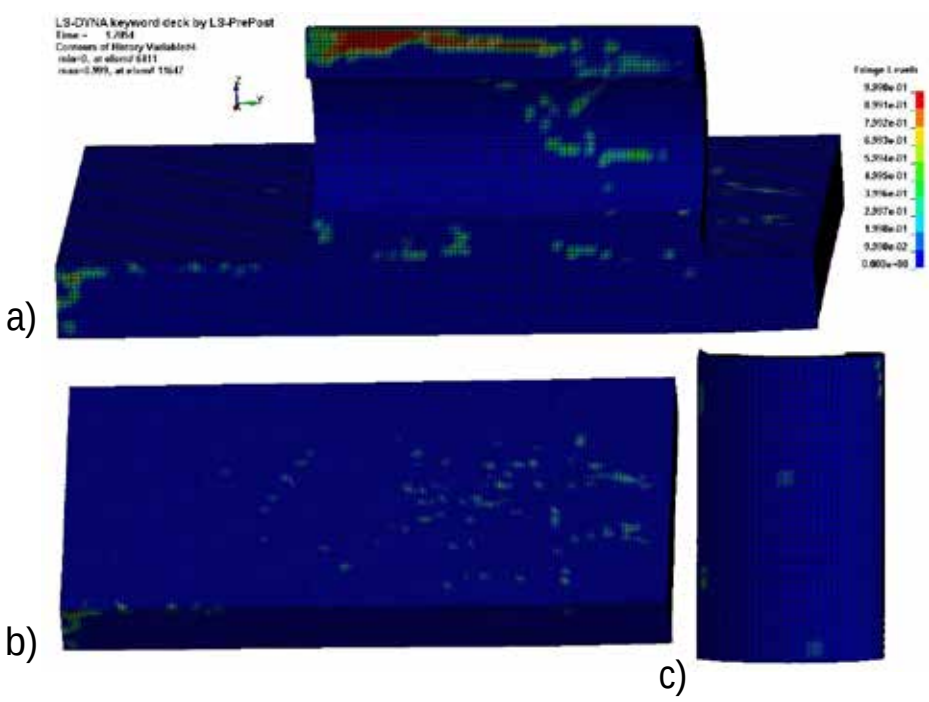

Figure 6-84 Contours of brittle damage at t=1.7054 sec (a) side view, (b) pad, (c) elevation view.

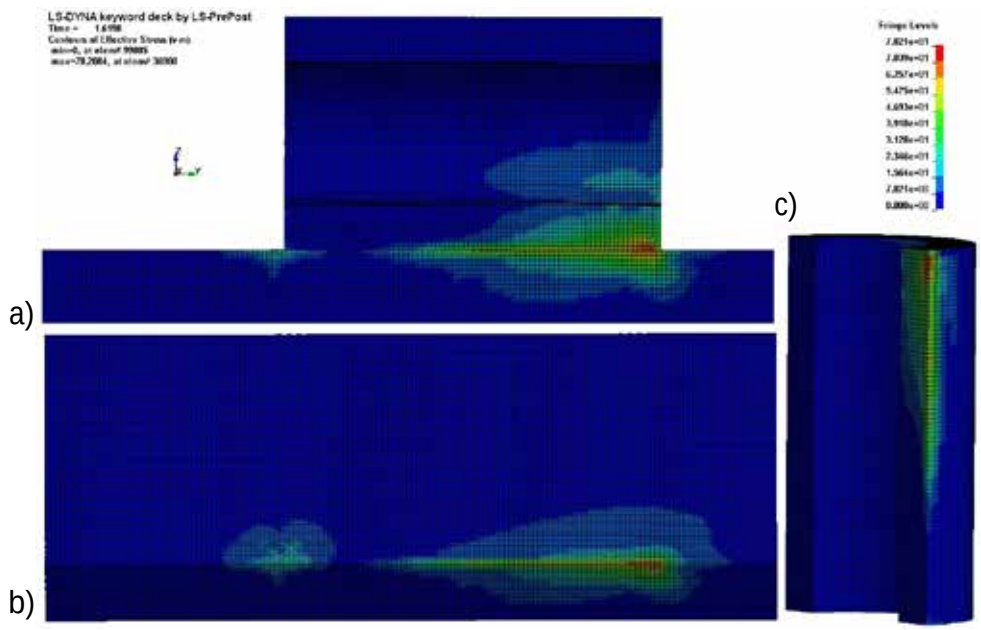

Figure 6-85 Contours of von-Mises stress (MPa) at t=1.6198 sec (a) side view, (b) pad, (c) elevation view.

Element 894 is selected which is located at the top and outside of the cask in the contact-impact region to illustrate the stress and strain time histories in this element. Figure 6-86 shows the location of the selected element.

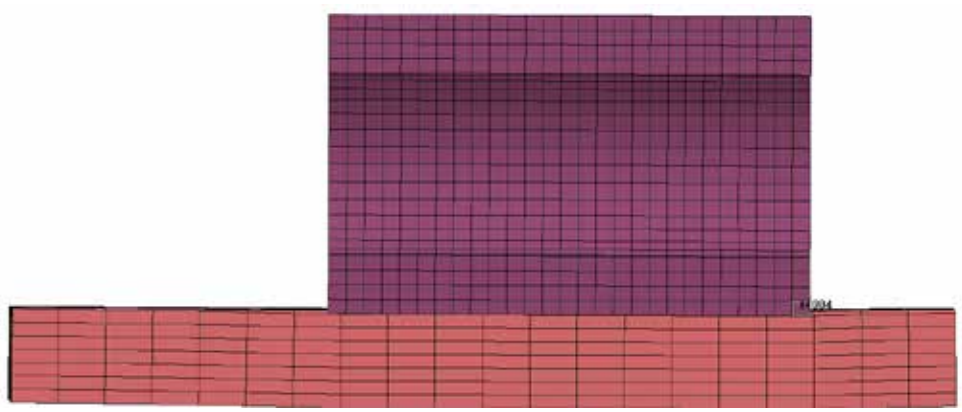

Figure 6-86 Deformed cask mesh and selected contact element for presenting the results.

Time histories of major principal stress (tensile stress) and minor principal stress (compressive stress) are shown in Figure 6-87; while, those for the von-Mises stress, pressure, and effective plastic strain are presented in Figure 6-88. Tensile strength is one-tenth of ultimate compressive strength equal to 41 MPa. It is seen that this element did not reach the tensile strength, but it exceeds the compressive uniaxial capacity of concrete due to triaxiality.

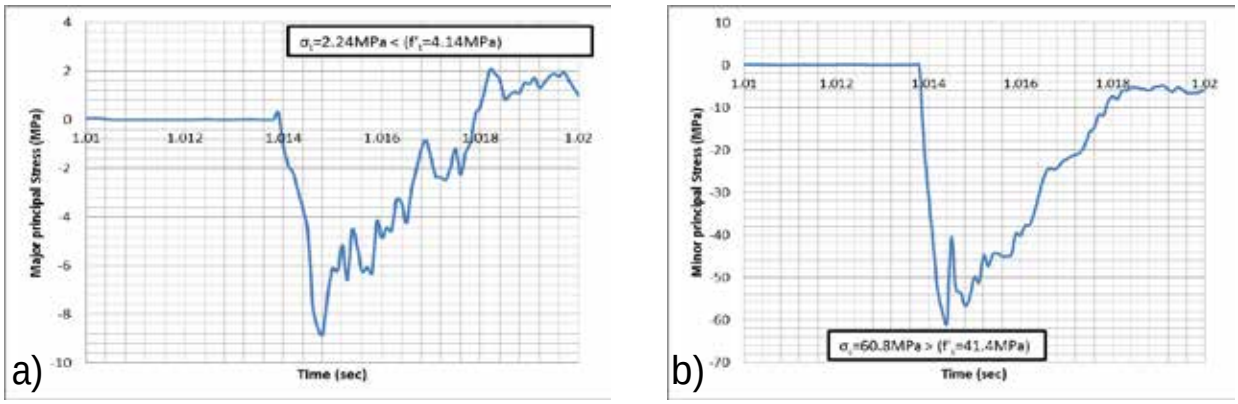

Figure 6-87 Major and minor principal stress for the element shown in Figure 6-86.

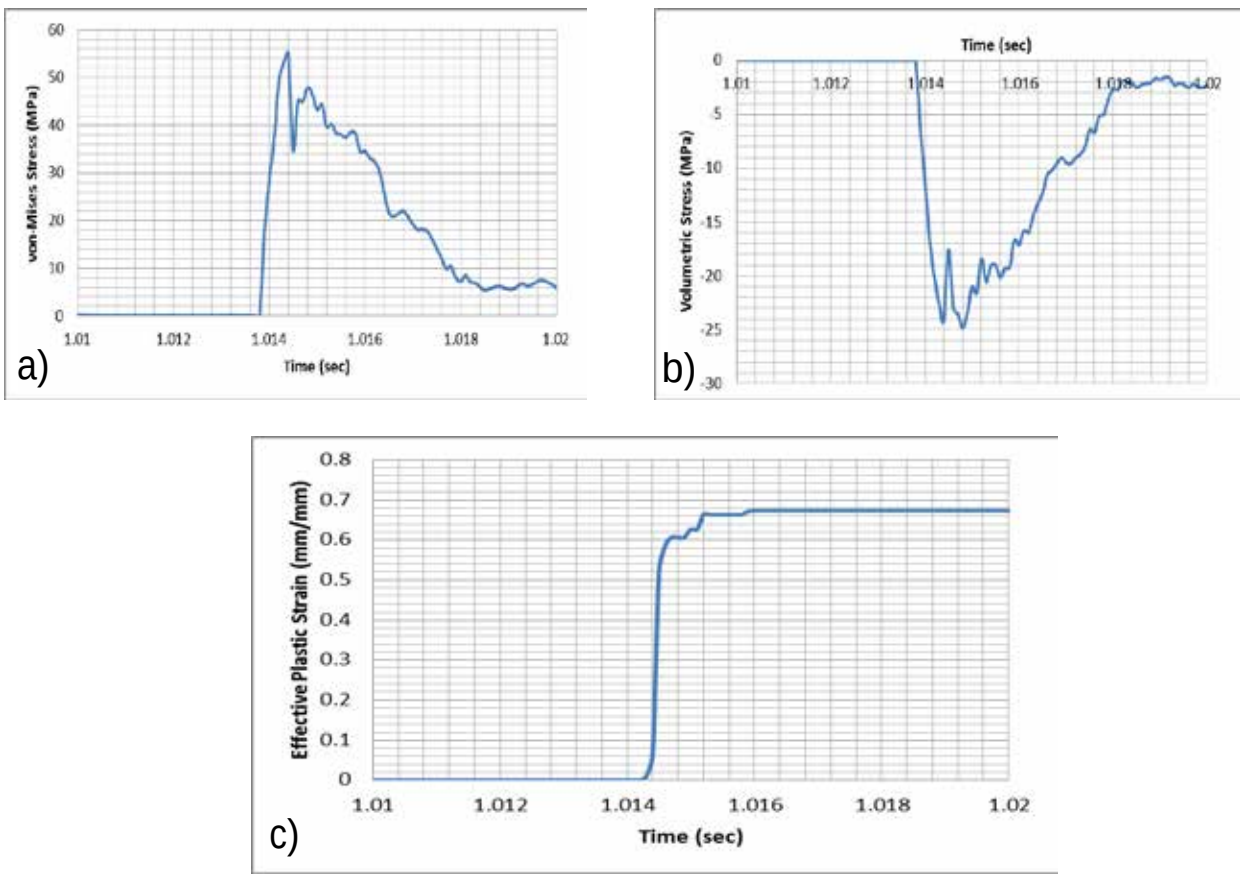

Figure 6-88 von-Mises, volumetric and effective plastic strain for the element shown in Figure 6-86.

The effective plastic strain reached a large value of 68% during contact, indicating large inelastic deformations far beyond the strain level for tensile cracking and compressive crushing of concrete.

Total energy reported in LS-DYNA is the sum of internal energy, kinetic energy, contact (sliding) energy, hourglass energy and system damping energy. In LS-DYNA software, internal energy

includes elastic strain energy and work done in permanent deformation. External work includes work done by applied forces and pressures as well as work done by velocity, displacement or acceleration boundary conditions. Time histories of total energy, kinetic energy, internal energy, hourglass energy, and sliding energy are presented in Figure 6-89. It is noted that internal energy suddenly increases at t=1.0146 sec because of contact between the pad and cask. After impact, kinetic energy decreases because of deceleration during contact.

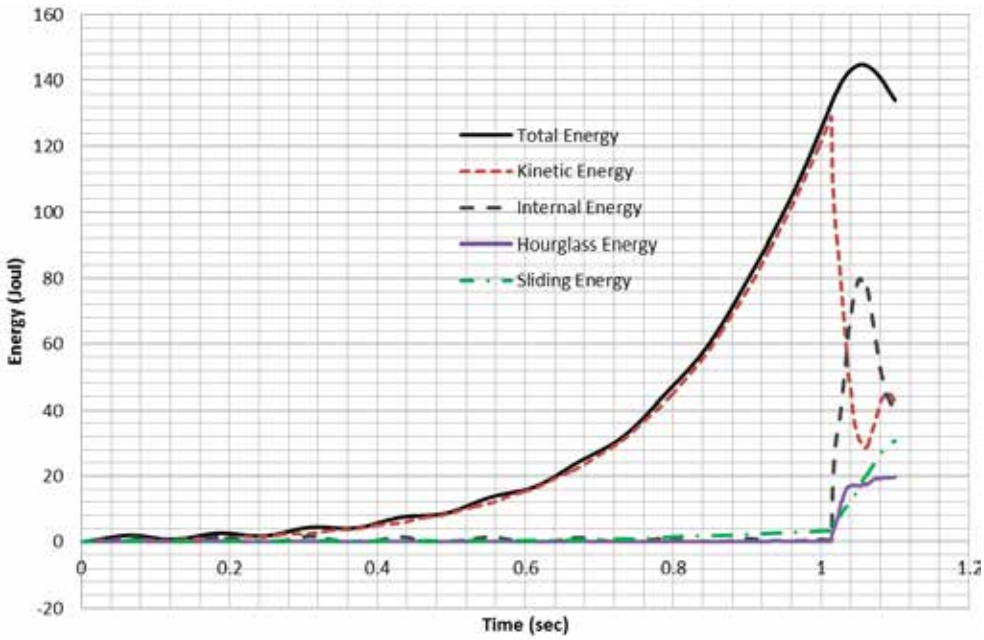

Figure 6-89 Time history of total, kinetic, and internal energy.

6.5.3.c. Sensitivity analysis of the soil thickness under contact-impact problem

In this section, different thicknesses of the soil foundation have been considered to determine the appropriate thickness for soil based on the accelerations in the different layers of the soil and pad. For this purpose, five thicknesses including 762 mm, 1270 mm, 2540 mm, 5080 mm and 7620 mm are considered and the results of acceleration are presented in the following. Length and width of the soil are 5080 mm and elastic material is considered to evaluate soil behavior under this scenario. Figure 6-90 illustrates the distribution of vertical acceleration along different depths of the cask-pad-soil interaction. At the bottom of soil, we have zero acceleration due to the pre-defined boundary condition. The presented values are for one element up from the bottom. As it can be seen the maximum values of the acceleration for bottom of the soil with thickness of 2540 mm is about 0.08 g and increasing the thickness does not further decrease this value. In addition, this thickness shows better behavior than thicknesses 762 mm and 1270 mm and has a comparable behavior to 5080 mm and 7620 mm. Therefore, a thickness of 2540 mm is used for future simulations.

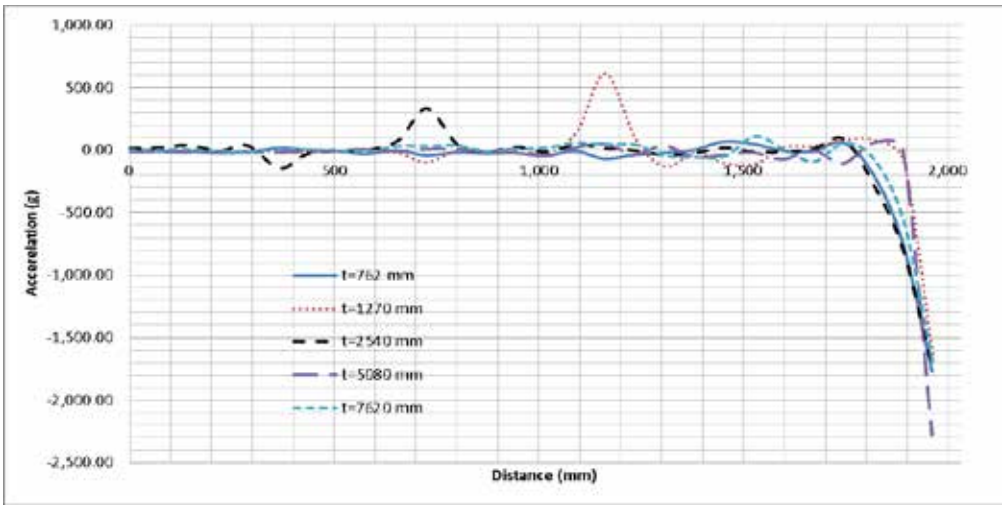

(a) Contact edge along the concrete cask

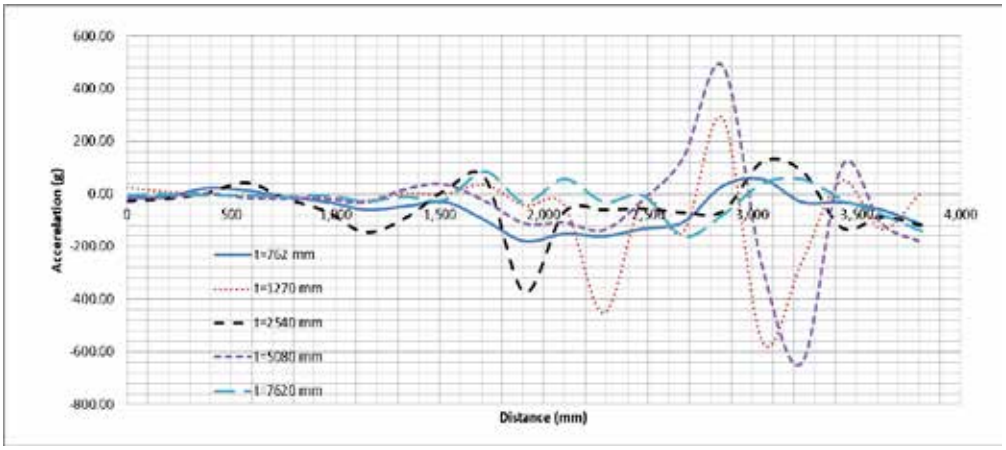

(b) Top surface of concrete pad

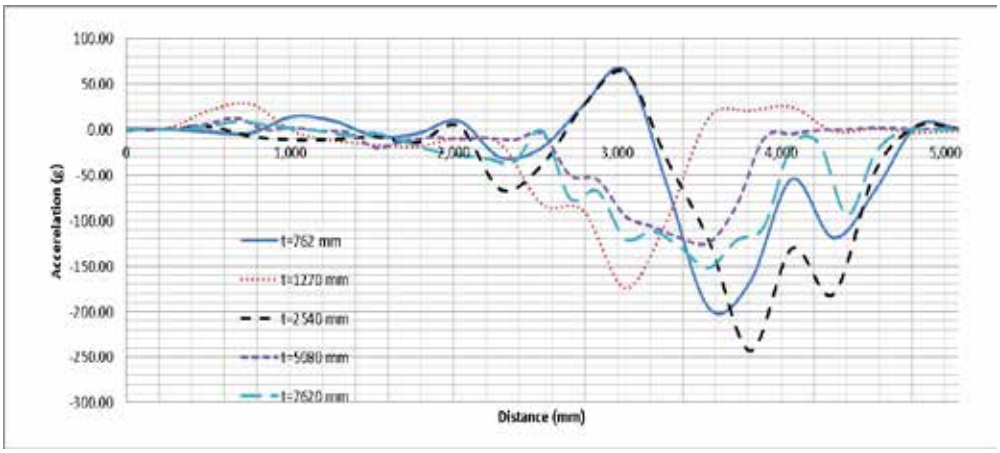

(c) Top surface of soil

Figure 6-90 Acceleration time histories at different locations.

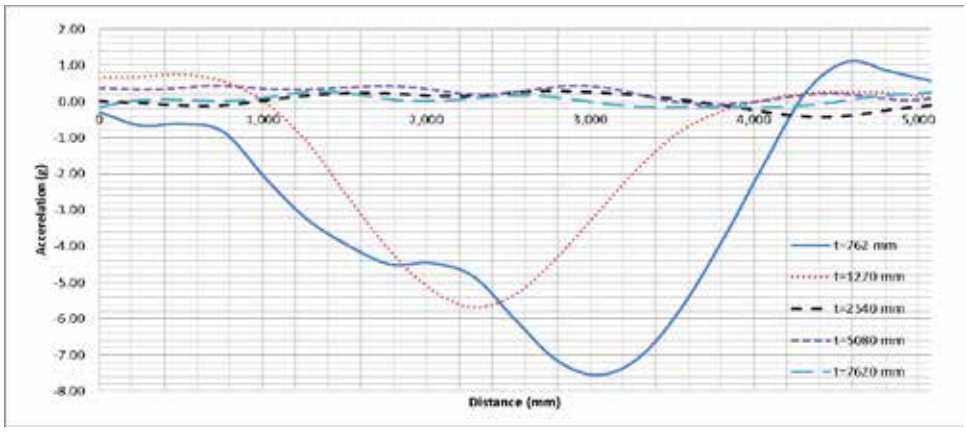

(d) Middle surface of soil

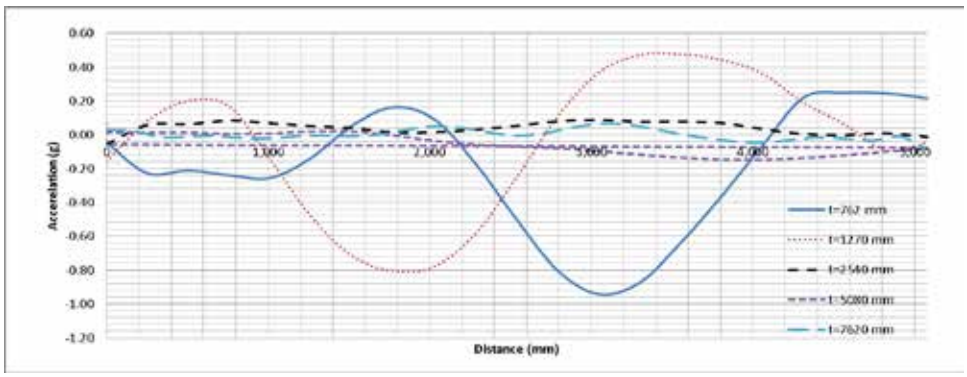

(e) Bottom surface of soil

Figure 6-90 (continued) Acceleration time histories at different locations.

6.5.3.d. Failure analysis of tip-over of 1:3 model dry cask structures

In this section, failure modes of the dry cask structure will be investigated. Geometry, boundary and initial conditions, and material properties are the same as previous sections, but in this section a fine mesh was used (80 elements along the length of the cask). Contact surface to surface was used for concrete cask-pad surface, pad-soil surface, base plate-pad surface, canister-base plate, and canister-liner surface. Static and dynamic friction coefficients between the contact surfaces were taken equal to 0.25. For contact between cask, steel liner and lid, tied contact surface to surface offset was used to activate penalty method instead of constraint method (tied contact surface to surface is a constraint method contact). Penalty method shows better behavior in most cases than constraint method while both of them have the same computational cost.

Failure Criteria

Elements can be deleted in LS-DYNA when they reach a failure criterion using *keyword_MAT_Add_Erosion. Different failure criteria are introduced in this keyword, but mainly the following criteria are used for concrete parts:

Maximum principal strain. Erosion is initiated when a maximum principal strain is reached according to

$$e_1 \geq (e_1)_{\lim} \qquad 6.111$$

Where, ε_1 is the maximum principal strain of an element in a specific time, and $(\varepsilon_1)_{lim}$ is the entered value as a limit for maximum principal strain. Once the element satisfies this criterion, it will be deleted, and can no longer be recovered, and its stiffness will be zero. This is a limit in tension strain and can be applied to brittle materials like concrete and can be used as a criterion in crack opening and can represent tensile fracture and spalling of concrete.

Maximum shear strain. Erosion is initiated when a maximum shear strain is reached according to

$$g_1 = (g_1)_{\lim} \qquad 6.112$$

Where, γ_1 is the maximum shear strain of an element at a specific time, and $(\gamma_1)_{lim}$ is the entered value as a limit for maximum shear strain. This criterion can be used for shear failure in concrete elements subjected to contact explosion or close blast loads, or to concrete plates under projectile perforation. The important issue about this criterion is that the estimation of the shear strain erosion limit from concrete is not straightforward.

Pressure. Erosion is initiated when a maximum (minimum) pressure is reached according to

$$P \geq P_{\lim} \quad or \quad P \leq P_{\lim} \qquad 6.113$$

Where, P the pressure of an element at a specific time, and P_{lim} is the entered value as a limit for maximum or minimum pressure. When this criterion is used in tension, it is similar to tension cut off in classical plasticity.

Principal stress. Erosion is initiated when a principal stress is reached according to

$$s_1 \geq (s_1)_{\lim} \qquad 6.114$$

Where, σ_1 the principal is stress of an element at a specific time, and $(\sigma_1)_{lim}$ is the entered value as a limit for principal stress. This criterion can represent a limitation to the tensile strength of concrete.

Damage. Erosion is initiated when a damage parameter is reached according to

$$D \geq D_{\lim} \qquad 6.115$$

where D is the level of damage in an element at a specific time, and D_{lim} is the entered value as a limit for damage. This criterion is highly dependent to the constitutive models used for concrete.

Many researchers used different criteria for failure analysis of structures in finite element software. Mostly, principal strain and shear strain were used for concrete structures, but also some researchers used tensile damage and tensile stress for evaluation of failure in structures. An extensive literature review has been performed in order to find a suitable failure criterion for tip-over impact of concrete casks in LS-DYNA. The results are summarized in Table 6-14.

Table 6-14 Failure Criteria in the Literature for Concrete in LS-DYNA.

Problem	Material	Criteria	Limit	Mesh size	Reference
Impact	Concrete 27.5 MPa	Principal strain	0.003	$80 \times 80 \times 60\ mm$	Huang C. Wu, T (2009)
Blast	Concrete 40 MPa	Principal strain	0.01	$18.75 \times 18.75 \times 25\ mm$	Xu K. Lu Y. (2006)
Blast	Concrete 24 MPa	Principal strain	0.15	$50\ mm$	Shi et al (2010)
Blast	Concrete 24 MPa	Shear strain	0.9	$50\ mm$	Shi et al (2010)
Blast	Concrete 60 MPa	Tensile strain	5MPa	6.25 to $100\ mm$	Tang and Hao (2010)
Blast	Concrete 60 MPa	Principal strain	0.1	6.25 to $100\ mm$	Tang and Hao (2010)
Blast	Concrete 40 MPa	Maximum strain	0.1	$50\ mm$	Wu et al (2011)
Blast	FRC 1% 28 MPa	Shear strain	0.4		Wang et al (2009)
Blast	FRC 1% 28 MPa	Tensile Stress	5.4MPa		Wang et al (2009)
Blast	FRC 1.5% 30 MPa	Shear strain	0.4		Wang et al (2009)
Blast	FRC 1.5% 30 MPa	Tensile stress	6MPa		Wang et al (2009)
Blast	FRC 2% 32 MPa	Shear strain	0.4		Wang et al (2009)
Blast	FRC 2% 32 MPa	Tensile stress	7.5MPa		Wang et al (2009
Blast	FRC 45 MPa	Damage	0.99	$25 \times 25\ mm$	Cuoghin et al (2010)
Dynamic	Concrete 35 MPa	Principal strain	0.002	$6\ to\ 8\ mm$	Tu and Lu (2009
Impact	Concrete 40 MPa	Strain limit	1.5		Tu and Lu (2010)
Impact	Concrete 48 to 140 MPa	Strain failure	-1(comp) 0.5(tens)	2mm	Islam et al (2011)
Impact	FRC 28 to 32 MPa	Tension stress failure	5.4MPa	1.25 mm	Teng et al (2008)
Impact	FRC 28 to 32 MPa	Shear strain failure	0.4	1.25 mm	Teng et al (2008)
Impact	HPFRC	Ultimate shear strain	0.012	$6 \times 8\ mm$	Farnam et al (2010)

In our case, several simulations were performed to obtain the suitable criteria for the concrete cask structure during tip-over simulation. A fine mesh was chosen for the concrete cask. The size of each element is $25 \times 25 \times 25\ \mathrm{mm}$ $(1 \times 1 \times 1\ \mathrm{in})$, which is about three times finer than the regular mesh which was used to perform the tip-over simulation. Decreasing the element dimensions increased the computational time highly. Each run took about 4 days to complete using this fine mesh.

It was discovered that using only the maximum compressive strength as an erosion criterion is not a good approach because the stiffness of the structure is highly decreased when the element is deleted, in other words, the stiffness of elements in the softening part is neglected. Therefore, damage based criterion was used. A damage parameter of 0.99 was used. However, it was seen that this criterion cannot capture the shear band and shear cracks correctly. Therefore, a combination of damage and maximum shear strain was used. Selecting a value for maximum shear strain is not straightforward and it is highly dependent on the material model. A value between 0.1 to 0.9 is highly used in the literature. It was concluded that 0.1 can better describe this criterion for MAT_159 (continuous surface cap material model) during this contact-impact problem.

Analysis Results

Figure 6-91 show the failure modes of the concrete after impact. As seen in the figure, the dominant failure modes are shear bond, concrete crushing and tensile cracking. Additionally, several micro-macro cracks are seen. Figure 6-92 shows the contours of the absolute value brittle and ductile damage) in the concrete cask.

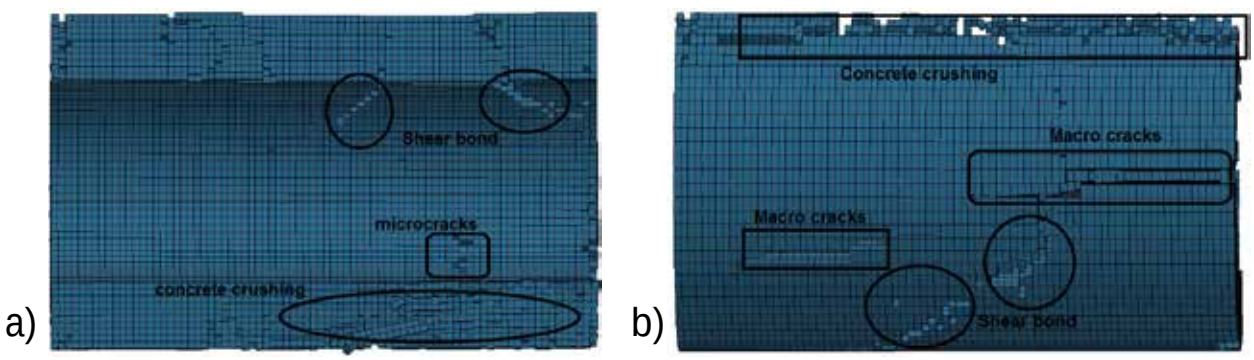

Figure 6-91 (a) inside of the concrete cask (b) outside of the concrete cask

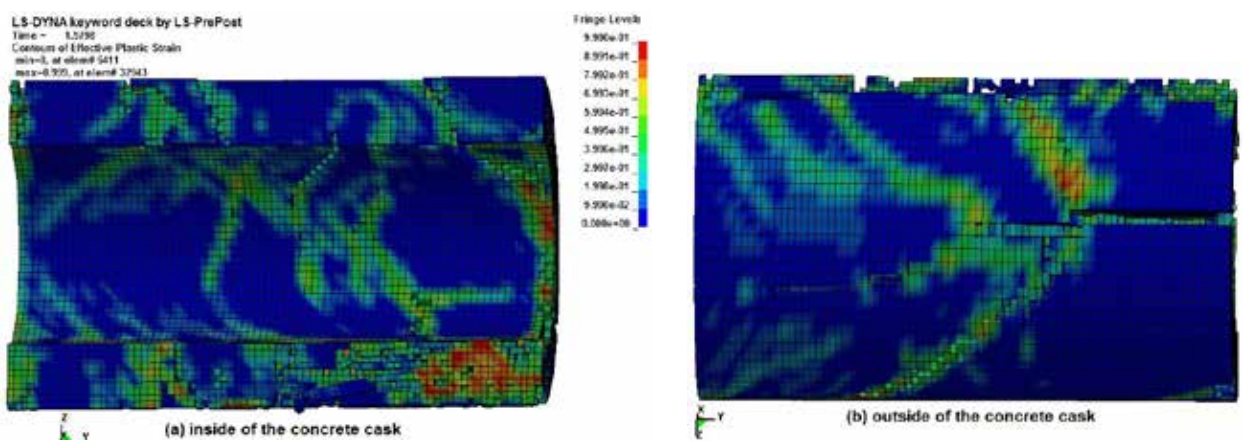

Figure 6-92 Failure modes of concrete cask.

6.5.3.e. Discussion

A simplified 1:3 scale model of the dry cask structure (physical model of which will be tested) was analyzed for the contact-impact scenario of tip-over. Ten parts including concrete cask, steel lid, concrete pad, steel liner, steel base plate, steel lid rib (two parts), concrete section inside of the lid, canister and soil were idealized with 22,627 nodes, and 17,736 elements. Internal time step for this explicit computation was *Δt=4.45E-08* sec. Strains and stresses were investigated in the critical region of cask at the top. There is no interpenetration during the contact. It was seen that the cask is subjected to considerable distress during this impact. Further investigations will be necessary to evaluate the interface between the lid and concrete cask and for the contact interaction between the cask and pad.

6.5.4. Tip-Over Simulation of Prototype Dry Cask Made of Reference Concrete

To validate the result of tip-over analysis of the 1:3 dry cask structures, a similar study of the 1:1 prototype cask has been performed in this section. In the FE simulation, only half of prototype cask is considered due to symmetry. Similar assumptions have been made here for prototype modeling. However, a finer mesh has been used to provide a better mechanism of contact-impact simulation. The geometric properties are summarized in Table 6-15. The internal time step of this analysis is 9.79E-07 sec. This simulation takes 13 hours to complete using 8 processors in parallel. Contact happened at time equal to 1.819 sec (corresponding to the maximum acceleration at tip of the cask) after starting tip-over simulation from initial condition. In this case, coarser mesh was selected for pad and soil which decreases the computational time significantly (Num_{ele} = 82,384 and Num_{nod} =98,531).

Table 6-15 Dimensions for Simulating the Impact Problem for Prototype Cask Model.

Part	Height (mm)	Length (mm)	Width (mm)	Internal radius (mm)	External radius (mm)	Thickness (mm)
Rectangular concrete pad	1143.0	11430.0	11430.0	-	-	-
Subgrade soil	7620.0	15240.0	15240.0	-	-	-
Steel liner	5557.5	-	-	1009.7	1054.1	44.5
Concrete model cask	5557.5	-	-	1054.1	1727.2	673.1
Lid-Top	-	-	-	-	1117.6	19.1
Lid-Bottom	-	-	-	-	1003.3	7.9
Lid-Rib	145.7	-	-	995.4	1003.3	7.9
Concrete Lid	145.7	-	-	-	995.4	995.4
Base plate	-	-	-	-	1727.2	146.1
Canister	5397.5	-	-	995.4	1003.3	7.9

Figure 6-93 and Figure 6-94 show ductile and brittle damage contour due to compressive and tensile stress, respectively, in different regions of prototype cask.

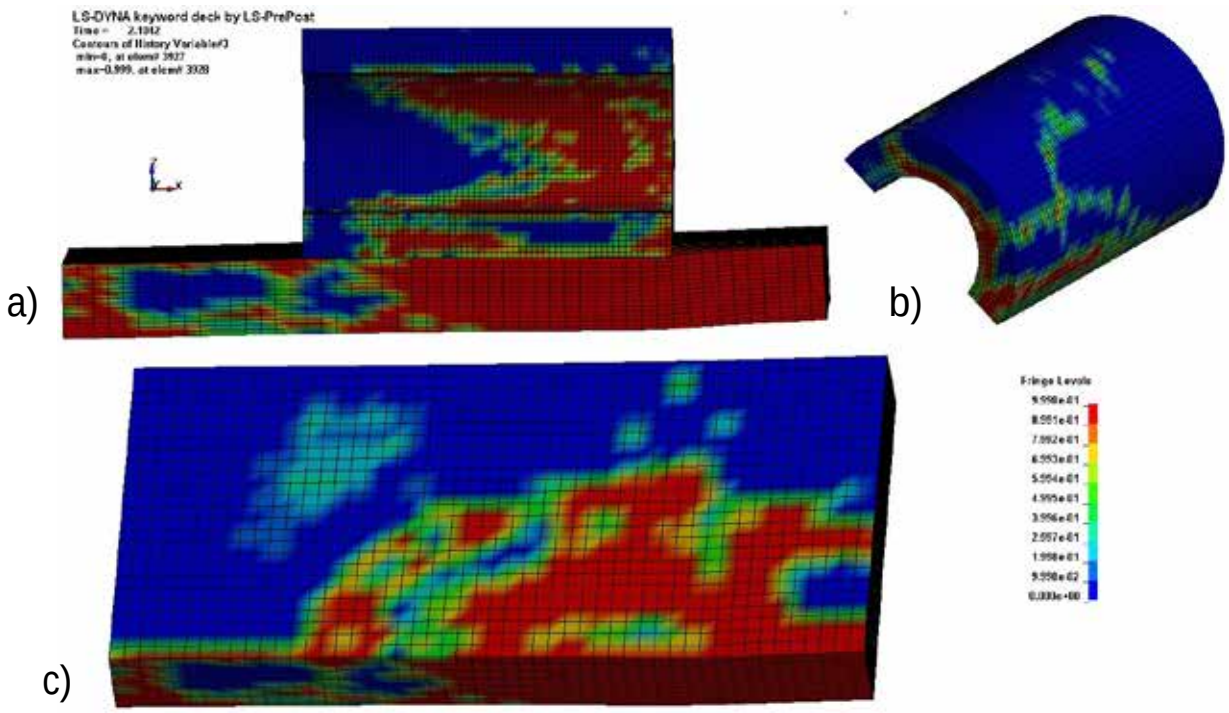

Figure 6-93 Contours of ductile damage at t=2.1042 sec (a) side view, (b) cask, (c) pad.

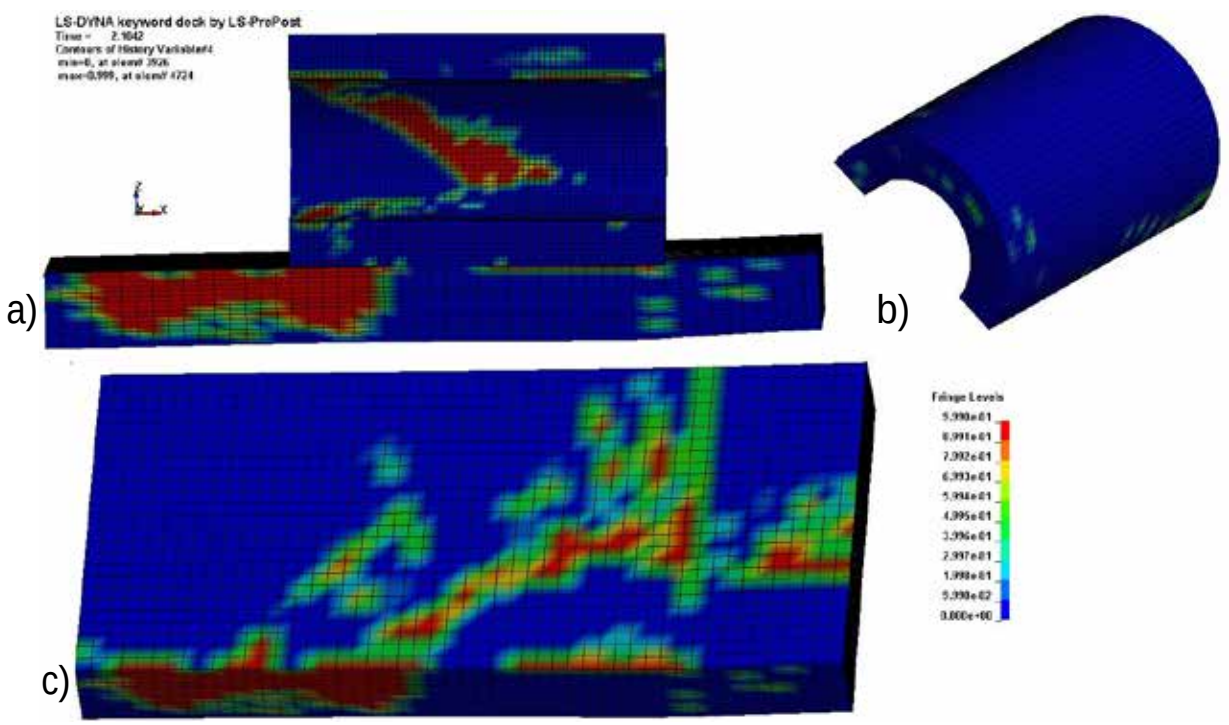

Figure 6-94 Contours of brittle damage at t=2.1042 sec (a) side view, (b) cask, (c) pad.

Figure 6-95 shows the contour of von-Mises stress.

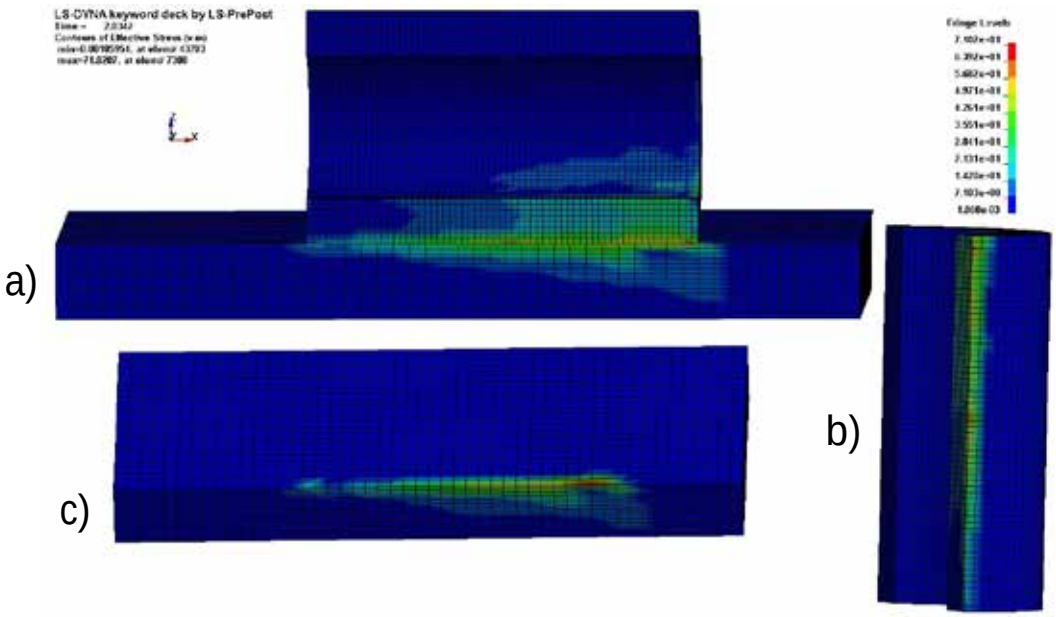

Figure 6-95 Contours of von-Mises stress (MPa) at t=2.0342 sec (a) side view, (b) cask, (c) pad.

Same location as the model cask on the tip is selected to present the results of strain and stress. Time histories of major (tensile) and minor (compressive) principal stress are provided in Figure 6-96 and Figure 6-97.The von-Mises stress, pressure and effective plastic strain are presented in Figure 6-98. In addition, the results of the 1:3 scale model cask are presented in the figures for making a better comparison. It is noted that the contact times are different for these two cases and the contact time of the model cask has been shifted to the contact time of the prototype cask (1.0146 sec to 1.8190 sec).

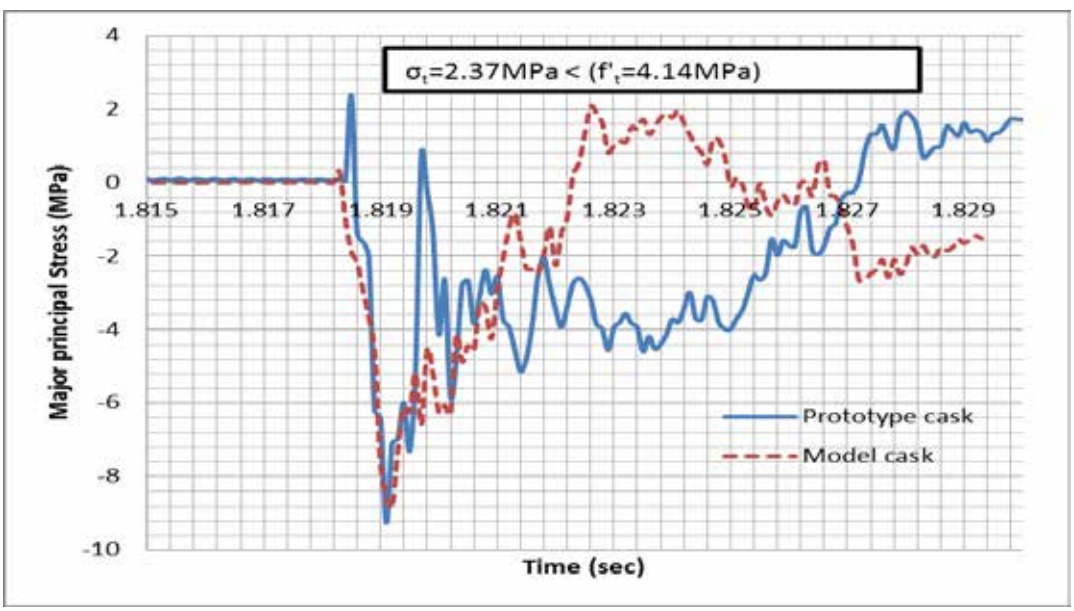

Figure 6-96 Major principal stress for the selected element shown in Figure 6-86.

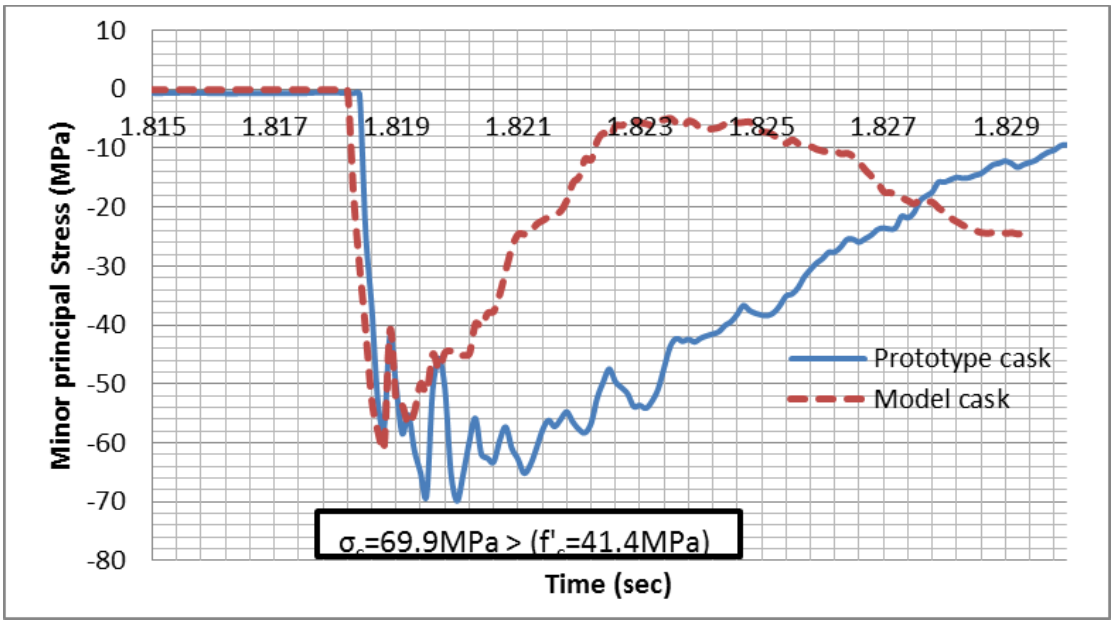

Figure 6-97 Minor principal stress for the element shown in Figure 6-86.

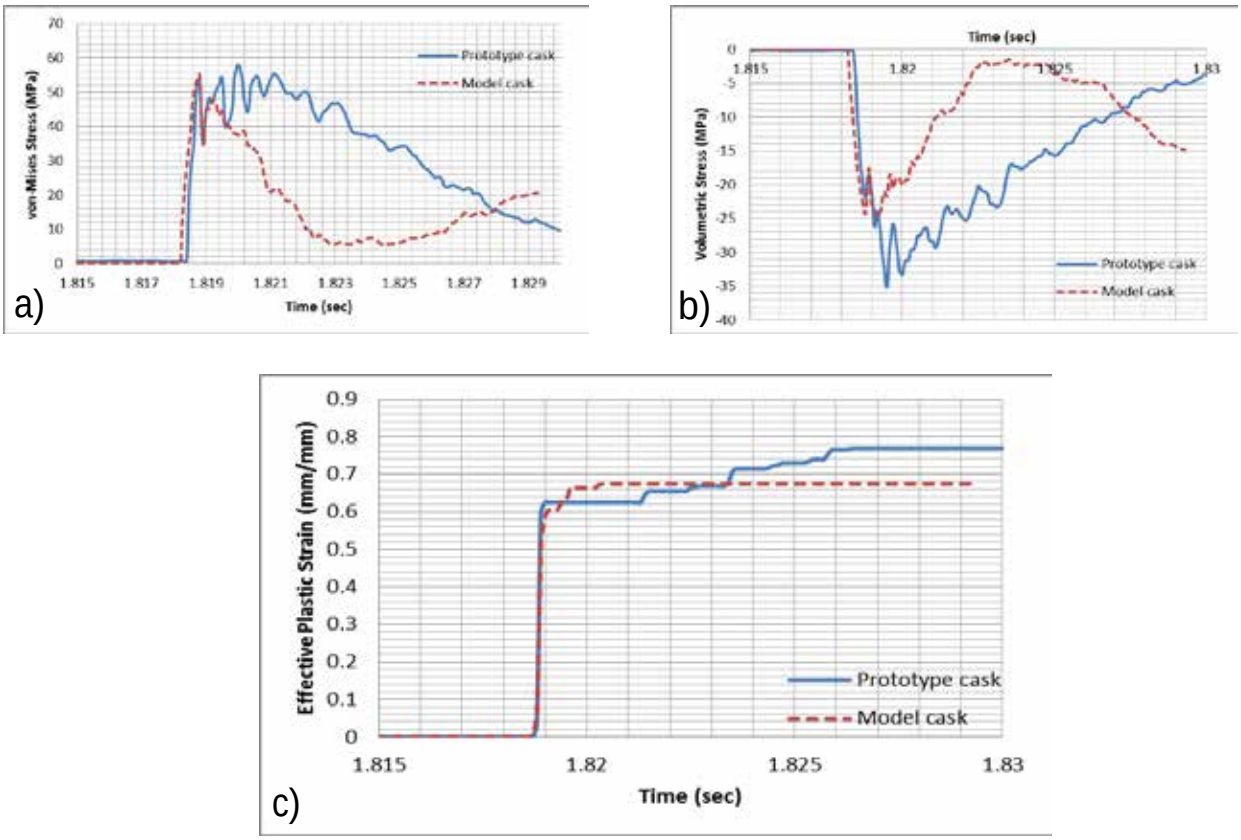

Figure 6-98 von-Mises, volumetric and effective plastic strain for the element shown in Figure 6-86.

The effective plastic strain reached a large value of 76% during contact indicating large inelastic deformations far beyond the strain level for tensile cracking and compressive crushing. The time histories of total energy, kinetic energy, and internal energy are presented in Figure 6-99.

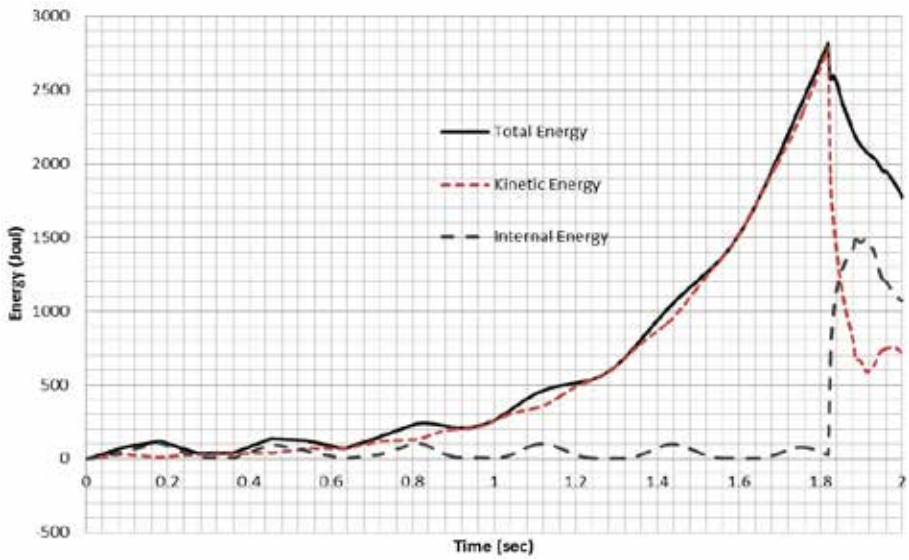

Figure 6-99 Time history of total, kinetic, and internal energy.

Global damping is implemented in all models. This option reduces the acceleration of the impact significantly and can be validated with the experimental work. A coefficient of 0.5 is implemented to the entire models. Vertical acceleration time history is depicted for tip of the cask indicated in Figure 6-100.

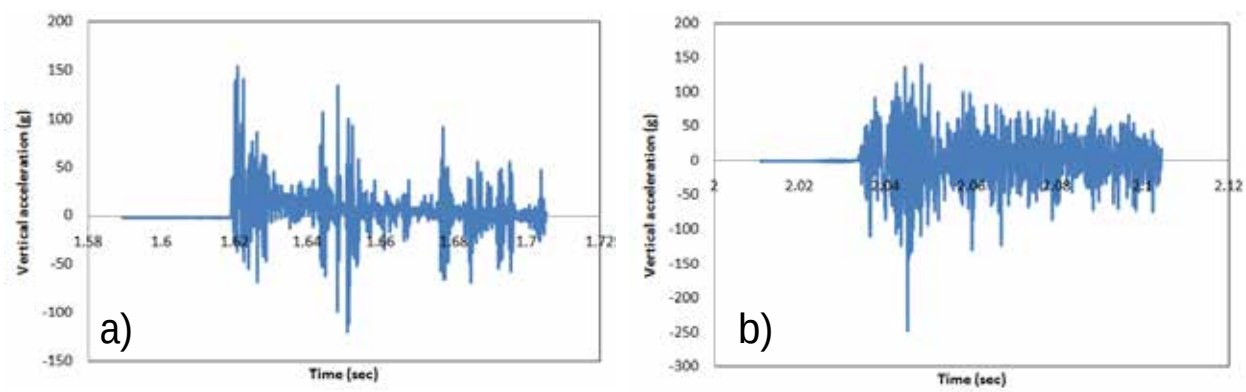

Figure 6-100 Time history of vertical acceleration at selected nodes for the model and prototype cask (acceleration in g).

A simplified version of the dry cask structure was analyzed for the contact-impact scenario of tip-over. A comparison between the model cask and the prototype cask shows that the results of strain and stresses are comparable with applying the extra mass to the model cask.

6.5.5. Tip-Over Simulation of Model Dry Cask Using the ASR Affected Concrete

6.5.5.a. Finite element model

An ASR model was introduced in section 6.4, and later this model was implemented to capture the behavior of the dry cask structure. ASR degrades the concrete outerpack from two aspects:

- Mechanical degradation: The reduction of modulus of elasticity and tensile strength was computed in section 6.4.4. The results are implemented to the concrete outerpack in this section in order to model tip-over scenario. *E* is considered to be 15.5 GPa where it was originally 29.2 GPa. Using ACI formulation or CEB standard makes us capable to compute the reduction of uniaxial compression strength. Here, it's assumed that $f_c' = 12.5\ \mathrm{MPa}$, where it was originally $41.1\ \mathrm{MPa}$.
- Environmental degradation: ASR strain was computed in three directions in Section 6.4.4. It was shown that $\varepsilon_r = \varepsilon_\theta = 0.0087$ and $\varepsilon_z = 0.0076$. This initial strain can be translated into LS-DYNA model as initial strains in form of the temperature gradient using different values for the thermal coefficient (α) in each direction.

Element erosion with the prescribed parameters in Section 6.5.4 is activated in this model for both the concrete outerpack and the concrete pad.

Isotropic elastic plastic material model is assumed for steel part. Concrete cap surface material model (CSCM_159) is used for mechanical behavior of cask and pad as described in Table 6-16. Elastic material behavior is considered for soil with ρ=1.5 gr/cm^3 $E = 34,474\,MPa,$ and n=0.3.

Table 6-16 Material Properties for Tip-over simulation

Structural Steel properties		Concrete properties	
Name	Value	Name	Value
Density	7850 [kg/m^3]	Density	2450 [kg/m^3]
Poisson's ratio	0.26	Poisson's ratio	0.15
Young's modulus	206E+9 [Pa]	Young's modulus	15.5E+9 [Pa]
Initial yield stress	250 [MPa]	Uniaxial tensile strength	2.2 [MPa]
Tangent Modulus	2E+9[Pa]	Uniaxial compressive strength cask	12.5 [MPa]

6.5.5.b. Analysis results

The internal time step of this analysis is 4.44E-07 sec. This simulation takes 2 days to complete using 8 processors in parallel. Contact happened at time equal to 1.2078 sec (corresponding to the maximum acceleration at tip of the cask) after starting tip-over simulation from initial condition.

Figure 6-101 Contours of ductile damage at t=1.2078 sec shows ductile damage contours due to compressive stress in different regions of the 1:3 scale cask. Figure 6-102 shows brittle damage contour due to tensile stress in different regions of 1:3 scale cask. Figure 6-103 shows the contours of von-Mises stress.

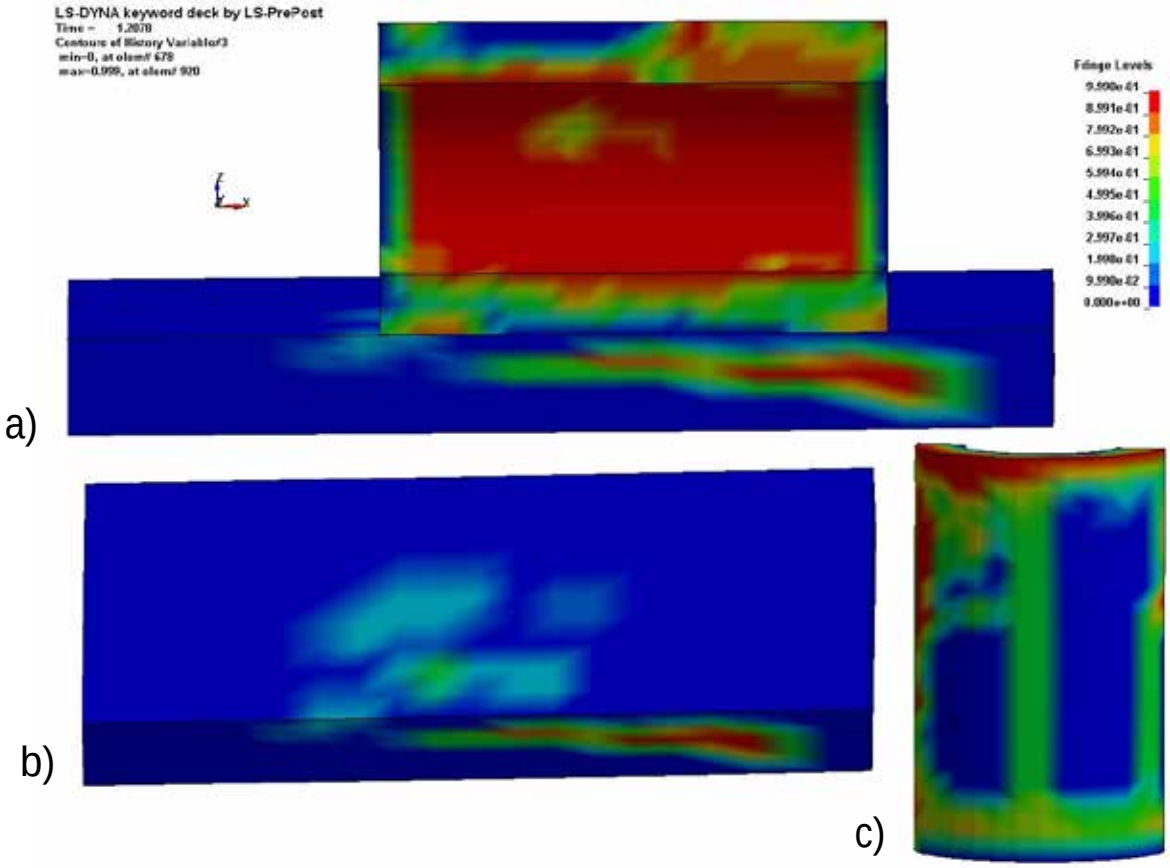

Figure 6-101 Contours of ductile damage at t=1.2078 sec (a) side view, (b) pad, (c) cask.

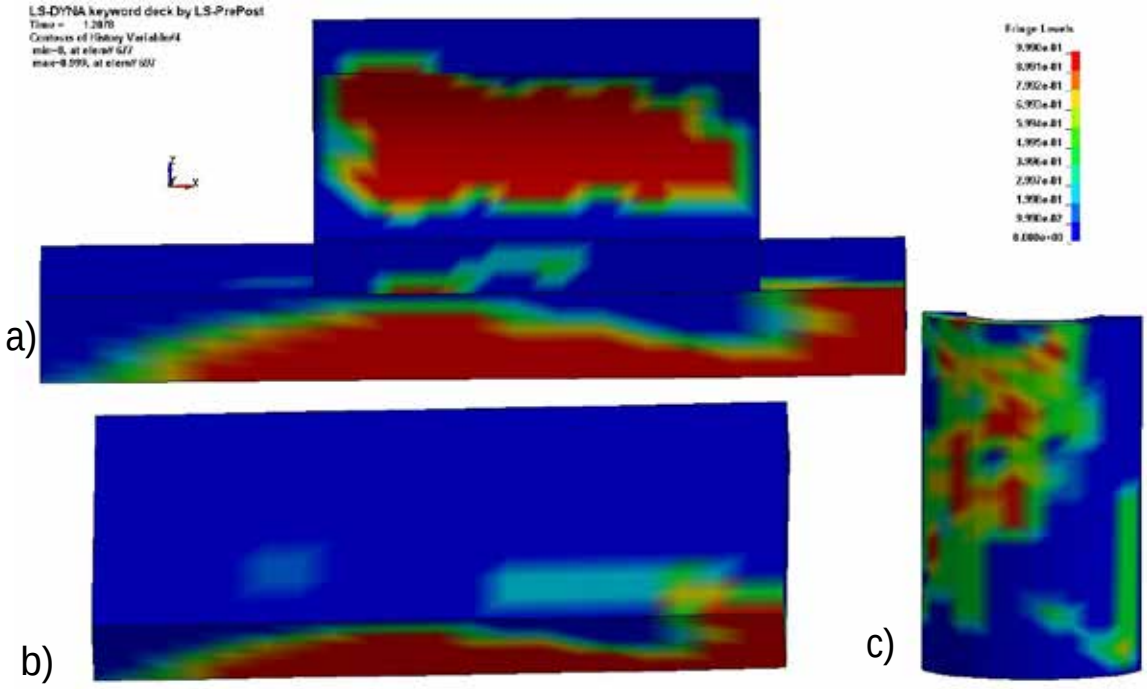

Figure 6-102 Contours of brittle damage at t=1.2078 sec (a) side view, (b) pad, (c) cask.

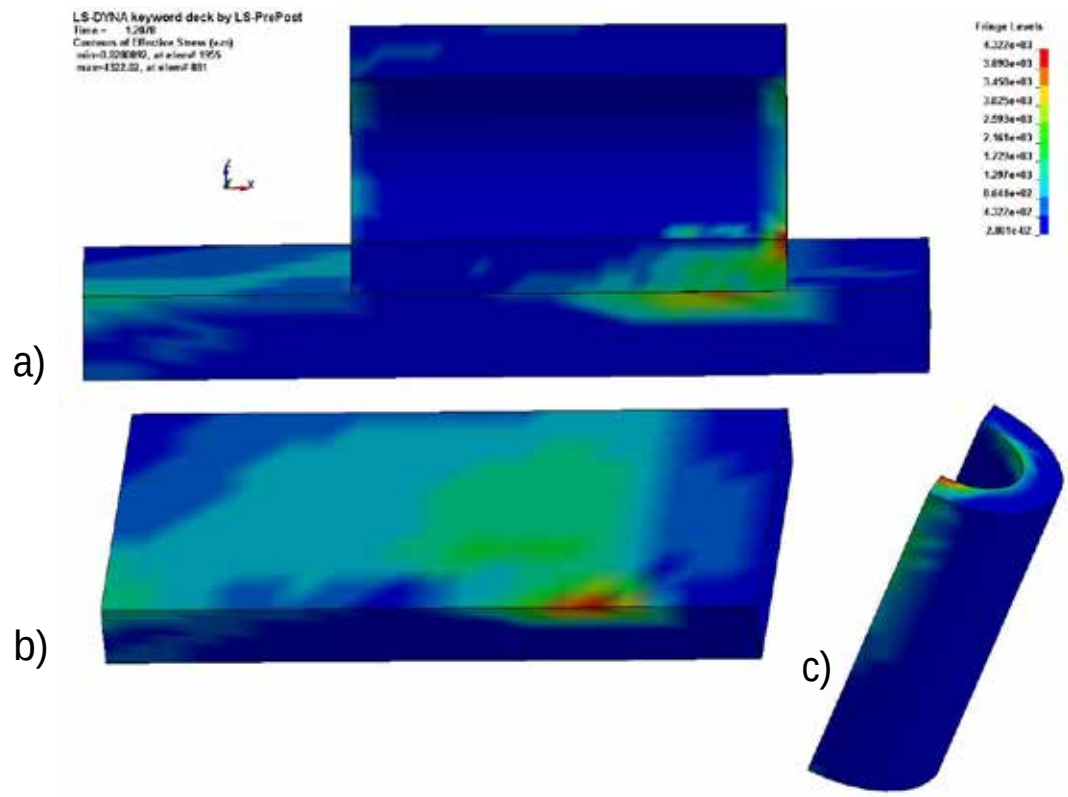

Figure 6-103 Contours of von-Mises stress at t=1.2078sec (a) side view, (b) pad, (c) cask.

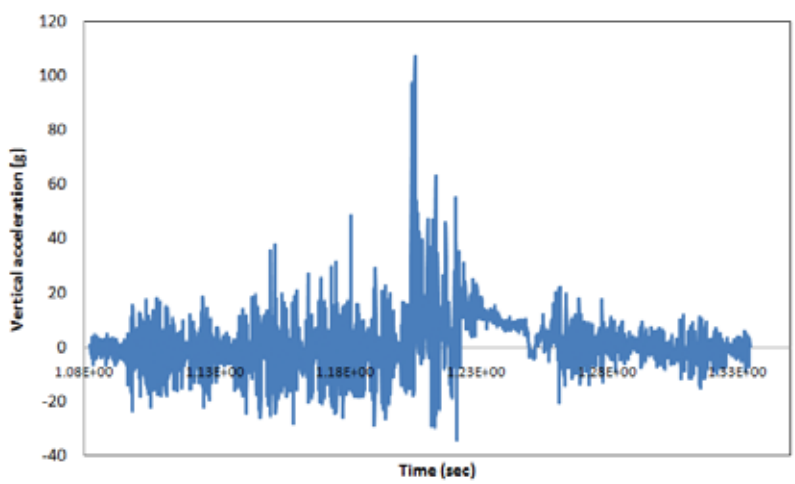

Figure 6-104 Time history of vertical acceleration at the tip of the cask.

It can be seen that in this case, the cask is fully damaged. Time history of vertical acceleration is shown in Figure 6-104.

<u>Discussion:</u> Implementing the results of ASR study to the cask for tip-over study which degrades the concrete cask mechanically and environmentally, makes the cask fully damaged. Brittle damage and ductile damage contours show that the damage is spread within the cask under this contact-impact scenario.

6.6. CONCLUSIONS

In this chapter, different scenarios were addressed computationally to capture the behavior of degraded concrete structures using the finite element method. Creep and shrinkage were modeled using B4 model which was developed by RILEM committee (RILEM, 2014). Implementing the developed model in the cask structure showed that the creep and shrinkage do not induced a large stress and strain on structure since the structure is self-weighted.

Then, a thermo-hygro model was introduced and was verified based on some published experimental data available in the literature. This model was implemented in the cask structure and results showed that the relative humidity and temperature are fully coupled. Moisture function dramatically changes during 3 years of analysis.

An ASR model is introduced which is a coupled of thermo-hygro-chemo-mechanical (THCM) model. Also this model was verified using some experimental results published in the literature and then the developed approach was implemented in the cask structure. The results showed that ASR strain is almost same in all directions, but it reduced the strength and modulus of elasticity of concrete significantly.

In order to evaluate the performance of degraded concrete dry cask structure, the behavior of cask under a crash scenario was evaluated considering temperature gradient, creep, shrinkage and ASR. Degradation of concrete has two effects on the structure. One is the environmental effects and the other one is the mechanical effects. To calculate the environmental effects, the strains due to temperature gradient, creep, shrinkage and ASR were calculated and can be applied on each element of the structure.

This strain was implemented for each element as an initial strain before the tip-over crash scenario. Mechanical effects of degraded concrete in form of elastic modulus and compressive strength also were calculated and implemented in the tip-over study.

The result of this study was compared to the 28 days concrete and prototype cask, to see how it affects the failure mode of the cask during contact-impact crushing in the form of the distribution of damage parameters which control the performance and disintegration of the cask during tip-over contact-impact crashing. ASR cask is fully damaged under this scenario.

6.7. REFERENCES

ACI Committee 209 (1972), *Prediction of creep, shrinkage and temperature effects in concrete structures, ACI-SP27, Designing for Effects of Creep, Shrinkage and Temperature*, American Concrete Institute (ACI), pp. 51–93 (re-approved 2008), Detroit.

ACI Committee 209 (2008). *Guide for Modeling and Calculating Shrinkage and Creep in Hardened Concrete ACI Report 209.2R-08*, American Concrete Institute (ACI), Farmington Hills, MI.

ASCE (1992). *Structural fire protection*, ASCE committee on fire protection, structural division, American society of civil engineers, new york, NY, USA.

ASTM C 199/C 109M (2007). *Standard Test Method for Compressive Strength of Hydraulic Cement Mortars,* ASTM International, West Conshohocken, PA, USA.

ASTM C 186 (2005). *Standard Test Method for Heat of Hydration of Hydraulic Cement,* West Conshohocken, PA, USA.

Bary, B., Morais, M., Poyet, S., Durand, S. (2012). "Simulations of the thermohydro-mechanical behaviour of an annular reinforced concrete structure heated up to 200°c," Engineering Structures, 36:302–315.

Bazănt, Z. P. (1975). "Theory of creep and shrinkage in concrete structures," Re-printed from Mechanics Today, Vol. 2, *Pergamon Press*, Chapt. I, pp. 1-93, Northwestern University, Evanston, Illinois.

Bažant, Z. P., and Thonguthai, W. (1979). "Pore pressure in heated concrete walls: theoretical prediction," Magazine of Concrete Research, 31(107):67–76.

Bažant, Z. P., Chern, J.C., and Thonguthai, W. (1982). "Finite element program for moisture and heat transfer in heated concrete," Nuclear Engineering and Design, 68(1):61–70.

Bažant, Z. P., Wender, R. and Hubler, M. H. (2012). *Multi-decade creep model B4 for concrete creep and shrinkage including multi-decade prediction: description and application*, Report of RILEM committee TC-MDC.

Bažant, Z.P., and Yu, Q. (2012). "Excessive long-time deflections of prestressed box girders," ASCE J. of Structural Engrg. 138 (6), 676-686, 687-696.

Belytschko, T. and Bindeman, L. P. (1993). "Assumed strain stabilization of the eight node hexahedral element," Computer Methods in Applied Mechanics and Engineering, 105, 225-260.

Bentz, P. (1997). "Three-dimensional computer simulation of Portland cement hydration and microstructure development," J. Am. Ceram. Soc., 80(1) 3-21.

Bentz, P., Feng, X., Haecker, C.-J., Stutzman, P. E. (2000). *Analysis of CCRL proficiency cements 135 and 136 using CEMHYD3S*, Technical report of NIST, NISTIR 6545.

Bentz, P. (2001).*The virtual cement and concrete testing laboratory consortium*, Annual Report of NIST, NISTIR 6840.

Bermejo, M., Goicolea, J., Gabaldón, F., Anastasio P. Santos (2011). "Impact and explosive loads on concrete buildings using shell and beam type elements," 3rd ECCOMAS Thematic Conference on Computational Methods in Structural Dynamics and Earthquake Engineering, Corfu, Greece.

Betten, J. (2008), *Creep Mechanics*, ISBN-10: 3540850503, ISBN-13: 978-3540850502, Auflage: 3rd ed.

Borrvall T., and Riedel, W. (2011). "The RHT concrete model in ls-dyna," *in Preceedings of the 8th European LS-DYNA Users Conference*, Strasbourg.

Brannon, R. M., and Leelavanichkul, S. (2004). *Survey of four damage models for concrete,* Sandia report, SAND2009-5544, Sandia National Laboratories, California.

Brooks, J.J. (2005), "30-year creep and shrinkage of concrete," Magazine of Concrete Research, 57(9), 545–556. Paris, France.

CEB-FIP Model Code, (1990), *Model Code for Concrete Structures*. Thomas Telford Services Ltd., London, Great Britain; also published by Comité euro-international du béton (CEB), Bulletins d'Information No. 213 and 214, Lausanne, Switzerland.

CEB-FIP Model code (2010), *Model code for concrete structures*, first draft, Bulletin d' information No. 195, Comite-Euro-International Du Beton-Federation Internationale De La Precontrainte, Paris.

Champiri, M. D., Attar, A., Hanifehzadeh, M., Willam, K., Gencturk, B. (2015a). "Long-termperformance of dry storage structures." *CONCREEP-10 conference*, September 21-23, Vienna, Austria.

Champiri, M. D., Attar, A., Hanifehzadeh, M., Willam, K., Gencturk, B. (2015b). "Tip-over simulation of degraded dry cask storage structures." *Proceedings of the ASME 2015 International MechanicalEngineering* Congress & Exposition (IMECE15), November 13-19, Houston, Texas, USA.

Champiri, M. D., Mousavizadegan, S. H., Moodi, F. (2012). "A Decision support system for diagnosis of distress cause and repair in marine concrete structures," International journal of Computers and Concrete, Techno press, Vol. 9, No. 2, pp. 99-118.

COMSOL Multiphysics® (2015). "The Platform for Physics-Based Modeling and Simulation," <http://www.comsol.com/comsol-multiphysics>.

Dilger, F., Halstead, R. J., Ballard, J. D. (2012). "Full-scale cask testing and public acceptance of spent nuclear fuel shipments-12254." *WM 2012 conference*, February 26-March 1, Phoenix, Arizona, USA.

Elfahal, M. M. (2003). "Size effect in normal and high-strength concrete cylinders subjected to static and dynamic axial compressive loads," Ph.D dissertation, The Pennsylvania State University.

Fossum, A. F., and Brannon, R. M. (2004). *The sandia geomodel: theory and users guide*, Sandia report, Sandia National Laboratories, California.

Gupta, N.K. (1997). *Simplified analytical solution for free drops during NCT for radioactive materials packaging*. US DOE report DE-AC09-96SR18500.

Hallquist, J.O. (2006). "LS-DYNA Theory Manual. Livermore Software and Technology Corporation (version 970)". Livermore, California.

Halstead, R. J., Dilger, F. (2006). "Full-scale cask testing revisited, again." *WM 2006 conference,* February 27-March 2, Tuscon, Arizona, USA.

Hansson, H., and Skoglund, P. (2002). *Simulation of concrete penetration in 2d and 3d with the RHT material model*, Swedish Defense Research Agency.

Harboe, E.M., et al. (1958), *A comparison of the instantaneous and the sustained modulus of elasticity of concrete*, Concr. Lab. Rep. No. C-354, Division of Engineering Laboratories, US Dept. of the Interior, Bureau of Reclamation, Denver, Colorado.

Harmathy, T., and Allen, L. (1973). "Thermal properties of selected masonry unit concretes," In ACI Journal Proceedings, volume 70. ACI.

Holt, E. (2001), *Early Age Autogenous Shrinkage of Concrete*, Technical Research Center of Finland-ESPOO, VTT PUBLICATIONS, 446.

Huang, C-.C., Wu, T-.Y. (2009). "A study on dynamic impact of vertical concrete cask tip-over using explicit finite element analysis procedures," Annals of Nuclear Energy, 36(2), 213-221.

Islam J., Liu Z. and Swaddiwudhipong S. (2011). "Numerical study on concrete penetration/perforation under high velocity impact by ogive-nose steel projectile," Computers and Concrete, Vol. 8, No. 1, 111-123.

Jirásek, M., and Bažant, Z.P. (2001). "Inelastic analysis of structures," J. Wiley, London (chapters 27, 28).

Larive, C. (1998). “Apportscombin’es de l’experimentation et de la modelisation a la comprehension del’ a lcalireaction et de seseffetsmecaniques,” PhD thesis, Thése de Doctorat, Laboratoire Central des PontsetChaussées, Paris.

Lee, Y. S., Ryu, C. H., Kim, H. S., Choi, Y. J. (2005). “A study on the free drop impact of a cask using commercial FEA codes,” Nuclear Engineering and Design, 235, 2219–2226.

Malvar, L., Crawford, J., Wesevich, J., and Simons, D. (1997). “A plasticity concrete material model for dyna3d," International Journal of Impact Engineering, vol. 19, no. 9-10, pp. 847-873.

Multon, S., Toutlemonde, F. (2006). “Effect of applied stresses on alkali–silica reaction-inducedexpansions,” Cement and Concrete Research, 36(5):912–920.

Murray, Y. D. (2007). *Users manual for ls-dyna concrete material model 159*, tech. rep. Federal Highway Administration, Report no. FHWA-HRT-05-062.

NCHRP 350 (1993). *Recommended Procedures for the Safety Performance Evaluation of Highway Features*, National Cooperative Highway Research Program, National academy press, Washington, D.C.

NIST (2012). *Cement Hydration,* Available from: http://ciks.cbt.nist.gov/bentz/phpct/database/images, Accessed on December 29, 2012.

Nuclear Regulatory Commission (NRC), *A Tutorial on packaging and transportation of nuclear materials*, Institute of Nuclear Materials Management, Packaging and Transportation Technical Division.

NUREG-1536, (1997), *Standard Review Plan for Dry Cask Storage Systems*. US Nuclear Regulatory Commission.

NUREG-1567, (2000), *Standard Review Plan for Spent Fuel Dry Storage Facilities*. US Nuclear Regulatory Commission.

NUREG-6608, (1998), *Summary and Evaluation of Low-Velocity Impact Tests of Solid Steel Billets onto Concrete Pads*. US Nuclear Regulatory Commission.

Parrot, L. J., Killoh, D. C. (1984). “Prediction of cement hydration,” British Ceramic Proceedings, British Ceramic Society, Stoke-on-Trent.

Ranc, G., Sercombe, J., and Rodrigues, S. (2003). “Comportement a haute temperature du beton de structure: impact de la fissuration sur les transferts hydriques,” Revue française de génie civil, 7(4):397–424.

RILEM (1988), *Mathematical Modeling of Creep and Shrinkage of Concrete*, Committee TC 69, Chapters 2 and 3 , Z.P. Bažant, ed., J. Wiley, Chichester and New York, 1988, 57–215.

RILEM Report (2014), *Multi-decade creep mpdel B4 for concrete creep and shrinkage including multi-decade prediction: description and application,* Report of RILEM committee TC-MDC (Bazant, Z. P., Wender, R., Hubler, M. H.).

Saegusa, T., Mayuzumi, M., Ito, C., SHirai, K. (1996), “Experimental studies on safety of dry cask storage technology of spent fuel: allowable temperature of cladding and integrity of cask under accidents,” Journal of nuclear science and technology, Vol. 33, No. 3, p. 250-258.

Saouma, V.E., Perotti, L. (2006), “Constitutive model for alkali-aggregate reactions,” ACI Materials Journal, 103: 194–202.

Saouma, V.E., Hariri-Ardebili, M. A. (2014), “A proposed aging management program for alkali silica reactions in a nuclear power plant,” Nuclear Engineering and Design, 277, 248–264.

Saouma, V., Puatatsananon; W., and Le Pape, Y. (2015). *Alkali-silica reaction in nuclear power plants*. ORNL/TM-xxxx/xx, Oak Ridge National Laboratory.

Shi Y., Li Z-X, Hao H. (2010). “A new method for progressive collapse analysis of RC frames under blast loading,” Engineering Structures, 32: 1691-1703.

Simo, J., Kennedy, J., and Govindjee, S. (1988). “Non-smooth multisurface plasticity and viscoplasticity. loading/unloading conditions and numerical algorithms," International Journal for Numerical Methods in Engineering, vol. 26, no. 10, pp. 2161-2185.

Tang E.K.C. and Hao H. (2010). “Numerical simulation of a cable-stayed bridge response to blast loads, Part I: Model development and response calculations,” Engineering Structures, 32: 3180-3192.

Tazawa, E. (1999), *Autogenous Shrinkage of Concrete*, London, E. & FN Spon.

Teng, T. L., Chu, Y. A., Chang, F. A., Chin, H. S., and Lee, M.C. (2003). “The dynamic analysis of nuclear waste cask under impact loading,” Annals of Nuclear Energy, 30, 1473–1485.

Troxell, G.E., Raphael, J.E. and Davis, R.W. (1958). “Long-time creep and shrinkage tests of plain and reinforced concrete,” *Proc. ASTM 58*, pp. 1101–1120.

Ulm, F., Coussy, O., Kefei, L., and Larive, C. (2000). “Thermo-Chemo-Mechanics of ASR Expansion in Concrete Structures,” Journal of Engineering Mechanics, V. 126, No. 3, pp. 233-242.

Wittmann, F.H. (1982), *Creep and shrinkage mechanisms, Creep and shrinkage of concrete structures*, Z.P. Bažant and F.H. Wittmann, eds., J. Wiley, London 129–161.

Wu K-C, Li B. and Tsai K-C. (2011). “The effects of explosive mass ratio on residual compressive capacity of contact blast damaged composite columns,” Journal of Constructional Steel Research, 67: 602-612.

CHAPTER 7

PROBABILISTIC SEISMIC AND IMPACT ANALYSIS OF CASKS

7.1. INTRODUCTION

Regarding the permanent storage of the spent nuclear fuel, the construction of a permanent storage repository in Yucca Mountains, Nevada, did not progress as expected. In fact, a functioning long-term storage option seems to be decades away (Rosner and Lordan, 2014). In the absence of a permanent storage option, the spent nuclear fuel has to be stored in spent fuel pools and dry cask structures. NUREG-1864 (NRC, 2007) requires the analysis of the casks' performance subject to different hazards. In this regard, the seismic performance of vertical concrete casks is studied in Section 7.2 in which finite element models of the casks' seismic response are developed and used to generate virtual experimental data. Probabilistic seismic demand models (PSDM) for the maximum sliding distance and maximum angle of rotation of the casks are developed based on the generated virtual data, and seismic fragility curves for a sliding limit state and tip-over are constructed upon using the PSDMs. In addition, the response of a dry cask to impact loads induced in a tip-over event is explored in Section 7.3, and impact fragility curves are presented in this section.

7.2. PROBABILISTIC SEISMIC ANALYSIS OF THE VERTICAL DRY CASK

7.2.1. Model Development

A finite element software package, LS-DYNA, was used to develop and analyze nonlinear dynamic models of the seismic response of the dry casks. To verify the finite element models used in this project, the rocking response of the cask was first compared with the results of an experimental test from the literature (Shirai et al, 2003). A numerical model was developed in LS-DYNA based upon the cask details presented in the paper by Shirai et al. (2003). Since a two-dimensional shake table was used in the experiment and the problem geometry was symmetric, it was possible to consider half of the cask and its foundation in the modeling process. This model, shown in Figure 7-1, was analyzed under the Kobe earthquake record, the ground motion that was used in the experiment, and the results for the angle of rotation are compared with those coming from the paper in Figure 7-2. As Figure 7-2 shows, the frequency content of the numerical results and experimental results match. Moreover, the amplitude of the response is almost captured by the finite element model.

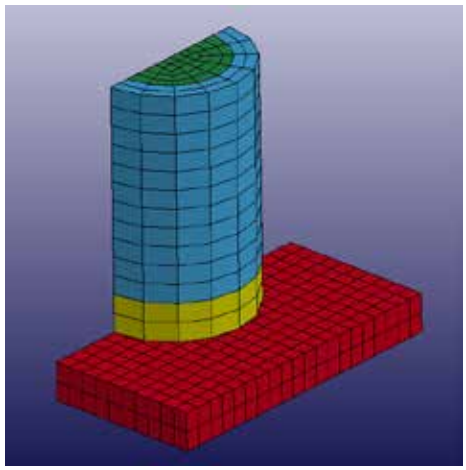

Figure 7-1 Finite element model used for the verification of seismic response with experimental results from the literature.

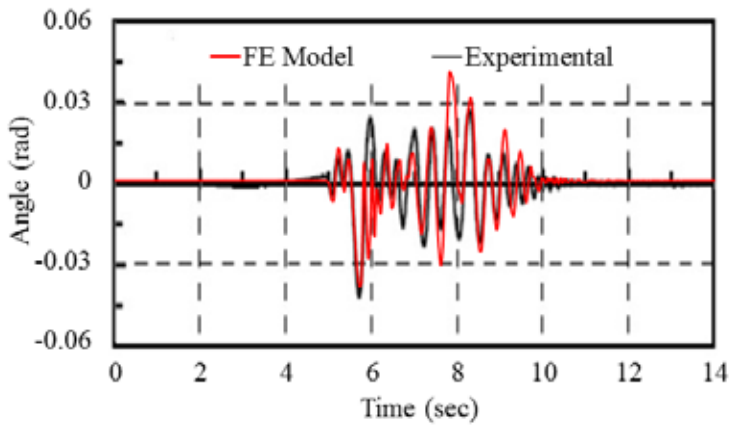

Figure 7-2 Comparison between the response obtained from an experimental test conducted by Shirai et al. (2003) and the response obtained from the corresponding finite element model.

Since the model used for verification included half of the problem geometry, it could save computational resources yet was still adequate to reflect lab conditions of the shake table testing. Although this modeling strategy was sufficient for verification with existing experimental data, the realistic field condition and seismic exposure of casks necessitated three dimensional modeling with three components of earthquake motion as observed in the field. Therefore, it was necessary to compare the results of the models considering half geometry with those that included full geometry as well as other details. To improve the modeling, models that included full geometry of the problem were developed. These models also include all the three components of the applied earthquakes. The sliding and rocking responses resulting from these models were compared with those coming from models with half geometry. Figure 7-3 and Figure 7-4 show examples of such comparisons. As these figures show, the effect of the minor horizontal component of earthquake is considerable, and it should be included in models used for probabilistic seismic demand modeling.

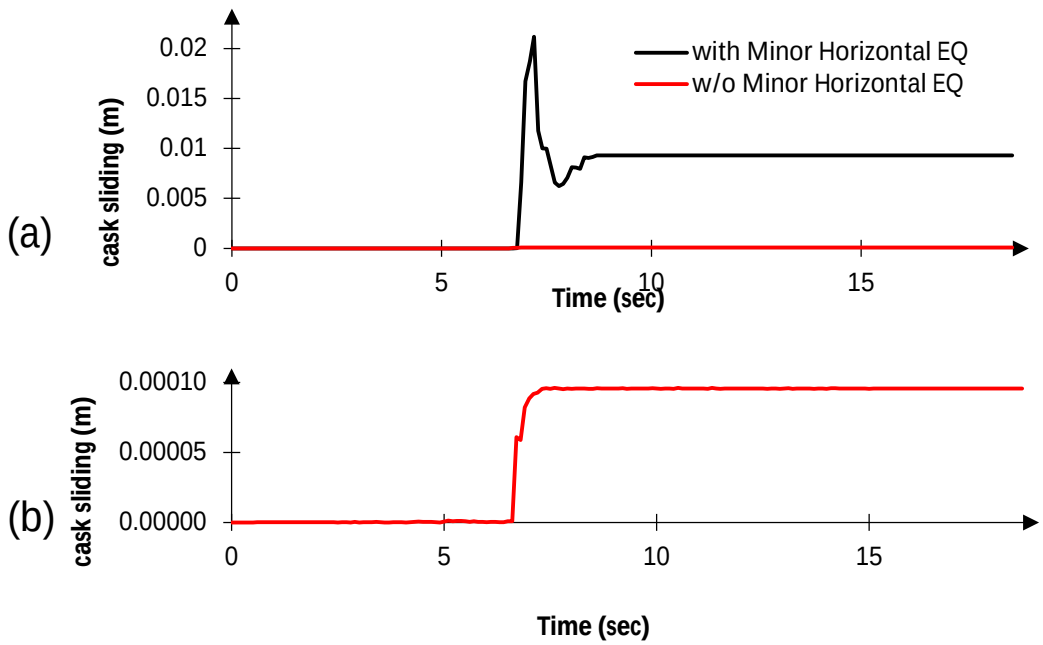

Figure 7-3 Cask sliding response. Top: time history comparison between models with and without minor horizontal earthquake component. Bottom: close up view of time history response of the model without minor horizontal earthquake component (note different scale).

Figure 7-5 shows the final model used in this study for probabilistic seismic analysis and generating virtual data needed for probabilistic seismic demand modeling. The final models include full geometry of the cask, canister, pad, and the soil. The seismic response of the cask is similar to a rigid body motion in which nonlinear material behavior is not expected. Therefore, the material behavior of all the parts was considered by elastic material models. The cask, canister, and pad were modeled by eight-node solid elements with one integration point, and an hourglass technique was used to avoid spurious deformations. Common nodes were used at the interface of the cask and canister. The canister was modeled by two cylinders that had common nodes at their interface. The canister cylinders had the same height but different mass densities. This strategy enabled considering height of the cask's center of gravity as a variable in the seismic analysis of the dry casks. The mass densities of the canister parts were determined by knowing the total mass of the cask and the location of its center of gravity. To simulate the soil mass effect, the soil was modeled with vertical and horizontal springs and dashpots based on NIST GCR 12-917-21 (NIST, 2012) formulas. According to NIST GCR 12-917-21, there are two methods to consider the soil-structure interaction effects: direct analysis and substructure approach. In the "direct analysis" method, the soil is modeled as a continuum with the foundation and the structure's elements. However, in the "substructure approach", the stiffness and damping effects of the soil are modeled by spring and dashpots at the soil-foundation interface. In this study, the substructure approach was used because it models the soil mass with fewer elements and degrees of freedom, which leads to lower computational costs. As mentioned, in the employed method, spring and dashpot elements in horizontal and vertical directions simulated the stiffness and damping effects of the soil in the translational degrees of freedom. In addition, the constants

of the springs and dashpots located at the end regions of the rectangular foundation were modified by correction coefficients to consider the rotational degrees of freedom of the foundation as well (for more details, see NIST GCR 12-917-21 (NIST, 2012)). The nonlinear contact between the cask's bottom surface and the pad was simulated by using "Automatic-Surface-to-Surface" contact. This type of contact is a two-way search algorithm in which penalty method is used to determine the contact forces between the two parts in contact. A viscous damping was introduced to the model by "Damping-Global" which applies mass-proportional damping forces to the nodes in the model.

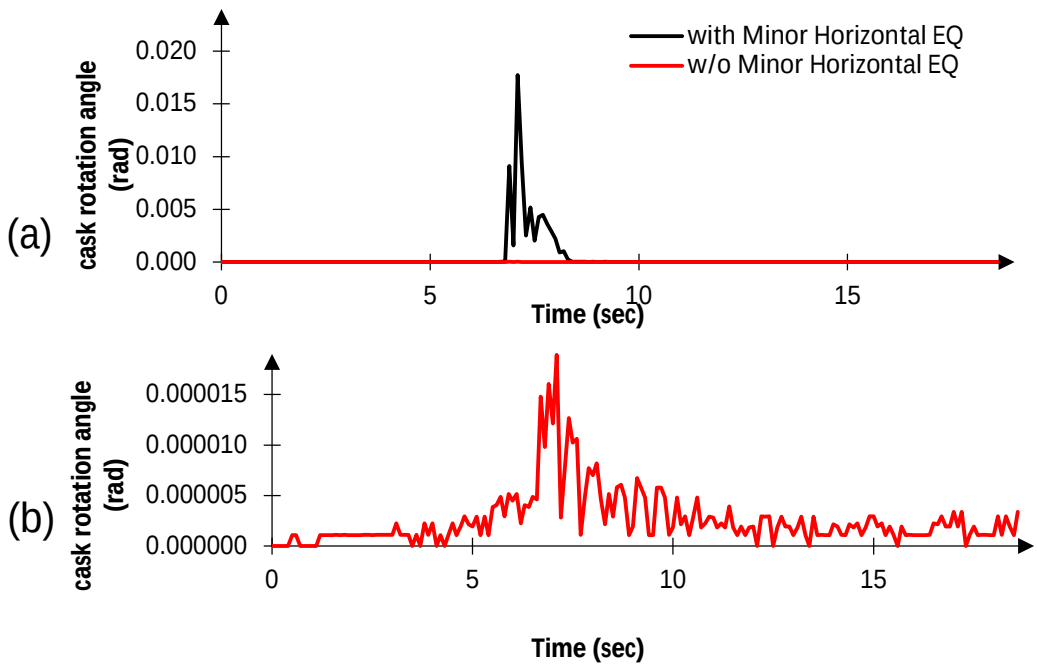

Figure 7-4 Cask rocking response. Top: time history comparison between models with and without minor horizontal earthquake component. Bottom: close up view of time history response of the model without minor horizontal earthquake component (note different scale).

Three-component earthquake accelerations were applied to the springs and dashpots, and the system was analyzed by LS-DYNA's explicit solver. The cask maximum sliding and angle of rotation were calculated from the analysis results. Sliding in each time step was calculated by subtracting the cask horizontal movement vector from the pad horizontal movement vector, and the magnitude of the resultant vector was considered as the cask's (relative) sliding. The cask angle of rotation (with respect to the vertical axis) in each time step was determined by computing the angle between the bottom surface of the cask and the horizontal plane. Finally, the maximum values of these responses were determined as the desired responses for probabilistic seismic analysis since they are key indicators of potential damage.

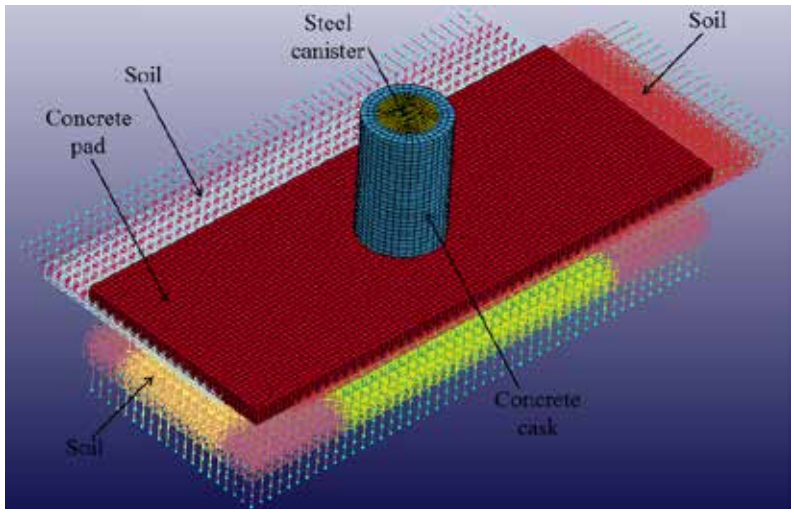

Figure 7-5 Final finite element model used for the probabilistic seismic analysis and probabilistic seismic demand modeling.

7.2.2. Virtual Experimental Design

Based on a literature review, twelve parameters that might affect the seismic behavior of the dry casks were considered. These parameters and their associated ranges are listed in Table 7-1. The considered ranges are broad enough to cover realistic cask configurations designed by different manufacturers in the U.S. 160 different configurations were generated for the analysis by using Latin hypercube sampling (McKay et al, 1979), which is a space filling technique that maximizes the minimum distance between the data points. In addition, the seismic analysis model described in Section 7.2.1 was parameterized so that it is capable of getting the values for the parameters and generating the corresponding finite element models. Using the parameterized model, the 160 finite element models were completed for analysis.

7.2.3. Earthquake Selection

To take into account earthquake characteristics of different regions in the U.S., the country was divided into three regions where dry casks are present in seismic zones, which are western, central, and eastern U.S. Earthquake selection was performed for each region, and 80 earthquake records were selected for each of them. The earthquake selection was conducted by using the method proposed by Baker et al. (2010), in which ground motions whose response spectra match a target response spectrum were selected for the region. The target response spectra were determined by using the U.S. Geological Survey (USGS) hazard curve application for the 2% probability of exceedance in 50 years hazard level for various locations across the U.S. This application took geographical coordinates of the desired location as input and determines hazard curves and uniform hazard response spectra (UHRS) for different hazard levels.

Table 7-1 Geometric, Material, and Structural Parameters Considered in Generating Seismic Analysis Models.

Variable	Symbol	Unit	Range
Cask wall thickness	t_C	m	0.5 – 0.8
Cask height	H_C	m	5.5 – 6.0
Cask outer diameter	D_C	m	3.2 – 4.0
Cask weight	W_C	ton	120 – 180
Height of the cask's center of gravity over the cask's total height	α_G	---	0.48 – 0.52
Cask concrete compressive strength	f'_{cc}	MPa	20 – 55
Pad thickness	t_P	m	0.5 – 1.2
Pad length	L_P	m	9 – 60
Pad concrete compressive strength	f'_{cp}	MPa	20 – 55
Cask-pad friction coefficient	μ	---	0.2 – 0.8
Soil shear wave velocity	C_S	m/s	150 – 2000
Damping ratio	ξ	---	0 – 0.1

As mentioned, three regions were considered (western, central, and eastern U.S.) for which an initial set of UHRS with different shapes were selected. The UHRS selection took into account the locations of current dry cask structures, locations with appreciable seismic hazards, and locations with different soil types. From the initial response spectra selection, eight spectra were finally selected as the target response spectra for ground motion selection. These final eight spectra were chosen so that they reflect different spectral shapes and different intensities. This approach produced ground motions with different frequency content and intensity measure ranges, while still respecting the seismic hazard characteristics of the region. Using Baker's tool, ten ground motions were selected for each target response spectrum. In some cases for the west region, scale factors were applied to obtain ground motion response spectra that match the target spectrum. In addition, NUREG-0800 (NRC, 1987) requires that NPP be analyzed under earthquakes with horizontal peak ground accelerations (PGA) larger than 0.1 g. As a result, some of the records from the original ground motion selection were scaled up. In addition, to produce a broader range of earthquake intensity measures and significant responses for the probabilistic seismic demand modeling, additional earthquakes were scaled so that half of the final suite of ground motions were scaled. The following criteria were considered in the scaling process: scaled peak ground displacement < 250 cm, scaled peak ground velocity < 300 cm/s, scaled vertical PGA < 2.2 g, and scale factor < 10. The selected ground motions for each region were randomly assigned to the developed finite element models, and the models were analyzed by the LS-DYNA explicit solver. It should be mentioned that each selected ground motion for each region was assigned to two different cask configurations. As a result, 480 different models were generated and analyzed, whose results were used to develop PSDMs for the dry casks.

7.2.4. Probabilistic Seismic Demand Modeling

Since excessive sliding and tip-over of the casks could lead to collision between adjacent casks and impact of the cask to the pad, respectively, this study considered maximum sliding distance

and maximum angle of rotation of the casks as engineering demand parameters (EDP). The results of the finite element analyses provided a data set which was used in probabilistic demand modeling for the EDPs in this section. A two-step model, presented in Figure 7-6, was developed to estimate the seismic responses. In the first step of this model, maximum horizontal and vertical accelerations of the cask's center of gravity (CG) were determined, and the results of this step were used in the second one to calculate maximum sliding distance and maximum angle of rotation of the cask in a seismic event. The geometric mean of the horizontal components of earthquake ($PGA = \sqrt{PGA_X PGA_Y}$, in which PGA_X and PGA_Y are the horizontal PGAs of the ground motion) was chosen as the earthquake intensity measure (IM). This choice for IM is consistent with the seismic hazard curves developed by the USGS, which could be helpful in seismic risk estimation of dry storage facilities. In order to develop the PSDMs, response surface methodology was used. A response surface model approximates the target response (e.g., maximum sliding distance) by a polynomial function comprised of the predictors (e.g., geometric parameters, friction coefficient, earthquake PGA, etc.) or functions of them. In this study, different transformations were applied to the response and predictors to improve the final PSDM. Moreover, to use the best set of predictors in the final models, stepwise regression was used, in which the model development started with a simple model, and a predictor/explanatory function was added to the model each time. The added term was kept if it improves the model performance based on a selected criterion. 5-fold cross validation (CV) was employed to evaluate the performance of the developed models. In this method, the data set was divided into five subsets, called folds, and the model was trained on the union of four folds and was tested on the left-out fold. This process was repeated five times, using a new fold as the test set in each run. The average R^2 of the five runs shows the accuracy of the developed model.

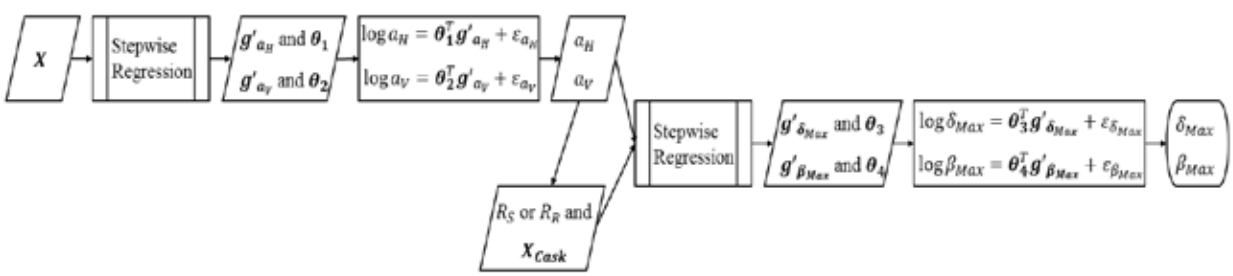

Figure 7-6 Two-step process of probabilistic seismic demand model development.

The PSDMs for the maximum horizontal and vertical accelerations of the cask's CG weere developed in the first step of the process in Figure 7-6, in which the set of geometric, material, and structural parameters along with earthquake PGA were inputted as $\boldsymbol{X}$, and the resulting models are presented in Eq. 7.1 and 7.2.

$$\log a_H = 0.381 - 0.162 PGA + 1.18 \log PGA + 0.142 \log \frac{pW_{eq}}{1 + \left(\frac{W_{eq}}{p}\right)} + e_{aH} \qquad 7.1$$

$$\log a_v = 0.733\mu + 1.1\log PGA + 0.771\mu\log PGA + 0.27\log\frac{p\omega_{eq}}{1+\left(\frac{\omega_{eq}}{p}\right)^2} + \varepsilon_{av} \qquad 7.2$$

where a_H and a_V are the maximum horizontal and vertical accelerations of the cask's CG in g. μ is the friction coefficient between the cask and the pad, and PGA is the geometric mean of the horizontal PGAs in g. p and ω_{eq} are the characteristic frequency of the cask and the dominant angular frequency of the earthquake, respectively. p is calculated by Eq. 7.3 in which m is the mass of the cask, Z is the distance between the cask's CG and a point on the circumference of the bottom facet of the cask (point O) ($Z = \sqrt{(D_c/2)^2 + H_{CG}{}^2}$ in which D_C is the cask outer diameter, and H_{CG} is the height of the cask's center of gravity), and I_O is the moment of inertia with respect to O. To determine the dominant angular frequency of earthquake (ω_{eq}), the period corresponding to the maximum spectral acceleration of ground motion (based on Boore et al. (2006) definition) is used. The model errors in Eqs. 7.1 and 7.2 are normal variables as follows: $\varepsilon_{a_H} \sim N(0, 0.018)$ and $\varepsilon_{a_V} \sim N(0, 0.067)$ (0.018 and 0.067 are the variances of the models).

$$p = \sqrt{\frac{mgz}{I_O}} \qquad 7.3$$

The R^2 values reported by 5-fold CV and the p-values associated with the explanatory functions are presented in Table 7-2. The cross validation method results show that the models perform acceptably in predicting the maximum accelerations, and the low p-values indicate that the explanatory functions are good predictors of the responses. The actual versus predicted values for the PSDMs presented in Eqs. 7.1 and 7.2 are also plotted in Figure 7-7(a) and Figure 7-7(b).

Table 7-2 Performance of the PSDMs Developed for the Cask's CG Maximum Accelerations.

Model	5-Fold CV R^2	p-Value				
		μ	PGA	$\log PGA$	$\mu\log PGA$	$\log\frac{p\omega_{eq}}{1+\left(\frac{\omega_{eq}}{p}\right)^2}$
Eq. 7.1	0.90	Not Used	*	*	Not Used	*
Eq. 7.2	0.86	*	Not Used	*	*	*

*: less than 0.0001

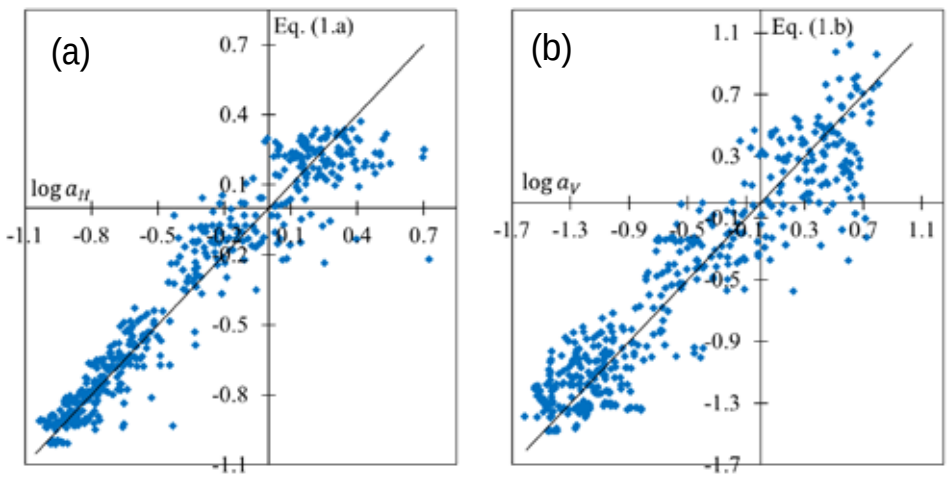

Figure 7-7 Predictions against actual values of (a) $\log a_H$ (b) $\log a_V$.

The outputs of Eqs. 7.1 and 7.2, geometric, material, and structural parameters of the cask, and two dimensionless parameters ($R_S = \frac{\mu}{a_H/(g-a_V)}$ and $R_R = \frac{D_C/2H_{CG}}{a_H/(g-a_V)}$), derived from pseudo static analysis, were used in the second step of the PSDM development process to determine probabilistic models for the maximum sliding distance and maximum angle of rotation of the casks. The probabilistic model for the maximum sliding of the cask (relative to the pad) is presented in Eq. 7.4:

$$\log d_{Max} = -2.1 - 0.863\log m + 3.393\log a_H + 0.788R_s' + e_{d_{Max}} \qquad 7.4$$

$$R_s' = \begin{cases} 1 & if \ \dfrac{m}{\dfrac{a_H}{g - a_V}} \leq 1 \\ 0 & if \ \dfrac{m}{\dfrac{a_H}{g - a_V}} > 1 \end{cases} \qquad 7.5$$

In Eq. 7.4, δ_{Max} is the maximum sliding distance of the cask in m, D_C is in m, $\log a_H$ is defined in Eq. 7.1, R'_S is defined in Eq. 7.5, and $\varepsilon_{\delta_{Max}} \sim N(0,0.253)$ (0.253 is the variance of the model). According to Table 7-3, which displays the goodness of fit measures of this model, Eq. 7.4 has a high accuracy in predicting the response ($R^2 = 0.93$), and the explanatory functions, with p-values smaller than 0.05, are good predictors of the response. Figure 7-8(a) shows actual and predicted values by Eq. 7.4 for comparison as well. In addition to the statistical metrics, the model is consistent with the physics of the problem. That is, larger friction coefficients result in smaller sliding distances, and larger horizontal accelerations at the cask's CG induce larger sliding, as expected. Moreover, pseudo static analysis shows that for $R_S = \frac{\mu}{a_H/(g-a_V)}$ larger than one, the cask is not expected to slide, but for values smaller than 1, it starts the sliding motion. This observation is consistent with the definition of R'_S and its role in Eq. 7.4.

Table 7-3 Performance of the PSDM for the Maximum Sliding of the Dry Casks.

Model	5-Fold CV R^2	p-Value		
		$\log \mu$	$\log a_{CG,H}$	R'_S
Eq. 7.4	0.93	*	*	*

*: less than 0.0001

The process illustrated in Figure 7-6 resulted in Eq. 7.6 for the rocking PSDM:

$$\log b_{Max} = 1.276 - 1.1Z \sin b_{Cr} + 1.592 m R'_R + 2.495 \log a_H + e_{b_{Max}} \qquad 7.6$$

$$R'_R = \begin{cases} 1 & if \ \dfrac{\dfrac{D_C}{2H_{CG}}}{\dfrac{a_H}{g - a_V}} \leq 1 \\ 0 & if \ \dfrac{\dfrac{D_C}{2H_{CG}}}{\dfrac{a_H}{g - a_V}} > 1 \end{cases} \qquad 7.7$$

where β_{Max} is the maximum angle of rotation in degrees, Z is in m, β_{Cr} is the angle of rotation at the onset of tip-over ($\beta_{Cr} = \tan^{-1} D_C/2H_{CG}$), R'_R is defined in Eq. 7.7, and $\varepsilon_{\beta_{Max}} \sim N(0,0.328)$ (0.328 is the variance of the model). Criteria assessing the performance of this model are presented in Table 7-4, which indicate the acceptable accuracy of the predictions (R^2 = 0.86) and capability of the explanatory functions (p-values less than 0.05) in estimating the response. The actual and predicted values are also presented in Figure 7-8(b). Moreover, the model and the physics of the problem are consistent. That is, casks with larger dimensions or larger critical angle of rotation experience smaller rocking angles, which was observed in previous studies on the rocking response of rigid blocks. In addition, larger coefficients of friction hinder the cask sliding, and at the same time, generate larger driving moments for the rocking motion, which can induce large angles of rotation. Large accelerations at the cask's CG are expected to increase the maximum angle of rotation, which is expressed in Eq. 7.6. Finally, pseudo static analysis shows that for $R_R = \frac{D_C/2H_{CG}}{a_H/(g-a_V)}$ larger than one, the cask is not expected to experience rocking, but for values smaller than 1, it starts the rocking motion. This observation is consistent with the definition of R'_R and the rocking PSDM in Eq. 7.6.

Table 7-4 Performance of the PSDM for the Maximum Angle of Rotation of the Dry Casks.

Model	5-Fold CV R^2	p-Value			
		$Z \sin \beta_{Cr}$	$\mu R'_R$	$\log a_H$	R'_R
Eq. 7.6	0.86	*	*	*	*

*: less than 0.0001

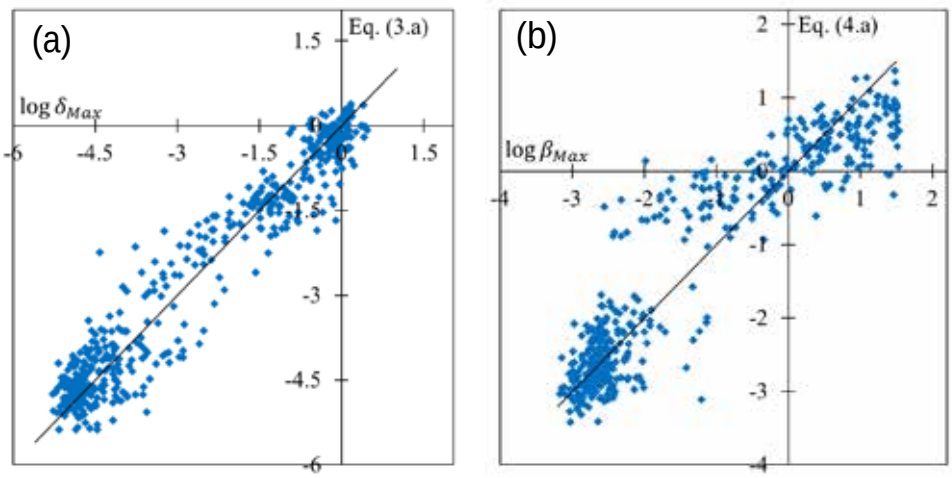

Figure 7-8 Predictions against actual values of (a) $\log \delta_{Max}$ (b) $\log \beta_{Max}$.

7.2.5. Seismic Fragility Analysis

Seismic fragility is the conditional probability of reaching or exceeding a limit state for an engineering demand parameter given the earthquake intensity measure and other parameters defining the problem (e.g., geometrical parameters). In this study, the fragilities were developed for the sliding and rocking responses. Singh et al. (2001) recommended $1/4 \times D_C$ as the maximum allowable sliding distance of dry casks. The same limit state was used in this study to develop sliding fragility curves because this limit is independent of the configuration of the dry casks on the foundation of dry storage facilities. Tip-over fragility was also developed considering the critical angle of rotation as the rocking angle limit state. To develop the fragility at each PGA, Monte Carlo method was applied on the developed PSDMs presented in Section 7.2.4. In this regard, 5×10^6 samples were generated for each PGA in the first step assuming that $\log a_H$ and $\log a_V$ have a bivariate normal distribution with the mean values and standard deviations defined in Eq. 7.1 and Eq. 7.2 and a correlation coefficient of 0.88. The generated samples of the cask CG accelerations were used in the second step to generate samples of the target EDP (maximum sliding distance or maximum angle of rotation) based on the appropriate mean values and variances presented in Eq. 7.4 and Eq. 7.6. The generated samples for the EDPs were compared with the above-mentioned limit states to determine the failed and safe cases. For each PGA, the probability of failure was estimated as the number of failures divided by the total number of samples (5×10^6). As an illustration the fragility curves for the sliding limit state and tip-over are presented in Figure 7-9(a) and Figure 7-9(b), respectively, for a sample cask with $D_C = 3.45$ m, $H_C = 5.72$ m, $W_C = 160$ ton, $\mu = 0.5$, and $\alpha_G = 0.5$ where α_G is the ratio between the height of the cask's CG and the cask's overall height.

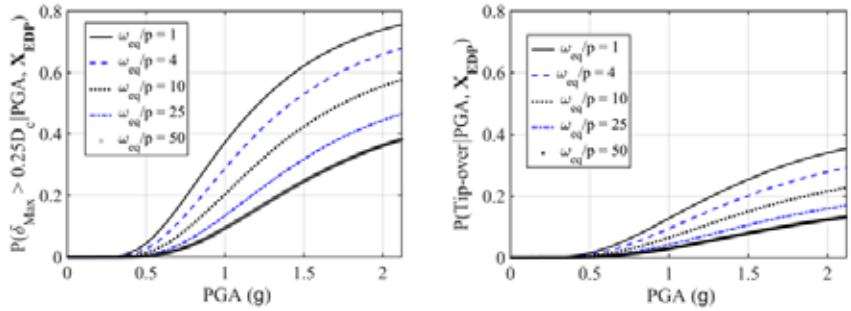

Figure 7-9 (a) Sliding fragility curves for a sample cask with $D_C = 3.45$ m, $H_C = 5.72$ m, $W_C = 160$ ton, $\mu = 0.5$, and $\alpha_G = 0.5$ (b) Tip-over fragility curves for a sample cask with $D_C = 3.45$ m, $H_C = 5.72$ m, $W_C = 160$ ton, $\mu = 0.5$, and $\alpha_G = 0.5$.

As the figures show, the conditional probabilities of failure depend on the ratio of ω_{eq}/p, which is due to the presence of $p\omega_{eq}/\left(1 + (\omega_{eq}/p)^2\right)$ in the probabilistic models developed for the cask CG maximum accelerations. In this regard, $p\omega_{eq}/\left(1 + (\omega_{eq}/p)^2\right)$ might be written as $\alpha p^2/1 + \alpha^2$ in which $\alpha = \omega_{eq}/p$ is a constant, and the maximum value of this function $\alpha p^2/1 + \alpha^2$ happens at $\alpha = 1$. Therefore, the maximum seismic responses of the casks are expected at ω_{eq}/p close to 1. In this study, ω_{eq} corresponds to the period at which the maximum spectral acceleration of the earthquake happens (per Boore et al. (2006) definition), and including ω_{eq}/p in the developed PSDMs aims to capture the effect of earthquake frequency content on the seismic response of the dry casks.

7.2.6. Parameter Study

This section studies the effect of changing parameters such as friction coefficient, Z, and critical angle of rotation on the seismic fragilities. The effect of different coefficients of friction on the sliding fragility of the sample cask with $\omega_{eq}/p = 25$ is illustrated in Figure 7-10. As the figure shows, the probability of maximum sliding distance exceeding the predefined limit state is larger for smaller friction coefficients. However, for larger friction coefficients, the fragilities are less affected by friction coefficient variations. That is because as the friction force between the cask and pad increases, the seismic motion of the cask is dominated by rocking motions, and therefore, the sliding motion and sliding fragilities are less influenced by larger friction coefficients.

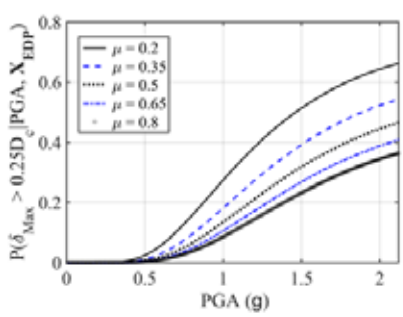

Figure 7-10 Effect of different friction coefficients on the sliding fragilities for the sample cask with $D_C = 3.45$ m, $H_C = 5.72$ m, $W_C = 160$ ton, and $\alpha_G = 0.5$ $(\omega_{eq}/p = 25)$.

The effect of different friction coefficients, Z, and critical angles of rotation on the tip-over fragility of the sample cask is illustrated in Figure 7-11. As the figures show, the tip-over probability is very sensitive to the friction coefficient variations, and it increases as the friction between the cask and its foundation increases. In comparison, the tip-over fragility decreases with the increase of cask dimensions or cask critical angle of rotation.

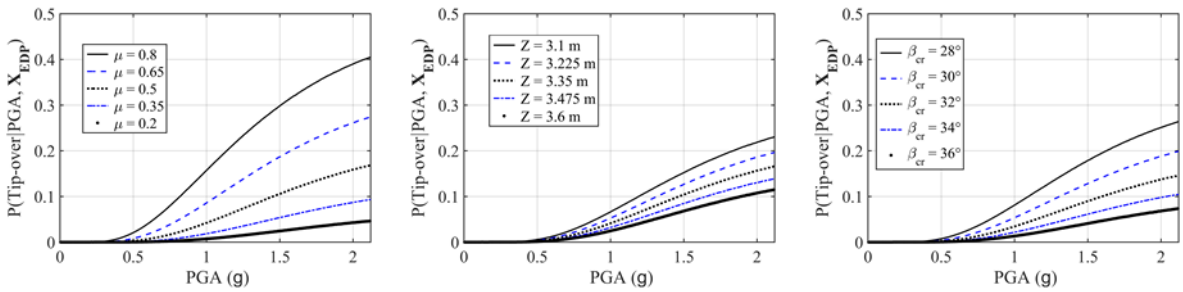

(a) (b) (c)

Figure 7-11 Effect of parameter variations on the tip-over fragilities assuming $\omega_{eq}/p = 25$ (a: effect of friction coefficient, b: effect of Z, c: effect of critical angle of rotation).

7.2.7. Seismic Risk Estimation for Sliding and Tip-Over

Having constructed fragility curves for the sliding limit state and tip-over, this section performs a risk analysis for three locations in the United States where dry casks are located in Western, Central, and Eastern U.S. In order to assess the seismic risk, seismic hazard information about PGA, ω_{eq} and the joint occurrence of them is required. The USGS hazard tool provides seismic hazard curves for PGA at each location in the U.S. However, the required information on ω_{eq} is not available. This study used the period corresponding to the maximum spectral acceleration of UHRS for 2% probability of exceedance in 50 years at the target location to estimate ω_{eq}. For the sites chosen in this study, this period equals 0.2 sec for the Western U.S. location and 0.1 sec for the Central and Eastern U.S. locations. Considering the parameters' effect on the seismic fragilities, the sliding fragility is maximum for $\mu = 0.2$, and the tip-over fragility is maximum for $\mu = 0.8$. Therefore, to estimate the highest risk to the dry casks, the fragility curves corresponding to $\mu = 0.2$ were used to estimate the seismic sliding risk, and fragilities corresponding to $\mu = 0.8$ were employed for the seismic tip-over risk estimation.

Risk is defined as the annual probability of exceeding a predefined limit state as shown in Eq. 7.8

$$p_f = \int_{PGA} P(EDP > LS \mid PGA, X_{EDP}) \left| \frac{dv}{dPGA} \right| dPGA \qquad 7.8$$

In Eq. 7.8, $P(EDP > LS|PGA, \boldsymbol{X_{EDP}})$ is the seismic fragility that was explained in Section 7.2.5, and $|dv/dPGA|$ is estimated by fitting a hyperbolic function, with the general form in Eq. 7.9, to the seismic hazard curves provided by the USGS. The hazard curves for the selected locations and fitted curves are plotted in Figure 7-12, and the results for the risk analysis are presented in Table 7-5. Although extreme values were assumed for the coefficient of friction for the risk analysis, the annual probabilities of failure are on the order of 10^{-5} to 10^{-6} for different sites, and the

highest risks are observed for the Western location, which is about an order higher than the other locations.

$$n = c_1 \exp[c_2 \left(\ln\left(\frac{PGA}{c_3}\right)\right)^{-1}] \qquad 7.9$$

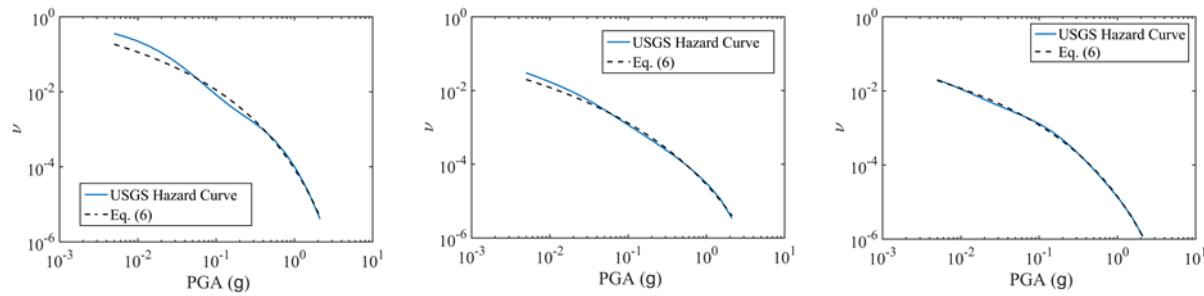

(a) (b) (c)

Figure 7-12 The USGS hazard curves and the fitted curves used in the seismic risk analysis (a: San Luis Obispo, CA, b: Decatur, TN, c: Hartsville, SC).

Table 7-5 Seismic Risk Analysis Results for the Sliding Limit State and Tip-Over of the Sample Cask with $D_C = 3.45$ m, $H_C = 5.72$ m, $W_C = 160$ ton, and $\alpha_G = 0.5$.

Location	Mean annual probability of failure, p_f	
	Sliding ($\mu = 0.2$)	Tip-over ($\mu = 0.8$)
Western U.S. (San Luis Obispo, CA) ($\omega_{eq} = 31.42\ rad/s$)	9.8×10^{-5}	6.4×10^{-5}
Central U.S. (Decatur, TN) ($\omega_{eq} = 62.83\ rad/s$)	1.6×10^{-5}	10^{-5}
Eastern U.S. (Hartsville, SC) ($\omega_{eq} = 62.83\ rad/s$)	9.8×10^{-6}	6.5×10^{-6}

7.3. ANALYSIS OF IMPACT FROM TIP-OVER

7.3.1. Model Development

In order to analyze the structural response of the dry casks to impact loads induced in a tip-over event, nonlinear dynamic analysis should be performed. In this section, a finite model of the tip-over experiment, explained in Chapter 5, was developed and verified versus the experimental results. As mentioned in previous chapters, the test was performed on a scaled cask, tilted to make a 45-degree angle with the pad surface. The cask was at rest at the beginning of the experiment and fell down due to gravity and hit the pad. A finite element model of the problem was developed in LS-DYNA, in which all the parts, including the cask and its components, the pad, and the soil, were modeled by eight-node solid elements. In order to avoid spurious deformations due to using one-point integration elements, an hourglass technique was employed. The

concrete and steel material nonlinearity was considered with appropriate material models available in the library of LS-DYNA. The material model used for concrete is a continuous surface cap model, which can be activated by the Mat_CSCM_Concrete in LS-DYNA. To model the steel material, Mat_Plasticity_Kinematic was used, which is suited to model isotropic and kinematic hardening plasticity. Contact between different parts of the model was defined by using Contact_Automatic_Surface_to_Surface and Contact_Tied_Surface_to_Surface. Viscous damping was introduced into the model by the Damping_Global option. In order to prevent stress waves from propagating back into the model at the soil boundaries, absorbing boundary conditions were used on the surfaces of the soil. Since the geometry and motion of the cask in the tip-over event are symmetric, half of the geometry was considered in the final model. In addition, in order to save computational resources, the cask's motion before impact was replaced by applying appropriate angular velocity to the cask and starting the analysis from an angle of 5 degrees instead of 45. The angular velocity at the beginning of the analysis was determined by using energy conservation law. Figure 7-13 shows the finite element model of the scaled cask's tip-over at the beginning of the analysis, and the crack patterns observed in the experiment are compared with the plastic strain results from finite element analysis in Figure 7-14 and Figure 7-15. The analysis results for the maximum accelerations, provided by the explicit solver of LS-DYNA, are compared with the experimental results in Table 7-6, which shows that the average difference between the experimental and numerical results is approximately 10%.

Finite element models of a full scale cask's tip-over were generated based on the verified model explained in this section and used to generate virtual experimental data needed for the probabilistic study of the tip-over problem. It should be mentioned that the cask considered for the probabilistic analysis had a fixed geometry ($D_C = 3.45\ \mathrm{m}, H_{CG} = 5.72\ \mathrm{m}, H_{CG} = 2.71\ \mathrm{m}, t_C = 0.67\ \mathrm{m}, W_C = 160\ \mathrm{ton}$) while material and structural parameters varied per the experimental design as explained in Section 7.3.2. In this regard, the structural response is highly affected by the material properties which are the focus of this study. The pad length and width and also the soil dimensions were similar to Huang et al.'s study (Huang et al., 2009), and the pad thickness was considered as a variable in the experimental design. The time history of element strains and nodal displacements were recorded at multiple locations on the cask and used to assess the structural response of the selected dry cask to the impact loads.

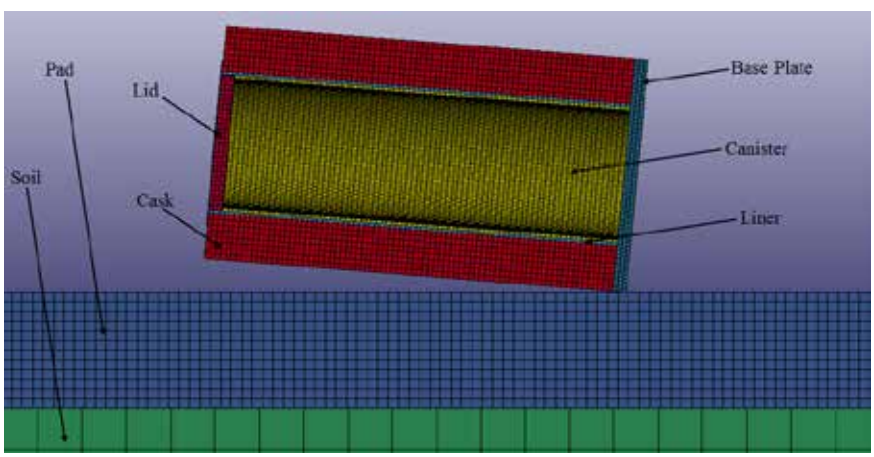

Figure 7-13 Finite element model of the tip-over experiment.

(a) (b) 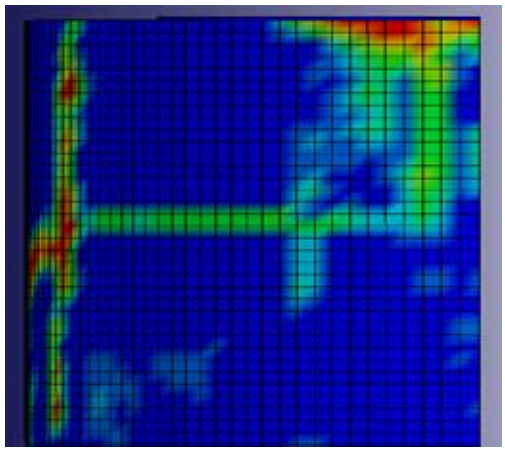

Figure 7-14 Crack patterns on the impact side of the cask in the experiment and finite element model.

(a) (b) 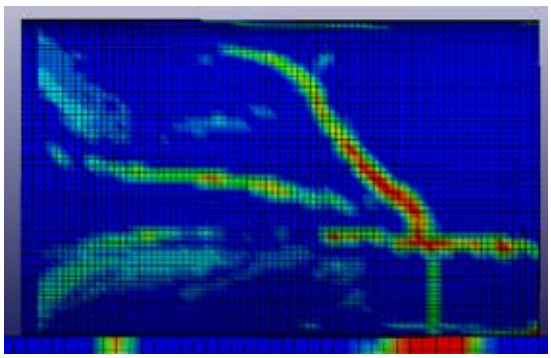

Figure 7-15 Crack patterns on the side of the cask in the experiment and finite element model.

Table 7-6 Comparison of Maximum Accelerations (in g) at Different Locations on the Cask in Two Experiments and the Finite Element Model.

Accelerometer location	Test 1	Test 2	Average of tests	Finite element model results	Difference with Test 1	Difference with Test 2	Difference with average of tests
Left side - Mid height	90	62.4	76.2	65.4	27.3%	4.8%	14.2%
Left side - Top	120	112.5	116.25	122.3	1.9%	8.7%	5.2%
Left side - Top surface	124	143	133.5	132	6.5%	7.7%	1.1%
Back side - Top surface	---	192.6	---	143.6	---	25.4%	---
Back side - Top	140	---	---	135.8	3%	---	---
Back side - Mid height	98	79.9	88.95	80.1	18.3%	0.3%	9.9%
				Average	11.4%	9.4%	7.6%

7.3.2. Virtual Experimental Design

In order to consider parameters that might affect the structural response of the selected dry cask to the impact loads in the tip-over event, the parameters and associated ranges shown in Table 7-7 were considered. Using Latin hypercube sampling (McKay et al, 1979), 200 different configurations of the tip-over problem were generated for the analysis, and parameterized finite element models of the full cask's tip-over scenario were developed based on the experimental design. The models were analyzed by LS-DYNA's explicit solver, and the analysis results were used to develop probabilistic models for the structural response of the cask to the tip-over impact loads.

Table 7-7 Geometric, Material, and Structural Parameters Considered in Generating Finite Element Models of the Tip-Over Scenario.

Variable	Symbol	Unit	Range
Cask concrete compressive strength	f'_{cc}	MPa	28 – 55
Pad concrete compressive strength	f'_{cp}	MPa	28 – 55
Pad thickness	t_P	m	0.5 – 1.2
Initial angular velocity	ω_0	rad/s	0 – 1
Soil shear wave velocity	C_S	m/s	150 – 2000
Soil Poisson ratio	ν_S	---	0.1 – 0.45
Damping ratio	ξ	---	0.01 – 0.1
Liner steel yielding stress	σ_{yL}	MPa	200 - 300
Canister steel yielding stress	σ_{yC}	MPa	140 - 205

7.3.3. Impact Demand Model Development

Investigating the plastic strain results for the 200 simulations throughout the canister showed that the maximum plastic strains varied between 0.06 mm/mm to 0.1 mm/mm in different models. On the other hand, NUREG-1864 (NRC, 2007) considers the mean failure plastic strain as 0.52 mm/mm with a standard deviation of 0.097. Therefore, for the largest plastic strain observed in the analysis results (0.1 mm/mm), the probability of failure was about 7×10^{-6}, which means the canister is highly unlikely to fail in a tip-over event. Another parameter of interest in the tip-over problem is the acceleration response of the system. In this study, probabilistic models were developed for the mean maximum acceleration (a_{Max}) in the cask. This response parameter was selected because it is of key interest to designers when considering loads for cask design; furthermore it can correlate to prospective damage to the basket and fuel rods depending upon the design details of the system. To determine the target response for each model, maximum values in the time history of the total acceleration at 25 locations in the cask were determined, and the average value of them was considered as the mean maximum acceleration of the cask. To develop a probabilistic model for the target response, the process explained in Section 7.2.4 was used and the parameters presented in Table 7-7 along with the cask's kinetic energy at the impact instance were used as potential predictors. The best set of

predictors was selected by using stepwise regression, which resulted in the following equation for the mean maximum acceleration of the cask in a tip-over event

$$a_{Max} = 638.94 + 1.2 f_{cp} - \frac{182.95}{\sqrt{t_p}} - 5.854\sqrt{C_S} - 131.29E_{imp} - \frac{4196.6}{\sqrt{C_S}} + \frac{35290}{C_S} + 28.276E^2_{imp} + 3.9737\sqrt{\frac{C_S}{t_P}} - 15.391\frac{f'_{cp}}{\sqrt{C_S}} + e_{\mathrm{Im}\,p} \qquad 7.10$$

where a_{Max} is in g, f'_{cp} is the pad concrete strength in MPa, t_P is the pad thickness in m, C_S is the shear wave velocity of soil in $\mathrm{m/s}$, E_{imp} is the kinetic energy of the cask at the instance of impact in $\mathrm{MN.m}$, and ε_{Imp} is the model error which is $\varepsilon_{Imp} \sim N(0,64)$ (64 is the model's variance). E_{imp} can be calculated as

$$E_{imp} = mg\sqrt{(\frac{D_C}{2})^2 + H^2_{CG}} - \frac{D_C}{2}) + \frac{1}{2}I_o w_0^2 \qquad 7.11$$

In Eq. 7.11, which was developed by using energy conservation law, ω_0 is the angular velocity of the cask at the instance of tip-over with respect to the pivot point (point O) in $\mathrm{rad/s}$, and other parameters were defined in previous sections. The performance of the probabilistic model developed in this section is presented in Figure 7-16 and Table 7-8, which show acceptable prediction performance of the model ($R^2 = 0.81$) and good explanatory functions (p-values<0.05) in Eq. 7.10. In addition, studying the variations of a_{Max} with respect to the model parameters show that the mean maximum acceleration of the cask increases as the pad concrete strength and thickness, soil shear wave velocity, and cask's impact kinetic energy increase. In other words, stiffer supports (pad or soil) and higher impact energy result in larger accelerations in the tip-over event.

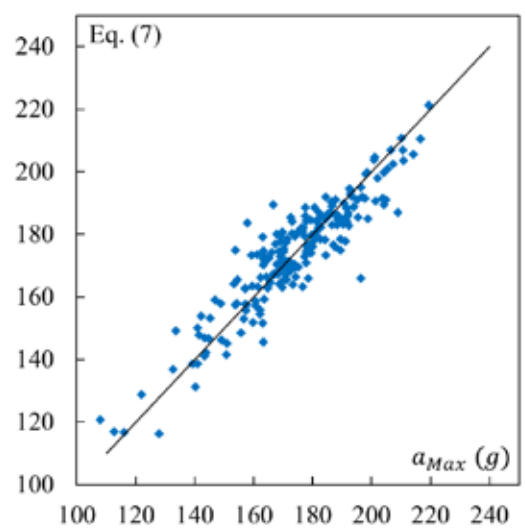

Figure 7-16 Predictions against actual values of a_{Max}.

Table 7-8 Performance of the Probabilistic Model for the Mean Maximum Acceleration of the Dry Cask in a Tip-Over Event.

Model	5-Fold CV R^2	p-Value								
		f'_{cp}	$\frac{1}{\sqrt{t_P}}$	$\sqrt{C_S}$	E_{imp}	$\frac{1}{\sqrt{C_S}}$	$\frac{1}{C_S}$	E_{imp}^2	$\sqrt{\frac{C_S}{t_P}}$	$\frac{f'_{cp}}{\sqrt{C_S}}$
Eq. 7.10	0.81	***	***	***	**	**	**	***	***	*

*: less than 0.05 **: less than 0.001 ***: less than 0.0001

7.3.4. Impact Fragility Analysis

Since the canister is not expected to fail in the tip-over event (i.e., the P_f was approximately 10^{-6} or less), fragility curves are developed for the mean maximum acceleration of the cask in this section, which show the sensitivity of the structural response of the cask to the impact loads. As Eq. 7.10 shows, the acceleration response depends on the cask kinetic energy at the impact instance, thickness and concrete strength of the pad, and soil shear wave velocity. In this section, effect of pad and soil properties on the fragility curves is studied by calculating the integral

$$P\left(a_{Max} > LS \mid f'_{cp}, t_p, C_s, S\right) = \int_{\omega_0} P\left(a_{Max} > LS \mid f'_{cp}, t_p, C_s, S, \omega_0\right) f\left(\omega_0\right) d\omega_0 \qquad 7.12$$

In Eq. 7.12, $\boldsymbol{S}$ includes mass and geometrical properties of the cask ($\boldsymbol{S} = \{m, D_C, H_{CG}, I_0\}$), and $f(\omega_0)$ is the probability density function of the cask's initial angular velocity. Since E_{imp} depends on $\boldsymbol{S}$ components, which are constant, and ω_0, integrating over ω_0 removes the dependency of the fragility on the impact kinetic energy. The integration was performed over ω_0, assuming a uniform distribution for that for the range of 0 to 1 rad/s. Using Eq. 7.12 to estimate the impact fragility led to results that included the uncertainty due to the cask's impact kinetic energy. The integral in Eq. 7.12 was estimated for the cask parameters: $m = 160\ \mathrm{ton}$, $D_C = 3.45\ \mathrm{m}$, $H_{CG} = 2.71\ \mathrm{m}$, and $I_O = 2206.4\ \mathrm{ton.m}^2$ by employing Monte Carlo method and using 10^7 samples for each set of parameters. For illustration purposes, the limit state chosen for fragility development was 150 g, however, other limit states might be considered as well if the cask components or fuel rods should be analyzed subject to other acceleration limits. Figure 7-17 to Figure 7-19 present the impact fragility curves developed in this section. As the figures show, the fragility is very sensitive to the variation of pad thickness and soil shear wave velocity. For example, the probability of exceeding the predefined limit state is very close to 1 for the curves with $t_P = 0.85\ \mathrm{m}$ in Figure 7-17 and Figure 7-19. However, when $t_P = 0.5\ \mathrm{m}$, the failure probability is low for small values of the pad concrete strength and soil shear wave velocity, and it approaches 1 for very large pad concrete strength and soil shear wave velocity. The same trend is observed for shear wave velocity of soil in Figure 7-17 and Figure 7-18. Based on this observation, the pad thickness should be as small as possible to reduce the impact loads applied to the cask in tip-over events. In comparison, larger pad concrete strength leads to larger accelerations (and consequently larger impact loads to the cask). Interestingly, this may suggest that although the potential cracking and spalling of the cask may increase with aging, the associated cask accelerations may decrease due to associated decrease in concrete strength. However, as Figure

7-18 and Figure 7-19 show, the sensitivity of the response to the variations of pad concrete strength is not as large as previous cases.

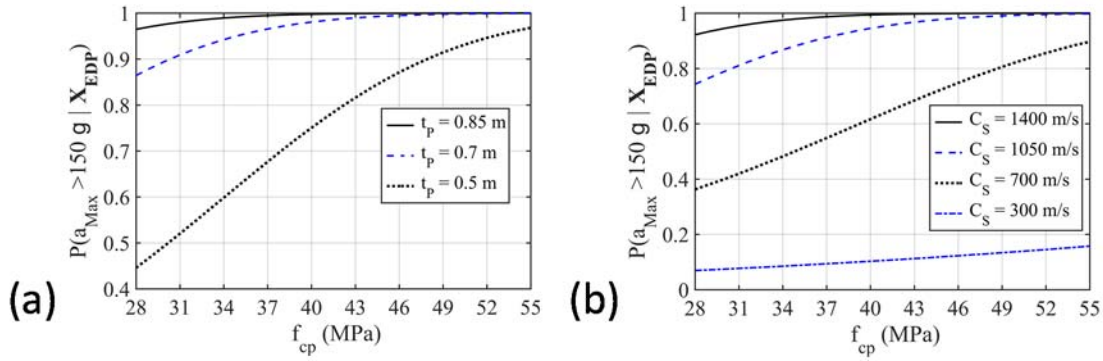

Figure 7-17 Impact fragility curves of the sample cask with $m = 160$ ton, $D_C = 3.45$ m, $H_{CG} = 2.71$ m for the pad concrete strength (Left: effect of pad thickness. Right: effect of soil shear wave velocity).

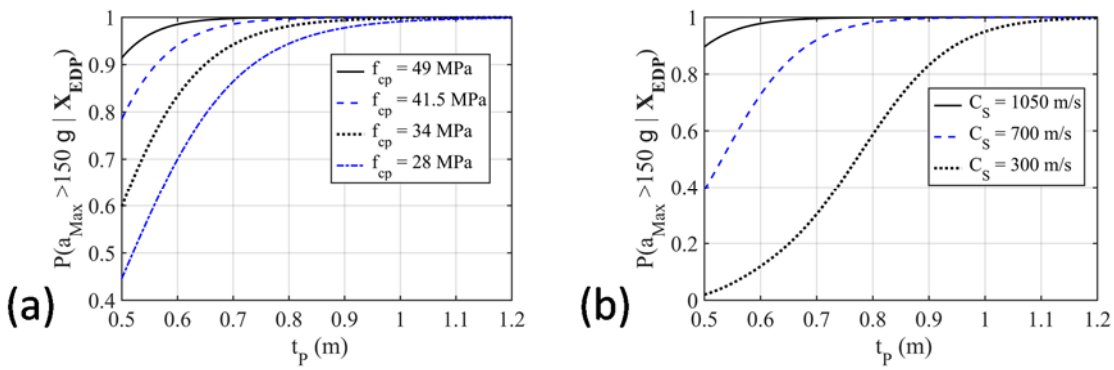

Figure 7-18 Impact fragility curves of the sample cask with $m = 160$ ton, $D_C = 3.45$ m, $H_{CG} = 2.71$ m for the pad thickness (Left: effect of pad concrete strength. Right: effect of soil shear wave velocity).

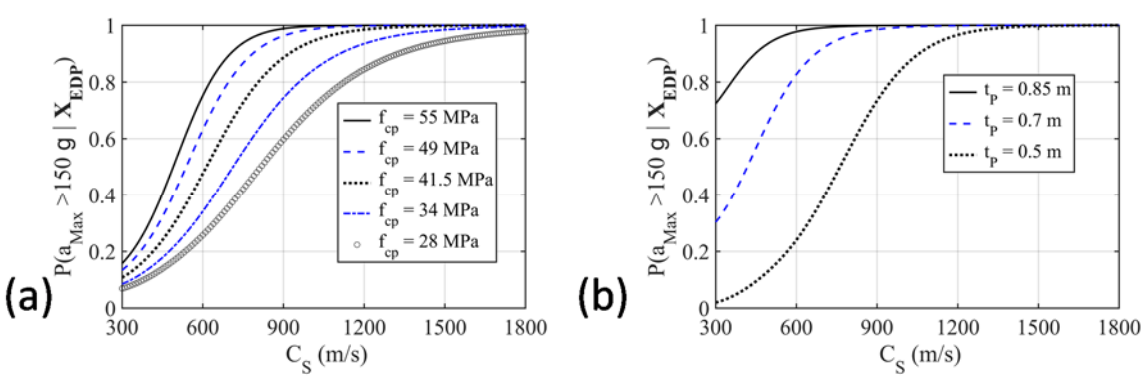

Figure 7-19 Impact fragility curves of the sample cask with $m = 160$ ton, $D_C = 3.45$ m, $H_{CG} = 2.71$ m for shear wave velocity of soil (Left: effect of pad concrete strength. Right: effect of pad thickness).

7.4. CONCLUSIONS

Probabilistic seismic analysis of vertical concrete dry casks was performed in this section. A finite element model of the seismic response of a scaled cask on a shaking table test was developed and verified with experimental results. This base model along with an experimental design and an earthquake selection were used to develop finite element models generating virtual experimental data needed for probabilistic seismic demand modeling. PSDMs were developed for maximum sliding distance and maximum rocking angle of the casks in seismic events. Fragility curves were developed for a select sliding limit state and for the tip-over scenario. The results showed that the casks' seismic response and fragility is very sensitive to the friction coefficient between the cask and the pad. Risk analysis performed for extreme values of friction coefficient revealed that the annual probability of exceeding the predefined sliding limit state ($\frac{1}{4}D_C$) and tip-over are on the order of 10^{-5} to 10^{-6} for locations in Western, Central, and Eastern U.S.

The structural response of a dry cask configuration to impact loads induced by tip-over events was further studied with a probabilistic approach. A finite element model of the tip-over problem was developed and verified against experimental results provided in Chapter 5. The model was used to generate virtual experimental data for probabilistic model development and impact fragility analysis. The analysis results showed that the canister is not expected to fail due to tip-over impact loads. Instead, a probabilistic model was developed for the mean maximum acceleration of the cask in tip-over events, which is a parameter linked to practical design practices and one that may be correlated to basket or fuel rod damage. Fragility curves were developed based on the developed probabilistic model for an illustrative acceleration limit, noting that the model is flexible to evaluate alternative limits. The results of the fragility analysis showed the high sensitivity of the response and fragility to thickness of the pad and the soil shear wave velocity. Based on this observation, in order to minimize the impact loads applied to dry casks in case of tip-over, the pad thickness should be as small as possible, acknowledging that there are practical limits to ensure adequate foundation. Furthermore, the pad concrete strength which may be affected by aging can also influence the impact fragility; although if minimization of cask accelerations is of key interests this phenomenon may actually have a beneficial effect. This may not be the case for other limit states, however, such as impact related cask cracking or spalling which may be adversely affected by aging.

7.5. REFERENCES

ASCE/SEI (2005). *Seismic Design Criteria for Structures, Systems, and Components in Nuclear Facilities,* ASCE/SEI Standard 43-05, American Society of Civil Engineers and Structural Engineering Institute, VA, USA.

FEMA (2000). *Prestandard and Commentary for the Seismic Rehabilitation of Buildings*, FEMA 356, Federal Emergency Management Agency, Washington, District of Columbia, USA.

Baker, J.W., Lin, T., Shahi, S.K. and Jayaram N. (2011). *New Ground Motion Selection Procedures and Selected Motions for the PEER Transportation Research Program*, PEER Report 2011/03 prepared by University of California, Berkeley, CA.

Baker Research Group. *A Computationally Efficient Ground Motion Selection Algorithm for Matching a Target Response Spectrum Mean and Variance*, Available form: http://web.stanford.edu/~bakerjw/gm_selection.html, Accessed on August 17, 2016.

Boore, D., Watson-Lamprey, J., Abrahamson, N. A. (2006). "Orientation-Independent Measures of Ground Motion," Bulletin of the Seismological Society of America, 96(4A).

Housner, G.W. (1963). "The Behavior of Inverted Pendulum Structures during Earthquakes," Bulletin of the Seismological Society of America 53(2).

Huang, C.C., Wu, T.Y. (2009). "A Study on Dynamic Impact of Vertical Concrete Cask Tip-over Using Explicit Finite Element Analysis Procedures," Annals of Nuclear Energy, 36(2).

Livermore Software Technology Corporation (2007). "LS-DYNA Keyword User's Manual, Version 971," Livermore, CA, USA.

McKay, M.D., Beckman, R.J. and Conover, W.J. (1979). "A Comparison of Three Methods for Selecting Values of Input Variables in the Analysis of Output from a Computer code," Technometrics, 22(2).

NIST (2012). *Soil-Structure Interaction for Building Structures*, NIST GCR 12-917-21, prepared by NEHRP Consultant Joint Venture.

Rosner, R., Lordan R. (2014). "Why America Should Move toward Dry Cask Consolidated Interim Storage of Used Nuclear Fuel," Bulletin of the Atomic Scientists, 70(6).

Shirai, K., Hirata, K. and Saegusa, T. (2003). "Experimental Studies of Free-Standing Spent Fuel Storage Cask Subjected to Strong Earthquakes," *17th International Conference on Structural Mechanics in Reactor Technology (SMiRT 17)*, August 17-22, Prague, Czech Republic.

Singh K.P., Soler A.I, Smith M. (2001). "Predicting the Structural Response of Free-Standing Spent Fuel Storage Casks under Seismic Events," *16th International Conference on Structural Mechanics in Reactor Technology (SMiRT 16)*, August 12-17, Washington, District of Columbia, USA.

USGS. *U.S. Geological Survey Hazard Curve Application*, Available form: http://geohazards.usgs.gov/hazardtool/application.php, Accessed on August 17, 2016.

NRC (1987). *Standard Review Plan for the Review of Safety Analysis Reports for Nuclear Power Plants*, NUREG-0800, U.S. Nuclear Regulatory Commission

NRC (2007). *A Pilot Probabilistic Risk Assessment of a Dry Cask Storage System at a Nuclear Power Plant*, NUREG-1864, U.S. Nuclear Regulatory Commission, Washington, District of Columbia, USA.

CHAPTER 8
CLOSURE

8.1. CONCLUSIONS

The key findings of this research project are reiterated here.

- Three scaled (approximately 1/3 scale) physical models of concrete dry casks with an exposed concrete surface have been manufactured. Two of the casks were subjected to accelerated aging due to corrosion and alkali-silica reactivity (ASR). After 2 years of degradation, the casks were tested under tip-over impact to compare their performance under aged conditions to the condition of the control (unaged) cask.
- Material studies on plain and reinforced concrete indicated that addition of $CaCl_2$ and NaOH work effectively for accelerators of rebar corrosion and ASR of concrete, respectively. Based on the outcomes of the material level studies, these techniques were successfully applied to accelerate the degradation in concrete outerpacks of scaled physical models of dry casks.
- 4% and 0.8% by weight of cement addition of $CaCl_2$ and NaOH to fresh concrete and has resulted in observable degradation (cracking) due to reinforcing bar corrosion and ASR in scaled models.
- Three tip-over impact tests were performed on each scaled cask model. It was observed that the degraded casks underwent substantially more distress in the form of cracking and spalling compared to the control (unaged) cask. Particularly, the corrosion damaged cask showed substantial spalling of the cover concrete. Some yielding of the steel liner was also observed. However, the overall performance of all three casks were found to be satisfactory with no major disintegration of the cask. Furthermore, the deformations of the steel liner were limited and canister integrity in this regard is not compromised although the damage due to severe decelerations reaching to over 100 g should be investigated separately.
- Detailed probabilistic simulations and analysis were performed and it was found out that the annual probability of exceeding the predefined sliding limit state (of a quarter of the cask diameter) and tip-over are on the order of 10^{-5} to 10^{-6} for locations in Western, Central, and Eastern U.S. These probabilities are considerably lower than those of the major failures modes of other key infrastructure such as bridges.
- The results of the fragility (probabilistic) analysis showed the high sensitivity of the response and fragility to thickness of the pad and the soil shear wave velocity. Based on this observation, in order to minimize the impact loads applied to dry casks in case of tip-over, the pad thickness should be as small as possible, acknowledging that there are practical limits to ensure adequate foundation.

- It was found through detailed computational fluid dynamics analysis that the temperature difference between the inside and outside surfaces of the dry cask concrete over pack might as high as 39 °C in winter conditions. The same number is 32 °C and 22 °C for summer and normal conditions, respectively. This temperature gradient might result in the deterioration of the concrete in the long term and needs to be investigated in more detail in future studies. The highest temperature on the interior surface of concrete was found to be 104 °C in summer conditions. This high temperature might also accelerate degradation processes such as corrosion of steel reinforcement and alkali-silica reactivity of aggregates in concrete.
- It was also found through thermal analysis that conventional scaling laws do not work to obtain the temperature distributions and a fully detailed analysis is required to obtain the temperature distributions in scaled models.
- Numerical simulations using state-of-the-art creep and shrinkage formulations indicate that the stresses induced in the concrete due these phenomena is negligible due to the nature of the applied loads (gravity only). However, the ASR degradation simulations followed by tip-over numerical experiments confirmed the findings of tests performed on the scaled casks that this issue needs to be investigated for even longer durations of ASR aging.

8.2. RECOMMENDATIONS FOR FUTURE RESEARCH

The following recommendations are made for future research:

- End- and side-drop testing of aged casks with more realistic representation of the fuel basket and fuel rods to investigate the effects of these probable loading conditions in aged casks on spent nuclear fuel assemblies.
- In-depth investigation of the microstructural changes in concrete when corrosion and ASR accelerating agents are added, and related crack development at the micro level.
- The influence of high temperature and temperature gradient on the integrity of the concrete outerpack in the long-term and its influence on the rate of corrosion and ASR.
- Scaling analysis to include thermal radiation effects in dry cask structures.
- Further studies to relate the laboratory accelerated aging experiments to field conditions.
- Simulation of various cask configurations with different types and number of spent nuclear fuel assemblies, loading conditions, and dimensions subjected to tip-over impact loading at various levels of aging.

APPENDIX A
MATERIAL LEVEL TEST DATA

Table A-1 Sieve Analysis of Fine Aggregate.

Sieve Size (mm)	Weight of fine aggregate retained (g) Determination No.				Percent Retained	Cumulative Percent Retained	Percent Passing
	I	II	III	Avg.			
9.5	0.0	0.0	0.0	0.0	0.0	0.0	100.0
4.75	5.6	4.5	8.2	6.1	0.6	0.6	99.4
2.36	84.5	99.6	122.6	102.2	10.2	10.8	89.2
0.85	270.5	287.7	310.5	289.6	29.0	39.8	60.2
0.6	282.0	250.9	223.9	252.3	25.2	65.0	35.0
0.3	202.3	202.3	201.8	202.1	20.2	85.2	14.8
0.15	130.1	128.4	114.0	124.2	12.4	97.6	2.4
0.075	22.0	23.1	16.1	20.4	2.0	99.7	0.3
Pan	3.0	3.5	2.9	3.1	0.3	100.0	0.0
Total	1000	1000	1000	1000	100	-	-

Table A-2 Sieve Analysis of Coarse Aggregate.

Sieve Size (mm)	Weight of Coarse aggregate retained (g) Determination No.				Percent Retained	Cumulative Percent Retained	Percent Passing	Size Number	Nominal Size
	I	II	III	Avg.					
25.4	23.0	25.2	0.0	16.1	1.3	1.3	98.7	6 & 67	3/4 to 3/8" & 3/4" to No.4
19.0	190.8	128.0	128.6	149.1	12.4	13.8	86.2		
12.7	225.4	228.2	187.7	213.8	17.8	31.6	68.4		
9.5	195.2	205.2	211.7	204.0	17.0	48.6	51.4		
4.75	388.3	415.8	421.5	408.5	34.0	82.6	17.4		
2.36	155.0	169.0	185.2	169.7	14.1	96.8	3.2		
Pan	22.3	28.6	65.3	38.7	3.2	100.0	0.0		
Total	1200	1200	1200	1200	100	-	-		

Table A-3 Density of Fresh Concrete, Phase 1.

Mix	Density (g/cm^3)	Average Density (g/cm^3)
SCC_PH1	2.339	2.325
	2.344	
	2.297	
NaOH-8_PH1	2.322	2.319
	2.317	
	2.314	
$CaCl_2$-4_PH1	2.355	2.347
	2.338	
	-	

Table A-4 Density of Fresh Concrete, NaOH Mixtures, Phase 2.

Mix	Density (g/cm^3)	Average Density (g/cm^3)
NaOH-0_PH2	2.35	2.36
	2.36	
	2.37	
NaOH-2_PH2	2.43	2.41
	2.40	
	2.40	
NaOH-4_PH2	2.42	2.42
	2.42	
	2.42	
NaOH-8_PH2	2.38	2.38
	2.39	
	2.38	

Table A-5 Density of Fresh Concrete, $CaCl_2$ Mixtures, Phase 2.

Mix	Density (g/cm^3)	Average Density (g/cm^3)
$CaCl_2$_0_PH2	2.31	2.31
	2.32	
	2.31	
$CaCl_2$_1_PH2	2.35	2.36
	2.38	
	2.34	
$CaCl_2$_2_PH2	2.31	2.33
	2.33	
	2.34	
$CaCl_2$_4_PH2	2.27	2.30

Table A-6 Slump Test Results, Phase 1.

Mix	Slump (mm)	Average Slump (mm)
SCC_PH1	279.4	271.8
	254.0	
	241.3	
NaOH-8_PH1	190.5	228.6
	241.3	
	254.0	
$CaCl_2$-4_PH1	266.7	275.1
	266.7	
	292.1	

Table A-7 Density of Hardened Concrete at 28 Days, NaOH Mixtures, Phase 2.

Mix	Bulk Density, Dry (g/cm^3)	Bulk Density after Immersion (g/cm^3)	Apparent Density (g/cm^3)
NaOH-0_PH2	1.66	1.74	1.81
NaOH-2_PH2	1.64	1.72	1.78
NaOH-4_PH2	1.64	1.71	1.77
NaOH-8_PH2	1.65	1.73	1.79

Table A-8 Absorption and Voids of Hardened Concrete at 28 Days, NaOH Mixtures, Phase 2.

Mix	Absorption after Immersion (%)	Absorption after Immersion and Boiling (%)	Volume of permeable pore space (voids) (%)
NaOH-0_PH2	4.6	4.8	8.0
NaOH-2_PH2	4.5	4.7	7.6
NaOH-4_PH2	4.2	4.4	7.3
NaOH-8_PH2	4.7	4.9	8.1

Table A-9 Density of Hardened Concrete at 28 Days, $CaCl_2$ Mixtures, Phase 2.

Mix	Bulk Density, Dry (g/cm^3)	Bulk Density after Immersion (g/cm^3)	Apparent Density (g/cm^3)
$CaCl_2$-0_PH2	1.67	1.75	1.82
$CaCl_2$-1_PH2	1.65	1.73	1.80
$CaCl_2$-2_PH2	1.65	1.73	1.79
$CaCl_2$-4_PH2	1.66	1.74	1.80

Table A-10 Absorption and Voids of Hardened Concrete at 28 Days, $CaCl_2$ Mixtures, Phase 2.

Mix	Absorption after Immersion (%)	Absorption after Immersion and Boiling (%)	Volume of permeable pore space (voids) (%)
$CaCl_2$-0_PH2	4.4	4.9	8.1
$CaCl_2$-1_PH2	4.7	5.0	8.3
$CaCl_2$-2_PH2	4.5	4.8	8.0
$CaCl_2$-4_PH2	4.6	4.9	8.1

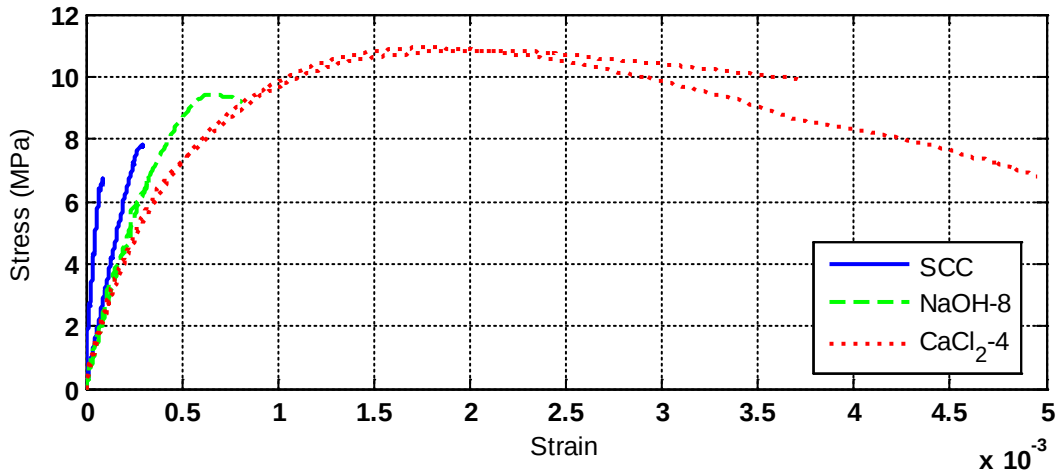

Figure A-1 Compression test, phase 1, 1st day.

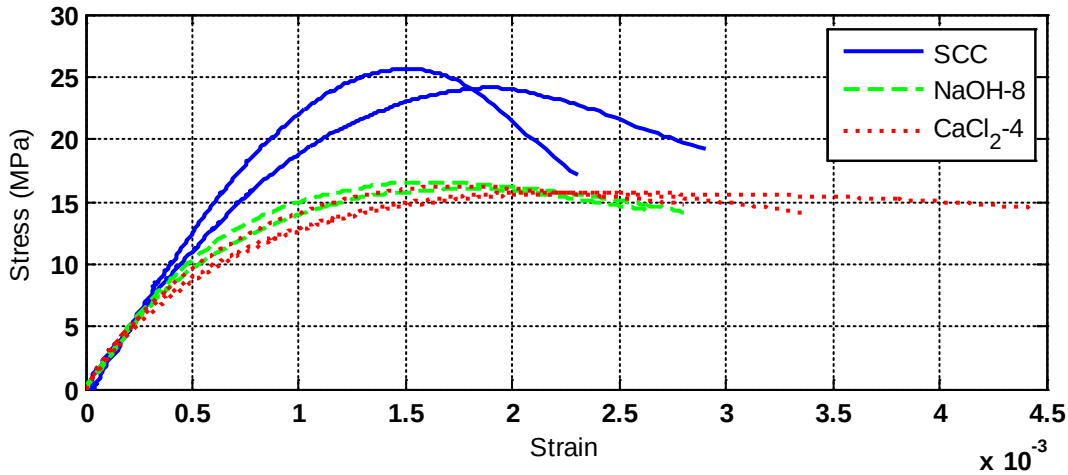

Figure A-2 Compression test, phase 1, 3rd day.

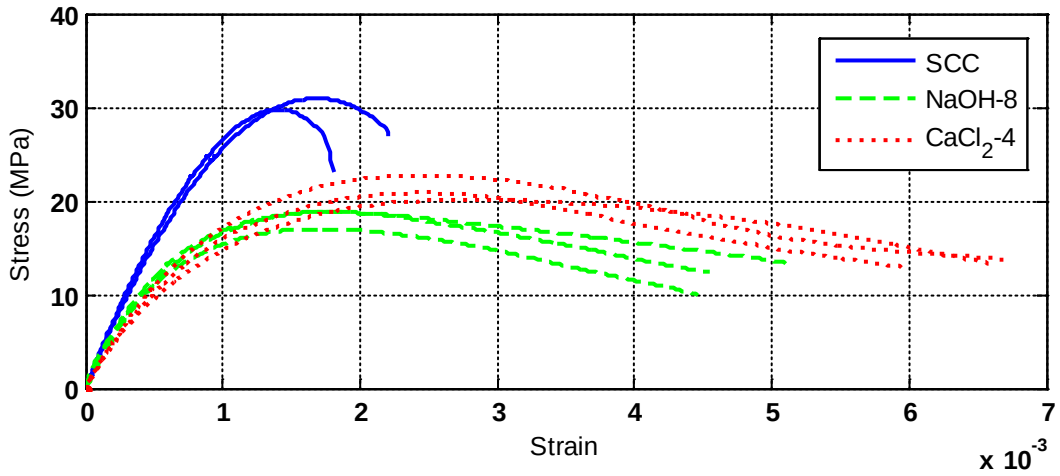

Figure A-3 Compression test, phase 1, 7th day.

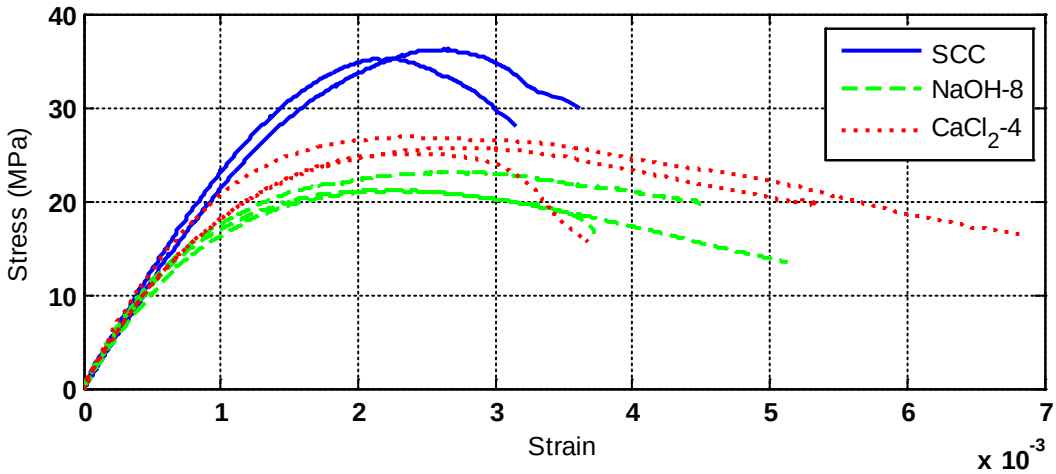

Figure A-4 Compression test, phase 1, 28th day.

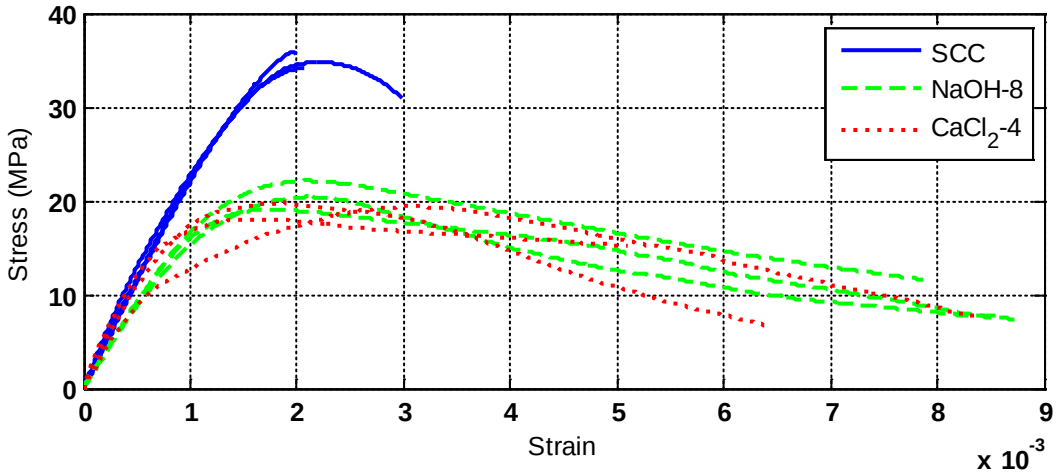

Figure A-5 Compression test, phase 1, 210th day.

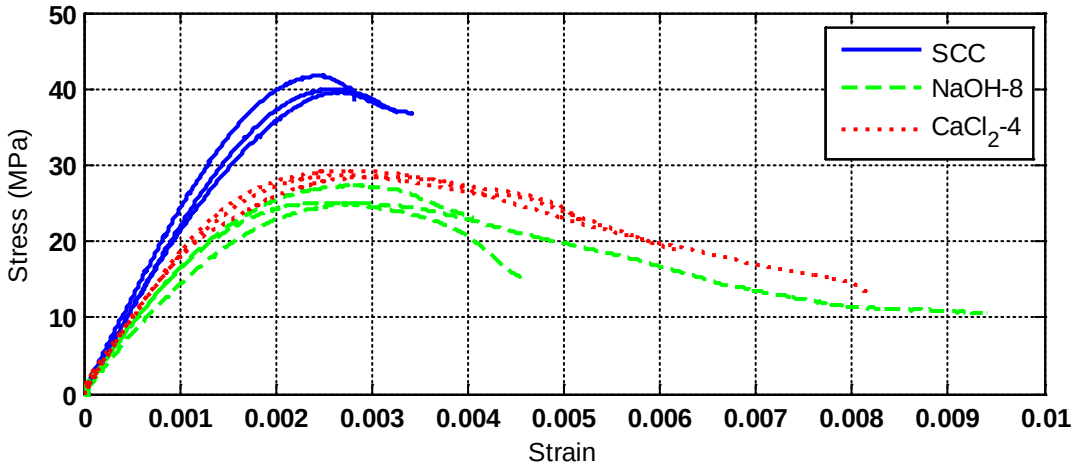

Figure A-6 Compression test, phase 1, 365th day.

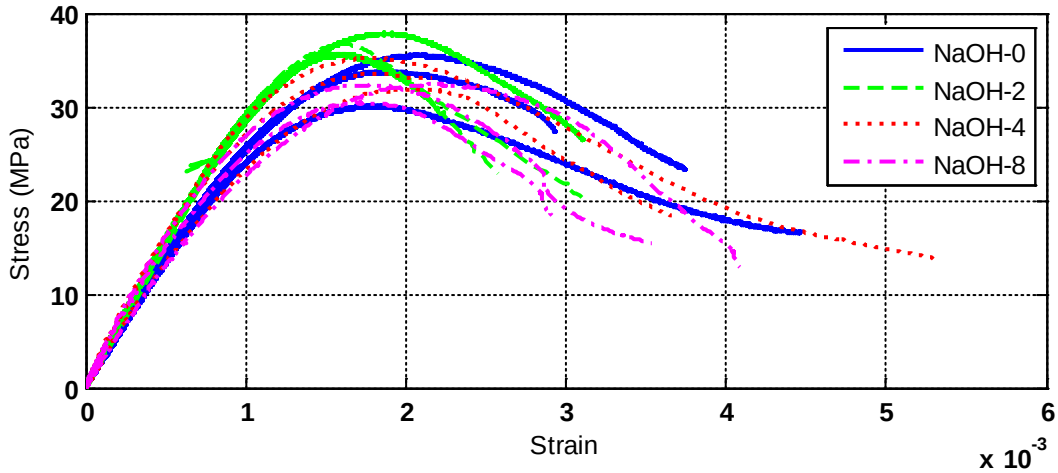

Figure A-7 NaOH compression test, vertical strain, phase 2, 7th day.

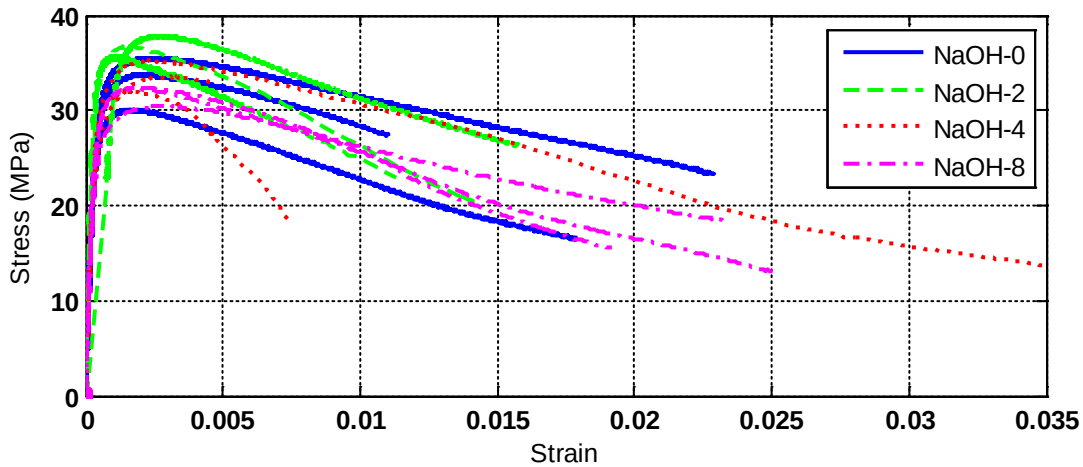

Figure A-8 NaOH compression test, horizontal strain, phase 2, 7th day.

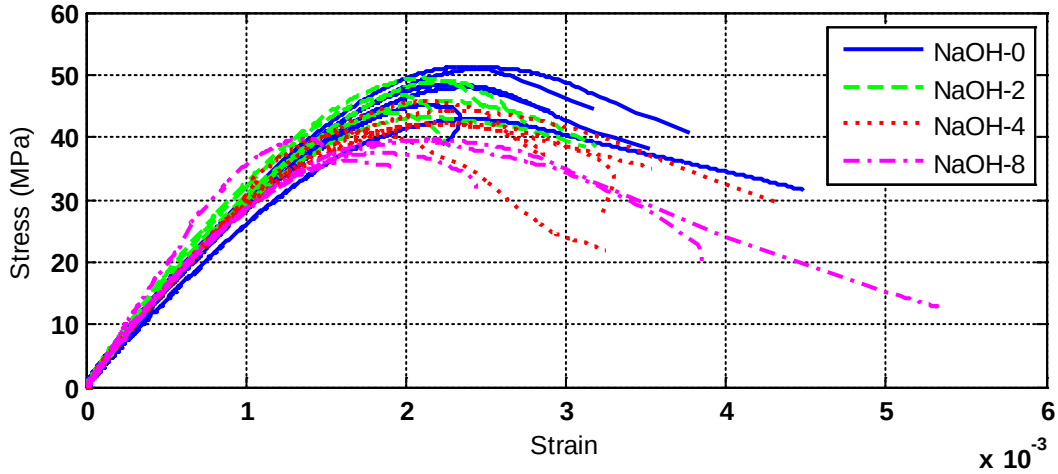

Figure A-9 NaOH compression test, vertical strain, phase 2, 28th day.

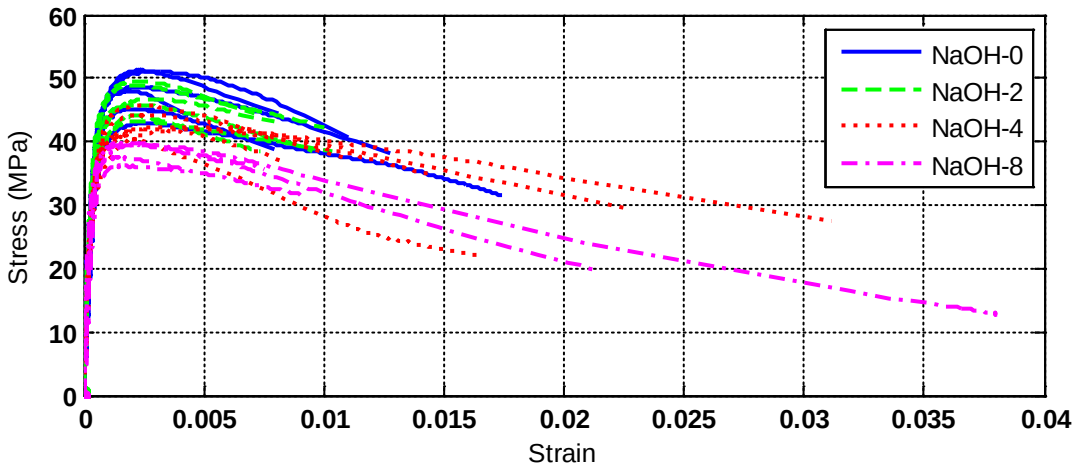

Figure A-10 NaOH compression test, horizontal strain, phase 2, 28th day.

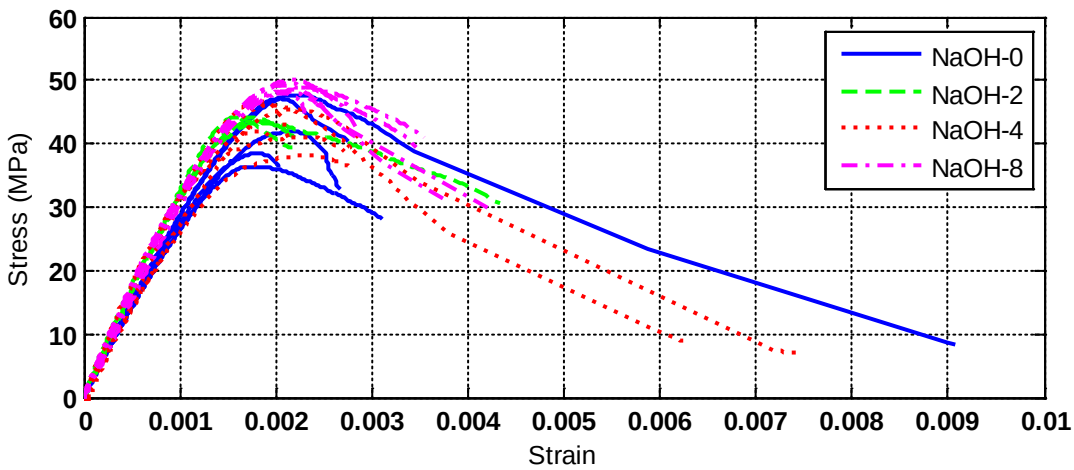

Figure A-11 NaOH compression test, vertical strain, phase 2, 180th day.

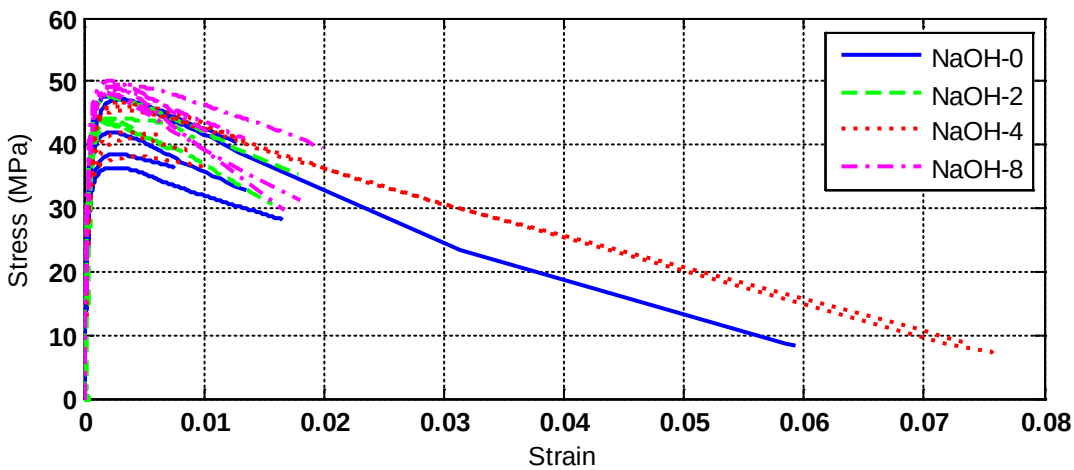

Figure A-12 NaOH compression test, horizontal strain, phase 2, 180th day.

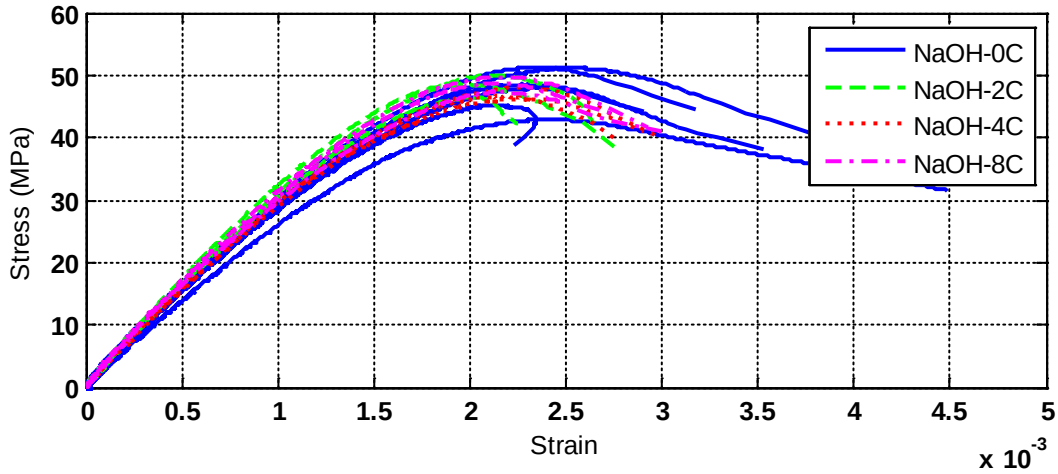

Figure A-13 NaOH control compression test, vertical strain, phase 2, 28th day.

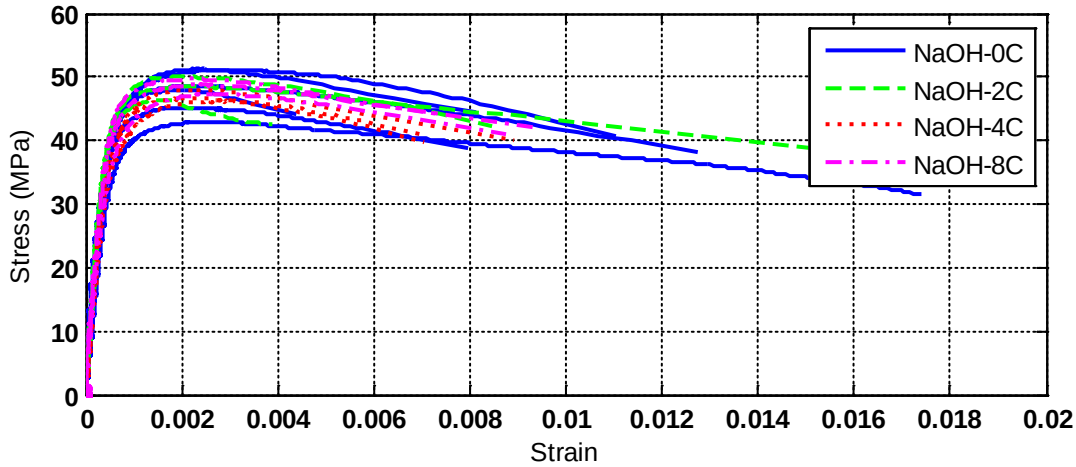

Figure A-14 NaOH control compression test, horizontal strain, phase 2, 28th day.

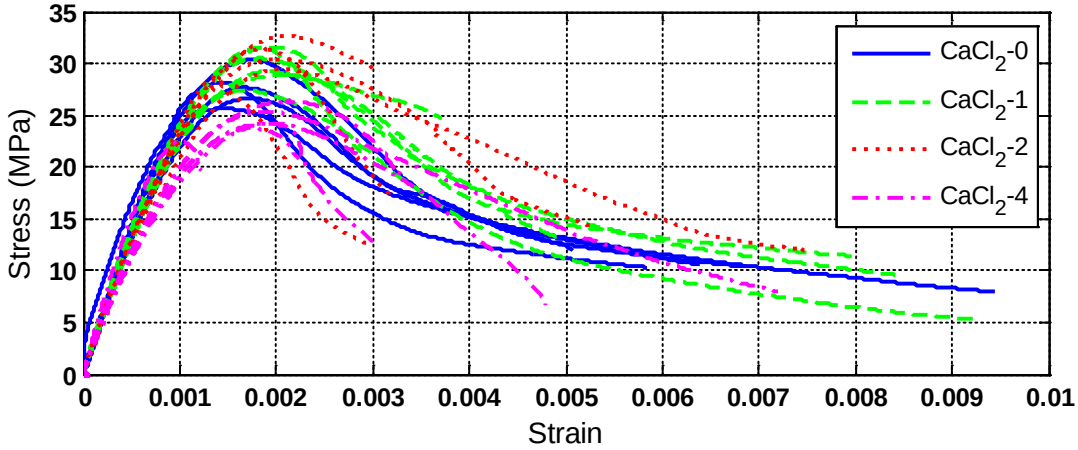

Figure A-15 $CaCl_2$ compression test, vertical strain, phase 2, 7th day.

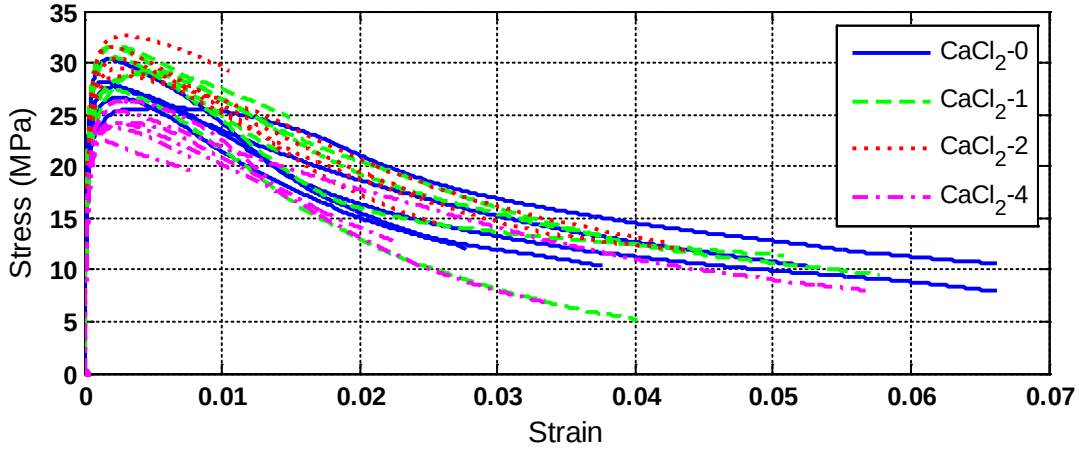

Figure A-16 $CaCl_2$ compression test, horizontal strain, phase 2, 7th day.

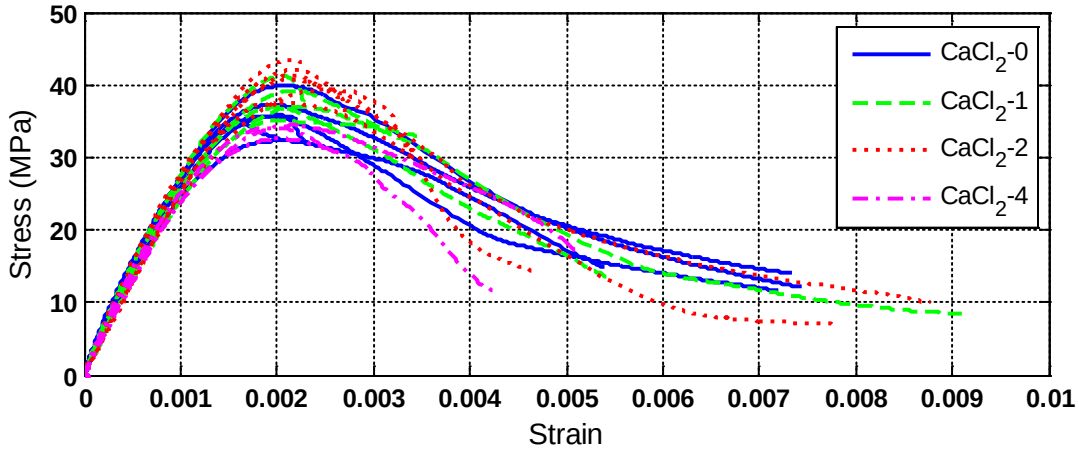

Figure A-17 $CaCl_2$ compression test, vertical strain, phase 2, 28th day.

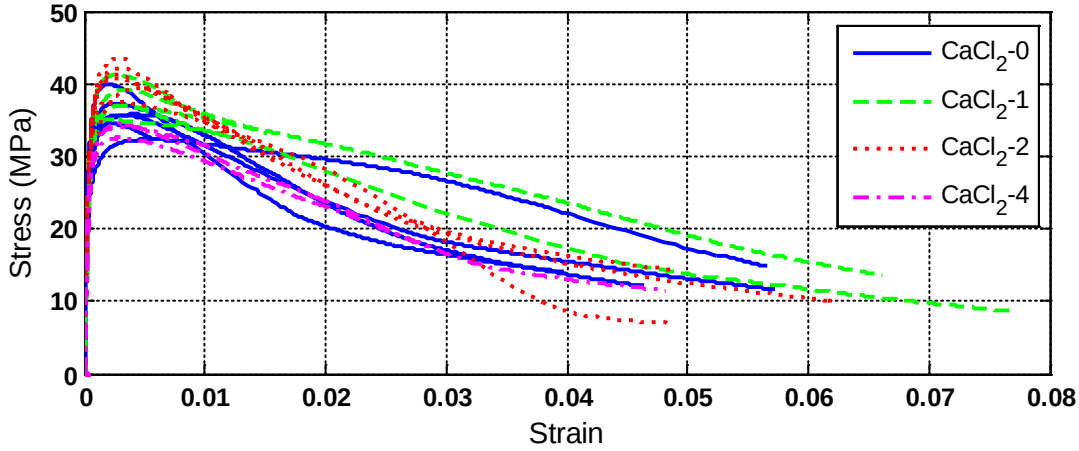

Figure A-18 $CaCl_2$ compression test, horizontal strain, phase 2, 28th day.

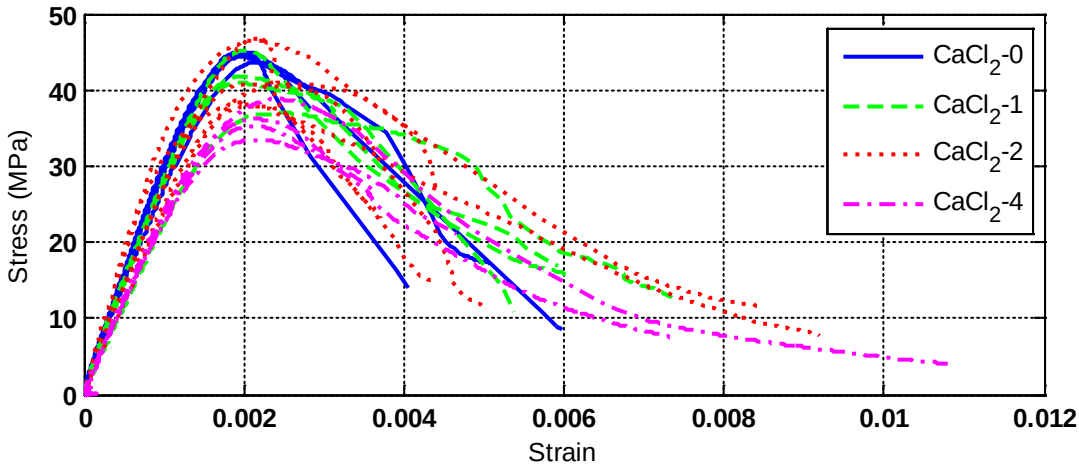

Figure A-19 $CaCl_2$ compression test, vertical strain, phase 2, 90th day.

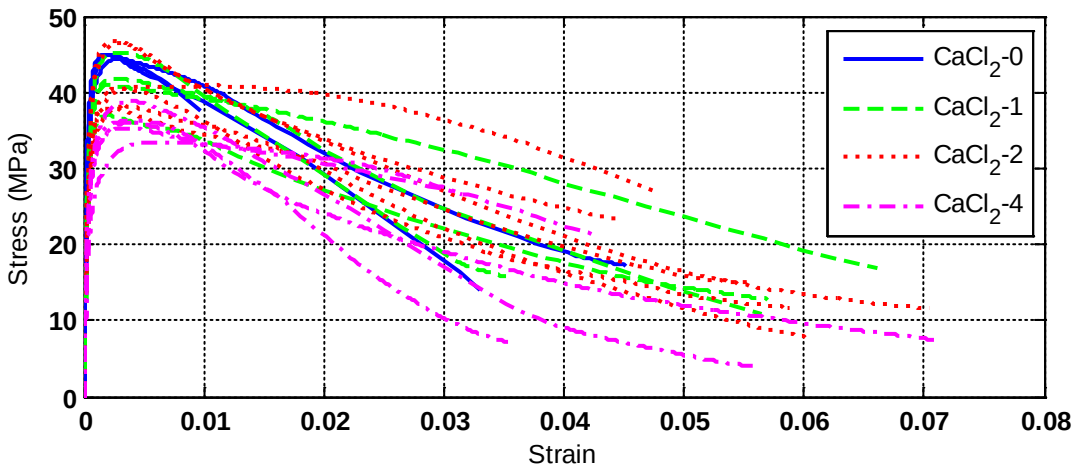

Figure A-20 $CaCl_2$ compression test, horizontal strain, phase 2, 90th day.

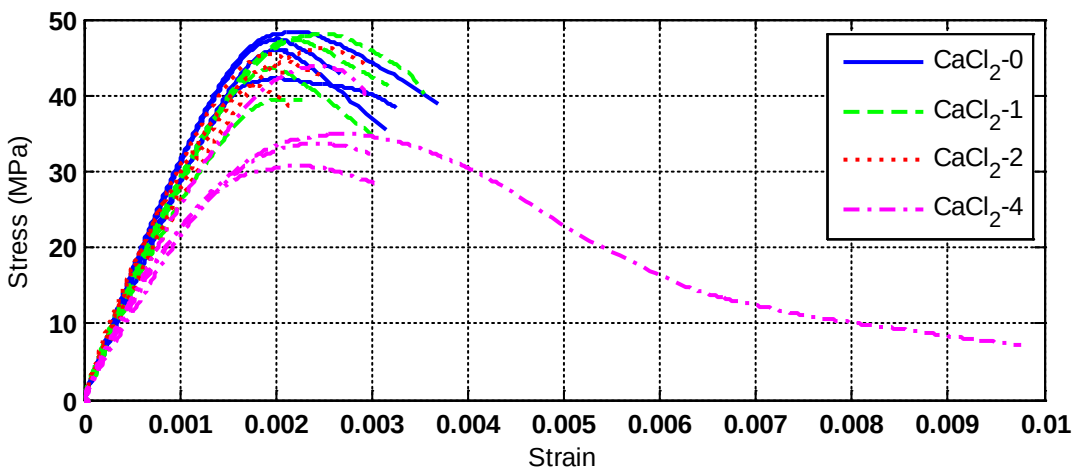

Figure A-21 $CaCl_2$ compression test, vertical strain, phase 2, 180th day.

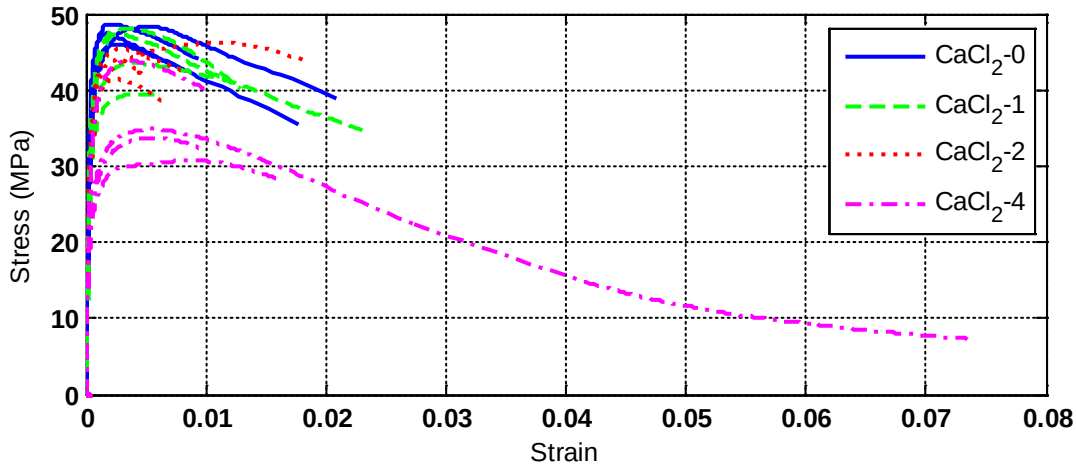

Figure A-22 $CaCl_2$ compression test, horizontal strain, phase 2, 180th day.

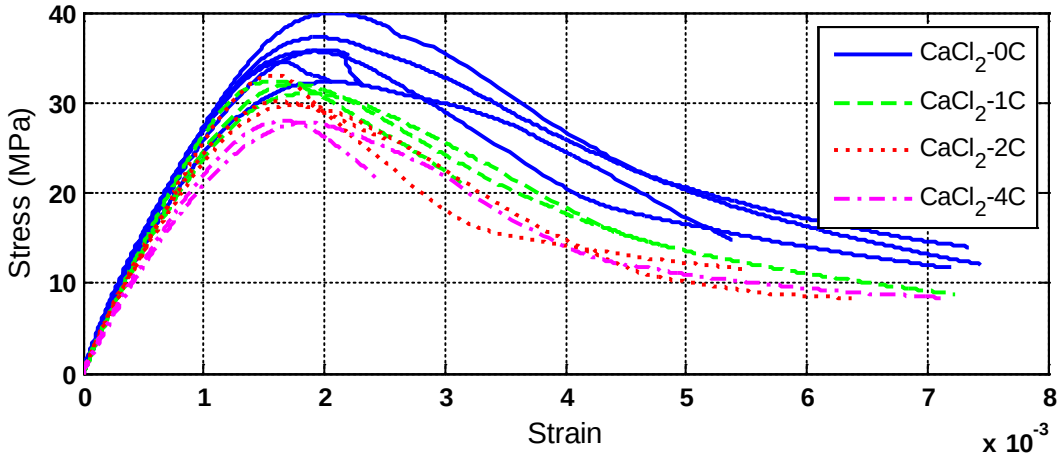

Figure A-23 $CaCl_2$ control compression test, vertical strain, phase 2, 28th day.

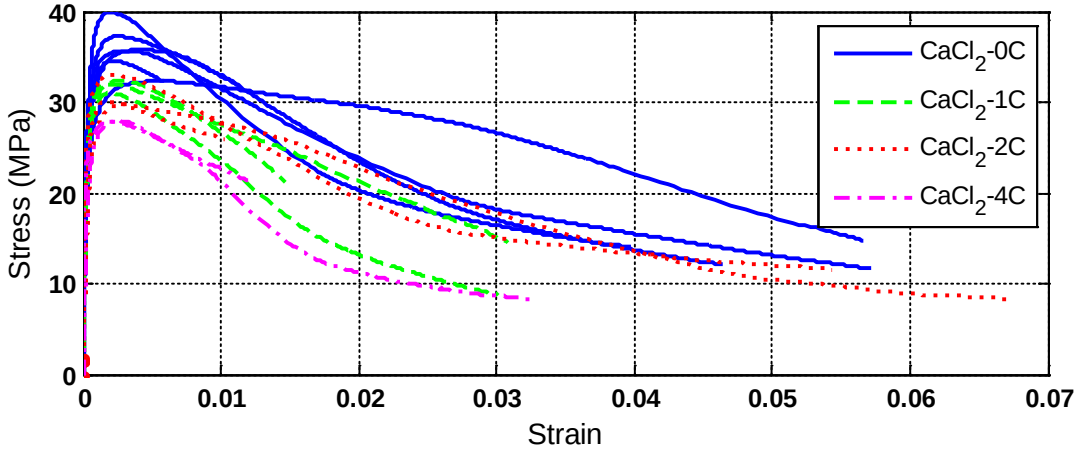

Figure A-24 $CaCl_2$ control compression test, horizontal strain, phase 2, 28th day.

Table A-11 Strength of Control Specimens of NaOH Mixtures, Phase 2.

Mix	Max Stress (MPa)	Average	MOE (MPa)	Average	Poisson's Ratio	Average
NaOH-0_PH2	45.1	47.8	29722	30042	0.29	0.31
	48.5		30584		0.30	
	51.1		30098		0.35	
	47.9		30622		0.30	
	42.9		27142		0.33	
	51.1		32085		0.32	
NaOH-2_PH2	48.5	48.3	33635	32783	0.32	0.30
	46.3		31938		0.29	
	50.0		32776		0.31	
NaOH-4_PH2	46.2	46.9	30578	30537	0.36	0.34
	46.6		30838		0.31	
	48.0		30194		0.34	
NaOH-8_PH2	49.7	48.6	33209	32207	0.32	0.34
	47.3		31672		0.37	
	48.7		31741		0.32	

Table A-12 Strength of Control Specimens of $CaCl_2$ Mixtures, Phase 2.

Mix	Max Stress (MPa)	Average	MOE (MPa)	Average	Poisson's Ratio	Average
$CaCl_2$-0_PH2	32.3	36.0	27748	29593	0.30	0.30
	35.9		29538		0.31	
	37.3		29497		0.32	
	35.7		30879		0.23	
	39.9		29269		0.31	
	34.5		30627		0.34	
$CaCl_2$-1_PH2	32.4	31.8	29117	27869	0.32	0.32
	32.0		27114		0.33	
	31.0		27376		0.31	
$CaCl_2$-2_PH2	29.8	31.0	26832	27025	0.35	0.32
	30.1		27812		0.29	
	33.1		26431		0.31	
$CaCl_2$-4_PH2	28.0	27.9	24492	24266	0.37	0.33
	27.8		24040		0.29	

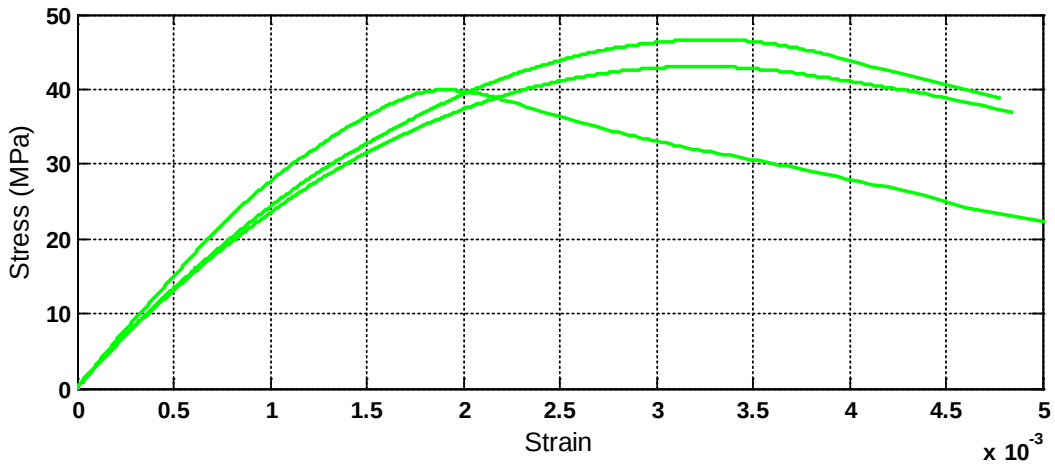

Figure A-25 TRIGA compression test, vertical strain.

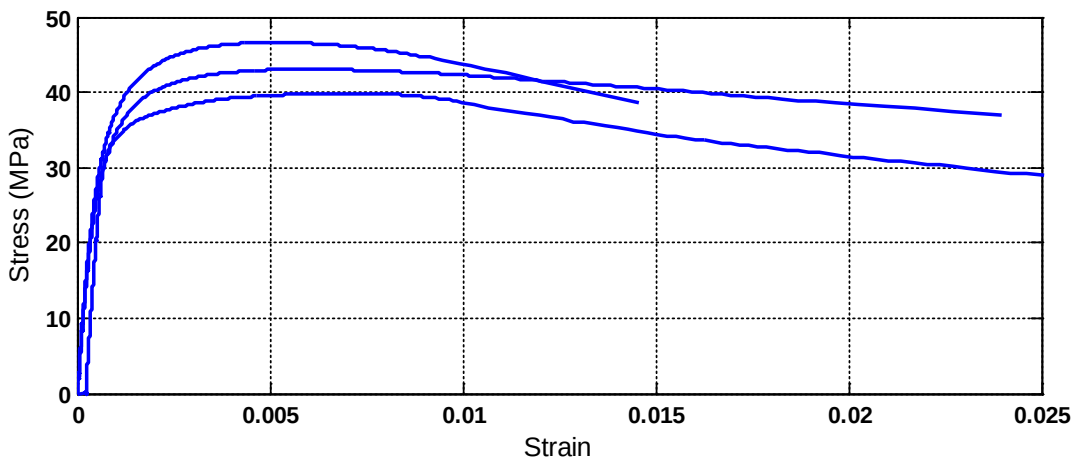

Figure A-26 TRIGA compression test, horizontal strain.

Table A-13 Modulus of Elasticity of Concrete Mixtures, Phase 1, at 210 and 365 Days.

Mix	210 Days		365 Days	
	E (MPa)	Average	E (MPa)	Average
SCC_PH1	25358.0	25250.9	22099.0	23503.4
	25143.8		24907.8	
	-		22466.7	
NaOH-8_PH1	17397.7	17878.1	15193.7	16549.1
	-		16581.9	
	18358.5		17904.5	
$CaCl_2$-4_PH1	22809.4	20455.3	19102.1	18783.3
	17802.6		19093.4	
			18154.4	

Table A-14 Modulus of Elasticity of NaOH Concrete Mixtures, Phase 2.

Mix	7 Days		28 Days		180 Days	
	E (MPa)	Average	E (MPa)	Average	E (MPa)	Average
NaOH-0_PH2	28291	27813	29722	30042	29477	28837
	28560		30584		-	
	26586		30098		27666	
	-		30622		29748	
	-		27142		29303	
	-		32085		27990	
NaOH-2_PH2	31470	31948	35486	32805	33156	34662
	32117		31612		-	
	32258		31039		33771	
	-		31146		38106	
	-		34526		35146	
	-		33020		33132	
NaOH-4_PH2	32613	30768	32403	31231	27930	31710
	32649		30039		36137	
	27042		31257		33369	
	-		30747		27971	
	-		31294		31946	
	-		31647		32906	
NaOH-8_PH2	33138	29971	41597	34195	33495	33057
	30761		31655		31104	
	26012		34981		32065	
	-		32551		35323	
	-		32472		32725	
	-		31912		33633	

Table A-15 Modulus of Elasticity of $CaCl_2$ Concrete Mixtures, Phase 2.

Mix	7 Days		28 Days		90 Days		180 Days	
	E (MPa)	Average	E (MPa)	Average	E (MPa)	Average	E (MPa)	Average
$CaCl_2$-0_PH2	-	28417	27748	29593	30805	30057	28627	32768
	27199		29538		27559		31026	
	29688		29497		29777		33271	
	28908		30879		31410		-	
	27539		29269		31263		31845	
	28751		30627		29528		39071	
$CaCl_2$-1_PH2	28171	27082	27248	27822	22645	27564	-	29277
	26554		30740		-		28223	
	25534		-		28660		28410	
	26808		28793		29913		30372	
	26185		25445		-		-	
	29239		26883		29039		30104	
$CaCl_2$-2_PH2	25486	26331	30822	28043	23771	29902	26312	29775
	22669		29638		28428		33490	
	33001		25928		35356		-	
	26154		28717		28082		27451	
	26819		27298		25831		27928	
	23856		25854		37941		33694	
$CaCl_2$-4_PH2	24357	24918	27046	27439	-	25236	-	24745
	23628		28322		26762		22077	
	33684		-		25096		25554	
	22354		28708		24330		-	
	22384		25678		23582		26474	
	23100		-		26411		24875	

Table A-16 Poisson's Ratio of Concrete Mixtures, Phase 1, at 210 and 365 Days.

Mix	210 Days		365 Days	
	Poisson's Ratio	Average	Poisson's Ratio	Average
SCC_PH1	0.24	0.27	0.29	0.29
	0.31		0.29	
	-		0.24	
NaOH-8_PH1	0.46	0.38	0.23	0.29
	0.29		0.29	
	0.31		0.34	
$CaCl_2$-4_PH1	0.31	0.353	0.27	0.29
	0.43		0.26	
	-		0.33	

Table A-17 Poisson's Ratio of NaOH Concrete Mixtures, Phase 2.

Mix	7 Days		28 Days		180 Days	
	Poisson's Ratio	Average	Poisson's Ratio	Average	Poisson's Ratio	Average
NaOH-0_PH2	0.29	0.31	0.29	0.31	0.29	0.31
	0.31		0.30		0.30	
	0.33		0.35		0.35	
	-		0.30		0.30	
	-		0.33		0.33	
	-		0.32		0.32	
NaOH-2_PH2	0.26	0.30	0.32	0.31	0.38	0.34
	0.32		0.28		-	
	0.32		0.29		0.31	
	-		0.33		0.34	
	-		0.36		0.35	
	-		0.28		0.32	
NaOH-4_PH2	0.39	0.37	0.35	0.33	0.27	0.33
	0.38		0.31		0.35	
	0.35		0.32		0.32	
	-		0.32		0.28	
	-		0.37		0.39	
	-		0.29		0.35	
NaOH-8_PH2	0.39	0.34	0.36	0.34	0.32	0.32
	0.35		0.35		0.31	
	0.27		0.28		0.30	
	-		0.40		0.32	
	-		0.34		0.29	
	-		0.34		0.36	

Table A-18 Poisson's Ratio of $CaCl_2$ Concrete Mixtures, Phase 2.

Mix	7 Days		28 Days		90 Days		180 Days	
	Poisson's Ratio	Ave.	Poisson's Ratio	Ave.	Poisson's Ratio	Ave.	Poisson's Ratio	Ave.
$CaCl_2$-0_PH2	-	0.30	0.30	0.30	0.24	0.31	0.32	0.31
	0.29		0.31		-		0.28	
	0.33		0.32		0.26		0.33	
	0.28		0.23		0.28		-	
	0.26		0.31		0.30		0.25	
	0.32		0.34		0.28		0.39	
$CaCl_2$-1_PH2	0.28	0.32	0.31	0.35	0.29	0.34	-	0.29
	0.27		0.35		-		0.26	
	0.28		-		0.28		0.38	
	0.37		0.42		0.33		0.23	
	0.36		0.31		-		-	
	0.37		0.37		0.32		0.30	
$CaCl_2$-2_PH2	0.36	0.35	0.37	0.35	0.28	0.33	0.24	0.29
	0.31		0.36		0.31		0.33	
	0.48		0.31		0.38		-	
	0.27		0.36		0.29		0.30	
	0.38		0.39		0.27		0.24	
	0.32		0.33		0.31		0.31	
$CaCl_2$-4_PH2	0.35	0.37	0.35	0.35	-	0.32	-	0.32
	0.37		0.34		0.44		0.28	
	0.45		-		0.32		0.35	
	0.34		0.36		0.37		-	
	0.34		0.35		0.30		0.31	
	0.38		-		0.35		0.33	

Table A-19 Modulus of Rupture of Concrete Mixtures, Phase 1.

Mix	28 Days (MPa)	Average	365 Days (MPa)	Average	455 Days (MPa)	Average
SCC_PH1	3.95	3.95	4.16	4.67	5.86	5.19
	3.26		4.74		5.13	
	4.10		5.11		4.58	
	4.49					
	3.13					
NaOH-8_PH1	2.84	2.92	2.86	2.95	2.44	2.32
	2.91		2.97		2.42	
	2.86		3.02		2.06	
	2.99					
	2.98					
CaCl2-4_PH1	3.69	3.65	3.88	3.89	3.42	3.35
	3.62		3.50		3.67	
	3.62		4.23		2.95	
	3.31					
	4.30					

Table A-20 Modulus of Rupture of NaOH Concrete Mixtures, Phase 2.

Mix	28 Days (MPa)	Average
NaOH-0_PH2	5.12	4.57
	4.07	
	4.50	
NaOH-2_PH2	4.53	4.29
	4.52	
	3.81	
NaOH-4_PH2	3.59	3.83
	3.33	
	4.57	
NaOH-8_PH2	4.03	4.24
	4.39	
	4.30	

Table A-21 Modulus of Rupture of $CaCl_2$ Concrete Mixtures, Phase 2.

Mix	28 Days (MPa)	Average
$CaCl_2$-0_PH2	3.43	3.68
	4.05	
	3.56	
$CaCl_2$-1_PH2	3.61	3.60
	3.76	
	3.45	
$CaCl_2$-2_PH2	4.36	4.49
	4.35	
	4.76	
$CaCl_2$-4_PH2	3.45	3.43
	3.32	
	3.51	

Table A-22 Crack Widths of Specimens with #10 Rebar, Phase 1 (Note that the Crack No. are Indicated in Figure 3-45).

Bar No.	No.	Crack Width (mm)						
		117 Days	171 Days	225 Days	276 Days	342 Days	432 Days	492 Days
4	1	0.6	0.8	0.8	0.8	1.0	3.0	4.2
	2	0.4	0.5	0.5	0.5	0.8	1.2	1.8
	3	0.2	0.2	0.2	0.3	0.3	Spalling	Spalling
	4	0.2	0.3	0.4	0.5	2.0	4.6	5.1
	5	0.2	0.2	0.4	0.5	0.9	1.3	1.8
	6	0.4	0.5	0.6	0.6	0.8	1.0	1.3
	7	0.1	0.2	0.3	0.5	0.5	0.8	1.0
	8	-	-	0.2	0.3	0.4	0.4	0.7
	9	-	-	0.2	0.2	0.2	0.2	0.3
5	1	0.3	0.4	0.4	0.4	0.4	0.4	0.8
	2	0.1	0.2	0.2	0.2	0.3	0.3	0.5
	3	0.1	0.2	0.2	0.2	0.2	0.5	0.8
	4	0.1	0.2	0.4	0.5	0.5	3.8	4.2
	5	0.2	0.3	0.3	0.3	0.3	0.3	0.3
	6	0.2	0.2	0.2	0.3	0.3	1.0	0.3
	7	-	0.1	0.2	0.3	0.3	0.6	1.3
	8	-	0.1	0.2	0.2	0.3	0.9	0.8
	9	-	-	0.1	0.2	0.3	0.6	0.7
	10	-	-	0.1	0.2	0.3	0.7	0.8
	11	-	-	0.1	0.1	0.1	0.2	0.4

Table A-23 Crack Width of Specimens with #19 Rebar, Phase 1 (Note that the Crack No. are Indicated in Figure 3-45).

Bar No.	No.	Crack Width (mm)						
		117 Days	171 Days	225 Days	276 Days	342 Days	432 Days	492 Days
14	1	-	0.1	0.2	0.3	0.4	1.3	1.3
	2	-	0.1	0.2	0.3	0.3	0.6	0.8
	3	-	-	0.1	0.2	0.2	0.3	0.4
	4	-	-	0.1	0.2	0.3	0.4	0.7
	5	-	-	-	0.1	0.2	0.4	0.7
17	1	0.2	0.4	0.4	0.5	0.7	0.8	Spalling
	2	0.2	0.2	0.5	0.6	0.7	1.0	2.1
	3	0.3	0.4	0.5	0.6	0.6	0.7	0.9
	4	0.4	0.4	0.5	0.8	1.2	3.4	4.1
	5	0.2	0.4	0.4	1.0	Spalling	Spalling	Spalling
	6	0.1	0.2	0.3	0.4	0.5	0.7	1.5
	7	0.1	0.2	0.3	0.5	0.5	0.5	0.5
	8	-	-	0.2	0.2	0.2	0.4	0.4

Table A-24 Half-Cell Potential Measurements in Specimens with #10 Rebar, Phase 1 (Corresponds to #3 in the US system), Phase 1.

Age	163 Days		236 Days		267 Days		291 Days		325 Days		357 Days		389 Days		422 Days		452 Days		482 Days		512 Days		536 Days		563 Days		590 Days	
Mix	Potential	Temp. (˚C)	Potential	Temp. (˚C)	Potential	Temp. (˚C)	Potential	Temp. (˚C)	Potential	Temp. (˚C)	Potential	Temp. (˚C)	Potential	Temp. (˚C)	Potential	Temp. (˚C)	Potential	Temp. (˚C)	Potential	Temp. (˚C)	Potential	Temp. (˚C)	Potential	Temp. (˚C)	Potential	Temp. (˚C)	Potential	Temp. (˚C)
SCC_PH1	-80.59**	9.2	-88.30	20.7	-53.11	17.9	-64.23	25.6	-66.10	23.7	-13.80	32.0	-105.40	22.0	-5.11	22.1	-2.38	22.8	-37.44	21.4	-141.09	17.9	-107.23	17.3	-59.70	28	-15.07	26.7
NaOH-8_PH1	-55.41	13.1	-104.19	19.9	-109.25	18.5	-70.56	22.6	-98.57	20.7	-56.83	32.3	-104.44	21.4	-5.60	21.0	-33.81	22.1	-79.01	20.1	-144.74	17.4	-154.5	17	-23.19	27.9	-17.04	26.4
$CaCl_2$-4_PH1	-546.5	7	-424.97	21.7	-462.08	18.8	-423.75	26.5	-439.23	24.3	-254.90	32.0	-494.73	22.3	-204.93	23.3	-157.14	23.4	-308.92	24.2	-435.94	18.4	-512.44	18.4	-280.99	27.9	-374.58	26.8

*CSE: Copper-sulfate electrode

**Measurements shown in this table are corrected based on JSCE-E 601-2000

Table A-25 Half-Cell Potential Measurements in Specimens with #19 Rebar (Corresponds to #6 in the US system), Phase 1.

Age	163 Days		236 Days		267 Days		291 Days		325 Days		357 Days		389 Days		422 Days		452 Days		482 Days		512 Days		536 Days		563 Days		590 Days	
Mix	Potential	Temp. (˚C)	Potential	Temp. (˚C)	Potential	Temp. (˚C)	Potential	Temp. (˚C)	Potential	Temp. (˚C)	Potential	Temp. (˚C)	Potential	Temp. (˚C)	Potential	Temp. (˚C)	Potential	Temp. (˚C)	Potential	Temp. (˚C)	Potential	Temp. (˚C)	Potential	Temp. (˚C)	Potential	Temp. (˚C)	Potential	Temp. (˚C)
SCC_PH1	-76.99**	5.9	-86.99	23.9	-102.15	18.5	-81.12	26.2	-87.32	25.2	-84.56	33.6	-97.48	22.8	-2.06	25.6	-39.33	24.3	-38.55	26.5	-141.14	20.4	-70.55	20.5	-12.91	26.1	-18.24	24.4
NaOH-8_PH1	-104.03	12.4	-134.8	23	-115.86	18.6	-104.85	26.5	-91.51	25.1	-28.61	35.1	-108.87	22.7	-41.90	25.0	-15.8	24	-119.4	26	-108.53	19.3	-138.96	19.6	-44.68	25.8	-45.34	23.4
$CaCl_2$-4_PH1	-416.29	7	-480.6	24	-491.4	19	-482.27	26.7	-529.32	25.2	-351.36	33.6	-507.18	22.8	-335.90	26.0	-228.05	24.5	-348.75	27.5	-411.23	21.3	-463.93	21.3	-240.06	26.6	-338.36	25.6

*CSE: Copper-sulfate electrode

**Measurements shown in this table are corrected based on JSCE-E 601-2000

Table A-26 Half-Cell Potential Measurements in $CaCl_2$ Specimens with #10 Rebar (Corresponds to #3 in the US system), Phase 2.

Age	28 Days		60 Days		90 Days		120 Days		150 Days		180 Days	
Mix	Potential (mV/CSE*)	Temp. (˚C)	Potential (mV/CSE)	Temp. (˚C)	Potential (mV/CSE)	Potential (mV/CSE)	Potential (mV/CSE)	Temp. (˚C)	Potential (mV/CSE)	Temp. (˚C)	Potential (mV/CSE)	Temp. (˚C)
SCC_PH1	-135.6**	17.1	-227.3	19.2	-123.0	17.2	-119.2	19.7	-98.0	14.5	-107.4	18.8
$CaCl_2$-1_PH2	-207.8	17.3	-311.3	19.0	-171.2	17.5	-161.5	21.3	-122.5	14.5	-125.2	21.8
$CaCl_2$-2_PH2	-241.3	17.7	-316.7	18.8	-199.3	17.6	-155.7	22.8	-137.8	14.5	-138.7	20.5
$CaCl_2$-4_PH2	-384.4	17.8	-474.1	18.8	-434.9	17.6	-396.5	23.9	-355.7	14.6	-400.0	19.4

*CSE: Copper-sulfate electrode

**Measurements shown in this table are corrected based on JSCE-E 601-2000

Table A-27 Surface Resistivity of Specimens, Phase 1.

		115 Days	171 Days	202 Days	230 Days	261 Days	291 Days	318 Days	349 Days	382 Days	412 Days	440 Days	470 Days	500 Days	530 Days	563 Days	593 Days
Mix	No.	ρ (KΩ.com)	ρ (KΩ.com)	ρ (KΩ.com)	ρ (KΩ.com)	ρ (KΩ.com)	ρ (KΩ.com)	ρ (KΩ.com)	ρ (KΩ.com)	ρ (KΩ.com)	ρ (KΩ.com)	ρ (KΩ.com)	ρ (KΩ.com)	ρ (KΩ.com)	ρ (KΩ.com)	ρ (KΩ.com)	ρ (KΩ.com)
SCC-PH1	1	16.1	21.2	22.3	23.2	25.3	26.1	28.5	29.0	26.4	32.8	35.3	32.9	33.9	34.8	38.1	37.0
	2	14.3	18.6	21.3	21.7	23.8	25.5	27.1	28.7	28.1	34.9	36.5	34.3	34.1	37.3	37.1	35.8
	3	12.1	16.0	16.9	18.2	20.5	21.5	23	25.1	24.5	30.9	37.5	31.2	32.5	33.3	33.9	31.5
NaOH-8-PH1 (in water)	1	5.7	6.3	6.8	8.9	7.5	7.6	8.2	9.2	9.4	12.1	12.3	13.4	14.4	14.0	13.7	15.5
	2	5.4	6.1	6.5	7.1	6.9	7.2	8.1	9.2	9.2	11.1	13.7	12.2	12.3	15.5	14.7	15.2
NaOH-8-PH1 (in NaOH solution)	1	4.7	6.9	5.4	6.0	7.1	6.2	6.4	6.8	6.9	7.1	7.4	7.4	8.6	9.0	8.1	7.7
	2	5.7	6.7	6.4	7.0	7.3	9.3	7.5	7.7	8.0	8.5	8.7	8.9	8.9	10.0	9.5	9.3
$CaCl_2$-4-PH1 (in water)	1	5.2	6.4	6.8	7.4	8.2	8.7	9.7	11.1	11.4	14.5	22.8	17.8	19.8	20.8	21.3	22.0
	2	5.2	6.2	6.7	9.7	8.1	8.4	9.1	10.6	10.2	13.2	16.5	16.3	16.0	18.6	18.8	20.4
$CaCl_2$-4-PH1 (in $CaCl_2$ solution)	1	4.9	9.1	7.3	8.1	12	16.8	21.7	28.7	36.6	38.5	64.3	74.4	41.4	43.4	44.8	44.0
	2	4.6	5.9	7.2	7.6	11.2	14.8	20	26.3	34.9	37.4	64.4	75.9	42.4	46.5	47.9	48.0

Table A-28 Surface Resistivity of NaOH Specimens, Phase 2.

		28 Days	60 Days	90 Days	120 Days	150 Days	180 Days	210 Days	240 Days
Mix	No.	ρ (KΩ.com)	ρ (KΩ.com)	ρ (KΩ.com)	ρ (KΩ.com)	ρ (KΩ.com)	ρ (KΩ.com)	ρ (KΩ.com)	ρ (KΩ.com)
NaOH-0_PH2	1	6.5	10.5	12.5	12.1	12.8	14.6	15.0	16.5
	2	6.8	10.5	11.4	12.3	12.6	13.4	15.2	16.9
	3	6.8	10.5	11.9	12.4	12.9	14.1	14.6	16.2
NaOH-0.2_PH2	1	8.5	13.3	16.0	17.9	17.6	19.6	19.5	19.8
	2	9.8	14.3	16.7	18.3	19.5	20.2	19.5	21.1
	3	9.8	14.6	15.4	17.0	18.6	19.9	16.8	20.4
NaOH-0.4_PH2	1	9.8	14.3	15.3	16.2	17.3	18.8	17.3	20.1
	2	11.0	14.8	15.2	17.7	18.5	19.7	19.1	21.3
	3	9.6	14.1	15.6	15.9	17.1	18.6	15.9	21.1
NaOH-0.8_PH2	1	11.5	17.0	21.6	23.3	23.2	25.2	21.9	25.9
	2	11.0	16.7	18.8	21.6	21.9	23.4	22.6	24.4
	3	12.4	17.0	20.2	21.8	22.5	23.7	20.2	24.4

Table A-29 Surface Resistivity of $CaCl_2$ Specimens, Phase 2.

		28 Days	60 Days	90 Days	120 Days	150 Days	180 Days
Mix	No.	ρ (KΩ.com)	ρ (KΩ.com)	ρ (KΩ.com)	ρ (KΩ.com)	ρ (KΩ.com)	ρ (KΩ.com)
SCC_PH2	1	6.5	12.3	20.1	22.5	26.2	32.0
	2	7.3	14.2	21.6	26.2	30.3	36.2
	3	6.2	12.7	18.2	23.5	27.6	31.1
$CaCl_2$-1_PH2	1	5.2	9.9	15.6	19.0	22.7	26.0
	2	5.2	10.4	16.0	19.6	23.8	27.4
	3	4.9	10.1	14.8	17.9	21.1	24.8
$CaCl_2$-2_PH2	1	6.3	14.1	23.4	26.9	33.8	37.4
	2	7.3	15.7	25.6	28.8	36.7	42.0
	3	7.2	15.5	26.0	29.7	37.6	42.4
$CaCl_2$-4_PH2	1	4.7	8.1	10.6	12.6	15.0	18.6
	2	4.9	8.0	11.2	12.8	16.0	20.3
	3	4.7	8.4	11.5	13.5	16.7	19.0

Table A-30 Ultrasonic pulse velocity (UPV) Measurement Results, Phase 1.

Mix	129 Days	176 Days	207 Days	235 Days	261 Days	286 Days	318 Days	348 Days	378 Days	408 Days	438 Days	468 Days	498 Days	528 Days	561 Days	594 Days
	V_{avg} (m/sec)	V_{avg} (m/sec)	V_{avg} (m/sec)	V_{avg} (m/sec)	V_{avg} (m/sec)	V_{avg} (m/sec)	V_{avg} (m/sec)	V_{avg} (m/sec)	V_{avg} (m/sec)	V_{avg} (m/sec)	V_{avg} (m/sec)	V_{avg} (m/sec)	V_{avg} (m/sec)	V_{avg} (m/sec)	V_{avg} (m/sec)	V_{avg} (m/sec)
SCC_PH1	4294	4520	4495	4412	4255	4171	4109	4146	4134	3977	4229	4176	4196	4291	4309	4225
NaOH-8_PH1 Spec. 1	3837	4098	4109	4052	3904	3886	3768	3914	3480	3691	3671	3864	4099	3934	3946	3957
NaOH-8_PH1 Spec. 2	3944	4062	4070	4033	3888	3814	3732	3835	3516	3723	3684	3864	3886	3916	3916	3924
NaOH-8_PH1 Spec. 3	3799	4109	4102	3998	3901	3916	3828	3859	3493	3649	3660	3797	3842	3906	3881	3874

Table A-31 UPV Measurement Results for NaOH Mixtures on Prisms, Phase 2.

Mix	7 Days	28 Days	60 Days	90 Days	120 Days	150 Days	180 Days
	V_{avg} (m/sec)	V_{avg} (m/sec)	V_{avg} (m/sec)	V_{avg} (m/sec)	V_{avg} (m/sec)	V_{avg} (m/sec)	V_{avg} (m/sec)
NaOH-0_PH2	4470	4548	4467	4359	4383	4463	4495
NaOH-0.2_PH2	4623	4627	4635	4589	4566	4624	4592
NaOH-0.4_PH2	4672	4596	4597	4580	4578	4624	4584
NaOH-0.8_PH2	4669	4569	4615	4606	4622	4642	4622

Table A-32 UPV Measurement Results for $CaCl_2$ Mixtures on Prisms, Phase 2.

Mix	7 Days	28 Days	60 Days	90 Days	120 Days	150 Days	180 Days
	V_{avg} (m/sec)	V_{avg} (m/sec)	V_{avg} (m/sec)	V_{avg} (m/sec)	V_{avg} (m/sec)	V_{avg} (m/sec)	V_{avg} (m/sec)
$CaCl_2$-0_PH2	4343	4510	4401	4565	4521	4636	4554
$CaCl_2$-1_PH2	4349	4344	4239	4389	4421	4436	4393
$CaCl_2$-2_PH2	4296	4362	4163	4363	4444	4451	4414
$CaCl_2$-4_PH2	4167	4290	4150	4244	4337	4394	4332

Table A-33 Schmidt Hammer Test Results for NaOH Specimens, Phase 2.

	15 Days	28 Days	90 Days	180 Days
	Stress (MPa)	Stress (MPa)	Stress (MPa)	Stress (MPa)
NaOH-0_PH2	23.1	29	30.0	25.1
NaOH-0.2_PH2	20.3	28.8	29.3	30.3
NaOH-0.4_PH2	19.2	24.7	28.3	27.7
NaOH-0.8_PH2	17.0	22.1	27.7	26.9

Table A-34 Schmidt Hammer Test Results for $CaCl_2$ Specimens, Phase 2.

	7 Days	28 Days	90 Days	180 Days
	Stress (MPa)	Stress (MPa)	Stress (MPa)	Stress (MPa)
$CaCl_2$-0_PH2	10.4	16.6	26.0	26.4
$CaCl_2$-1_PH2	11.2	17.8	27.2	28.1
$CaCl_2$-2_PH2	12.1	19.5	28.7	30.8
$CaCl_2$-4_PH2	8.9	14.7	23.6	21.1

Table A-35 Crack Widths for $CaCl_2$ Cask.

No.	Crack Width (mm)					
	163 Days	186 Days	225 Days	295 Days	512 Days	569 Days
1	0.2	0.3	0.3	0.3	0.5	0.5
2	0.1	0.1	0.1	0.1	0.1	0.2
3	0.05	0.05	0.05	0.05	0.1	0.1
4	0.1	0.1	0.1	0.1	0.2	0.3
5	0.15	0.15	0.15	0.25	0.4	0.5
6	0.1	0.1	0.1	0.1	0.2	0.2
7	0.05	0.05	0.05	0.1	0.1	0.1
8	0.05	0.1	0.1	0.1	0.2	0.2
9	0.05	0.05	0.05	0.05	0.1	0.1
10	0.15	0.15	0.15	0.2	0.2	0.2
11	0.1	0.1	0.1	0.1	0.3	0.3
12	0.1	0.1	0.1	0.15	0.2	0.2
13	0.1	0.1	0.1	0.1	0.1	0.2
14	0.1	0.1	0.1	0.15	0.3	0.4
15	0.1	0.15	0.15	0.2	1	1
16	0.15	0.15	0.2	0.2	0.4	0.5
17	0.05	0.1	0.1	0.1	0.2	0.2
18	0.1	0.15	0.15	0.2	0.2	0.2
19	0.1	0.1	0.1	0.15	0.5	0.5
20	0.1	0.15	0.15	0.2	0.4	0.5
21	0.1	0.1	0.1	0.2	0.5	0.5
22	0.05	0.1	0.1	0.1	0.2	0.2
23	0.05	0.1	0.1	0.1	0.2	0.2
Mean	0.10	0.12	0.12	0.14	0.29	0.32

Table A-36 Diameter of Rebar in Corrosion Accelerated Cask.

No.	Diameter of Rebar #1 (mm)	Diameter of Rebar #2 (mm)
1	9.3726	9.779
2	9.2964	9.8298
3	9.3218	9.8044
4	9.2964	9.1186
5	9.4488	9.525
6	9.525	9.4996
7	9.4742	9.8298
8	9.4996	9.8298
9	9.2202	9.7536
10	9.144	9.652
11	9.0678	9.4996
12	9.525	9.4488
13	9.4996	9.7536
14	9.1948	9.7282
15	9.2964	9.7536
16	9.144	9.6774
17	9.3472	9.7028
18	9.3726	9.6266
19	9.398	9.5504
20	9.4996	9.779

APPENDIX B
SCALED CASK DESIGN AND FABRICATION DETAILS

B.1. CASK DESIGN AND FABRICATION

B.1.1. Overall Geometry

An elevation view cross section of the model cask is shown in Figure B-1.

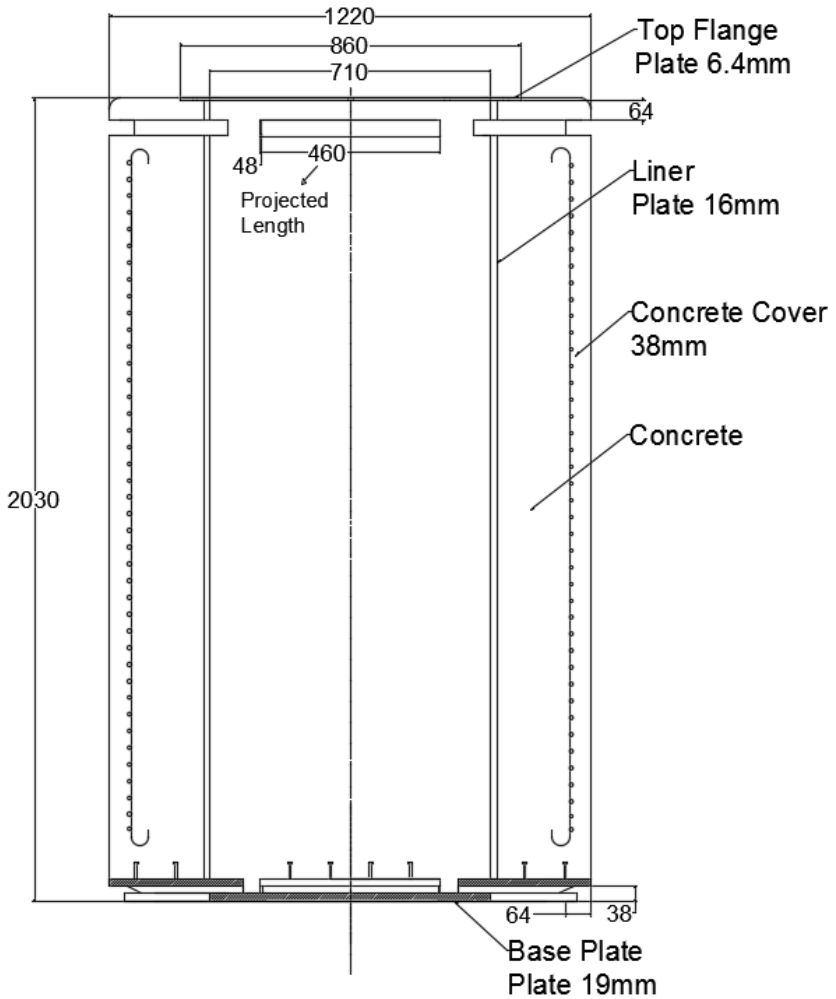

Figure B-1 Concrete elevation view cross section (all dimensions are in mm).

Base plate design includes the air inlet ducts. Since in this project the canister will be not fabricated, the sitting plate for the canister is removed from the model. The quantity and orientation of the nelson studs are similar to existing cask designs. Four alignment guides are installed on top of the air inlets to facilitate placement of the steel tube, which do not exist in the prototype. They are also used as lifting points. As for the studs, H4L, 6.35 X 50.8 mm (mild steel) was used, which is one of standard products of Nelson. The base plate assembly is shown in Figure B-2.

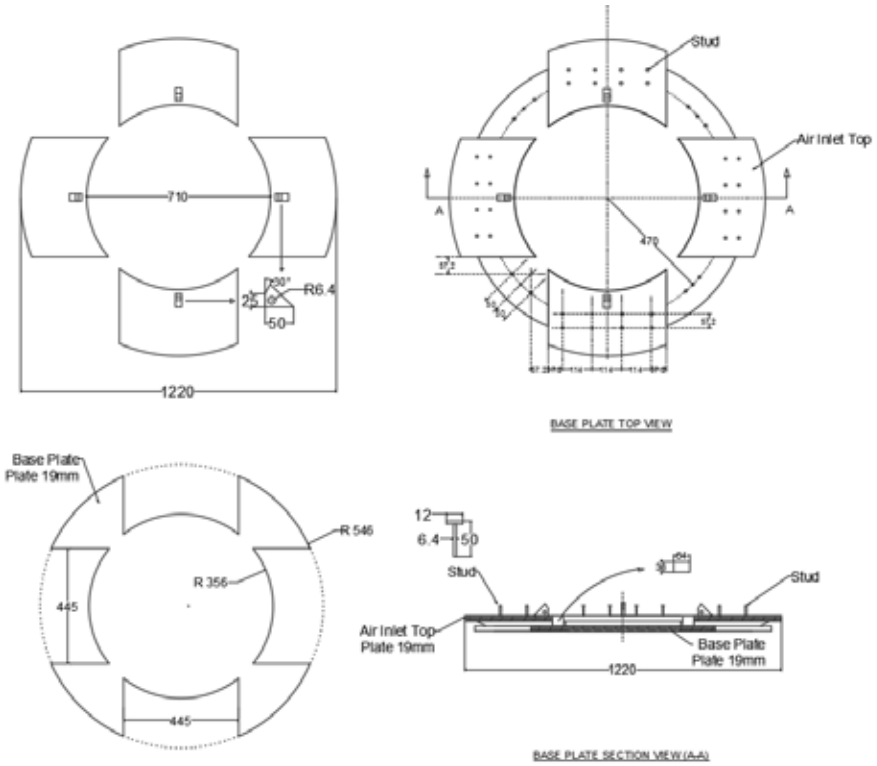

Figure B-2 Base plate configuration (dimensions are in mm).

The lid is made of a circular steel plate and a steel basket filled with concrete. The hole diameter is 15.8 mm, which is suitable for a 12.7 mm threaded rod. The baskets are filled with concrete on the day of casting and they are welded to the circular plates. The lid assembly is shown in Figure B-3.

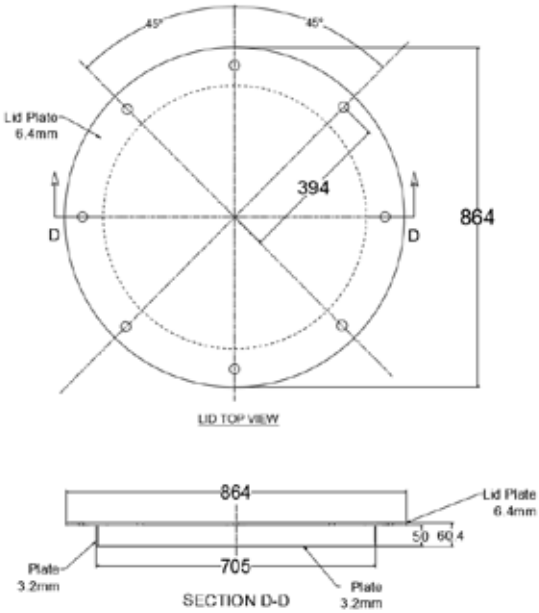

Figure B-3 Lid assembly (dimensions are in mm).

B.1.2. Flanges

To secure the lid to the flange, threaded rods and nuts are used (see Figure B-4). Eight holes are drilled into the flange and concrete having a depth of 50.8 mm, high strength threaded rods are inserted into the holes, and the threaded anchors are fixed in place by high strength expansive grout. The flange plan view is shown in Figure B-5.

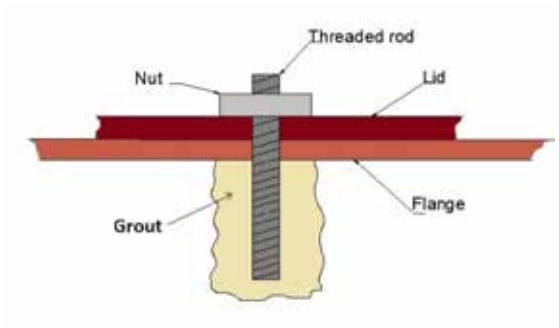

Figure B-4 Nut and threaded rod configuration.

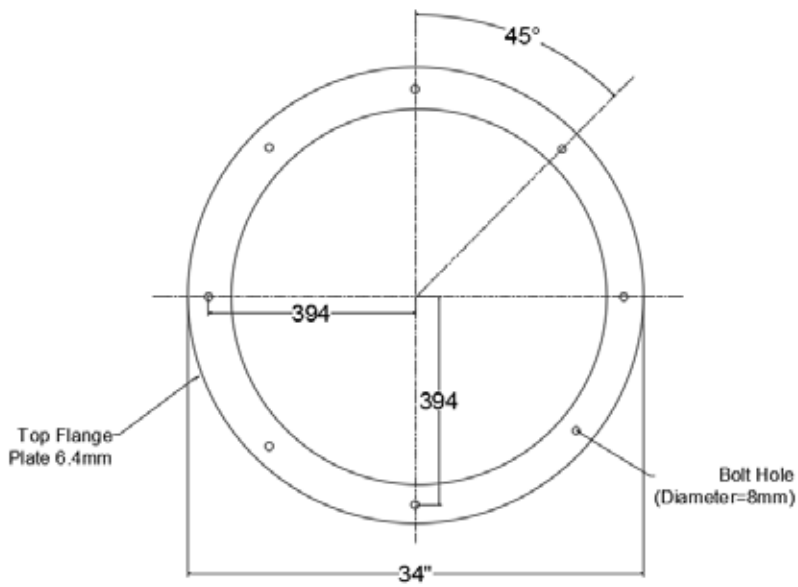

Figure B-5 Flange (dimensions are in mm).

B.1.3. Air Channels

Four sets of outlet channels are made from 3.18 mm plate for each cask. The drawings of the air channels is provided in Figure B-6.

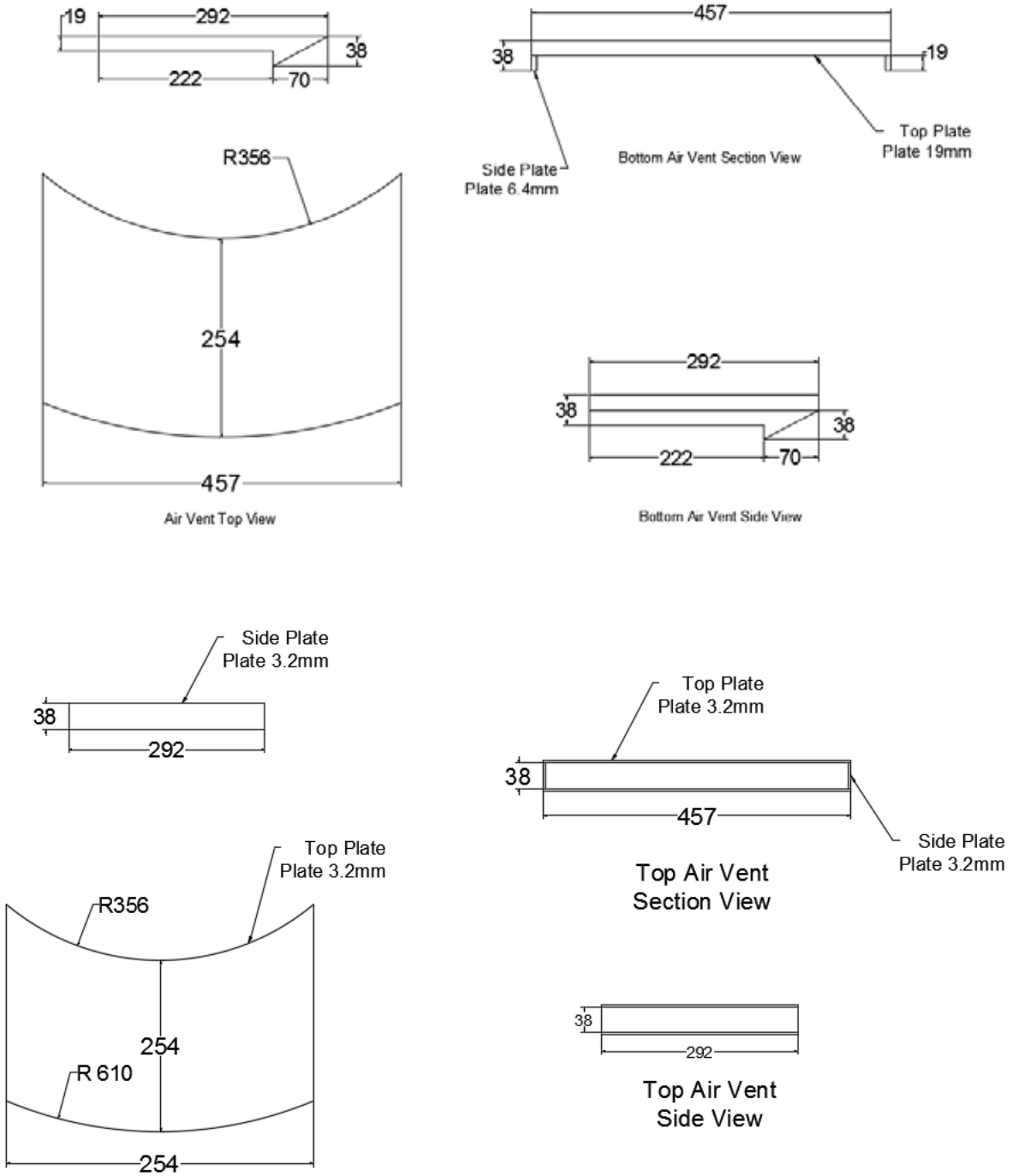

Figure B-6 Air inlet and outlet channels (dimensions are in mm).

Two sets of lift anchors are fabricated for each cask. The capacity of the anchors are checked to support the dead weight of the model. The lift anchor dimensions are provided in Figure B-7.

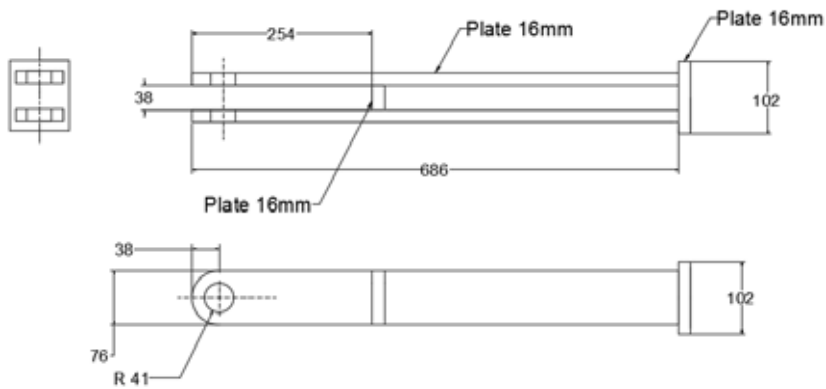

Figure B-7 Lift anchors (dimensions are in mm).

In the original design, outer surface of the liner is not completely coated due to presence of the thick concrete layer, which protects steel surface from corrosion. However, in the scaled model owing to presence of corrosive chemicals in one of the mixtures, corrosion could initiate immediately after concrete placement. Therefore, to protect the outer surfaces of the steel liners and to better represent the degradation mechanisms in real casks, all of the surfaces of the steel parts were coated. DIMETCOTE 9 (PPG Industries, Inc., 2016) is a commercial brand of inorganic zinc silicate primer made by PPG Protective & Marine Coatings. This type of coating provides effective corrosion and abrasion resistance at temperatures up to 400°C. All exposed surfaces of the steel parts are coated with this product before being shipped to University of Houston Structural Testing Laboratory. Figure Figure B-8 shows the steel components prior to the coating.

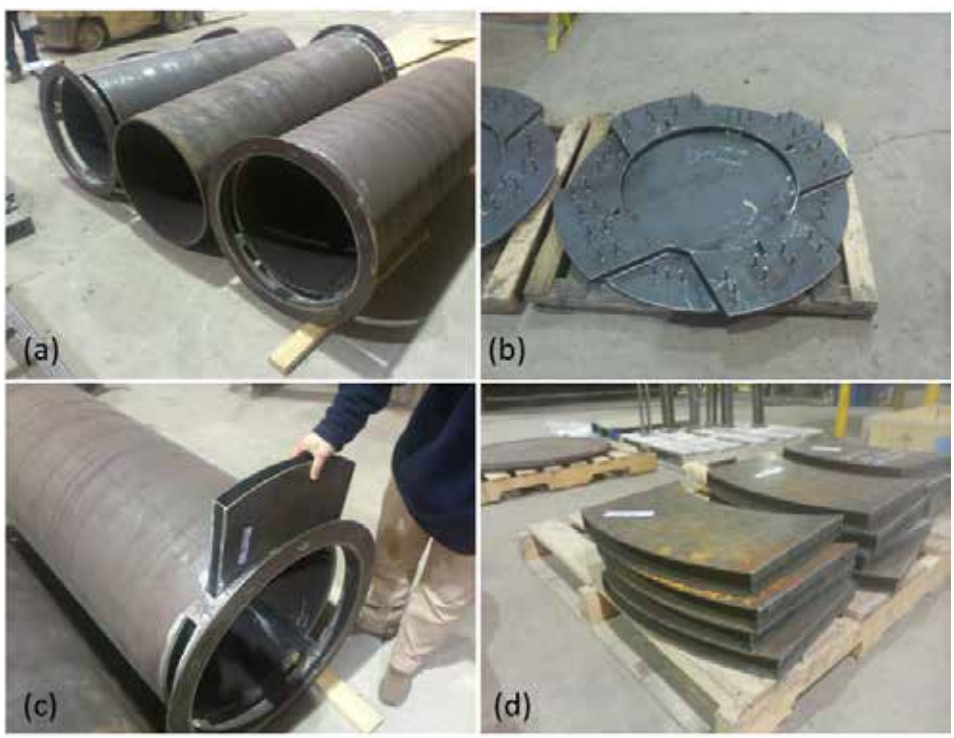

Figure B-8 Fabricated Steel parts (a) liner, (b) base, (c) and (d) air vent.

General design and dimensions of the canister is shown in Figure B-9. After welding a disc to enclose one side of the pipe, the rods were placed inside the canister.

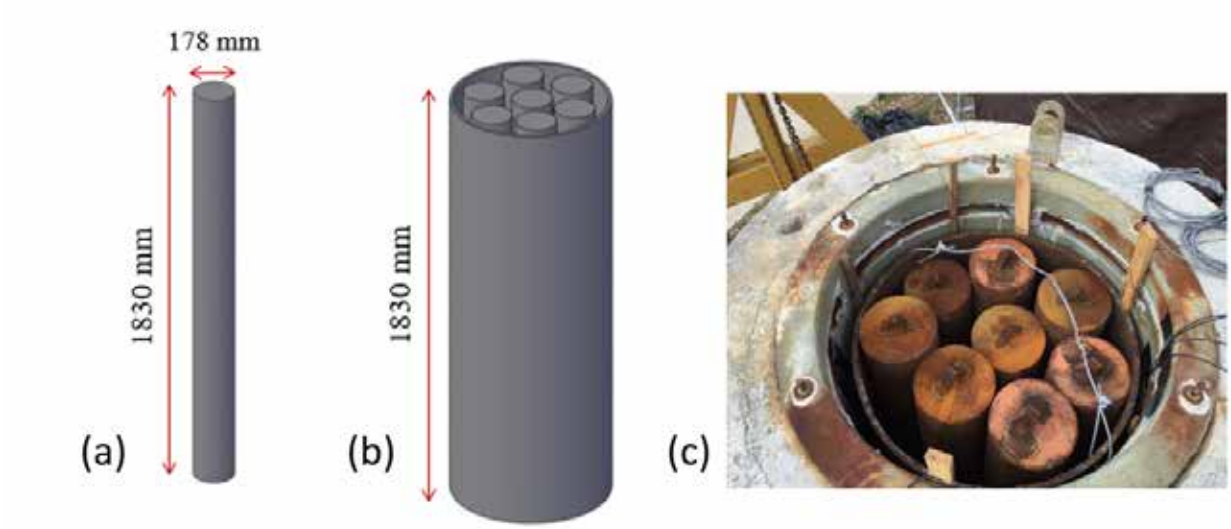

Figure B-9 Model configuration, (a) steel rod, (b) canister, (c) cask loaded with the basket.

In addition, to determine the material properties of the steel used in fabricating the casks, tension coupons were obtained from the steel supplier (see Figure B-10). From each steel batch, three steel coupons were prepared in accordance with ASTM E8/E8M (2016).

Figure B-10 Dogbone shaped steel coupons prepared for tension tests.

Detailed quantity, spacing and steel reinforcement area were calculated based on the specified scaling factor. Figure B-11 and Figure B-12 below show the reinforcement layout for the model casks.

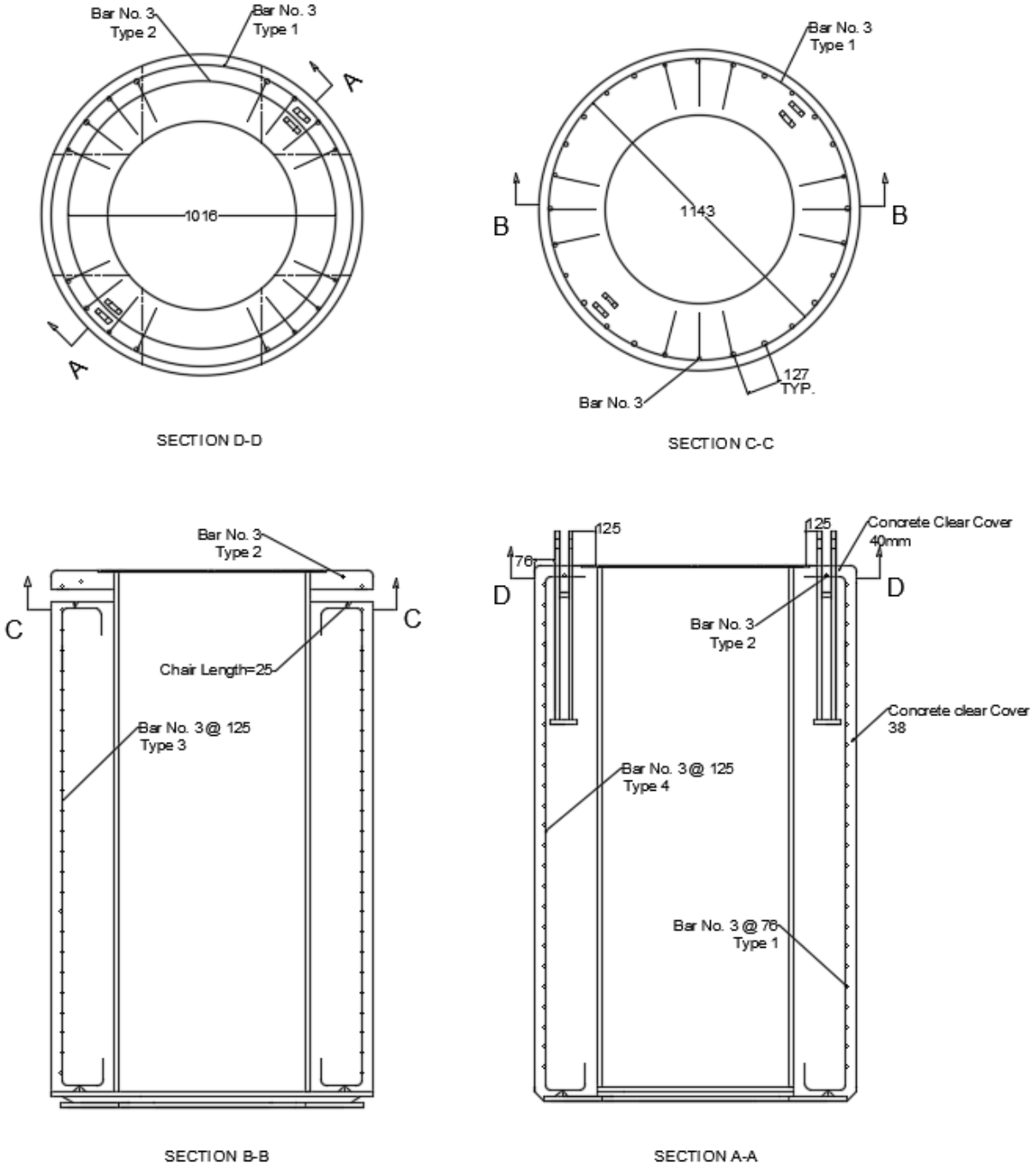

Figure B-11 Reinforcement layouts for the model casks (dimensions are in mm).

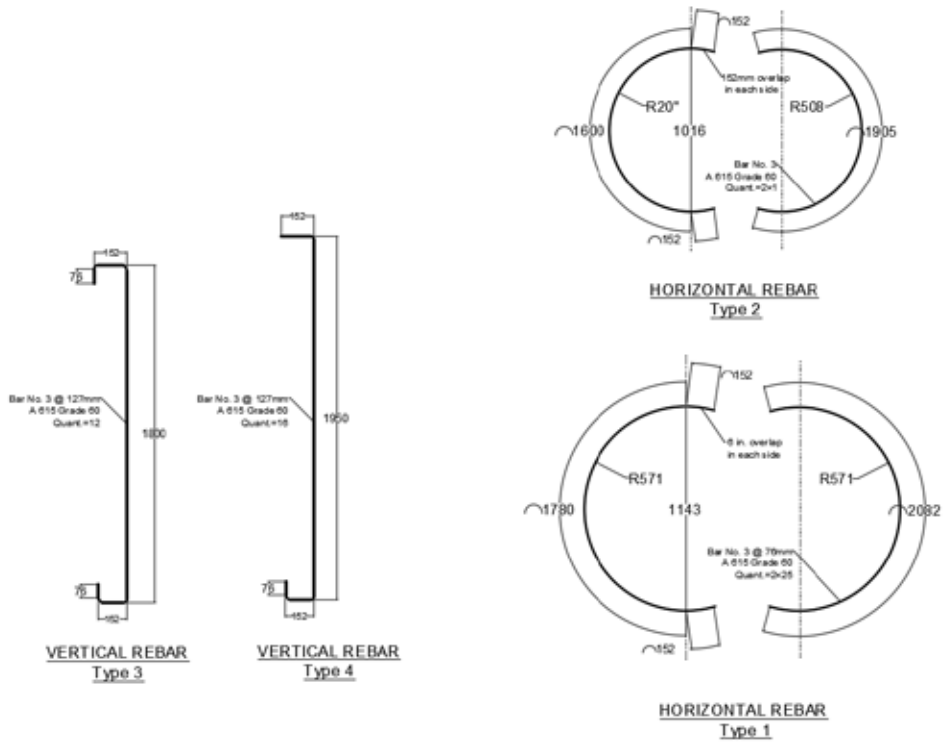

Figure B-12 Reinforcement layouts for the model casks (dimensions are in mm).

Reinforcement pieces were fabricated at the precast concrete facilities and shipped to the University of Houston Structural Research Laboratory. They were fixed in place around the steel liner tubes in the laboratory. Some extra steel pieces from the same batch were also provided for the further material tests. Figure B-13 shows the positioned reinforcement cages. Plastic spacers were used to ensure that proper cover concrete is provided to rebar. Cardboard tubes, specially produced for concrete casting were procured and used as formwork (see Figure B-14). Bolt holes and seams were covered with duct tape.

Figure B-13 Positioned reinforcement cages.

Figure B-14 Fixing the formworks in place and preparing for concrete pouring.

The casting was performed on Wednesday, July 30, 2014 with the help of concrete contractor (see Figure B-15). For each concrete mixture, first casks were poured and then material test specimens (cubes, cylinders, etc.) were filled and compacted. After pouring the casks, top of the formwork was sealed with plywood and plastic sheet to prevent rapid loss of moisture.

Figure B-15 Concrete pouring.

About a month after casting the cardboards formworks were removed and currently the non-destructive testing initiated to monitor degradation due to aging (see Figure B-16).

Figure B-16 Fabricated casks located in University of Houston testing lab.

B.2. SLAB DESIGN AND FABRICATION

SAFE software (SAFE, 2000) was used for design of the concrete pad. In the first attempt, the thickness of the slab was considered 0.381 m. However, a large area on the impact side did not satisfy the shear and flexural demand. Thus, the thickness of the slab was increased to 0.61 m. In the model, seven horizontal strips and 16 vertical strips were considered. Note that the computational modeling was performed using U.S. Customary Units. Therefore, conversion factors are provided for the outputs. A linear loading was applied on the impact area according to the tip over simulations as shown in Figure B-17 and Figure B-18.

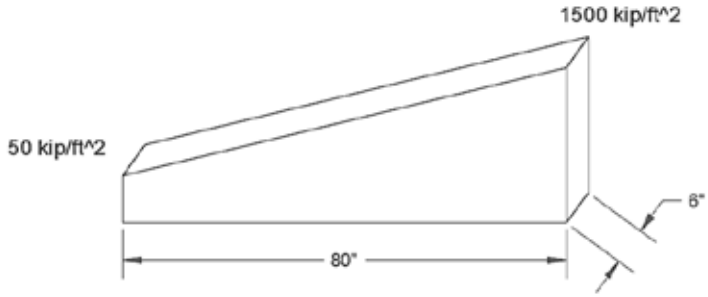

Figure B-17 Applied linear impact load for design of the pad.

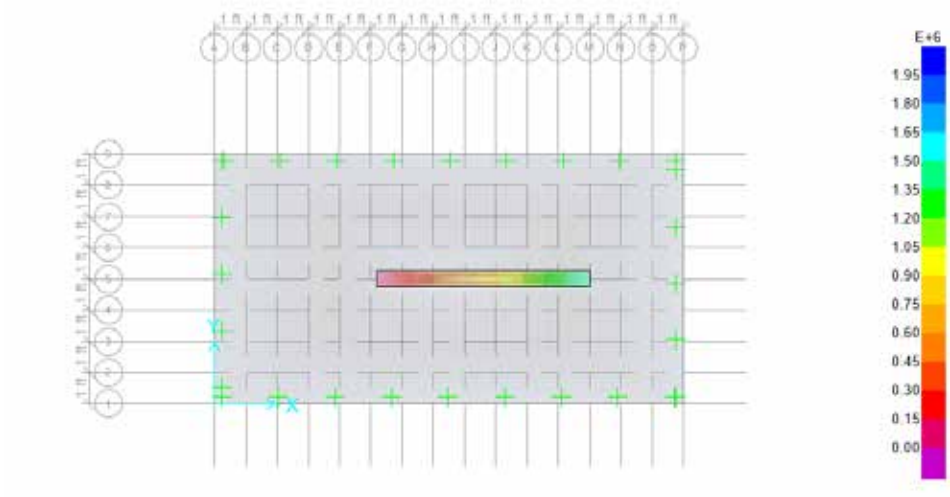

Figure B-18 Pad loading $(1\frac{kip}{ft^2} = 49.44\frac{kN}{m^2})$**.**

Qualitative distribution of moment along X- and Y- directions are shown in Figure B-19 and Figure B-20, respectively.

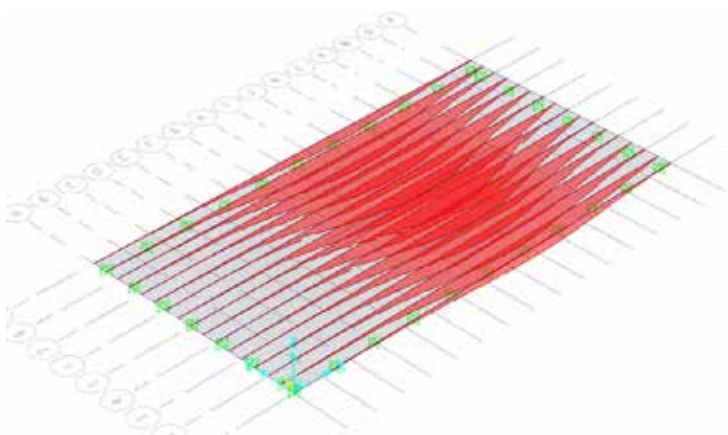

Figure B-19 Moment diagram along X direction.

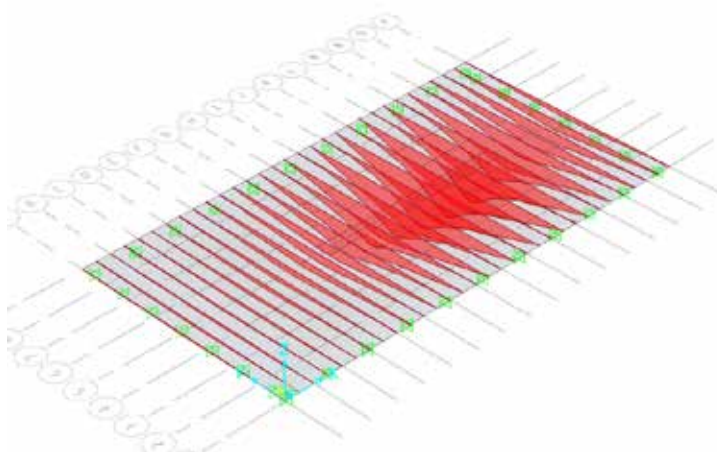

Figure B-20 Moment diagram along Y direction.

Maximum moment along X direction calculated by software was 496.6 kN.m at the middle of the pad. Reinforcement needed along X and Y direction for bottom layer due to flexure are shown in Figure B-21 and Figure B-22, respectively.

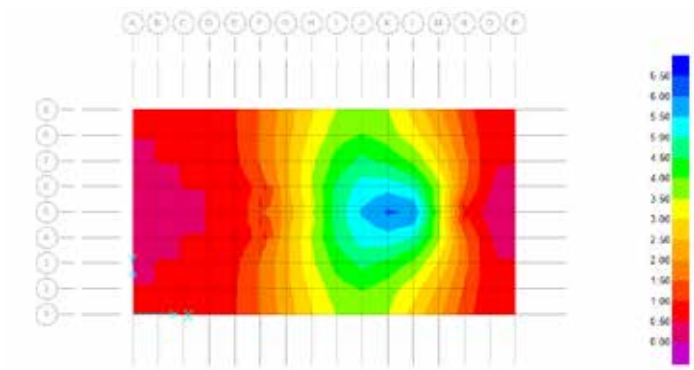

Figure B-21 Reinforcement distribution for flexure along X axis $(1\ in^2 = 645.15\ mm^2)$.

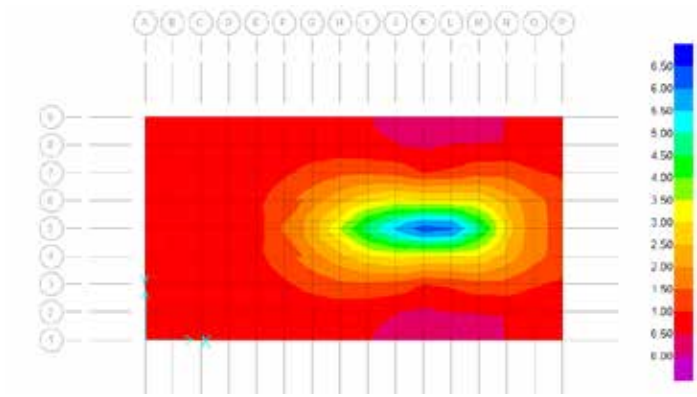

Figure B-22 Reinforcement distribution for flexure along Y axis $(1\ in^2 = 645.15\ mm^2)$.

Table B-1 shows the specification of the pad. Flexural and shear reinforcement detailing are shown in Figure B-24 and Figure B-25.

Table B-1 General Specification of the Pad.

Variable	Symbol	Value
Footing Width (m)	B	2.44
Footing Length (m)	L	4.57
Footing Thickness (m)	t	0.609
Footing Area (m^2)	A	11.15
Effective Depth (m)	d	0.58
Footing Volume (m^3)	V	7.08
Concrete Density (kg/m^3)	ρ	2400
Footing Weight (kg)	W	16994
Compressive Strength (MPa)	f'_c	27.6
Yield Strength of Reinforcement (MPa)	f_y	413.7

As shown in the Figure B-23 four lifting hooks were considered on top of the pad for lifting. The anchor rods were placed symmetrically as shown in Figure B-23. Due to the high cost of fabrication, the pad was highly reinforced (Figure B-24, Figure B-25 and Figure B-26) and the compressive strength increased to minimum 38 MPa in order to reduce the risk of damage to the pad under multiple tip over tests.

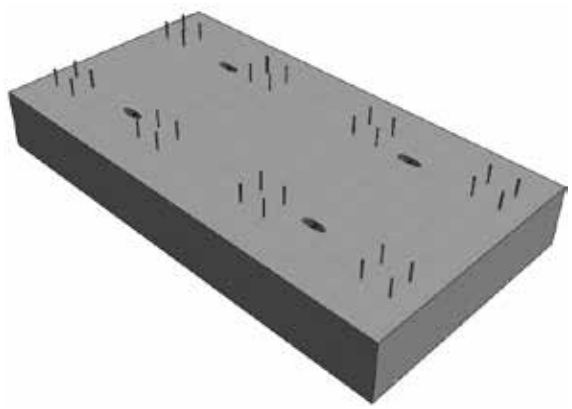

Figure B-23 Isometric view of the concrete pad.

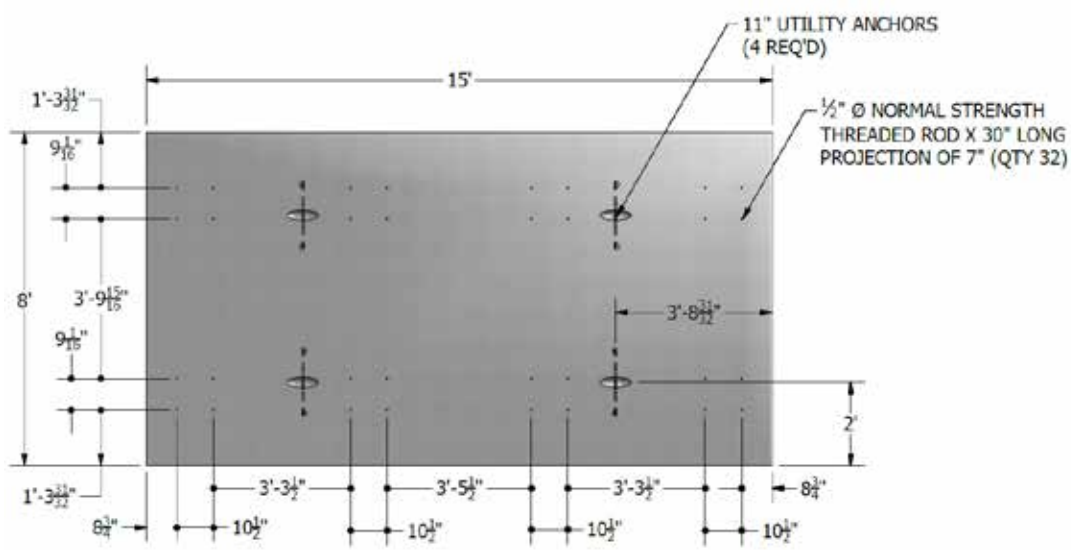

Figure B-24 Plan view of the pad (1 ft = 0.3048 m, 1 in = 0.0254 m).

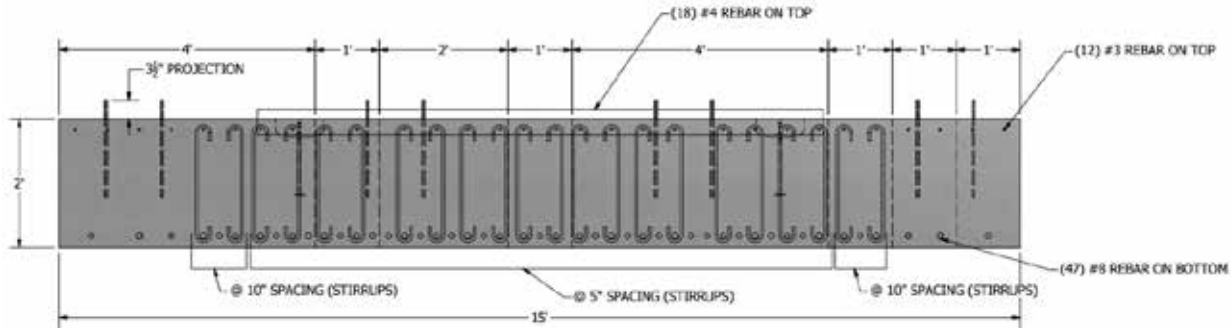

Figure B-25 Cross section of the pad along long side (1 ft = 0.3048 m, 1 in = 0.0254 m).

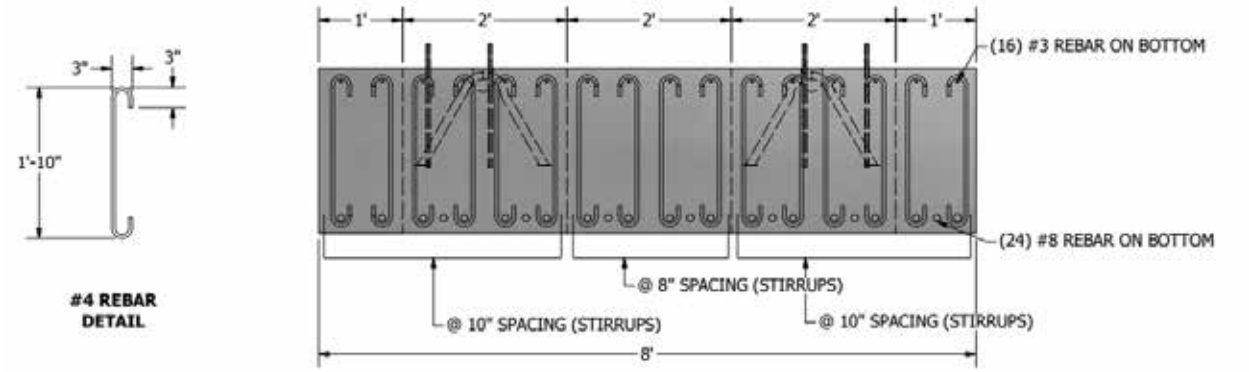

Figure B-26 Cross section of the pad along short side (1 ft = 0.3048 m, 1 in = 0.0254 m).

For more structural integrity in the pad, it was decided to place the reinforcement uniformly in both directions (Figure B-27(a)). Due to the high density of the reinforcement it was decided to use a high strength SCC mixture for the pad (Figure B-27(b)). As shown in the

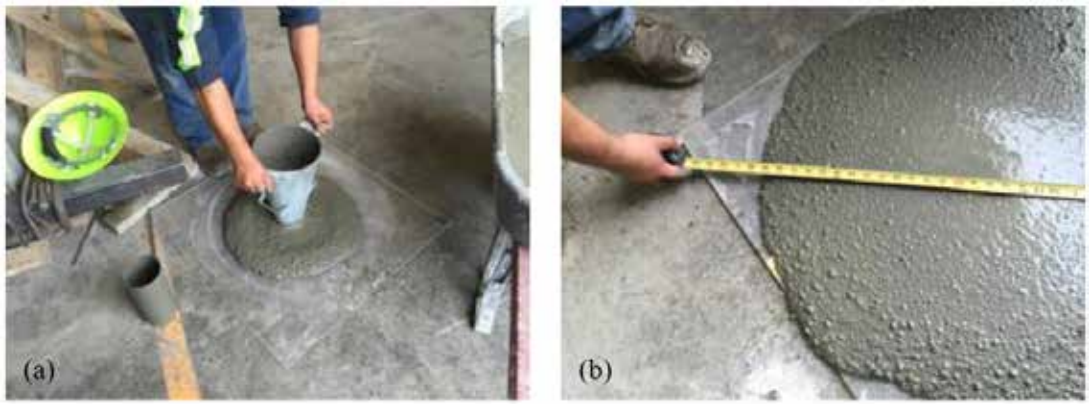

Figure B-28 the slump of the mixture was about 730 mm. Thus compaction of the concrete with vibrator was not necessary (see Figure B-28). On August 2015, and after curing, it was shipped to the University of Houston Structural Laboratory.

Figure B-27 (a) Mold and reinforcement of the pad (b) pouring self-consolidating concrete.

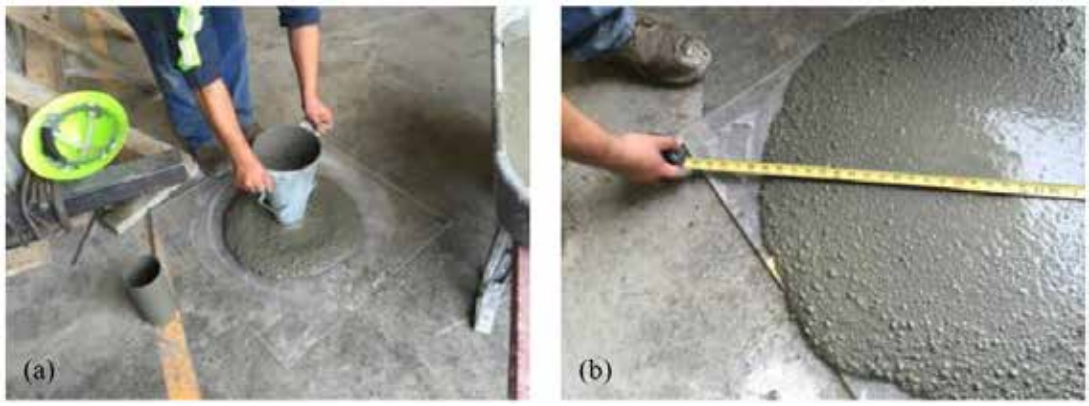

Figure B-28 Measuring the slump flow (ASTM, 2009) for the concrete (a) lifting the slump cone (b) diameter measurement (965mm).

Several $100 \times 100 \times 200$ mm prisms and 100×200 mm cylinder specimens prepared to measure mechanical properties of concrete as shown in Figure B-29. The compression and split tensile test were performed at 7 days and 28 days after the casting. The compressive strength of the concrete was designed to be around 38 MPa. The strength resulted from the compression test at the University lab was between 35 to 40 MPa. The results of split tensile and compression tests were used for the finite element modeling and to check the integrity of the concrete.

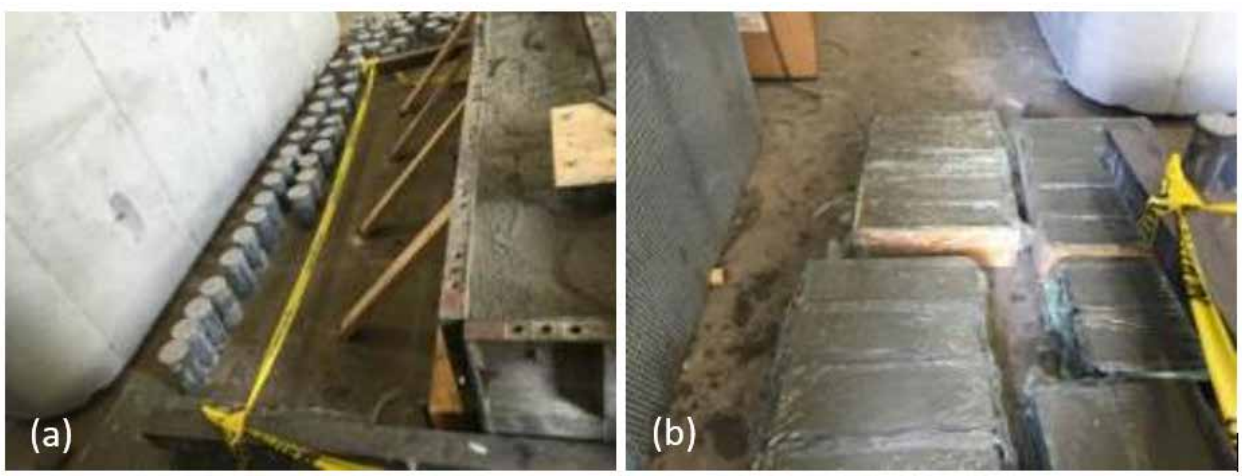

Figure B-29 Prism and cylinder specimens (a) cylinders (b) prisms.

In order to guide the cask during the impact and to prevent rolling after impact, a retaining frame was designed (see Figure B-30 through Figure B-33). The frame is made of HSS 5 x 5 x 1/2 with 317 MPa yield strength. The steel frame for supporting the cask during the test was fabricated and delivered to University of Houston, Structural Engineering Research Laboratory.

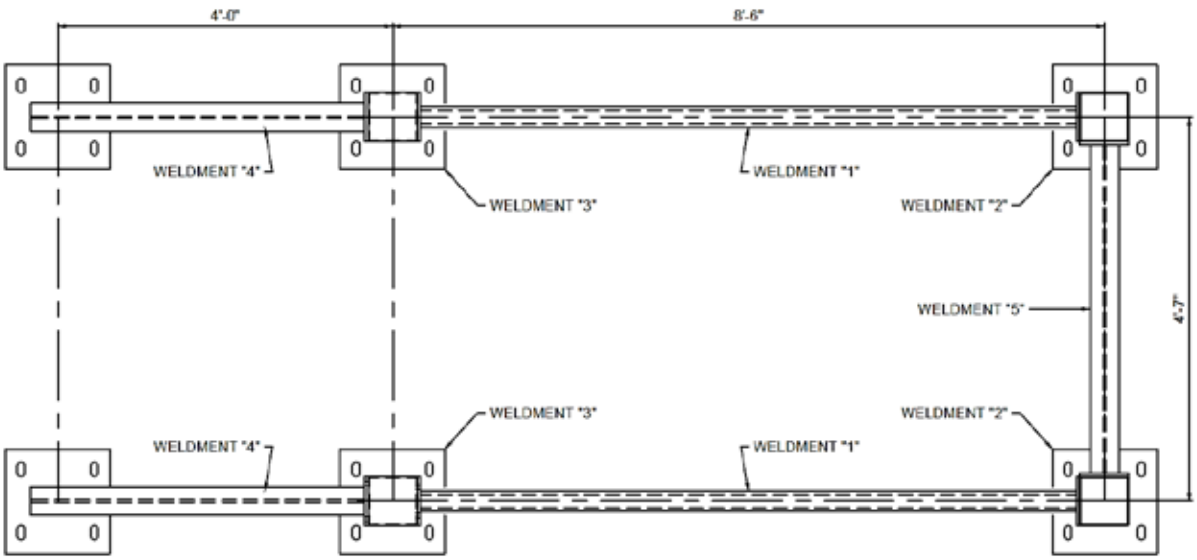

Figure B-30 Plan view of engineering drawings for the frame (1 ft = 0.3048 m, 1 in = 0.0254 m).

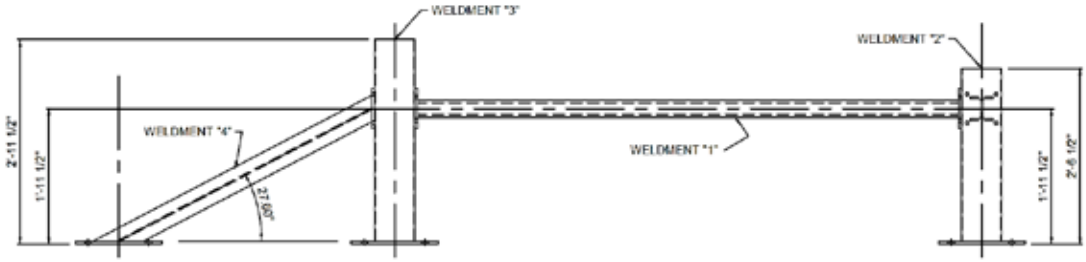

Figure B-31 Elevation view of engineering drawings for the frame (1 ft = 0.3048 m, 1 in = 0.0254 m).

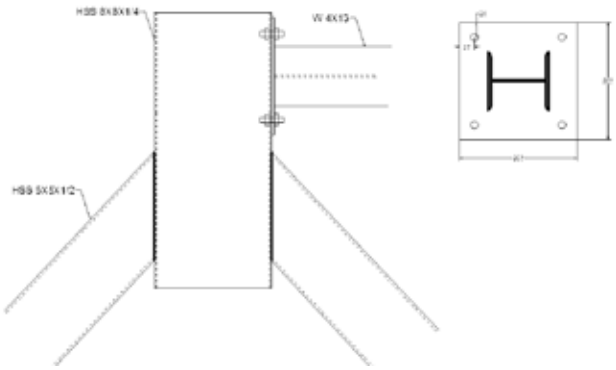

Figure B-32 Connection details, Parts 1 and 2 (all dimensions are in mm).

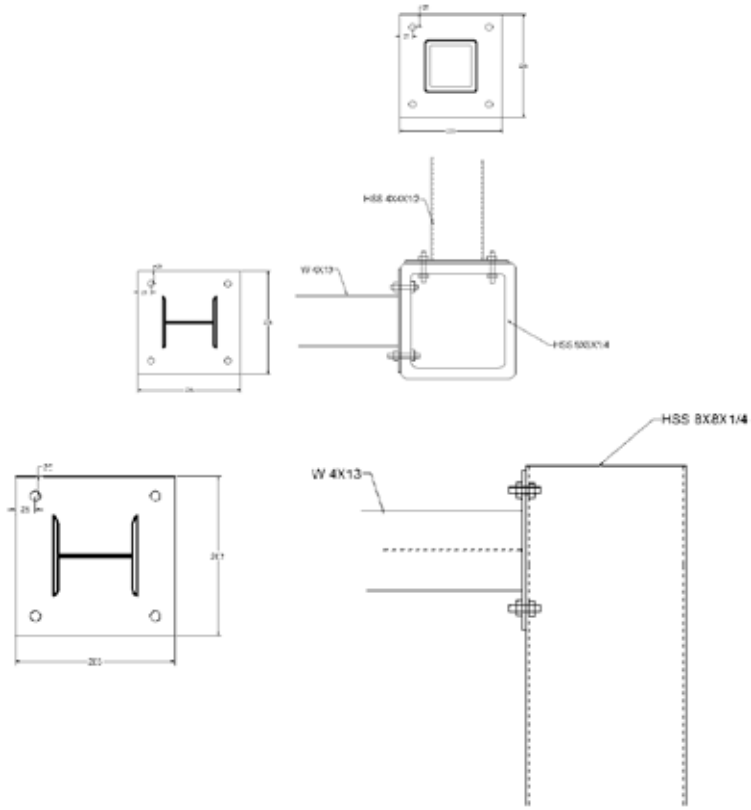

Figure B-33 Connection details, Parts 3 and 4 (all dimensions are in mm)

A 2700 × 4900 mm hole with 900 mm depth was excavated as shown in

Figure B-34 for placement of the pad. The composition of the soil in Houston mostly consists of silt and clay which has low bearing capacity. Therefore, there was a concern about non-uniform settlement of the pad especially after the first impact test. To address this issue, bottom of the hole was covered with 180 mm large gravel to increase the stiffness of the subgrade and minimize the settlement due to the weight of the structure and the impact load. Several bags of cements mixed with gravel to increase the integrity of the subgrade. Then the guard frame and the gantry crane installed on the pad. By placement of the SCC cask, the system was ready for the first end drop test (Figure B-35).

Figure B-34 (a) Excavated site for the pad, (b) twenty-five tons forklift used for placement of the pad

Figure B-35 Configuration of the test setup for end drop and tip over test

B.3. CANISTER FABRICATION

Eight steel rods with 180 mm diameter were used to fill the canister as simulated spent nuclear fuel. The general design and dimensions of the canister is shown in Figure B-36. A steel tube with 710 mm diameter and a disc welded to the bottom is used as the canister. Two holes were drilled on the sides closer to the top for lifting purpose. The rods were inserted into the canister and the whole package was placed inside the SCC cask for the first test. No significant damage and deformation was observed to the canister after the tip-over test therefore, the same package was used for all three specimens.

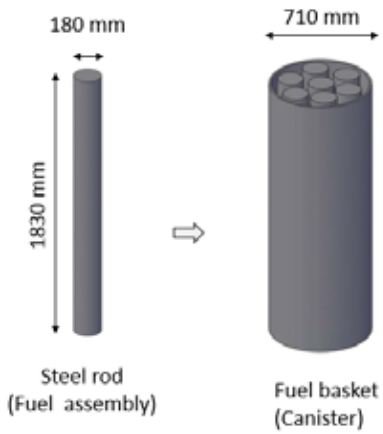

Figure B-36 General design and dimensions of the canister

Weight of each rod is about 360 kg and the weight of the basket itself is about 450 kg. Considering 8 bars inside the basket, the total weight of the canister is 3,260 kg. The fabrication of the canister is shown in Figure B-37.

Figure B-37 Canister fabrication (a) steel rod (b) cutting to 1830 mm pieces (c) steel tube (canister) (d) simulated spent fuel package placed into the cask.

B.4. REFERENCES

ASTM. (2009). Standard Test Method for Slump Flow of Self-Consolidating Concrete. West Conshohocken, PA: American Society of Testing and Materials Academic & Science (ASTM).

ASTM E8 / E8M-16a. (2016). Standard Test Methods for Tension Testing of Metallic Materials. West Conshohocken, PA.

CSI SAFE (2016). DESIGN OF SLABS, BEAMS AND FOUNDATIONIS REINFORCED AND POST-TENSIONED CONCRETE COMPUTERS & STRUCTURES.

PPG INDUSTRIES INC. "Steel Caoting Supplier." Accessed on 26 Dec. 2016. Available from: http://www.ppgpmc.com/Products/P108/DIMETCOTE-9-VOC.aspx.